ASME
SETTING THE STANDARD
1880 2005

Transactions of the ASME, Journal of Turbomachinery (ISSN 0889-504X) is published quarterly (Jan., Apr., July, Oct.) by The American Society of Mechanical Engineers, Three Park Avenue, New York, NY 10016. Periodicals postage paid at New York, NY and additional mailing offices. POSTMASTER: Send address changes to Transactions of the ASME, Journal of Turbomachinery, c/o THE AMERICAN SOCIETY OF MECHANICAL ENGINEERS, 22 Law Drive, Box 2300, Fairfield, NJ 07007-2300. **CHANGES OF ADDRESS** must be received at Society headquarters seven weeks before they are to be effective. Please send old label and new address. **STATEMENT from By-Laws.** The Society shall not be responsible for statements or opinions advanced in papers or ... printed in its publications (B7.1, Par. 3).

Journal of Turbomachinery

Published Quarterly by ASME

VOLUME 128 • NUMBER 1 • JANUARY 2006

TECHNICAL PAPERS

(Contents continued on inside back cover)

This journal is printed on acid-free paper, which exceeds the ANSI Z39.48-1992 specification for permanence of paper and library materials. ♾™
♻ 85% recycled content, including 10% post-consumer fibers.

Journal of Turbomachinery Volume 128, Number 1 JANUARY 2006

TECHNICAL BRIEF

ERRATA

The ASME Journal of Turbomachinery is abstracted and indexed in the following:

Aluminum Industry Abstracts, Aquatic Science and Fisheries Abstracts, Ceramics Abstracts, Chemical Abstracts, Civil Engineering Abstracts, Compendex (The electronic equivalent of Engineering Index), Corrosion Abstracts, Current Contents, Ei EncompassLit, Electronics & Communications Abstracts, Energy Information Abstracts, Engineered Materials Abstracts, Engineering Index, Environmental Science and Pollution Management, Excerpta Medica, Fluidex, Fuel and Energy Abstracts, INSPEC, Index to Scientific Reviews, Materials Science Citation Index, Mechanical & Transportation Engineering Abstracts, Mechanical Engineering Abstracts, METADEX (The electronic equivalent of Metals Abstracts and Alloys Index), Metals Abstracts, Oceanic Abstracts, Pollution Abstracts, Referativnyi Zhurnal, Shock & Vibration Digest, Steels Alert

A Unified Correlation for Slip Factor in Centrifugal Impellers

Theodor W. von Backström
Department of Mechanical Engineering,
University of Stellenbosch,
Private Bag X1,
Matieland 7602, South Africa

A method that unifies the trusted centrifugal impeller slip factor prediction methods of Busemann, Stodola, Stanitz, Wiesner, Eck, and Csanady in one equation is presented. The simple analytical method derives the slip velocity in terms of a single relative eddy (SRE) centered on the rotor axis instead of the usual multiple (one per blade passage) eddies. It proposes blade solidity (blade length divided by spacing at rotor exit) as the prime variable determining slip. Comparisons with the analytical solution of Busemann and with tried and trusted methods and measured data show that the SRE method is a feasible replacement for the well-known Wiesner prediction method: it is not a mere curve fit, but is based on a fluid dynamic model; it is inherently sensitive to impeller inner-to-outer radius ratio and does not need a separate calculation to find a critical radius ratio; and it contains a constant, F_0, that may be adjusted for specifically constructed families of impellers to improve the accuracy of the prediction. Since many of the other factors that contribute to slip are also dependent on solidity, it is recommended that radial turbomachinery investigators and designers investigate the use of solidity to correlate slip factor. [DOI: 10.1115/1.2101853]

Introduction

The rate at which fans, compressors, and pumps do flow work is less than that calculated with the assumption that the relative flow at the exit of a rotor follows the blade trailing edges. The angular momentum imparted to the flow is reduced by a factor known as the slip factor in radial flow machines.

Despite the recent advances in computational fluid dynamics, engineers and students still need a reliable method for first estimates of the slip factor in centrifugal impellers. Such a method should be direct (no iteration or conditional procedures), have a sound fluid dynamic basis, be widely applicable in terms of basic impeller geometry such as blade number, blade angle, and impeller radius ratio, and be relatively accurate.

Background

The main mechanism usually considered when predicting the slip factor in radial flow machines is the so-called relative eddy. This is an inviscid flow effect. A fluid element entering a radial flow impeller does not rotate around its own axis with an angular velocity equal to that of the rotor, but moves around the machine axis while maintaining a constant orientation relative to the machine casing. Relative to the rotor, however, the fluid element rotates at an angular velocity equal but opposite to the angular velocity of the rotor. The relative vorticity of the flow entering the rotor will set up a recirculating flow pattern relative to the rotor. In centrifugal impellers it affects the primary flow by causing underturning across the rotor exit plane.

Other mechanisms that cause slip are the relaxation of the cross passage pressure gradient near the blade trailing edges and the unequal boundary layer displacement thicknesses on the pressure and suction sides of the blades. The thicker boundary layers associated with lower Reynolds numbers enhances this effect. The existence of a wake region in the passages of radial flow machines may also play a part, as may hub and shroud drag and tip leakage flow. The wake develops in the suction side shroud corner of the flow passage, as the pressure gradients associated with the flow turning from axial to radial, and the Coriolis force turns low momentum fluid in the boundary layers more than the main flow. At lower Reynolds numbers, the thicker boundary layers will result in larger wakes. Concerning Mach number, Stanitz (in the discussion attached to Wiesner [1]) reported that his results showed only a small effect up to tip Mach numbers of 2.0.

Directly, or by implication, textbooks generally treat the relative eddy as the major factor causing slip in radial flow turbomachines, for example, Stodola [2], Eckert and Schnell [3], Ferguson [4], Wislicenus [5], Osborne [6], Eck [7], Dixon [8], Watson and Janota [9], Cumpsty [10], Logan [11], Johnson [12], Wilson and Korakianitis [13], Aungier [14], and Saravanamuttoo et al. [15]. At least, they generally do not attempt to model the other contributing factors. Dean and Young [16] and Japikse and Baines [17] do, however, consider the effect of the wake region in the blade passage, but jet-wake models still require a slip factor correlation in the jet flow region where viscous effects do not dominate.

Stodola [2] presented a simplified and popular approximate derivation followed by many textbooks. He inserted a circular-shaped control volume between the blades, near the outer radius of the rotor. The circle touches the suction side trailing edge of one blade and is tangent to the pressure surface of its neighbor. For a rotor with exit radius r_e and number of blades, Z, the blade spacing is $2\pi r_e/Z$, the eddy diameter is $2e=(2\pi r_e/Z)\cos\beta$, with β the blade exit angle, measured from the radial direction. Stodola assumed the slip velocity caused by the relative eddy to be equal in magnitude to the speed of rotation of the eddy at its rim: $\Delta w = \Omega e = \pi\Omega r_e(\cos\beta)/Z = \pi U_e(\cos\beta)/Z$. A recent example of such an approach is the paper of Paeng and Chung [18]. The present study was started because the assumption that the eddy rim velocity Δw may be applied along the rotor perimeter (the edge of another control volume) as the so-called slip velocity was difficult to justify, especially in a teaching situation.

Busemann [19] proposed a remarkable slip factor prediction method that was sensitive to the blade radius ratio. The blade radius ratio is the radial distance of the blade leading edge from the axis divided by that of the blade trailing edge. He analytically solved the inviscid flow field through a series of two-dimensional impellers with logarithmic spiral blades. He generated maps of slip factor versus the impeller radius ratio, with the blade number as a parameter, for various blade sweep angles for logarithmic spiral blades. Wislicenus [5] and Wiesner [1] reproduced these maps (for example, Fig. 3). The Busemann maps indicated that slip factor depends on RR, but below a critical value of RR it is relatively constant. The popular method of Wiesner [1] was de-

Contributed by the Computational Fluid Dynamics Committee of ASME for publication in the JOURNAL OF TURBOMACHINERY. Manuscript received April 1, 2004; final manuscript received August 10, 2005. Review conducted by M. Casey.

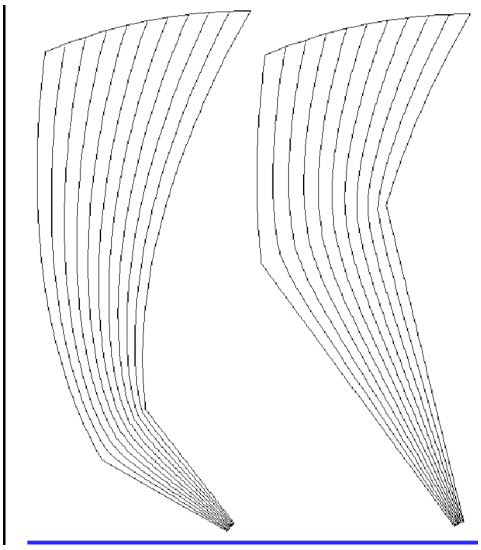

Fig. 1 Control volumes and streamlines for nonrotating low and high radius ratio impellers

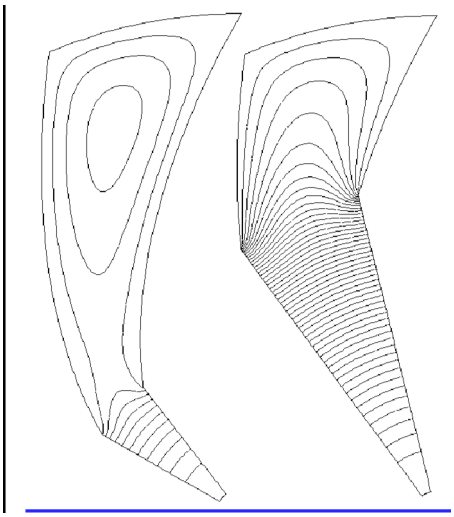

Fig. 2 Control volumes and relative-eddy-induced streamlines for low and high radius ratio impellers

signed to fit the Busemann data in the range where RR has virtually no influence, and includes an empirical correction for the effect of the blade radius ratio on the slip factor, once the critical value is exceeded.

Objectives

The overall objective of this paper is to formulate a simple, approximate but relatively accurate approach to predict eddy-induced slip factor in centrifugal impellers. Specific objectives are as follows:

(1) To propose a suitable control volume for the calculation of a relative-eddy-induced slip factor.
(2) To propose an appropriate relative-eddy-induced flow pattern.
(3) To propose a model for the calculation of the magnitude of the recirculating flow caused by the relative eddy.
(4) To present a new, generally applicable relationship for the slip factor.
(5) To compare the derived relationship to other, commonly used relationships and to experimental data.

The Single Relative-Eddy Method

The approach presented below follows, in principle, from that of Stodola [2], who assumed one relative eddy per blade passage, but it is applied here with the new assumption of a single eddy in the rotor. The detailed assumptions are as follows:

(1) Two-dimensional (2D) flow in a plane perpendicular to the axis.
(2) Logarithmic spiral rotor blades.
(3) The 2D control volume consists of a curved sector bounded by five lines: two logarithmic spirals representing adjacent blades, two radial lines between the blade leading edges and the axis, and by the rotor perimeter between the trailing edges (Fig. 1).
(4) The flow consists of the fixed-rotor flow pattern for flow through the stationary rotor and, superimposed on it, the relative-eddy flow.
(5) The fixed-rotor flow consists of the flow that would occur if the rotor does not rotate, i.e., a radial flow upstream of the rotor and a flow following the blades in the region between them (Fig. 1 is a very rough representation of such a flow).
(6) The throughflow upstream of the rotor blade leading edges has no rotation in the absolute frame, but its radial component is assumed to be proportional to the radius, to ensure a logarithmic spiral flow pattern upstream of the rotor, once the forced vortex relative-eddy-induced flow pattern is added. (This flow pattern is achieved in practice when flow enters the rotor axially.)
(7) The flow induced by the relative eddy causes no throughflow, and, in agreement with Stodola [2] is shown as if the rotor exit area is closed along the rotor perimeter (Fig. 2). Hassenpflug [20] has shown that such flow patterns do indeed resemble the eddy-induced flow component in Busemann's analytical approach reasonably well.
(8) There is only one relative eddy in the whole rotor: it revolves around the axis and protrudes into the blade passages, and when it forms separate cells associated with each blade passage as in Fig. 2, these cells are included in the main cell centered on the rotor axis.
(9) At radial positions inside the rotor leading edges the flow rotates approximately as a solid body relative to the rotor.

With reference to its most distinguishing feature, a suitable name for the method is the single relative-eddy (SRE) method.

Derivation of Equations

The fundamental principles in the derivation are as follows:

(1) Each fluid particle in the rotor has a vorticity equal in magnitude to twice the rotor angular velocity, relative to the rotor.
(2) There is a single average circulation velocity around the edges of the relative eddy.
(3) The integral of the circulation velocity around the control volume divided by the control volume area is equal to the vorticity.
(4) The integration path follows the suction surface from leading to trailing edge, then the rotor exit rim from the blade trailing edge to the next blade pressure side trailing edge, then to its leading edge, and then around its leading edge from the pressure to the suction side.

The eddy-induced velocities along the suction, exit, and pressure surfaces are $f_s \Delta w$, $f_e \Delta w$, and $f_p \Delta w$, where Δw is the average eddy-induced velocity along the control volume boundaries, and the f factors allow for deviations from the average along each section of the boundary. The component of the velocity induced by the relative eddy along the radial lines extending inward from

the blade leading edges is $f_i \Delta w$. The magnitude of the vorticity induced by the relative eddy is $\omega = 2\Omega$, where Ω is the angular velocity of the rotor in radians per second.

Circulation is the integral of the velocity, taken around the edges of the control volume:

$$\Gamma_{cv} = \int_{cv} V\, ds \tag{1}$$

The average vorticity is:

$$\omega = \Gamma_{cv}/A_{cv}. \tag{2}$$

The blade length is:

$$c = (r_e - r_i)/\cos\beta \tag{3}$$

The blade spacing is:

$$s_e = 2\pi r_e/Z \tag{4}$$

The next step is to calculate the circulation by adding the contributions along each section of the control volume boundary. There is no net contribution from the two boundary sections extending inward toward the rotor axis from the blade-leading edges since the velocity components along these two boundaries are equal due to periodicity, but the integration direction is opposite when integrating around the boundary. The circulation is then:

$$\Gamma_{cv} = f_e \Delta w\, 2\pi r_e/Z + (f_p \Delta w + f_s \Delta w)(r_e - r_i)/\cos\beta$$
$$= (f_e \Delta w\, 2\pi r_e/Z)\left(1 + \frac{f_p + f_s}{f_e}\frac{(1 - r_i/r_e)Z}{2\pi\cos\beta}\right) \tag{5}$$

and

$$\Omega = \frac{\omega}{2} = \frac{1}{2}\frac{\Gamma_{cv}}{A_{cv}} = \frac{\Gamma_{cv}}{2\pi r_e^2/Z} \tag{6}$$

$$\therefore \Omega = \frac{(f_e \Delta w\, 2\pi r_e/Z)}{2\pi r_e^2/Z}\left(1 + \frac{(f_p + f_s)}{f_e}\frac{(1 - \mathrm{RR})Z}{2\pi\cos\beta}\right) \tag{7}$$

with $\mathrm{RR} = r_i/r_e$. Then:

$$\frac{\Delta w_s}{U_e} = \frac{f_e \Delta w}{\Omega r_e} = \left(1 + \frac{(f_p + f_s)}{f_e}\frac{(1 - \mathrm{RR})Z}{2\pi\cos\beta}\right) \tag{8}$$

where the average slip velocity along the exit boundary is $\Delta w_s = f_e \Delta w$, and $\Omega r_e = U_e$.

The normal definition of blade row solidity is the blade chord divided by the spacing, but to keep things simple, we shall replace the chord by the blade length (in a plane perpendicular to the rotor axis) and use the spacing at the radius, r_e, of the blade trailing edges (rotor rim). The solidity is then:

$$c/s_e = \frac{(r_e - r_i)/\cos\beta}{(2\pi r_e)/Z} = \frac{(1 - \mathrm{RR})Z}{2\pi\cos\beta} \tag{9}$$

Define the solidity influence coefficient as:

$$F = \frac{f_p + f_s}{f_e} \tag{10}$$

Since it depends on the relative magnitudes $\int V\, ds$ over the blade surfaces, compared to the value over the blade passage exit surface, F can be expected to be a function of the blade angle and of the aspect ratio (or solidity) of the blade passage. The normalized slip velocity is then simply:

$$\frac{\Delta w_s}{U_e} = \frac{1}{1 + F(c/s_e)} \tag{11}$$

Typical values of solidity extracted from the data of Wiesner [1] range from 0.5 to 2.5, with a few values as high as 3.5 and an average of 1.5. We shall see that the average value of F is about 4, implying that for $c/s_e = 1.5$ the normalized slip velocity $(\Delta w_s/U)$ is about 1/7 or 0.14.

Implications of the equation above are as follows:

(1) The eddy-induced slip velocity is dependent on blade solidity.
(2) The eddy-induced slip velocity is independent of the blade number, blade angle, and blade radius ratio individually, but depends on them collectively insofar as they affect solidity.
(3) The factors that determine the influence coefficient F must still be determined, and may include any or all of the above.
(4) When blade solidity is zero (no blades or infinitely short blades), the equation correctly predicts that the slip velocity is equal in magnitude to the rotor rim speed.
(5) Impellers with splitter vanes can be handled by using a control volume that includes two adjacent blade passages, containing two rotor perimeter pitches and a suction and pressure side of each of the main and splitter blades. This will be equivalent to using the mean blade length.
(6) The assumption of logarithmic spiral blades turns out to be unnecessary at this point, but the blade shape may affect the value of F.

Definition of Slip Factor

There are basically two definitions of slip factor. Both are equal to one minus the normalized slip velocity. In the one definition the amount of slip is normalized by dividing the slip velocity by the rotor rim speed and in the other by the ideal (slipless) circumferential fluid velocity component. The second one introduces the complication that the circumferential fluid velocity component is dependent on the flow through the impeller, except in the case of radial blades ($\beta_e = 0$), when the two definitions are equivalent. As the second definition contradicts the assumption made in the derivation that eddy-induced slip is independent of throughflow, we shall follow Wiesner [1] and use the first definition:

$$\sigma_s = 1 - (\Delta w_s/U) = 1 - 1/[1 + F(c/s_e)] \tag{12}$$

Since the magnitude of the other factors affecting slip, like the trailing edge pressure gradient relaxation and boundary layer blockage effect (including the existence of wakes) are also primarily dependent on solidity, solidity should correlate measured slip factors well, at worst with a different coefficient F for each family of impellers.

It is known that in practice slip factors are not independent of flow, but the relative eddy can, in terms of its definition, not be the cause of these variations.

The Dependence of F on Blade Angle

The next step is to determine the dependence of F on Z, β, and RR. As a first approximation the dependence on β alone will be investigated, since Busemann drew separate figures for each blade angle. Busemann [19] (also Wiesner [1] and Wislicenus [5]) presented graphs for each of the following blade angles $\beta_B = 90$ deg, 60 deg, 40 deg, 20 deg, 10 deg, and 5 deg (measured from the circumferential direction), corresponding to our angles $\beta = 0$ deg, 30 deg, 50 deg, 70 deg, 80 deg, and 85 deg (measured from the radial direction). Wiesner's graphs show Busemann's slip factor as a function of radius ratio for blade numbers 1, 2, 4, 8, and 16 with the graph for 30 blades estimated by Wiesner. Figure 3 shows the Busemann graph for $\beta = 30$ deg, with the line for 1 blade removed, to make room for a legend, and Fig. 4 shows the corresponding graph calculated from Eq. (12) with $F = 4.45$. The graphs have roughly the same shape, but the SRE method predicts that the slip factor continues to increase with a decrease in RR, even at low values of RR, say, below RR = 0.4. An inspection of the data reported by Wiesner, however, shows that, if we disregard the pump data of Varley (from Wiesner [1]), who presented a set of data for RR = 0.338, then 90% of the rest falls within the range $0.4 < \mathrm{RR} < 0.6$.

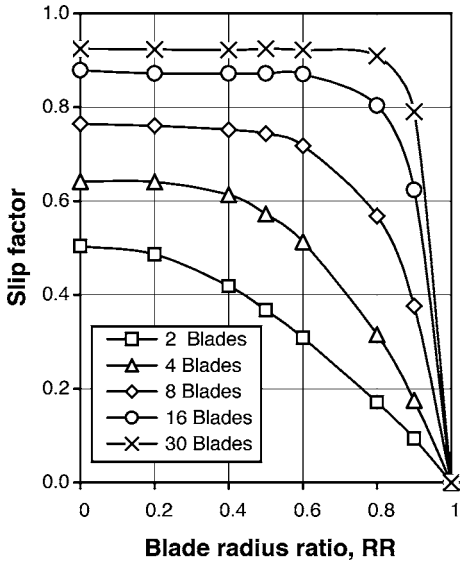

Fig. 3 The Busemann slip factor for β=30 deg versus radius ratio for various blade numbers

Now find, for each of the above blade angles, the value of F that would minimize the sum of the square of the differences between the slip factors calculated with Eq. (12) and the corresponding Busemann values. The nine points selected were those with RR=0.4, 0.5, and 0.6, and blade numbers 8, 16, and 30. Figure 5 shows the resulting relationship between F and $\cos\beta$. The equation $F=F_0(\cos\beta)^{0.5}$, with $F_0=5.0$, presented the trend well enough, except for one point at β=80 deg. It can be shown by differentiating Eq. (12) with respect to F that $\partial\sigma/\partial F=\sigma(1-\sigma)$. At β=80 deg, and for the blade numbers and radius ratios considered, a typical value of slip factor is σ=0.91, so that $\partial\sigma/\partial F$ has a value of 0.08, implying that a 30% error in F would cause only a 2.5% error in slip factor. Conversely, a small error in estimating the Busemann values from Wiesner's graphs would result in a large variation in F.

The SRE slip factor equation then becomes:

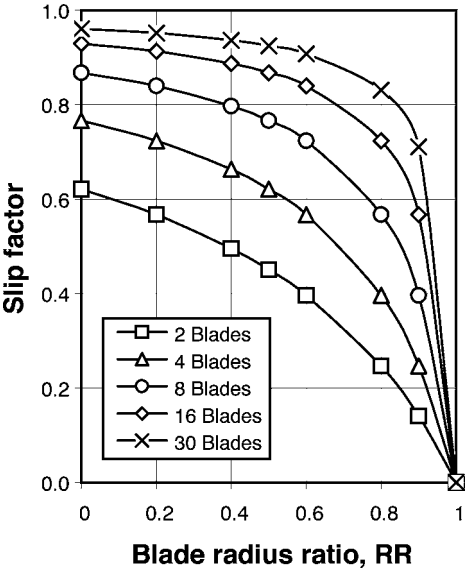

Fig. 4 The SRE slip factor for β=30 deg versus the radius ratio for various blade numbers

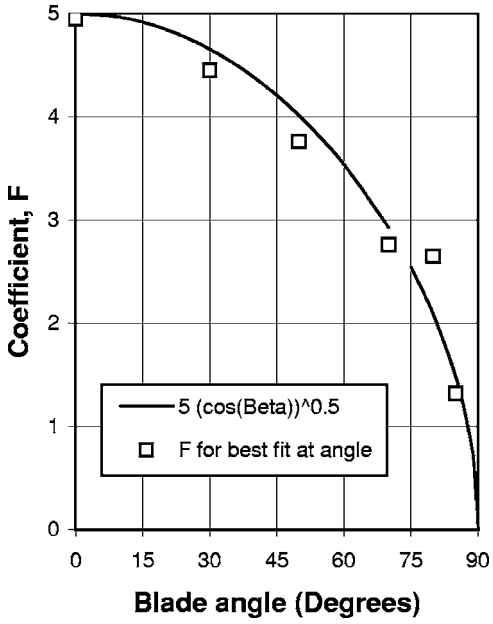

Fig. 5 The relationship between solidity coefficient, *F*, and blade angle, β, in the SRE model

$$\sigma_s = 1 - \frac{1}{1 + 5(c/s_e)(\cos\beta)^{0.5}} \tag{13}$$

Figure 6 is a graphical representation of Eq. (13). It shows the variation of slip factor with solidity, with β as a parameter. Note that for $\beta \leqslant 50$ deg the influence of β is small, and the slip factor is then to a good approximation a function of solidity alone.

The SRE slip factor can also be written in terms of the basic parameters as:

$$\begin{aligned}\sigma_s &= 1 - 1/[1 + 5(\cos\beta)^{0.5}(c/s_e)] \\ &= 1 - 1 \Big/ \left(1 + 5(\cos\beta)^{0.5}\frac{Z(1-\mathrm{RR})}{2\pi\cos\beta}\right) \\ &= 1 - 1 \Big/ \left(1 + 5\frac{(1-\mathrm{RR})Z}{2\pi(\cos\beta)^{0.5}}\right)\end{aligned} \tag{14}$$

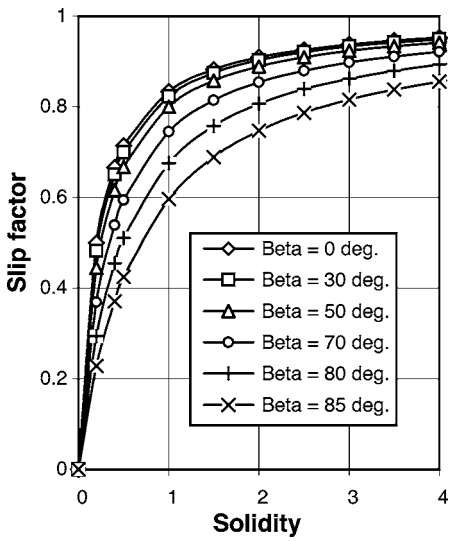

Fig. 6 Variation of the SRE slip factor with solidity, c/s_e, with blade angle, β, as a parameter

Table 1 SRE slip factors compared to Stodola, for RR=0.5 and β=50 deg and 65 deg

Z	4	8	16	32
Exact SRE (50 deg)	0.665	0.799	0.888	0.941
Approximate SRE (50 deg)	0.496	0.748	0.874	0.937
Stodola (50 deg)	0.495	0.748	0.874	0.937
Exact SRE (65 deg)	0.710	0.830	0.907	0.951
Stodola (65 deg)	0.668	0.834	0.917	0.959

Comparison to Equation of Stodola

One problem in comparing the SRE equation (14) above with some other slip factor equations, is that they are insensitive to blade radius ratio, RR. For the 66 cases summarized by Wiesner [1] RR varied between 0.338 and 0.6. The average value was 0.47.

Substituting the Stodola derived slip velocity, $\Delta w = \pi U_e(\cos\beta)/Z$, into the slip factor definition normalized with respect to the rotor speed U, leads to:

$$\sigma_s = 1 - \pi(\cos\beta)/Z \tag{15}$$

For average RR, say 0.5 and large Z, say 24, so that in Eq. (14) the second term in the large parentheses $\approx 10 \gg 1$, the first term may be ignored and the SRE method, (Eq. (14)) may be approximated as below:

$$\sigma_s = 1 - 1 \Big/ \left(1 + 5\frac{(0.5)Z}{2\pi(\cos\beta)^{0.5}}\right) \approx 1 - 0.8\pi\sqrt{(\cos\beta)}/Z \tag{16}$$

The major difference between Eq. (16) and Eq. (15) is in the square root, but they are exactly equivalent for β=50.2 deg for any number of blades. Dixon [8] states that the Stodola equation gives the best results in the range of 60 deg to 70 deg. Table 1 compares exact and approximate SRE predictions to Stodola. For 8 or more blades the agreement is within 0.01, but the Stodola equation is inaccurate for small Z, and incorrectly predicts that in the limit of zero blades the slip factor equals minus infinity, whereas the SRE method (in its exact form) correctly predicts it to be equal to zero.

Comparison to Equation of Stanitz

A commonly used expression for the slip factor of radial bladed impellers (β=0 deg) is one proposed by Stanitz [21], based on numerical solution of flow fields in impellers with radius ratio 0.445:

$$\sigma_s = 1 - 0.63\pi/Z \tag{17}$$

Note that this equation does not agree with the Stodola equation (15) for β=0 deg, which gives:

$$\sigma_s = 1 - \pi/Z \tag{18}$$

For β=0 deg and RR=0.5, the approximate SRE equation (16) above reduces to:

$$\sigma_s \approx 1 - 0.8\pi/Z \tag{19}$$

This equation gives values that are about halfway between the Stodola equation (18) for β=0 deg, and the Stanitz equation. For β=0 deg and RR=0.4, however, the approximate equation (14) above reduces to:

$$\sigma_s \approx 1 - \frac{2}{3}\pi/Z = 1 - 0.67\pi. \tag{20}$$

The agreement between Eqs. (17) and (20) is striking. The full SRE is compared to the Stanitz equation in Table 2 and shows that for RR=0.4 agreement is within 0.025 for 8 or more blades. The Stanitz equation, unlike the Stodola equation, consistently predicts higher values of slip factor than the SRE method. It is gratifying to see that the approximation to the SRE equation, in its simplified form exhibits fundamentally the same dependence on the blade number as the Stodola and Stanitz equations, and in its exact form agrees with the two different equations as far as they are reconcilable with each other.

Table 2 SRE slip factors compared to predictions by Stanitz, for RR=0.4 and 0.5

Z	4	8	16	32
SRE, β=0 deg, RR=0.5	0.614	0.761	0.864	0.927
SRE, β=0 deg, RR=0.4	0.656	0.793	0.884	0.939
Stanitz	0.706	0.828	0.906	0.951

Comparison to Equations of Wiesner and Analytical Values of Busemann

Wiesner [1] proposed an empirical equation, valid for RR less than a limiting value, RR_{lim}, stating, in our angle notation, that:

$$\sigma_s = 1 - \sqrt{\cos\beta}/Z^{0.7} \tag{21}$$

We have seen that the SRE equation may, for small RR, say 0.5, to avoid exceeding RR_{lim}, and large Z, be approximated as:

$$\approx 1 - 0.8\pi\sqrt{(\cos\beta)}/Z \tag{22}$$

The approximate SRE equation resembles the Wiesner equation in its dependence on $\sqrt{\cos\beta}$, but not in its dependence on Z, but Eqs. (21) and (22) predict exactly the same value of slip factor for Z =21.6, for any blade angle. The 0.7 exponent for Z in the Wiesner equation disagrees with the Stodola, Stanitz, and approximate SRE equations. The fundamental Wiesner equation (Eq. (21)), like the Stodola and Stanitz equations, predicts that as Z approaches zero, the slip factor approaches minus infinity, but because of the lower valued exponent (0.7) it does so more slowly. As the fundamental equation also assumes that slip factor is independent of RR, Wiesner proposed an empirical correction factor to force the slip factor to zero as RR approaches unity (and blade length approaches zero). The correction factor is:

$$F_{RR} = 1 - [(RR - RR_{lim})/(1 - RR_{lim})]^3 \tag{23}$$

where $RR_{lim}=\exp[8.16(\cos\beta)/Z]$ is the limiting radius ratio. It must be applied only when the limiting radius ratio is exceeded. Note that Wiesner [1] did not attempt to model the physics by correcting the slip velocity, but applied the correction to the slip factor directly.

Table 3 compares SRE predictions with Busemann and Wiesner for a typical RR value of 0.5, and a wide range of blade angles. The Busemann data is given to two decimals only, having been measured off figures in Wiesner [1]. The asterisk (*) denotes val-

Table 3 SRE slip factors compared to values predicted by Busemann and Wiesner, for RR=0.5

Z	4	8	16	30
Busemann, β=0 deg	0.56	0.76	0.86	0.91
SRE, β=0 deg	0.614	0.761	0.864	0.923
Wiesner, β=0 deg	0.575*	0.763*	0.856	0.908
Busemann, β=50 deg	0.63	0.79	0.88	0.92
SRE, β=50 deg	0.665	0.799	0.888	0.937
Wiesner, β=50 deg	0.676*	0.813	0.885	0.926
Busemann, β=70 deg	0.71	0.83	0.91	0.94
SRE, β=70 deg	0.731	0.845	0.916	0.953
Wiesner, β=70 deg	0.778	0.864	0.916	0.946
Busemann, β=80 deg	0.83	0.92	0.96	0.96
SRE, β=80 deg	0.793	0.884	0.939	0.966
Wiesner, β=80 deg	0.841	0.903	0.940	0.961

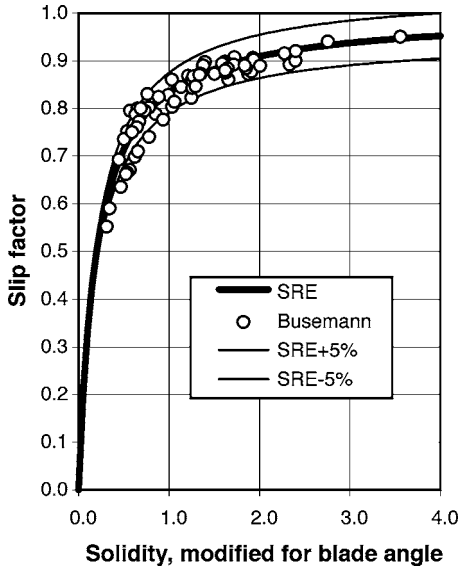

Fig. 7 SRE and Busemann predictions of the slip factor for Wiesner test cases, versus $(c/s_e)\sqrt{\cos\beta}$

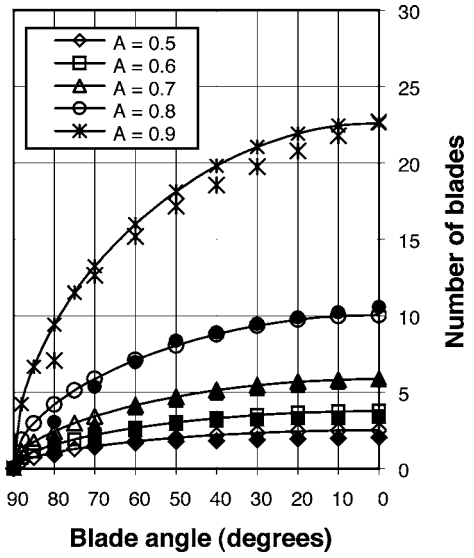

Fig. 9 A comparison of *A*-contours by SRE and Csanady (1960)

ues corrected for exceeding Wiesner's limiting radius ratio. The average value of the SRE value minus the Busemann value is +0.0068 and the standard deviation of the difference is 0.054, compared to +0.0113% and 0.057 for Wiesner. For the 16 points considered, SRE performs slightly better in terms of the average difference and the standard deviation of the difference when compared to Busemann. Although Wiesner typically predicts slip factors to be about 0.005 higher than SRE, the standard deviation based on the difference between them is only 0.002.

Figure 6 is a graphical representation of the SRE slip factor prediction, Eq. (14). It presents the slip factor as a function of solidity, with the blade angle as a parameter. All the lines in the figure can, however, be collapsed onto a single line if the x-axis value is changed to $(c/s_e)\sqrt{\cos\beta}$, the so-called modified solidity. Figures 7 and 8 present comparisons between Eq. (14) and the Busemann and Wiesner slip factors, respectively, for all the applicable test cases in Wiesner [1]. The agreement is good in both cases. Both figures support the notion that a prime factor that determines the slip factor is the modified blade solidity, $(c/s_e)\sqrt{\cos\beta}$.

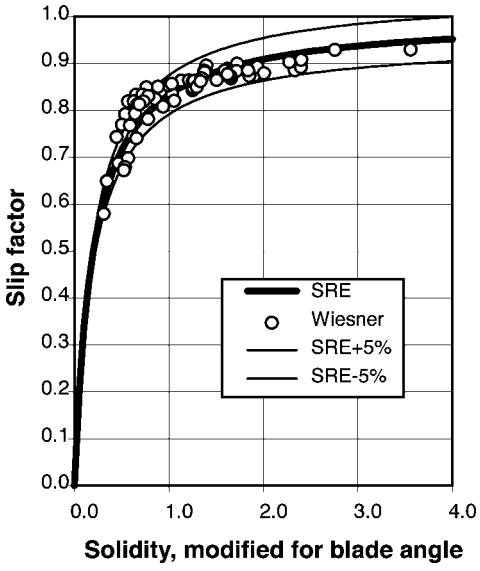

Fig. 8 SRE and Wiesner predictions of the slip factor for Wiesner test cases, versus $(c/s_e)\sqrt{\cos\beta}$

Comparison to Equation of Eck

In the Discussion section attached to Wiesner's paper [1], Love proposed an equation for the slip factor derived by Eck [7], who derived his equation by using pressure gradient arguments. The equation is:

$$\sigma_s = 1 \Big/ \left(1 + \frac{(\pi/2)\cos\beta}{Z(1-\mathrm{RR})}\right) \tag{24}$$

It may be rewritten as:

$$\sigma_s = 1 \Big/ \left(1 + \frac{2\pi}{4}\frac{\cos\beta}{Z(1-\mathrm{RR})}\right) = 1 - 1 \Big/ \left(1 + 4\frac{Z(1-\mathrm{RR})}{2\pi\cos\beta}\right) \tag{25}$$

Equations (14) and (25) are very similar. The only difference is that in the Eck equation the coefficient Z has a constant value of 4 instead of $5(\cos\beta)^{0.5}$. At $\beta=50.2$ deg the two equations are identical. The comparisons with Stodola, Stanitz, and Wiesner have, however, confirmed that the $5(\cos\beta)^{0.5}$ coefficient as a good approximation. As the coefficient Z varies between 1.00 at 0 deg and 0.30 at 85 deg, it is unlikely that a constant value would be adequate over a wide range of blade angles.

Neither Eck nor Love pointed out that the fundamental parameter influencing slip factor is solidity.

Comparison With Csanady

Csanady (1960) (reported by Ferguson [4], and Dixon [8]) published curves showing contours of a coefficient A, which is equivalent to the slip factor definition we use. Each curve basically gives the number of blades required to achieve a desired solidity, given the blade angle. The equivalent curves, using SRE, can be drawn by assuming RR=0.5 and rewriting Eq. (14) in the following form:

$$Z = \frac{\sigma_s}{1-\sigma_s}\frac{2\pi\sqrt{\cos\beta}}{5(1-0.5)} \tag{26}$$

Equation (26) opens up the possibility of explicitly calculating the number of blades required to achieve a desired slip factor, for any

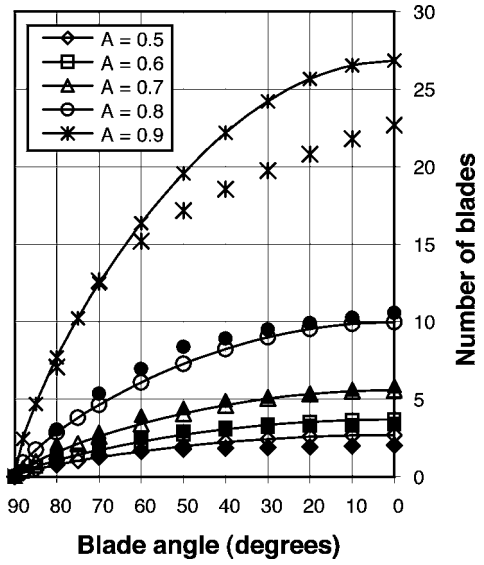

Fig. 10 A comparison of *A* contours by Wiesner and Csanady (1960)

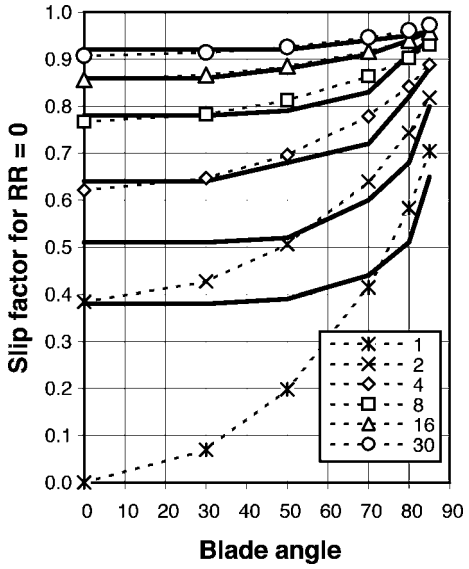

Fig. 12 A comparison of Wiesner and Busemann slip factors for RR=0

blade angle and radius ratio. It is apparent from Fig. 9 that Eq. (26) above (represented by the lines) predicts Csanady's data points surprisingly well. Since these curves were derived from Busemann's data they demonstrate once more how well SRE approximates the Busemann calculations. Figure 10 shows a similar graph using Wiesner's correlation, but the agreement is not nearly as good, except at blade angles exceeding 65 deg, and it cannot model the effect of RR explicitly.

Slip Factor For Low Radius Ratio

The study so far has shown that the SRE method predicts slip factor well for RR≈0.5, but initial comparisons (Figs. 3 and 4) showed that it overpredicted at low values of RR. The simplest way of removing this discrepancy is to assume that if RR$<$0.5, then RR=0.5. This is equivalent to assuming that blade-leading edges extending inward beyond RR=0.5, do not contribute to the control of slip. Figure 11 compares SRE slip factors (for RR=0.5) to those of Busemann (measured from the graphs in Wiesner, for example, Fig. 3) for RR=0. The agreement is generally within three percentage points, but it deteriorates as the blade number decreases. The Wiesner correlation (Fig. 12) is very good for 16 blades (and for 30, where Busemann data did not exist, but were estimated by Wiesner), but it is relatively inaccurate for lower blade numbers or large blade angles.

Figures 13 and 14 present comparisons between Eq. (14) and the Busemann and Wiesner slip factors respectively, as before, but with RR values of less than 0.5 changed to 0.5. The agreement is improved and can be described as excellent in both cases. It is remarkable that the simple SRE correlation manages to represent Busemann's predictions accurately for all Wiesner's data points. SRE agrees better with Busemann than with Wiesner's prediction method.

Although assuming a fixed value of RR=0.5 as the cutoff point may be regarded as simplistic, it works very well. The author has derived a more complicated method, but does not consider it

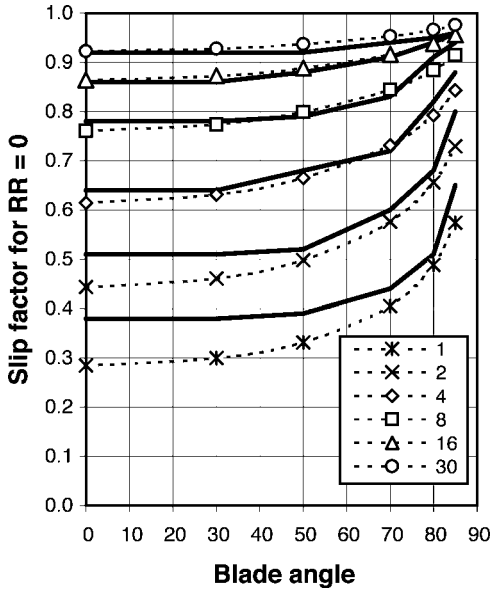

Fig. 11 A comparison of SRE (with RR=0.5) and Busemann slip factors for RR=0

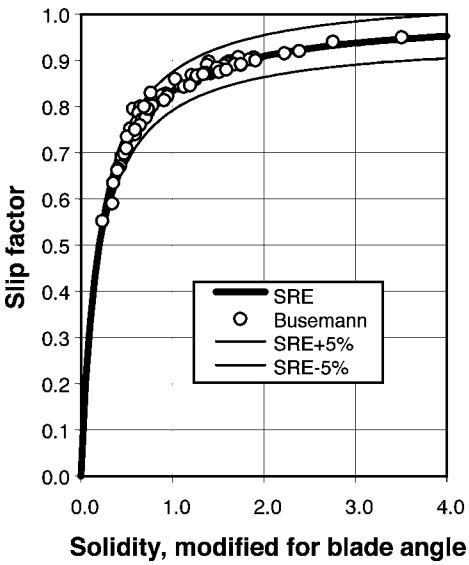

Fig. 13 SRE (with RR≥0.5) and Busemann predictions of the slip factor for Wiesner test cases, versus $(c/s_e)\sqrt{\cos\beta}$

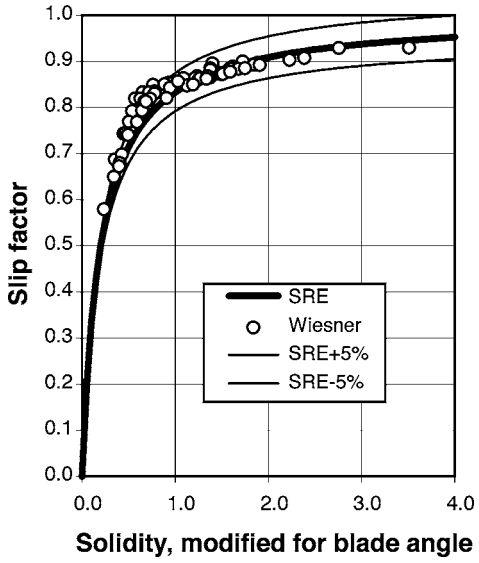

Fig. 14 SRE (with RR≥0.5) and Wiesner predictions of the slip factor for Wiesner test cases, versus $(c/s_e)\sqrt{\cos\beta}$

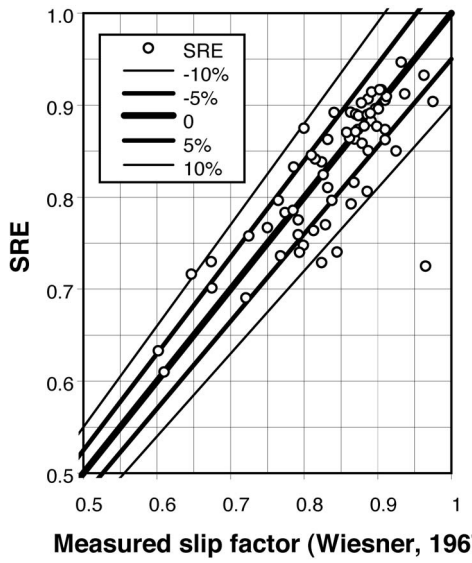

Fig. 16 The slip factor comparison between the SRE prediction and Wiesner test cases

worthwhile since, like the Wiesner method, it would require a conditional procedure involving the calculation of a critical radius ratio.

Comparisons With Measured Data of Wiesner

To qualify as an accepted general method of predicting slip factor the SRE method should show that it represents a considerable body of measured data with sufficient accuracy. Conveniently available experimental results are those reported by Wiesner [1]. Measured slip factors reported by Wiesner were used wherever the blade radius ratio and the so-called "test slip coefficients" were given. In the comparisons that follow we make the standard, tacit assumption that the rotor blade angle at the trailing edge (rotor exit) represents the rotor blade angle, even for nonlogarithmic-spiral blades.

Figure 15 presents a comparison between Eq. (14) (with no limitation on minimum RR values) and the so-called test slip coefficients presented by Wiesner. Here the agreement is not as good as with the Wiesner and Busemann predictions, because of a combination of experimental scatter and nonviscous fluid effects. The figure is, however, experimental confirmation of the notion that a prime factor that determines the slip factor is indeed the modified blade solidity, $(c/s_e)\sqrt{\cos\beta}$.

Figures 16 and 17 show how well the SRE compares to Wiesner in predicting the measured data reported by Wiesner. Wiesner has more points within the ±5% range, but SRE has more within the ±10% range, and is less prone to overpredict. SRE has the potential advantage that each family of impellers may be fitted with its own constant F or F_0, but this needs further investigation.

The question of how much of the scatter is attributable to poor prediction models and how much to the experimental inaccuracies is addressed in the next section.

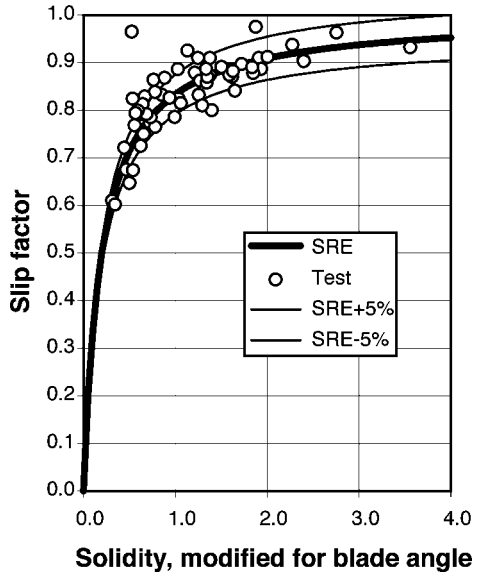

Fig. 15 SRE prediction and Wiesner test cases for slip factors versus $(c/s_e)\sqrt{\cos\beta}$

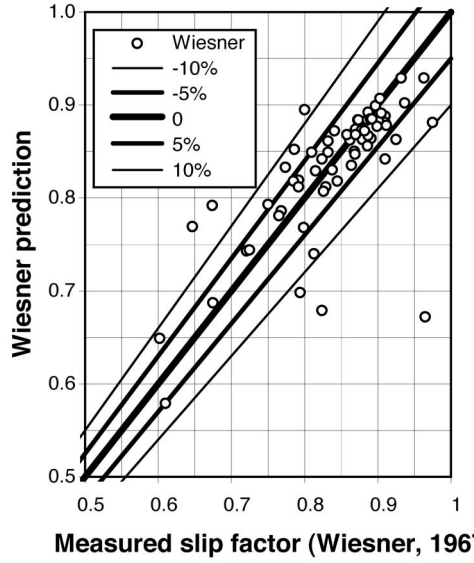

Fig. 17 The slip factor comparison between the Wiesner prediction and Wiesner test cases

Table 4 Estimation of standard deviation of slip factor measurement error, S_σ

Blade exit angle, β_2(deg)	0	30	50	70	80	85
Blade number, Z	20	17	16	7	5	4
Wiesner slip factor, σ	0.877	0.871	0.884	0.850	0.864	0.888
Guessed efficiency, η	0.80	0.80	0.80	0.80	0.80	0.80
Flow coefficient, ϕ	0.300 000	0.300 000	0.200 000	0.150 000	0.100 000	0.050 000
Head coefficient, μ	0.701 742	0.576 735	0.539 194	0.399 930	0.299 746	0.304 936
S_μ	0.007 017	0.005 767	0.005 392	0.003 999	0.002 997	0.003 049
$(S_\mu\ \partial\sigma/\partial\mu)^2$	0.000 077	0.000 052	0.000 045	0.000 025	0.000 014	0.000 015
S_η	0.010 000	0.010 000	0.010 000	0.010 000	0.010 000	0.010 000
$(S_\eta\ \partial\sigma/\partial\eta)^2$	0.000 120	0.000 081	0.000 071	0.000 039	0.000 022	0.000 023
S_ϕ	0.003 000	0.003 000	0.002 000	0.001 500	0.001 000	0.000 500
$(S_\phi\ \partial\sigma/\partial\phi)^2$	0.000 000	0.000 003	0.000 006	0.000 017	0.000 032	0.000 033
S_β	0.017 500	0.017 500	0.017 500	0.017 500	0.017 500	0.017 500
$(S_\beta\ \partial\sigma/\partial\beta)^2$	0.000 028	0.000 049	0.000 072	0.000 503	0.003 360	0.013 203
S_σ	0.014 991	0.013 608	0.013 922	0.024 168	0.058 553	0.115 207

Error Estimate For Experimental Data Reported by Wiesner

Experimental slip factors in Wiesner's paper are calculated as: $\sigma=\mu/\eta+\phi_2\tan\beta_2$, where μ is the pressure or head coefficient, η is the efficiency, ϕ_2 is the impeller discharge flow coefficient, and β_2 is the impeller discharge angle. (The subscripts 2 are omitted from hereon.) If one can estimate the typical standard deviation S_i in determining each of the four independent variables, the variance S_σ^2 and standard deviation of the value of the dependent variable, σ may be derived, by doing a sensitivity analysis. According to Granger [22] the relationship between the standard deviations, S is for the present case:

$$S_\sigma^2=\left(\frac{\partial\sigma}{\partial\mu}S_\mu\right)^2+\left(\frac{\partial\sigma}{\partial\eta}S_\eta\right)^2+\left(\frac{\partial\sigma}{\partial\phi}S_\phi\right)^2+\left(\frac{\partial\sigma}{\partial\beta}S_\beta\right)^2$$

where, for the equation under consideration:

$$\frac{\partial\sigma}{\partial\mu}=\frac{1}{\eta};\ \frac{\partial\sigma}{\partial\eta}=\frac{-\mu}{\eta^2};\ \frac{\partial\sigma}{\partial\phi}=\tan\beta;\ \frac{\partial\sigma}{\partial\beta}=\frac{\phi}{\cos^2\beta}$$

In Table 4 the typical assumption is that the standard deviation of the measurement error is 1%, implying that 95% of the measured values are accurate to within ±2%. The standard deviations are taken as either one percent of the value or one percentage point (for efficiency), and that of the angle measurement error as 1 deg, as summarized below: $S_\mu=0.01\mu$; $S_\eta=0.01$; $S_\phi=0.01\phi$; $S_\beta=0.0175$ rad=1 deg.

The values of the variables were selected as typical ones from Wiesner's data table. Note that the low blade number typically goes with high blade angles to give high slip factors (as in Fig. 9).

For $\beta_2\leqslant 70$ deg and $Z\geqslant 7$, the standard deviation is 0.015 to 0.024, but it is much higher at larger blade angles and lower blade numbers. It implies that in 95% of the cases with $\beta_2<70$ deg and blade numbers $Z\leqslant 7$, the slip factor experimental error should be less than ±0.05, but that for cases with larger blade angles and fewer blades the error may be much larger (±0.12 to ±0.23). Since these conservative guesses for measurement error result in fairly large standard deviations for the slip factor, it may be assumed that a relatively large part of the differences between the predictions and the measured data reported by Wiesner is attributable to inaccuracies in measurement.

Discussion

In the paper we present a simple method for deriving the relative-eddy-induced slip factor in centrifugal impellers. The derivation proposes the concept of a single relative-eddy recirculation zone in the rotor, in contrast to previously used separate recirculation cells. The resulting equation reduces to well-known and trusted equations for the calculation of slip factor when assuming realistic radius ratios and excluding rotors with a few blades, where many trusted methods start to approach an unrealistic limiting value.

The SRE equation is, next to Eck's, the only one to intrinsically predict the zero slip factor for zero blades. It also correctly predicts the zero slip factor for blades of zero length (RR=1), independent of the number of blades, without the need to calculate a limiting radius ratio, and it can handle splitter blades in a logical way. It turned out that the prime variable that determines slip is the blade solidity, c/s_e:

$$c/s_e=\frac{(1-\mathrm{RR})Z}{2\pi\cos\beta}$$

The proposed general equation for relative-eddy-induced slip factor is:

$$\sigma_s=1-\frac{\Delta w_s}{U}=1-\frac{1}{1+F_0(c/s_e)(\cos\beta)^{0.5}}$$

with the constant $F_0=5.0$, but its value may be adjusted for specific families of impellers.

Assuming that radius ratios of less than 0.5 are equal to 0.5 in the previous equations, gives better agreement with Busemann's analytical values, but does not improve agreement with Wiesner's test cases.

Conclusions

Two slip factor correlations are presented: both assume that $\sigma_s=1-[1+F(c/s_e)]^{-1}$ where the solidity influence coefficient is: $F=F_0(\cos\beta)^{0.5}$, with $F_0=5$, but the second one additionally assumes that radius ratios of less than 0.5 should be taken to be 0.5.

Agreement with the methods of Stodola, Stanitz, Wiesner, Eck, and Csanady, with the analytical solutions of Busemann, and with measured data presented by Wiesner, show that the SRE method is a feasible replacement for the Wiesner method: it is not a mere curve fit, but is based on a fluid dynamic model; it is inherently sensitive to an impeller inner-to-outer radius ratio and does not need a separate calculation to find a critical radius ratio; and it contains a constant, F_0, that may be adjusted for specifically constructed families of impellers to improve the accuracy of the prediction.

The three main contributions of this work are as follows: the derivation of a slip factor in terms of a single relative eddy centered on the rotor axis, instead of multiple eddies (one per blade passage); the recognition that blade solidity is the prime variable determining the relative-eddy-induced slip factor; the presentation of a simple, reliable method, that analytically and numerically unifies the tried and trusted methods of Stodola, Stanitz and Wiesner, Eck, Csanady, and Busemann over a wide range of impeller geometries.

Since the effect of many of the other factors that contribute to slip (potential flow and boundary layer effects) are also dependent on solidity, it is recommended that radial turbomachinery investigators and designers investigate the use of solidity to correlate the slip factor.

Acknowledgment

Graduate students René Heise and Louwrens Marais helped with the numerical solutions for finding the streamlines in Figs. 1 and 2.

List of Symbols

A = control volume area, Csanady coefficient
c = blade length
d = rotor diameter
e = eddy radius in Stodola derivation
F = solidity coefficient
f = velocity coefficient
RR = radius ratio
r = rotor radius
s = blade spacing, distance along integration path
U = rotor speed
V = velocity
w = circulation velocity
Z = number of rotor blades

Greek Symbols

β = blade angle
Γ = circulation
η = efficiency
μ = pressure or head coefficient
π = circle circumference to radius ratio
σ = slip factor
ϕ = impeller discharge flow coefficient
ω = vorticity
Ω = rotor angular velocity

Subscripts

cv = control volume
e = exit
i = inner
p = pressure side of blade
s = suction side of blade, slip
β = blade angle
η = efficiency
μ = pressure or head coefficient
φ = impeller discharge flow coefficient
0 = zero blade angle

References

[1] Wiesner, F. J., 1967, "A Review of Slip Factors for Centrifugal Impellers." Trans. ASME: J. Eng. Gas Turbines Power **89**, pp. 558–572.
[2] Stodola, A., 1945, *Steam and Gas Turbines*, McGraw-Hill, 1927, reprinted by Peter Smith, New York.
[3] Eckert, B., and Schnell, E., 1961, *Axial- und Radial-Kompressoren*, Springer-Verlag, Berlin, p. 345.
[4] Ferguson, T. B., 1963, *The Centrifugal Compressor Stage*, Butterworths, London, pp. 85–90.
[5] Wislicenus, G. F., 1965, *Fluid Mechanics of Turbomachinery*," 2nd ed. (in two volumes), Vol. 1, Dover, New York, p. 269.
[6] Osborne, W. C., 1966, *Fans*, Pergamon, Bell and Bain Ltd., Glasgow, p. 129.
[7] Eck, B., 1973, *Fans*, Pergamon, Germany, p. 37.
[8] Dixon, S. L., 1978, *Fluid Mechanics*, Thermodynamics of Turbomachinery, Pergamon, New York, pp. 201–206.
[9] Watson, N., and Janota, M. S., 1986, *Turbocharging the Internal Combustion Engine*, MacMillan Education Ltd., London, p. 89.
[10] Cumpsty, N. A., 1989, "*Compressor Aerodynamics*," Longman Scientific & Technical, England, pp. 245–249.
[11] Logan, E., Jr., 1993, "*Turbomachinery, Basic Theory and Applications*," 2nd ed. revised and expanded, Marcel Dekker, New York, pp. 167, 248.
[12] Johnson, R. W., 1998, "*The Handbook of Fluid Dynamics*," CRC Press, Springer, New York, pp. 41-12–41-14.
[13] Wilson, D. G., and Korakianitis, T., 1998, *The Design of High-Efficiency Turbomachinery and Gas Turbines*, 2nd ed., Prentice–Hall, Englewood Cliffs, NJ, p. 240.
[14] Aungier, R. H., 2000, *Centrifugal Compressors–A Strategy for Aerodynamic Design and Analysis*, ASME Press, New York, p. 55.
[15] Saravanamuttoo, H. I. H., Rogers, G. F. C., and Cohen, H., 2001, *Gas Turbine Theory*, 5th ed., Prentice–Hall, Englewood Cliffs, NJ, pp. 153, 155.
[16] Dean, R. C., and Young, L. R., 1976, "The Fluid Dynamic Design of Advanced Centrifugal Compressors," Creare TN-244, pp. 5–27.
[17] Japikse, D., and Baines, N. C., 1997, *Introduction to Turbomachinery*, Concepts ETI and Oxford University Press, Oxford, pp. 4-6–4-7.
[18] Paeng, K. S., and Chung, M. K., 2001, "A New Slip Factor For Centrifugal Impellers," Proc. Inst. Mech. Eng., Part A, pp. 645–649.
[19] Busemann, A., 1928, "Das Förderhöhenverhältniss Radialer Kreiselpumpen Mit Logarithisch-Spiraligen Schaufeln," Z. Angew. Math. Mech., **8**, pp. 371–384.
[20] Hassenpflug, W. C., 2004, personal communication.
[21] Stanitz, J. D., 1952, "Some Theoretical Aerodynamic Investigations of Impellers in Radial- and Mixed-Flow Centrifugal Compressors," Trans. ASME, **74**, pp. 473–476.
[22] Granger, R. A., 1988, *Experiments in Fluid Mechanics*, Holt, Reinhart and Winston, New York.

Multistage Aspects and Unsteady Effects of Stator and Rotor Clocking in an Axial Turbine With Low Aspect Ratio Blading

T. Behr
e-mail: behr@lsm.iet.mavt.ethz.ch

L. Porreca

T. Mokulys

A. I. Kalfas

R. S. Abhari

Turbomachinery Laboratory,
Swiss Federal Institute of Technology,
8092 Zurich, Switzerland

This paper presents the outcome of a recent study in clocking-related flow features and multistage effects occurring in high-pressure turbine blade geometries. The current investigation deals with an experimentally based systematic analysis of the effects of both stator-stator and rotor-rotor clocking. Due to the low aspect ratio of the turbine geometry, the flow field is strongly three-dimensional and is dominated by secondary flow structures. The investigation aims to identify the flow interactions involved and the associated effects on performance improvement or degradation. Consequently a three-dimensional numerical analysis has been undertaken to provide the numerical background to the test case considered. The experimental studies were performed in a two-stage axial research turbine facility. The turbine provides a realistic multi-stage environment, in which both stator blade rows and the two rotors can be clocked relative to each other. All blade rows have the same blade number count, which tends to amplify clocking effects. Unsteady and steady measurements were obtained in the second stage using fast response aerodynamic probes and miniature pneumatic five-hole probes. The current comprehensive investigation has shown that multistage and unsteady flow effects of stator and rotor clocking in low aspect ratio turbines are combined in a nonlinear fashion caused by axial and radial redistribution of low energy fluid. The integral result of clocking on stage efficiency is compensated by competing loss generating mechanisms across the span. [DOI: 10.1115/1.2101855]

Introduction

The relative clocking positions of the stator vanes and the rotor blades affect the overall performance of multistage axial turbines. An optimal clocking position of stators and rotors in a multistage turbine aims to maximize the overall efficiency as well as to optimize the unsteady mechanical loading on the airfoils. The prerequisite of an overall successful design are prediction tools that incorporate the effects caused by clocking.

Finding an optimal relative circumferential position of stators and rotors in a multistage axial turbine is the subject of extensive investigations in the last decade. The prospect of increasing turbine efficiency by consciously positioning the blade rows drives the study of understanding the aspects of the flow physics, which are responsible for this effect. Thereby the main focus lies on unsteady effects caused by the relative motion of adjacent blade rows.

Experimental findings could show the effect of clocking on turbine efficiency, however the level of variation is not yet clear. Jouini et al. [1] conducted a series of tests on a two-stage turbine facility to investigate the effect of stator-stator and rotor-rotor clocking on the aerodynamic efficiency. It was found that for both options this efficiency revealed a sinusoidal shape with respect to the clocking position with a peak-to-peak difference of 4% in a relative basis. Spanwise variation in efficiency was detected to be small. However, the region at 90% span showed a shift in phase and higher reaction on clocking with respect to the mean due to secondary flows offsetting the wake position. Huber et al. [2] conducted an investigation of different vane clocking positions in a two-stage test turbine with low aspect ratio blading. The peak-to-peak value of aerodynamic efficiency variation was determined to be at 0.3% overall and up to 0.8% for the midspan region. Efficiencies of five radial positions showed differences in periodical shape, position of minimum and maximum, as well as their difference when plotted against the vane clocking position. Reinmöller et al. [3] measured a maximum difference in relative aerodynamic efficiency in a 1.5-stage turbine of 1.0% when clocking the stator blade rows. Gombert et al. [4] determined aerodynamic efficiency for different clocking positions of the first stator in a three-stage turbine with high aspect ratio blading. Although the mean peak-to-peak value of the relative efficiency at different span positions is around 1.5%, the optimum efficiency occurs at different clocking positions.

The change in efficiency due to circumferential clocking of blade rows is caused by redistributing loss areas within the blade passages. It was commonly found that a maximum in efficiency could be observed when the wake of an upstream stator hits the leading edge of the subsequent stator. If the wake passes between two stator blades, degradation in efficiency occurs. In the referenced test cases [1–3], low aspect ratio blade rows were investigated. In such cases a highly three-dimensional flow field dominated by secondary flow structures exists. Walraevens et al. [5] gives an interpretation of the unsteady flow around a second stator of a 1.5-stage turbine with low aspect ratio blading. Tiedemann et al. [6] investigated unsteady stator-rotor interactions in a single-stage high-pressure turbine with its effect on a downstream stator.

Höhn et al. [7] classifies effects in a multistage turbine that are acting on a stat or wake that passes eventually through a subsequent stator. In this context spanwise differences in aerodynamic efficiency behavior as an effect of circumferential clocking might be consequential. Corresponding phenomena, such as phase shifts between the optimum clocking positions, could be detected in [1–4].

Various numerical simulations were conducted to predict the

Contributed by the Turbomachinery Division of ASME for publication in the JOURNAL OF TURBOMACHINERY. Manuscript received by June 28, 2004; final manuscript received June 28, 2005. Review conducted by C. Scrivener.

effects of clocking in multistage turbines. Griffin et al. [8] correctly predicts the sinusoidal pattern of the efficiency at midspan of the test case in [2] using a 2D algorithm. However, the magnitude of the maximum efficiency change is less than in the experiment (±0.15%). Differences in 2D and 3D numerical calculations of stator-stator clocking phenomena were observed by Dorney and Sharma [9] and Dorney and Sondak [10]. When applying a 2D algorithm a maximum change in efficiency of 2% was predicted, while the 3D simulation resulted in 1%. Different opinions exist about the effect of flow unsteadiness on the variation of efficiency in downstream blade rows caused by stator clocking. Dorney and Sharma [9] found highest efficiency at maximum unsteadiness, whereas Griffin et al. [8] observed the opposite.

The current study intends to shed further light on the issue of clocking by investigating the steady and unsteady effects of stator-stator and rotor-rotor clocking in a two-stage high-pressure turbine. It will focus on the effects of clocking on performance and flow features that are especially related to the low aspect ratio of the used blade rows.

Experimental Method

Research Turbine Facility. The facility accommodates two axial turbine stages. The air-loop is of a quasi-closed type and includes a radial compressor, a two-stage water to air heat exchanger, and a calibrated venturi nozzle for mass flow measurements. Downstream of the turbine the air-loop is open to atmospheric conditions. A dc generator absorbs the turbine power and controls the rotational speed of the turbine. The first and the second rotor are mechanically decoupled by a twin spool shaft design. A torque meter measures the torque of the second rotor.

The turbine design allows quick and precise assembly and an easy access to the measurement planes. A number of different intrusive and nonintrusive measurement methods can be applied. The facility is equipped with a four-axis numerically controlled probe positioning system with high accuracy in every direction. The turbine entry temperature (TET) is controlled to an accuracy of 0.3% and the rpm is kept constant within ±0.5 min^{-1} by a dc generator. The pressure difference across the turbine is stable within 0.3%. The turbine is operated at constant pressure difference across the stages. With this strategy even minor changes in mechanic efficiency due to clocking can be detected by the systems high sensible torquemeters. The alternative way of operation at constant power would not reach an equivalent level of accuracy.

The interested reader can find a more detailed description of the research facility in Sell et al. [11]. A cross section of the turbine module is shown in Fig. 1. The first stator blade row can be continuously positioned in the circumferential direction relative to the second stator. In addition, both rotor blade rows can be clocked relatively to each other with increments of 0.25 deg.

Key parameters of the rig are presented in Table 1. The Reynolds number based on axial chord is in the order of 2×10^5. The blade row geometries tested for this clocking investigation are designed to model high-pressure turbine blade geometries. In gas turbines the effects of transition are known to be crucial for the performance of the blades especially in low-pressure rather than high-pressure turbines [12]. In the current investigation, any possible effects caused by transition on the blades would apply in all of the tested clocking positions since all Reynolds number relevant parameters are kept constant.

Measurement Technology. A number of unsteady as well as steady measurement techniques are available at the Turbomachinery Laboratory (LSM). Flow parameters at frequencies up to 40 kHz, including total and static pressure, flow angles, velocity components, and Mach number, can be captured with fast response pressure probes. The steady flow field is measured with miniature five-hole probe with a tip diameter as small as 0.9 mm [13]. The unsteady pressure measurement technology of the Fast Response Aerodynamic Probes (FRAP) was developed at the

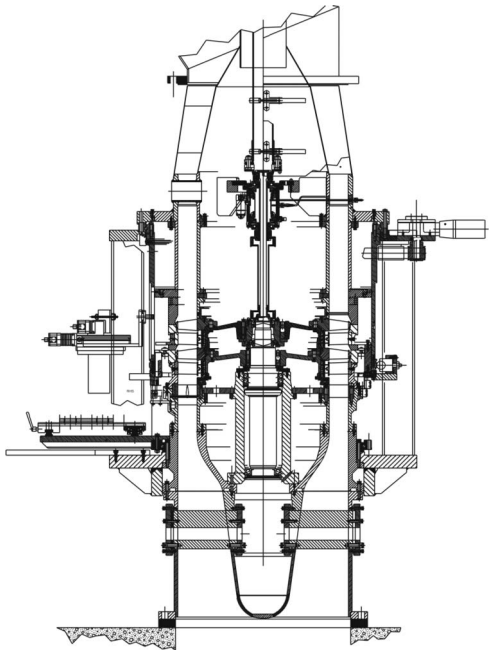

Fig. 1 "LISA" Two stages axial turbine facility

LSM [14,15]. The mainstream flow field is typically measured using a 1.8 mm tip diameter single sensor FRAP probe in virtual-three-sensor mode providing two-dimensional, time-resolved flow field information. The FRAP probe technology provides also temperature data at a frequency of up to 10 Hz.

Clocking Test Cases. The nomenclature to identify the stator-stator (SS) and rotor-rotor (RR) clocking cases has the format SSxxRRyy. The placeholder xx and yy represent the clocking position as a percentage of the pitchwise chord (Fig. 2).

Two shrouded test cases (TC1, TC2) with identical profile geometries have been investigated during this clocking study.

TC1 measurements were taken in a 2×2 matrix containing two stator-stator clocking positions (SS00, SS50) and two rotor-rotor clocking positions (RR00, RR50). For all four combinations the flow was measured in all three measurement planes with the steady technique. In addition both stator clocking positions were tested in all measurement planes with the unsteady technique at 0% rotor clocking (RR00).

In TC2 unsteady measurements were conducted in all planes for SS00RR00, SS50RR00, and SS50RR50. For a performance evaluation both rotor exit planes were tested with the coarse grid at eight different stator clocking position at RR00 and RR50.

Two different measurement grids per pitch have been used during the campaign for the area traverses. In order to investigate a flow field in a measurement plane (MP) a grid of 20 equidistant circumferential and 30 radial positions has been used. This grid is the standard for the conducted measurements. A coarse grid was

Table 1 Main parameter of "LISA" 2-stages axial turbine research facility

Rotor speed (RPM)	2625
Pressure ratio	1.38
Mass flow (kg/s)	10.65
Blades	42/42
Aspect ratio	1.8
Tip diameter (mm)	800
Mach number at rotor exit/stator exit	0.1/0.35
Reynolds number based on axial chord	2×10^5

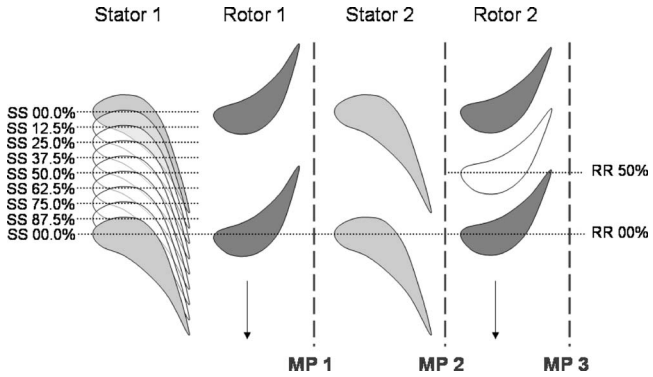

Fig. 2 Relative circumferential stator-stator (SS) and rotor-rotor (RR) clocking positions in percent of circumferential chord. Position of measurement planes

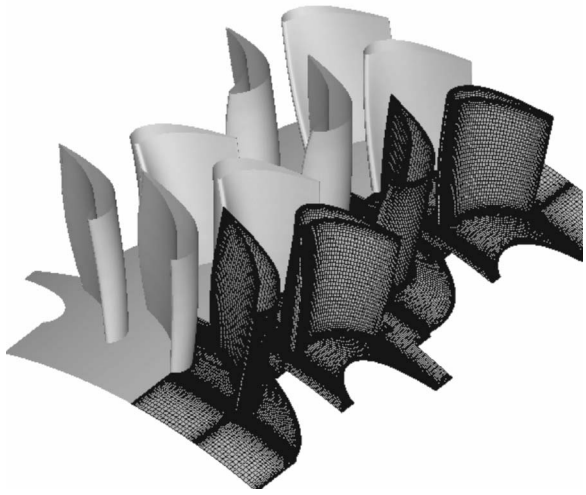

Fig. 3 CFD—Mesh of "LISA" two-stage axial turbine configuration

used once for TC2 to get sufficiently representative values of the MP for an efficiency evaluation. This measurement grid consists of 7 equidistant circumferential and 15 radial positions.

All area plots shown is this paper are views in the upstream direction and contain the area of two pitches. In there, the rotational direction of the rotor blades is from the right to the left.

Numerical Method

The 3D steady and unsteady Navier-Stokes multistage solver Stage3D has been derived from the original Dawes code BTOB3D [16], running a new discretization scheme from Jameson and Baker [17]. The validation on low speed turbines, comparable to LISA, has been undertaken by Emunds et al. [18], where the validity of the computational approach on low Mach number axial turbines has previously been shown. The solver has an explicit five-step, fourth-order Runge-Kutta cycle, using three level multigrid convergence acceleration. The spatial discretization uses a second-order central differencing scheme. It is equipped with several turbulence models, from which the one-equation of Spalart and Allmaras [19] has been chosen for the investigation in this paper. When running steady state the solver uses a so-called mixing-plane between rotating and nonrotating cascades, which mixes out circumferential variations. The averaging for the mixing planes is done, using a consistent approach from Denton [20].

A nonreflective treatment of outflowing characteristics is applied, which creates a high level of independency from axial spacing between blade rows and mixing planes [21]. The unsteady treatment makes use of fourth-order-accurate sliding meshes at the interfaces, direct periodicity at circumferential borders, as LISA is of integer blade ratio nature, and dual time stepping with a second-order time stepping scheme.

The LISA rig has been modeled in this investigation using simple straight H-meshes, without discretization of shroud leakages (see Fig. 3).

Results and Discussion

The following presentation and interpretation of the measurement and calculation results of the flow field will refer to the three measurement planes in the order as the flow passes through them. In this context, comparisons between experimental and numerical results will be commented. Effects occurring due to stator-stator and rotor-rotor clocking will be commented on in the corresponding sections. An evaluation of performance measurements will be given in the last part of the paper.

Flow Behind First Stage (MP 1). The flow in between the first and the second stage is dominated by secondary flow structures created within the first rotor blade row. Remaining flow features from the first stator are seen as quasi-stationary effects. The flow field in this measurement plane is exposed to the potential field of the second stator, which has a dominating influence in the following flow parameters such as static pressure and flow yaw angle.

Due to the application of five-hole probes, the measurements are pneumatically averaged and do not show pitchwise resolution of the high-frequency signal of the passing rotor blades. However, the rotor signal is still resolved in the radial direction. This fact allows the detection of quasi-steady flow features, which originate in the first stator blade row. These features are quasi-stationary in the absolute frame of reference, since they are not moving relative to the stators, but they are modulated in time by the rotor blades.

According to the relative circumferential position of the first stator, the location varies, where its secondary flow structures approach the leading edge of the second stator. This dependence can be seen in the pneumatically averaged distribution of the total pressure coefficient Cpt downstream of the first rotor for eight different stator-stator clocking positions (Fig. 4). The distribution of Cpt in the pneumatically averaged area plots shows only a minor influence on the position of the second stators potential field. Regions of higher and lower Cpt values can be observed from 20% to 80% span, which are corresponding to the position of the first stator. The span region from 0% to 20% is dominated by the passing rotor hub passage vortex and the flow, which is going into the second stators cavity. At the tip region the leakage jet from the rotor cavity is seen as low Cpt values from 90% to 100% span. At around 85% span, the trace of the passing rotor tip passage vortex appears.

The first stator's secondary flow structure forms a region of low total pressure (see dotted line in Fig. 4), which is inclined relative to the radial direction. This flow structure can be viewed as a wake-vortex secondary flow "package." Hence, by clocking the stators relatively to each other, it cannot be achieved that all parts of the package are aligned with the second stator's leading edge at one certain clocking position. In the opinion of the authors the reasons for the inclination are remaining exit swirl out of the blade rows of the first stage as well as a nonconstant spanwise loading distribution on rotor one.

The pneumatically averaged values of the absolute flow angles downstream of the first rotor blade row reflect the position of the secondary flow package that originates from the first stator. Depending on whether a part of the secondary flow package of the first stator hits the second stator LE or passes in between the two stator blades, it creates a more or less uniform flow angle distribution across the pitch. This effect is demonstrated in Fig. 5 for two exemplary span positions, 29% and 79%. The absolute flow

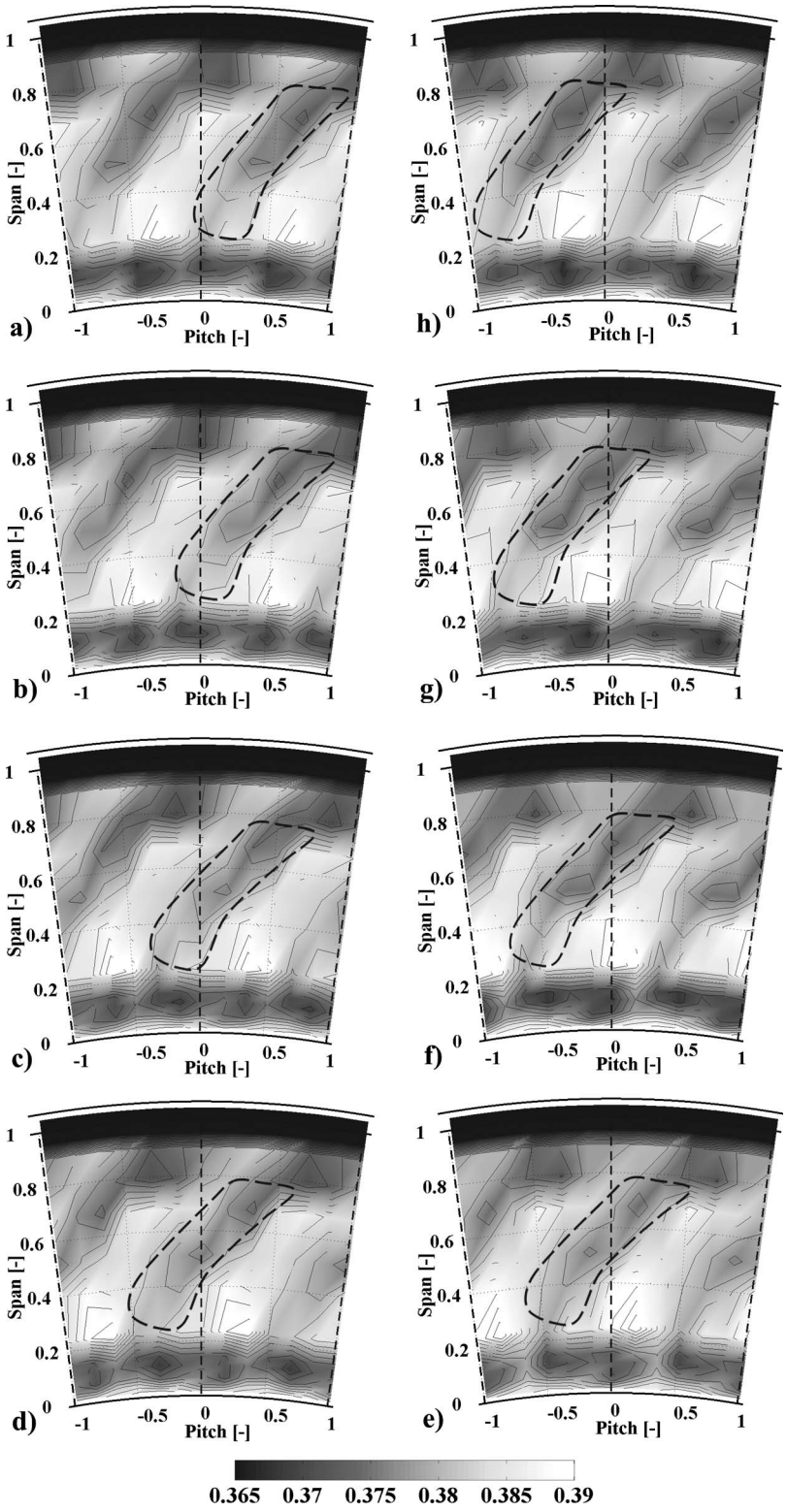

Fig. 4 TC2—total pressure coefficient Cpt [−] downstream of Rotor 1 at eight different stator-stator positions at RR00 (coarse grid measurement, pneumatically averaged). (*a*) SS00, (*b*) SS12.5, (*c*) SS25, (*d*) SS37.5, (*e*) SS50, (*f*) SS62.5, (*g*) SS75, and (*h*) SS87.5.

angle distribution across two pitches is shown at the stator clocking positions where it has its minimum and maximum amplitude. The shaded area represents the variation of flow angles, which occurs at the intermediate stator clocking positions. The following four cases can be distinguished for these two span positions:

Case I—SS000: The part of the secondary flow package at 79% span passes in between two stator blades. A maximum peak-to-peak value of the flow yaw angle can be observed at this pitch

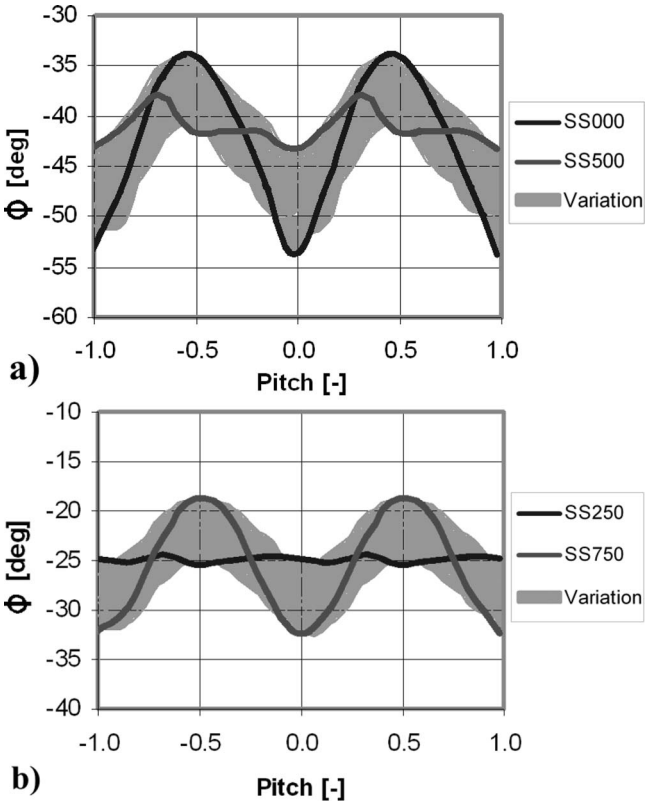

Fig. 5 TC2—pitchwise distribution of absolute flow yaw angle downstream of rotor 1 at (*a*) 79% and (*b*) 23% span (eight stator clocking positions at RR00)

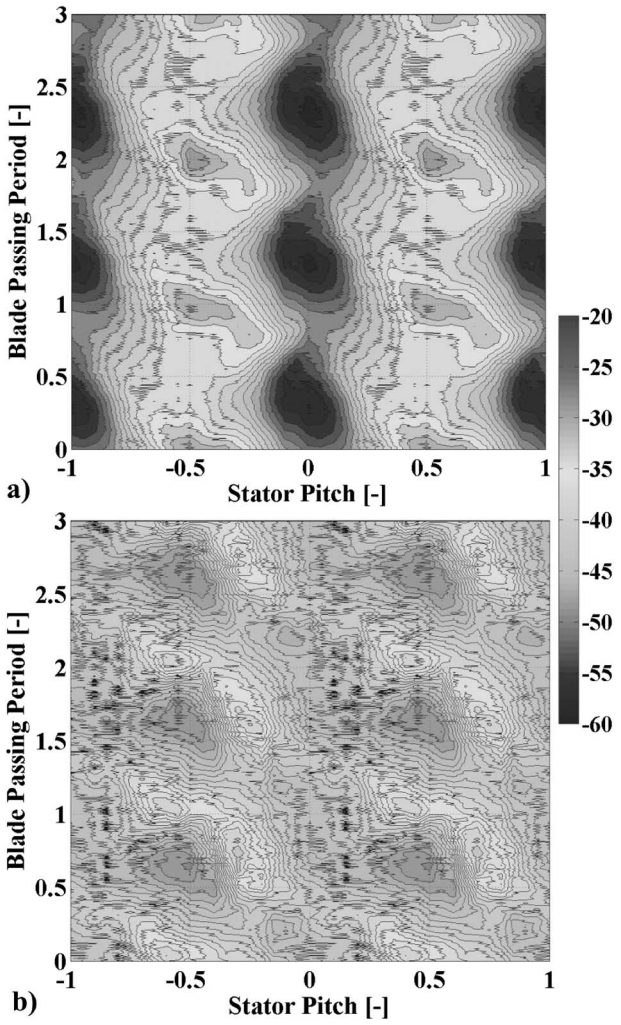

Fig. 6 TC2—time resolved pitchwise distribution of absolute flow yaw angle downstream of rotor 1 at 79% span (*a*) SS00RR00 and (*b*) SS50RR00

position ($\Delta\phi$=20 deg).

Case II—SS250: The part of the secondary flow package at 23% span hits the LE of the second stator. The flow angle at this span position shows the smallest variation across the pitch compared to the other clocking positions ($\Delta\phi<1$ deg).

Case III—SS500: The part of the secondary flow package close to the tip (79% span) hits the LE of the second stator. The flow angle at this span position shows the smallest variation across the pitch compared to the other clocking positions ($\Delta\phi$=5 deg).

Case IV—SS750: The part of the secondary flow package at 23% span passes in between two stator blades. A maximum peak-to-peak value of the flow yaw angle can be observed at this pitch position ($\Delta\phi$=14 deg).

In order to verify this observation, unsteady measurement results for cases I and III are available and presented in Fig. 6. The time-distance diagrams show the flow angle variation across two stator pitches during a time of three rotor blade passing periods. Stationary flow features, i.e., a potential field around a stator LE, will be expressed in such plots as parallel to the vertical axis. Flow features moving with the rotor, i.e., rotor wakes, are detectable as diagonal lines oriented from the lower right to the upper left, according to the rotational direction of the rotor. In the case of the current geometry, one stator pitch corresponds to one blade passing period due to an identical number of blades in the stator and rotor stages. Both unsteady plots underline the findings from the steady measurements (Fig. 5(*a*)). The 50% stator clocking case at 79% span shows much more evenly distributed flow angles across the pitch compared to the 0% stator clocking case.

What was explained on that exemplary span position can be applied to the whole pitch. Due to the inclined shape of the secondary flow structure created in the first stator, it is not possible to have evenly distributed flow angles across the pitch at all span positions at one certain stator clocking position. To visualize this fact, two different stator clocking cases are shown in Fig. 7, SS00 and SS50. The previously discussed span positions are marked as dotted lines across the circumference. The minima in flow angle at 79% span and SS00 can be located in front of the stator leading edge. If both cases are subtracted from each other, the effect of clocking on flow yaw angles can be observed (Fig. 8). Each radial position shows an alternating distribution of minima and maxima of flow yaw angle differences across the span. A pitchwise averaged distribution across the span helps to evaluate the integral effect for each span position. For this case, the 50% clocking of the stators results in an underturning at the tip region down to 80% span. In the midspan region, no significant change is noticeable. From 0% to 25% span an over-under-turning effect can be observed, which results from the interaction of the rotor hub passage vortex and the derivative of the shed stator hub passage vortex. During the time of a rotor blade passage, when these two features interact with each other, the rotor hub passage vortex is weakened. The position of the second stator's leading edge relative to this interaction zone is of high importance. If the interaction happens in front of the leading edge, a weaker rotor hub passage vortex approaches the second stator's leading edge. Hence, the potential of loss production is reduced. If the interaction occurs in the midpitch area, the rotor vortex with its full strength approaches the leading edge of the second stator. The effect of this phenomenon can be observed in reduced performance of this span region at a stator clocking position of 50%

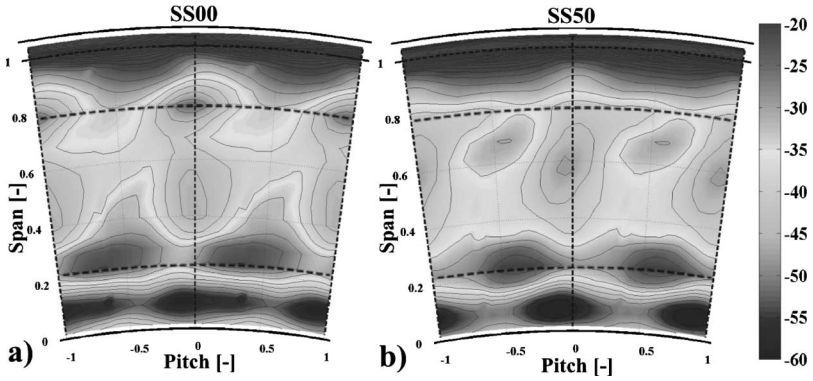

Fig. 7 Flow yaw angle distribution downstream of rotor 1 at (*a*) 0% and (*b*) 50% stator clocking (RR00)

when compared to the 0% position.

Resulting from this discussion it can be stated that, in the current case, the inlet angle distribution of the second stator depends especially on the position of the derivatives of the first stators passage vortices. The wake structure appears only in a very limited area and has minor influence. In addition the impact of the cavity flow has to be considered when clocking the stators.

After the potential of the stator clocking on incidences on the second stator has been shown, now the rotor-rotor clocking will be evaluated. Figure 9 shows for the SS00 and SS50 test cases the difference in flow yaw angles between rotor clocking of 50% and 0% pitch. When the stators are aligned the rotor clocking has very little influence on the flow angles in front of stator 2. Whereas in the SS50 case, there are significant differences, which are observed in the hub region up to 20% span, as well as close to the casing endwall. However the midspan region remains unchanged. This comparison leads to the conclusion that at the endwalls, the potential field of the downstream second rotor can have an upstream effect on the inlet flow angles of the second stator, if an appropriate stator-stator clocking position has been chosen.

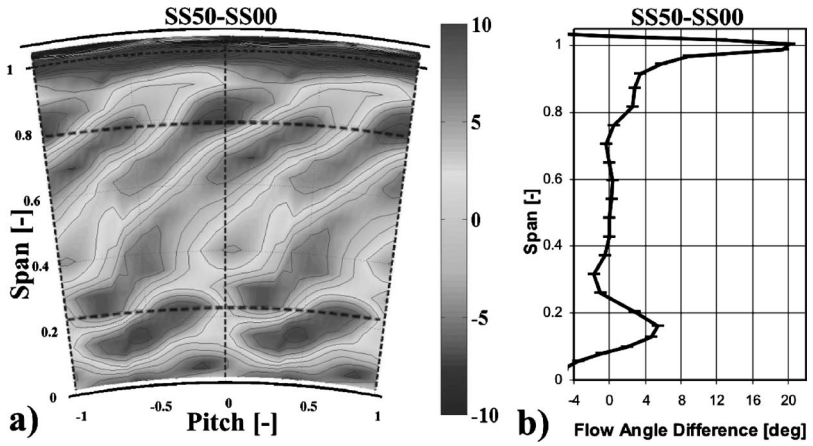

Fig. 8 Difference of flow yaw angles between 50% and 0% Stator clocking (RR00) downstream of rotor 1. (*a*) Pitchwise distribution and (*b*) circumferentially massaveraged and spanwise distribution

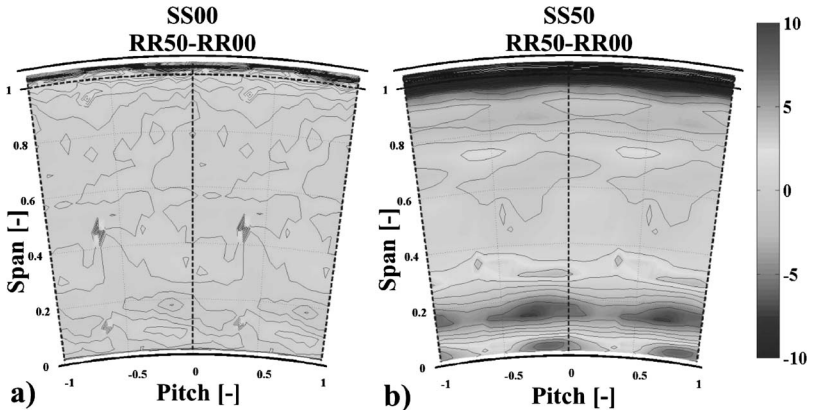

Fig. 9 Difference between 50% and 0% rotor clocking in flow yaw angle distribution downstream of rotor 1 at (*a*) SS00 and (*b*) SS50

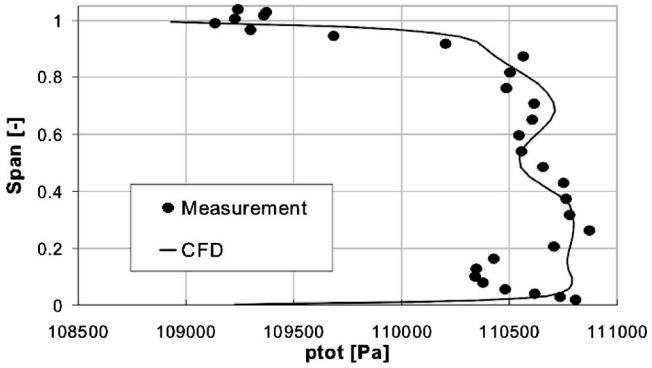

Fig. 10 Spanwise total pressure distribution downstream of rotor 1—comparison of CFD and experiment

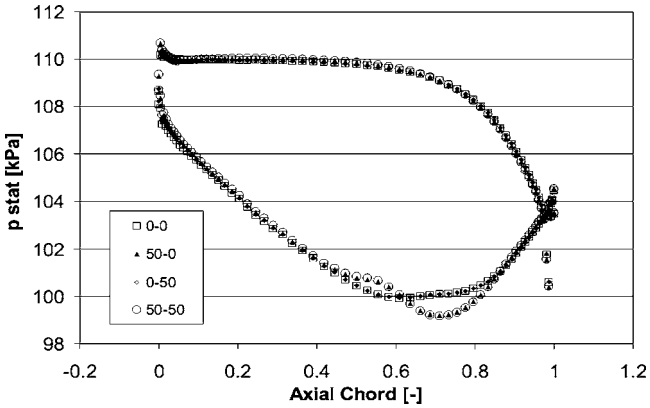

Fig. 12 CFD—static surface pressure distribution of stator 2 at 79% span for four different stator and rotor clocking cases

In order to evaluate the accuracy of the CFD prediction for the current case a comparison of pitchwise averaged total pressures downstream of rotor 1 between experimental and numerical results is presented in Fig. 10. The CFD model seems to predict the midspan region from 20% to 85% span, being accurate to within 70 Pa. The neighboring areas at the endwalls are affected by cavity flows and the CFD prediction is not as good. To show also the applicability to clocking studies, the area distribution of total pressure coefficients derived from experiments and CFD at stator clocking positions 0% and 50% are shown in Fig. 11. From 0% to 20% span the measurement detects underturned fluid coming from the stator 1 cavity, which propagates through the rotor. It appears as a band of low Cpt in the plot. In the tip region the cavity flow bypassing the blades of the first rotor can be recognized. Due to energy dissipation in the labyrinth of the shroud, the area from 90% to 100% span shows Cpt values, which are 10% lower compared to the unaffected region of this plane.

Flow of Second Stator (MP 2). The variation of inlet flow angles in front of the second stator LE was discussed in the previous section. The modified inlet condition of the second stator blade row will have an effect on the static surface pressure distribution of this stage, and therefore an influence on the stator blade loading. CFD results of the static surface pressure distribution at 90% span are presented in Fig. 12. Differences between stator positions of 0% and 50% are noticeable, whereas rotor clocking does not have a significant influence. While the frontloading of the stator does not change, the aft-loading increases when clocking the stators to 50%. This difference shows an effect of the incidence on stator 2 in this span region.

The way in which a changed stator loading translates into a change in turning angle across this stator is demonstrated in Fig. 13. Experimental and numerical results show a good agreement in the midspan region from 20% to 75% span. This range has now decreased compared to the rotor 1 exit plane, due to the added rotor cavity leakage. However, both plots show strong similarities between both rotor clocking positions of the same stator clocking case. They agree as well in a span region (50% to 70%) where the turning angle has decreases, and a region (20% to 40%) where it increases, with setting the stator clocking to 50% of a pitch.

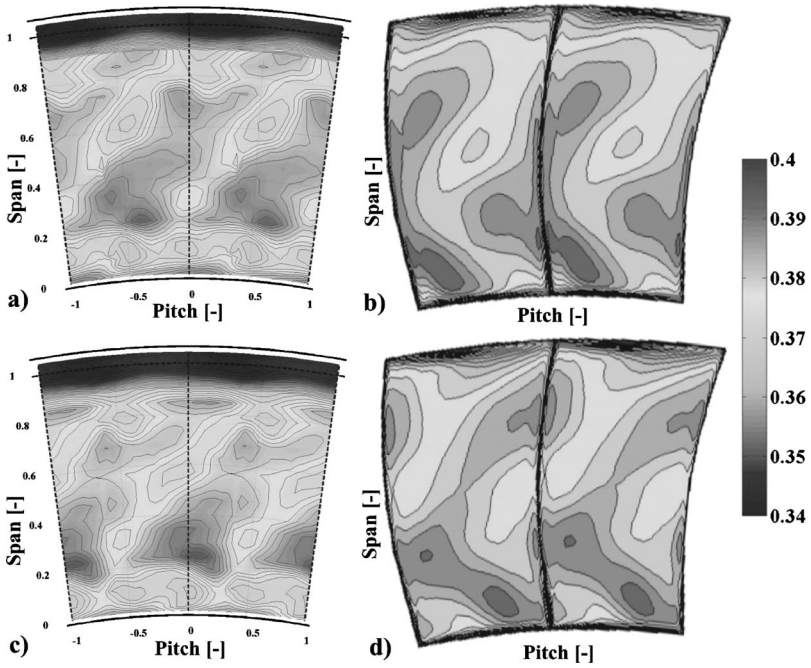

Fig. 11 TC1, CFD—comparison of total pressure coefficient distribution of experiment and CFD downstream of rotor 1 at RR00. (*a*) SS00 (Exp.), (*b*) SS00 (CFD), (*c*) SS50 (Exp.), and (*d*) SS50 (CFD)

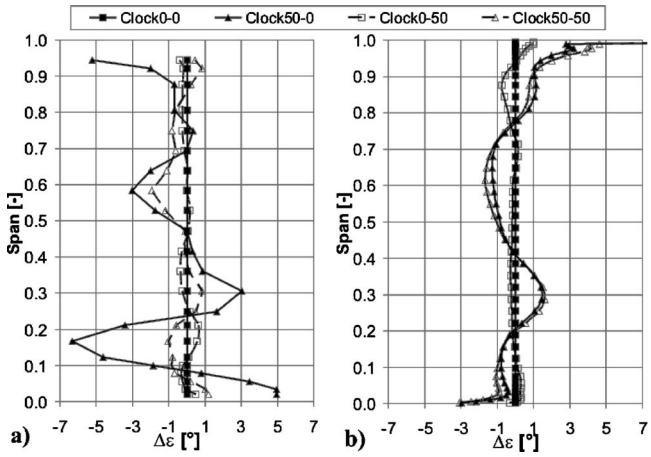

Fig. 13 Turning angle differences $\Delta\varepsilon$ across stator 2 of four clocking configurations (reference case is SS00RR00): (*a*) Experiment (TC1) and (*b*) CFD

The actual effect for the second rotor is expressed in the absolute exit angle of the stator. The same similarities between the four different cases as stated for the turning angle also apply here. Figure 14 shows that at the 50% stator clocking cases the stator exit swirl increased from 70% to 90% span, and it decreased from 50% to 70%. The maximum change in these regions of 2 deg in absolute flow yaw angle was achieved by clocking only the stator 50%. Additional clocking of the rotors by 50% reduced this effect. Hence, it is possible to achieve a change in incidence on the second rotor over a wide range of the span of up to 2 deg by clocking the stators.

The unsteady exit flow yaw angle development downstream of the second stator for two stator clocking positions is presented in Fig. 15. A pitchwise averaged spanwise distribution of the flow angle is plotted versus time, which is expressed in rotor blade passing periods. Due to the mass averaging, one vertical line represents the whole effective flow field at a certain moment in time. The contained information is therefore different from regular time-distance diagrams, which show only one pitch or span position. The comparison of both clocking positions shows higher flow yaw angles between 40% and 70% span for the 0% case. With that, the findings from the steady measurements (Fig. 14) can be underlined also with the unsteady results. From the comparison of the two unsteady cases it becomes clear that the stator

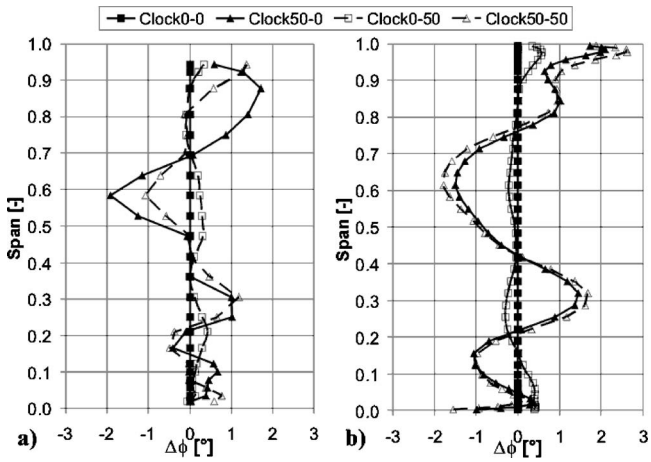

Fig. 14 TC1—absolute flow angle differences $\Delta\phi$ of four clocking configurations (reference case: SS00RR00) at stator 2 exit: (*a*) experiment (TC1) and (*b*) CFD

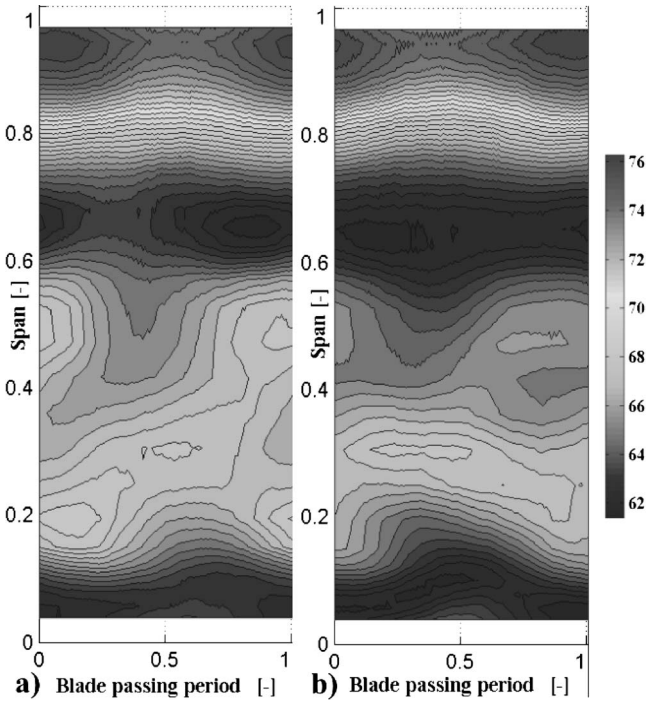

Fig. 15 TC2—time distance diagram of flow yaw angle downstream of stator 2, pitchwise massaverages spanwise distribution versus time: (*a*) SS00 and (*b*) SS50 at RR00

clocking on the tested configuration has strong influences on certain span regions, however there are others, which are much less affected. The modified flow conditions through the stator blade row between 0% and 50% stator clocking appear also in the entropy production of this stage.

In Fig. 16 the distribution of static entropy difference across the second stator is shown for both cases. The entropy was calculated according to Denton [20]. Comparing both cases, an overall increase in entropy across the span can be stated when clocking the stators to 50%. At the 50% clocking case the entropy is considerably higher in the region from 0% to 40% span. These different levels of entropy reflect the result of the interaction of the first rotor hub passage vortex and the secondary flow structure from the first stator. The stator trailing edge vortex that appears in the midspan region of the 0% clocking case seemed to have merged with the upper stator passage vortex at the 50% clocking case. Furthermore, the loss cores of the latter case are more detached from the trailing edge of the stator. In the opinion of the authors this is caused by the observed changes in incidence on the stator. Therefore it is reasonable that they can grow in a more unobstructed way and involve more massflow, which in the end results in a higher entropy level.

Flow Behind Second Stage (MP 3). Unlike the case of the exit of the first rotor, downstream of rotor 2 no potential field of a subsequent blade row is present. The secondary flow field at this point mainly comprises of the following three influences:

1. secondary flow generated in the second stator,
2. the secondary flow structures originated in the first rotor blade row, and
3. cavity leakage flows of each upstream blade row.

Isolation of every single influence is difficult since they are all interacting with each other. The impact of the secondary flows in this plane is significant. The exit plane of rotor 2 reflects the downstream effects of the given stator clocking position. In addition the effect of the rotor clocking becomes apparent. The super-

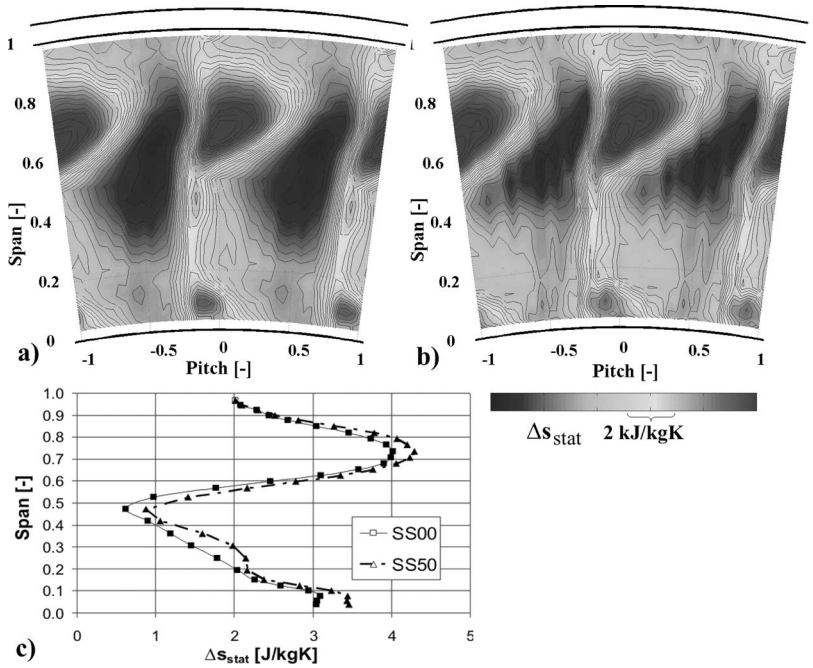

Fig. 16 TC2—measured static entropy difference across the second stator of (*a*) SS00 and (*b*) SS50 positions (both at RR00) and (*c*) corresponding pitchwise averaged spanwise distributions

position of both, the stationary and the rotating clocking of the two sets of blade rows, defines the flow condition of the second rotor. Consequently the performance of the second rotor should show an influence of the stator and the rotor clocking. This can be confirmed when evaluating the turning angles of the second rotor (Fig. 17).

A strong underturning effect occurs for the 50% stator clocking cases from 40% to 75% span, which is a result of the change in incidence in front of the stator blade row. For the adjoining span regions (80% to 100% and 20% to 40%) this changes into overturning. However, the integral value across the span of the change in turning angle is around zero. Changing the clocking position seems to improve and reduce the performance of a stage at the same time, depending on the radial position. The comparison with the numerical results shows again a good agreement with the experiment at the midspan region from 25% to 75%. Out of this region the influence of the cavity flow introduces a strong deviation between the results.

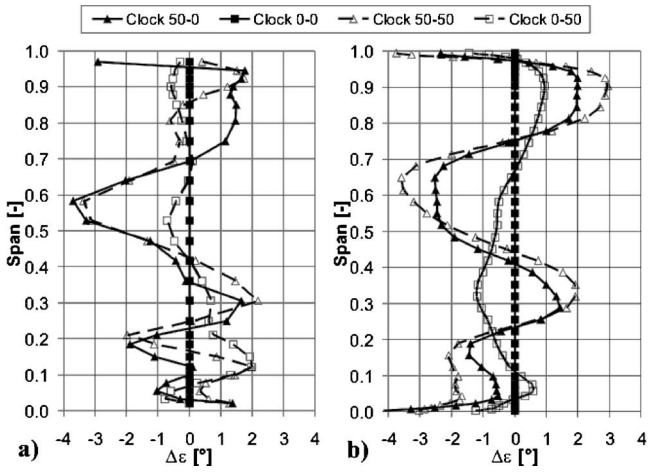

Fig. 17 Relative turning angle differences $\Delta\varepsilon$ across rotor 2 of four clocking configurations (reference case is SS00RR00): (*a*) experiment (TC1) and (*b*) CFD

Besides the characteristic differences between the stator clocking positions, the influence of the rotor clocking can be also observed. Keeping the stator clocking position constant and varying the rotor clocking position causes only minor changes in the shape and level of the flow yaw angle distribution. At SS00 an increase in the relative turning angle of $\Delta\varepsilon=1$ deg can be observed from 10% to 40% span when clocking the rotors from 0% to 50%. However, the difference in this span region at SS50 for the same rotor clocking positions is less than $\Delta\varepsilon=0.2$ deg. The opposite picture appears for the span region from 70% to 90%. There the difference is in the order of $\Delta\varepsilon=1.3$ deg at the 50% stator clocking position, when clocking the rotors. Both span regions happen to be in the area of the rotor passage vortices. The given combination of stator and rotor clocking positions defines whether there is an increase or decrease in performance in these regions.

Performance Evaluation

Experimental. Thermodynamic efficiencies of the three unsteady measured clocking configurations of TC2 are presented in Fig. 18. The graphs show the results of efficiency balances across both stages (turbine), stage 1 and stage 2. The thermodynamic total-to-total efficiency has been calculated from

$$\eta_{th}=\left(1-\frac{T_{t,\text{out}}}{T_{t,\text{in}}}\right)\Bigg/\left[1-\left(\frac{p_{t,\text{out}}}{p_{t,\text{in}}}\right)^{(\kappa-1)/\kappa}\right] \tag{1}$$

All three clocking cases show the difference in efficiency with respect to the reference case at 0% stator and 0% rotor clocking. The reference case has the highest thermodynamic efficiency of the evaluated cases when balancing both stages together. A maximum difference in relative thermodynamic efficiency between the clocking cases of 0.33% has been determined.

When clocking the stators to 50% the efficiency of the first stage increases, while the one of the second stage drops considerably. The first stage reveals a relative increase in efficiency of 0.32%, whereas the second stage decreases by 1.3%. This trade-

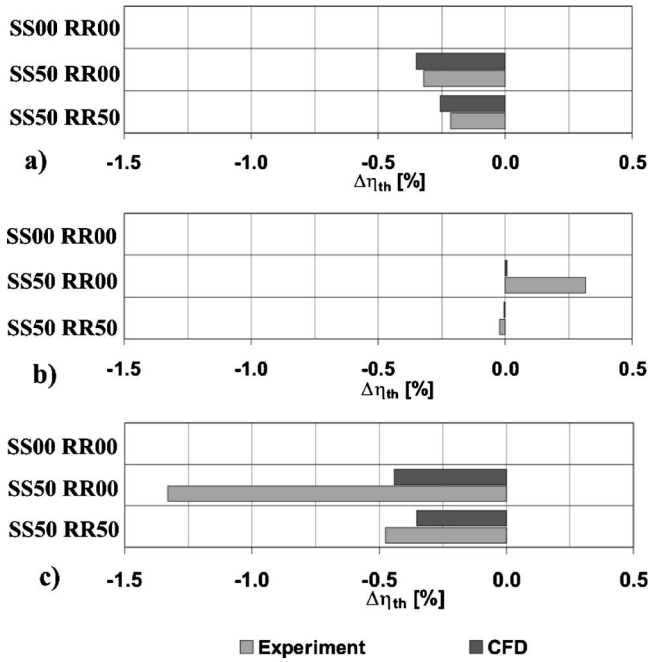

Fig. 18 TC2, CFD—relative thermodynamic efficiency difference to the reference case of three characteristic clocking configurations: (*a*) stage 1, (*b*) stage 2, and (*c*) turbine

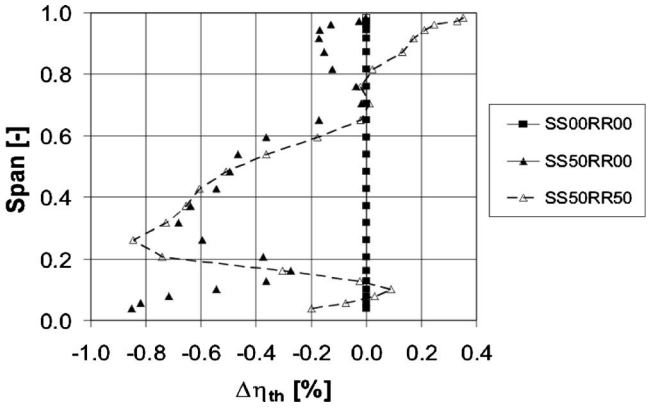

Fig. 19 TC2—spanwise distribution of turbine relative thermodynamic efficiency difference to the reference case of three characteristic clocking configurations

off between efficiency gain in one stage and efficiency loss in the other stage reveals the multistage effect of the clocking. It shows that it cannot be assumed that clocking has only an efficiency effect on downstream stages. In the present case the flow has a highly subsonic character, which increases the potential for flow effects to be transmitted upstream. This kind of phenomena was also observed by Haldeman et al. [22] when clocking a low-pressure turbine vane in a 1.5-stage transonic turbine.

If in addition the rotors are also clocked to 50%, the efficiencies of both stages again come closer to the one of the SS00RR00 position. This counterbalancing effect due to the clocking of the rotors compensates in the present case to a certain extent the negative effect of the stator clocking.

The observed effects of the experiments on relative efficiency between the clocking cases can also be seen in the numerical results. The CFD model shows the same trend, however it the underpredicts the effect of clocking on the efficiency of both stages, due to the insufficient modeling of endwall flows and numerical diffusion.

The radial distribution of thermodynamic efficiency balanced across both stages (Fig. 19) shows which span regions are affected most by the clocking. The plot shows the difference from the reference case SS00RR00. The regions where vortical structures were identified, 0% to 40% span and 80% to 100% span, show locally significant relative changes in thermodynamic efficiency up to −0.7%. The integral change in efficiency across the span corresponds with the values presented in Fig. 18(*c*). The higher overall efficiency of the SS50RR50 case compared to the SS50RR00 case comes due to a higher efficiency value close to the endwalls. Haldeman et al. [22] reported as well significant spanwise differences in the effect of clocking based on static pressure measurements. They have found the effect of clocking at 10% span to be most apparent.

The error analysis [23] shows that the relative uncertainty in efficiency between different test cases is in the order of 0.3%. The relative uncertainty between clocking cases of the same measurement campaign will be even less, since identical test and measurement conditions apply.

Due to the instrumentation of the test facility it is possible to measure rig operation parameters, such as the torque of the second stage and massflow. This allows the calculation of mechanic efficiency. The integral character of this value does not resolve any spanwise efficiency distribution. It is defined as the ratio of specific shaft power over the enthalpy difference of the isentropic expansion:

$$\eta_m = \left(\frac{\omega \cdot M}{\dot{m}}\right) \Bigg/ \left[c_p T_{in}\left(1 - \left(\frac{p_{t,\text{out}}}{p_{t,\text{in}}}\right)^{(\kappa-1)/\kappa}\right)\right] \tag{2}$$

The resulting values are plotted for comparison as the ratio of the actual value over the average of all values from a data set:

$$\Delta\eta_{m,\text{rel}} = \left[\eta_m \Bigg/ \left(\frac{1}{n}\sum_{i=1}^{n}\eta_{m,i}\right)\right] - 1 \tag{3}$$

The differences from the mean are plotted in Fig. 20. From the variation of the efficiencies versus clocking positions no systematic change can be observed. The maximum peak-to-peak variation is in the order of 0.3%. This magnitude of changes in mechanic efficiency is within the relative accuracy of the test facility. Reasons for these minor changes are suspected to be the strong three-dimensional character of the flow at each clocking position. Especially the second stage receives a highly complex flow field, containing secondary flow features from the upstream blade rows. The mixture of positive and negative effects of the current clocking position across the span results in a rather small change in mechanical efficiency.

Numerical. A series of 2D and 3D unsteady computations was performed for the different clocking cases (SS-RR: 0-0, 50-0, 0-50, 50-50). The 2D calculation considered only the midspan position, whereas the 3D method evaluates the whole span. In

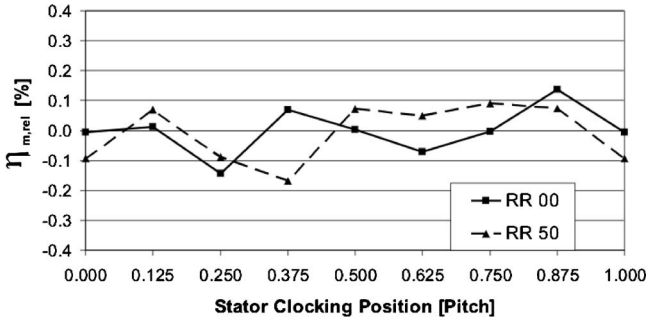

Fig. 20 TC2—total-to-total mechanic efficiency of the second stage at eight stator and two rotor clocking positions

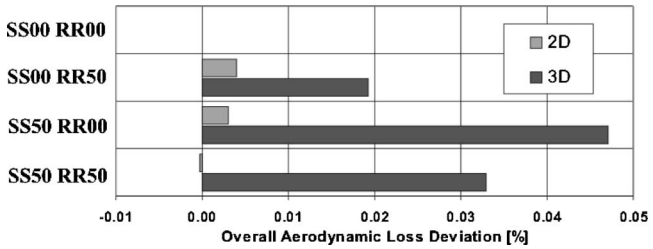

Fig. 21 CFD—overall aerodynamic loss deviation from reference case SS00 RR00

contrast to the 2D, which only accounts for profile losses, the 3D calculation realizes the full modeling of secondary flow propagation through the engine and the influences due to wall friction.

In Figs. 21 and 22 the results of both kinds of calculations are presented. All plots show difference values of the aerodynamic loss compared to the reference case of 0% stator clocking and 0% rotor clocking. The direct comparison shows several systematic differences, which illustrates the insufficiency of the 2D algorithms for the current low aspect ratio application.

In Fig. 21 the differences in aerodynamic loss are presented for each clocking case. The 2D results show a variation of the losses at midspan only in the order one-tenth of what has been calculated with the 3D algorithm. The reason for this is the strong influence of vortical structures in the flow field. Hence, the losses due to vortices and endwalls have a predominant character over losses created by wakes, which makes the midspan region not representative for the overall flow. However, in both calculations the reference case 0-0 has the lowest losses compared to the clocking positions. A closer look at the development of losses per row is given in Fig. 22. The most significant difference between the 2D and 3D methods appears in the losses of the second stator. An opposite result has been derived for this blade row with the two methods. There at the midspan, only the influence of the wake

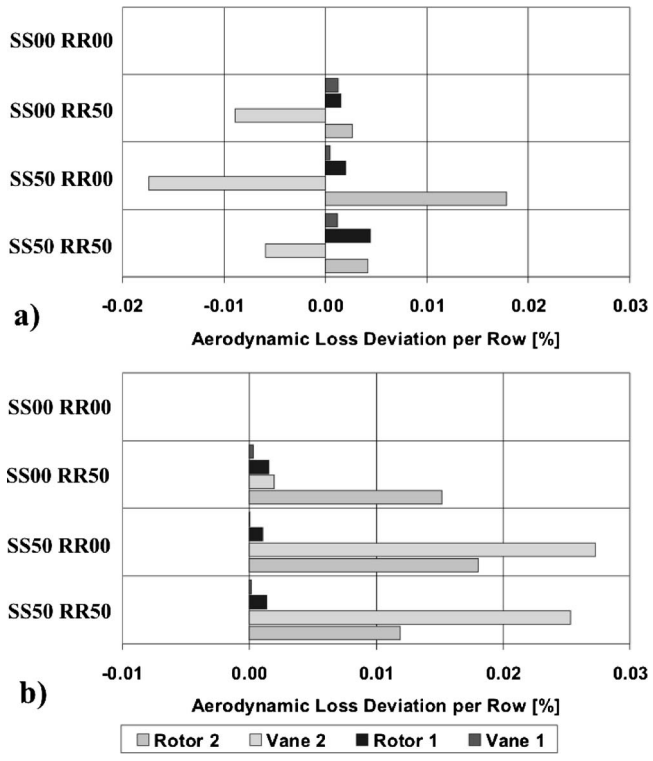

Fig. 22 CFD—aerodynamic loss deviation from reference case 0-0 clocking for each blade row: (*a*)) 2D and (*b*) 3D

clocking appears since vortices are not existent in the model. The more realistic result comes therefore again from the 3D calculation, where the influence of the clocking on the vortex propagation is also taken into account. The second stage shows generally a higher reaction on clocking than the first one and has also the bigger contribution to the overall losses. It can be concluded from the 3D numerical results that the rotor clocking, compared to the stator clocking, has only low impact on the stator losses. However, the relatively high loss generation of the second rotor for all clocking cases seems to indicate that the loss of rotor 2 depends on the same order of magnitude on two influences: (1) the relative position of rotor 2 to the first rotor's secondary flow remainders and (2) changes in loading of the second stator due to the clocking of the stators.

The second rotor seems to be the weakest part in the development of losses, as it can suffer under its own clocking position as well as ill-conditioned inflow characteristics from previous stator rows.

Observed efficiency changes are in the order of −0.35% from the reference case for the stator clocking and about −0.32% for the rotor clocking, while the combined case 50-50 differs in the order of −0.25%.

Conclusions

Stator-stator as well as rotor-rotor clocking effects have been investigated in a comprehensive experimental and numerical effort. The test case was a two-stage low aspect ratio axial turbine. Thus, a combined view on the flow field and the performance of blade rows and turbine was achieved. In addition, a 2D and 3D numerical study was performed to study the numerical effects of the current clocking case.

An overall change of relative mechanical efficiency of ±0.15% was experimentally determined. The maximum relative change in thermodynamic efficiency between two oppositional stator clocking positions was in the order of 0.3%.

Evaluating the applied measurement techniques it was found that steady, pneumatically averaged five-hole probe measurements are sufficient to derive overall performance values of turbine stages. In order to understand the influence of clocking on the interaction of flow features between neighboring blade rows, highly resolved unsteady measurements of the related flow fields are necessary.

The application of numerical methods for clocking investigations on turbines with low aspect ratio blading requires the use of 3D unsteady algorithms with a full nonlinear treatment. It allows correct modeling of secondary flow propagation through different blade rows and accurate prediction of flow angles. In 2D approaches the use of mixing algorithms between blade rows prevents the modeling of convective flow features that are dominant in such kinds of geometries. In the current case, the region from 0% to 40% span behind the first rotor is clearly dominated by a strong vortical structure, which is a combination of cavity leakage from the first stator and vortices of the first rotor.

The current study has demonstrated that the evaluation of overall performance of a certain clocking position requires the consideration of all stages. The performance of a downstream stage is set by its relative clocking position with respect to the preceding stage. However, in the upstream direction an effect influencing efficiency was detected. In the current test case the change from 0% to 50% stator clocking position caused a relative degradation of thermodynamic efficiency of the second stage by 1.3%. This was accompanied by an efficiency increase in the first stage of the order of 0.3%. The applied numerical methods show the same trend. However, due to insufficient modeling of cavity leakage flows involved in the experiment as well as numerical diffusion, this effect is underpredicted. At this point it has to be pointed out again that this rather small effect on efficiency is characteristic for the tested geometry. It must not lead to a general conclusion, that clocking has a minor influence on efficiency.

In the flow field of the investigated low aspect ratio blading vortex, interaction and propagation are more important than the influence of wakes. Vortices close to the endwalls are enhanced by leakage flows from the cavities. The wakes of the stators and the rotors are strongly affected by their adjoining vortical structures. Due to the resulting deformation of the wakes they cannot be clearly distinguished anymore in the flow field. Therefore an alignment of wakes relative to the leading edges of a subsequent bladerow is not as important as it is in high aspect ratio geometries.

Vortical structures can be seen as the instrument of redistributing low energy fluid in the radial direction. The convection and interaction of secondary flow structures results in local variations of flow angles, incidences, and loading. Therefore, clocking is affecting the performance characteristic of each radial position differently. The combination of the resultant performance characteristics across the span causes a nonlinear behavior of the overall stage. In order to have an overall efficiency benefit due to clocking, the blade design has to ensure that an efficiency increase can be achieved on the majority of the span by setting up a certain clocking position.

Acknowledgment

The authors gratefully acknowledge the support and the precious suggestions of Dr. Pfau and Dr. Schlienger. The geometries of the blades used in this investigation were developed during the course of the AG-Turbo project "500 MW auf einer Welle" funded by the German Federal Ministry of Economy (BMWI) under File Nos. 0327060D and 0327060F. In particular, Dr. E. Janke, Dr. H.-P. Schiffer, and Dr. H. Richter of Rolls-Royce Deutschland are acknowledged for their continuous support and kind permission to publish the results presented in this paper.

Nomenclature

c_p = Specific heat capacity at constant pressure, J/kg K
c_v = Specific heat capacity at constant volume, J/kg K
Cps = Static pressure coefficient, $Cps=(p-p_3)/(p_{t0}-p_3)$
Cpt = total pressure coefficient, $Cpt=(p_t-p_3)/(p_{t0}-p_3)$
$\dot{m}$ = massflow, kg/s
M = torque, N m
P = pressure, Pa
R = perfect gas constant, J/kg K
R = radius, m
S = specific entropy, J/kg K
T = temperature, K

Greek

ε = turning angle, deg
ϕ = flow yaw angle, deg
κ = isentropic coefficient, $\kappa=c_p/c_v$,
ω = rotational velocity, 1/s

Abbreviations

5HP = five-hole probe
CFD = computational fluid dynamics
FRAP = fast response aerodynamic probe
LE = leading edge
MP = measurement plane
RR = relative rotor-rotor clocking position
SS = relative stator-stator clocking position
TC = test case
TE = trailing edge
TET = turbine entry temperature

Subscripts

t = total
th = thermal
rel = relative frame of reference
m = Mechanical
0 = turbine inlet
1 = measurement plane 1
2 = measurement plane 2
3 = measurement plane 3

Superscripts

$\bar{}$ = circumferentially averaged
$\tilde{}$ = average across the pitch area

References

[1] Jouini, D. B. M., Little, D., Bancalari, E., Dunn, M., Haldeman, C., and Johnson, P. D., 2003, "Experimental Investigation of Airfoil Wake Clocking Impacts on Aerodynamic Performance in a Two Stage Turbine Test Rig," ASME Paper No. GT-2003–38872.
[2] Huber, F. W., Johnson, P. D., Sharma, O. P., Staubach, J. B., and Gaddis, S. W., 1996, "Performance Improvement Through Indexing of Turbine Airfoiles: Part 1—Experimental Investigation," J. Turbomach., **118**, pp. 630–635.
[3] Reinmöller, U., Stephan, B., Schmidt, S., and Niehuis, R., 2002, "Clocking Effects in a 1.5 Stage Axial Turbine—Steady and Unsteady Experimental Investigations Supported by Numerical Simulations," J. Turbomach., **124**, pp. 52–60.
[4] Gombert, R., and Höhn, W., 2001, "Unsteady Aero-dynamical Blade Row Interactions in a New Multistage Research Turbine—Part I: Experimental Investigation," ASME Paper No. 2001-GT-0306.
[5] Walraevens, R. E., Gallus, H. E., Jung, A. R., Mayer, J. F., and Stetter, H., 1998, "Experimental and Computational Study of the Unsteady Flow in a 1.5 Stage Axial Turbine with Emphasis on the Secondary Flow in the Second Stator," ASME Paper No. 98-GT-254.
[6] Tiedemann, M., and Kost, F., 2001, "Some Aspects of Wake-Wake Interactions Regarding Turbine Stator Clocking," J. Turbomach., **123**, pp. 526–533.
[7] Höhn, W., and Heinig, K., 2000, "Numerical and Experimental Investigation of Unsteady Flow Interaction in a Low-Pressure Multistage Turbine," J. Turbomach., **122**, pp. 628–633.
[8] Griffin, L. W., Huber, F. W., and Sharma, O. P., 1996, "Performance Improvement Through Indexing of Turbine Airfoiles: Part II—Numerical Simulation," J. Turbomach., **118**, pp. 636–642.
[9] Dorney, D. J., and Sharma, O. P., 1996, "A Study of Turbine Performance Increase Through Airfoil Clocking," AIAA Paper No. 96–2816.
[10] Dorney, D. J., and Sondak, D. L., 1996, "Three-Dimensional Simulation of Airfoil Clocking in a 1–1/2 Stage Turbine," AIAA Paper No. 96–2816.
[11] Sell, M., Schlienger, J., Pfau, A., Treiber, M., and Abhari, R. S., 2001, "The 2-stage Axial Turbine Test Facility LISA," ASME Paper No. 2001-GT-0492.
[12] Hourmouziadis, J., 1989, "Aerodynamic Design of Low Pressure Turbines," Lecture 8, AGARD LS-167.
[13] Treiber, M., Kupferschmied, P., and Gyarmathy, G., 1998, "Analysis of the Error Propagation Arising from the Measurements with a Miniature Pneumatic 5-hole Probe," XIVth Symposium on Measuring Techniques for Transonic and Supersonic Flows in Cascades and Turbomachines, Limerck.
[14] Kupferschmied, P., Köppel, O., Gizzi, W. P., and Gyarmathy, G., 2000, "Time Resolved Flow Measurements with Fast Aerodynamic Probes in Turbomachinery," Meas. Sci. Technol., **11**, pp. 1036–1054.
[15] Pfau, A., Schlienger, J., Kalfas, A. I., and Abhari, R. S., 2002, "Virtual Four Sensor Fast Response Aerodynamic Probe (FRAP)," Proceedings of the XVIth Bi-Annual Symposium on Measuring Techniques in Transonic and Supersonic Flows in Cascades and Turbomachines, Cambridge, UK, September 23–24.
[16] Dawes, W. N., BT0B3D, 1991, "A Computer Program for the Analysis of Three-Dimensional Viscous Compressible Flow in Tubomachinery Blade Rows," Manual for BT0B3D.
[17] Jameson, A., and Baker, T. J., 1984, "Multigrid Solutions of the Euler Equations for Aircraft Configurations," AIAA Paper No. 84–0093.
[18] Emunds, R., Jennions, I. K., Bohn, D., and Gier, J., 1997, "The Computation of Adjacent Blade-Row Effects in a 1.5 Stage Axial Flow Turbine," ASME Paper No. 97-GT-81.
[19] Spalart, P. R., and Allmaras, S. R., 1992, "A One-Equation Turbulence Model for Aerodynamic Flows," AIAA Report 92–0439.
[20] Denton, J. D., 1993, "Loss Mechanisms in Turbomachines," ASME J. Turbomach., **115**, pp. 621–656.
[21] Saxer, A. P., and Giles, M. B., 1993, "Quasi-Three-Dimensional Nonreflecting Boundary Conditions for Euler Equations Calculations," J. Propul. Power, **9**(2), pp. 263–271.
[22] Haldeman, C., Dunn, M. G., J., Barter, J. W., Green, B. R., and Bergholz, R. F., 2004, "Experimental Investigation of Vane Clocking in a One and 1/2 Stage High Pressure Turbine," ASME Paper No. GT2004–53477.
[23] Pfau, A., 2003, "Loss Mechanisms in Labyrinth Seals of Shrouded Axial Turbines." ETH Ph.D. dissertation no. 15226.

Design and Testing of a Transonic Linear Cascade Tunnel With Optimized Slotted Walls

Aldo Rona
Department of Engineering,
University of Leicester,
Leicester LE1 7RH, UK
e-mail: ar45@leicester.ac.uk

Renato Paciorri
e-mail: paciorri@dma.ing.uniroma1.it

Marco Geron

Department of Mechanics and Aeronautics,
University of Rome "La Sapienza,"
Via Eudossiana 18,
Rome 00184, Italy

In linear cascade wind tunnel tests, a high level of pitchwise periodicity is desirable to reproduce the azimuthal periodicity in the stage of an axial compressor or turbine. Transonic tests in a cascade wind tunnel with open jet boundaries have been shown to suffer from spurious waves, reflected at the jet boundary, that compromise the flow periodicity in pitch. This problem can be tackled by placing at this boundary a slotted tailboard with a specific wall void ratio s and pitch angle α. The optimal value of the s-α pair depends on the test section geometry and on the tunnel running conditions. An inviscid two-dimensional numerical method has been developed to predict transonic linear cascade flows, with and without a tailboard, and quantify the nonperiodicity in the discharge. This method includes a new computational boundary condition to model the effects of the tailboard slots on the cascade interior flow. This method has been applied to a six-blade turbine nozzle cascade, transonically tested at the University of Leicester. The numerical results identified a specific slotted tailboard geometry, able to minimize the spurious reflected waves and regain some pitchwise flow periodicity. The wind tunnel open jet test section was redesigned accordingly. Pressure measurements at the cascade outlet and synchronous spark schlieren visualization of the test section, with and without the optimized slotted tailboard, have confirmed the gain in pitchwise periodicity predicted by the numerical model. [DOI: 10.1115/1.2101856]

Introduction

In a linear cascade wind tunnel, tests of compressor and turbine blade profiles can suffer from spurious end-wall interference in pitch. In transonic tests, such interference can lead to passage-to-passage variations in blade loading, stage loss, stage outflow angle, and other performance parameters relevant to the design of a turbine stage.

Design guidelines for interference-free transonic test sections are given by Goethert [1]. Wall interface-free tests are typically achieved through the use of perforated or slotted boards, placed at the wind tunnel test section boundary. Goethert [1] reports theoretical models for both perforated and slotted end-walls. These models study the interference between these surfaces and a single impinging wave and they can be used to design interference-free test sections where the impinging wave pattern is known beforehand, like in the testing of simple aerodynamic shapes. More complex aerodynamic shapes, such as transonic cascade profiles, generate a flow-boundary interference of greater complexity. In such tests, the end-wall wave pattern is unknown beforehand, preventing the use of such a simple design approach by itself to perform a low interference wind tunnel end-wall design.

One empirical approach to design a low interference wall for a specific transonic wind tunnel is reported in Davis [2]. The simple geometry of a tapered cylinder was tested in this tunnel. Davis [2] obtained an empirical correlation for the variation of the optimal wall void ratio with the inflow Mach number. This correlation was obtained through intensive wind tunnel testing. The availability of an alternative end-wall design method that gives a more optimal low-interference test section with minimal wind tunnel testing would be useful to the industrial experimentalist. It could reduce the wind tunnel setup time for cascade tests, reducing the cost of tunnel tests.

The aim of this work is to gain an additional insight into the causes of end-wall interference in transonic cascade tunnels and to provide an effective computational fluid dynamic tool to design a wind tunnel test section with a reduced end-wall interference in pitch.

A new computational optimization is developed to design a specific transonic cascade wind tunnel geometry. The innovative aspect of this approach is that the optimization uses a computational fluid dynamic model to predict out-going disturbances at the cascade end-wall and a wave reflection model for slotted walls. This approach is different from previous designs of wind tunnel nonreflecting end-walls, which mainly addressed the effectiveness of slotted boundaries by considering the suppression of impinging single waves. Such studies often neglected to include in detail the geometry of the model being tested in the wind tunnel.

The remainder of this article is structured in four main sections. In the first section the performance limitations of the University of Leicester cascade wind tunnel are exposed, when this is operated with non-optimal open jet end-walls, are exposed. Wind tunnel tests show that the test section is affected by significant flow-boundary interference. This survey sets the benchmark to evaluate improved end-wall geometries. The second section gives an analytical description of the end-wall interference in the transonic wind tunnel flow, leading to a validated numerical model for such interaction, applicable to computational fluid dynamic methods. In the third section, the original University of Leicester wind tunnel test section is studied, by computational fluid dynamics, with several alternative end-walls and a low end-wall interference configuration is identified that is tailored to this specific cascade geometry and wind tunnel inflow. The fourth section verifies by experiment the performance improvement of the configuration optimized by computational fluid dynamics.

Performance Limitations of an Open Jet Cascade Wind Tunnel

Experimental Facility. The University of Leicester cascade wind tunnel is a useful tool to study wall interference effects in linear cascade test. The wind tunnel working section features re-

Contributed by Turbomachinery Aero Division of ASME for publication in the JOURNAL OF TURBOMACHINERY. Manuscript received October 6, 2004; final manuscript recieved June 23, 2005. Review conducted by D. Prasad.

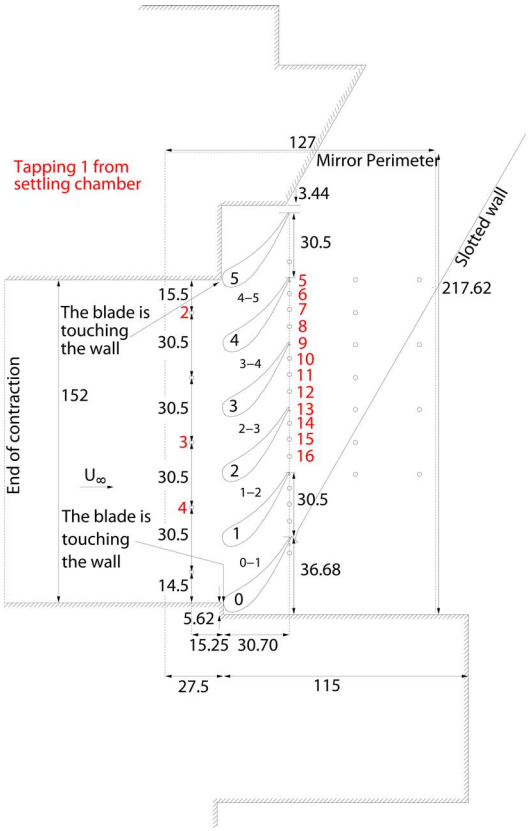

Fig. 1 Side view of the wind tunnel test section. All dimensions are in mm.

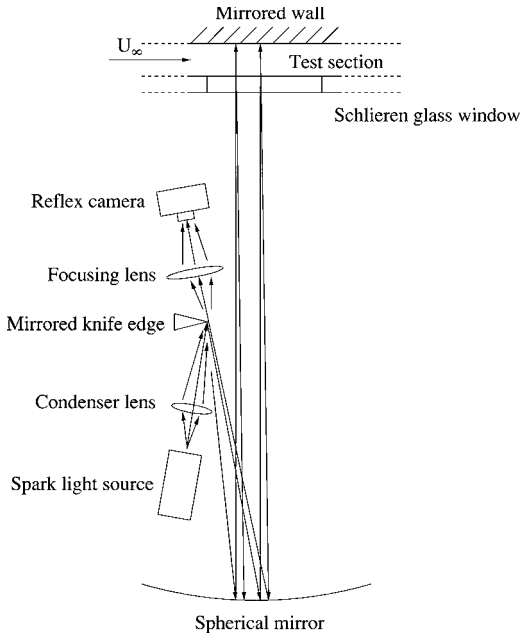

Fig. 2 Double pass schlieren schematics

movable boundaries in pitch, to perform open jet discharge tests. The tunnel is an intermittent transonic blow-down test facility, supplied by a 6 MPa gauge 6 m^3 air reservoir. Compressed air is admitted to a settling chamber by a Fisher valve with pneumatic feedback, which controls the settling chamber pressure. A 20 to 1 convergent contraction admits the flow from the settling chamber to a 152 mm high × 50 mm span working section that discharges in the ambient laboratory air with no diffuser.

To study end wall interference effects, a transonic test was setup, in which a linear nozzle cascade was used at a pressure ratio higher than its design value, to produce supersonic flow at the cascade exit. Six nozzle blades of Rolls Royce T2 profile [3] were tested in the linear cascade assembly shown in Fig. 1. The blade chord $\bar{c}$ is 45.27 mm. The design cascade isentropic exit Mach number M_d is 0.955. Tests were conducted at a nominal laboratory ambient to settling chamber pressure ratio $p_a/p_0 = 0.3728$, which corresponds to an isentropic exit Mach number $M_e = 1.27$ and a typical exit flow velocity $u_e = 383$ m/s.

Measurement Techniques. Synchronous spark schlieren flow visualization [4,5] and wall pressure measurements are used to assess the pitchwise periodicity in the discharge and to visualize nonperiodic features in the flow. The University of Leicester cascade tunnel is instrumented with a double-pass schlieren flow visualization system. The optical setup for the schlieren system is described in Fig. 2. White light is provided by an argon jet spark light source. The flash time is about 200 μs and the flash intensity halves in about 150 μs. A condenser lens focuses the light on the mirror side of a half-mirrored knife edge which reflects it towards a 0.3 m diameter $f = 2.44$ m (8 ft) spherical mirror. The knife edge is located one focal length away from the mirror, therefore this alignment results in a parallel light beam from the spherical mirror that illuminates the cascade test section. The test section is front-faced by a 25.4 mm thick schlieren grade glass window. As the beam passes through the test section, local variations in air density change the air refractive index, bending the incident rays in response to the density gradients in the flow [4]. The light beam is then reflected by the back wall of the test section, which is made of mirror polished stainless steel. The beam passes twice through the test section, augmenting the refraction of these rays with respect to a conventional single pass schlieren setup. The beam then converges back onto the knife edge, past a focusing lens and an image is collected by a Reflex camera body. The camera has no lens and the chassis is used to support a 35 mm black and white 400 ASA film. The camera trigger activates the flash of the argon jet spark source. A conservative $\frac{1}{60}$ of a second shutter speed ensures that the film is fully exposed to the 200 μs flash, which, at the discharge flow conditions, adequately freezes the flow. To improve the contrast in the black and white photographs, the laboratory illumination is subdued.

The mirror at the back of the test section is equipped with 0.5 mm diameter static pressure holes from which measurements of the wall static pressure are made [5]. Sixteen pressure holes, or tappings, are used in this study. Tapping 1 is located in the settling chamber. Tappings 2–16 are located as shown in Fig. 1. Specifically, tappings 2–4 are upstream of the nozzle blades and tappings 5–16 are located $\frac{1}{4}$ blade pitch apart along the cascade trailing edge line, as detailed in Fig. 3. These tappings are connected via 2 mm manometer piping to a 16-port DSA3017 electronic differential pressure transducer. This transducer has a range from −101.3 kPa to 206.7 kPa and is activated by the Reflex camera trigger via a Stanford Research Systems 535 signal generator, to improve the synchronization of the pressure record acquisition with the flash arriving on the film.

During a typical tunnel blow down, the settling chamber pressure p_0 fluctuates about the test point $p_a/p_0 = 0.3728$. A number of pressure acquisitions, synchronous to the schlieren photographs, are acquired during each test, giving a time-accurate record of the stagnation to ambient pressure ratio history, sampled at about 1 Hz. To estimate the normalized wall pressure distribution at $p_a/p_0 = 0.3728$, the zero crossings of the sampled function $f(t) = p_a/p_0 - 0.3728$ are obtained by linear interpolation of the ambient to stagnation pressure history. The normalized pressure p/p_0 at

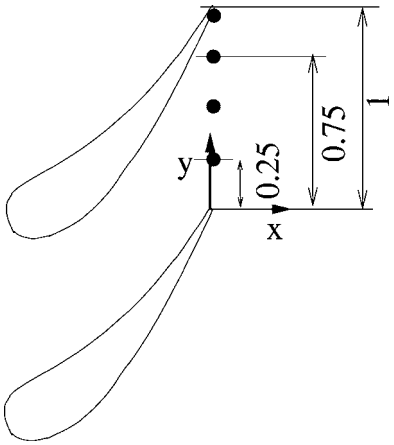

Fig. 3 Blade passage exit geometry in the cascade linear assembly, showing the wall pressure tappings (•). All dimensions are normalized by the blade pitch *h*.

every wall pressure tapping is then linearly interpolated in time, synchronous to the $p_a/p_0=0.3728$ crossings, and ensemble averaged.

Open Jet Cascade Flow. Figure 4 shows a selected schlieren record of the linear nozzle cascade tested at an isentropic exit

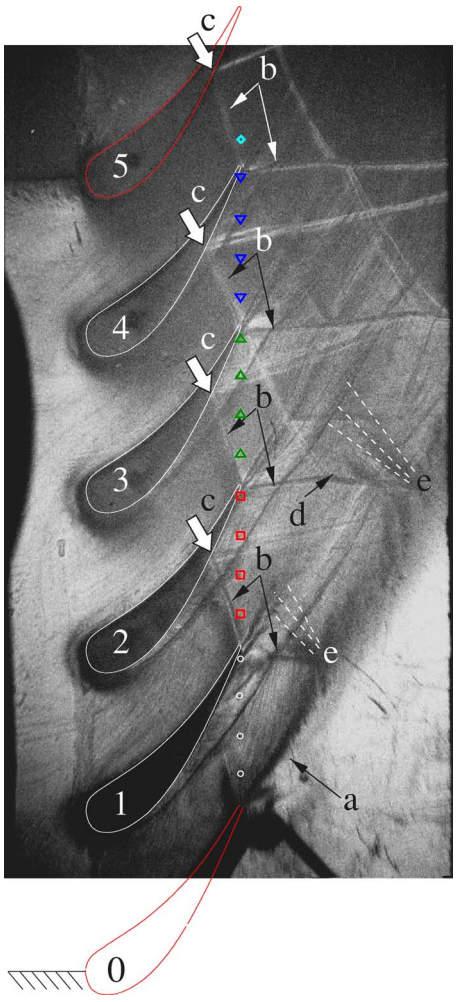

Fig. 4 Experimental schlieren visualization of the cascade flow discharge without a slotted wall

Mach number $M_e=1.27$. As the discharge is supersonic, disturbances generated at the discharge pitchwise boundaries follow downstream propagating characteristic lines. It is therefore possible to define the area affected by the presence of the open jet boundaries in this high Reynolds number flow. The profile leading edge of each blade is upstream of the open jet boundaries and is therefore unaffected by end-wall disturbances. Such disturbances can only affect the suction side trailing edge of a blade, as the leading edge is shielded by the neighboring blade, as shown in Fig. 4. Similarly, each blade pressure side faces away from the outer pitchwise boundary and it is thus shielded from these disturbances. This pattern drives the analysis of the cascade flow to focus on the passage outlet and on the discharge, where the effects of the cascade pitchwise boundaries are expected to take place.

Downstream of the blade 0 trailing edge, a thick shear layer separates the high-speed discharge from passage 0-1, between blades 0 and 1, from the surrounding low-speed air in the laboratory. The initial development of this shear flow is driven by the supersonic expansion in the rear section of passage 0-1, which continues past the trailing edge. Downstream of blade 0, the shear layer bulges outwards, similarly to an underexpanded jet, driven by a streamwise pressure gradient at the cascade outlet. This shear layer is significantly thicker compared to the mixing regions downstream of the trailing edges of the other blades in the cascade. These narrower mixing regions also run more parallel to the each other. The discharge through passage 0-1 differs with respect to the outflow from other passages, making the cascade discharge nonperiodic.

In Fig. 4, tailing edge shocks are identified by arrows **b**. These stem from the neighborhood of the blade surface and form a fish-tail shock pattern. In passage 0-1, the supersonic expansion changes the trailing edge fish-tail structure beneath blade 1, creating a lambda shock, close to the trailing edge. This shock stems more normal to the flow, compared to the corresponding shocks from the other blades. On each internal blade, the pressure side branch of the trailing edge shock impinges against the suction side of the neighboring blade and is reflected in the downstream direction. Arrows **c** in Fig. 4 mark the point of impingement of this shock on each blade surface. The reflected shock off blade 2 is oriented differently with respect to the ones from all other blades, indicating that the overexpansion in passage 0-1 has also affected the discharge through passage 1-2.

The blade trailing edge shear layers intercept the suction side branch of the trailing edge shock from neighboring blades as they deploy downstream. Shock-shear layer interactions produce reflected and refracted waves. The location of one of such interactions is shown by arrow **d** in Fig. 4. A refracted wave, propagating beyond the shear layer, is obtained when one of the suction side trailing edge shock branches crosses one of the thin shear layers shed by blades 1–4. In the interaction with the thick shear layer from blade 0, the impinging shocks are fully reflected back towards the inner passages as expansion fans. Two such reflections are identified by label **e** in Fig. 4, marking the shock impingement point. This shock-shear layer interaction, specific to the blade 0 shear layer, leads to further nonperiodic shock-shear layer interactions over the cascade pitch. The path of the expansions from **e** are traced by dashed white lines. They propagate through passage 0-1 and continue through the other internal passages. These expansions overexpand the whole flow field with respect to a periodic model flow discharge [6]. These expansion fans are another significant cause of loss of pitchwise periodicity in the cascade. Further details on these flow features, aided by the tracing of selected characteristic lines, are available in Rona et al. [6] to the interested reader.

Figure 4 also provides evidence of secondary flows at the mirror end of the cascade. Horseshoe vortices are captured in the schlieren record around the blades. These are due to the interaction of the on-coming boundary layer over the 127×218 mm^2 mirrored back wall with the blade profiles. These vortices are

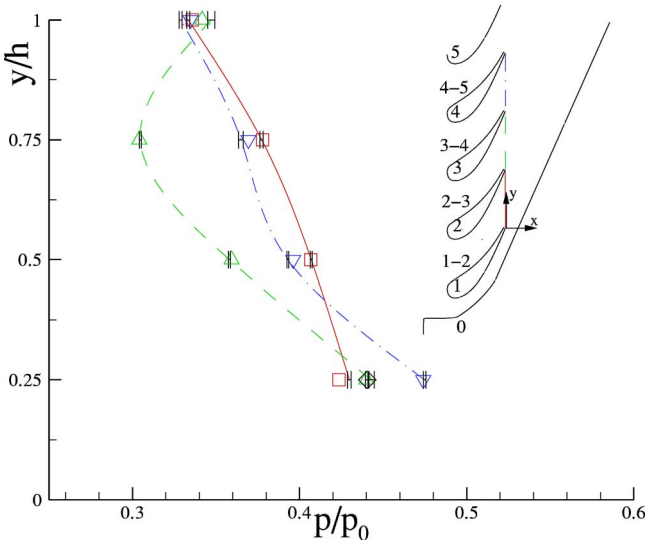

Fig. 5 Normalized wall pressure distribution in the discharge from a free jet cascade along the trailing edge line. (–, □) passage 1-2, (– –, △) passage 2-3, (– · –, ▽) passage 3-4, (◇) passage 4-5

most noticeable below the suction side of blades 1 and 2 and are denoted by thin dark lines running parallel to the passage outflow shear layers. To capture these secondary flow features, the focal plane of the schlieren setup was made to coincide with the mirrored wall. This arrangement makes secondary flows very prominent in the photographic record. However, a three-dimensional numerical study by Rona et al. [7] indicated that these secondary flows are of limited spanwise extent and that, at the selected test conditions, the discharge at the wind tunnel mid-span is essentially two-dimensional.

A quantitative insight into the periodicity of the discharge from the cascade with a free jet boundary is given by the measured normalized wall pressure distribution in Fig. 5. In this figure, the wall pressure distribution along the blade trailing edge line is normalized by the settling chamber stagnation pressure p_0. The vertical axis y covers one blade pitch, between two consecutive blade trailing edges in the linear cascade, such as between blades 0 and 1. The y axis is normalized by one blade pitch $h=0.67\bar{c}$, which is the same pitch as in Oldfield et al. [3]. Measurements of wall static pressure are obtained from passages 1-2, 2-3, and 3-4. From each passage, four pressure measurements are taken along the pitch, at $0.25h$, $0.50h$, $0.75h$, and $1.00h$, as shown in Fig. 3. From the schlieren photograph of Fig. 4, the positions of these 0.5 mm diameter ports were directly visible as dark dots on an electronic enlargement of this photographic record. These ports have been remarked by hollow symbols to render their location more visible in Fig. 4. In Fig. 5, the experimental values use the same symbols of the corresponding pressure ports.

Symbols □, △, and ▽ in Fig. 5 report the pressure distribution acquired from a single acquisition, synchronous to the schlieren record of Fig. 4. The diamond symbol (◇) and the lines show the wall pressure distribution at $p_a/p_0=0.3728$ obtained from up to 44 acquisitions by ensemble averaging, to reduce the effects of the settling chamber fluctuations during these tests. A cubic spline curve fit is used to interpolate in pitch between the ensemble averaged measurements, to give a qualitative view of the wall pressure trends across the passages.

There is a good overlap between the synchronous pressure measurements and the ensemble average results, indicating that the selected schlieren record is a close match to the test design conditions. In the range $0 \leqslant y/h \leqslant 0.25$, the wall static pressure is expected to increase approaching the pressure side of the blades, generating localized wall pressure maxima that have not been extrapolated from the experimental results.

The pressure distribution at the outlet of passage 1-2, denoted by squares (□) in Fig. 5, is higher than the distributions from the other passages. This indicates that the discharge between blades 1 and 2 is comparatively underexpanded. In passage 2-3, the experimental pressure record, reported by triangles (△), is lower than the other ones, indicating an overexpansion of the flow. Passage 3-4 is underexpanded with respect to passage 2-3, resulting in a pressure distribution that is in between those of the two preceding passages. This gives a pattern of alternating underexpansions and overexpansions. Such pattern is driven by the complex wave structure induced by the cascade pitchwise outer boundary, visualized in Fig. 4. This wall pressure distribution confirms and assesses, through a quantitative measurement, the presence of pitchwise nonperiodicity in the cascade flow.

The pressure data in Fig. 4 have a good repeatability, as indicated by the error bars crossing the lines in Fig. 5. The error bars show the 95% confidence interval [8] of the local pressure at pressure tappings 5–15, in the range $1.50 \leqslant y/h \leqslant 4.00$, obtained from the 44 test ensemble conducted at the same nominal isentropic exit Mach number $M_e=1.27$. The 95% confidence interval at $y/h=1.25$ is obtained from an ensemble of 26 measurements. The average uncertainty is $\pm 0.0010 p_0$. The largest statistical spread is associated to the trailing edge pressure from blade 3 and is $\pm 0.0022 p_0$.

The data ensemble was collected at different times over a time span of 48 months. In the blow-down tunnel, the Mach and Reynolds number are interdependent and the cascade exit Reynolds number $\mathrm{Re}=u_e\bar{c}/\nu_e$ varied in the range $1.82\times10^6 \leqslant \mathrm{Re} \leqslant 1.90\times10^6$ during these tests. This modest variation in Reynolds number had only a negligible effect on ensemble mean wall pressure measurements, as indicated by the small size of the 95% confidence intervals in Fig. 5.

Nonperiodicity Index. Experimental cascade tests most often concern the determination of lift and drag. Therefore, it would be useful to estimate the nonperiodicity index from the scatter in the profile lift. Instrumenting all blade surfaces to determinate each profile's lift coefficient is often impractical. This work considers the alternative approach of quantifying the pitchwise periodicity in a free jet cascade wind tunnel flow by defining a nonperiodicity index based on the cascade exit pressure distributions. In an ideal pitchwise periodic cascade test, the measured end-wall pressure should repeat at the corresponding pitchwise coordinates y over successive passages, so that, for instance, $p_{1\text{-}2}(0.5h) = p_{2\text{-}3}(0.50h) = p_{3\text{-}4}(0.50h)$, where each subscript of p denotes passages 1-2, 2-3, and 3-4, respectively, defined in Fig. 1. The nonperiodic pressure scatter at 0.5 blade pitch can be defined as

$$\Delta p_{0.5} = [|p_{1\text{-}2}(0.50h) - p_{2\text{-}3}(0.50h)| + |p_{1\text{-}2}(0.50h) - p_{3\text{-}4}(0.50h)| + |p_{2\text{-}3}(0.50h) - p_{3\text{-}4}(0.50h)|]/3 \quad (1)$$

and similarly for other fractions of the blade pitch. The pitch average nonperiodicity index is then obtained by integrating along the pitch with Simpson's rule and dividing the result by $(p_a h)$, p_a being the laboratory ambient pressure. This gives

$$\bar{E} = \tfrac{1}{2}\left(\tfrac{1}{3}\Delta p_{0.25} + \tfrac{4}{3}\Delta p_{0.50} + \tfrac{1}{3}\Delta p_{0.75}\right)/p_a \quad (2)$$

From the measurements in Fig. 5, the cascade test with open jet boundaries yields a nonperiodicity index $\bar{E}=0.093\,53$, as shown in Table 1. This is a measure of the lack of periodicity in pitch within the cascade flow.

This test has clearly shown the performance limitations of an open jet cascade wind tunnel in producing a pitchwise periodic discharge from a linear cascade. In a transonic discharge, disturbances generated at the open jet boundary propagate to all other cascade passages, leading to an uncertainty margin of about 9% in

Table 1 Predicted and measured pitchwise nonperiodicity index

Test	$\bar{E}_{exp}$	$\bar{E}_{CFD}$
No tailboard	0.093 53	0.107 70
50% void ratio	0.124 88	0.179 60
15% void ratio	0.021 79	0.023 41

the measured pitch averaged exit pressure. Numerical simulations presented later on show that these variations in exit pressure produce differences between 5% and 6% in blade loading across the cascade. This is a very significant uncertainty for practical blade performance tests of an industrial turbine blade design.

Thick Slotted Wall Models

Background. The flow past slots in a slotted wall transonic wind tunnel typically generates a spanwise nonuniformity in mass and momentum transfer through the slots. Provided the slot size is adequately small, the spanwise nonuniform flow is limited to the immediate neighborhood of the walls and does not affect the wind tunnel interior flow.

When designing a computational fluid dynamic model of a slotted wind tunnel test section, it is interesting to consider the use of an appropriate numerical boundary condition to model the spanwise averaged slot flow without resolving the slot geometry, nor its induced the near-wall flow. This boundary condition is likely to reduce the computational mesh density at the wind tunnel boundaries, focusing the available computational resources along the wind tunnel centerline, to resolve the interior flow.

To design such a numerical boundary condition, a compressible flow geometry simpler than a cascade tunnel is considered first. Figure 6 shows a slotted flat plate, wetted on one side by a compressible flow, tangent to the surface. A weak shock reflects off the plate. The slots link a supersonic region (state 1) to the upper region (state 2) where the medium is at rest. Since the pressure in region 2 is the same as that in the supersonic region (state 1), no mass flow occurs across the plate. If a wave, for instance a weak shock, impinges on the wall at point A, this wave is usually reflected by the wall and a new wave originates from point A. If the wall is not slotted, the reflected wave will be a shock, the strength of which will be approximately equal to that of the impinging shock, since the deflection angles of both waves must be equal in order to satisfy a tangent flow condition at the wall ($\theta_4=0$). This behavior is significantly altered by the presence of slots through the flat plate in Fig. 6. In fact, the pressure difference that occurs between regions 2 and 4 causes a mass flow across the wall and, therefore, the flow direction in region 4 does not satisfy the tangent condition ($\theta_4 \neq 0$). The reflected wave strength is different from the impinging one and, under certain conditions, the reflected wave can become an expansion wave. In this analysis, the state referenced as 4 denotes a region far enough from the wall where the flow can be considered uniform. Closer to the wall, there is a near-wall region where the flow is nonuniform, because of the slots. The thickness of this region scales with the slot width. The pressure in regions 3 and 4, normalized by the reference pressure p_1, are related to the Mach number M_1 and the angles θ_3 and θ_4 by nonlinear implicit relations

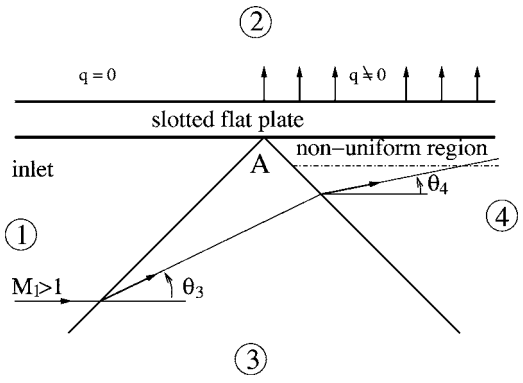

Fig. 6 Shock reflecting over a slotted flat plate

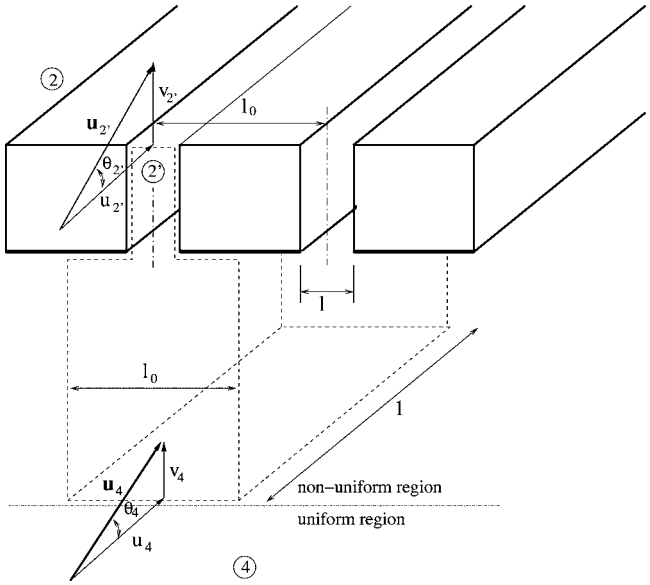

Fig. 7 Control volume around a slot

$$f_1\left(\frac{p_3}{p_1}, M_1, \theta_3\right) = 0 \tag{3}$$

$$f_2\left(\frac{p_4}{p_1}, M_1, \theta_3, \theta_4\right) = 0 \tag{4}$$

Assuming the perturbations in the flow are weak, p_3/p_1 and $p_4/p_1 \ll 1$ and θ_3 and $\theta_4 \ll 1$, these relations can be rewritten as

$$\frac{p_3}{p_1} = 1 + \frac{\gamma M_1^2}{\sqrt{M_1^2 - 1}}\theta_3 \tag{5}$$

$$\frac{p_4}{p_1} = \frac{p_4}{p_2} = 1 + \frac{\gamma M_1^2}{\sqrt{M_1^2 - 1}}(2\theta_3 - \theta_4) \tag{6}$$

The pressure difference between regions 2 and 4 causes a mass flow rate per unit area q through the wall and a flow deflection by an angle θ_4 with respect to the inlet flow direction. The mass flow rate and the deflection angle are a function of the pressure ratio p_4/p_2, of the wall void ratio s, and of the inflow Mach number M_1. Specifically,

$$\frac{q}{\rho_1 u_1} = \theta_4 = f\left(M_1, \frac{p_4}{p_2}, s\right) \tag{7}$$

The solution of the shock reflection problem requires knowledge of the explicit expression for f in Eq. (7). This relation is provided by Eq. (12) in the next subsection.

Analytical Formulation and Model Validation. Consider the dashed line control volume in Fig. 7. This includes the volume inside one slot and an external region extending from the wall surface to the boundary of the nonuniform near-wall flow. Due to the flow spanwise symmetry, the two lateral open boundaries do not provide a net contribution in the mass, momentum, and energy

balance. Therefore the outgoing fluxes in the slot exit section depend only on the fluxes coming through the side neighboring region 4 and on the mechanical and thermal actions of the walls.

The flow crossing the control volume is taken to be equivalent to an omentropic and adiabatic quasi-1D flow between two sections, whose area ratio l/l_0 is equal to the tailboard void ratio s, and where the working gas has the following total temperature and pressure,

$$p_0 = p_4\left[1 + \frac{\gamma-1}{2}\left(\frac{v_4}{a_4}\right)^2\right]^{\gamma/(\gamma-1)} \tag{8}$$

$$T_0 = T_4\left[1 + \frac{\gamma-1}{2}\left(\frac{v_4}{a_4}\right)^2\right] \tag{9}$$

and where the exit pressure is set to

$$p_{2'} = p_2 = p_1 \tag{10}$$

To this crosswise flow is superimposed a constant velocity flow aligned to the longitudinal direction

$$u_{2'} = u_4 \tag{11}$$

Assuming that the perturbations in the flow are weak and that the flow in the exit section is subsonic ($M<1$), it is possible to obtain an explicit expression for Eq. (7), which is

$$\theta_4 = s\frac{1}{M_1}\sqrt{\frac{2}{\gamma-1}}\left(\frac{p_4}{p_1}\right)^{-(\gamma+1)/2\gamma}\sqrt{\left(\frac{p_4}{p_1}\right)^{(\gamma-1)/\gamma} - 1} \tag{12}$$

The flow state 4 is determined by solving Eqs. (12), (5), and (6). To determine the conditions for the suppression of the reflected wave, the strength of the reflected wave is imposed to be zero by

$$p_4 = p_3 \tag{13}$$

$$\theta_4 = \theta_3 \tag{14}$$

Combining Eqs. (5) and (12), the optimal void ratio that suppresses the reflected wave is determined as

$$s_{opt} = \frac{\left(\frac{p_3}{p_1} - 1\right)\left(\frac{p_3}{p_1}\right)^{(\gamma+1)/2\gamma}}{\frac{\gamma M_1}{\sqrt{M_1^2-1}}\sqrt{\frac{2}{\gamma-1}}\sqrt{\left(\frac{p_3}{p_1}\right)^{(\gamma-1)/\gamma} - 1}} \tag{15}$$

Equation (15) indicates that s_{opt} depends on the pressure ratio (p_3/p_1) and on the Mach number (M_1) of the free stream inflow. If the perturbations in the flow are strong, rather than weak, an explicit expression for θ_4 and s_{opt}, analogous to Eqs. (12) and (15), cannot be written. Nevertheless, the state 4 and the value of s_{opt} can be computed numerically from M_1 and p_3/p_1 by means of the oblique shock relations and the quasi-1D omentropic flow relations.

Several experiments have been performed in the past to study the aerodynamics of slotted walls. A selection of experimental results is reported in Goethert [1]. Figure 8 reports measurements of the mass flow rate across a wall with a single longitudinal slot in a transonic tunnel. Specifically, Fig. 8 shows the variation of the dimensionless pressure drop through the slotted wall, $\Delta p/(\frac{1}{2}\rho_1 u_1^2)$, against the normalized mass flow rate per unit area through the slot, $q/(\rho_1 u_1)$. These measurements were obtained at two different inflow Mach numbers, $M_1=0.75$ and 1.2, using a 3.18 mm $(\frac{1}{8}$ in.) thick board with a single slot slot 33.02 mm (1.3 in.) wide. The wall void ratio was 0.11.

Three different lines are plotted in Fig. 8 together with the experimental data. The continuous line traces Goethert's empirical correlation [1]

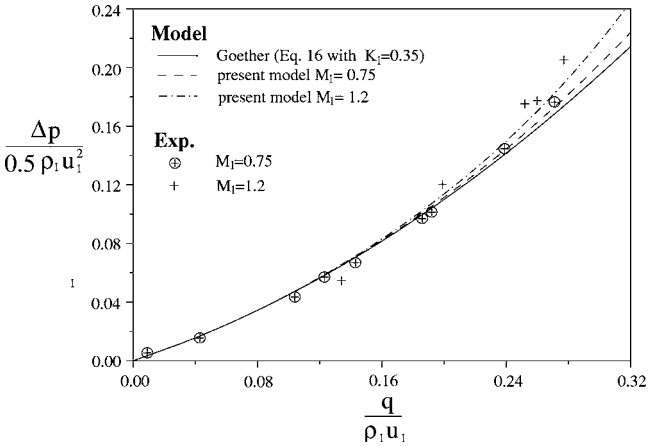

Fig. 8 Differential pressure across a slotted wall versus normalized slot mass flow rate

$$\frac{\Delta p}{\frac{1}{2}\rho_1 u_1^2} = K_1\frac{q}{\rho_1 u_1} + \left(\frac{q}{\rho_1 u_1}\right)^2 \tag{16}$$

The right-hand side of Eq. (16) has two terms. The linear term models the pressure loss caused either by friction on the side walls of the slot or by the flow separating along the slot edges. The quadratic term is the normalized pressure loss due to the inviscid flow through the slot. Although in Goethert [1] the constant K_1 is set at 0.4, a better fit with the measured Δp at low values of slot mass flow rate is obtained by setting $K_1=0.35$. In Fig. 8, the agreement between Eq. (16) and the experimental data is excellent at a low mass flow rate. As the mass flow rate becomes larger, a discrepancy builds up between experiment and prediction. Figure 8 shows two further lines, which plot the Δp predicted at $M_1=0.75$ and 1.2 from a new slotted wall model. Specifically, these curves are computed by solving the following equation

$$\frac{\theta_4}{s} = \frac{q}{\rho_1 u_1} \tag{17}$$

$$\frac{p_4}{p_1} = \frac{\Delta p}{\frac{1}{2}\rho_1 u_1^2}\frac{\gamma M_1^2}{2} + 1 \tag{18}$$

together with Eq. (12). Since this slotted board model only takes into account the effects of the inviscid flow through the slot, a viscous contribution equal to that of Eq. (16) has been added.

This new slotted wall model shows a small but significant improvement over Eq. (16). In fact, in Fig. 8, the new model shows a weak dependence on the Mach number. In particular, at $M_1 \neq 0$ the slotted board model predicts a higher pressure drop than Eq. (16), improving the agreement with the experimental data. As $M_1 \to 0$, all predictions of Δp tend to overlap, as shown in Fig. 8. The new slotted wall model better predicts the dependence of Δp on the Mach number and improves the correlation with the experimental data, compared to Eq. (16), at $M_1 > 1$.

Numerical Implementation and its Verification. The slotted wall model discussed in the previous subsection has been implemented in a computational fluid dynamic scheme as a boundary condition. This scheme is based on a finite volume Godunov-type method that integrates the discrete Euler equations. The numerical integration is up to second-order accurate. A detailed description of this scheme is presented by Di Mascio and Favini [9].

The computational boundary condition for a slotted wall is formulated without assuming the disturbances in the flow to be small. Specifically, the computation of the mass, momentum, and energy fluxes at the computational cell boundaries, where the slotted wall model boundary condition is applied, is performed by

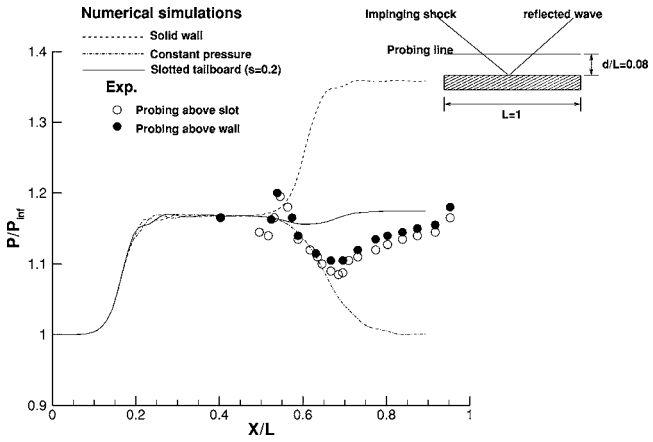

Fig. 9 Reflection of an impinging oblique shock over a straight boundary. Thick wall model.

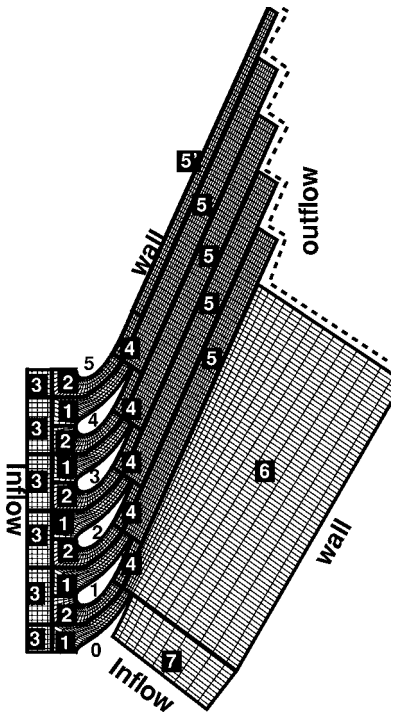

Fig. 10 Mesh and boundary conditions of the cascade model

modeling an isentropic quasi-1D steady flow through a convergent nozzle with an area ratio equal to the wall void ratio. Where the flow across the slotted tailboard is from the test section towards the outside, the quasi-1D flow is computed assuming (i) that the total temperature and pressure are constant and equal to the cell average static temperature and pressure, respectively, plus the dynamic contribution due to the crosswise velocity component, and (ii) that the exit section pressure of the convergent nozzle is the same as the laboratory ambient one. Where the flow is reversed, (i) the total pressure and the total temperature are set equal to the laboratory ambient conditions and (ii) the exit section pressure of the nozzle is the average static pressure of the cells bordering with the slotted tailboard.

The numerical method with this new boundary condition has been verified against a shock reflection test case by Goethert [1]. In a Mach 1.75 flow, an oblique shock wave of $\Delta C_p=0.079$ impinges on a flat plate with 0.2 void ratio streawise slot. From Eq. (15), the optimal void ratio s_{opt} at these flow conditions is about 0.2.

The outcome of this simulation is reported in Fig. 9, which shows the pressure distribution along a line parallel to the slotted wall and placed at twice the distance between two adjacent slots, 15.24 mm (0.6 in.). The pressure distributions obtained when the slotted wall boundary is replaced by (i) a solid wall and (ii) a constant pressure boundary condition are included for comparison in Fig. 9. These pressure distributions clearly show that the solid wall and the constant pressure boundary condition produce a reflected wave which causes a pressure variation about equal in magnitude to that caused by the impinging wave. No reflection is observed when the slotted wall boundary condition with $s=0.2$ is applied, the pressure distribution being approximately constant downstream of the impinging wave. This verifies the correct implementation of the wall interference model in the numerical scheme.

Figure 9 reports, for validation purposes, the pressure distribution measured by Goether [1] when the shock impinges a tailboard with the optimal void wall ratio $s=0.2$. Figure 9 shows measurements obtained along two probing lines parallel to the wall. The filled circles denote measurements performed above the solid area of the slotted wall whereas the hollow circles denote measurements performed above a slot. The difference between these experimental pressure distributions and the irregularities of such distributions indicate the presence of a complex system of secondary shocks above the slotted wall. The effects of this shock structure are local and are likely to become negligible as the distance from the wall is increased. Despite the presence of these localized effects, the experimental pressure distributions show the absence of any significant wave reflection. This is inferred from the static pressure, downstream of the oscillations due to the secondary shocks, which settles at about the same value as just downstream of the impinging shock. This result confirms that the void ratio $s_{opt}=0.2$ is about optimal for this flow, validating the analytical prediction method for s_{opt}. The numerical simulations computed using the slotted tailboard boundary condition do not show any near-wall pressure oscillation, because the numerical model estimates the far wall flow state and does not resolve the local three-dimensional flow through the slots.

Cascade Flow Predictions

The flow in the cascade wind tunnel is computed using the numerical method described in subsection "Numerical Implementation and its Verification." The cascade is modeled at the same inflow conditions as those detailed in section "Performance Limitations of an Open Jet Cascade Wind Tunnel." In addition to this numerical test, further flow simulations are carried out altering the test section configuration. Specifically, the original test section is modified by placing a tailboard along the cascade discharge boundary, hinged to the trailing edge of blade 0, as shown in Fig. 1. The model tailboard has a streamwise constant wall void ratio s and is inclined at an angle α to the cascade axial inflow direction. The aim of these simulations is to identify the optimal tailboard configuration able to minimize spurious wave reflections coming from the cascade pitchwise boundary, or tailboard, which compromise the flow periodicity across the cascade discharge.

The cascade flow models use two kinds of structured mesh. The mesh shown in Fig. 10 is used to compute the numerical solutions inside the test section with no slotted tailboard. For clarity, one of every four mesh points is plotted in Fig. 10. This mesh is built by clustering eight blocks: Blocks 1, 2 and 4 surround each blade profile like a "C" mesh. Blocks 3 and 5 are Cartesian grids placed, respectively, upstream and downstream of each blade. Block 5′ is half a block 5 and two additional blocks, 6 and 7, discretize the low speed region downstream of the blade 0 suction side. The total number of cells is 42,760. Blocks 1 and 2 have the same number of cells, therefore the number of cells bordering each blade suction side differs from that bordering each blade pressure

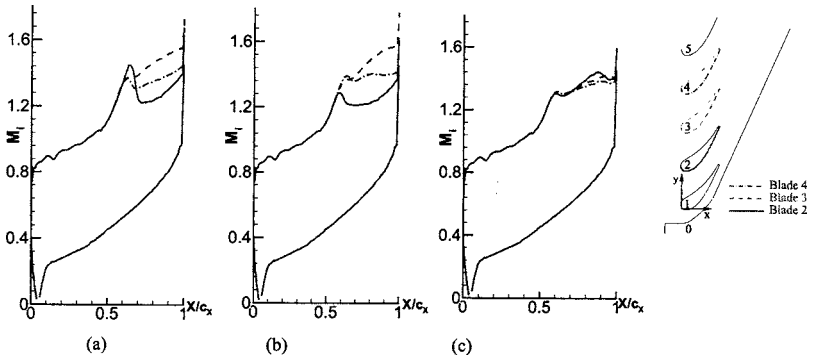

Fig. 11 Isentropic Mach number distributions along the blades: (*a*) open jet cascade, (*b*) tailboard with $s=0.5$ and $\alpha=62$ deg, and (*c*) tailboard with $s=0.143$ and $\alpha=64$ deg

side by 42 cells. This arrangement gives a quasi-orthogonal multiblock mesh. Linear mesh stretching is used in blocks 6 and 7. The mesh used to compute the solution where the slotted tailboard is present is obtained from the mesh shown in Fig. 10 by replacing blocks 6 and 7 with half a block 5. In fact, the presence of a slotted tailboard reduces the numerical domain, removing the free shear layer which separates the cascade flow from the low speed flow region downstream of the blade 0 suction side. A convergence study indicates that the spatial resolution of this mesh provides numerical predictions that are essentially mesh independent. The maximum numerical uncertainty estimated by means of the GCI [10] in the predicted pressure field is less than 2%.

At the inflow boundary, the air stream is subsonic. Accordingly, the total pressure, the total temperature, and an axial inflow velocity are imposed. At the outflow boundary, indicated by a dashed line in Fig. 10, only the static pressure is imposed where the outflow is subsonic. Where the outflow is supersonic, the flow state is extrapolated from the computational domain interior. An inviscid wall condition applies at the blade perimeter. The inflow and outflow conditions imposed when a slotted tailboard is used are identical to those used in the open jet boundary cascade test case, except for the block 7 inflow boundary, where a lower total pressure and total temperature are imposed, to obtain an inflow isentropic Mach number M_i of 0.3. Along the tailboard, the computational boundary condition for a slotted wall from subsection "Numerical Implementation and its Verification" is used.

Among the numerous cascade configurations studied, three configurations have been selected and their numerical results are reported hereinafter. The first configuration considers the test section without the tailboard. This test case represents the reference case with respect to which to assess the gain in flow periodicity introduced by adding a tailboard. A test section with a tailboard with $s=0.5$, angled at 62°, is the second test case. This configuration is the authors' first attempt at restoring the cascade flow periodicity by the use of a tailboard. The third test case is a model cascade with a slotted tailboard with $s=0.143$ and $\alpha=64°$. This is the result of a numerical optimization process to find a tailboard configuration that minimizes the nonperiodicity index with respect to the values of the s-α pair. Less than 10 s-α combinations were required to find the optimal end wall geometry for the University of Leicester cascade tunnel. Each s-α model configuration required between 3 and 4 h of CPU time on a 1 GHz class workstation.

For each of these three configurations, the predicted isentropic Mach number distribution along the blade surface is shown in Fig. 11, plotted against the nondimensional axial chord x, in the range $0 \leqslant x \leqslant 1$. The surface isentropic Mach number is computed by normalizing the cascade inlet total pressure by the static pressure distribution predicted along each blade surface. This ratio is converted into an isentropic Mach number by Eq. (8).

In Fig. 11, the isentropic Mach number distribution M_i around each blade perimeter forms a loop. The lower part of the loop, closest to the abscissa and delimited by the M_i extrema $M_i=0$ and $M_i \sim 1.6$, is the isentropic Mach number distribution over each blade pressure side. These pressure side M_i predictions from blades 1 to 5 overlap. This indicates that the pressure distribution over the pressure side of all blades is pitchwise periodic.

The isentropic surface Mach number predicted over the suction side is also pitchwise periodic towards the leading edge, in the range $0 \leqslant x/c_x \leqslant 0.6$, as shown by the good overlap among the traces from different blades in Fig. 11. Downstream of $x \sim 0.6$, Fig. 11(*a*) and 11(*b*) show significant blade-to-blade differences in M_i, indicating a marked departure from a pitchwise periodic flow towards the trailing edge of the blades. The nonpitchwise periodic cascade exit flow gives corresponding blade-to-blade variations in exit static pressure. These variations are shown in Fig. 12(*a*) and 12(*b*), which plot the predicted normalized static pressure distribution (p/p_0) at each passage exit versus the normalized blade pitch y/h. Figure 12(*a*) is the numerical analogous of Fig. 5. To ease the comparison with Fig. 5, the measured ensemble averages of Fig. 5 are reproduced in Fig. 12(*a*) using the same pressure port symbols as Fig. 4. The variation in exit static pressure among the cascade passages reported in Figs. 12(*a*) and 12(*b*) are significant and confirm that the predicted flow is not pitchwise periodic at the cascade outlet. The overlap between predictions and experiment is Fig. 12(*a*) in coarse. The inviscid flow model is unable to correctly describe shear layer mixing, as it does not include viscous nor Reynolds stresses. This affects the trailing edge wave refractions through the modeled shear layers in the discharge, affecting the cascade exit pressure distribution that deviates from the measurements. However, the measured scatter in the wall static pressure from different passages at the same passage height (y/h) is similar to that in the predictions. This indicates that the inviscid numerical model is reproducing the main cause of the flow pitchwise nonperiodicity affecting the measurements.

The source of the pitchwise nonperiodicity shown in Figs. 11 and 12 is the spurious wave reflection radiating from the cascade pitchwise outer boundary towards the interior passages. The cascade exit Mach number is supersonic, as shown by the predictions of Fig. 11 at $x/x_c=1$ and by the presence of shocks in Fig. 4. This prevents the cascade leading edge from being affected by such disturbances. Consequently, the isentropic Mach number distribution around the profile leading edge remains pitchwise periodic. The predictions of Fig. 11 display blade-to-blade differences in M_i as being confined to $0.6 \leqslant x \leqslant 1.0$ on the blade suction side. Still, such differences are responsible for a spread in the measured blade loading, this being given by the cyclic integral of surface pressure distribution.

In the model cascade, spurious wave reflections from the outer

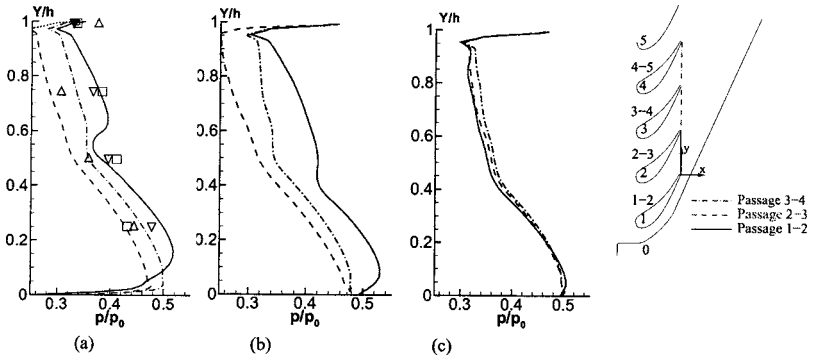

Fig. 12 Pressure distribution at the blade trailing edge lines: (*a*) open jet cascade, (*b*) tailboard with $s=0.5$ and $\alpha=62$ deg, and (*c*) tailboard with $s=0.143$ and $\alpha=64$ deg

boundary propagate through the cascade exit plane onto the blade suction side trailing edges. This gives a good correlation between the blade-to-blade spread of the surface isentropic Mach number at the rear end of the passage, in Fig. 11, and the corresponding blade-to-blade difference in exit pressure in Fig. 12. In Fig. 11(*b*) the spread of M_i is greater than in Fig. 11(*a*). Correspondingly, in Fig. 12(*b*) the spread in p/p_0 is greater than in Fig. 12(*a*). This is because the same disturbances that are causing a spread in M_i are affecting the normalized exit static pressure distribution in pitch.

The large differences in static pressure and M_i occurring in the open jet cascade configuration, shown in Figs. 11(*a*) and 12(*a*), denote a significant lack of flow periodicity throughout the cascade. The predicted nonperiodicity index $\bar{E}$ is 0.1077, as reported in Table 1. The same level of flow nonperiodicity is observed in the second test case, from Figs. 11(*b*) and 12(*b*), despite the presence of a slotted tailboard with $s=0.5$. The second test case shows no reduction in the spread between the pressure distributions at the exit of different passages with respect the open jet cascade prediction. The predicted nonperiodicity index $\bar{E}$ is 0.179 60 and is higher than in the open jet configuration. The spread among the exit pressure distributions and M_i are significantly reduced in the last configuration, which features an optimized tailboard with $s=0.143$ at $\alpha=64°$. In this case, the pressure distributions are sufficiently close to consider the flow through the passages as periodic, for engineering purposes. The predicted nonperiodicity index $\bar{E}$ reduces to 0.023 41 and the differences in blade loading are less than 1%.

The two-dimensional inviscid computational fluid dynamic model does not provide a locally accurate prediction of the three-dimensional turbulent flow. Using a computationally more expensive three-dimensional model does not appear to be cost-effective in the present framework, where the fluid dynamic solver is used inside an optimization procedure. The main objective of the numerical simulation is to predict the strength of the shock and expansion waves reflected by the cascade pitchwise boundary. This pattern has been shown not to change significantly between a three-dimensional Navier-Stokes model and a two-dimensional inviscid model of the cascade at the same inflow conditions [7], with pitchwise periodic boundaries. Therefore, there is some confidence that three-dimensional and viscous effects are not dominant in this flow and the inviscid two-dimensional model is adequate for the purpose of the present work.

Using a slotted tailboard with a constant wall void ratio does not completely suppress the spurious reflections from the pitchwise boundary. A complete cancellation of these reflections would require a shaped slotted board with a streamwise varying wall void ratio, to account for the dependence of the optimal void ratio and tailboard angle on the streawise Mach number distribution along the board. This dependence can be quantified through Eq. (15). Still, the tailboard performance predicted in the numerical test with $s=0.143$ at $\alpha=64°$, in terms of restored cascade periodicity, can be considered adequate for a good range of practical cascade wind tunnel applications, where engineering measurements are required.

Wind Tunnel Measurements With the Optimized Tailboard. The numerical tests reported in section "Cascade Flow Predictions" identify a slotted tailboard that promises to deliver a significant improvement in the cascade flow pitchwise periodicity with respect to an open jet cascade. Following these encouraging numerical predictions, a slotted tailboard was manufactured at the University of Leicester with a 15% void ratio, to stand at 64° to the inflow direction [11]. The 15% void ratio is slightly higher than the 14.3% optimal void ratio predicted by the inviscid model, to compensate for boundary layer blockage through the slots. This tailboard is diagrammatically shown in Fig. 13. The tailboard is made from a 2 mm thick steel shim and is supported on a chassis that secures it to the test section. The chassis is detailed in Fig. 13(*a*). This chassis is 219 mm long and 50 mm wide, spanning the test section from side to side once assembled in the cascade tunnel. The leading edge of the chassis is secured to the trailing edge of blade 0 via a brass hinge that allows the tailboard angle to be adjusted with respect to the cascade outflow direction. The trailing edge of the chassis is secured to the mirrored back wall frame and to the frame of the front schlieren glass by grooved T pieces, which allow the tailboard angle to be adjusted between tests. In the present work, tests have been conducted with a tailboard angle

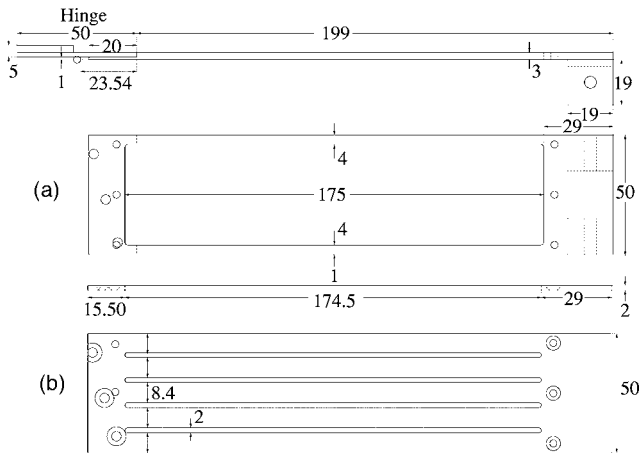

Fig. 13 Tailboards tested in the cascade tunnel: (*a*) support chassis for slotted board (b) and (*b*) 15% void ratio board. All dimensions are in mm.

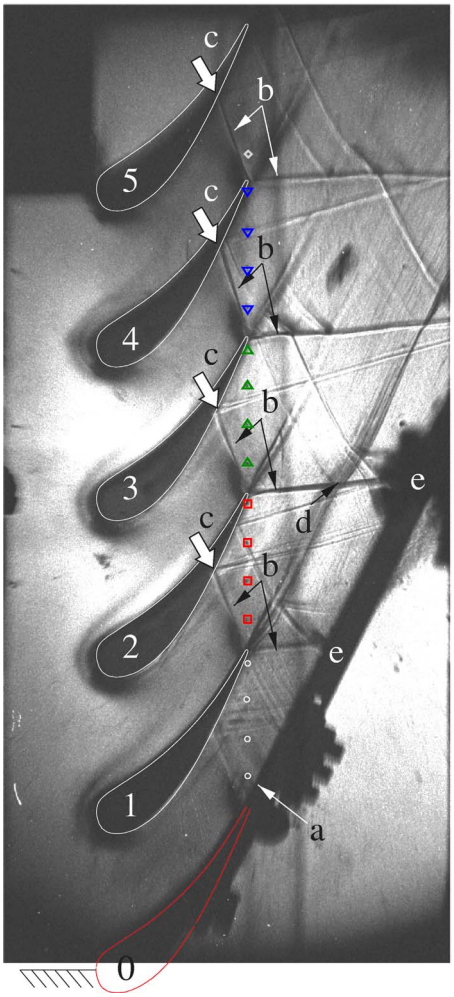

Fig. 14 Experimental schlieren visualization of cascade flow discharge with a 15% void ratio tailboard.

of $64° \pm 0.083°$ to the inflow direction. The chassis has a 175×42 mm^2 open area at its center. Overlapping this central area, the tailboard shim is 200×50 mm^2 in wetted area and has four evenly spaced 2 mm wide streamwise slots. This pattern, shown in Fig. 13(*b*), gives a void ratio of approximately 15% above the chassis open area. An aluminium in-fill has been cut and filed from a $3 \times 50 \times 2$ mm^3 thick shim to fill a small gap between the 15% void ratio tailboard leading edge and the suction side of the blade 0 trailing edge.

With the tailboard fitted, the linear cascade was tested at the same inflow conditions as the free jet open boundary configuration, detailed in section "Performance Limitations of an Open Jet Cascade Wind Tunnel." Figure 14 shows a selected experimental schlieren visualization from these tests. The shadow of the tailboard is shown in the bottom right-hand quadrant of Fig. 14. Three bolts fix the tailboard to the supporting hinge. The ends of these three bolts are visible below the tailboard. They are secured by M5 nuts whose shadows have merged in a single rectangular shape. The metal hinge, supporting the tailboard, is visible at the bottom right-hand side of Fig. 14 as a round shadow below the bolt assembly.

The flow pattern visualized in Fig. 14 suggests that the tailboard has corrected the overexpansion through passage 0-1, between blades 0 and 1. The metal in-fill above the hinge, indicated by arrow **a** in Fig. 14, is acting as a splitter plate at the blade 0 trailing edge, channeling the outflow from passage 0-1 in the direction parallel to the tailboard, which is set close to the design outflow angle of this cascade. Rectifying the discharge from passage 0-1 has straightened the shear layer shed by the blade 1 trailing edge. The shear layer runs more parallel to the trailing edge wakes from the more internal blades and it is considerably thinner with respect to the corresponding feature in Fig. 4. The symmetric growth of the blade 1 shear layer about its centerline indicates that the discharges from passages 0-1 and 1-2 are similar to each other. The same inference can be drawn from the approximately symmetric wakes downstream of blades 2, 3, and 4, indicating that the discharges from all passages are more similar to one another in Fig. 14 than in Fig. 4. Contrary to Fig. 4, in Fig. 14 there is no evidence of any alternating pattern of underexpansions and overexpansions across successive passages.

The shock pattern visualized in Fig. 14 gives further evidence that the tailboard has improved the cascade discharge pitchwise periodicity at the selected test conditions. The fish tail shocks stemming from the trailing edge of each blade run more parallel to one another than in the flow without a tailboard. Specifically, the lambda shock structure on the trailing edge suction side of blade 1 has been replaced by a single more oblique shock, indicating a milder flow recompression in the cascade with tailboard with respect to the passage 0-1 discharge in Fig. 4, leading to a more pitchwise periodic discharge.

As the suction side branch of the blade 1 trailing edge shock impinges against the tailboard, it causes an arc-shaped reflection that propagates towards the blade 2 trailing edge. The shape of this reflected wave is similar to the one produced by the blade 4 suction side shock interfering with the shear layer from blade 3. This suggests that the slotted tailboard is imposing a pressure field similar to that around the blade 3 shear layer, resulting in a shock-shear layer interaction similar to the one from a more internal passage. This substantiates the numerical prediction that a 15% tailboard void ratio is about optimal at the selected test conditions. Further downstream along the tailboard, the suction side trailing edge shock from blade 2 also generates an arc-shaped reflection from the tailboard. The strength of this wave seems to be greater than the corresponding upstream tailboard reflection, judging from the more pronounced turning angle that this reflection imposes on the blade 1 shear layer. This is a welcomed feature, as it compensates for the steeper turning angle imposed on the blade 1 shear layer by the blade 2 suction side shock. The end result is that, as the blade 1 shear layer leaves this downstream shock system, it runs again almost parallel to the other shear layers shed by blades 2, 3, and 4.

The flow visualization in Fig. 14 contains some non-flow-related features worthy of clarification. The dark line running from top to bottom in Fig. 14 is the shadow of the collimator line, used to align the optics. The dark spot between the blade 2 and 3 shear layers is due to chipping on the schlieren glass. A hazy shadow of the knife edge support appears on the right margin of the picture.

The measured wall pressure distribution with a 15% void ratio tailboard quantitatively confirms the gain in pitchwise periodicity predicted by the numerical model in Figs. 11(*c*) and 12(*c*). This result is presented in Fig. 15, where the normalized pressure distribution synchronous to the schlieren record of Fig. 14 is plotted with symbols □,△,▽. To obtain precise measurements at the test condition of $p_a/p_0 = 0.3728$, a set of 88 acquisitions have been ensemble averaged, following the same procedure described in subsection "Measurement Techniques." The ensemble-averaged measurements are reported in Fig. 15 with the diamond symbol (◇) and lines. The proximity of the ensemble averages to the single synchronous schlieren acquisition confirms that the schlieren record of Fig. 14 is a good visualization of the flow near the design test point.

Cubic splines are constructed through the ensemble-averaged data to interpolate the experimental wall pressure in pitch. The resulting trends are a good qualitative match with the numerical predictions of Fig. 12(*c*). Specifically, the normalized wall pres-

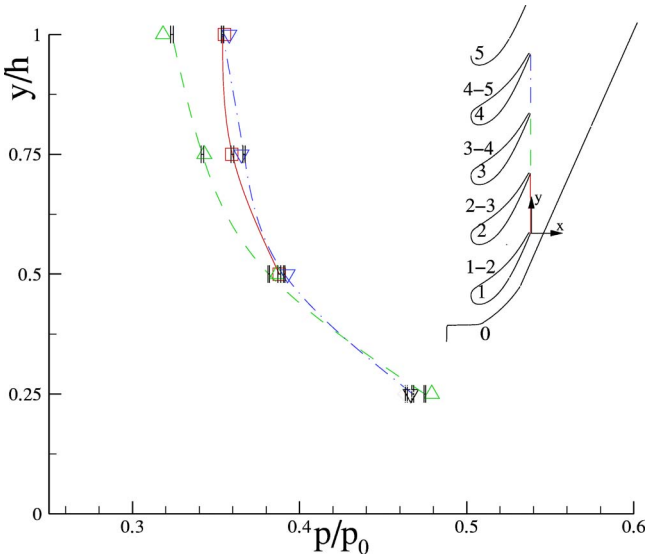

Fig. 15 Normalized wall pressure distribution in the discharge from a cascade with 15% void ratio tailboard at 64° to the inflow direction. (–, □) passage 1-2, (– –, △) passage 2-3, (– · –, ▽) passage 3-4, (◇) passage 4-5

sure is low through the upper section of the passage, in the range $0.75 \leqslant y/h \leqslant 1$, close to the suction side of the blades. The normalized wall pressure then increases monotonically towards each blade pressure side, for reducing values of y/h. The $0.25h$ spacing between monitoring points is not fine enough to resolve localized flow features, such as the crossing of the pressure side trailing edge shock towards each neighboring blade suction side. Still, the main trend of a consistent increase in wall pressure from each blade suction side to its pressure side is recorded in all passages, with a good data overlap from different passages over the range $0.25 \leqslant y/h \leqslant 0.50$. Passages 1-2 and 3-4 are comparatively underexpanded with respect to passage 2-3 but their pressure distributions are more similar to each other than the ones from passages 1-2 and 3-4 in Fig. 5, suggesting a tangible improvement in the flow periodicity with respect to the result with a free jet open boundary.

Figure 14 displays at each measurement location the 95% confidence interval of the ensemble mean by an error bar across each small symbol. In Fig. 15, the average uncertainty shown by the error bars is $\pm 0.0006 p_0$. The largest uncertainty is associated with the measurement at $y/h=0.25$ in passage 1-2 and is $\pm 0.0009 p_0$, which is $\leqslant 0.24\%$ of the ensemble mean at this location. This indicates a good consistency in the measurements through the ensemble. This modest data scatter is in line with the measured uncertainties in Fig. 5.

From Table 1, the nonperiodicity index measured with the $s=15\%$, $\alpha=64°$ tailboard configuration is 0.023 41, which is within 7.2% of $\bar{E}$ predicted by the numerical model. Table 1 shows that the numerical model consistently underestimates the nonperiodicity index in all test cases. The nonperiodicity index reduces by a factor of 4.6 with respect to the open jet cascade. This is a close match to the relative improvement in the nonperiodicity index predicted by the numerical model, in which it reduces by a factor of 4.37.

Conclusions

Measurements on a transonic cascade, tested in an open jet wind tunnel above its design pressure ratio, highlighted significant passage-to-passage differences in the cascade exit pressure distribution. This study identified the source of this lack of pitchwise flow periodicity, by flow visualization and synchronous pressure measurements. When the cascade discharge is supersonic, shocks and expansion waves from the cascade interior impinge upon the free jet boundary, causing spurious wave reflections. It is concluded that there is scope for replacing the free jet boundary with a more suitable nonreflecting test section end-wall, to suppress such spurious reflected waves and thus restore some pitchwise periodicity throughout the cascade flow.

Improvements in the cascade flow quality were sought by replacing the open jet boundary with a slotted tailboard, designed by a numerical method based on an inviscid flow model and a special boundary condition that simulates the effects of the presence of slots, away from a slotted wall, and predict the macroscopic or spanwise-averaged flow through them. The boundary condition and the numerical method were verified and validated against experimental data in simple shock reflection tests.

The inviscid numerical method was then used to obtain an inviscid model of the cascade flow with an open jet boundary. The predictions closely reproduced the pitchwise nonperiodicity index experimentally determined, validating the numerical model.

Introducing the slotted-wall boundary condition in the model enabled the authors to identify a void ratio and a slotted wall pitch angle that minimized spurious end-wall wave reflections. Wind tunnel cascade tests using this optimal tailboard configuration verified the level of spurious end-wall suppression predicted by the numerical model. It is concluded that the flow physics modeled by the inviscid method captures those flow details that determine the level of interference between the wind tunnel pitchwise boundary and the interior cascade flow. By reducing this source of interference, a more uniform discharge is obtained. The nonperiodicity index of the test case considered hereinforth reduces by a factor of 4.6 and the cascade flow is more pitchwise periodic. Consequently, the predicted blade-to-blade difference in lift coefficient decreases from between 5% and 6% to about 1%.

The inviscid numerical method, coupled with the new macroscopic model for a slotted wall boundary, represents an important improvement with respect to past empirical techniques for the design of transonic cascade wind tunnels with low end-wall interference. This numerical method can identify an end-wall geometry that is optimal for a given blade profile and at a given wind tunnel running condition.

As the numerical method is inviscid, two-dimensional, and does not resolve the near-wall flow through slots, it represents a computationally efficient approach to optimize cascade end-wall geometries with respect to the alternative of a more onerous three-dimensional Reynolds averaged computation, which resolves the flow through slots. This streamlined computational approach makes this technique particularly attractive to use in an industrial turbomachinery design environment.

Nomenclature

a = speed of sound
E = nonperiodicity index
M = Mach number
p = pressure
q = mass flow rate per unit area
s = tailboard void ratio
T = temperature
u = streamwise velocity
v = crosswise velocity
α = tailboard pitch angle
γ = specific heat ratio, Cp/Cv
ν = kinematic viscosity
ρ = density
θ = flow deflection angle

Subscripts

a = ambient conditions
e = cascade exit
0 = reservoir conditions
$\|$ = absolute value

References

[1] Goethert, B., 1961, *Transonic Wind Tunnel Testing*, Pergamon Press, Oxford, UK.

[2] Davis, J. W., 1974, "Optimization of Wave Cancellation in Variable Porosity Transonic Wind Tunnel Flows," NASA Technical Report TR-TN-D-7432, November.

[3] Oldfield, M., Kiock, R., Holmes, A., and Graham, C., 1981, "Boundary Layer Studies on Highly Loaded Cascades Using Heated Thin Films and a Traversing Probe," ASME J. Eng. Power, **103**, pp. 237–246.

[4] Holder, D., and North, R., 1963, *Schlieren Methods*, Her Majesty's Stationary Office, London, UK.

[5] Rona, A., Gostelow, J. P., Paciorri, R., and Geron, M., 2003, "Wall Interference in the Discharge Flow in a Linear Cascade Wind Tunnel," Conference Paper 2003-0455, AIAA, January, 41st AIAA Aerospace Sciences Meeting and Exhibit, Reno, NV.

[6] Rona, A., Paciorri, R., and Sabetta, F., 2001, "Experimental and Numerical Evaluation of Non-Reflecting Porous Tailboards for Transonic Cascade Wind Tunnels," Conference Paper ATI-CST-019/01, March, in Proceedings of 4th European Conference on Turbomachinery Fluid Dynamics and Thermodynamics.

[7] Rona, A., Paciorri, R., Geron, M., and Ince, N., 2004, "Slot Width Augmentation in a Slotted-Wall Transonic Linear Cascade Wind Tunnel," Conference Paper 2004-0608, AIAA, January, 42nd AIAA Aerospace Sciences Meeting and Exhibit, Reno, NV.

[8] Calvert, J., and Farrar, R., 1999, *An Engineering Data Book*, MacMillan Press, Houndmills, UK.

[9] Di Mascio, A., and Favini, B., 1991, "A Two-Step Godunov-Type Scheme for the Euler Equation," Meccanica, **26**, pp. 179–188.

[10] Roache, P., 1997, "Quantification of Uncertainty in Computational Fluid Dynamics," Annu. Rev. Fluid Mech., **29**, pp. 123–160.

[11] Paciorri, R., Sabetta, F., and Rona, A., 2002, "Wave Reflection of Porous Walls: Numerical Modelling and Application to Transonic Wind Tunnels," Conference Paper 2002-1060, AIAA, January, 40th AIAA Aerospace Sciences Meeting and Exhibit, Reno, NV.

Unsteady Aerodynamics and Interactions Between a High-Pressure Turbine Vane and Rotor

Ryan M. Urbassik

J. Mitch Wolff
e-mail: mitch.wolff@wright.edu

Department of Mechanical and Materials Engineering,
Wright State University,
Dayton, OH 45435

Marc D. Polanka[1]
Air Force Research Laboratory, Turbines Branch,
Wright-Patterson Air Force Base,
Wright-Patterson AFB, OH 45433
e-mail: marc.polanka@wpafb.af.mil

A set of experimental data is presented investigating the unsteady aerodynamics associated with a high pressure turbine vane (HPV) and rotor blade (HPB). The data was acquired at the Turbine Research Facility (TRF) of the Air Force Research Laboratory. The TRF is a transient, blowdown facility generating several seconds of experimental data on full scale engine hardware at scaled turbine operating conditions simulating an actual engine environment. The pressure ratio and freestream Reynolds number were varied for this investigation. Surface unsteady pressure measurements on the HPV, total pressure traverse measurements downstream of the vane, and surface unsteady pressure measurements for the rotor blade were obtained. The unsteady content of the HPV surface was generated by the rotor potential field. The first harmonic decayed more rapidly than the second harmonic with a movement upstream causing the second harmonic to be most influential at the vane throat. The blade unsteadiness appears to be caused by a combination of shock, potential field, and vane wake interactions between the vane and rotor blade. The revolution averaged data resulted in higher unsteadiness than a passing ensemble average for both vane and rotor indicating a need to understand each passage for high cycle fatigue (HCF) effects. [DOI: 10.1115/1.2098752]

Introduction

In turbomachinery, periodic unsteadiness is prevalent. This unsteadiness is usually created from vanes or rotors interacting with the freestream flow. There has been extensive research both computationally and experimentally to try to characterize these effects and the resulting aeromechanical forces acting on vanes and blades in turbomachinery. These aeromechanical forces can result in HCF of the engine components. They can also cause a decrease in efficiency. Relatively little aeromechanical research on full scale high pressure turbine hardware operating at realistic conditions has been reported.

Experimentally investigations into vane/rotor interactions have been completed in both compressors and turbines. Fleeter et al. [1] characterized the effects of a rotor on a downstream stationary compressor stator. Johnston et al. [2] quantified the response of an upstream rotor and inlet guide vane on a downstream rotor. Further study on the effects of upstream vanes and rotors on downstream vanes and rotors was done in a low speed turbine by Johnston and Fleeter [3]. Kielb et al. [4] studied the forced response on a rotor blade caused by vane wakes from an upstream vane row. They also studied the effect of axial spacing on the unsteady pressure at 50% and 85% span showing a 10% increase in unsteady pressure at the closer spacing. More recently Miller et al. [5] investigated the affects of vane-rotor interaction in a high-pressure turbine stage, characterizing the rotor response at 50% span using experimental data and CFD analysis.

Clark et al. [6] demonstrated that it is possible to mitigate resonant stresses in a turbine engine using state-of-the-art design tools and analysis techniques. First, they validated a 3D unsteady Reynolds-averaged Navier-Stokes (RANS) solver for the prediction of unsteady forcing (both phase and amplitude) on a single stage high pressure turbine (also see Clark et al. [7]). Next, they found that it was possible to correlate the peak to peak variation in the circumferential static pressure distortion exiting the HPV row with the largest magnitude of unsteadiness predicted on the blade surface. Then, they used a design optimization system in conjunction with a steady RANS solver to reduce the predicted vane exit static pressure distortion. In so doing, they were able to significantly reduce the unsteadiness on the blade predicted with the 3D time resolved solver, and this corresponded to a reduction of 42% in the predicted level of the first torsion mode resonant stress. Subsequent engine tests confirmed the reduction in stress with a measured decrease of 36%.

In this paper the objective was not only to investigate the unsteady aerodynamics associated with a high pressure turbine, but also to provide a set of experimental data for comparison with computational fluid dynamic (CFD) predictions. CFD analysis is important for continued improvements in turbomachinery. If CFD can accurately simulate the unsteady flow phenomena in turbomachinery, it can be used for the design of vanes and blades to avoid resonant stresses. For instance, Sharma et al. [8] and Manwaring and Wisler [9] used experimental data to test the accuracy of computational methods to improve CFD accuracy. Venable et al. [10] studied the affects of vane blade spacing on a transonic turbine stage and compared the results with four different CFD codes to determine which code could more accurately resolve the data and if using a 2D or 3D code would affect the analysis accuracy.

Experimental Facility

The experimental facility used was the TRF (Fig. 1) of the Air Force Research Laboratory (Haldeman et al. [11]). The TRF was designed to provide experimental data on full scale engine hardware for heat transfer and aero performance related research investigations. The TRF utilized full scale turbine hardware tested with aerodynamic and heat transfer dimensionless parameters matched to actual turbine engine conditions.

[1]Corresponding author.

Contributed by the International Gas Turbine Institute (IGTI) of ASME for publication in the JOURNAL OF TURBOMACHINERY. Manuscript received October 1, 2003; final manuscript received March 1, 2004. IGTI Review Chair: A. J. Strazisar. Paper presented at the International Gas Turbine and Aeroengine Congress and Exhibition, Vienna, Austria, June 13 – 17, 2004, Paper No. 2004-GT-53607.

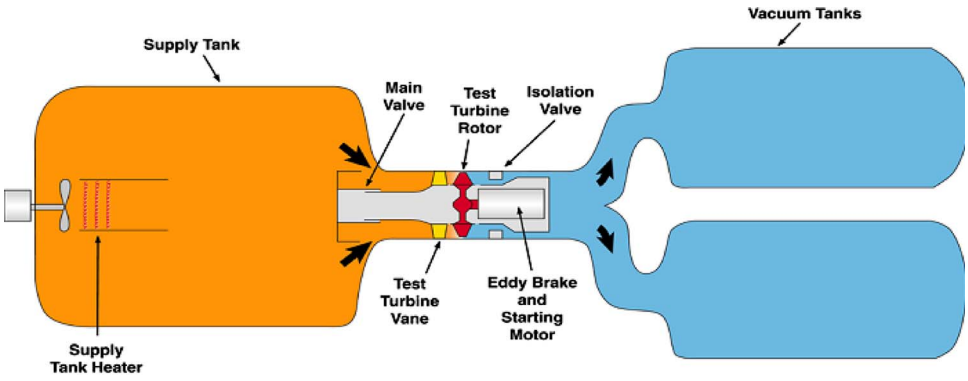

Fig. 1 TRF Schematic

The TRF is a transient, blowdown device. The facility was operated by releasing a properly scaled, heated, and pressurized nitrogen flow through a turbine section into two dump tanks. A typical test run resulted in about 3 seconds of experimental data. The gas to metal temperature ratio, stage pressure ratio, Reynolds number, axial Mach number, corrected speed, specific heat ratio and Prandtl number were matched between the TRF and actual engine conditions.

For this study the TRF was run in both a vane only configuration and as a full stage. Figure 2 is a schematic of the test section in both half (*a*) and full stage (*b*) configurations. Initially, the HPV's alone were installed and a series of different flow measurements were acquired for various freestream Reynolds numbers. Next, the rotor was added and the series of tests were repeated as well as a pressure ratio comparison enabling the effect of the vane-blade interaction to be measured.

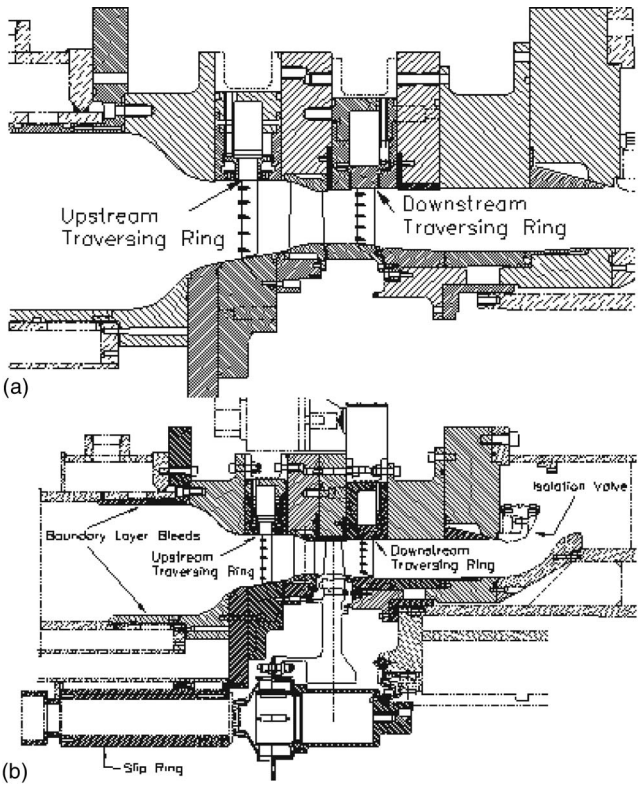

Fig. 2 (*a*) Schematic of test section with vane only. (*b*) Schematic of test section with vane and rotor

Instrumentation

Instrumentation for this analysis consisted primarily of Kulite high frequency response transducers. On the HPV, surface unsteady pressure measurements were obtained from seven (100 psia) Kulite pressure transducers mounted at 50% span. The surface pressure transducers and associated wiring were flush mounted with the vane surface. Four sensors were located on the suction surface at 48%, 69%, 84%, and 94% axial chord while three sensors were on the pressure surface at 0%, 53%, and 90% axial chord. Data for these transducers was digitized at 100 kHz to ensure that higher harmonic content was obtained and to better understand the impact of the unsteady aerodynamics associated with the downstream rotor on the vane.

The rotor blade unsteady pressure measurements were obtained by Kulite pressure transducers surface mounted at 17.9%, 38%, 58.8%, and 75% axial chord on the pressure surface and 0%, 16.3%, 33.9%, 52.5%, 79.8%, 85.1%, and 89.7% axial chord suction surface at 50% span. Pressure measurements were also taken at 7.8%, 50%, 65.8%, 75.3%, and 85.2% axial chord pressure surface and 15.9%, 34.9%, 53%, 70.8%, 84.5%, 89.3%, and 94% axial chord on the suction surface at 96.5% span. A slip ring provided the electrical connection between the rotational and stationary planes.

To characterize the unsteady aerodynamics of the HPV flow entering the rotor, the total pressure distribution was measured at 107% axial chord downstream of the vane trailing edge with a total pressure rake without the rotor present. This was as close to the location where the rotor leading edge was (77% axial chord) as the hardware would allow. A circumferentially traversing instrumentation ring containing a nine headed total pressure rake was utilized. The rake location with respect to the test article is indicated in Fig. 2(*a*). The pressure rake traversed approximately 100° circumferentially during each run. Externally mounted Kulite pressure transducers measured the total pressure at the centroid of equal flow areas. The frequency response of these transducers as installed was 10 kHz.

Data Analysis

The experimental data acquired was analyzed using two methods, ensemble averaging and discrete fourier transform (DFT). Data reduction codes were developed for both of these analysis methods. These codes were thoroughly tested by using known functions to ensure that the data was being reduced properly. For the ensemble averaging analysis, different population sizes of data were analyzed to determine the optimum number of ensemble averages required. Ensemble averaging eliminates the fluctuations due to incoherent unsteadiness associated with turbulence (and any unsteadiness nonsynchronous with the rotor) and thereby clarifies the stationary periodic unsteadiness, which was of interest.

For the total pressure measurements downstream of the HPV's, the data was ensemble averaged. A DFT utilizing a Hanning window method was applied to the experimental data acquired by the circumferential traverse to obtain the unsteady harmonic content from the vane, impinging on the rotor.

Analysis of the vane and blade surface unsteady pressure measurements was accomplished by taking eighty 3 rotor revolution sections of data successively from the entire trace. Ensemble averaging of the HPV and HPB was achieved by linearly interpolating the three rotor revolution sections. These sections were then averaged on a revolution basis. A DFT of each three revolution section with respect to engine order was averaged to get a representative DFT output for the entire trace. The vane surface data was normalized by the upstream total pressure (PU_t) while the rotor surface data was normalized by the relative total pressure (P_t).

Uncertainty

The total uncertainty of the analysis was determined by taking the square root sum of squares of the different sources of uncertainty consistent with Moffat [12]. The different sources include code error, data resolution error, calibration error and repeatability error.

The pressure transducers were statically calibrated in situ prior to and after each run. A Ruska standard was used to monitor the test section pressure while it was filled and evacuated. A difference of about 0.40% in measured pressure was found between using the calibration coefficients from the pre calibration versus the post calibration for a typical run. Because the vane total pressure data is being normalized by the upstream total pressure (PUt) the maximum calibration error was 0.44% and the rms value was 0.40%. For the vane surface data the maximum calibration error was 0.20% with a rms of 0.10%. The rotor surface data maximum calibration error was 0.28% with a rms of 0.22%. The rotor calibration uncertainty includes uncertainty due to gravitational loading caused when the rotor was spinning. An additional strain was induced in the Kulite due to the centripetal acceleration of the rotor. A test was done with the rotor spinning in a vacuum at various speeds to account for the offset read by the Kulite pressure transducers.

The uncertainty introduced by using the ensemble average code for the total pressure traverse data was a bias error with a 0.11% maximum uncertainty and a rms uncertainty of 0.07%. The uncertainty in the data resolution for the ensemble averaging process was split up into two separate sections. The wake region, the maximum uncertainty was 0.8% with a rms uncertainty of 0.3%. For the freestream region the uncertainty was much smaller having a maximum of 0.09% and a rms uncertainty of 0.06%. For the vane and rotor surface data the ensemble averaging code had a bias error of 0.08% maximum with a rms of 0.05%. The vane surface data had a maximum uncertainty of 0.07% and a rms of 0.01%. The rotor surface data had higher uncertainties of 0.53% maximum and 0.25% rms.

The bias error caused by the DFT code for the total pressure traverse was 0.16% when inputting the ensemble averaged data. For the vane and rotor surface harmonic analysis the code error was less than 0.01%.

Analyzing multiple runs for the baseline condition it was determined that the repeatability error had a maximum uncertainty of 0.5% with a rms value of 0.3%. Combining these errors resulted in maximum total error for the ensemble averaged total pressure data of 1.05% for the wake region and a rms of 0.59% and a freestream region uncertainty of 0.68% maximum and a rms of 0.51%. The total pressure harmonic analysis had a maximum uncertainty of 1.06% for the wake region and a rms of 0.61%. The freestream region maximum uncertainty was 0.70% and a rms of 0.53%. The surface pressure data had much lower uncertainties. The vane and rotor surface data had maximum uncertainties of 0.55% and 0.78%, respectively, with rms uncertainties of 0.32% and 0.45%.

Results

The full-scale high-pressure turbine data was first acquired downstream of the HPV utilizing a circumferential traverse assembly without a downstream rotor blade row. The vane surface unsteady pressures were also acquired. The goal of this testing was to quantify the unsteadiness caused by the vane. A second experiment was performed with the HPB row in place where both vane and rotor surface measurements were taken. The measurements on the vane are assumed representative of the forcing function to the vane from the upstream propagating potential field generated by the downstream rotor. The measurements on the rotor were assumed caused by shock, potential field, and wake effects.

HPV Total Pressure Measurements. The vane only test was performed to determine if the unsteadiness leaving an upstream vane row could be quantified and seen on a downstream rotor in a subsequent vane and rotor test. Therefore tests were run in this configuration to matched vane and rotor cases. The baseline condition was defined as a pressure ratio of 1.018, a Reynolds number of 3.67E5, a Mach number of 0.17, and inlet turbulence level less than 1.0%. The pressure ratio was calculated by dividing the total pressure entering the vane by the total pressure exiting the vane

$$PR = \frac{PU_t}{P_{t\,ex}} \tag{1}$$

The Reynolds number for the HPV total pressure traverse was based on inlet conditions:

$$\mathrm{Re}_i = \frac{\rho V x_V}{\mu} \tag{2}$$

where x_v is the vane axial chord. For these tests three Reynolds numbers of 5.78E4, 3.67E5, and 4.63E5 were used. The corresponding inlet Mach numbers were 0.21, 0.17, and 0.15, respectively.

A higher pressure ratio case was not presented because the effects seen in the vane only configuration would not be representative of a vane and rotor configuration. The addition of a rotor would choke the flow causing a higher pressure ratio case to follow the baseline until the rotor choke point as seen later.

Figure 3 is a plot of the normalized exit total pressure versus circumferential angular position for the baseline case at eight of nine radial positions. The 18.2% span transducer was not functional therefore the data was not analyzed. Approximately twelve vane passages of data were acquired for each span location. The variation in the wake location was 16% maximum. The data shows that the normalized pressure fully recovers to the upstream value away from the wakes, except near the end walls, where the secondary flow results in an overall loss. A $7\pi/4$ radian phase shift in the data was observed with a change in spanwise location as suggested in Fig. 3. This was attributed to a change in the exit flow angle. A change of only 2 deg in the HPV flow exit angle would cause the time trace to be π radians out of phase and this vane is expected to have a 3 deg change from hub to tip (or $3\pi/2$ radians).

For aeromechanical design the frequencies associated with the unsteady aerodynamics that coincide with structural resonances is of primary interest. Therefore, a harmonic analysis of the HPV total pressure circumferential traverse data for the baseline was performed. Figure 4 contains the magnitudes of the first five harmonics. The first and second harmonics are significant, therefore, highlighting the need to consider both of these harmonics in the high pressure turbine aeromechanical design analysis. Higher unsteadiness levels near the end walls were seen indicative of sec-

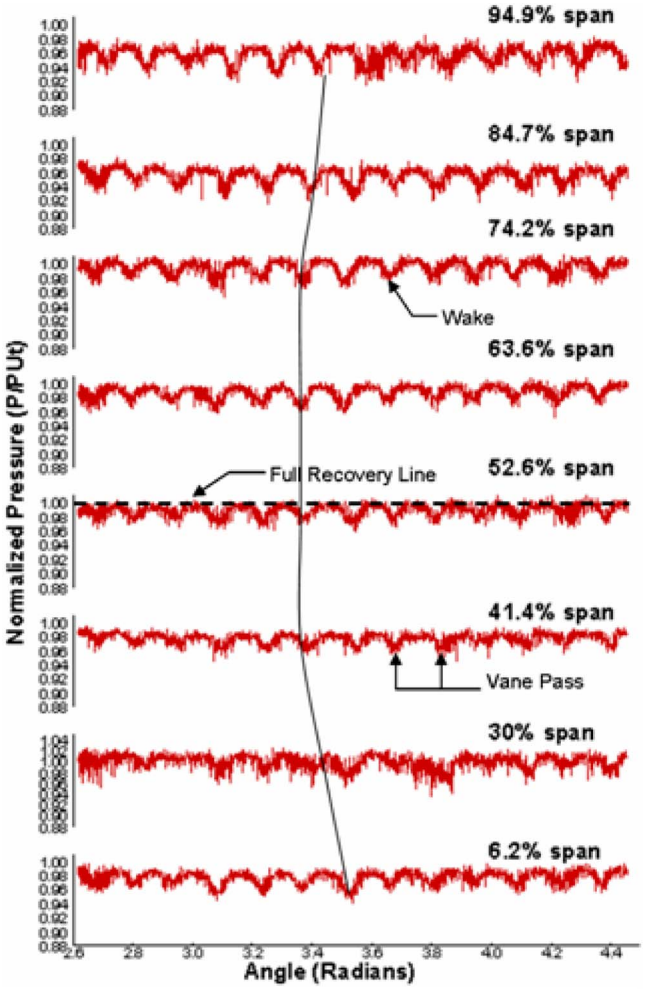

Fig. 3 Baseline HPV total pressure exit traverse

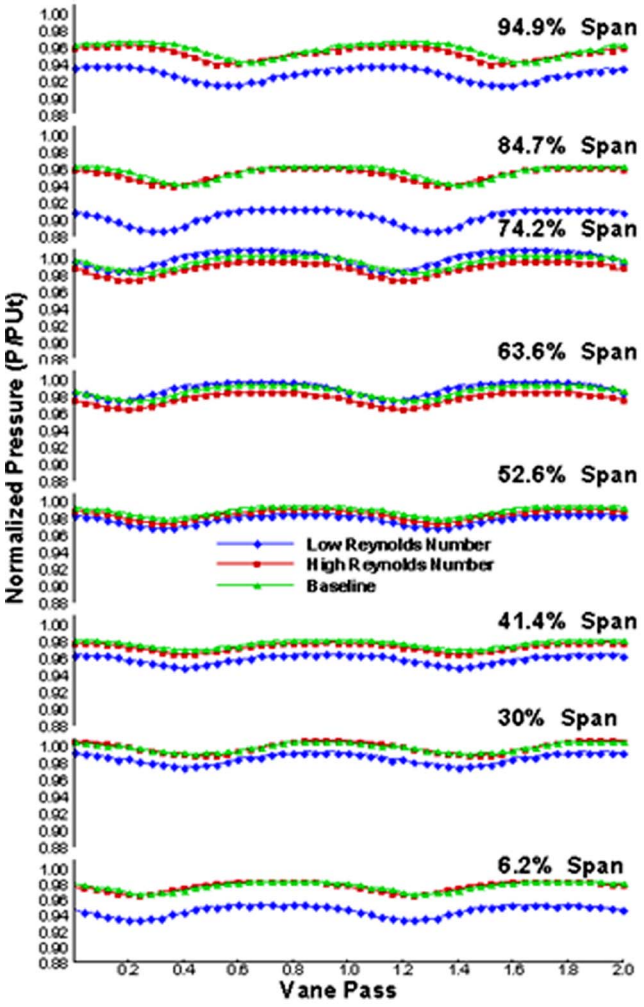

Fig. 5 Reynolds number effects on the HPV total pressure exit flow

ondary flow.

Figure 5 is an ensemble average comparison of each spanwise location for the three Reynolds numbers. The lower Reynolds number data shows more overall loss, particularly in the 3D sections of the airfoil which is consistent with an off design point. An increase in Reynolds number had no noticeable effect on the total pressure traverse.

Figure 6 contains the first harmonic (44E) magnitudes of the HPV total pressure measurements for all three freestream Reynolds numbers. The first harmonic trends were nominally the same for all three cases. In the midspan region both the high and low Reynolds number cases had the higher unsteadiness levels consistent with being off design. The low Reynolds number case had in general higher pressure magnitudes consistent with greater secondary flows. The higher Reynolds number case had the oppo-

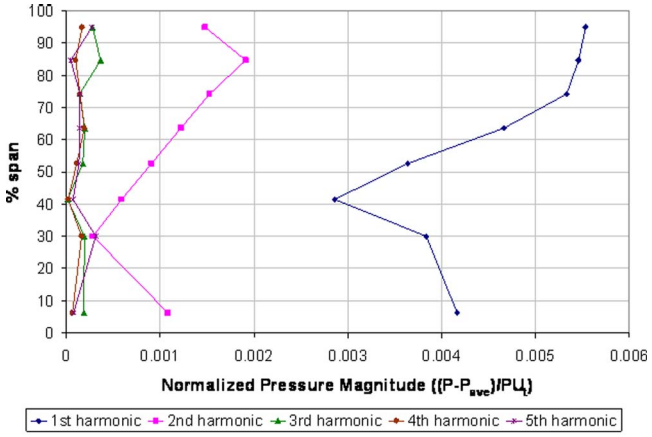

Fig. 4 Harmonic comparison for baseline vane exit flow

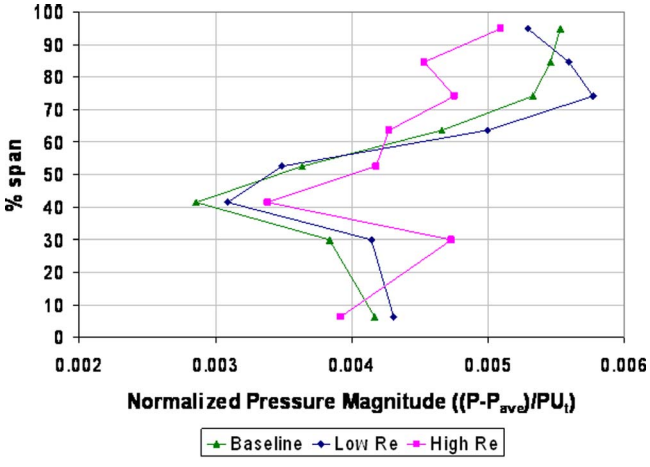

Fig. 6 Reynolds number effects on HPV 1st harmonic exit flow

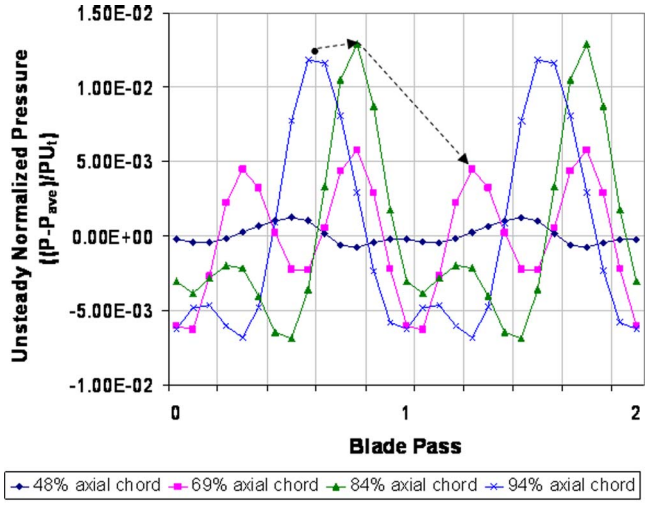

Fig. 7 Unsteady pressure on the HPV for the baseline condition at 50% span

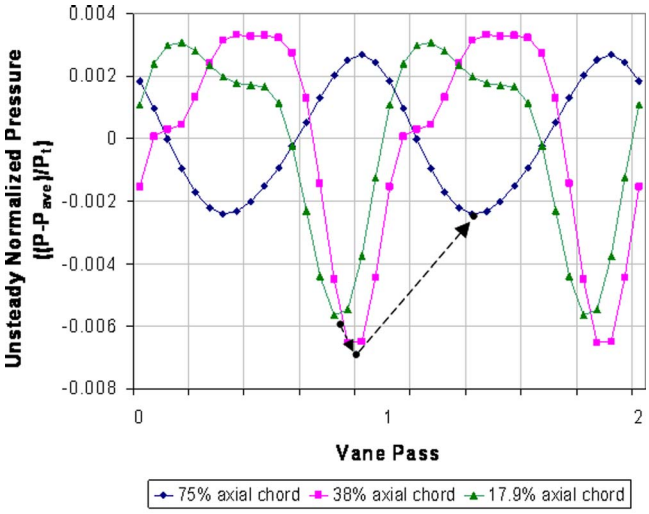

Fig. 8 Unsteady pressure on the pressure side of the HPB for the baseline condition at 50% span

site trend as expected. The vane only test was able to quantify the unsteadiness leaving an upstream vane. The results show that the unsteadiness increases with an increase in span. The unsteadiness leaving the vane at 52.6% span was around 0.004 while the unsteadiness at 94.9% span is about 0.0055. These results were compared later to the stagnation points on the rotor blade at 50% and 96.5% span.

Vane-Rotor Interaction. The baseline case for the vane and rotor had the same inlet conditions as the vane only baseline case. This resulted in a pressure ratio of 2.76, Reynolds number of 3.80E5, and Mach number of 0.163. The pressure ratio was calculated the same as Eq. (1) except the total pressure exiting the rotor was used. Similarly, the Reynolds number was based on exit conditions and was calculated the same as Eq. (2) except the rotor axial chord length was used instead of vane axial chord length. For the vane and rotor experiments tests were performed to analyze what effect changes in Reynolds number and pressure ratio would have on the unsteadiness on the vane and blade surface. The Reynolds number was held constant while pressure ratio was changed to 3.09. The Reynolds number was varied the same as the vane only cases resulting in Reynolds numbers of 2.33E5 and 4.10E5 at constant pressure ratio. The corresponding Mach numbers were 0.177 and 0.160, respectively.

As stated earlier the data was analyzed using two different methods, ensemble averaging and DFT. A DFT analysis was performed for the pressure transducer closest to the trailing edge of the vane to find the frequency of the unsteady excitation. This frequency (6871 Hz) was then compared to the calculated rotor blade pass frequency of 6846 Hz. This agreement suggests that the vane forcing function was driven primarily by the downstream rotor.

An ensemble averaging analysis was done on the vane and rotor surface at 50% span to understand the unsteady pressure waves due to the vane/rotor interaction. For the vane the unsteady pressure has the greatest influence on the suction surface therefore the four suction surface pressure sensors were ensemble averaged and plotted in Fig. 7. The 69% vane surface axial chord location is located just aft of the vane throat. The unsteady pressure signal in front of the vane throat (48% axial chord) was negligible, as were the pressure surface unsteady signal. This emphasizes that the rotor has the greatest effect in the uncovered portion of the vane as expected.

The unsteadiness shown in Fig. 7 was the vane forcing function and was found to be due to the potential field from the rotor. This propagating potential field was defined as the V−c characteristic and was determined by calculating the local speed of sound (429.5 m/s) and subtracting it from the exit HPV freestream velocity (347.9 m/s). This propagation speed (−81.6 m/s) was compared with the speed (−77.7 m/s) obtained from the experimental data using the axial distance between sensors and the maximum unsteady pressure response from Fig. 7 with an excellent agreement obtained. A potential field should also be moving downstream at a propagation speed of the V+c characteristic. Figure 8 is the vane pass ensemble average of the 50% span surface unsteady pressure measurements on the rotor pressure surface. A propagation speed (574.6 m/s) was calculated using the known axial distance between sensors and the time difference between unsteady responses between sensors. This was compared to the propagation speed (545 m/s) determined by the local speed of sound (429.5 m/s) and axial velocity (115.5 m/s) with good agreement. This is consistent with work of Miller et al. [5] which found the blade pressure side to be strongly influenced by the potential field.

To further analyze the variation on the vane and blade, a DFT analysis was performed on the vane and rotor surface. A harmonic comparison was performed for both the vane and rotor to determine which harmonics were influential. Consistent with aeromechanical design procedures, the results are presented in the RMS of the harmonic amplitudes.

Again analysis was done on the vane suction surface which was influenced by an upstream propagating potential field. Figure 9 compares the first three harmonics (58E, 116E, and 174E). From Fig. 9, the first harmonic decay significantly increased between 84% and 69% axial chord. This resulted in the second harmonic being more influential at 69% and 84% axial chord. Therefore both harmonics would need to be accounted for in the design process.

Figures 10 and 11 contain the 1st and 2nd harmonic unsteady magnitudes respectively on the vane surface for all four flow conditions. The baseline and high pressure ratio 1st harmonic results show similar trends of a significant reduction forward of the 84% axial chord location which is consistent with the flow being choked in the rotor. Airfoil loading is only affected downstream of the choke point on the blade for increased pressure ratio. Before the vane throat (69% axial chord) all cases show similar levels of unsteadiness. After the vane throat however, only the baseline, higher pressure ratio, and lower Reynolds number cases were similar. An increase in Reynolds number however caused a decrease in unsteady pressure.

The second harmonic results show similar trends with the low

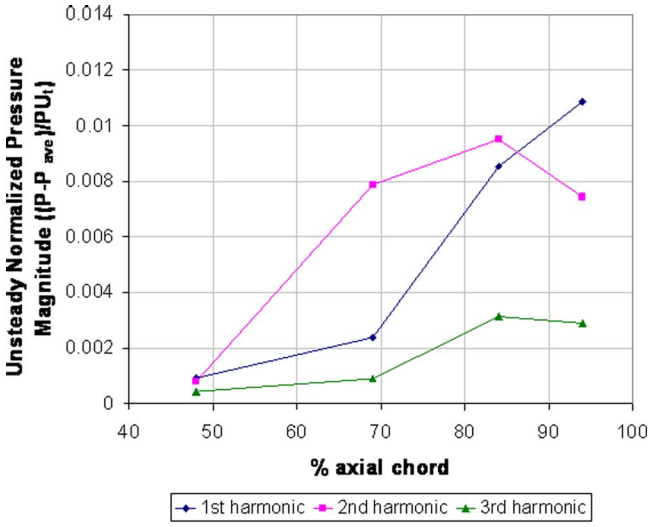

Fig. 9 Harmonic comparison of unsteady vane surface pressure for baseline

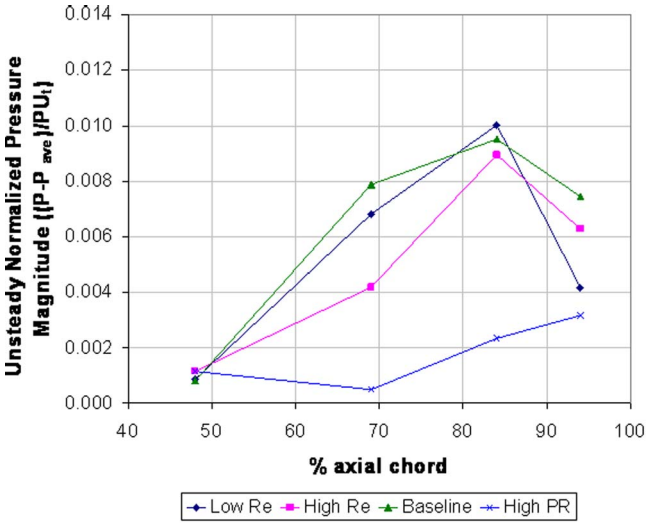

Fig. 11 2nd harmonic Reynolds number and pressure ratio effects of unsteady surface pressure acting on the vane

Reynolds number case following the baseline. For the second harmonic with an increase in Reynolds number a decrease in unsteady pressure at the vane throat occurred compared to the baseline. The high pressure ratio case had the most dramatic results in that the values were negligible compared to the first harmonic results. These results highlight a clear need to consider higher harmonic content and the freestream Reynolds number effects when performing a high pressure turbine vane aeromechanical design.

The first four harmonics (44E, 88E, 132E, 176E) of the unsteady pressure on the HPB were compared on Fig. 12. The harmonic analysis revealed that the first harmonic drives the unsteadiness on the rotor. But the other harmonics are not negligible.

Also investigated was the variation in blade surface unsteady pressure at 50% and 96.5% span. The 1st harmonic shows that the peak unsteadiness on the suction surface was almost three times greater than the pressure surface. Comparing, 50% to 96.5% span (Fig. 13 and 14), the unsteady pressure decreases on the pressure side with increase in span. On the suction surface, the unsteady pressure decreased rapidly from the peak unsteadiness near the leading edge to the trailing edge of the HPB for both spans.

Comparing the results at the stagnation point in Fig. 13 with the vane only analysis results in Fig. 6 at 52.6% span the unsteadiness appears to be primarily driven by the potential field and wakes from the upstream HPV. The first harmonic unsteadiness measured from the vane only analysis was 0.0035 while the rotor stagnation measured 0.006. From the ensemble average analysis earlier the potential field was seen to be the major source of unsteadiness on the pressure surface with levels around 0.005. Therefore similar unsteadiness levels would be expected to be from potential field effects on the suction surface. This shows that the potential field effects had greater influence than the wake from the upstream vane row. At 96.5%, Fig. 14, however the data does not agree as well. The levels seen from the vane only analysis at 94.9% span were 0.0055 while the vane/blade analysis at 96.5% was around 0.003. This could have been due to tip gap flow influencing the unsteadiness as will be discussed later.

Analysis of Fig. 13 and 14 show much higher levels between 16% and 52.5% on the suction surface. After 52.5% axial chord the unsteadiness on the suction surface of the rotor blade returns to levels consistent with that expected from the potential field and

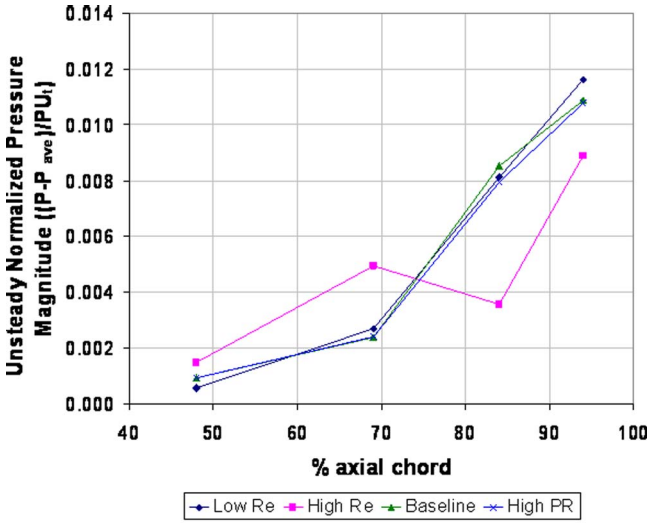

Fig. 10 1st harmonic Reynolds number and pressure ratio effects of unsteady surface pressure acting on the vane

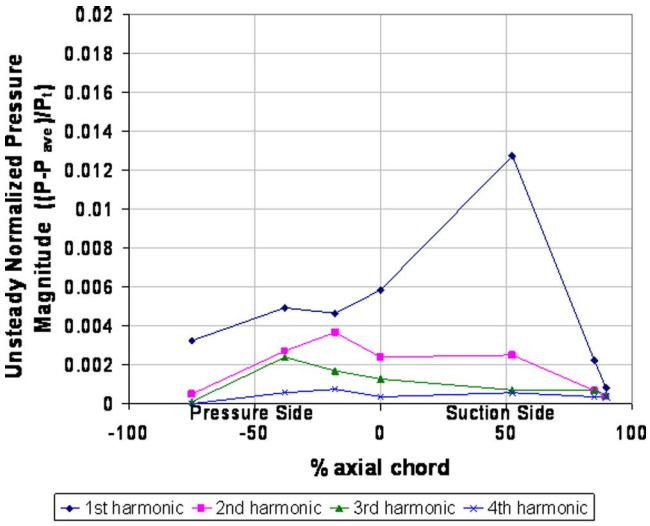

Fig. 12 Comparison of unsteady harmonics on the rotor at 50% span

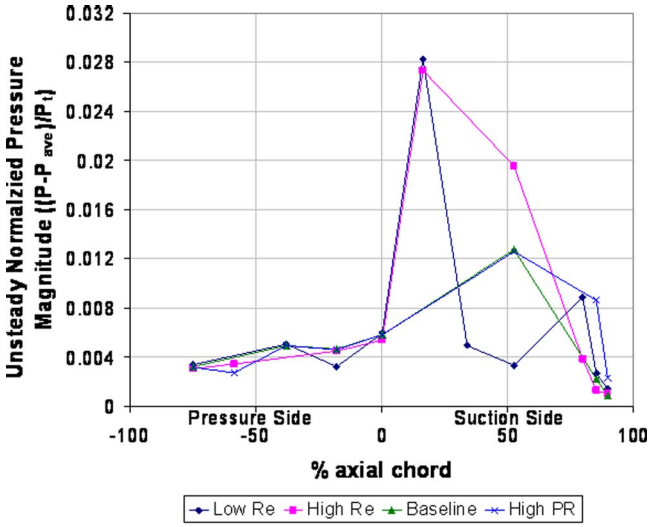

Fig. 13 Comparison of the 1st harmonic of unsteady pressure on the rotor at 50% span

vane wakes. Levels higher than the potential field unsteadiness must be from another source. Miller et al. [5] had similar results with high levels of unsteadiness towards the leading edge of the suction surface on the HPB. Using CFD they concluded these effects were due to the trailing edge shock impinging on the suction surface. The current data suggests the same results. The shock impingement location appears to be between 52.5% and 85.1% axial chord which is consistent with the rotor crown. The shock then moves upstream on the blade surface.

An investigation of the four cases revealed that there was no influence of increased pressure ratio for the unsteadiness on the rotor except aft of the rotor choke point as expected at both spans. At 50% span a decrease in Reynolds number caused the shock to form closer to the leading edge while increased Reynolds number caused the shock effect on the suction surface to have a stronger effect at 52.5% axial chord. On the pressure surface unsteadiness levels are nominally the same magnitude for all cases. At 96.5% span a decrease in Reynolds number caused an increase in unsteadiness on the pressure surface. The suction surface has nearly constant values for all cases. Polanka et al. [13] showed that the 96.5% span loading and the tip pressure distribution do not

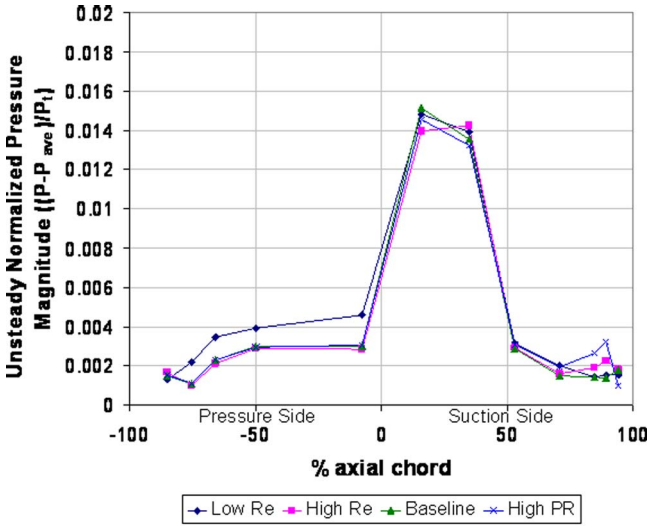

Fig. 14 Comparison of the 1st harmonic of the unsteady pressure on the rotor at 96.5% span

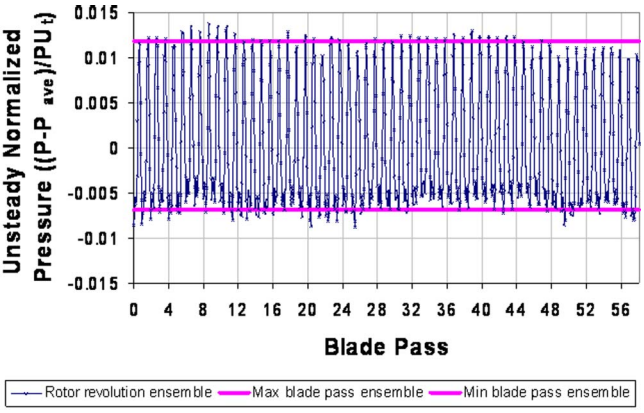

Fig. 15 Comparison between revolution ensemble and blade pass ensemble at 94% vane axial chord

change in front of the rotor choke point with changes in Reynolds number. This implies that the tip gap flow is constant (regardless of Reynolds number) and a more similar flow pattern was established. This consistent flow could have had significant impact on the local unsteadiness, resulting in the nearly constant levels shown in Fig. 14. The tip gap flow may also have contributed to the lower unsteadiness levels seen on the stagnation point at 96.5% span as the secondary flow was accelerating to enter the tip gap, thus reducing the unsteadiness.

The vane and blade surface data was acquired at a high enough frequency resolution to quantify each vane and rotor passage through ensemble averaging. A comparison between a revolution ensemble and the maximum and minimum window of the blade passing ensemble at the 94% axial chord location on the vane is shown in Fig. 15. The blade to blade variation in the data of the revolution ensemble is not much outside the blade pass ensemble suggesting weak lower order harmonics. A similar comparison is shown in Fig. 16 for the stagnation point on the HPB. The peak to peak variation for each vane passing cycle varies dramatically compared to the average vane passing period. This shows that if the vane or rotor is designed to the average unsteadiness, passages whose unsteadiness falls outside of this could easily fail. On the rotor this was especially important because the variation was so dramatic that at least half the passage fall outside the average. This variation was thought not to be due to variability of the vane throat areas as they were within 4% from the average, but according to Miller [5] small variations in vane trailing edge thickness or blade to blade throat areas can cause a relatively large variation.

The variation seen in the vane and rotor revolution ensembles

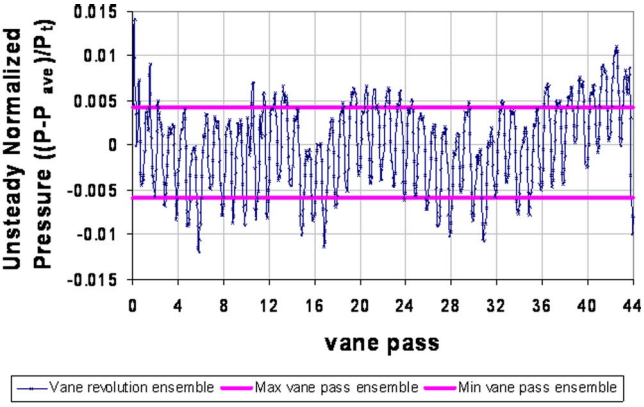

Fig. 16 Comparison between revolution ensemble and vane pass ensemble at the rotor stagnation point

was due to lower engine orders. It is important for designers to look at the Campbell diagrams and make sure these lower engine order levels will not cause vane or blade failure. The vane showed a maximum variation of 6% (<0.001) of the 58E at 2E with 4% at 5E and 3% at 1E. At 50% span at the stagnation point the variation was 41% (0.002) of the 44E at 2E and 24% at 1E, 3E, and 4E.

Conclusion

Detailed measurements of the unsteady aerodynamics associated with a vane and rotor of a modern full scale high pressure turbine have been completed. A total of four different flow conditions were investigated using surface unsteady pressure measurements and circumferential traverses of a total pressure rake downstream of the vane. The unsteadiness on the HPB was primarily driven by shock and potential field interaction while the HPV unsteadiness was driven by potential field interaction. The upstream vane wakes appeared to have little or no effect on the rotor unsteadiness as Miller et al. [5] suggest. The lack of significant effects in the unsteady aerodynamics of the HPV and HPB with changes in pressure ratio is consistent with the stage being choked. In addition, the freestream Reynolds number was shown to have an effect on the unsteady aerodynamics related to the vane and rotor, therefore, this effect should be considered in the design process. This data highlights that both second harmonic content and individual vane/blade passages should be considered in the design process because they contain substantial unsteadiness associated with the vane and blade surface.

Acknowledgment

The authors would like to acknowledge the support of the AFRL/PRT and the Dayton Area Graduate Studies Institute (DAGSI). In particular, AFRL contract F33615-98-C-2895, under contract monitor Dr. Charles Cross, and DAGSI project PR-UC-01-17. We would especially like to thank Dr. John Clark for his helpful input throughout this research.

Nomenclature

P = pressure
PR = pressure ratio
PU = upstream pressure
Re = Reynolds number
V = velocity
c = speed of sound
x = axial chord length
μ = dynamic viscosity
ρ = density

Subscripts

R = rotor
V = vane
ex = exit conditions
i = inlet conditions
s = static
t = total

References

[1] Fleeter, S., Jay, R. L., and Bennett, W. A., 1978, "Rotor Wake Generated Unsteady Aerodynamic Response of a Compressor Stator," ASME J. Eng. Power, **100**, pp. 664–675.

[2] Johnston, R. T., Feiereisen, J. M., and Fleeter, S., 1998, "Measured Rotor Wake and Potential Forcing Functions, Including Blade Row Interactions," J. Propul. Power, **14**(2), pp. 191–198.

[3] Johnston, D. A., and Fleeter, S., 1998, "Three-Dimensional Turbine Rotor Forcing Functions and Linear Theory Analysis," J. Propul. Power, **14**(2), pp.183–190.

[4] Kielb, J. J., Dunn, M. G., and Abhari, R. S., 2001, "Experimental and Numerical Study of Forced Response in a Full-Scale Rotating Turbine," ASME Paper No. 2001-GT-0263.

[5] Miller, R. J., Moss, R. W., Ainsworth, R. W., and Harvey, N. W., 2003, "Wake, Shock, and Potential Field Interactions in a 1.5 Stage Turbine–Part I: Vane–Rotor and Rotor–Vane Interaction," J. Turbomach., **125**, pp.33–39.

[6] Clark, J. P., Aggarwala, A. S., Velonis, M. A., Gacek, R. E., Magge, S. S., and Price, F. R., 2002, "Using CFD to Reduce Resonant Stresses on a Single-stage High-pressure Turbine Blade," ASME Paper No. GT-2002-30320.

[7] Clark, J. P., Stetson, G. M., Magge, S. S., Ni, R. H., Haldeman, C. W., Jr., and Dunn, M. G., 2000, "The Effect of Airfoil Scaling on the Predicted Unsteady Loading on the Blade of a 1 and Stage Transonic Turbine and a Comparison with Experimental Results," ASME Paper No. 2000-GT-0446.

[8] Sharma, O. P., Pickett, G. F., and Ni, R. H., 1992, "Assessment of Unsteady Flows in Turbines," ASME J. Turbomach., **114**, pp. 79–90.

[9] Manwaring, S. R., and Wisler, D. C., 1993, "Unsteady Aerodynamics and Gust Response in Compressors and Turbines," ASME J. Turbomach., **115**, pp. 724–740.

[10] Venable, B. L., Delaney, R. A., Busby, J. A., Davis, R. L., Dorney, D. J., Dunn, M. G., Haldeman, C. W., and Abhari, R. S., 1999, "Influence of Vane-Blade Spacing on Transonic Turbine Stage Aerodynamics: Part I—Time-Averaged Data and Analysis," J. Turbomach., **121**, pp. 663–682.

[11] Haldeman, C. W., Dunn, M. G., MacArthur, C. D., and Murawski, C. G., 1992, "The USAF Advance Turbine Aerothermal Research Rig," *NATO AGARD Propulsion and Energetics Panel Conference Proceedings*, No. 527, Antalya, Turkey, 1992.

[12] Moffat, R. J., 1988, "Describing the Uncertainties in Experimental Results," Exp. Therm. Fluid Sci., **1**, pp.3–17.

[13] Polanka, M. D., Hoying, D. A., Meininger, M., and MacArthur, C. D., 2002, "Turbine Tip and Shroud Heat Transfer and Loading Part A: Parameter Effects Including Reynolds Number, Pressure Ratio, and Gas to Metal Temperature Ratio," ASME Paper No. GT-2002-30186.

Fan-Shaped Hole Effects on the Aero-Thermal Performance of a Film-Cooled Endwall

Giovanna Barigozzi
e-mail: giovanna.barigozzi@unibg.it

Giuseppe Benzoni

Giuseppe Franchini

Antonio Perdichizzi
e-mail: antonio.perdichizzi@unibg.it

Dipartimento di Ingegneria Industriale,
Università degli Studi di Bergamo,
Viale Marconi 24044,
Dalmine (BG), Italy

The present paper investigates the effects of a fan-shaped hole endwall cooling geometry on the aero-thermal performance of a nozzle vane cascade. Two endwall cooling geometries with four rows of holes were tested, for different mass flow rate ratios: the first configuration is made of cylindrical holes, whereas the second one features conical expanded exits and a reduced number of holes. The experimental analysis is mainly focused on the variations of secondary flow phenomena related to different injection rates, as they have a strong relationship with the film cooling effectiveness. Secondary flow assessment was performed through downstream 3D aerodynamic measurements, by means of a miniaturized 5-hole probe. The results show that at high injection rates, the passage vortex and the 3D effects tend to become weaker, leading to a strong reduction of the endwall cross flow and to a more uniform flow in spanwise direction. This is of course obtained at the expense of a significant increase of losses. The thermal behavior was then investigated through the analysis of adiabatic effectiveness distributions on the two endwall configurations. The wide-banded thermochromic liquid crystals (TLC) technique was used to determine the adiabatic wall temperature. Using the measured distributions of film-cooling adiabatic effectiveness, the interaction between the secondary flow vortices and the cooling jets can be followed in good detail all over the endwall surface. Fan-shaped holes have been shown to perform better than cylindrical ones: at low injection rates, the cooling performance is increased only in the front part of the vane passage. A larger improvement of cooling coverage all over the endwall is attained with a larger mass flow rate, about 1.5% of core flow, without a substantial increase of the aerodynamic losses. [DOI: 10.1115/1.2098788]

Introduction

The demand for the continuous increase of gas turbine performance requires the enhancement of thermal protection all over the turbine surfaces, including the endwall region. In fact, turbine inlet temperature increase and combustor design improvement combine to give higher and flatter temperature distributions approaching the turbine first-stage nozzle vane. Moreover, inside the vane passage, secondary flows move high-temperature gas from the midspan region towards the endwalls. All these aspects lead to the requirement of a quite effective endwall cooling. The achievement of high cooling performances requires the improvement of injection modes, getting higher effectiveness with minimum coolant consumption.

Because of the impact of endwall cooling on secondary flow and related losses, combined aero-thermal investigations are required to analyze the cooling performances. Endwall cooling is usually performed through slots (Blair [1], Roy et al. [2], Oke and Simon [3]) or discrete holes located upstream of the leading edge (Oke et al. [4]). Cooling schemes with holes located inside the passage were also proposed (Jabbari et al. [5], Friedrichs et al. [6–8], Kost and Nicklas [9], Nicklas [10], Knost and Thole [11]). Endwall flow injection upstream of the vane passage also has been used to control secondary flows (Zhang and Jaiswal [12]).

Endwall heat transfer is strongly influenced by the presence of the corner vortex, which was proved to be responsible for the large heat transfer coefficient variations inside the vane passage [1]. Friedrichs et al. [6–8] found that endwall coolant injection strongly alters the secondary flow structure, with the lift-off line of the horseshoe vortex moving closer to the leading edge when coolant injection is present. Concerning the coolant-to-mainstream mixing loss, a reduction was found for mass flow rates above 2%, when compared with the uncooled case. When coolant is injected at large mass flow rate, it re-energizes the boundary layer, thus weakening the secondary flows.

More recently, Kost and Nicklas [9] and Nicklas [10] investigated the aero-thermal behavior of a transonic cascade with endwall film cooling. A strong interaction between the coolant and the main flow was detected. Again, coolant injection strengthens the endwall boundary layer, thus reducing the endwall crossflow. A similar investigation, but on a different endwall cooling scheme, was also performed by Knost and Thole [11]. They found that coolant behavior is strongly dependent upon local blowing conditions for the cooling holes, and especially upon the momentum flux ratio. The leading edge region and the pressure side were found to be the most difficult regions to be efficiently cooled.

The most common geometry used for endwall cooling through hole is based on cylindrical holes inclined in the axial direction and showing a compound angle. Thole et al. [13] and Gritsch et al. [14,15] demonstrated that the addition of an expanded exit can provide better cooling performances in terms of larger adiabatic effectiveness, larger lateral spreading, and reduced heat transfer coefficient, when applied to a simple flat plate configuration. No information is available, to the authors' knowledge, on the effect of the use of expanded exits in endwall film-cooling configurations in a cascade.

The present paper deals with the effect of endwall film-cooling geometry and overall mass flow ratio on the aero-thermodynamic performance of a nozzle vane cascade. The same cascade was already extensively tested on both a full coverage film cooling and a solid (i.e., without film cooling) configurations (Barigozzi et al. [16]). In the present study, two endwall cooling geometries were

Contributed by the International Gas Turbine Institute (IGTI) of ASME for publication in the JOURNAL OF TURBOMACHINERY. Manuscript received October 1, 2004; final manuscript received February 1, 2005. IGTI Review Chair: K. C. Hall. Paper presented at the ASME Turbo Expo 2005, Land, Sea and Air, Reno, NV, June 6–9, 2005, Paper No. GT2005-68544.

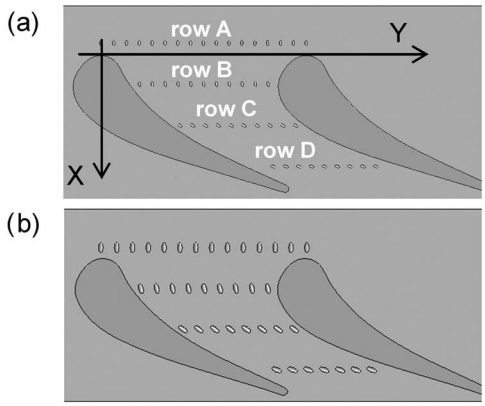

Fig. 1 Cascade and endwall cooling geometry—(*a*) CONF1 and (*b*) CONF2

tested: the first one consists of four rows of cylindrical holes regularly distributed inside the vane passage. This simple configuration has been already aerodynamically tested (Barigozzi et al. [17]). The distinguishing features of the second geometry are a smaller number of holes and a diffusion section. The goal is to analyze the effect of the introduction of fan-shaped holes on the aero-thermal performances of a nozzle vane cascade, under different overall coolant to mainstream mass flow ratios.

Experimental Details

Geometry and Test Conditions. Tests were performed in the subsonic wind tunnel for linear cascades at the Thermo-Fluid Dynamic Laboratory of Bergamo University. A description of the wind tunnel, including the cascade geometry and the secondary air supply system, is given in Ref. [16]. The facility consists of a 7-blade cascade, whose geometry is typical of a first-stage nozzle vane. Figure 1 shows the tested vane together with the cooled endwall geometries (CONF1 and CONF2). For both configurations, only one endwall was cooled, with cooling assured by the presence of 4 rows of cylindrical holes of 1.5 mm diameter connected to a single plenum. The holes are distributed over only one passage. Hole locations and geometrical characteristics are summarized in Table 1. For both geometries, row A is located upstream of the leading edge plane. The following three rows are evenly positioned inside the vane channel, with the last one located at 81.2% c_{ax} downstream of the leading edge plane. Row C is located where the passage vortex separation line impacts on the suction side surface. The definition of hole axial positions has been determined on the basis of oil flow visualizations (Barigozzi et al. [17]), identifying the saddle point and separation line positions. The hole injection angle has been set to 30 deg with respect to the radial direction. In the blade-to-blade plane, each row has a compound angle equal to the mean flow angle at midspan. Following Friederichs et al. [6], this mean flow angle has been computed on the basis of midspan blade-to-blade measurements (Barigozzi et al. [16]), by pitchwise averaging the flow angles from pressure to suction side.

Table 1 Cooling system geometrical characteristics

	CONF1				CONF2			
Row	*A*	*B*	*C*	*D*	*A*	*B*	*C*	*D*
X/c_{ax}	−0.08	0.35	0.65	0.82	−0.08	0.35	0.65	0.82
$N°$	17	11	10	9	14	9	8	7
γ		0°				20°		
B/D		4.8				6		
L/D				10.7				
α				30°				

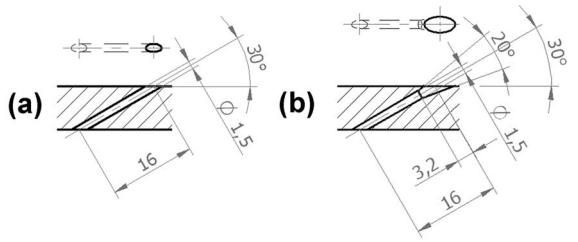

Fig. 2 Detail of hole geometry—(*a*) CONF1 and (*b*) CONF2

CONF2 cooling scheme has a lower number of holes (≈20% less) compared to CONF1, with a conical expanded exit: the final portion of each hole has a divergence angle of 20 deg (Fig. 2), with the fan-shaped portion extending approximately 2*D* inward. The hole length over diameter ratio is the same for both configurations ($L/D=10.7$), while the CONF2 hole pitch is larger (6*D* against 4.8*D*). Exit-to-inlet area ratio (normal to hole axis) is 3.1.

A good film-cooling effectiveness will be attained when coolant is injected at a momentum high enough to resist to the passage vortex, but not too large to give rise to jet lift-off. The presence of expanded exits, maintaining the same number of holes and injected massflow, is expected to reduce the local blowing and momentum flux ratios. This will also alter the jet-to-secondary flow interaction and the cooling capabilities. On the opposite, when reducing the number of holes, still holding the same mass flow ratio (MFR), the mass flow injected through each hole will increase, together with local blowing and momentum flux ratios. When the two modifications are combined, it is not easy to predict the way the two aforementioned aspects will interact.

The cascade geometry and the operating conditions are summarized in Table 2. Tests were performed at low isentropic Mach number (Ma=0.2), and low inlet turbulence intensity, namely 1%. Air was blown as cooling flow (DR=1); during thermal tests, the secondary air was slightly heated, while the core flow was at ambient temperature. Small density differences (as large as 6%) between the two data sets do exist. An overall mass flow ratio MFR was used to identify each test condition; it is defined as the ratio of the injected mass flow measured by an orifice device, and the overall mass flow rate related to one vane passage (full span). Tests were carried out for MFR ranging between 0.5% and 2.5%. Several authors ([6–8,13]) use a different parameter, named inlet blowing ratio M_1, to identify the injection conditions

$$M_1 = \sqrt{\frac{p_{t,c} - p_1}{p_{t,1} - p_1}} \tag{1}$$

If results are compared at a constant MFR, different local blowing conditions will take place for the two configurations, as a consequence of the different hole exit areas and hole number. If data are compared at a constant inlet blowing ratio, local injection conditions will be the same, while the overall injected mass flow will not. Figure 3 shows the linear dependency of overall mass flow ratio MFR on the inlet blowing ratio M_1 for the two endwall geometries.

The inlet boundary layer was characterized using a flattened

Table 2 Cascade geometry and operating conditions

$s/c=0.86$	$H/c=1.04$
$c=133.7$ mm	7 blades
$\beta_1=90°$	$\beta'_2=21°$
$Ma_1=0.06$	$Ma_{2is}=0.2$
$Re_{2is}=0.66\ 10^6$	$Tu_1=1\%$

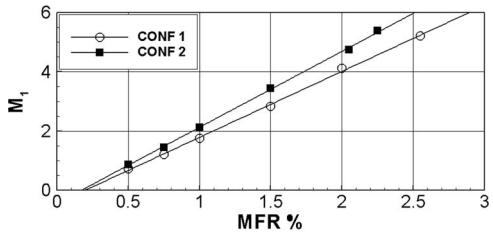

Fig. 3 M_1 **versus MFR**

Pitot tube at 80% c_{ax} upstream of the leading edge. Boundary layer profile and integral parameters are reported in Fig. 4 and Table 3, respectively.

Measurement Techniques. Aerodynamic measurements were performed downstream of the trailing edge plane by using a 5-hole miniaturized aerodynamic pressure probe (1.6 mm head). Uncertainties have been estimated to be ±0.15% of dynamic pressure. Testing conditions were controlled through a continuous monitoring of the global coolant to mainstream mass flow rate. Coolant total pressure and temperature were measured inside of the plenum by means of a pressure tap and a T-type thermocouple.

The measurement plane is located 50% of the axial chord downstream of the trailing edge (X/c_{ax}=150%) and it covers three blade passages. The measurement grid consists of 30 points per pitch in tangential direction times 30 points along the blade height up to midspan. The grid spacing was reduced approaching the endwall surface.

Spryable wide-banded thermochromic liquid crystals (TLC) (Hallcrest BM/R20C10 WC17-10) and the transient technique were used for the evaluation of film-cooling effectiveness distributions. TLC images were acquired using a CCD camera, with a 767×573 pixels resolution. The primary lighting system consists of two 150 W white light sources, each one connected to two optical fibers. A proper in situ calibration of TLCs was performed. The Hue capturing technique proposed by Camci et al. [18] was applied to the recorded data. During tests, cooling air was slightly heated while the mean flow was at room temperature. The relatively large thickness of the Plexiglas endwall (externally insulated) assured the satisfaction of wall adiabatic condition during test duration. Nonadiabatic spurious effects due to heat conduction took place anyway just upstream and in between the holes, as the material thickness was too small. The film-cooling effectiveness uncertainty ranges from ±3.3% with η=0.3, up to ±10% when η=0.1.

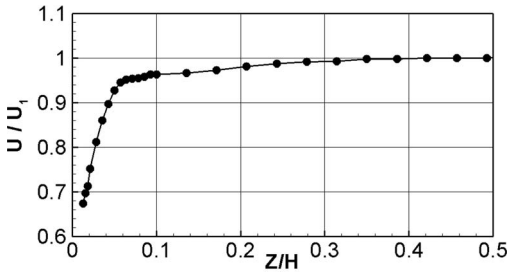

Fig. 4 **Inlet boundary layer profile** (X/c_{ax}**=−80%**)

Table 3 **Inlet boundary layer integral parameters**

δ	8.4 mm
δ^*	1.36 mm
H_{12}	1.95

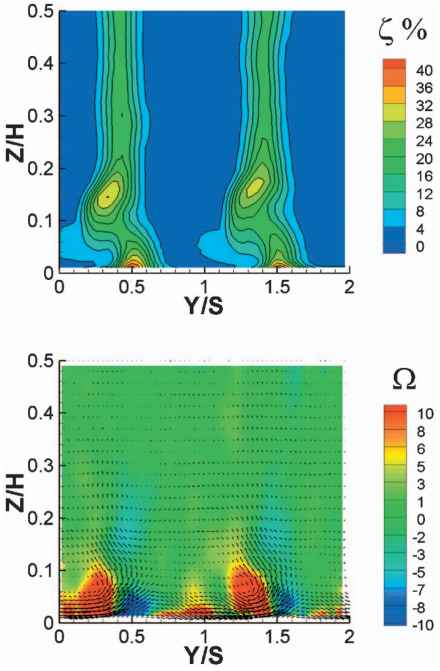

Fig. 5 **Secondary kinetic energy loss coefficient, vorticity, and velocity vectors** (X/c_{ax}**=150%)—solid endwall**

Aerodynamic Results

Due to the crucial role played by secondary flows in determining the endwall cooling effectiveness, the first part of the investigation was devoted to establishing how the secondary flow is modified by different blowing conditions and to determine the loss production variation. Five-hole probe measurements have been carried out for both the endwall configurations, but in the following, only CONF2 results are reported, as only small differences have been found between the two cases. Moreover, results for the baseline configuration CONF 1 were already presented and discussed by Barigozzi et al. [17].

Figure 5 presents contour plots of secondary kinetic energy loss coefficient and secondary flow field, superimposing the vorticity distribution, for the uncooled (i.e., solid) endwall. The streamwise vorticity was computed for each measurement point following the procedure suggested by Gregory-Smith et al. [19] based on the Crocco relation. The vorticity values are normalized by using the inlet free-stream velocity and the vane chord.

The typical secondary flow vortex structure can be clearly recognized. The flow field is dominated by the presence of a well-defined passage vortex, corresponding to the positive vorticity region and to the loss core on the suction side of the wake. Due to the large distance from the cascade exit plane (x/c_{ax}=150%), only very weak traces of the trailing shed vorticity could be found. A significant cross flow, embedding the corner vortex, can be observed in the endwall region.

Figure 6 shows the results for the CONF2 geometry, in the MFR range 0.5%–2.5%. Each picture shows three wakes and two complete channels; the one extending between Y/s=0.5 and 1.5, as Fig. 6(a) shows, corresponds to the cooled channel. The central wake is the one that is affected by coolant injection.

Looking at the results for MFR in the low range (0.5%–0.75%), it can be seen that losses related to the passage vortex are much higher with respect to the uncooled case (compare the middle with the first and third wakes traces of Fig. 6(a) and 6(b)). The loss core related to the passage vortex becomes wider and moves towards midspan, with the peak growing up to more than 32%. The injected low momentum fluid is entrained by the passage vortex, and is driven inside the loss core on the suction side of the wake,

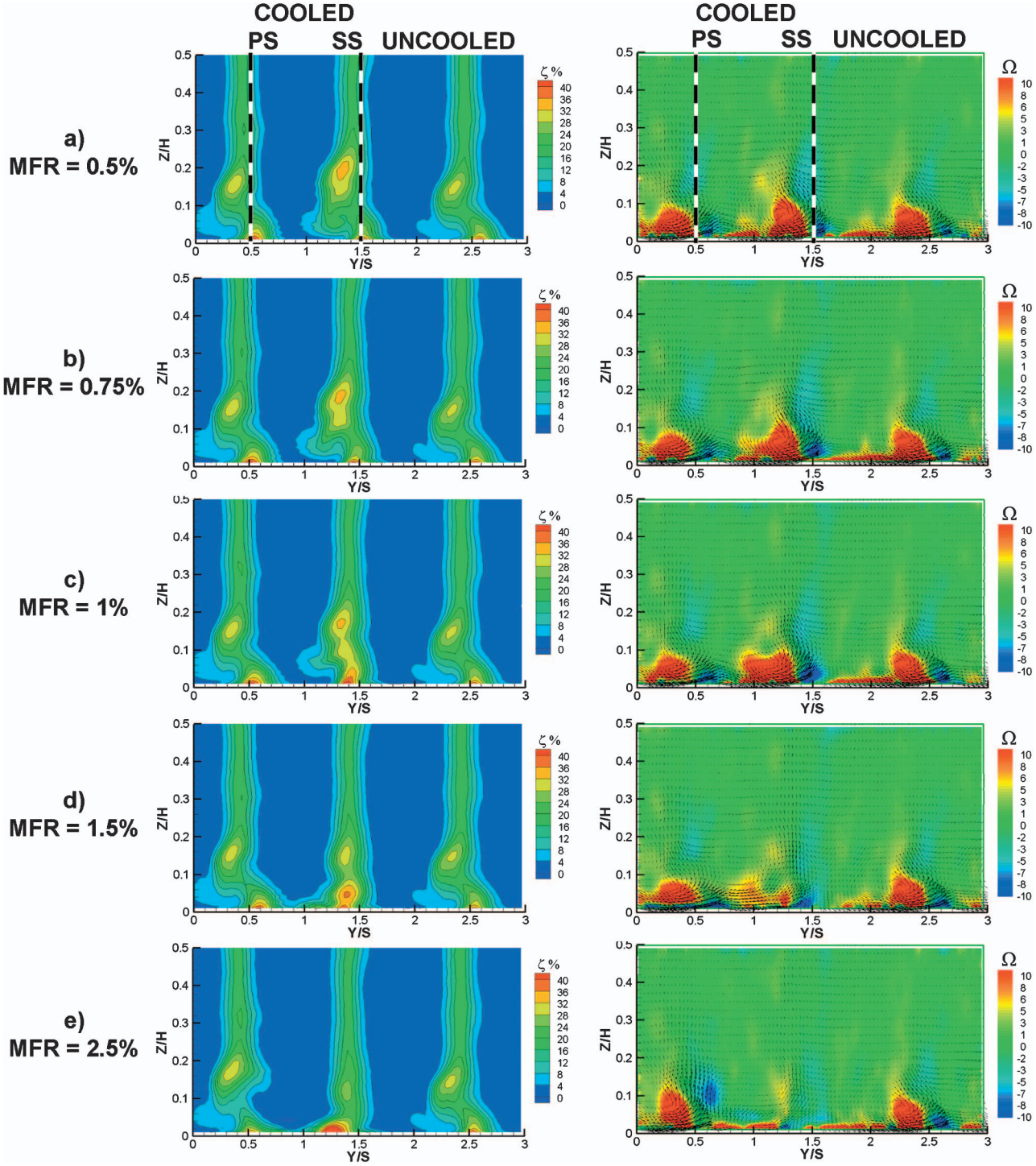

Fig. 6 CONF2 Secondary kinetic energy loss coefficient (primary), vorticity, and velocity vectors—(*a*) MFR=0.5%; (*b*) MFR =0.75%; (*c*) MFR=1%; (*d*) MFR=1.5%; and (*e*) MFR=2.5%

increasing the loss peak value. A similar behavior was also found by Friedrichs et al. [7]. Looking at the vorticity and secondary flow distributions, it can be observed that upon increasing MFR (up to 1%) the passage vortex undergoes an enlargement in the pitchwise direction, with a small displacement of its center towards the pressure side.

With a further increase of MFR up to 1.5% (Fig. 6(*d*)), the positive vorticity core corresponding to the passage vortex weakens and migrates towards the pressure side of the vane passage, against the endwall cross flow. As far secondary loss distribution, the low-energy fluid region connected to the passage vortex is vanishing, while the corner vortex loss core undergoes a slight increase. When large mass flow ratios are injected, the high-energy fluid introduced at the endwall along the flow channel interacts with the passage vortex, increasing the streamwise velocity and producing a stretching of the vortex structure.

With a further increase of the mass flow ratio (MFR=2.5%), the passage vortex cannot be identified (the positive vorticity core has vanished) and there is no trace of the cross flow at the endwall

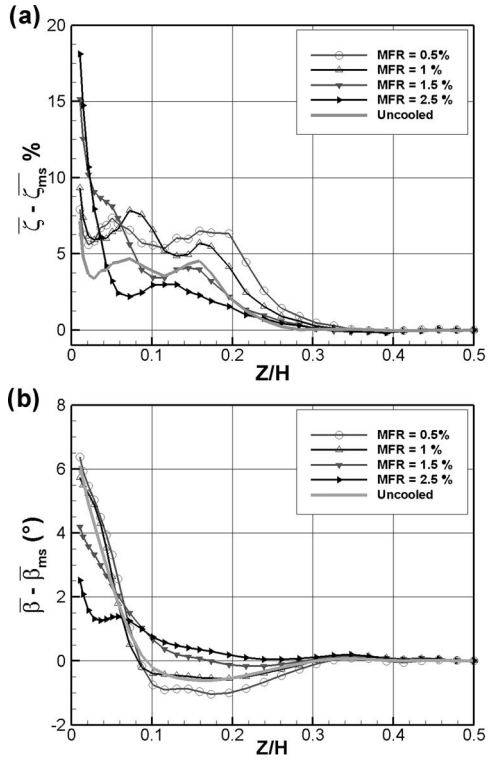

Fig. 7 Spanwise (*a*) loss distribution (primary) and (*b*) flow angle deviation at different MFR—CONF2

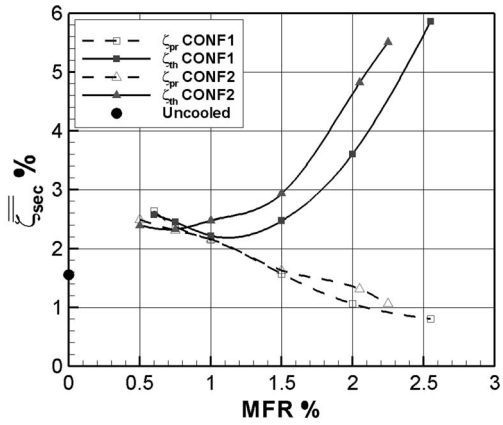

Fig. 8 Mass-averaged primary and thermodynamic secondary energy loss coefficients versus MFR percent

due to secondary flows. It has to be noticed that a negative vorticity region instead appears on the pressure side of the vane passage. A similar but enhanced feature was also detected for the CONF1 geometry at the same MFR.

Looking at the secondary loss distribution, the central wake, i.e., the one interested by the injection, is practically 2D, without showing a loss core on the suction side. The loss core at the endwall associated with the corner vortex is shifted towards the pressure side, as a consequence of the disappearing of the cross flow. Furthermore, there is a modification of the configuration of the first wake, due to the appearance of the negative vorticity core previously mentioned. Regardless, it is clear that it should be better to use a two-channel cooling configuration in such extreme injecting conditions.

Pitch-Averaged Results. Local flow-field data were mass averaged over the pitch corresponding to the cooled endwall, to obtain the spanwise distributions of deviation angle and loss coefficient (Fig. 7), the latter defined as

$$\bar{\zeta} - \bar{\zeta}_{ms} = \frac{\bar{U}_{2s}^2 - \bar{U}_2^2}{\bar{U}_{2s,ms}^2} \tag{2}$$

The uncooled loss distribution is also presented for comparison. It can be observed that even small injection rates produce a significant loss increase with respect to the uncooled case. The loss core associated with the passage vortex moves towards the midspan up to $Z/H=0.2$. According to the flow-field analysis, for larger MFR values there is a gradual reduction of the loss core (Fig. 7(*a*)), showing a clear trend of the flow towards a 2D configuration. In fact, the peak value reduces from approximately 6.5% for the lower MFR of 0.5%, down to 3% for MFR=2.5%. Moreover, its spanwise extent also reduces, affecting a more limited spanwise portion of the vane passage. The loss level at the endwall instead increases for MFR larger than 1%. It is of the order of 20% for an MFR of 2.5%.

Concerning the deviation angle (Fig. 7(*b*)), for low injection rates the underturning angle is of the order of 1 deg, whereas the overturning at the endwall is as large as 6 deg. For MFR of 1.5%, the underturning disappears, while the extent of the overturning region widens, with the maximum value decreasing down to 4 deg. Increasing MFR further, the overturning angle is reduced even more, as a consequence of the weakened secondary flow activity. This means that, for high injection rates, the flow exiting the vane is much more uniform along the span, with a benefit for the incidence angle on the following blade.

Mass-Averaged Results. In order to quantify the effect of coolant injection on the cascade aerodynamic performance, overall energy loss coefficients have been estimated by mass averaging the flow data all over the vane half passage. Following Kost and Holmes [20], two different energy loss coefficients were computed. The primary loss is defined as

$$\bar{\bar{\zeta}}_{pr} = \frac{\bar{\bar{U}}_{2s}^2 - \bar{\bar{U}}_2^2}{\bar{U}_{2s,ms}^2} \tag{3}$$

and the thermodynamic loss coefficient is defined as

$$\bar{\bar{\zeta}}_{th} = \frac{m_\infty(\bar{\bar{U}}_{2s}^2 - \bar{\bar{U}}_2^2) + m_c(U_{2s,c}^2 - \bar{\bar{U}}_2^2)}{(m_\infty + m_c)\bar{U}_{2s,ms}^2} \tag{4}$$

where m_∞ is the mass flow rate related to the full span channel. It is well known that the primary loss coefficient may give misleading results, because it neglects the coolant flow energy. The thermodynamic loss coefficient takes into account the energy related to the injected flow, but it also includes losses inside the cooling holes.

The secondary loss is obtained by subtracting the pitchwise-averaged loss at midspan from the total loss. Figure 8 presents both primary and thermodynamic secondary losses for the tested injection conditions and the two geometries. In agreement with the local flow-field results, secondary losses for small injection rates increase with respect to the uncooled case, in a quite similar way for both geometries: they are about 2.4%, i.e., 0.85 more than the solid case (1.55%). Increasing the mass flow rate over 0.5%, a significant continuous reduction of primary losses can be observed. This trend is of course related to the larger coolant kinetic energy introduced in the main flow. For both CONF1 and CONF2 cases, it decreases down to a level of about 1.0%–1.3% for MFR=2%.

Concerning the thermodynamic losses, there is an initial decrease with a minimum MFR value of 0.75% for CONF2 and 1% for CONF1. Then, it begins to grow for both configurations. The geometry with the expanded exits (CONF2) shows lower thermodynamic losses only at low MFR values, if compared with

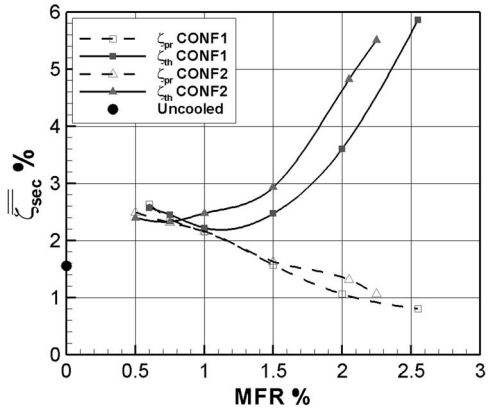

Fig. 9 Mass-averaged primary and thermodynamic secondary energy loss coefficients versus M_1

CONF1 results, while for higher MFR the opposite takes place. This can be simply explained by considering that CONF2 has a smaller number of holes and so larger losses take place inside the cooling holes because of higher coolant velocities. If the same results are plotted against the inlet blowing ratio parameter M_1 (Fig. 9), the two geometries show the same performance in terms of thermodynamic loss coefficients, with a minimum around $M_1 = 2$.

These results appear to be consistent with the previous discussed reduction of the passage vortex intensity for MFR in the range 0.5%–1%, which corresponds to M_1 variations between 0.7 and 2. Concerning the aerodynamic performance, it can be concluded that there is an optimal injection inlet blowing ratio for both geometries, corresponding to about 2.

Adiabatic Effectiveness Results

In order to compare the performance of different cooling geometries, the thermal analysis can be limited to the adiabatic effectiveness alone, because it will give enough information on the coolant protection capabilities. High film-cooling performances can be reached if the jets have a minimal penetration. In this way they remain attached to the wall. They must have a high enough mass flow rate to cover a large area, and a low turbulent mixing to avoid dilution by the mainstream. It has been shown that the use of expanded exits is a way to achieve this feature (Thole et al. [13] and Gritsch et al. [14,15]).

Local Blowing Ratio Variations. Before discussing the results, the reader is reminded that local injection conditions are strongly influenced by the local values of parameters like blowing and momentum flux ratios. Since all the holes are fed by a single plenum, such parameters experience large variations in both the pitchwise and streamwise directions. Local injection parameters like blowing and momentum flux ratios were estimated from coolant/main flow inlet total pressure, the measured injected mass flow, and blade-to-blade velocity distribution at midspan (measured by a 2D LDV system). The coolant velocity at hole exit was computed on the basis of a unique value of the discharge coefficient, and assuming an isentropic expansion from plenum total pressure and local static conditions. The discharge coefficient was defined just to obtain the measured injected coolant flow. Of course, these parameters have been computed assuming that the static pressure distribution at the endwall is the same as at midspan, and that it is not affected by coolant injection. Regardless, they will give useful information on the share of the injected flow between the different holes. Figures 10 and 11 report the local blowing rate (BR) values obtained for the CONF1 and CONF2 geometries, for the tested MFR. The two geometries show very similar distributions, but CONF2 always has lower values, as a consequence of the presence of expanded exits. It has to be noted that, to define the local blowing ratios for CONF2, the hole exit area has been computed starting from the upper edge of the hole.

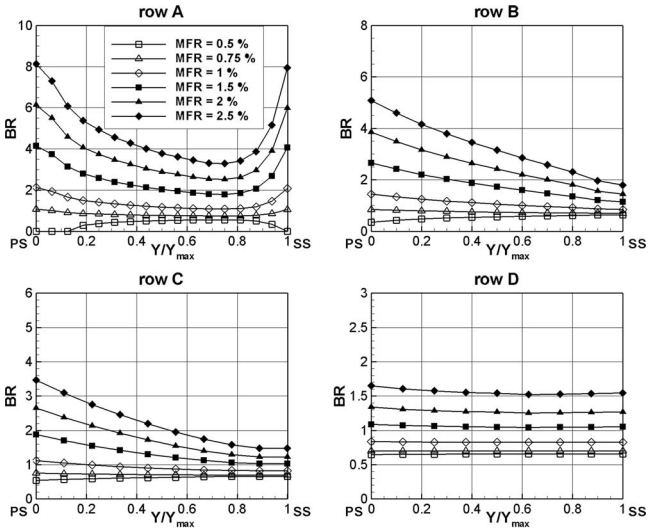

Fig. 10 CONF1 local BR values for variable MFR

Due to the very low mainstream velocity, BR values of row A increase approaching the leading edge for all MFR tested, with the exception of the 0.5% case. Holes located very close to the stagnation region do not blow at all. The following two rows, located inside of the vane passage, are characterized by progressively decreasing BR values that also decrease going from the pressure to the suction side of the channel. This happens for all MFR, except the lowest one: in this condition low BR values, smaller than 1, can be found close to the pressure side. The last row holes have almost constant blowing ratios, smaller than the previous ones.

CONF1 η Results. Figure 12 shows the adiabatic effectiveness η distributions for the two tested geometries (CONF1 and CONF2) and five of the tested MFR values. Superimposed to the lower MFR value is the separation line for the uncooled case. Looking at the CONF1 distribution corresponding to MFR = 0.5% (Fig. 12 at the top), the pressure side region extending up to half of the axial chord downstream of the leading edge is poorly cooled. This is due to the fact that row A holes located close to the

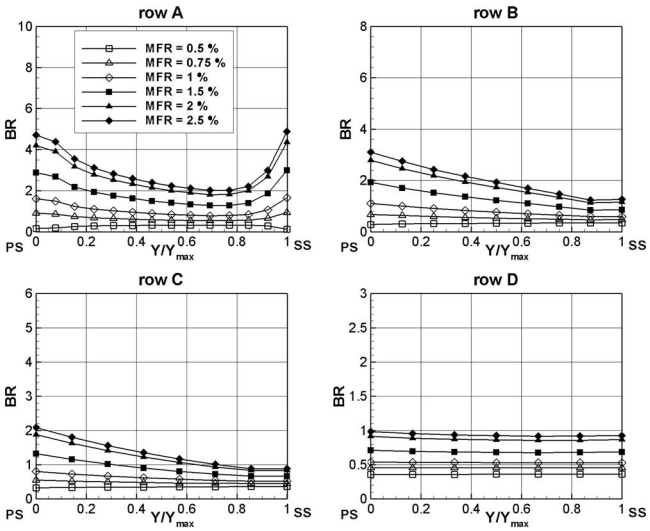

Fig. 11 CONF2 local BR values for variable MFR

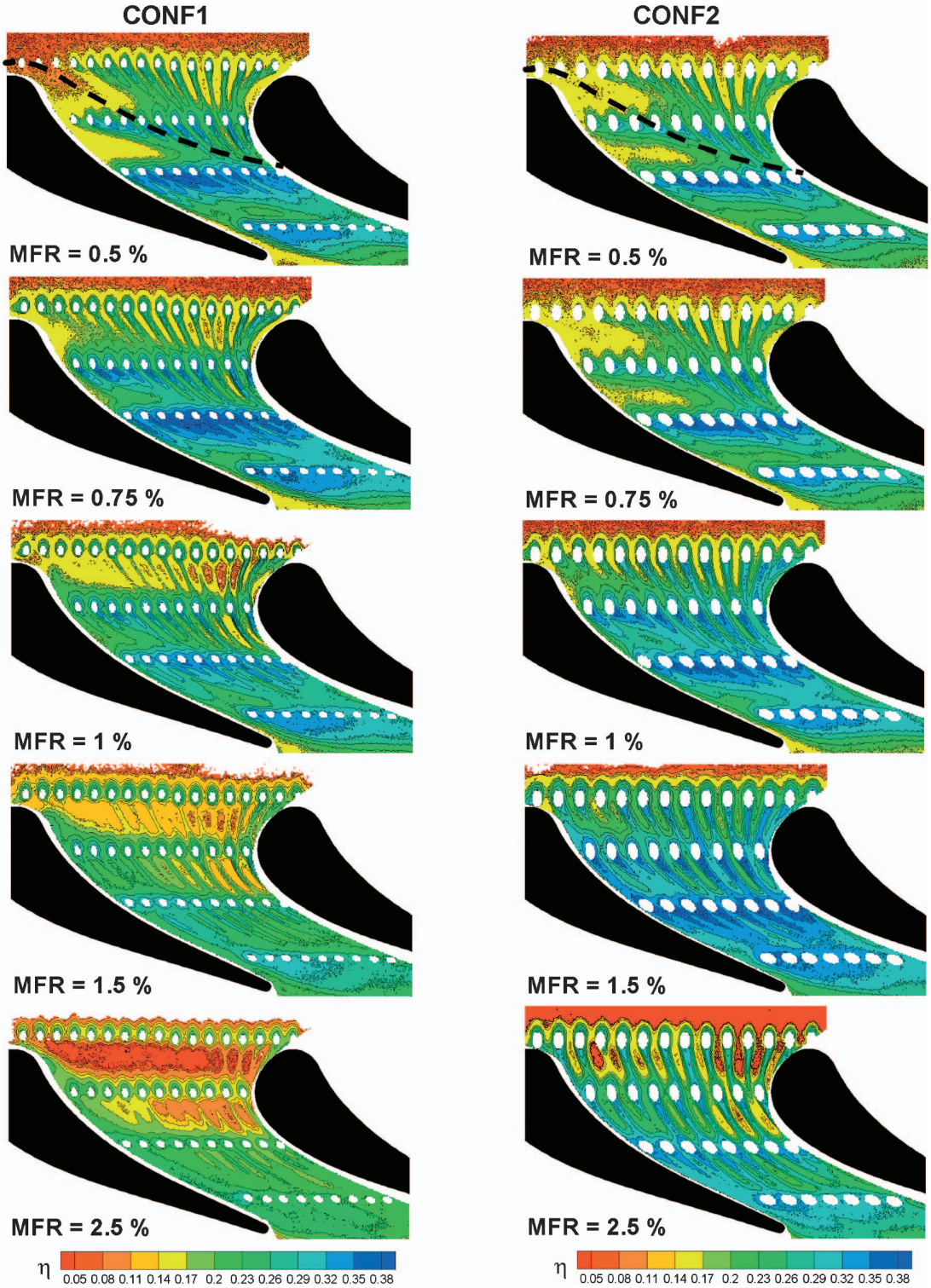

Fig. 12 Adiabatic effectiveness distributions for the different injection conditions and the two geometries

pressure side do not blow, as shown by the local blowing ratios of Fig. 10. It can be also observed that, in the opposite side, the coolant flow injected in front of the leading edge is deflected by the suction side leg of the horseshoe vortex away from the vane surface. Row B injection is dominated by the cross flow related to the passage vortex, which moves the injected flow towards the suction side. Jets exiting the following row (row C), that is located downstream of the separation line, exhibit two different behaviors, depending on their relative position to the pressure side. In fact, the jet coming out from the first two holes located closer to the pressure side follows the potential flow direction, while the others are strongly deflected under the cross-flow action. Going further downstream, after the last row, holes closer to the suction side are influenced by the action of the passage vortex. The jet traces merge to create a unique insulating layer that quickly decays in the streamwise direction.

Increasing MFR up to 0.75%, the degree of cooling coverage improves all over the endwall. Jets exiting row A holes located

close to the leading edge pressure side are swept off the vane surface by the pressure side leg of the horseshoe vortex. The front part of vane pressure side remains practically uncooled. Looking at the second row of holes (row B), which is located across the separation line, three different kind of traces can be identified. Starting from the pressure side, the first hole trace follows the potential flow direction, while the following three hole traces merge, showing a strong dependency on the passage vortex cross flow. The remaining holes lay in between the separation line and the suction side leg of the horseshoe vortex, giving rise to a good surface coverage. The following row looks to be the most effective: large local adiabatic effectiveness values (as large as 0.38) can be found just downstream of injection holes. Furthermore, a quite good spreading and a good persistency characterize the jet traces. This is consistent with the sharing of the endwall in four different regions as proposed by Friedrichs et al. [8], with the unique difference that now region 3 seems to become narrower approaching the trailing edge plane. In fact, downstream of row D, the jets merge as in the previous case, but now the cooling layer persists over a longer distance downstream.

For MFR larger than 0.75%, cooling coverage decays almost everywhere, particularly in the front part. The degradation of cooling performance can be explained by the larger local blowing conditions, leading to an important jet lift-off, especially in the first row. However, due to their large momentum, jets coming out from row A close to the leading edge contribute to contrast the horseshoe vortex. Looking at what happens in the middle of row A, it is clear that cooling at large MFR is totally inefficient. This is clearly shown by the red region downstream of a large portion of row A in the last picture (MFR=2.5%), indicating that this region is not cooled at all, with cooling jets that penetrate inside of the mainstream and never reattach. Concerning the following rows, it can be observed that flow deviation by the endwall cross flow is progressively lower, in agreement with the aerodynamic results.

CONF2 η Results. When comparing the results of the two tested geometries, the reader is reminded that CONF2 endwall differs from CONF1 not only because of the presence of fan-shaped holes, but also because of the lower number of holes. In fact, whereas the presence of expanded exits will reduce the coolant momentum, the reduction of hole number (at constant MFR) will have exactly the opposite effect. Nevertheless, as Figs. 10 and 11 clearly show, CONF2 always presents lower BR values everywhere. As a consequence, coolant flow is injected at a lower momentum, regardless of coolant condition. The introduction of fan-shaped holes thus allows the jets to remain more attached to the wall, with a better lateral spreading.

Looking at the overall differences between the two test sets, it is evident that, at lower MFR, when the injected flow momentum is low, the above-mentioned benefits are practically overcome by the action of secondary flow vortices. Increasing MFR, the higher momentum jets become able to contrast the washing action of the vortices, thus making it possible to take advantage of beneficial effects of fan shaping.

Going into details, for the lower MFR values of 0.5% and 0.75%, the overall cooling performance are worse if compared with CONF1 results. Holes located in front of the leading edge blow, but their momentum is not strong enough to resist to both the horseshoe vortex legs. Coolant traces for CONF2 are wider, but the decay in downstream direction is stronger. This is especially true for the MFR=0.75% that was the optimum cooling condition for the CONF1 case. Row B holes, located between the pressure side and the passage vortex separation line, blow a limited amount of coolant flow; their momentum is so small that their traces are immediately deflected in the tangential direction by the passage vortex-related cross flow, resulting in a poor effectiveness region.

Increasing the mass flow ratio, cooling performance increases (the opposite happened for CONF1). At MFR=1%, similar features as in the first cylindrical hole case can be observed. Again, the endwall surface can be divided into different regions, each one showing peculiar film-cooling performances: (i) the upstream region, which shows a good coverage, also close to the vane surface, especially on the suction side; (ii) the region between the separation line and the suction side leg of the horseshoe vortex, where the jet traces remain visible further downstream; (iii) the region very close to the pressure side, where jets follow the potential flow direction; and (iv) the region in the middle of the passage, where the influence of the passage vortex is dominant.

The optimum cooling condition takes place for an MFR =1.5%, with the jets that are able to resist to the endwall cross flow, giving rise to a very satisfactory adiabatic effectiveness distribution all over the endwall. The coverage due to the first row of holes is quite good, even in the stagnation region, where the jets are able to contrast both horseshoe vortex legs. Downstream of row B, the pressure side is very well protected by the first hole. Going towards the middle of the channel, jets better resist to the cross flow. This is also true for the following rows. The lower coverage of the suction surface downstream of row C can be related to the action of the corner vortex. Only the pressure side trailing edge region is not so well cooled.

Increasing the MFR even more, the cooling performance starts to decrease, and this already happens at 2% (not shown). Jets belonging to the first row start to separate (see the bottom picture of Fig. 12), with large, uncooled regions between the jets. The coverage improves going downstream, where the cooling of the endwall is more efficient than in the CONF1 case, because of the lower blowing ratios. The pressure side surface is now the most cooled region. The traces of the jets look like the potential flow streamlines at midspan, confirming the suppression of the passage vortex, as found in the aerodynamic analysis.

Pitch-Averaged Results. Starting from the local adiabatic effectiveness distributions shown in Fig. 12, pitchwise-averaged values were computed for each axial position, excluding the hole and the zone extending approximately $4D$ upstream, where conduction effects are relevant. Figure 13 reports the pitch-averaged adiabatic effectiveness distributions for the two geometries and for the different injection conditions.

Comparing the $\bar{\eta}$ distributions downstream of row A, it is evident that, whatever injection condition is concerned, CONF2 leads to a better or at least equal endwall protection than CONF1, with averaged values as large as 0.26 (only 0.2 for CONF1 as a maximum).

CONF1 shows larger $\bar{\eta}$ values (as large as 0.28 for the optimum MFR of 0.75%) downstream of the following row (row B) that gradually reduce going further downstream and also varying the MFR.

The passage vortex cross flow is responsible for the quick decay in the axial direction of the two low MFR $\bar{\eta}$ distributions of CONF2 (see Fig. 13(b)). In fact, with such mass flow rates, the low momentum injected flow cannot provide resistance to cross flow, and it is quickly moved towards the suction side. A similar behavior also characterizes the following two rows of both geometries. Both the geometries exhibit similar values, but the best distribution for the two tested configurations takes place at a different MFR: 0.75% for CONF1 and 1.5% for CONF2. However, the presence of the expanded exits gives an optimum distribution that better resists to secondary flows, maintaining a large value all over the endwall portion. Downstream of the last injection row, the surface protection persists only when injecting with large MFR ($>1\%$).

Averaging all the pitch-averaged effectiveness values also in the axial direction, excluding the hole region and the regions affected by conduction, a single global value for the adiabatic effectiveness $\bar{\bar{\eta}}$ was computed. This value will give an idea of the global capability of the cooling scheme to protect the whole endwall surface. Figure 14 shows the $\bar{\bar{\eta}}$ distribution as a function of the MFR.

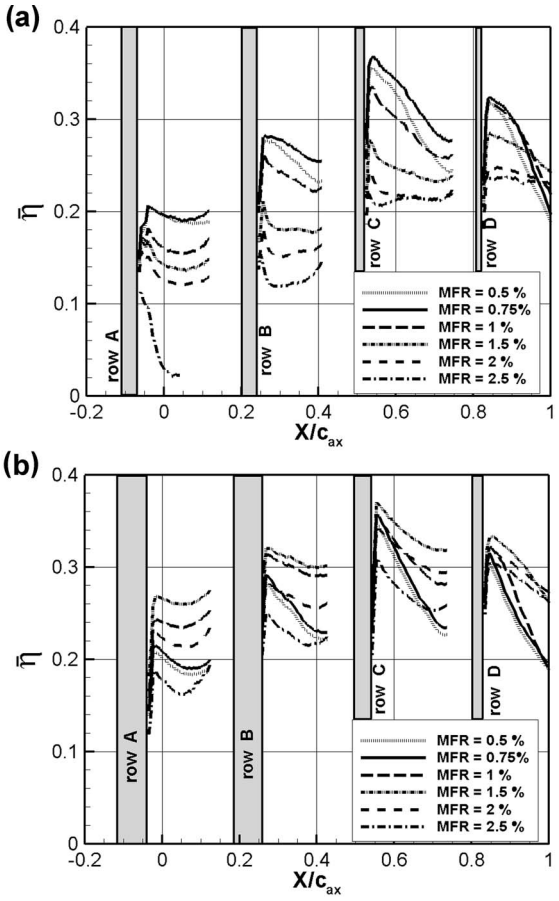

Fig. 13 Pitch-averaged adiabatic effectiveness distributions at different MFR—(*a*) CONF1 and (*b*) CONF2

CONF1 gives a better cooling protection only at low MFR, and also in these conditions the gain is limited. CONF2 performance results are always higher than CONF1 for MFR greater than 1%.

Conclusions

The presented investigation drew a comprehensive picture of the complex aero-thermal flow field in the endwall region, showing in detail the different behavior of two endwall cooling geometries (cylindrical and fan-shaped holes). From the presented results the following aerodynamic conclusions can be drawn:

- Concerning the secondary flow behavior, no relevant differences were found between the cylindrical and fan-shaped endwall.
- At constant MFR, larger thermodynamic losses have been found for the fan-shaped geometry.
- A minimum loss condition has been found for MFR value equal to 1% for CONF1 and 0.75% for CONF2.
- Increasing the MFR, secondary vortex and related cross flow undergo a strong reduction, leading to an almost 2D flow-field configuration.

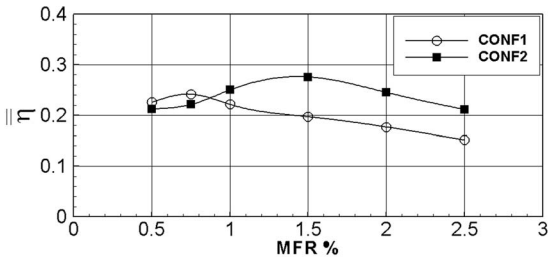

Fig. 14 Axial and pitch-averaged adiabatic effectiveness distributions versus MFR

Concerning the film-cooling adiabatic effectiveness, the following results have been found:

- The adiabatic effectiveness distribution is strongly influenced by secondary flows: in the stagnation region cooling jets interact with the horseshoe vortex legs, while inside of the channel the passage vortex and the related cross flow strongly influence the cooling performance.
- Fan-shaped holes allow injection of larger mass flow rate at a lower momentum flux ratio, assuring a better film cooling coverage of the whole endwall.
- The cylindrical hole endwall presents the optimum film cooling coverage for MFR=0.75%, while the fan-shaped holes reach the optimum at a greater MFR=1.5%. Comparing the two optimal film-cooling effectiveness conditions, the fan-shaped endwall gives rise to an average effectiveness of 0.29, against 0.24 attained by the cylindrical one. However, it must be underlined that fan-shaped holes provide a much more uniform distribution.

It has been shown that the optimum MFR values for the aerodynamic losses do not match the optimum for the adiabatic effectiveness (1% against 0.75% for the cylindrical holes and 0.75% against 1.5% for the fan-shaped holes). Regardless, the loss increase is small, and thus the associated penalty is not so relevant for the overall performance.

Acknowledgment

The authors wish to thank S. Carrara, M. Quattrore, and G. Pellegrinelli for the work they did during their Mechanical Engineering degree final project, and Mr. E. Gatti and V. Biondi for the appreciated technical support.

Nomenclature

B = hole spacing
$\mathrm{BR}=(\rho_c U_c)/(\rho_\infty U_\infty)$ = local blowing rate
c = blade chord
D = hole diameter
$\mathrm{DR}=\rho_c/\rho_\infty$ = density ratio
H = blade height
H_{12} = shape factor
L = hole length
m = mass flow rate
Ma = Mach number
M_1 = inlet blowing ratio
$\mathrm{MFR}=m_c/m_\infty$ = overall coolant to mainstream mass flow ratio
$\mathrm{Re}_{2is}=U_{2is}c/\nu$ = isentropic outlet Reynolds number
s = blade pitch
T = temperature
$\mathrm{Tu}=\sqrt{0.5(\overline{u'^2}+\overline{v'^2})}/U_1$ = turbulence intensity, percent
$U=\sqrt{u^2+v^2+w^2}$ = local mean velocity
u,v,w = streamwise, transverse, and spanwise velocity components
X,Y,Z = cascade coordinate system
α = injection angle
β = flow angle (tangential direction)
γ = expansion angle
δ = boundary layer thickness
δ^* = displacement thickness
$\eta=(T_{aw}-T_\infty)/(T_c-T_\infty)$ = film cooling adiabatic effectiveness
ν = kinetic viscosity
ρ = flow density

$\zeta = (U_{2is}^2 - U_2^2)/U_{2is,ms}^2$ = local energy loss coefficient
Ω = vorticity

Subscripts

1 = inlet
2 = exit
a = adiabatic
c = cooling flow
is = isentropic condition
ms = at midspan
pr = primary
th = thermodynamic
∞ = free stream
w = local wall condition

Overbars

$\bar{}$ = time averaged, pitch averaged
$\tilde{}$ = mass averaged
$'$ = rms

References

[1] Blair, M. F., 1974, "An Experimental Study of Heat Transfer and Film Cooling on Large-Scale Turbine Endwalls," ASME J. Heat Transfer, **96**, pp. 524–529.

[2] Roy, R. P., Squires, K. D., Gerendas, M., Song, S., Howe, W. J., and Ansari, A., 2000, "Flow and Heat Transfer at the Hub Endwall of Inlet Vane Passages—Experiments and Simulations," ASME Paper No. 2000-GT-198.

[3] Oke, R. A., and Simon, T. W., 2002, "Film Cooling Experiments With Flow Introduced upstream of a First Stage Nozzle Guide Vane through Slots of Various Geometries," ASME Paper No. GT-2002–30169.

[4] Oke, R. A., Simon, T. W., Burd, S. W., and Vahlberg, R., 2000, "Measurements in a Turbine Cascade Over a Contoured Endwall: Discrete Hole Injection of Bleed Flow," ASME Paper No. 2000-GT-214.

[5] Jabbari, M. J., Marston, K. C., Eckert, E. R. G., and Goldstein, R. J., 1996, "Film Cooling of the Gas Turbine Endwall by Discrete-Hole Injection," ASME J. Turbomach., **118**, pp. 278–284.

[6] Friedrichs, S., Hodson, H. P., and Dawes, W. N., 1996, "Distribution of Film-Cooling Effectiveness on a Turbine Endwall Measured With the Ammonia and Diazo Technique," ASME J. Turbomach., **118**, pp. 613–621.

[7] Friedrichs, S., Hodson, H. P., and Dawes, W. N., 1997, "Aerodynamic Aspects of Endwall Film-Cooling," ASME J. Turbomach., **119**, pp. 786–793.

[8] Friedrichs, S., Hodson, H. P., and Dawes, W. N., 1999, "The Design of an Improved Endwall Film-Cooling Configuration," ASME J. Turbomach., **121**, pp. 772–780.

[9] Kost, F., and Nicklas, M., 2001, "Film-Cooled Turbine Endwall in a Transonic Flow Field: Part I-Aero-dynamic Measurements," ASME Paper No. 2001-GT-0145.

[10] Nicklas, M., 2001, "Film-Cooled Turbine Endwall in a Transonic Flow Field: Part II-Heat Transfer and Film-Cooling Effectiveness," ASME Paper No. 2001-GT-0146.

[11] Knost, D. G., and Thole, K. A., 2004, "Adiabatic Effectiveness Measurements of Endwall Film-Cooling for a First Stage Vane," ASME Paper No. GT-2004-53326.

[12] Zhang, L. J., and Jaiswal, R. S., 2001, "Turbine Nozzle Endwall Film Cooling Study Using Pressure Sensitive Paint," ASME Paper No. 2001-GT-0147.

[13] Thole, K., Gritsch, M., Schulz, A., and Wittig, S., 1996, "Flowfield Measurements for Film-Cooling Holes With Expanded Exits," ASME Paper No. 96-GT-174.

[14] Gritsch, M., Schulz, A., and Wittig, S., 1997, "Adiabatic Wall Effectiveness Measurements of Film-Cooling Holes With Expanded Exits," ASME Paper No. 97-GT-164.

[15] Gritsch, M., Schulz, A., and Wittig, S., 1998, "Heat Transfer Coefficient Measurements of Film-Cooling Holes With Expanded Exits," ASME Paper No. 98-GT-28.

[16] Barigozzi, G., Benzoni, G., and Perdichizzi, A., 2001, "Boundary Layer and Loss Analysis in a Film Cooled Vane," ASME Paper No. 2001-GT-0136.

[17] Barigozzi, G., Benzoni, G., Franchini, G., and Perdichizzi, A., 2005, "Aerodynamic Measurement over a Film Cooled Nozzle Vane Endwall," accepted for presentation at the 6th European Conference on Turbomachinery Fluid Dynamics and Thermodynamics, to be held in Lille (France).

[18] Camci, C., Kim, K., and Hippensteele, S. A., 1992, "A New Hue Capturing Technique for the Quantitative Interpretation of Liquid Crystal Images Used in Convective Heat Transfer Studies," ASME J. Turbomach., **114**, pp. 765–775.

[19] Gregory-Smith, D. G., Graves, C. P., and Walsh, J. A., 1988, "Growth of Secondary Losses and Vorticity in an Axial Turbine Cascade," ASME J. Turbomach., **110**, pp. 1–8.

[20] Kost, F. H., and Holmes, A. T., 1985, "Aerodynamic Effect of Coolant Ejection in the Rear Part of Transonic Rotor Blades," *AGARD CP 390 "Heat Transfer and Cooling in Gas Turbines,"* Bergen, Norway, May.

Heat Transfer and Film-Cooling Measurements on a Stator Vane With Fan-Shaped Cooling Holes

W. Colban

A. Gratton

K. A. Thole

Mechanical Engineering Department,
Virginia Polytechnic and State University,
Blacksburg, VA 24061

M. Haendler
Siemens Power Generation,
Muelheim an der Ruhr, Germany

In a typical gas turbine engine, the gas exiting the combustor is significantly hotter than the melting temperature of the turbine components. The highest temperatures in an engine are typically seen by the turbine inlet guide vanes. One method used to cool the inlet guide vanes is film cooling, which involves bleeding comparatively low-temperature, high-pressure air from the compressor and injecting it through an array of discrete holes on the vane surface. To predict the vane surface temperatures in the engine, it is necessary to measure the heat transfer coefficient and adiabatic film-cooling effectiveness on the vane surface. This study presents heat transfer coefficients and adiabatic effectiveness levels measured in a scaled-up, two-passage cascade with a contoured endwall. Heat transfer measurements indicated that the behavior of the boundary layer transition along the suction side of the vane showed sensitivity to the location of film-cooling injection, which was simulated through the use of a trip wire placed on the vane surface. Single-row adiabatic effectiveness measurements without any upstream blowing showed jet lift-off was prevalent along the suction side of the airfoil. Single-row adiabatic effectiveness measurements on the pressure side, also without upstream showerhead blowing, indicated jet lifted-off and then reattached to the surface in the concave region of the vane. In the presence of upstream showerhead blowing, the jet lift-off for the first pressure side row was reduced, increasing adiabatic effectiveness levels. [DOI: 10.1115/1.2098789]

Introduction

In an effort to increase overall efficiency and power output of industrial gas turbines, the combustor exit temperatures have continued to rise. This has placed an ever increasingly difficult task on engine designers to effectively cool turbine components. The turbine inlet guide vanes are subjected to the most extreme conditions and are therefore one of the most difficult components to cool. Most turbine guide vanes contain a complicated internal cooling scheme, as well as external film-cooling holes, which are designed to cover the surface of the vane with a thin protective film of relatively cooler air.

There are three main regions of the vane where film cooling is used: the leading edge, the pressure side, and the suction side. Multiple rows of cylindrical holes are typically used near the leading edge to make sure that the stagnation region is adequately cooled. On the pressure and suction sides, rows of film-cooling holes are spaced such that the downstream row is placed where the upstream row ceases to be effective. Different film-cooling hole shapes are used in an effort to keep the jet attached to the surface over a range of blowing ratios.

One film-cooling hole shape that is a consideration for a designer is the so-called fan-shaped hole, or laid-back diffuser hole. This hole expands in the lateral direction, effectively reducing the jet's momentum before it ejects onto the downstream surface. The reduced momentum helps the jet stay attached to the surface for high blowing ratios. The fan-shaped hole also promotes lateral spreading of the jet compared with a cylindrical hole, causing the jet to more effectively cover the entire surface.

This study is the first to present parallel heat transfer coefficients and adiabatic film-cooling effectiveness for a scaled-up turbine guide vane with fan-shaped film-cooling holes. Heat transfer coefficients are presented for a dry airfoil at different span heights noting the effect of endwall contouring. Heat transfer coefficients are also presented with trip wires used to simulate the boundary layer transition caused by a row of film-cooling holes. Adiabatic effectiveness data are presented for the leading edge, as well as eight individual fan-shaped cooling rows on the pressure and suction sides for engine representative blowing ratios.

Past Studies

Past studies involving surface heat transfer on a gas turbine vane include the effects of Reynolds number, free-stream turbulence, acceleration, transition, and surface roughness. The transition location is particularly important because of the increase that occurs in heat transfer coefficients as the boundary layer becomes turbulent. The film-cooling rows on the vane surface also cause the boundary layer to transition from laminar to turbulent.

There have been a few studies investigating the effect of boundary layer transition on vane surface heat transfer using a trip wire to force the boundary layer to transition. Riess and Bölcs [1] used a trip wire on the suction side to transition the boundary layer upstream of a single row of cooling holes and showed a decrease in adiabatic film-cooling effectiveness with an incoming turbulent boundary layer.

Polanka et al. [2] studied leading-edge film cooling experimentally for blowing ratios ranging from 0.3 to 2.9. They had six rows of showerhead holes that were directed along the span of the vane and had a 25 deg angle relative to the surface. Results from Polanka et al. [2] showed increasing adiabatic effectiveness with increasing blowing ratio. This was attributed to the small surface angle facilitating jet attachment.

There have been many studies investigating the benefits of film cooling of many different hole shapes on flat plates. Gritsch et al. [3], Yuen et al. [4], and Dittmar et al. [5] all studied fan-shaped film-cooling holes on a flat plate for blowing ratios ranging from 0.33 to 2.83. All reported that fan-shaped film-cooling holes performed better than cylindrical holes for all measured blowing ratios, particularly the higher blowing ratios. The fan-shaped hole

Contributed by the International Gas Turbine Institute (IGTI) of ASME for publication in the JOURNAL OF TURBOMACHINERY. Manuscript received October 1, 2004; final manuscript received February 1, 2005. IGTI Review Chair: K. C. Hall. Paper presented at the ASME Turbo Expo 2005: Land, Sea, and Air, Reno, NV June 6–9, 2005, Paper No. GT2005-68258.

performed better because its reduced jet momentum allowed the jet to stay attached to the surface and spread out and cover a larger surface area. Dittmar et al. [6] studied fan-shaped holes on a flat surface designed to simulate the Reynolds number and acceleration parameter distribution along the pressure side of a gas turbine vane. Dittmar et al. [6] showed that fan-shaped holes have higher levels of adiabatic film-cooling effectiveness than cylindrical holes for the same amount of coolant flow, especially at blowing ratios above one.

Film cooling is a topic that has been studied extensively; yet, despite all the work done there has not been much published research with fan-shaped cooling holes on turbine vanes. Guo et al. [7] studied the adiabatic film-cooling effectiveness on a fully cooled nozzle guide vane with fan-shaped holes in a transonic annular cascade using thin-film technology. On the suction side they found that fan-shaped holes had a consistently higher level of adiabatic film-cooling effectiveness than cylindrical holes. On the pressure side, Guo et al. [7] found that initially downstream of the hole exit the fan-shaped hole had a higher adiabatic film-cooling effectiveness than the cylindrical hole. However, the fan-shaped hole had a much faster decay of adiabatic effectiveness on the pressure side than the cylindrical hole.

Zhang et al. [8] researched vane film cooling with one row of shaped holes on the suction side using the pressure-sensitive paint technique. They found that adiabatic film-cooling effectiveness increased from blowing ratios of 0.5 to 1.5. Zhang et al. [8] also reported that for a blowing ratio of 1.5, a small separation region occurred downstream of the hole exit before the jet reattached. Using the same setup and technique, Zhang and Pudupatty [9] studied one row of fan-shaped holes on the pressure side. They found that the adiabatic film-cooling effectiveness decreased as blowing ratios increased from 1.5 to 2.5.

Sargison et al. [10] studied a converging slot-hole design on a flat plate and compared the results with cylindrical and fan-shaped holes. They found that the fan-shaped holes and converging slot holes had similar adiabatic effectiveness levels downstream of the hole exit, and both performed better than cylindrical holes. Sargison et al. [11] did the same comparison on a transonic nozzle guide vane placed in an annular cascade. Again, fan-shaped holes and converging slot holes both performed similarly in terms of adiabatic film cooling effectiveness, and both performed better than cylindrical holes at the same blowing ratios.

Schnieder et al. [12] studied vane film cooling with showerhead blowing and three rows of fan-shaped film-cooling holes on the pressure side. They presented laterally averaged adiabatic effectiveness data for each row for three blowing ratios. Schnieder et al. [12] investigated the superposition approach for individual rows, and found that it matched quite well with the complete coverage data. Polanka et al. [13] also examined the effect of showerhead blowing on the first downstream pressure side row. They found that at higher blowing ratios the pressure side row separated without upstream showerhead cooling. With showerhead cooling, the adiabatic effectiveness downstream of the separating pressure side row increased. This was attributed to the upstream showerhead coolant increasing turbulence levels and dispersing the downstream detached jet down towards the surface.

Despite the work that has been done to study fan-shaped film cooling on a gas turbine vane, there still is not a complete study offering high-resolution measurements of adiabatic film-cooling effectiveness that characterizes the entire pressure and suction side surfaces. The current study offers a complete characterization by giving measurements at eight surface locations for different blowing ratios. It is important to understand the jet–free-stream interaction at each location on the vane surface, since film-cooling effectiveness is affected by many different factors which vary along the vane surface including surface curvature, acceleration, the state of the boundary layer, and pressure gradient.

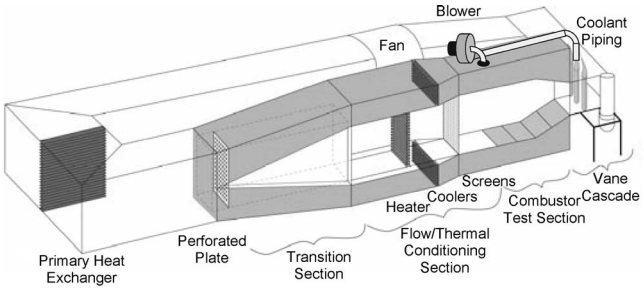

Fig. 1 Schematic of the low-speed recirculating wind tunnel facility

Experimental Facilities

The heat transfer on a nozzle guide vane is difficult to predict with boundary layer codes due to factors such as surface curvature, pressure gradients, boundary layer transition location, and free-stream turbulence. This study used a large-scale test facility to obtain high-resolution heat transfer and adiabatic film-cooling effectiveness data. All experiments were done in the low-speed, large-scale, closed-loop wind tunnel shown in Fig. 1. Heat was removed from the flow by the main heat exchanger before entering the flow split section. A perforated plate provided the correct pressure drop to split the flow into a center flow channel and two secondary channels. The core flow was heated by a 55 kW heater bank, while the outer two channels were cooled by heat exchangers and served as the coolant flow supply. The measurements were taken on the center vane of the two passage cascade (shown in Fig. 2), which had one contoured endwall. The free-stream turbulence level entering the turbine cascade was measured with a hot wire anemometer to be 1.2%. A description of the vane geometry, as well as some nominal operating conditions, is listed in Table 1. Inlet temperatures were 30°C for the heat transfer coefficient tests and 60°C for the film-cooling measurements, while inlet pressures were nominally atmospheric.

Vane Test Section Design. Whenever a nozzle guide vane is placed in a low-speed experimental facility, the lack of compressibility effects changes the location of the minimum static pressure on the suction surface. There are two options available for doing low-speed simulations, the first of which is to redesign the turbine vane profile so that the low-speed pressure distribution matches

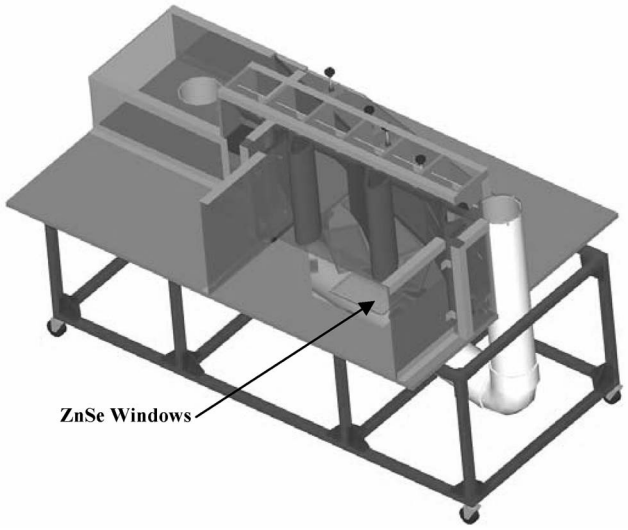

Fig. 2 Two-passage, three-vane test section with a contoured endwall

Table 1 Operating conditions and vane parameters

Scale	3X
C (m)	0.53
$Z_{max,inlet}/C$ (-)	1.05
$Z_{max,exit}/C$ (-)	0.54
$S_{max,PS}$ (m)	0.52
$S_{max,SS}$ (m)	0.68
U_{inlet} (m/s)	10
Re_{inlet} (-)	3.0×10^5
ΔT_{FC} (°C)	20

the engine surface pressure distribution. The second option, which was taken in this study, is to incorporate a contoured endwall to accelerate the flow, which maintains the vane's geometric integrity from the engine design. The finished contour is shown in Fig. 3 nondimensionalized by the maximum span height. The contraction occurs earlier along the surface of the suction side. Figure 4 shows the nondimensional pressure distribution, *Cp*, before and after the contoured endwall compared with the engine conditions. The film-cooling hole exit locations are shown in Fig. 4 as well. The low-speed pressure distributions were predicted with FLUENT 6.0, a commercially available computational fluid dynamics (CFD) solver, and verified experimentally.

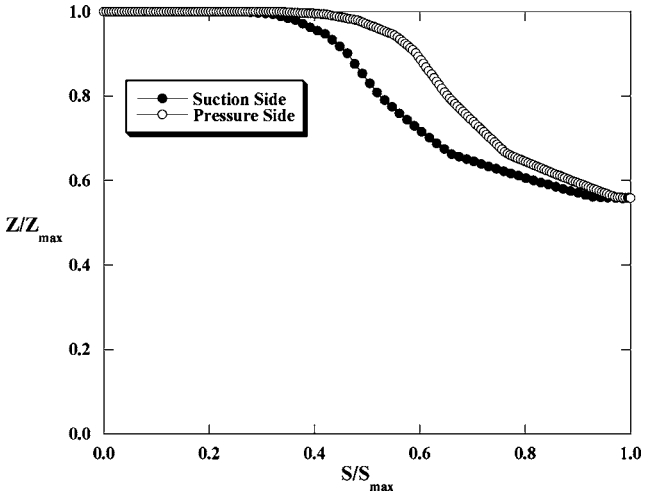

Fig. 3 Contoured endwall surface definition

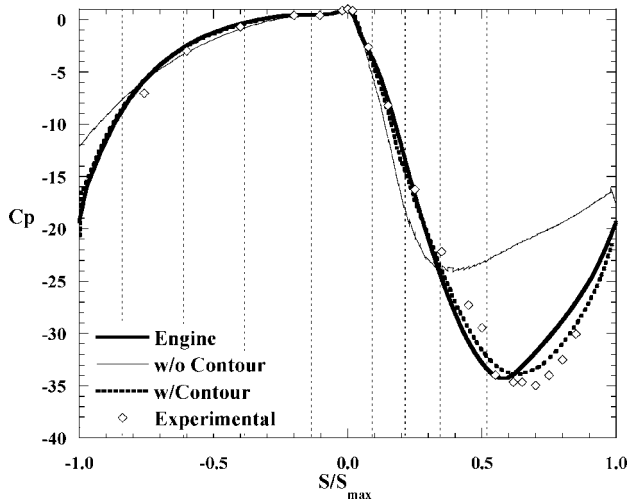

Fig. 4 *Cp* distribution around the vane before and after the contoured endwall compared with engine conditions (dashed lines indicate locations of film-cooling rows)

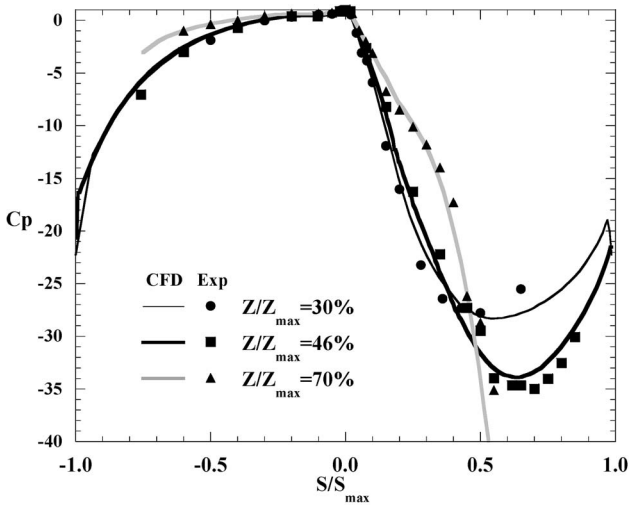

Fig. 5 The effect of span height on the *Cp* distribution

An iterative process was used to design the contour that involved altering the contour shape, modeling the resulting geometry in FLUENT, and comparing the modified *Cp* distribution to the engine *Cp* distribution. A systematic iterative approach of altering the contour based on the desired difference between pressure distributions was used by implementing the definition of the pressure coefficient as well as Bernoulli's equation. Note that the *Cp* distribution at the vane midspan was the design location for these iterations. The final contour shape had a sharp contraction, with the span reduced by 46% from the leading edge to trailing edge across the vane passage.

The effect of the contour on the pressure distribution can be seen in Fig. 5 by measurements at three span heights. The *Cp* distribution at the lowest span height ($Z/Z_{max}=30\%$) did not vary significantly from the midspan location ($Z/Z_{max}=46\%$), indicating a nearly two-dimensional flow on the bottom half of the vane. At the highest span height ($Z/Z_{max}=70\%$) the flow on the suction side initially had a much lower acceleration, indicating a stagnating flow in the region just upstream of the contraction. However, as the contour began to contract the flow showed a much greater acceleration at the 70% span.

Vane Construction. The center vane was made from a low-density foam with a low thermal conductivity ($k=0.028$ W/m K) in order to minimize conduction losses through the surface. For the heat transfer tests, the vane was covered with 13 Inconel 600 thin metal foils, which provided a constant surface heat flux. Between each foil there was a gap of 0.38 cm, which allowed enough room for pressure taps and insured that current did not conduct between foils. The foils were connected in series, with copper bus bars soldered to the ends of each foil to promote a uniform distribution of the current and insure a good electrical connection. The vane was instrumented with 214 type E thermocouples that were placed just below the heat transfer surface at five span heights to measure the surface temperature. Pressure taps were installed at 74 locations along the vane at three span heights, concentrating them in regions of high-pressure gradients as predicted by FLUENT.

The convective heat flux was calculated using the total power supplied to the metal foils minus radiation losses and conduction losses and gains. For the radiation correction the emissivity, $\varepsilon=0.22$, of the Inconel foils was assumed to be the same value as stainless-steel foils (Incropera and DeWitt [14]). The surrounding temperatures were measured and found to agree with the free-

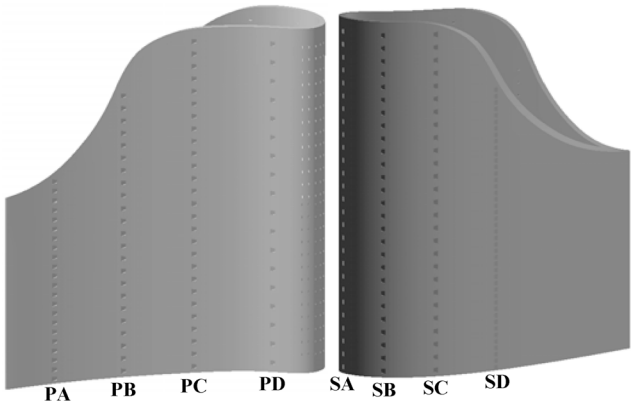

Fig. 6 Film-cooling vane showing hole designations

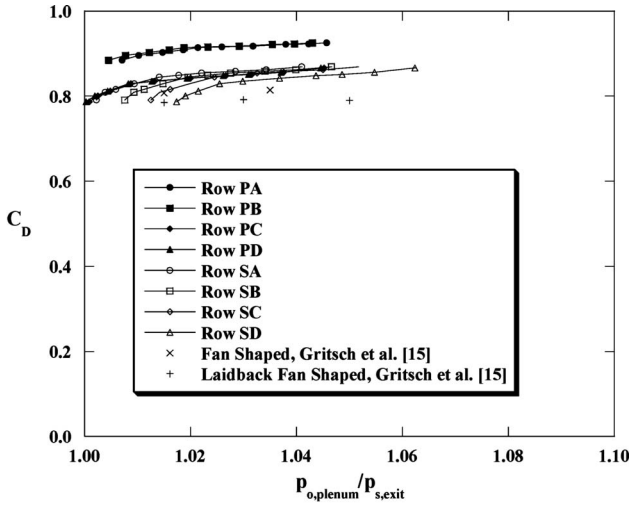

Fig. 8 Fan-shaped hole discharge coefficients

stream temperature. The radiation losses amounted to 4% of the total heat flux. Conduction corrections were calculated based on a one-dimensional conduction model driven by the temperature difference through the foam vane, and accounted for a maximum of about 2% of the total heat flux for the worst case.

Adiabatic film-cooling effectiveness measurements were performed in the same large-scale test facility as the heat transfer measurements. Coolant flow was provided by the upper flow channel of the wind tunnel shown in Fig. 1, using a blower to increase the coolant supply pressure before it was fed into the film-cooling vane. The temperature difference between the freestream and coolant flows was typically 20°C for the film-cooling tests, yielding density ratios near 1.06. The center vane of the two-passage cascade contained five rows of cylindrical showerhead film-cooling holes and eight rows of fan-shaped film-cooling holes, four rows each on the suction and pressure sides. The experimental film-cooling vane is shown in Fig. 6. A detailed schematic of the fan-shaped film-cooling hole geometry is shown in Fig. 7, while the important film-cooling parameters are listed in Table 2 for both the showerhead and fan-shaped holes. The cylindrical showerhead holes had a 60 deg surface angle and a 90 deg compound angle. The centerlines of the fan-shaped holes were angled 30 deg with respect to the surface. The fan-shaped holes also had a 10 deg lateral diffusion angle from the hole centerline and a 10 deg forward expansion angle.

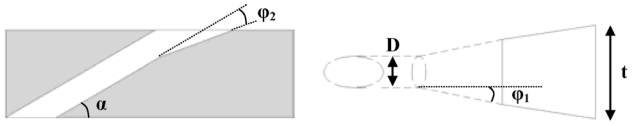

Fig. 7 Fan-shaped cooling hole detailed geometry

Table 2 Film-cooling hole parameters

Fan shaped			Showerhead	
D (cm)	0.38		D (cm)	0.24
α (°)	30		α (°)	60
φ_1 (°)	10		β (°)	90
φ_2 (°)	10		t (cm)	0.48
t (cm)	0.81		t/P (-)	0.22
	t/P (-)	S_{exit}/S_{max} (-)		
Row *PA*	0.540	−0.840		
Row *PB*	0.405	−0.615		
Row *PC*	0.405	−0.384		
Row *PD*	0.270	−0.135		
Row *SA*	0.405	0.090		
Row *SB*	0.405	0.214		
Row *SC*	0.405	0.345		
Row *SD*	0.810	0.519		

The film-cooling vane was also constructed using low thermal conductivity foam ($k=0.028$ W/m K). The film-cooling holes were cut into the foam using a 5-axis water jet cutting machine. The manufacturing process did produce small nonuniformities in the diameter of the cylindrical portion of the hole. Each hole was measured individually to insure the correct flow areas were used in calculating the coolant mass flow. The nominal diameter for the cylindrical portion of the fan-shaped film-cooling hole was 0.38 ± 0.015 cm. Four plenums were placed inside the film-cooling vane to allow for the capability of independently varying individual row blowing ratios. To verify the nondimensional pressure distribution as discussed previously, pressure taps were placed at a 46% span. Type E thermocouples were also placed flush with the surface at various locations for calibration purposes.

To set the desired coolant flows, discharge coefficients were measured for the fan-shaped film-cooling holes and compared to data from Gritsch et al. [15], which had slightly larger lateral diffusion and forward expansion angles of $\varphi_1=14$ deg and $\varphi_2=15$ deg. Discharge coefficients shown in Fig. 8 increased with pressure ratio initially before leveling off, with C_D values falling in the range between 0.8 and 0.9. Generally good agreement is shown between most of the rows and also between the current study and Gritsch et al. [15], with slight differences in C_D attributed to the smaller lateral diffusion and forward expansion angles used in our study. C_D values were further verified by running multiple rows at the same time and comparing the calculated total mass flow rate using pressure ratios and C_D coefficients to the measured total flow rate, showing agreement within 1%.

An infrared (IR) camera was used to measure the surface temperature distribution on the vane during testing. Five images were taken at each location and averaged to minimize experimental uncertainty. Images were taken from beneath the test section through ZnSe windows placed in the lower flat endwall (illustrated in Fig. 2). For some of the rows, more than one image was necessary to capture the area downstream of the cooling holes. Because of the vane surface curvature and the 45 deg angle between the IR camera and the surface, the IR images needed to be transformed to accurately represent the true surface distance. Prior to testing, a 1×1 cm grid was placed on the surface of the vane and an IR image was taken at each viewing location. Next, the grid vertices in each of the images were used to perform a third- or fourth-order polynomial surface transformation for that image.

The transformed images were then calibrated using type E ther-

mocouples that were placed flush with the vane surface. The infrared camera measures the radiation from the surface, so an accurate knowledge of the surface emissivity and the surrounding ambient temperature yields the correct surface temperature. The values of ε and T_{amb} for each image were deduced by calibrating the image surface temperatures to match the measured thermocouple temperatures over the full measurement range. Values for ε were fairly consistent between image locations, varying from 0.6 to 0.7. The variation resulted because not all of the images were taken at the same viewing angle or the same distance from the surface. Following the calibration procedure, the surface temperatures were nondimensionalized and corrected for conduction errors using the method established by Ethridge et al. [16]. Values for η_o ranged from 0.04 to 0.12 around the vane surface, where the highest values occurred just downstream of row PB on the pressure side.

Blowing ratios for this study were defined in two ways, depending on the region. For the showerhead region, blowing ratios are reported based on the inlet velocity, U_{in}

$$M_\infty = \frac{m_c}{A_h U_{in} \rho_{in}} \tag{1}$$

However, for each row of fan-shaped holes, blowing ratios are reported in terms of the local surface velocity, U_{local}

$$M = \frac{m_c}{A_h U_{local} \rho_{in}} \tag{2}$$

Five blowing ratios were tested for the showerhead region, four blowing ratios were tested for each row on the pressure side, and three blowing ratios were tested for each row on the suction side. The range of blowing ratios was chosed to span typical engine operating conditions.

Experimental Uncertainty. The partial derivative and sequential perturbation method given by Moffat [17] was used to calculate uncertainties for the measured values. For a high reported value of St=0.0093 the uncertainty was ±3.23%, while the uncertainty for a low value of St=0.0023 was ±2.13%. The uncertainties for the adiabatic effectiveness measurements were ±0.012 for a high value of η_{AW}=0.9 and ±0.011 for a low value of η_{AW} =0.2.

Experimental Results

Heat transfer results will be discussed first, followed by adiabatic effectiveness results and a comparison to existing data from literature.

Heat Transfer Results. Heat transfer results are reported in terms of the Stanton number based on inlet velocity, with results shown in Fig. 9 for each of the five span locations. There was a local peak in heat transfer at the stagnation region for all span heights, followed by a decrease on the pressure side before Stanton numbers leveled off. On the suction side there was a decrease in heat transfer until the boundary layer transitioned from laminar to turbulent. The transition caused a large increase in heat transfer, followed again by decreasing Stanton numbers as the turbulent boundary layer developed.

A large increase in Stanton numbers also occurred at the higher span locations, which were closer to the contour, but the increase occurred at more upstream locations on the surface ($S/S_{max,SS}$ =0.4 for the 73% span location and $S/S_{max,SS}$=0.3 for the 88% span location). The sudden increase in Stanton numbers below 50% span was because of the boundary layer transition. However, the effect of the contour was to stagnate the flow in the region just upstream of the contraction, which led to the increase in Stanton numbers for the higher span locations. A midspan comparison with the prediction from the numerical boundary layer code TEXSTAN [18] shows the same general trends in Stanton numbers.

Trip wires were used to simulate film-cooling injection along

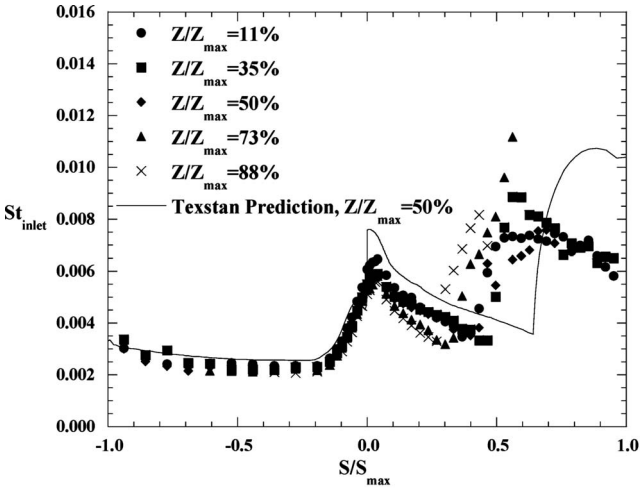

Fig. 9 Stanton number distribution around the vane for all span heights

the surface of the vane. The effect of a trip wire on the boundary layer is analogous to a film-cooling hole modifying the boundary layer. The desired effect was that of perturbing the laminar boundary layer and causing it to become turbulent at the trip location. The trip wires consisted of materials that would not conduct current across the heat transfer surface, and were sized based on the criterion by Schlichting [19], which stated that the critical Reynolds number based on the trip diameter should be greater than 900 to cause boundary layer transition. Trip wires were placed at four locations on the suction side as shown in Fig. 10. The critical Reynolds numbers based on the trip wire diameters and local velocities are also shown in Fig. 10. Note there were no cooling holes present during these tests; they are merely illustrated for reference.

Figure 11 shows the effect of the trip wires placed on the suction side in terms of a locally defined Stanton and Reynolds number, along with flat plate correlations for laminar and turbulent flow over a flat plate with constant surface heat flux developed by Kays and Crawford [20]. Trip 1, which was placed at the same surface location as the first row of suction side film-cooling holes, caused the boundary layer to transition. However, the boundary layer ultimately relaminarized because of the strong flow acceleration. Further downstream, the boundary layer transitioned at nominally the same location as the no-trip case. Trip 2, which was placed at the same surface location as the second row of suction side film-cooling holes, again forced the boundary layer to transition, which was shown by an increase in heat transfer. In this case, however, the boundary layer did not relaminarize as for trip 1. A resulting investigation of several more trip locations defined a

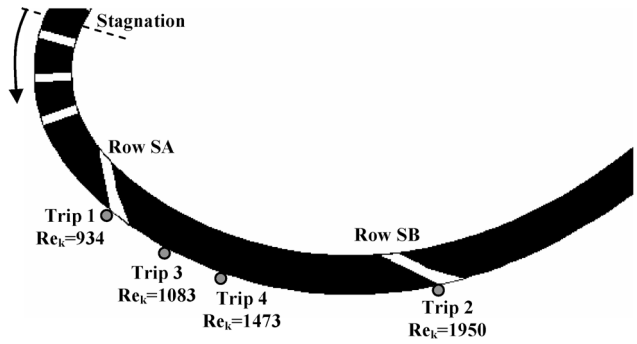

Fig. 10 Trip wire locations shown relative to hole exit locations on the vane

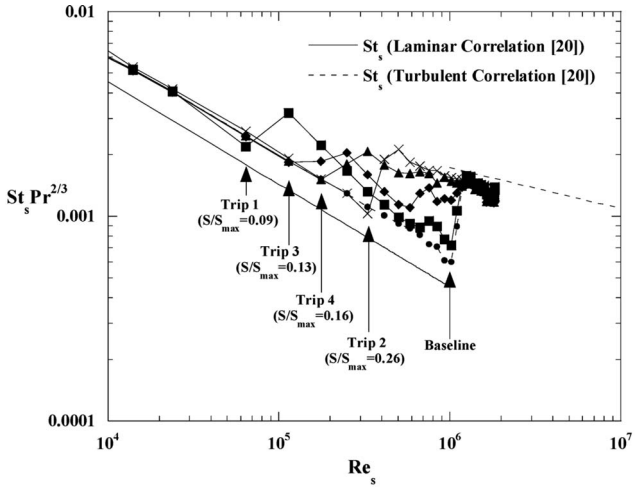

Fig. 11 Stanton numbers for the four suction side trip cases

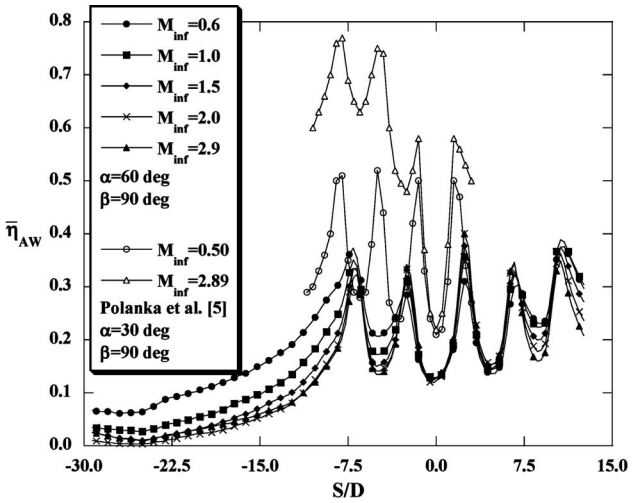

Fig. 13 Laterally averaged effectiveness for the showerhead cases

critical region along the surface bounded by trips 3 and 4 wherein the boundary layer would transition to turbulent flow and not relaminarize.

Showerhead Adiabatic Effectiveness Results. Showerhead film cooling was investigated independently, without downstream blowing, by measuring η_{AW} for five different blowing ratios ranging from $M_\infty=0.6$ to 2.9. These blowing ratios are reported as the average M_∞ value of the five showerhead rows when referring to a certain case, although M_∞ values varied slightly between rows. Film-cooling effectiveness contours for the highest and lowest blowing ratio cases are shown in Fig. 12. As M_∞ increased, the jets were directed up the span of the vane and started to lift off. At $M_\infty=0.6$ the coolant trickled out, causing the jets to spread laterally, while at $M_\infty=2.9$ the coolant offered little benefit downstream of the holes.

The pitch-averaged film-cooling effectiveness for the showerhead cases is shown in Fig. 13. It is interesting to see that the peaks increase with M_∞ while the valleys decrease with M_∞. This is due to the change in jet direction as the blowing ratio increased. Also shown in Fig. 13 is a comparison to Polanka et al. [2] for blowing ratios of 0.5 and 2.9. The showerhead holes in their study had a shallow surface angle of 25 deg, as compared with the much sharper 60 deg surface angle used in this study, although both studies had a 90 deg compound angle. In addition, the holes in the Polanka et al. [2] study were in a staggered configuration. These differences in geometry allowed the film-cooling jets to stay attached to the surface much better, even for the relatively low blowing ratio of 0.5, leading to the much greater levels of laterally averaged effectiveness by Polanka et al. [2].

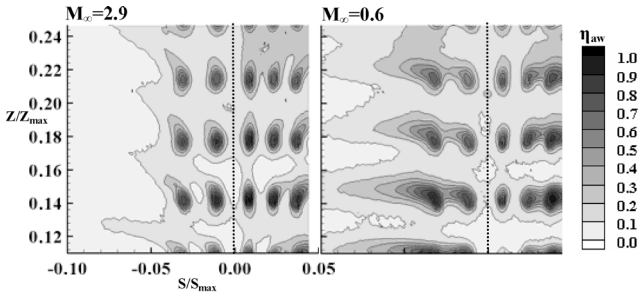

Fig. 12 Contours of adiabatic effectiveness for the $M_\infty=2.9$ and $M_\infty=0.6$ showerhead cases

Pressure Side Adiabatic Effectiveness Results. Single-row adiabatic film-cooling effectiveness measurements were taken for four rows on the pressure side, without any upstream showerhead blowing. Adiabatic effectiveness contours for the highest ($M=7.4$) and lowest ($M=2.9$) blowing ratios measured for the first pressure side row (row $PD: S/S_{\max,PS}=-0.14$) are shown in Fig. 14. The contours for row *PD* show a contraction of the jet downstream of the hole exit, indicating jet separation. After about 10 hole diameters a large lateral spreading of the jet occurs that yields an increase in both the level of adiabatic effectiveness and jet coverage. Jet separation occurred immediately downstream of

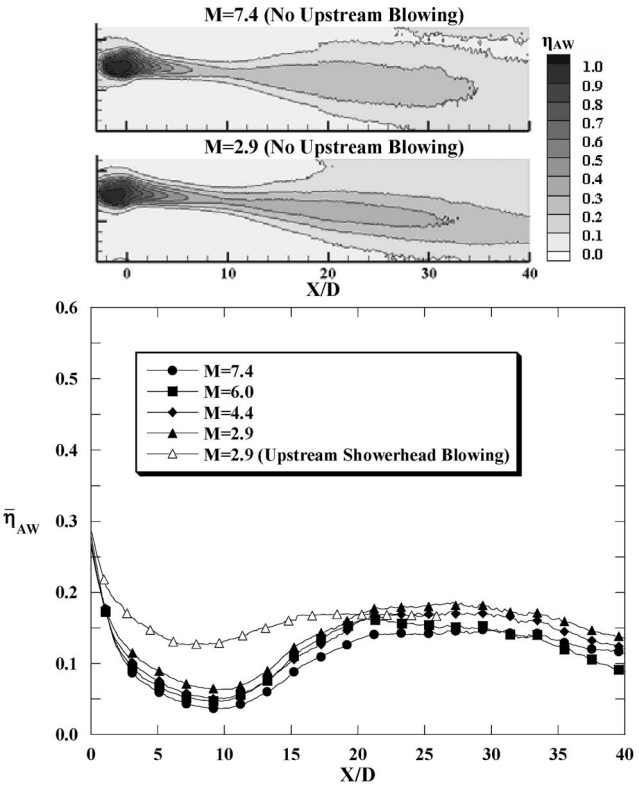

Fig. 14 Contours of adiabatic effectiveness for high and low blowing ratios for row *PD* and laterally averaged adiabatic effectiveness for row *PD*

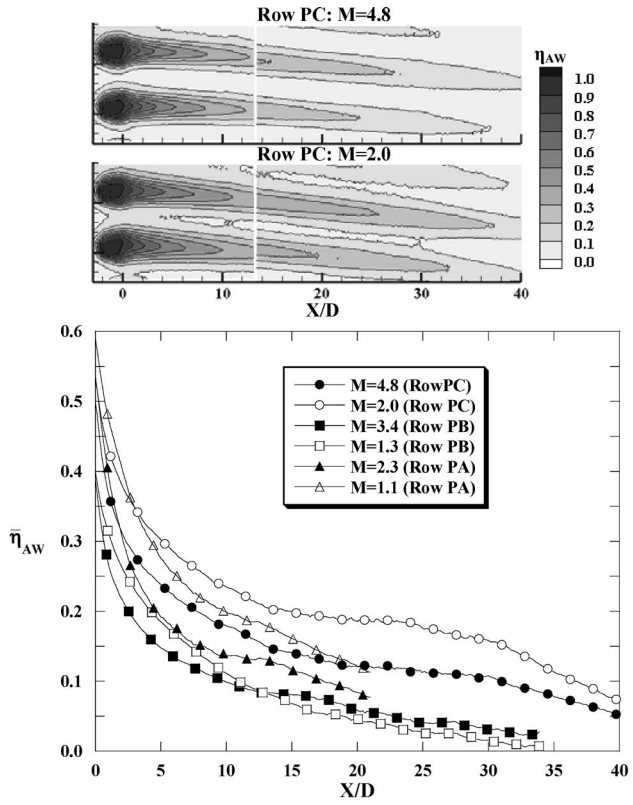

Fig. 15 Contours of adiabatic effectiveness for high and low blowing ratios for row *PC* and laterally averaged adiabatic effectiveness for rows *PC-PA*

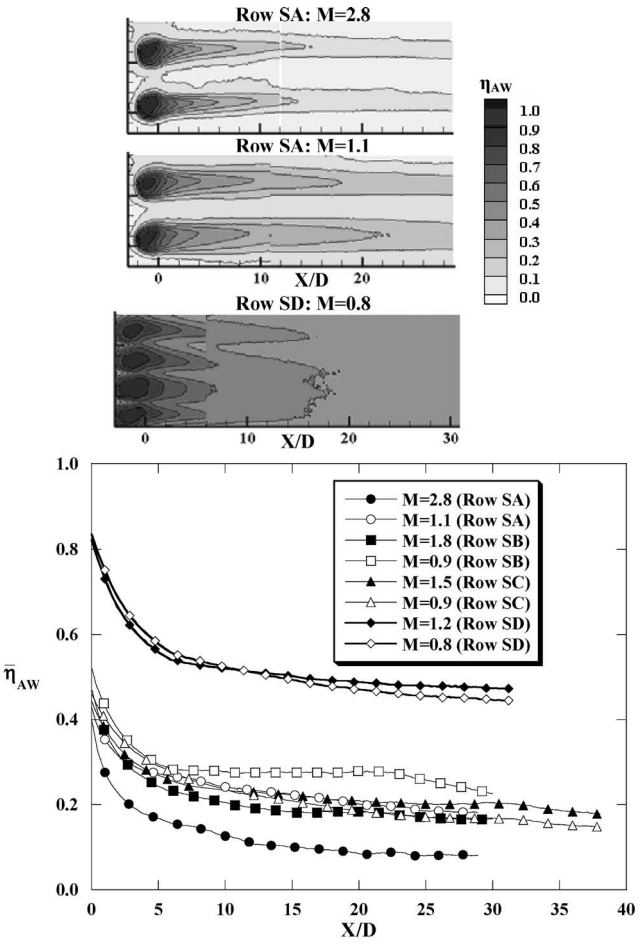

Fig. 16 Contours of adiabatic effectiveness for high and low blowing ratios for row *SA* and a representative case for row *SD*. Also laterally averaged effectiveness for the suction side rows.

the hole location due to relatively high local blowing ratios coupled with a concave surface curvature. However, as the vane surface curved back into the jet trajectory, the jet impinged and spread onto the vane surface. As expected, this phenomenon was accentuated with an increase in blowing ratio, which led to increased separation. Also shown in Fig. 14 is the laterally averaged effectiveness for row *PD*. For this configuration, increased blowing led to lower laterally averaged effectiveness due to the increasing separation.

Also investigated was the effect of upstream showerhead cooling on the first pressure side row of fan-shaped holes. Included in Fig. 14 is a comparison of the laterally averaged effectiveness for row *PD* at a blowing ratio of $M=2.9$ in which there was upstream showerhead blowing ($M_\infty=2.0$). The upstream blowing actually increased the adiabatic effectiveness downstream of row *PD*. This is consistent with the findings of Polanka et al. [13], who stated that for high blowing ratios the turbulence generated by the upstream blowing tended to disperse the jet down onto the vane surface, making it more effective at cooling the surface.

The other pressure side rows (row $PC:S/S_{\max,PS}=-0.38$, row $PB:S/S_{\max,PS}=-0.61$, row $PA:S/S_{\max,PS}=-0.84$) were located on a relatively flat section of the vane surface. Representative adiabatic effectiveness contours for these three rows for high (row *PC*, $M=4.8$) and low (row *PC*, $M=2.0$) blowing ratios are shown in Fig. 15. The jet contours taper immediately downstream of the holes. These three pressure side rows were located in a region of high acceleration, which tends to provide less resistance to jet lift-off. Also shown in Fig. 15 are laterally averaged effectiveness values for rows *PC*, *PB*, and *PA*, for the highest and lowest measured blowing ratios. Due to jet separation, higher blowing ratios actually reduced the adiabatic effectiveness of the fan-shaped rows.

Suction Side Adiabatic Effectiveness. Single-row adiabatic film-cooling measurements, without any upstream showerhead blowing, were also made on the suction side for four individual rows. The first three rows on the suction side, rows *SA* ($S/S_{\max,SS}=0.09$), *SB* ($S/S_{\max,SS}=0.21$), and *SC* ($S/S_{\max,SS}=0.35$), were located in a region of high convex curvature and high acceleration. The final suction side row (row $SD:S/S_{\max,SS}=0.52$) had much closer hole spacing and was located just upstream of the maximum throat velocity. Representative adiabatic effectiveness contours for high (row *SA*, $M=2.8$) and low (row *SA*, $M=1.1$) blowing ratios in the region of high curvature are shown in Fig. 16. The contours show a large amount of separation with increased blowing. This trend is seen further in the laterally averaged effectiveness values for rows *SA*, *SB*, and *SC*, which are also shown in Fig. 16 for a high and low blowing ratio. Clearly, the separation is due to the severe surface curvature in this region of the suction side. The results indicate that for this region it is more beneficial to eject less flow so that it remains attached to the surface.

A representative contour of adiabatic effectiveness for row *SD* (also see Fig. 16) shows a much higher effectiveness than the other suction side rows, in part because of the hole spacing, but also because of an absence of separation. There was less tapering of the jet contours downstream of the hole exit for row *SD*, indicating less separation. Individually defined jets are nearly indistinguishable downstream of about 16 hole diameters, indicating the excellent lateral diffusion typically seen in an attached fan-shaped cooling hole jet. Also shown in Fig. 16 are the laterally averaged effectiveness levels for row *SD*. The laterally averaged

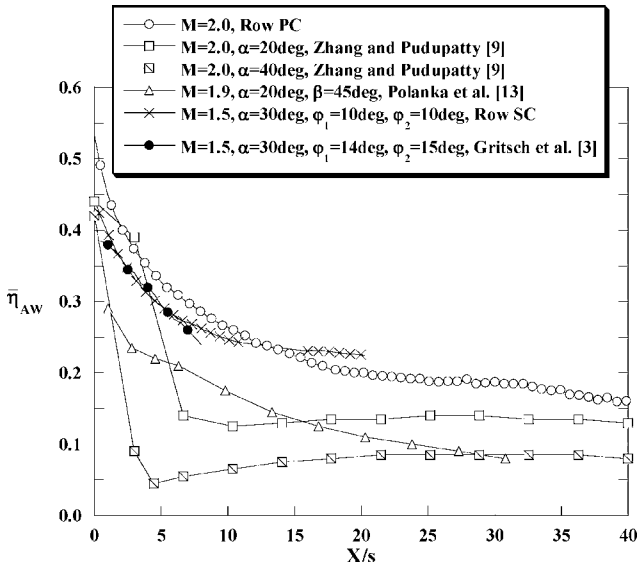

Fig. 17 Comparisons with published cylindrical hole vane film-cooling data and fan-shaped flat plate data

values are much higher than the separated cooling rows, and level out near a laterally averaged effectiveness value of 0.5.

Comparisons to Literature. A pressure side comparison between cylindrical and fan-shaped cooling holes for a blowing ratio near $M=2.0$ is shown in Fig. 17. The cylindrical holes studied by Zhang and Pudupatty [9] had surface inclination angles of $\alpha=20$ deg and $\alpha=40$ deg, while Polanka et al. [13] studied cylindrical holes on the vane pressure side with a surface inclination angle of $\alpha=30$ deg and a compound angle of 45 deg. Because of differences in hole geometry and spacing, the distance downstream of the hole exit was normalized with respect to the equivalent exit slot width s described by L'Ecuyer and Soechting [21], where s is the ratio of the hole breakout area to the hole spacing P (measured normal to the streamwise direction). This comparison shows that the fan-shaped hole geometry offers a significant increase in adiabatic effectiveness over cylindrical holes.

Although there have been some previous studies done with fan-shaped holes on a vane surface, it was not possible to make a direct comparison to these studies, as the equivalent slot width was not able to be determined. For a region on the suction side with relatively low surface curvature, a comparison was made between data from our study and fan-shaped data on a flat plate from Gritsch et al. [3] (also shown in Fig. 17). The flat plate study by Gritsch et al. [3] featured the same surface inclination angle as our study ($\alpha=30$ deg), with slightly larger lateral diffusion and forward expansion angles of $\varphi_1=14$ deg and $\varphi_2=15$ deg. In this region of relatively low surface curvature on the suction side, very good agreement is shown just downstream of the hole between the current study and the flat plate study by Gritsch et al. [3].

Conclusions

This paper has presented a coupled study of the heat transfer coefficients and adiabatic effectiveness for a large-scale turbine vane under low-speed conditions. A contoured endwall was designed in order to match the engine pressure distribution around the vane. Heat transfer results showed a peak in Stanton numbers near the leading edge. Stanton numbers decreased on the pressure side to a constant value. On the suction side, Stanton numbers decreased until a surface location of $S/S_{max}=0.5$, where Stanton numbers were increased because of the boundary layer transitioning from laminar to turbulent.

Trip wires were used to simulate the boundary layer transition caused by film-cooling holes on the vane suction side. It was noted that using a trip wire to transition the boundary layer increased the Stanton numbers as if the boundary layer had transitioned naturally. The trip wire placed at the location of the first film-cooling hole row tripped the boundary layer, but the boundary layer relaminarized before the natural transition location. An investigation of trip wire location showed the sensitivity to location in terms of the boundary layer transition and the relaminarizing process. This sensitivity should be considered by engine designers when determining film-cooling hole placement, as this will dictate the laminar-to-turbulent boundary layer transition.

Adiabatic effectiveness measurements for the showerhead region showed that increasing the blowing ratio changed the direction of the jets and reduced the amount of lateral spreading. Adiabatic film-cooling effectiveness measurements showed that in regions of high curvature just downstream of the leading edge the jets separated from the surface. However, on the pressure side where there was a concave surface curvature near the first cooling hole row, the coolant jets impinged on the surface about 10 hole diameters downstream and spread laterally. Along both the suction and pressure sides, increasing the blowing ratio tended to accentuate the jet lift-off, reducing overall film-cooling effectiveness. The presence of upstream showerhead blowing on the first pressure side row tended to increase the turbulent diffusion of the jet downwards onto the surface, increasing effectiveness. The suction side was particularly hard to cool due to the jet separation resulting from the convex curvature.

A comparison to previous cylindrical hole vane cooling studies further highlights the cooling benefit from fan-shaped holes over the traditional cylindrical cooling hole shape. This study emphasizes the difficulty of film-cooling hole placement, as there are many effects that play a role in the effectiveness of a cooling jet. These effects include boundary layer transition location, surface curvature, acceleration, hole spacing, and blowing ratio.

Acknowledgment

The authors are grateful to Siemens Power Generation for their funding and support of this project.

Nomenclature

A = area
C = vane chord
C_D = discharge coefficient
C_p = specific heat
Cp = static pressure coefficient, $Cp=(p_{s,\text{local}}-p_{s,\text{in}})/0.5\rho_{\text{in}}U_{\text{in}}^2$
D = film-cooling hole diameter
h = heat transfer coefficient
k = thermal conductivity
m = mass flow rate
M = blowing ratio using local velocity, $m_c/A_hU_{\text{local}}\rho_{\text{in}}$
M_∞ = blowing ratio using inlet velocity, $m_c/A_hU_{\text{in}}\rho_{\text{in}}$
p = pressure
P = hole spacing measured normal to streamwise direction
Re = Reynolds number, $\text{Re}=U_{\text{in}}C/\nu$
s = equivalent slot width, A_{break}/P
S = distance along the vane surface
St_{in} = Stanton number using inlet conditions, $\text{St}_{\text{in}}=h/\rho_{\text{in}}C_pU_{\text{in}}$
St_s = Stanton number using local conditions, $\text{St}_s=h/\rho_{\text{in}}C_pU_{\text{local}}$
t = hole breakout width
U = velocity
X = distance downstream of the hole exit
Z = distance measured along the vane span

Greek

α = inclination angle
β = compound angle
ε = surface emissivity
η_{AW} = adiabatic film-cooling effectiveness, $\eta_{AW}=(\eta_{\text{meas}}-\eta_o)/(1-\eta_o)$
η_{meas} = effectiveness with blowing, $\eta_{\text{meas}}=(T_\infty-T_{\text{surf}})/(T_\infty-T_c)$
η_o = effectiveness without blowing, $\eta_o=(T_\infty-T_{\text{surf}})/(T_\infty-T_c)$
ρ = density
υ = kinematic viscosity
φ_1 = lateral diffusion angle
φ_2 = forward expansion angle

Subscripts

amb = ambient
break = hole breakout area
c = coolant
h = metering area of film-cooling holes based on D
in = inlet condition
k = critical
local = local conditions
max = maximum
o = total
s = static pressure
surf = surface
∞ = free-stream conditions

References

[1] Riess, H., and Bölcs, A., 2000, "The Influence of the Boundary Layer State and Reynolds Number on Film-Cooling and Heat Transfer on a Cooled Nozzle Guide Vane," ASME Paper No. 2000-GT-205.

[2] Polanka, M. D., Witteveld, V. C., and Bogard, D. G., 1999, "Film-Cooling Effectiveness in the Showerhead Region of a Gas Turbine Vane Part 1: Stagnation Region and Near Pressure Side," ASME Paper No. 99-GT-48.

[3] Gritsch, M., Schulz, A., and Wittig, S., 1998, "Adiabatic Wall Effectiveness Measurements of Film-Cooling Holes With Expanded Exits," ASME J. Turbomach., vol. **120**, pp. 549.

[4] Yuen, C. H. N., Martinez-Botas, R. F., and Whitelaw, J. H., 2001, "Film-Cooling Effectiveness Downstream of Compound and Fan-Shaped Holes," 2001-GT-0131.

[5] Dittmar, J., Schulz, A., and Wittig, S., 2002, "Assessment of Various Film-Cooling Configurations Including Shaped and Compound Angle Holes Based on Large Scale Experiments," ASME Paper No. GT-2002–30176.

[6] Dittmar, J., Schulz, A., and Wittig, S., 2004, "Adiabatic Effectiveness and Heat Transfer Coefficient of Shaped Film-Cooling Holes on a Scaled Guide Vane Pressure Side Model," Int. J. Rotating Mach., **10**, pp. 345–354.

[7] Guo, S. M., Lai, C. C., Jones, T. V., Oldfield, M. L. G., Lock, G. D., and Rawlinson, A. J., 1998, "The Application of Thin-Film Technology to Measure Turbine-Vane Heat Transfer and Effectiveness in a Film-Cooled, Engine-Simulated Environment," Int. J. Heat Fluid Flow, **19**, pp. 594–600.

[8] Zhang, L., Baltz, M., Pudupatty, R., and Fox, M., 1999, "Turbine Nozzle Film-Cooling Study Using the Pressure Sensitive Paint (PSP) Technique," ASME Paper No. 99-GT-196.

[9] Zhang, L., and Pudupatty, R., 2000, "The Effects of Injection Angle and Hole Exit Shape on Turbine Nozzle Pressure Side Film-Cooling," ASME Paper No. 2000-GT-247.

[10] Sargison, J. E., Guo, S. M., Oldfield, M. L. G., Lock, G. D., and Rawlinson, A. J., 2001, "A Converging Slot-Hole Film-Cooling Geometry Part 1: Low-Speed Flat-Plate Heat Transfer and Loss," ASME Paper No. 2001-GT-0126.

[11] Sargison, J. E., Guo, S. M., Oldfield, M. L. G., Lock, G. D., and Rawlinson, A. J., 2001, "A Converging Slot-Hole Film-Cooling Geometry Part 2: Transonic Nozzle Guide Vane Heat Transfer and Loss," ASME Paper No. 2001-GT-0127.

[12] Schnieder, M., Parneix, S., and von Wolfersdorf, J., 2003, "Effect of Showerhead Injection on Superposition of Multi-Row Pressure Side Film-Cooling With Fan-Shaped Holes," ASME Paper No. GT-2003–38693.

[13] Polanka, M. D., Ethridge, M. I., Cutbirth, J. M., and Bogard, D. G., 2000, "Effects of Showerhead Injection on Film-Cooling Effectiveness for a Downstream Row of Holes," ASME Paper No. 2000-GT-240.

[14] Incropera, F. P., and DeWitt, D. P., 1996, *Fundamentals of Heat and Mass Transfer*, 4th ed., Wiley & Sons, New York.

[15] Gritsch, M., Schulz, A., and Wittig, S., 1997, "Discharge Coefficient Measurements of Film-Cooling Holes With Expanded Exits," ASME Paper No. 97-GT-165.

[16] Ethridge, M. I., Cutbirth, J. M., and Bogard, D. G., 2000, "Scaling of Performance for Varying Density Ratio Coolants on an Airfoil With Strong Curvature and Pressure Gradient Effects," ASME Paper No. 2000-GT-239.

[17] Moffat, R. J., 1988, "Describing the Uncertainties in Experimental Results," Exp. Therm. Fluid Sci., **1**, pp. 3–17.

[18] Crawford, M. E., 1986, *Simulation Codes for Calculation of Heat Transfer to Convectively-Cooled Turbine Blades* (a set of four lectures in Convective Heat Transfer and Film-cooling in Turbomachinery, T. Arts, ed., Lecture Series 1986–06), von Karman Institute for Fluid Dynamics, Rhode-Saint-Genese, Belgium.

[19] Schlichting, H., 1979, *Boundary Layer Theory*, 7th ed., McGraw-Hill, New York.

[20] Kays, W. M., and Crawford, M. E., 1991, *Convective Heat and Mass Transfer*, McGraw-Hill, New York.

[21] L'Ecuyer, M. R., and Soechting, F. O., 1985, "A Model for Correlating Flat Plate Film-Cooling Effectiveness for Rows of Round Holes," *Heat Transfer and Cooling in Gas Turbines*, AGARD CP-390, Paper 19.

Effect of Midpassage Gap, Endwall Misalignment, and Roughness on Endwall Film-Cooling

N. D. Cardwell

N. Sundaram

K. A. Thole

Mechanical Engineering Department,
Virginia Polytechnic Institute and State University,
Blacksburg, VA 24061

To maintain acceptable turbine airfoil temperatures, film cooling is typically used whereby coolant, extracted from the compressor, is injected through component surfaces. In manufacturing a turbine, the first stage vanes are cast in either single airfoils or double airfoils. As the engine is assembled, these singlets or doublets are placed in a turbine disk in which there are inherent gaps between the airfoils. The turbine is designed to allow outflow of high-pressure coolant rather than hot gas ingestion. Moreover, it is quite possible that the singlets or doublets become misaligned during engine operation. It has also become of interest to the turbine community as to the effect of corrosion and deposition of particles on component heat transfer. This study uses a large-scale turbine vane in which the following two effects are investigated: the effect of a midpassage gap on endwall film cooling and the effect of roughness on endwall film cooling. The results indicate that the midpassage gap was found to have a significant effect on the coolant exiting from the combustor-turbine interface slot. When the gap is misaligned, the results indicate a severe reduction in the film-cooling effectiveness in the case where the pressure side endwall is below the endwall associated with the suction side of the adjacent vane. [DOI: 10.1115/1.2098791]

Introduction

Traditional techniques to cool the hot section of a gas turbine engine involve the use of air from the compressor that has bypassed the combustion chamber and is used for impingement cooling, film cooling, and convective cooling in the turbine airfoils. The coolant is generally high-pressure air that has been routed to the turbine section through a secondary flow path. In the manufacturing of a turbine engine, the airfoils and their associated endwalls are typically cast as singlets or doublets that are then placed in the turbine disk. It is inherently difficult to seal interfaces between the singlets and doublets, particularly when considering the expansion and contraction of turbine components during engine operation. Given that there is high-pressure coolant that must be routed to the turbine through a secondary flow path to cool the blades and vanes, this high-pressure coolant can also leak through any gaps that may exist in the turbine. Moreover, since combustor profiles are not always uniform, it would be expected that the thermal contraction and expansion of adjacent vanes would be significantly different. This difference can lead to turbine airfoils that are misaligned. The question then becomes, how should a turbine designer account for a potential misalignment in airfoil components in their calculations of airfoil temperatures?

Airfoil roughness is an important problem in today's operation of gas turbines. With the push to use fuels other than natural gas, such as coal-derived fuels for industrial turbines, erosion and deposition are issues that must be accounted for. Moreover, propulsive gas turbines are being used in harsh environments in which sand or other foreign debris is ingested and deposited on components in the hot section.

The work presented in this paper compares measured adiabatic effectiveness levels of a well-sealed midpassage gap that is aligned and misaligned to determine the effect on endwall film cooling and slot cooling. Also compared in this paper is the effect that roughness can have on endwall film cooling.

Contributed by the International Gas Turbine Institute (IGTI) of ASME for publication in the JOURNAL OF TURBOMACHINERY. Manuscript received October 1, 2004; final manuscript received February 1, 2005. IGTI Review Chair: K. C. Hall. Paper presented at the ASME Turbo Expo 2005: Land, Sea, and Air, Reno, NV, June 6–9, 2005, Paper No. GT2005-68900.

Relevant Past Studies

There have been turbine endwall studies in the literature that have documented the effects of an upstream slot, discrete film-cooling holes, and combined upstream slot and film cooling. Only a few studies exist on the effect of a midpassage gap. There have been no studies documenting what happens in the case of having a misaligned midpassage gap in an actual airfoil passage. In addition, there have been no studies on the effect of roughness on endwall film cooling.

Most of the studies evaluating leakage flows have been concerned with an upstream slot that represents the leakage flow that might occur between the combustor and turbine. Some of the earliest work related to a leakage flow was performed by Blair [1], who used a two-dimensional aligned slot upstream of vane geometry. Enhancements in film-cooling effectiveness along the endwall were observed as the flow through the slot was increased. In a similar study of coolant upstream of a vane passage, Burd et al. [2] studied the effects of an upstream aligned, 45 deg slot. By using coolant flows as high as 6% of the total passage flow, better cooling was observed over the endwall and on both sides of the vanes relative to lower coolant flows. A study by Colban and Thole [3,4] measured the effects of changing the combustor liner film cooling and upstream slot flows on the effectiveness levels along the endwall of a first-stage turbine vane. Their results showed that the coolant from the slot was not uniform across the exit, with coolant accumulating along the endwall near the suction side of the vane. Coolant injection from the upstream combustor liner caused a different total pressure profile entering the vane passage, relative to a turbulent boundary layer, that in turn changed the secondary flow field.

Detailed endwall film-cooling results have been conducted by Friedrichs et al. [5–7]. The results of their first study [5], which were all surface measurements or visualization, indicated a strong

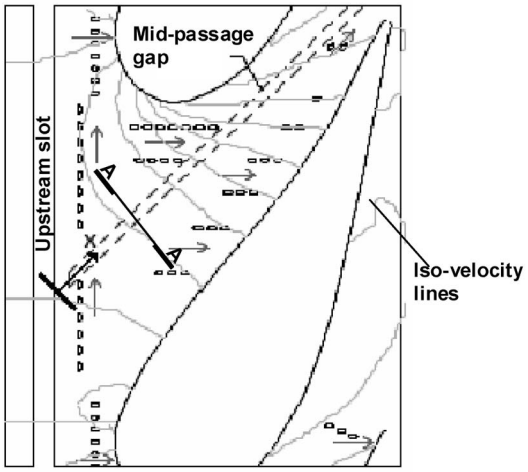

Fig. 1 Directions of the coolant hole injection along with isovelocity contours and the midpassage gap location for mating two turbine vane platforms

influence of the secondary flows on the film cooling and an influence of the film cooling on the secondary flows. Their data showed that the angle at which the coolant leaves the hole did not dictate the coolant trajectory except near the hole exit. Furthermore, the endwall cross flow was altered so that the cross flow was turned toward the inviscid streamlines, which was due to the film-cooling injection.

The only studies to have combined an upstream slot with film-cooling holes in the passage of the vane were those of Zhang and Jaiswal [8], Kost and Nicklas [9], Nicklas [10], and Knost and Thole [11,12]. One of the most interesting results from the Kost and Nicklas [9] and Nicklas [10] studies was that they found for the slot flow alone, which was 1.3% of the passage mass flow, that the horseshoe vortex became more intense. This increase in intensity resulted in the slot coolant being moved off of the endwall surface and heat transfer coefficients that were over three times that measured for no slot flow injection. They attributed the strengthening of the horseshoe vortex to the fact that for the no slot injection the boundary layer was already separated, with fluid being turned away from the endwall at the injection location. Given that the slot had a normal component of velocity, injection at this location promoted the separation and enhanced the vortex. Their adiabatic effectiveness measurements indicated higher values near the suction side of the vane due to the slot coolant migration. Knost and Thole reported a significant change in the streamlines in the near-endwall region resulting from the upstream slot flow. Their results also indicated that the momentum flux ratio was an important parameter in predicting the cooling jet behavior.

Using a flat plate geometry with no turbine airfoils, Yu and Chyu [13] studied the influence of gap leakage downstream of injection cooling holes. They observed that for a moderate level of film cooling upstream of a coolant slot, the combined presence with the gap promoted better coolant film protection. However, as the film-cooling flow was increased the coolant from the gap appeared to lift the slot flow coolant from the wall, resulting in decreased adiabatic effectiveness.

The only known studies of flow from a slot within the midpassage of adjacent airfoils were performed by Aunapu et al. [14], Ranson and Thole [15], and Yamao et al. [16]. Aunapu et al. used blowing through a passage gap in an attempt to reduce the effects of a passage vortex. They hypothesized endwall blowing in the blade passage could reduce the effects of the passage vortex. Aunapu et al. [14] observed that endwall jets in the center of the blade passage effectively altered the path of the pressure side leg of the vortex. Unfortunately, the increased blowing caused higher turbulence and higher aerodynamic losses. Ranson and Thole used

Table 1 Geometric and flow conditions

Scaling factor	9
Scaled up chord length (C)	59.4 cm
Scaled up axial chord length	29.3 cm
Pitch/chord (P/C)	0.77
Span/chord (S/C)	0.93
Re_{in}	2.1×10^5
Inlet and exit angles	0 & 72 deg
Inlet, exit Mach number	0.017,0.085
Inlet mainstream velocity	6.3 m/s

an aligned midpassage gap between two adjacent blades for their combined experimental and computational studies. Their results indicated that the flow leaving the gap was directed toward the blade pressure side, as a result of the incoming velocity vector, and then traversed towards the suction side of the adjacent airfoil. Yamao et al. [16] investigated the distribution of film-cooling effectiveness due to sealing air injected from combustor-vane interface and vane-to-vane interface on annular cascade test equipment. Their study indicated that the film-cooling effectiveness was enhanced with an increase in the sealing air flow rate between the vanes. Also, the increase in sealing air flow rate between the combustor-vane interfaces resulted in significant increase in film-cooling effectiveness near the leading edge, but a slight increase along the trailing edge.

In summary, it is important to understand the effect of coolant flow from leakage points in the endwall region under realistic surface conditions to further the technology of turbine blade cooling. To date, there have been only a few studies that have addressed roughness effects on an actual turbine airfoil but none of these studies has addressed the effect of roughness with adiabatic effectiveness levels on a film-cooled endwall.

Midpassage Gap Geometry

The flat endwall in the linear cascade used for these studies was comprised of five realistic features: a combustor to turbine (upstream) gap, endwall film cooling, a midpassage gap with accompanying strip seal, the capability of simulating an endwall misalignment, and surface roughness representative of that found in an engine. The first-stage vane endwall film-cooling pattern, which was originally designed and tested by Knost and Thole [12], is shown in Fig. 1, which also shows isovelocity contours and hole injection angles. All film-cooling holes were at an angle of 30 deg with respect to the endwall surface.

Also included in the endwall pattern is a two-dimensional slot representing the interface between the combustor and first stage of the turbine. This slot is located 30% of the axial chord upstream of the vane stagnation location, and is designed to be forward facing with an injection angle of 45 deg with respect to the endwall surface. This leakage interface will be referred to as the upstream slot. Table 1 provides a description of turbine vane geometry and

Table 2 Summary of endwall geometry

	Parameter	Experimental
Midpassage gap	W-Passage gap width	0.01C
	H-Seal strip thickness	0.5W
	A-Thermocouple location	6H
	B-Passage gap depth	10H
	C-Seal strip gap	2H
	D-Seal strip width	16.8H
	E-Passage gap plenum width	28H
Upstream slot	Upstream slot width	0.024C
	Slot flow length to width	1.88
Film cooling	FC hole diameter (cm)	0.46
	FC Hole L/D	8.3

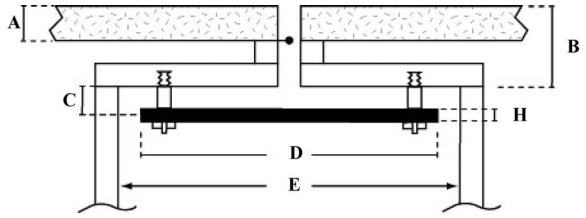

Fig. 2 Cross-section view (section AA, Fig. 1) of the midpassage gap plenum and accompanying seal strip (see Table 2)

operating conditions, and Table 2 provides a summary of parameters relevant to film cooling and upstream slot geometries.

The focus of this paper, as explained, is the interface between the combustor and turbine flows. Also, the midpassage gap does not open into the upstream slot and has its own supply plenum. The dimensions and arrangement of the midpassage gap plenum are shown in Table 2 and Fig. 2. The vane-to-vane interface has three distinct alignment modes: aligned, forward-facing step (dam), and backward-facing step (cascade). The aligned mode, which is shown in Fig. 3(*a*), represents no disparity in height between adjacent vanes and the combustor.

The offset that was considered for the misaligned endwall was 1.2% of vane height or 0.65 cm for the 9× scale geometry. The dam endwall refers to a condition where the suction surface of vane 1 (V1) is raised relative to the pressure side of vane 2 (V2), which is flush with the combustor wall. This configuration is referred to as a dam because, as the secondary flows are driven from the pressure side of one vane towards the suction side of the adjacent vane, the flow faces an upward step. Figure 3(*b*) shows the dam configuration has a raised step for V1 at the upstream slot location.

The cascade endwall refers to a condition where the suction surface of V1 is lowered relative to the pressure side of V2, which is flush with the combustor wall, as shown in Fig. 3(*c*). This configuration is referred to as a cascade because the secondary flows from the pressure to the suction side experience a waterfall, or cascade, effect. For the cascade case, the upstream slot has a recessed step for the vane 1 portion of the platform.

Relative to the work that was done by Knost and Thole [12], endwall roughness was also investigated. For this simulation, the study completed by Bons et al. [17] was referenced to model realistic surface roughness on a first-stage vane platform. Bons et al. lists measured values of endwall rms roughness height (R_a) as 28 μm. This rms value translates to an equivalent sand grain roughness (k_s) of 196 microns as described by Bogard et al. [18]. At 9× scale, which is the scaling factor for the test vane, it resulted in equivalent sand grain roughness (k_s) of 1.76 mm.

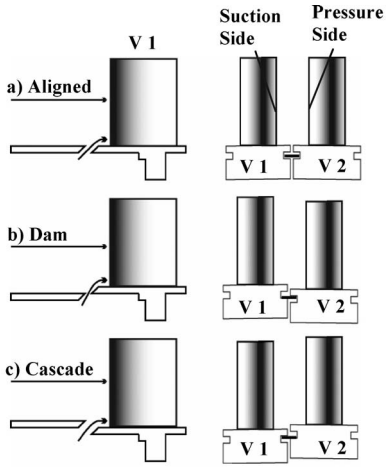

Fig. 3 Side and upstream views of the three alignment modes for two adjacent vane platforms

To simulate a uniformly rough surface, wide-belt industrial sandpaper was used to cover the entire endwall. It has a closed-coat 36-grit surface and grade Y cloth backing. The 36-grit sandpaper corresponds to an equivalent sand grain roughness of 418 microns at engine scale (www.sizes.com/tools/sandpaper.htm). A closed-coat surface has roughness elements arranged in a random array over 100% of the surface. Custom construction of the sandpaper was used to guarantee tight tolerances around each film-cooling hole. This ensured that the rough surface does not block the hole, and that the interaction between the rough surface and coolant jets is uniform for the entire endwall.

Experimental Methodology

The experimental facility included a test section placed in a wind tunnel, as shown in Fig. 4. The test section consisted of a vane scaled up by a factor of 9 with cooling holes and slot geometries. Adiabatic endwall temperature measurements were taken for different flow rates through film-cooling holes and through the slot representing the combustor turbine interface. For the present study, there was no flow through the midpassage gap at the interface of the vanes. This was primarily done to study the aerodynamic effect caused by the presence of the gap, and to simulate a perfectly sealed interface.

The test section was placed inside the closed-loop wind tunnel facility shown in Fig. 4, a detailed account of its construction has been previously described by Knost and Thole [12]. The difference in this test section from the one used by Knost and Thole is the presence of a rough endwall surface and the presence of a

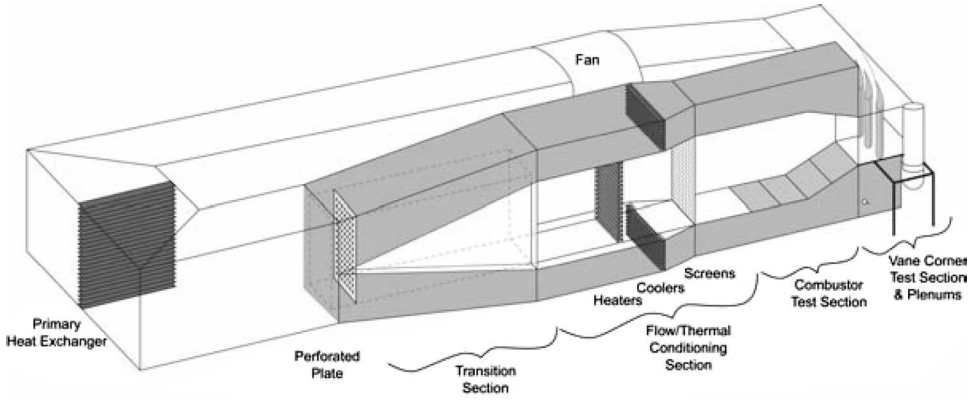

Fig. 4 Illustration of the wind tunnel facility

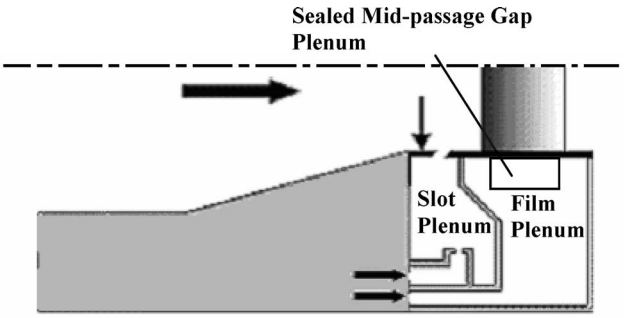

Fig. 5 Separate plenums for film cooling and upstream slot provided independent control of the flow through each of them

midpassage gap between the endwalls of the adjacent vanes. The flow in the wind tunnel is driven by a 50 hp axial vane fan, which is controlled by a variable frequency inverter. Downstream of the fan, the flow encounters a 90 deg turn and passes through a primary finned-tube heat exchanger used to cool the bulk flow. After the heat exchanger, the flow encounters a three-way flow split. Note that only the bottom channel was used for this study. This split was done to create a primary core flow and a cooled secondary flow. The primary core flow was made to pass through a heater bank consisting of three heaters where the air temperature was increased to 55°C. The secondary flow, in the outer channel, was made to pass through a secondary heat exchanger where the flow temperature was lowered to about 15°C. The secondary flow path represented the coolant flow through the film-cooling holes and the slots.

The test section consisted of two full passages with one center vane and two half vanes. It is important to note that film-cooling effectiveness studies were done only in the passage where the midpassage gap was simulated. The test section consisted of separate plenums for independent control of flow through the film-cooling holes and the upstream slot, as shown in Fig. 5. A temperature difference of about 40°C was maintained at all times between the mainstream and coolant flows under steady-state conditions.

Typical times to achieve steady state conditions were 3 h. The free-stream turbulence effects were not taken into consideration, as these studies were more focused on industrial gas turbines rather than on aero engines. Free-stream turbulence levels are generally higher for aero engines when compared to industrial gas turbines. The inlet turbulence effects and length scales were measured to be 1.3% and 4 cm, respectively. The endwall of the vane, which was the main focus of study, was constructed of foam because of its low thermal conductivity (0.033 W/m K). The endwall foam was 1.9 cm thick and was mounted on a 1.2 cm thick Lexan plate. The cooling hole pattern on the endwall was cut with a five-axis water jet to ensure precision and integrity. The upstream slot was constructed with hard wood, as it had a low conductivity and was stiffer.

Coolant Flow Settings. For every test condition the dimensionless pressure coefficient distribution was verified to ensure periodic flow through the passages. As stated earlier, two separate plenums were used to control the flow rate through the film-cooling holes and through the upstream slot. Friedrichs et al. [5] suggested that a global blowing ratio based on the inlet flow conditions could be characterized by the blowing ratio of a loss-free hole injecting into inlet conditions calculated from

$$M_{\text{ideal}} = \sqrt{\frac{\rho_c}{\rho_{\text{in}}} \frac{P_{o,c} - p_{s,\text{in}}}{P_{o,\text{in}} - p_{s,\text{in}}}} \tag{1}$$

A modification of this approach was done in this study, and a global discharge coefficient, C_D, was derived so that a cumulative flow rate through the film-cooling holes could be defined. These C_D values were obtained from computational fluid dynamics (CFD) studies done on a similar geometry, and were reported earlier by Knost and Thole [11]. Measurements of the inlet velocity, average inlet static pressure, and coolant total pressures were obtained which then allowed the fraction of coolant flow relative to the inlet core flow to be calculated from

$$\frac{\dot{m}_c}{\dot{m}_{\text{core}}} = M_{\text{ideal}} \cdot C_D \cdot \frac{A_{\text{hole}}}{A_{\text{in}}} \cdot \#\,\text{holes} \tag{2}$$

The upstream slot flow was assumed to have a discharge coefficient of 0.6, which is the assumed value for a flow through a sharp-edged orifice, and the flow rate was calculated accordingly. Table 3 gives a description of the actual and ideal global blowing ratios used for the different film-cooling and upstream slot mass flow rate settings.

Table 3 Summary of Coolant Settings

% Mass flow	C_D	M_{ideal}	M_{actual}
0.35 Film cooling	0.85	1.24	1.06
0.50 Film cooling	0.8	1.88	1.51
0.75 Film cooling	0.71	3.2	2.26
0.75 Upstream slot	0.6	0.48	0.29
0.95 Upstream slot	0.6	0.69	0.414
1.10 Upstream slot	0.6	0.72	0.43

Instrumentation and Temperature Measurements. An FLIR P20 infrared (IR) camera was used to capture the spatially resolved adiabatic wall temperatures on the endwall. Measurements were taken at seven different viewing locations to ensure that the entire endwall surface was mapped. The camera was placed perpendicular to the endwall surface at a distance of 55 cm. Each picture covers an area 24 by 18 cm, with the area being divided into 320 by 240 pixel locations. The spatial integration of the camera was 0.715 mm (0.16 hole diameters). Thermocouples were also placed on the endwall surface at different locations to directly measure the temperature to postcalibrate the infrared images. For the postcalibration the emissivity and background temperature were adjusted until the temperatures from the infrared camera images were within 1°C of the corresponding thermocouple data. Typical emissivity values and background temperatures were 0.92 and 45°C (note that the free-stream temperature was 55°C). Five images were taken at each of the viewing locations to obtain an averaged picture using an in-house MATLAB program. The same program was also used to assemble the averaged pictures at all locations to give a complete temperature distribution along the passage endwall.

Free-stream temperatures were measured at multiple locations along the pitch, and the average was determined by using a thermocouple rake consisting of three thermocouples along the span. It was found that the variations along the pitch were less than 0.2°C and those along the span were less than 1.5°C. Three thermocouples were attached in the upstream slot location at the combustor exit, and two thermocouples were attached in the film-cooling plenum. Eleven thermocouples were placed in the midpassage gap to measure the temperature profile along the gap. The thermocouples in the midpassage gap were placed 6 seal strip thicknesses beneath the surface, which was roughly one-third of the slot flow length beneath the surface (Table 2). Voltage outputs from the thermocouples were acquired by a 32-channel data acquisition module that was used with a 12-bit digitizing card. The temperature data were compiled after the system reached steady state.

An uncertainty analysis was performed on the measurements of adiabatic effectiveness using the partial derivative method described at length by Moffat [19]. The precision uncertainty was determined by taking the standard deviation of six measurement

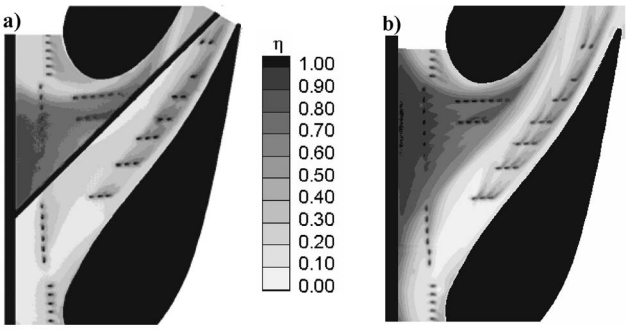

Fig. 6 Contours of adiabatic effectiveness for film-cooling cases (*a*) rough endwall with midpassage slot and (*b*) smooth endwall with no midpassage slot

sets of IR camera images, with each set consisting of five images. The precision uncertainty of the measurements was ±0.014°C. The bias uncertainty was ±1.0°C based on the calibration of the image. The bias uncertainty of the thermocouples was ±0.5°C. The total uncertainty was then calculated as ±1.0°C for the images and ±0.51°C for the thermocouples. Uncertainty in effectiveness, η, was found based on the partial derivative of η with respect to each temperature in the definition and the total uncertainty in the measurements. Uncertainties of $\partial\eta = \pm 0.082$ at $\eta = 0.2$ and $\partial\eta = \pm 0.029$ at $\eta = 0.9$ were calculated. A one-dimensional conduction analysis was performed at the entry and exit of the passage to calculate the conduction error. The resulting η correction was found to be 0.07 at the entrance and 0.02 at the exit region at a measured η value of 0.5.

Discussion of Results

As stated previously, all tests and data acquisition were completed for no flow through the midpassage gap. First, the effect of the presence of the midpassage gap and roughness will be discussed for an aligned endwall. The results from this test will be compared with an existing case having no midpassage gap. Second, a comparison of results obtained for aligned and misaligned midpassage gap will be discussed.

Film-Cooling Effectiveness With a Rough Endwall and a Midpassage Gap. The nominal film-cooling cases with and without a midpassage slot for 0.75% upstream slot flow and 0.5% film-cooling flow are shown in Figs. 6(*a*) and 6(*b*). Note that the percentages refer to the coolant flow relative to the hot gas path flow. There are two noticeable effects that can be determined by comparing these two cases that include the effect of the midpassage gap and the effect of roughness.

It can be seen from Fig. 6(*a*) that there is no coolant flow from the upstream slot crossing over the midpassage gap location. This condition becomes apparent when comparing the contours of Fig. 6(*a*) with those of Fig. 6(*b*) where, in the absence of the gap, the coolant from the upstream slot convects towards the suction side of the vane sweeping over a large area of the endwall. In the presence of the midpassage gap, Fig. 6(*a*) shows no coolant exiting the upstream slot on the pressure side of the midpassage gap. The reason for this lack of coolant is that the coolant from the upstream slot is ingested until the end of the vane passage where it then exits the gap. This effect will be discussed further in a later section of the paper. As a result of this degradation of the coolant on the pressure side of the midpassage gap, the hot streak through the center of the passage appears to be wider with the presence of a midpassage gap relative to the no-gap case. In determining the effect of roughness on the endwall film cooling, comparisons can also be made between Figs. 6(*a*) and 6(*b*).

Observing the coolant exiting from the leading edge holes upstream of the stagnation location on the suction side, one can see

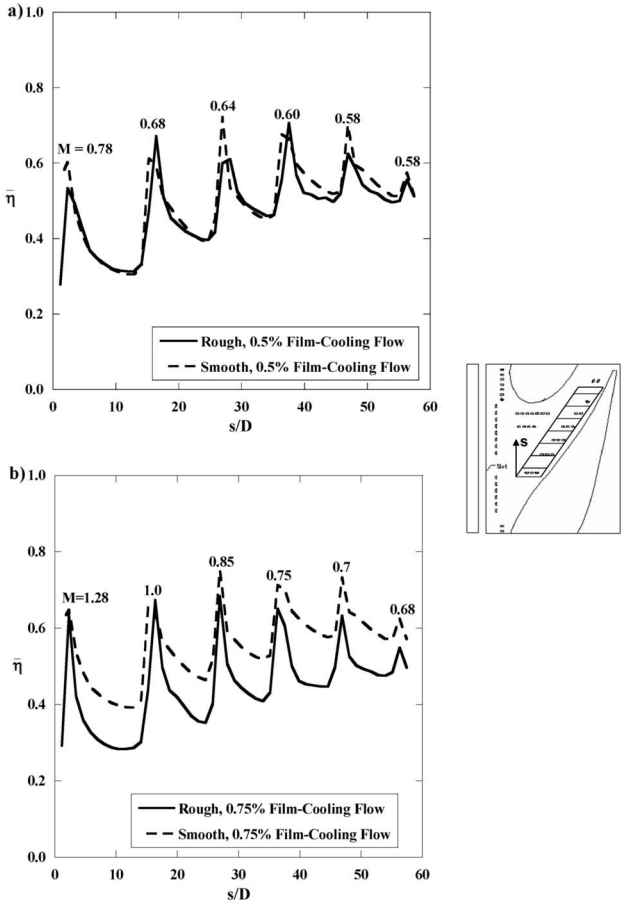

Fig. 7 Plots of laterally averaged adiabatic effectiveness on the film-cooling holes on the pressure side: (*a*) for 0.75% upstream slot flow and 0.5% film cooling and (*b*) 0.75% upstream slot flow and 0.75% film cooling

that the coolant is dispersed more rapidly for the case with the rough endwall relative to the smooth endwall. Along the pressure side, the jets merge more evenly in the case of the rough endwall relative to the smooth endwall, where in the case of the smooth endwall there are distinct jets.

To quantify the effects of roughness, a section of the endwall near the pressure side of the vane, as shown in Fig. 7, was further analyzed. Figures 7(*a*) and 7(*b*) show the effect of roughness on the laterally averaged effectiveness for 0.5% and 0.75% film-cooling flows, respectively. Also indicated in Fig. 7 are the row-averaged local blowing ratios for each row of holes along the pressure side. Note that CFD results were used to quantify the local coolant flows from each cooling hole, and the local static pressure was used to calculate the local free-stream velocity that was used in the blowing ratio definition. For the 0.5% case, where the local blowing ratios ranged from 0.58 to 0.78, the laterally averaged effectiveness values indicate that there is essentially no effect of roughness of the film-cooling performance. In looking at the contours in Figs. 6(*a*) and 6(*b*), however, there are some local differences indicated particularly with the jet merging.

For the higher coolant flow condition in Fig. 7(*b*), where the local blowing ratio ranges from 0.68 to 1.28, there is a dramatic decrease in the average effectiveness along the pressure side with roughness. The decrease in the laterally averaged effectiveness due to roughness is on the order of 30% midway between film-cooling rows. One plausible reason for the larger decrease at the higher blowing ratio relative to the lower blowing ratio is because for a rough wall the boundary layer is thicker, thereby allowing the jets to separate from the endwall. As the front jet separates

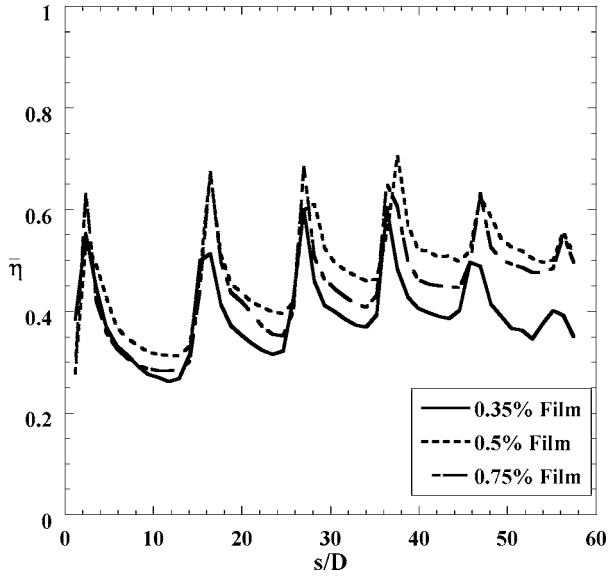

Fig. 8 Laterally averaged adiabatic effectiveness for 0.35%, 0. 5%, and 0.75% film-cooling flows for a rough endwall

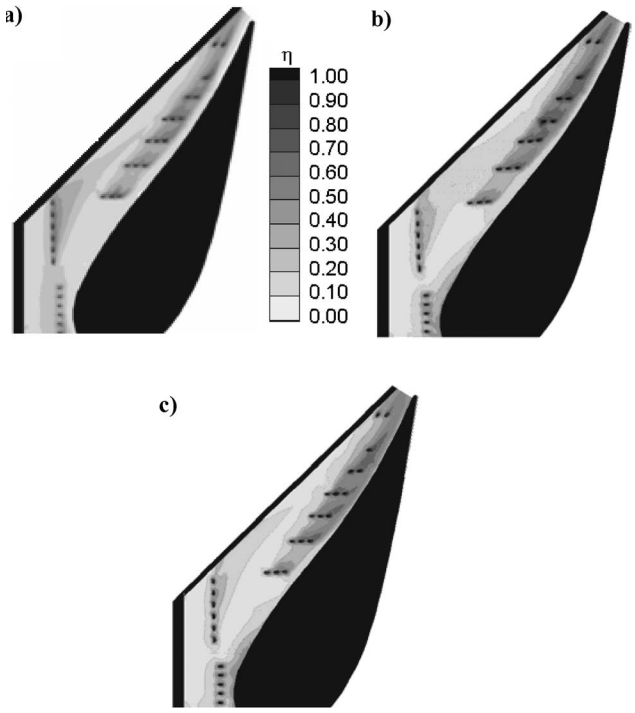

Fig. 9 Contours of adiabatic effectiveness with a rough endwall with 0.75% slot flow for (*a*) 0.35% film cooling; (*b*) 0.5% film cooling; (*c*) 0.75% film cooling

from the wall, this effect is compounded as one progresses downstream along the pressure side. This reduction in film-cooling effectiveness may also be attributed to increased interaction with hot mainstream. The rough surface greatly increases boundary layer thickness and turbulence levels, causing enhanced mixing between the coolant and mainstream and thereby lowering area-averaged values of adiabatic effectiveness.

In comparing Fig. 7(*a*) and Fig. 7(*b*), it is seen that there is a benefit in cooling when increasing the coolant flow from 0.5% to 0.75% for the smooth wall case. In contrast, when increasing the coolant flow for the rough wall case, the average adiabatic effectiveness levels actually decrease with an increase in blowing ratio. As such, Fig. 8 compares the laterally averaged effectiveness values for the rough endwall case along the pressure side holes for three different coolant flow rates: 0.35%, 0.5%, and 0.75%. The corresponding contours for these lateral averages just along the pressure side are shown in Figs. 9(*a*)–9(*c*). As is typically expected, by increasing the film-cooling flow from 0.35% to 0.5%, one sees that there is an increased gas performance in the film-cooling effectiveness levels. In comparing the contours shown in Figs. 9(*a*) and 9(*b*), it is clear that the first row of holes in the averaging area defined in Fig. 7 appears nearly the same between the two cases, but that cooling appears to be much better at the second row for the higher blowing ratio case.

By increasing the coolant flow to 0.75%, the laterally averaged effectiveness significantly decreases relative to the 0.5% coolant flow case but is better than the 0.35% coolant flow case, as shown in Fig. 8. The contours in Fig. 9(*c*) indicate better penetration towards the pressure side of the endwall for the 0.75% coolant flow case, but that the overall levels of effectiveness downstream of the film-cooling holes are significantly lower than for the 0.5% coolant flow case. These contours indicate that, as the jets penetrate closer to the pressure side surface, they are also lifted off the surface. Knost and Thole [11] observed a similar trend for the smooth wall case in that the pressure side film-cooling jets appeared to be lifted off the surface for the 0.75% coolant flow case, but as seen from Fig. 7(*b*) this effect is worsened with roughness.

Outside of the averaging area, at the most upstream row of film-cooling holes, the contours in Figs. 9(*a*)–9(*c*) indicate little change in effectiveness levels as a function of increased coolant levels. There was only slightly better performance for the 0.5% coolant flow condition relative to the 0.35% and 0.75% coolant flows. Just upstream of the stagnation location, the contours in Figs. 9(*a*)–9(*c*) indicate that, for the 0.5% and 0.75% coolant flow conditions, the leading-edge film-cooling jets are impacting the vane and then being washed back down onto the surface, indicating some coolant at the vane-endwall junction.

Effect of a Misaligned Midpassage Gap. One of the primary questions raised for this work was how to best design an endwall simulating the surface roughness and turbine vane misalignment. As was discussed previously, there is a possibility for an aligned endwall configuration, a cascade endwall configuration, and a dam endwall configuration. The misalignment value was set to 1.2% of the vane span. For these comparisons, both the film-cooling and upstream slot flows remained constant at 0.5% and 0.75% of the core flow, respectively. Figures 10(*a*)–10(*c*) correspond to aligned, dam, and cascade endwall configurations, respectively. Indicated on the vanes on these figures is the portion of the endwall that is raised (*U*) and lowered (*D*). For explanatory purposes, the section of endwall closest to the top vane picture is referred to as the suction side section, and the section of the endwall closest to the bottom vane will be referred to as the pressure side section.

In comparing the aligned case to the dam case, it can be seen that in the case of the dam the overall platform cooling is much worse than in the case of the aligned endwall. It appears that, because of the front slot misalignment, the leakage coolant from the upstream slot is directed into the hot gas path rather than along the endwall. It is also interesting to look at the end of the midpassage gap. Figure 10(*a*) for the aligned endwall indicates that at the midpassage gap exit, coolant exits the slot. This coolant was the upstream slot coolant and film coolant that was ingested into the slot and then exited at the lowest external static pressure location. In the case of the dam endwall, Fig. 10(*b*) indicates that there is no coolant exiting the end of the midpassage slot. It is also quite interesting to see the diminished effectiveness levels in the vicinity of the midpassage slot at about 20% of the slot length measured from the upstream slot shown in Fig. 10(*b*). This warmer region was also shown for aligned endwall in Fig. 10(*a*), but it is

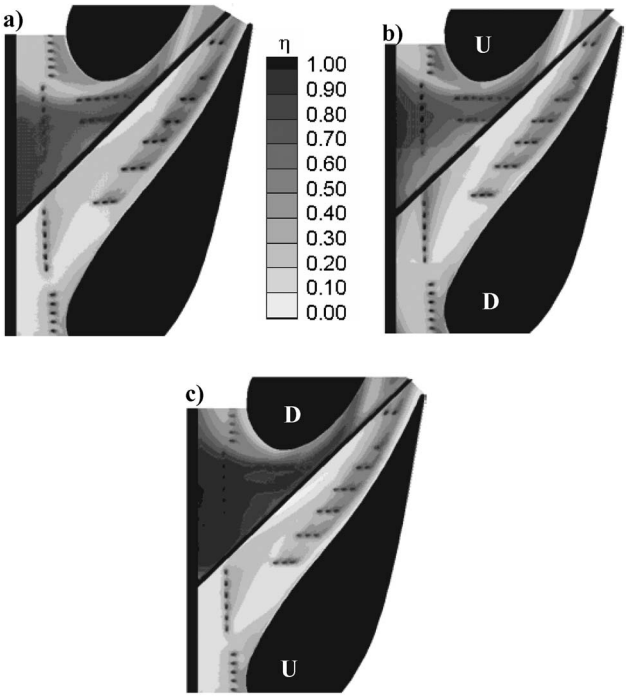

Fig. 10 Contours of adiabatic effectiveness on a rough endwall for the baseline film and slot cooling cases: (*a*) aligned, (*b*) dam, and (*c*) cascade endwall (note that *U* refers to raised side and *D* refers to lowered side)

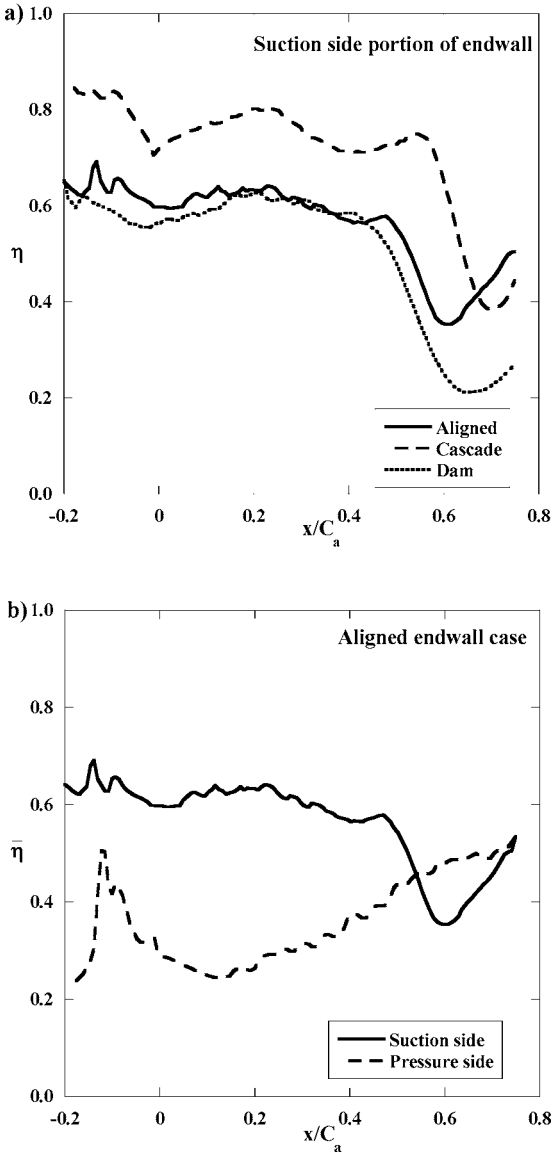

Fig. 11 Pitchwise-averaged adiabatic effectiveness for the baseline film and slot cooling cases: (*a*) along the suction side for the three endwall settings; (*b*) comparison between effectiveness on the suction and pressure side

not as dramatic. At this location, there is no upstream slot flow present, which was worsened for the dam configuration, nor is there any film-cooling flow present.

When the endwall surface is set to cascade configuration, coolant from the upstream slot can flow in an unobstructed manner onto the endwall. The effectiveness contours in Fig. 10(*c*) indicate a much improved performance for the cascade case relative to both the aligned and the dam configurations. The lowered endwall in the case of the cascade acts like a trough in which the upstream slot flow does not mix out as quickly with the mainstream hot gas. As a result, higher effectiveness values occur on the suction side portion of the endwall. For the cascade configuration, the pressure side contours are very similar to the aligned endwall configuration, because there is no blockage for the secondary flows, as compared with the dam case. At 20% slot length downstream from the upstream slot the warm region previously discussed is diminished for the cascade condition relative to both the dam and aligned cases.

Figure 11(*a*) compares the pitchwise-averaged effectiveness along the suction side of the endwall for the three endwall configurations, and Fig. 11(*b*) compares the effectiveness distribution along the suction and pressure sides for the aligned case. Figure 11(*a*) clearly substantiates the previous results that the cascade configuration results in better cooling along the suction side, and Fig. 11(*b*) strengthens the conclusion that there is better cooling on the suction side than on the pressure side for any kind of endwall configuration. It was also found that the pitchwise-averaged effectiveness on the pressure side for the three endwall settings remained the same. The area-averaged effectiveness was higher for the cascade configuration when compared to the aligned or dam. The area-averaged effectiveness levels, which include both the pressure and suction side portions of the endwall, were 0.49 for cascade, 0.45 for the aligned, and 0.42 for the dam, respectively.

As was previously discussed, the air temperature inside the gap was measured as indicated in Fig. 2. Recall that for the study reported in this paper there was no flow exiting the midpassage gap such that the temperatures measured were those of any flow that might ingest into the midpassage slot. The measured nondimensional gap temperatures for the aligned and misaligned cases are shown in Fig. 12. The nondimensionalization was based on the coolant temperature and hot gas free-stream temperatures. Also shown in Fig. 12 are the inviscid gap velocities that were calculated based on the local static pressure at the gap exit. Note that this inviscid analysis assumed a constant total pressure difference between the mainstream and the gap plenum. An iterative procedure was used to calculate the pressure difference which resulted in zero net mass flow from the slot (ingested flow balanced with exiting flow).

Figure 12 shows that, for the aligned and dam cases, a large amount of coolant is ingested into the leading edge of the midpassage gap region relative to the cascade case. In the location $0<x/L<0.2$ there is coolant ingestion from the upstream slot resulting in higher θ, with the amount of coolant being ingested decreasing with an increase in x/L. There is also increased ingestion of the mainstream flow, causing a rapid rise in the gap air

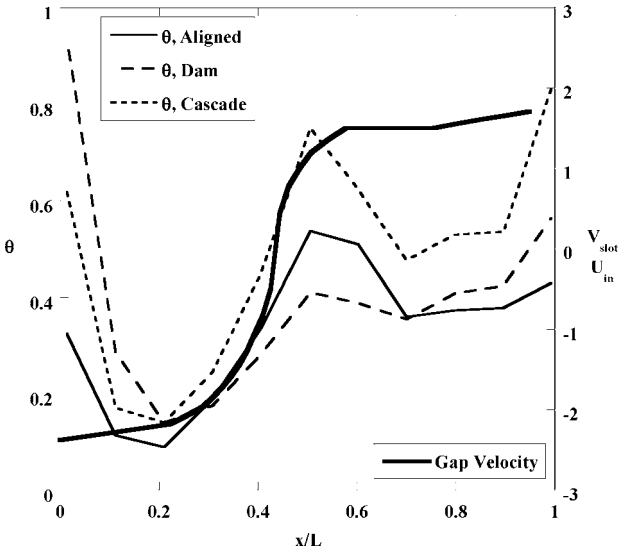

Fig. 12 Nondimensionalized gap temperature profiles for the three endwall alignment modes and the velocity profile for an aligned gap

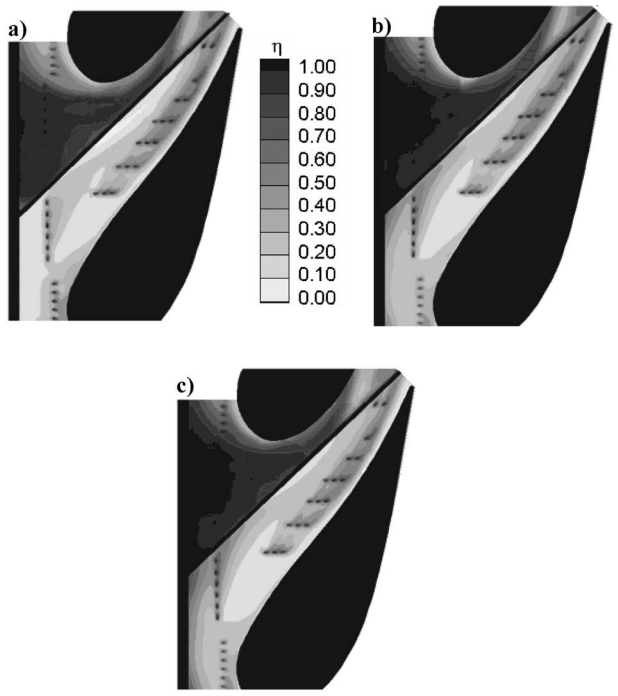

Fig. 13 Contours of adiabatic effectiveness on a rough endwall with cascade setting for different upstream slot flow rate with 0.5% film cooling: (*a*) 0.75% (*I*=0.08) slot flow; (*b*) 0.95% (*I*=0.12) slot flow; (*c*) 1.1% (*I*=0.16) slot flow

temperature and hence a decrease in θ. The nondimensional temperatures in the gap decrease dramatically as hot mainstream flow is ingested near $x/L=0.2$. For the midpassage gap location between $0.3<x/L<0.5$, all of the endwall cases show a decrease in the air temperature (increase in θ) along the midpassage gap, which results from a fresh influx of coolant from the two rows of film-cooling holes directly upstream of this region (see Figs. 10(*a*)–10(*c*)). The dam case benefits less because of the step, in conjunction with the cross-passage secondary flows that forces more hot flow into the gap. Figure 12 also shows that the temperatures inside the gap associated with the cascade endwall setting are cooler than that for the dam endwall setting, which is because of the cooler fluid from the upstream slot. Up to $x/L=0.5$, the inviscid velocity is indicated to be into the slot (static endwall pressure is higher than the plenum pressure), which is consistent with the fact that flow is ingesting into the slot.

Beyond $x/L=0.5$, Fig. 12 shows that flow exits the midpassage gap. Between $0.5<x/L<0.7$, there is an increase in the temperature within the midpassage gap, which is followed by a decrease beyond $x/L=0.9$. The slight increase at the exit results from any coolant that was channeled through the midpassage gap from the upstream slot.

Effect of Slot Flow with a Cascade Endwall. Because the best configuration appeared to be the cascade endwall, more studies were completed with this configuration whereby flow from the upstream slot was varied. As previously discussed, the coolant flow from upstream slot has little effect on the pressure side of the midpassage slot. Figure 13 compares adiabatic effectiveness contours for different slot flow rates (or different momentum flux ratios) with cascade endwall setting. The momentum flux ratios were calculated for all the flow rates through the slot using the relation

$$I = \frac{\rho_s u_s^2}{\rho_\infty U_\infty^2} = \frac{\rho_s (\dot{m}/\rho_s A_s)^2}{\rho_\infty U_\infty^2} \tag{3}$$

It can be seen in Fig. 13(*a*), that, for 0.75% slot flow, there is little cooling around the leading edge holes on the pressure side. With an increase in the slot flow rate, however, the adiabatic effectiveness near the upstream slot region increases, indicating some coolant exiting from the upstream slot onto the pressure side of the midpassage gap as seen in Fig. 13(*b*) and Fig. 13(*c*). It is also interesting that, as the upstream slot flow is increased, the warmer region is no longer present, which was shown at the 0.75% coolant flow condition about one-third of the way downstream of the midpassage slot. It is also interesting to note that the film-cooling holes on the pressure side of the midpassage gap showed better cooling as the slot flow was increased to 0.95% relative to 0.75%.

6 Conclusions

Measurements of endwall and midpassage gap adiabatic effectiveness were presented for an endwall surface with realistic features, namely a combustor-to-turbine interface gap, endwall film cooling, a vane-to-vane midpassage gap, a platform misalignment, and surface roughness. When compared to a smooth surface, it was observed that the effect of roughness could vary. For the higher blowing ratio, there was a definite decrease in adiabatic effectiveness due to roughness but, for the lower blowing ratio, there was essentially no difference in cooling. This difference was related to the boundary layer thickness, whereby a thicker boundary layer had a significant impact on the jet separation from the endwall in the case of a high blowing ratio.

The midpassage gap had a significant impact on the progression of the upstream coolant, whereby the gap limited the area of coverage for the upstream slot coolant flow. The cooling from the upstream slot had a beneficial effect only along the suction side surface of the vane. Measurements, along with an inviscid analysis, indicated that fluid from the platform was ingested into the midpassage gap. Near the start of the gap, most of the flow ingested was coolant, which rapidly decayed because of the hot gas ingested.

Platform misalignment proved to also have a substantial effect on endwall adiabatic effectiveness levels. Clearly, from a heat transfer standpoint, a cascade configuration would be the most desirable endwall alignment mode. The cascade setting showed considerably better adiabatic effectiveness levels relative to an aligned or dam endwall configuration, nearly removing the need for cooling holes on the suction side of the endwall. From a tur-

bine design standpoint, the cascade setting is ideal relative to a dam configuration, as the cascade acts like a trench where the coolant flow can reside.

This study has shown the drastic effects that realistic turbine features can have on first-stage nozzle platform cooling. Upstream slot flow and a cascade misalignment provide for better cooling on the endwall. Quite the opposite is the case for a misaligned dam, midpassage gap, and, in some cases, endwall surface roughness. These competing effects, when properly understood, can be used to better design endwall cooling arrangements.

Acknowledgment

This publication was prepared with the support of the U.S. Department of Energy, Office of Fossil Fuel, and National Energy Technology Laboratory. However, any opinions, findings, conclusions, or recommendations expressed herein are solely those of the authors and do not necessarily reflect the views of the DOE. The authors would also like to thank Mike Blair (Pratt & Whitney), Ron Bunker (General Electric), and John Weaver (Rolls-Royce) for their input on the modeling of realistic turbine features.

Nomenclature

C = true chord of stator vane
C_a = axial chord of stator vane
D = diameter of film cooling hole
I = momentum flux ratio
L = length of midpassage gap
$\dot{m}$ = mass flow rate
M = mass flux/blowing ratio
P = vane pitch; hole pitch
P_o or p = total and static pressures
$\mathrm{Re}_{\mathrm{in}}$ = Reynolds number defined as $\mathrm{Re}=CU_\infty/\nu$
s = distance along vane from flow stagnation
S = span of stator vane
T = temperature
x,y,z = local coordinates
u,v,w = local velocity components
U = velocity global
W = midpassage gap width

Greek Symbols

η = adiabatic effectiveness, $\eta=(T_\infty-T_{\mathrm{aw}})/(T_\infty-T_c)$
ρ = density
ν = kinematic viscosity
θ = nondimensionalized gap effectiveness, $\theta=(T_\infty-T_G)/(T_\infty-T_c)$

Subscripts

aw = adiabatic wall
c = coolant conditions
G = gap
in = inlet conditions
j = coolant flow through film-cooling holes
s = flow through upstream slot
∞ = free-stream conditions

References

[1] Blair, M. F., 1974, "An Experimental Study of Heat Transfer and Film-cooling on Large-Scale Turbine Endwall," ASME J. Heat Transfer, **96**, pp. 524–529.
[2] Burd, S. W., Satterness, C. J., and Simon, T. W., 2000, "Effects of Slot Bleed Injection Over a Contoured Endwall On Nozzle Guide Vane Cooling Performance: Part II—Thermal Measurements," ASME Paper No. 2000-GT-200.
[3] Colban, W. F., Thole, K. A., and Zess, G., 2002, "Combustor-Turbine Interface Studies: Part 1: Endwall Measurements," ASME J. Turbomach., **125**, pp. 193–202.
[4] Colban, W. F., Lethander, A. T., Thole, K. A., and Zess, G., 2002, "Combustor-Turbine Interface Studies: Part 2: Flow and Thermal Field Measurements," ASME J. Turbomach., **125**, pp. 203–209.
[5] Friedrichs, S., Hodson, H. P., and Dawes, W. N., 1996, "Distribution of Film-Cooling Effectiveness on a Turbine Endwall Measured Using the Ammonia and Diazo Technique," ASME J. Turbomach., **118**, pp. 613–621.
[6] Friedrichs, S., Hodson, H. P., and Dawes, W. N., 1997, "Aerodynamic Aspects of Endwall Film-Cooling," ASME J. Turbomach., **119**, pp. 786–793.
[7] Friedrichs, S., Hodson, H. P., and Dawes, W. N., 1999, "The Design of an Improved Endwall Film-Cooling Configuration," ASME J. Turbomach., **121**, pp. 772–780.
[8] Zhang, L. J., and Jaiswal, R. S., 2001, "Turbine Nozzle Endwall Film-cooling Study Using Pressure Sensitive Paint," ASME J. Turbomach., **123**, pp. 730–738.
[9] Kost, F., and Nicklas, M., 2001, "Film-Cooled Turbine Endwall in a Transonic Flow Field: Part I-Aerodynamic Measurements," ASME Paper No. 2001-GT-0145.
[10] Nicklas, M., 2001, "Film-Cooled Turbine Endwall in a Transonic Flow Field: Part II-Heat Transfer and Film-Cooling Effectiveness," ASME J. Turbomach., **123**, pp. 720–729.
[11] Knost, D. G., and Thole, K. A., 2003, "Computational Predictions of Endwall Film-Cooling for a First Stage Vane," ASME Paper No. GT2003-38252.
[12] Knost, D. G., and Thole, K. A., "Adiabatic Effectiveness Measurements of Endwall Film-Cooling for a First Stage Vane," ASME Paper No. GT2004–52236.
[13] Yu, Y., and Chyu, M. K., 1998, "Influence of Gap Leakage Downstream of the Injection Holes on Film-cooling Performance," ASME J. Turbomach., **120**, pp. 541–548.
[14] Aunapu, N. V., Volino, R. J., Flack, K. A., and Stoddard, R. M., 2000, "Secondary Flow Measurements in a Turbine Passage with Endwall Flow Modification," ASME J. Turbomach., **122**, pp. 651–658.
[15] Ranson, W., Thole, K. A., and Cunha, F., 2004, "Adiabatic Effectiveness Measurements and Predictions of Leakage Flows Along a Blade Endwall," IMECE2004–62021.
[16] Yamao, H., Aoki, K., Takeishi, K., and Takeda, K., 1987, "An Experimental Study for Endwall Cooling Design of Turbine Vanes," IGTC-1987, Tokyo, Japan.
[17] Bons, J. P., Taylor, R. P., McClain, S. T., and Rivir, R. B., 2001, "The Many Faces of Turbine Surface Roughness," ASME Paper No. 2001-GT-0163.
[18] Bogard, D. G., Schmidt, D. L., and Tabbita, M., 1998, "Characterization and Laboratory Simulation of Turbine Airfoil Surface Roughness and Associated Heat Transfer," ASME J. Turbomach., **120**, pp. 337–342.
[19] Moffat, R. J., "Describing the Uncertainties in Experimental Results," Exp. Therm. Fluid Sci., **1**, pp. 3–17.

Turbulent Transport in Pin Fin Arrays: Experimental Data and Predictions

F. E. Ames
Mechanical Engineering Department,
University of North Dakota,
Grand Forks, ND 98202
e-mail: forest_ames@mail.und.nodak.edu

L. A. Dvorak
Sandia National Laboratories,
P.O. Box 5800, MS 776,
Albuquerque, NM 87185

The objective of this research has been to experimentally investigate the fluid dynamics of pin fin arrays in order to clarify the physics of heat transfer enhancement and uncover problems in conventional turbulence models. The fluid dynamics of a staggered pin fin array has been studied using hot wire anemometry with both single- and x-wire probes at array Reynolds numbers of 3000, 10,000, and 30,000. Velocity distributions off the endwall and pin surface have been acquired and analyzed to investigate turbulent transport in pin fin arrays. Well resolved 3D calculations have been performed using a commercial code with conventional two-equation turbulence models. Predictive comparisons have been made with fluid dynamic data. In early rows where turbulence is low, the strength of shedding increases dramatically with increasing Reynolds numbers. The laminar velocity profiles off the surface of pins show evidence of unsteady separation in early rows. In row three and beyond, laminar boundary layers off pins are quite similar. Velocity profiles off endwalls are strongly affected by the proximity of pins and turbulent transport. At the low Reynolds numbers, the turbulent transport and acceleration keep boundary layers thin. Endwall boundary layers at higher Reynolds numbers exhibit very high levels of skin friction enhancement. Well-resolved 3D steady calculations were made with several two-equation turbulence models and compared with experimental fluid mechanic and heat transfer data. The quality of the predictive comparison was substantially affected by the turbulence model and near-wall methodology. [DOI: 10.1115/1.2098792]

Introduction

Pin fin arrays are common cooling features used in turbine vanes and blades. Flow in pin fin arrays is complex. The flow on the endwalls forms horseshoe vortices as flow approaches the stagnation region of the cylinder. In the midpassage flow stagnates on the pins, then accelerates over the surface before separating. The resulting shedding caused by unsteady separation is a significant driver of heat transfer on the backside of the pins. In the first few rows high levels of turbulence are produced as spanwise velocity gradients mix out in the wakes of the pins. The intense turbulence levels have a large effect on transport rates and the flow through the downstream pin rows. Considering the multifaceted nature of the flow, it is not surprising that gas turbine designers are constrained to use empirical correlations to estimate heat transfer rates and pressure drop in pin fin arrays. The overall focus of the present research is to comprehensively investigate turbulent transport in pin fin arrays. The present paper presents single-wire and x-wire measurements acquired within a pin fin array to examine the flow features and investigate aspects of turbulent transport. This research is expected to better clarify the flow physics of pin fin arrays and help lead to the development of more physically based turbulence models for internal flows.

Background

Research related to the present study on turbulent transport in pin fin arrays includes turbulence measurements made within arrays, local heat transfer measurements made on pins within arrays, research on the influence of shedding on backside heat transfer, research on the response of turbulence near surfaces, and research documenting average array heat transfer and pressure drop. This paper documents research in the area of turbulent transport in pin fin arrays. This current work is a portion of an ongoing study on the physics of heat transfer in pin fin arrays.

Turbulence Measurements. Metzger and Haley [1] acquired turbulence intensity measurements in a large-scale facility with a 5.08 cm diameter pin for two staggered arrays, both with spacings $S/D=2.19$ and $H/D=0.875$. One array had an axial spacing of $X/D=1.32$ and the other array had an axial spacing of $X/D=2.19$. The measurements were acquired 4.06 cm upstream of the pins at midspan in the passage. The turbulence intensity in both cases peaked at row 3 and decayed downstream to levels of 27% for an X/D of 1.32 and 18% for an X/D of 2.19. They suggested this upstream rise in turbulence was responsible for the higher heat transfer levels, which have been documented in the forward portion of a staggered array. Van Fossen and Simoneau [2] used a hot film probe to acquire local turbulence intensity measurements in between pin rows in a staggered array with an X/D and S/D of 2.67 and with an H/D of 3.0. They acquired turbulence intensity levels at array Reynolds numbers of 10,000, 50,000, and 118,000. Generally, they found that turbulence intensity increased until two or three rows were upstream of the measurement point, and then decreased. For three rows upstream they found that turbulence levels decreased with increasing Reynolds number. Ames, Dvorak, and Morrow [3] acquired turbulence measurements in the pin fin array described in this paper. They documented turbulence levels, velocities, turbulent scales, and dissipation rates between adjacent pins in an 8-row staggered array for array Reynolds numbers of 3000, 10,000, and 30,000. Similar to Metzger and Haley, and Van Fossen and Simoneau, they found turbulence levels peaked with two or three rows upstream from the measurement point for the highest two Reynolds numbers but had a more gradual rise for the lowest Reynolds number. In the downstream rows, similar to Van Fossen and Simoneau, they found turbulence levels for the 3000 and 10,000 Reynolds number were higher than the 30,000 Reynolds number case.

Contributed by the International Gas Turbine Institute (IGTI) of ASME for publication in the JOURNAL OF TURBOMACHINERY. Manuscript received October 1, 2004; final manuscript received February 1, 2005. IGTI Review Chair: K. C. Hall. Paper presented at the ASME Turbo Expo 2005: Land, Sea and Air, Reno, NV, June 6–9, 2005, Paper No. GT2005-68180.

Local Heat Transfer Measurements. (Pin midline) Metzger and Haley [1] acquired midline heat transfer distributions in a staggered pin fin array, described above, with an axial spacing of $X/D=1.32$. They found the relative level of backside heat transfer increased substantially with Reynolds number. They also found much higher heat transfer on the front half of the pin in rows 3 and beyond at an array Reynolds number of 52,800. Additionally, they reported that average heat transfer from pins increased with reduced axial spacing. Baughn and Saniei [4] acquired local heat transfer measurements in rows 1 through 3 in a staggered array with an X/D, S/D, and H/D of 2 at an array Reynolds number of 23,000. They found heat transfer increased with row position but only a small influence between rows 1 and 2. Ames, Dvorak, and Morrow [3] acquired pin midline heat transfer and static pressure measurements in the facility described in this paper. They were able to correlate stagnation region heat transfer for the pins in terms of $\mathrm{Nu}/\mathrm{Re}_{D_{\mathrm{eff}}}^{1/2}$ versus the TRL parameter of Ames and Moffat [5]. They found significant levels of turbulent augmentation at higher Reynolds numbers, but suggested that heat transfer increases in the array were also driven by an increase in the effective approach velocity, $V_{\max}$, due to the blockage caused by flow around pins and their wakes.

Cylinders in Cross Flow. Zukauskas and Ziugzda [6] report the impact of shedding on backside heat transfer to a cylinder in cross flow when measurements were acquired with and without a splitter plate. The splitter plate inhibited shedding and resulted in reduced backside heat transfer levels. The splitter plate had little influence on cylinder front side heat transfer. Ames and Moffat [5] also measured local cylinder heat transfer with and without a splitter, finding similar results. They found backside heat transfer increased with increasing Reynolds number from diameter Reynolds numbers of 4000 through 68,000. The splitter plate had a large effect at reducing backside heat transfer for 68,000 Reynolds number and none at a Reynolds number of 4000.

Attenuation of the Normal Component of Turbulence. Hunt and Graham [7] used rapid distortion theory to predict the influence of the wall-blocking effect on the wall-normal component of turbulence. They predicted the integral scale of v' was proportional to Y, and found v'^2 decreased as $Y^{2/3}$ in the near-wall region. Thomas and Hancock [8] developed a shear-free turbulence layer using grid-generated turbulence near a moving wall. They found that that lateral integral scale was proportional to the distance from the wall. They also noticed that low wave number v' power spectra were attenuated as the surface was approached, which explained the decrease in v' as the wall was approached. Ames and Moffat [5] measured v'^2 distributions outside a boundary layer subjected to high-intensity large-scale turbulence. They found that v'^2 was blocked by the presence of the wall outside the boundary layer and through it until near-wall production of turbulence began to become significant. They developed an empirical fit suggesting $v'^2/v_\infty'^2=(1-\exp[-2.9y/Lu])^{2/3}$ that correlated their data well.

Average Array Heat Transfer and Pressure Drop. Armstrong and Winstanley [9] review staggered array pin fin heat transfer and pressure drop data. They recommend Jacob's [10] long tube correlation, as well as Metzger's et al. [11] low and high Reynolds number correlations to predict flow friction factor across pin fin arrays. For array average Nusselt number, Armstrong and Winstanley recommend Metzger's et al. [12] correlation. More recently, Chyu et al. [13] determined array-averaged heat transfer using a naphthalene sublimation technique, and found a lower dependence on Reynolds number, 0.583 versus 0.685, which they attributed to a difference in the thermal boundary condition.

This paper presents a significant extension to previous turbulence measurements documenting all three components of turbulence and cross-span shear stress. Additionally, this paper develops a link between the measured intensity of shedding and backside heat transfer levels for early rows in pin arrays. Data also show how the normal component of turbulence is blocked by the endwall and pin's presence. In addition, numerical predictions are presented for pin heat transfer, pressure distributions, and array average heat transfer and pressure drop.

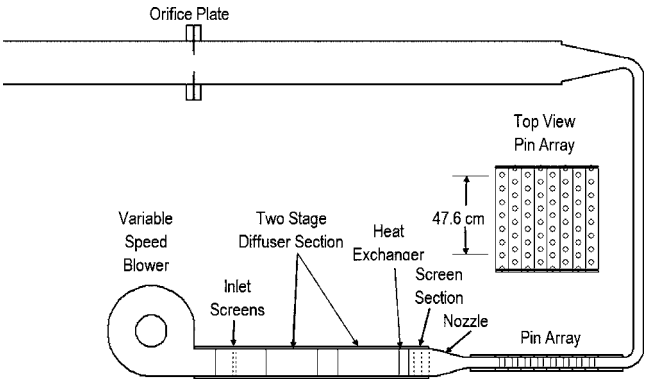

Fig. 1 Internal heat transfer and flow facility showing staggered pin fin array test section

Experimental Approach

Facility. This fluid dynamic investigation has been conducted in an internal flow facility designed to investigate the heat transfer and fluid dynamics of pin fin arrays. The wind tunnel, shown schematically in Fig. 1, is powered by a 2 kW blower controlled by a variable frequency drive. The blower is capable of moving 0.3 m^3/s of air at a static pressure rise of 2000 Pa. A high-efficiency filter is connected to the inlet of the blower to help eliminate dust particles which could foul hot wires. Flow at the exit of the blower is spread out and slowed using a two-stage multivane diffuser. The diffuser attaches to a heat exchanger with a recirculation system designed to control air temperatures for more accurate hot wire and heat transfer measurements. Next, a flow conditioning section connects the heat exchanger to the nozzle and uses three nylon screens to reduce velocity variations entering the nozzle. Finally, the nozzle takes a smooth 2.5 to 1 area ratio contraction into the pin fin test section.

The pin fin test section consists of eight staggered rows of seven and a half 2.54 cm diameter pins. The streamwise (X/D) and spanwise (S/D) spacing in the array are both 2.5 diameters, while the channel height to diameter ratio (H/D) is 2.0. Inlet static pressure, total pressure, and total temperature are monitored 5 diameters upstream from the streamwise centerline of the first row of pins. Five exit static pressures, spaced across 1 spanwise spacing, are monitored 5 diameters downstream from the last row of pins. The test section used for fluid dynamic measurements was fabricated from 1.2 cm acrylic sheets, used for the endwalls, and 2.54 cm diameter acrylic rod used for the pins. Slots were machined across 1 pin span at each row to allow acquisition of hot wire surveys in the region in between pins at the axial centerline.

The array Reynolds number was determined by measuring the test section flow rate using an orifice tube (see Miller [14]). Downstream from the test section the flow is directed through a rectangular channel connected to the test section and the orifice tube through two 90 deg rectangular turns. The hot wire data were acquired at array Reynolds numbers ($\mathrm{Re}_{D_{\max}}$) of 3000, 10,000, and 30,000 based on pin diameter and the average velocity ($V_{\max}$) in the area between adjacent pins. Array Reynolds number and flow friction factor (f), a dimensionless pressure drop parameter, were monitored for each hot wire survey.

Hot Wire Anemometry. Both single- and x-wire probes were powered using a TSI IFA 300 constant temperature anemometry (CTA) unit. A single-wire probe (Dantek 55P14) oriented in the z

direction was used to measure distributions of streamwise velocity in the normal direction off the endwall and to acquire velocity time records used to calculate spectra. A single-wire probe (Dantek 55P13) oriented in the y direction was used to acquire distributions of streamwise velocity in the spanwise direction off the pin surface. An x-wire probe (Dantek 55P63) with wires lying on the x-y plane was used to acquire instantaneous U and V velocity components off the endwall surface, and an x-wire probe (Dantek 55P64) with wires lying in the x-z plane was used to acquire instantaneous U and W velocity components off the pin. Here, the x direction is streamwise, the y direction is normal and upward from the bottom endwall, and the z direction is spanwise in the direction away from the pin surface. The U, V, and W velocity components are in the x, y, and z directions respectively.

Hotwire output voltages from the CTA were offset and amplified to maximize the resolution of the 12-bit data acquisition board used to sample the signals; x-wire signals were sampled simultaneously to provide instantaneous velocity vectors. Each hot wire was calibrated using both the high- and low-velocity calibration jet to allow calibrations from 0.4 to 40 m/s. The high-velocity jet calculated velocity based on the total to static pressure difference and had a useful range from 2.4 m/s to in excess of 40 m/s. The low end of the high-velocity jet was limited by the accuracy of the low-range Rosemount pressure transmitter, which had a full-scale output of 125 Pa and a reported accuracy of 0.1% of full scale. The low-speed jet used a 0.635 cm diameter nozzle to determine the mass flow rate through the larger jet (2.04 cm diameter). The exit velocity of the larger jet was determined based on continuity while accounting for boundary layer growth, and was typically varied from 0.4 to 4 m/s.

Hot wires were fit to a fourth-order polynomial assuming wire Reynolds number was a function of voltage. Voltages were compensated for changes in wire to air temperature differences and property variations. Posing the velocity in terms of the wire Reynolds number allowed compensation for ambient pressure variations. For a more complete discussion of the calibration technique, see Dvorak [15].

Streamwise and lateral velocities were determined for the x-wire using Jorgensen's decomposition [16]. Average velocities were determined based on the average of 8192 samples spaced in time at two to three integral time scales to ensure independent samples. Power spectra for instantaneous velocities were calculated from 40 records of 8192 samples sampled at 5, 15, and 40 kHz for the 3000, 10,000, and 30,000 Reynolds number cases. The autocorrelation in time was determined from the inverse fast Fourier transform (FFT) of the averaged power spectrum. The integral time scale was determined from the autocorrelation's integration to the first zero crossing. The integral length scale was calculated, assuming Taylor's hypothesis was valid, by multiplying the integral time scale by the local convective velocity. The energy scale ($Lu=1.5|u'|^3/\varepsilon$) was estimated using the dissipation rate (ε) determined from the power spectrum. The dissipation was calculated from a fit to the spectrum function assuming in the initial subrange that [Hinze, Eq. (3-152a)] [17]

$$E_1(k_1) = \frac{18}{55} A \varepsilon^{2/3} k_1^{-5/3} \tag{1}$$

taking A as 1.62 after Ames and Moffat [5]. Lateral components were assumed to be equal to four-thirds of $E_1(k_1)$ in the inertial subrange.

Pin Pressure Distributions. Pin midline surface pressure distributions were acquired using 20 static pressure taps equally spaced around the surface of the pin. Pressure coefficients were determined at 6 deg increments by rotating the pin.

Midline Heat Transfer Distributions. Pin midline heat transfer distributions were acquired using a combination of 24 fine-wire thermocouples and a constant heat flux foil technique. The type K thermocouples were used to determine surface temperature and to provide the boundary condition for the finite difference conduction analysis through the epoxy pin. The net surface heat flux was calculated from the heat flux dissipated in the foil plus the local conduction to the surface less the radiative heat transfer losses. A more detailed description of the surface heat transfer measurements is given in Ames, Dvorak, and Morrow [3].

Data Acquisition. The PC-based data acquisition system was used to acquire hot-wire, pressure, voltage, and temperature measurements and to control the lead screw drive tables and TSI IFA 300 CTA. Voltages from pressure transmitters, heaters, and thermocouples were read using an HP 3497A data acquisition unit which has an integral voltmeter with 1 μV sensitivity. Thermocouples voltages were acquired with the use of a passive constant temperature junction referenced to an ice bath. Pressures were acquired with the use of a custom-built pressure scanner, which used two Rosemount smart pressure transmitters in parallel and can scan 44 low-pressure ports and 4 high-pressure ports. The two pressure transmitters had full scale ranges of 125 and 1250 Pa with a full scale accuracy ±0.1%. The most sensitive reading was used for the measurement. Hot-wire measurements were acquired using a 12-bit data acquisition board with simultaneous sample and hold. The internal offset and amplification capabilities of the TSI IFA 300 were set to use the full resolution of the data acquisition board.

Data Uncertainties. Possible errors in the reported values of velocity, turbulence intensity, turbulent scale, Reynolds number, pressure coefficient, and Nusselt number were estimated using the root sum square method described by Moffat [18]. Uncertainties in the measurement of velocity using hot wire anemometry were estimated to be 3% for low turbulence situations. However, uncertainties in the very near-wall region could be much larger due to conduction effects and uncertainty in the wire location. At higher intensities Hinze [17] [Eq. (2-46a)] suggests that

$$\bar{U}_{\text{eff}} = \bar{U}\left[1 + \frac{\overline{v'^2}}{2\bar{U}^2} - \frac{\overline{u'v'^2}}{2\bar{U}^3} + \cdots\right] \tag{2}$$

where $\overline{v'^2}$ should be taken as $\overline{v'^2}$ for the normal traverses and $\overline{w'^2}$ for the spanwise traverses. The maximum turbulence intensity ranged to 22% in terms of $\overline{v'^2}$ and 32% in terms of $\overline{w'^2}$. This suggests an overestimation of U of up to 2% for normal single-wire traverses and up to 4% for spanwise single-wire traverses. The uncertainty in turbulence intensity was estimated to be approximately 3%. The experimental uncertainty in the determination of turbulence energy scale and integral scale was estimated to be ±13%. The uncertainty in Reynolds number was approximately 3%, primarily due to the uncertainty of the mass flow measurement. The absolute uncertainty in the pressure coefficient was as high ±0.12 for the lowest Reynolds number when uncertainties in the hole location are included and ±0.07 for the 10,000 and 30,000 Reynolds number cases. Finally, the worst case uncertainty in the heat transfer rates, reported as $\text{Nu}/\text{Re}_D^{1/2}$ is 6% at the lowest Reynolds number. Uncertainty estimates were assessed using a 95% uncertainty interval.

Analytical Approach

A well-resolved 3D CFD model of the pin fin array was developed to conduct analytical predictions of heat transfer and pressure drop through the current pin fin channel. The half-height half-pitch model had symmetry conditions at midspan and along even and odd row pin centerlines. The model was constructed with 163,000 hexahedral cells and was checked for grid independence with a significantly denser model. The steady segregated implicit method was selected as the solver, while the standard, realizable, and RNG k-ε models were all used as the turbulence closure models. Second-order upwind discretization schemes were chosen to solve the momentum, energy, kinetic energy, and dissi-

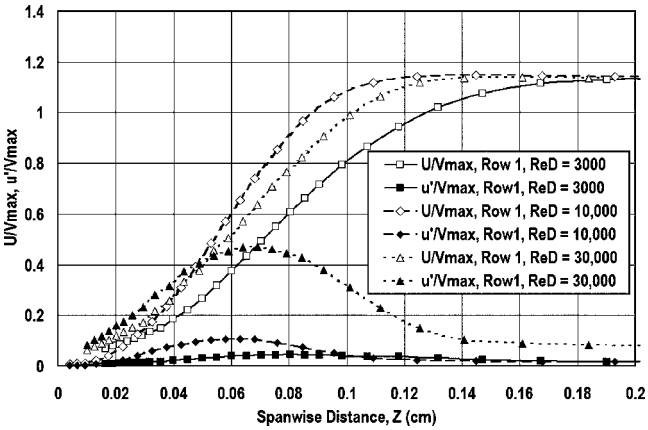

Fig. 2 Near-pin velocity and u' distributions off row 1 pin at 90 deg, normalized by V_{max}

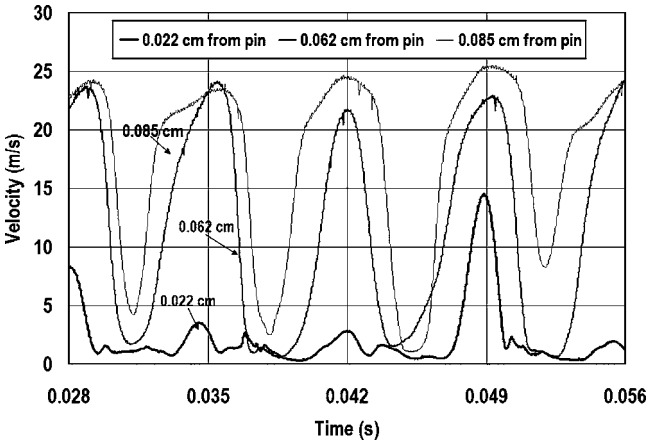

Fig. 3 Time-dependent near-pin velocity off row 1 pin, $Re_{D_{max}}$ =30,000, V_{max}=18.98 m/s

pation equations and the SIMPLE (semi-implicit method for pressure-linked equations) was chosen for pressure-velocity coupling. The PRESTO scheme was selected as the discretization scheme for pressure. All three GUI k-ε models in the commercial CFD program (FLUENT [19]) use the Wolfstein [20] one-equation turbulence model for the near-wall treatment. In the Wolfstein model, the k equation is retained. However, the eddy viscosity is calculated based on a mixing length approach, using an algebraic equation for mixing length.

Experimental Results

Hot-wire velocity traverses were acquired in the plane generated by the centerlines of two adjacent pins. Near-wall velocity distributions were acquired using single wires in the near-pin and near-endwall region to detail the condition of the pin and endwall boundary layers, and to clarify the near-wall mixing in the regions. Single-wire surveys also documented the velocity and u' distributions in the cross-span and normal directions. Streamwise velocity spectra were acquired to document the midpassage energy (Lu) and integral (Lx) scales of turbulence and the turbulent dissipation rate. Streamwise velocity spectra were also acquired in the near-pin region to characterize the shedding which occurred off pins. Spanwise surveys of instantaneous U and W were also acquired to document the streamwise and spanwise turbulent components and the turbulent shear stress in the cross-passage direction. Normal surveys of instantaneous U and V were acquired off the endwall to document streamwise and normal turbulence components and the turbulent shear stress. Velocity spectra were also acquired off the pin and off the endwall to look at the wall blocking effect of the pin and the endwall on the surface normal turbulent spectra approaching the surface. Finally, a few pin midline heat transfer and pressure coefficient distributions are reported with CFD predictions to highlight specific aspects of shedding and separation and difficulties with predictive models.

Near-Pin Velocity Distributions and Shedding, Row 1. Near-surface velocity distributions were acquired near pins to investigate the state of boundary layer in that region. Figure 2 presents near-pin surface velocity and u' distributions, normalized by V_{max}, taken at the pin midline, 90 deg from the stagnation line. In the very near-surface region all velocity profiles show near-wall inflections indicating separated flow. The 30,000 Reynolds number shows very high levels of u' due to strong shedding and intermittent separation. The 3000 Reynolds number case shows the shallowest velocity-gradients, expected due to viscous effects. However, the velocity gradient of the 30,000 Reynolds number is not as steep as the 10,000 Reynolds numbers due to the influence of shedding. Additionally, below 0.05 cm, u' is higher than U for the 30,000 Reynolds number, indicating a very unusual velocity-time record.

Time-dependent velocities are shown in Fig. 3 at three normal distances from the pin surface taken for the 30,000 Reynolds number case where V_{max}=18.98 m/s. At 0.085 cm the mean velocity is 16.4 m/s, but excursions range from above 26 m/s to below 1 m/s. The calculated turbulence intensity is 49%. These large periodic excursions in velocity result from the shedding caused by the flow instability around the cylinder. These periodic excursions are spaced at roughly 7 ms, suggesting a Strouhal number (Sh) of about 0.209 based on V_{max}. As we approach the surface to 0.062 cm, the periodicity and size of the velocity excursions are similar to the 0.085 cm profile, but the duration of the high velocity excursion is smaller and the peak is slightly lower. The duration and character of the low-velocity excursion suggests separated flow, noting the hot wire is largely sensitive to the magnitude of the wire normal fluctuation but not the direction. Here, the calculated mean velocity is 11.45 m/s and the turbulence intensity is calculated at 77.6%. At the closest near wall the profile indicates the flow is likely separated most of the time with weak positive velocities for small portion of the shedding cycle. Here, the calculated mean velocity is 2.17 m/s and the calculated turbulence intensity is 128%. Clearly, due to separated flow and the rectifying nature of the hot wire, these very near-surface values only provide a rough indication of streamwise velocity and u'.

Representative time-dependent near-pin velocities are shown for the three Reynolds numbers off a row 1 pin in Fig. 4. The velocities are presented in terms of $U(t)/V_{max}$ versus time $\times V_{max}/D$ to normalize velocity and time to allow direct comparisons between the three Reynolds numbers. The most distinguishing feature of the comparison is the intensity of the velocity excursions. The intensity of the shedding is shown to be strongly Reynolds number dependent. The relative size of the velocity excursions is much smaller for the two lower Reynolds numbers. Additionally, the shedding period appears a bit shorter for the lower Reynolds number cases.

Near-Pin Power Spectra, Row 1. One-dimensional power spectra for u' were acquired and calculated in the near-surface region of pin 1 to show the peak shedding frequencies. These spectra are presented in Fig. 5 as a function of wave number. The spectra indicate a definitive shedding frequency in addition to one or two secondary frequencies. The primary frequencies are reported in Table 1 along with a Strouhal number based on V_{max}. The Strouhal numbers were 0.231, 0.234, and 0.209 for the 3000, 10,000, and 30,000 Reynolds numbers, respectively. These values are near the typical 0.21 value reported for cylinders for subcriti-

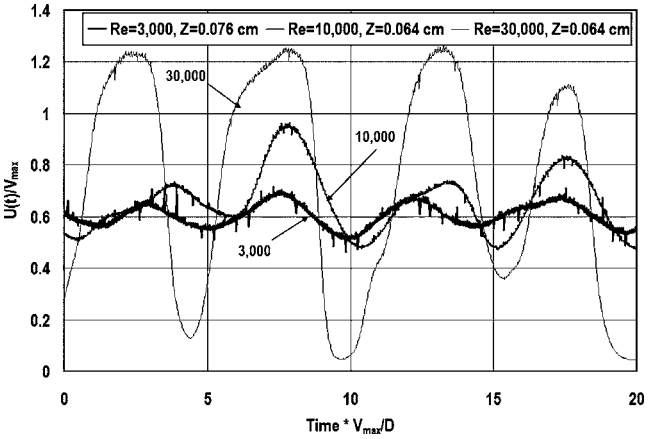

Fig. 4 Near-pin velocity normalized on V_{max} versus time normalized on D/V_{max}, pin 1, 90 deg, $Re_{D_{max}}$=30,000, 10,000, and 3000

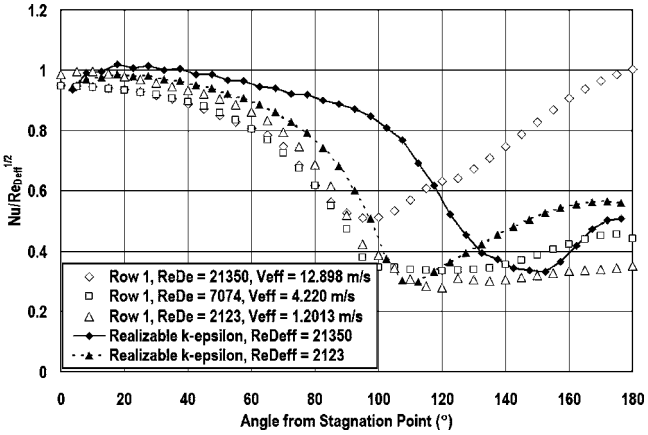

Fig. 6 Row 1 midline $Nu/Re_{D_{eff}}^{1/2}$ as a function of angle, showing the effect of shedding on pin backside heat transfer compared to realizable k-ε, $Re_{D_{max}}$=3000, 10,000, and 30,000

cal flow. However, trying to compare the shedding frequency on cylinders with shedding in pin fin arrays is complicated due to the difference between the effective approach velocity, V_{eff} and V_{max}, and the influence of downstream pins.

Backside Heat Transfer Row 1. Shedding is an important phenomenon in pin fin rows due to its influence of backside heat transfer. Figure 6 presents midline pin heat transfer in terms of $Nu/Re_{D_{eff}}^{1/2}$ as a function of angle for row 1 for the three Reynolds numbers. The effective approach velocity, V_{eff}, was determined by fitting the pin velocity distribution, inferred from the pressure profile, to $U(x)=1.81\times V_{eff}\times \sin\theta$. Using a Reynolds number based on V_{eff} allows clearer comparisons for heat transfer augmentation in the leading edge region (see Ames, Dvorak, and Morrow [3]). The experimental data, shown with open symbols, display high levels of backside heat transfer only for the highest Reynolds number. This backside enhancement correlates closely with the intensity of shedding. Shedding has previously been shown to have a strong influence on cylinder backside heat transfer with and without free-stream turbulence (see Zukauskas and Ziugzda [6]). CFD predictions are also shown on the figure using FLUENT's realizable k-ε model. Qualitatively, the prediction for the lowest Reynolds number is most accurate. However, the row 1 prediction indicates a delayed separation point and significant backside heat transfer, not present in the data. Predictions suggest separation occurs at 97 deg, while experimental pressure coefficient data combined with Thwaite's parameter [21] suggest separation at 83 deg. The FLUENT prediction for the 30,000 Reynolds number case overpredicts heat transfer near the expected point of separation (82 deg) and underpredicts the backside heat transfer. FLUENT predicts separation at 107 deg due to the half-pin symmetrical model, which acts like a splitter plate limiting the influence of shedding. Shedding has a substantial influence on backside heat transfer, and the steady half-pin symmetrical model, which eliminates shedding, misses this important effect.

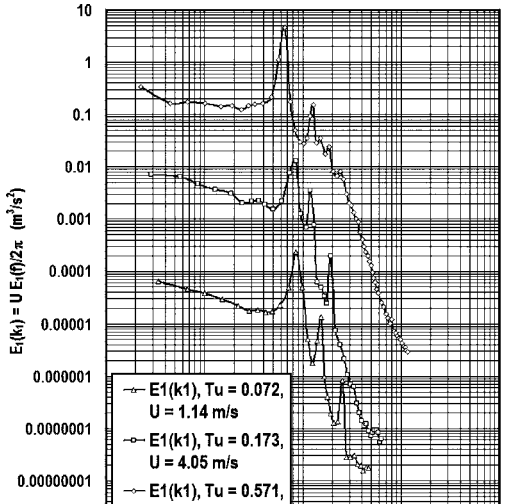

Fig. 5 One-dimensional power spectra of u' off row 1 pin showing peak shedding wave number, $Re_{D_{max}}$=30,000, 10,000, and 3000

Table 1 Strouhal number of row 1 pin shedding frequency, $Re_{D_{max}}$=3000, 10,000, and 30,000

$Re_{D_{max}}$	V_{max} (m/s)	f (Hz)	$St=fD/V_{max}$
3000	1.71	15.56	0.231
10,000	5.93	54.55	0.234
30,000	18.20	150.04	0.209

Near-Pin Velocity Distributions and Shedding, Row 2. Near-pin velocity and u' distributions, normalized on V_{max}, are presented in Fig. 7 acquired off the row 2 pin for the three Reynolds numbers. The near-pin velocity distribution for the 3000 and 10,000 Reynolds number cases suggest the flow here is predominately separated. However, the velocity profile taken at the higher Reynolds number indicates an intermittent separation based on the very high u'. The streamwise fluctuation velocity u' has increased from row 1 and is on the order of U in the near-wall region for 3000 and 10,000 Reynolds cases, indicating stronger shedding from row 2 pins.

Near-pin velocities for row 2 are presented in terms of $U(t)/V_{max}$ versus time$\times V_{max}/D$ in Fig. 8 to allow direct comparisons between the three Reynolds numbers. The strength of the velocity excursions has significantly increased from row 1 for the lower Reynolds numbers. In general, the flow appears less periodic in nature. The 30,000 Reynolds number case shows clear evidence of transition occurring in the mixing layer off the pin.

Backside Heat Transfer, Row 2. Pin midline heat transfer distributions are shown in Fig. 9 for row 2 for the three Reynolds numbers again in terms of $Nu/Re_{D_{eff}}^{1/2}$ as a function of angle. The

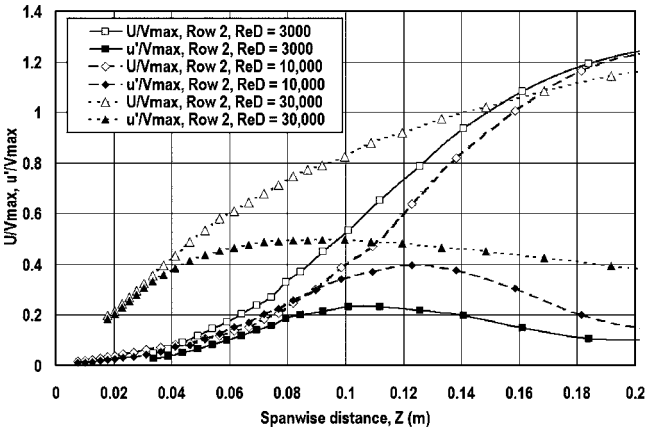

Fig. 7 Near-pin velocity and u' distributions off row 2 pin at 90 deg, normalized by V_{max}

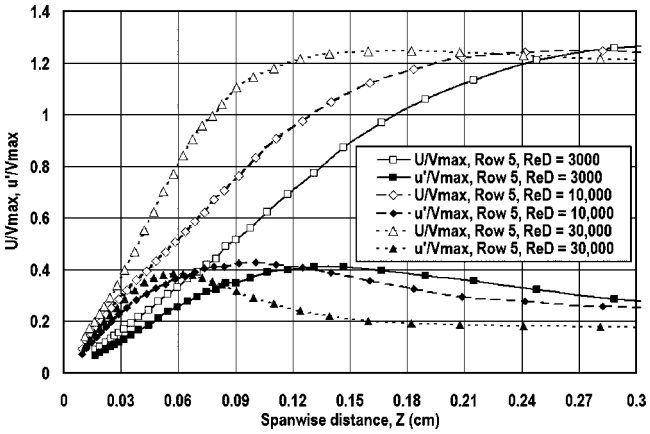

Fig. 10 Near-pin velocity and u' distributions off row 5 pin at 90 deg, normalized by V_{max}

increase in shedding intensity, shown in Fig. 8, has resulted in an increase in backside heat transfer. Backside heat transfer levels have increased by 27% and 39% for the 3000 and 10,000 Reynolds number cases, respectively. The 30,000 Reynolds number case shows about a 7% increase in average backside heat transfer. The FLUENT prediction overpredicts heat transfer in the front half of the cylinder and underpredicts heat transfer on the backside due to the half-pin symmetrical model, except in the 3000 Reynolds number case. At the 3000 Reynolds, the shedding has only a modest influence on backside heat transfer.

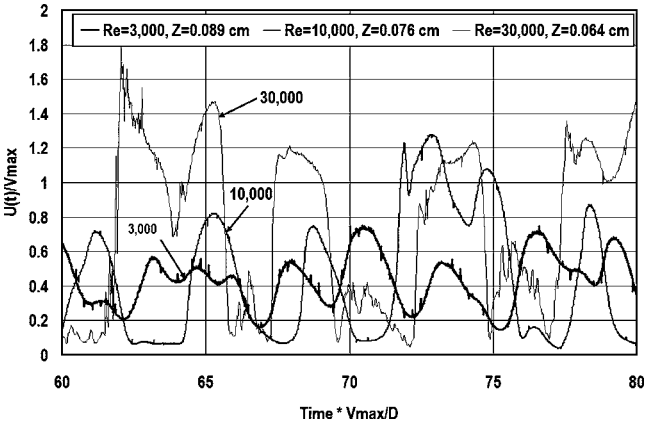

Fig. 8 Near-pin velocity normalized on V_{max} versus time normalized on D/V_{max}, row 2, 90 deg, $Re_{D_{max}}$=3000, 10,000, and 30,000

Near-Pin Velocities, Row 5. Near-pin velocity and u' distributions are presented for row 5 in Fig. 10. These distributions are representative of profiles taken downstream from row 5 as the turbulence levels in the array have reached a row to row equilibrium. Velocity profiles show increasing gradients with increasing Reynolds number as expected from viscous effects. Additionally, local turbulence levels for the near wall are around 80% for the three profiles, indicating strong streamwise variations and intermittent separation in spite of the absence of any significant inflection point in the profile.

Midline Pressure Coefficients, Row 5. Midline pressure coefficient distributions are shown for row 5 in Fig. 11 as a function of surface angle. The pressure coefficient in the attached region is reasonably consistent for the three Reynolds numbers. However, the backside pressure recovery is now a strong function of Reynolds number. While the pressure coefficient distribution for the lowest Reynolds number is similar to the upstream values from row 2, the 10,000 Reynolds number shows a noticeable pressure recovery. From 0 to 80 deg all three profiles are similar. However, by θ=180 deg the 10,000 Reynolds number case shows a significantly different backside recovery. At the 30,000 Reynolds num-

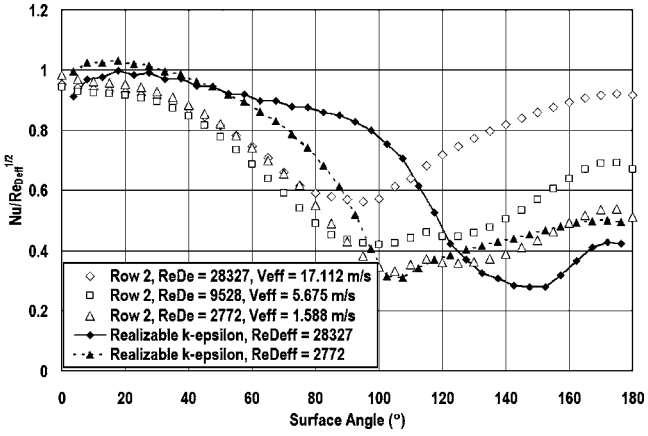

Fig. 9 Row 2 midline $Nu/Re_{D_{eff}}^{1/2}$ as a function of angle, showing the effect of shedding on pin backside heat transfer compared to realizable k-ε, $Re_{D_{max}}$=3000, 10,000, and 30,000

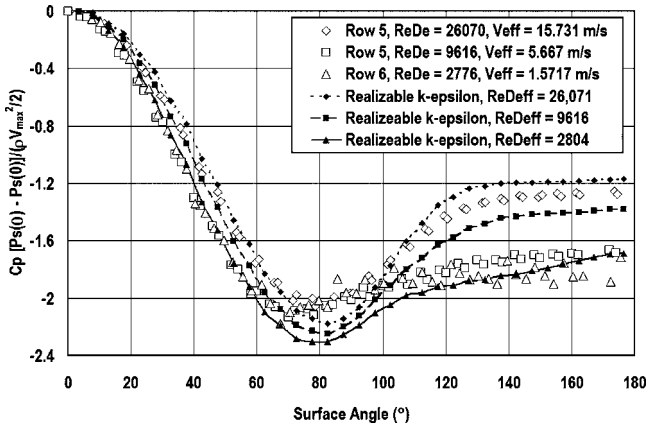

Fig. 11 Midline pressure coefficient distribution, row 5, $Re_{D_{max}}$=30,000, 10,000, and 3000 comparing realizable k-ε predictions

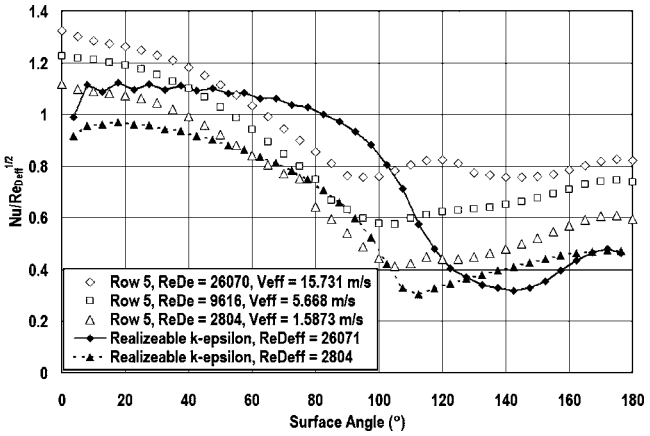

Fig. 12 Row 2 midline $Nu/Re_{D_{eff}}^{1/2}$ as a function of angle, showing the effect of turbulence on pin heat transfer and compared with realizable k-ε, $Re_{D_{max}}$=30,000, 10,000, and 3000

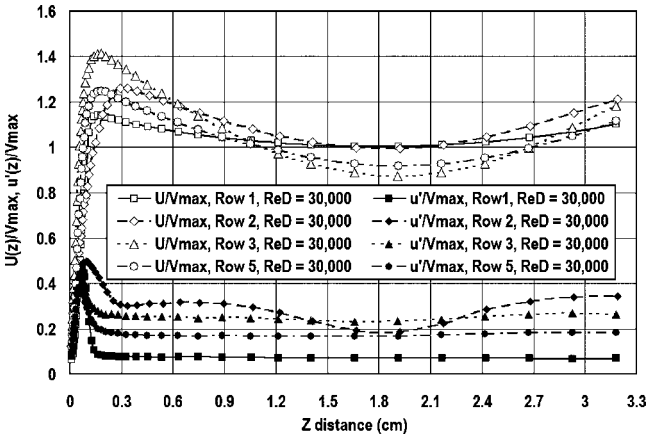

Fig. 13 Cross-span velocity and u' distributions, rows 1, 2, 3, and 5, normalized by V_{max}, $Re_{D_{max}}$=30,000

ber, the backside pressure recovery is 37% of the minimum value, suggesting the boundary layer is staying attached much further along the cylinder. Generally, FLUENT's pressure coefficient predictions show the proper trend with increasing recovery with increasing Reynolds number. However, in each case the relative backside pressure recovery is overpredicted.

Heat Transfer, Row 5. Midline heat transfer distributions presented in Fig. 12 in terms of $Nu/Re_{D_{eff}}^{1/2}$ as a function of angle show the influence of turbulence on stagnation region and front side heat transfer. Heat transfer in the stagnation region should produce a value of $Nu/Re_{D_{eff}}^{1/2}$ equal to 0.95 in air for a low turbulence, flow. On the front side of the pin, heat transfer is significantly augmented by turbulence, showing increased $Nu/Re_{D_{eff}}^{1/2}$ with increasing Reynolds number. However, FLUENT predictions show only a small increase in this region above row 1 and 2 values, suggesting the near-wall treatment for FLUENT's k-ε model inhibits heat transfer augmentation due to turbulence. On the backside of the cylinder, experimental distributions of $Nu/Re_{D_{eff}}^{1/2}$ are enhanced above early low-turbulence rows, but are flatter. The 30,000 Reynolds number case shows two minima in the backside heat transfer curve, indicating critical flow is occurring (see Zukauskas and Ziugzda [6]). The substantial backside pressure recovery shown in Fig. 11 is also an indication of possible separation bubble transition, reattachment, and later separation. Again, FLUENT underpredicts backside heat transfer substantially, due to the steady spanwise-symmetrical model.

Cross-Passage Velocity and u' Distributions. Cross-passage velocity and u' distributions for the 30,000 Reynolds number are presented in Fig. 13 for rows 1, 2, 3, and 5. These distributions help describe the midspan streamwise development of the flow. At row 1 a relatively flat velocity profile results from the uniform upstream flow, except in the near-pin region where velocities peak due to the convex curvature of the pin surface. In row 2 the midspan velocity profile is affected by the pin wake from row 1. However, due to the strong shedding the time-averaged velocity deficit at row 2 is significantly reduced. Row 3 sees the highest effective velocity due to the strong wake generated by the row 2 pin in the midspan. Near the pin surface u' levels, which are 40% of V_{max}, are measured in the near-pin region. Downstream from row 3 effective velocities and turbulence levels begin to diminish due to the strong backside pressure recovery on the row three pins. These effects are the result of the smaller separated region on the backside of the pin. Turbulence levels for row 1 are elevated primarily due to unsteadiness from shedding from row 1 pins. When this unsteadiness is filtered out of the spectra, calculated turbulence levels from row 1 are consistent with inlet values of about 1%. Downstream u' distributions will be discussed later.

Cross-passage velocity and u' distributions for row 3 are shown for the three Reynolds numbers in Fig. 14. The velocity profiles show steeper near-pin velocity gradients with increasing Reynolds number due to viscous effects. Midspan velocity deficits are deeper due to an increasing region of separation with lower Reynolds numbers. This near-wall and midspan blockage also causes higher near-pin velocities. The turbulence levels generated at lower Reynolds numbers can be attributed to the broader blockage on the backside of the pin. Near-pin u'/V_{max} levels are higher due to the instabilities caused by the subcritical flow of the lower Reynolds number flows.

Cross-Passage Distributions of u'/V_{max} and w'/V_{max}. Cross-passage distributions of u'/Vmax and w'/Vmax are shown in Fig. 15 for rows 2, 3, and 5. Distributions of u'/V_{max} show minor peaks off center and a midspan deficit. This double-peak distribution is quite common for wakes, since peak velocity gradients and consequently peak production occurs off centerline. However, much of the turbulence level seen in row 2 (u'/V_{max} and w'/V_{max}) is due to unsteadiness. Measured dissipation rates, the turbulence characteristic which really drives heat transfer augmentation, are substantially reduced compared to row 3. Row three has the highest dissipation rates and high midspan u'/V_{max} and u'/V_{max} distributions due to the turbulence generated by the large separation and the high effective velocities around the pins of row 2. Turbu-

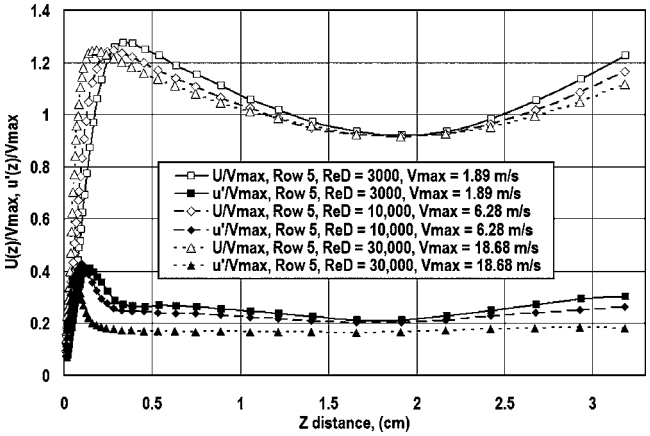

Fig. 14 Cross-span velocity and u' distributions, row 5 pin, normalized by V_{max}

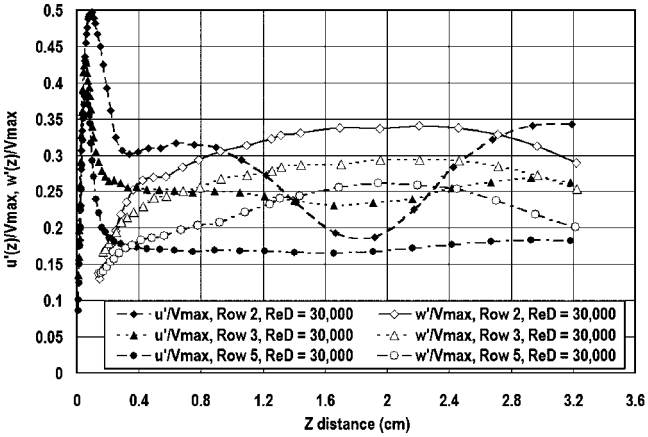

Fig. 15 Cross-span distributions of u'/V_{max}, w'/V_{max}, rows 2, 3, and 5 for $Re_{D_{max}}=30{,}000$

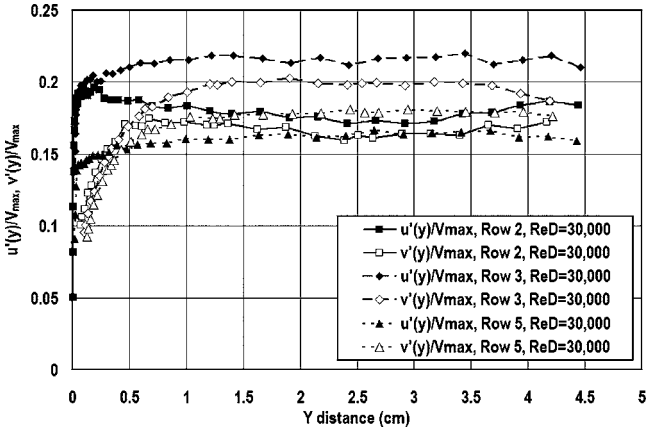

Fig. 17 Normal distributions of u'/V_{max}, v'/V_{max}, rows 2, 3, and 5 for $Re_{D_{max}}=30{,}000$

lence convected into row 3 generated in row 1 also contributes. The same double-peak behavior in u'/V_{max} can be observed. However, this effect is substantially diminished from row 2. The w'/V_{max} levels measured in row 3, like row 2, peak in the middle, similar to distributions seen in typical wakes. However, adding to this effect is the wall blocking of w'/V_{max} due to the attenuation of pin surface normal eddies in the near-pin region. By row 5 turbulence levels have decayed, dissipation rates are lower than row 3, but qualitatively distributions are similar. Row 5 dissipation rates are still substantially higher than row 2 levels, but the reduced separation regions on the pins have allowed turbulence levels to decay. In the near-pin region u'/V_{max} distributions all peak due to unsteadiness around the pin. This effect is clear as no similar peaks are found in u'/V_{max} in the near-endwall region.

Inner Variable Velocity Distributions, Row 5. Endwall normal velocity distributions taken midspan in row 5 are presented in Fig. 16 in terms of inner variables $U+$ versus $Y+$. The momentum deficit Reynolds number is given to provide a basis to compare skin friction levels. For the higher two Reynolds numbers the momentum deficit is sufficient to produce turbulent flow. Skin friction levels are 48% and 62% above values of skin friction estimated from the momentum thickness Reynolds number for the 10,000 and 30,000 Reynolds number (see Kays and Crawford [21], Eq. [11-20]). Skin friction levels are 134%, 53%, and 54% above values of skin friction for turbulent channel flow based on V_{max} and a hydraulic diameter equal to $2H$ for the 3000, 10,000, and 30,000 Reynolds number cases (see Kays and Crawford [21], Eqs. [12-11 and 12-13]). This pin fin array flow is complex and not easily compared with either boundary layers or fully developed channel flows In addition to the turbulent transport rates in the channel, these profiles show no signs of a wake midchannel. This effect has been observed in turbulent boundary layers subjected to high turbulence levels (see Ames and Moffat [5]). The most interesting aspect is the profile for the 3000 Reynolds number case does not even approach Spalding's formula (see White [22], Eq. [6-41]).

Endwall Normal Distributions of u'/V_{max} and v'/V_{max}. Endwall normal distributions of u'/V_{max} and v'/V_{max} taken midpassage for rows 2, 3, and 5 are shown in Fig. 17 for the 30,000 Reynolds number case. Generally, midspan levels of v' are approximately the same as u' levels. Average midspan levels of u'/V_{max} are 17.8%, 21.6%, and 16.3%, and midspan values of v'/V_{max} are 16.6%, 19.3%, and 17.8% for rows 2, 3, and 5. Ratios of v'/u' in the midspan are 0.94, 0.90, and 1.10 for rows 2, 3, and 5, respectively. Normal fluctuation velocities show near-wall attenuation due to the blocking effect of the endwall.

Wall Normal Blocking Effect on Normal Fluctuations. The blocking effect of the endwall on the v' component of turbulence is shown in Fig. 18 in terms of the power spectra of v' as a function wave number in log coordinates. The midspan energy

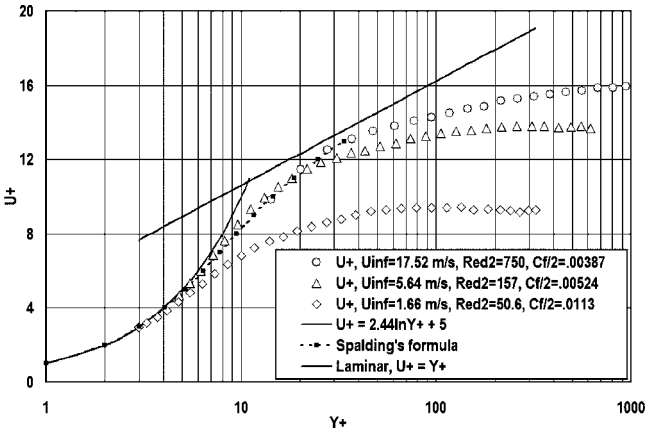

Fig. 16 Endwall normal velocity profiles taken midline in row 5 (inner variables) at $Re_{D_{max}}=30{,}000$, 10,000, and 3000

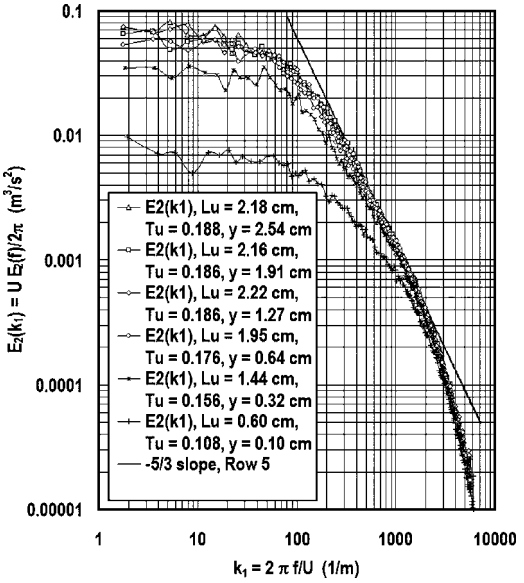

Fig. 18 Attenuation of low wave number v' power spectra approaching endwall, row 5, $Re_{D_{max}}=30{,}000$

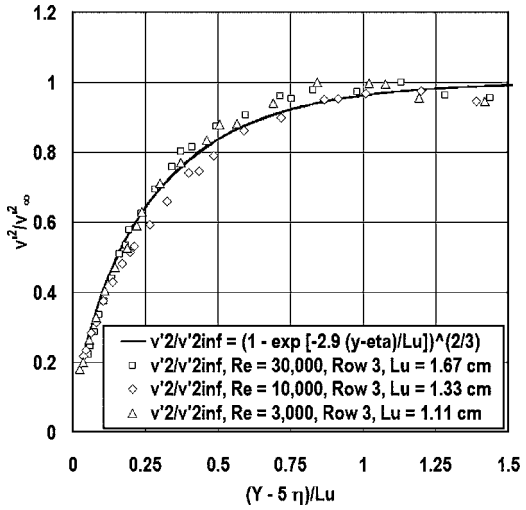

Fig. 19 Wall damping of v'^2 approaching endwall, row 3, $Re_{D_{max}}$=30,000, 10,000, and 3000

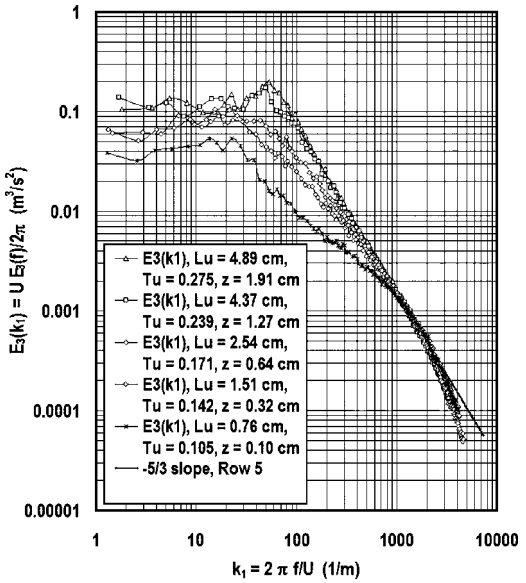

Fig. 21 Attenuation of low wave number w' spectra approaching pin, row 5, $Re_{D_{max}}$=30,000

scale, Lu, is less than the half channel height and the proximity to the wall has little influence until the wall normal distance is smaller than the energy scale. Then, the increasing attenuation of the low wave number eddies is apparent in the spectra.

This attenuation of the low wave number eddies by the wall can be seen in the near-wall v' distribution. Figure 19 shows v'^2/v'^2_∞ as a function of $(Y-5\eta)/Lu$ taken midpassage in row 3 for the three Reynolds numbers. Earlier, Ames and Moffat [5] and Ames [23] correlated v'^2/v'^2_∞ as a function of Y/Lu. However, in the present data a definitive influence of Reynolds number could be seen. This Reynolds number influence is due to the dissipation range of the spectrum, which results in a minimum size of turbulent eddies due to viscous dissipation. This cutoff wavelength is proportional to the Kolmogorov scale ($\eta=[\nu^3/\varepsilon]^{1/4}$). The data correlated best at a distance of $Y-5\eta$. For this constant size pin fin array η increases with decreasing Reynolds number. Figure 20 shows that same comparison taken at row 5 for the same three Reynolds numbers. Again, v'^2/v'^2_∞ correlates well as a function of $(Y-5\eta)/Lu$ and can be represented reasonably well as $[1-\exp(-2.9[Y-5\eta]/Lu)]^{2/3}$.

The blocking effect of the pin surface on the w' component of turbulence is presented in Fig. 21. The effect is similar to the endwall in that the low wave number spectra are clearly shown to attenuate due to their position from the surface of the pin. However, the character of the spectra is somewhat different. There exists an intermediate peak in the data, which in some cases can be explained by the shedding frequency. Additionally, flow around the pin accelerates strongly and has a positive W component of velocity. The source of this anomaly is unknown. The wall blocking effect of the pin surface on w' is similar to the wall blocking effect of the endwall on v'. Figure 22 shows w'^2/w'^2_∞ as a function of $(Z-5\eta)/Lu$ across the midspan of the passage. Based on Fig. 22, the w'^2 data do not appear to fit as well as the v'^2 data in Figs. 19 and 20. However, unlike v'^2, w'^2 is significantly greater in magnitude than u'^2. Consequently, Lu, which is based on u', is likely not the appropriate scale to correlate the near-pin blocking of w'^2. Additionally, the distribution of w' is expected to peak at the center of the wake. Also, with the strong spanwise velocity gradients of $U(dU/dz)$, a significant level of production is occurring between the center of the passage and the pin surface. As a result, the simple attenuation of w'^2 based on midpassage values may be too simple of a model.

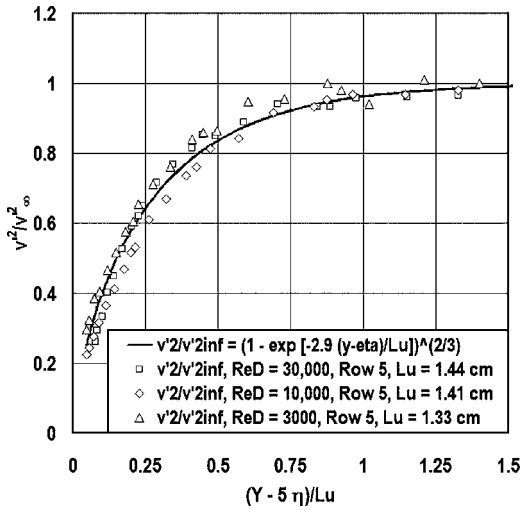

Fig. 20 Wall damping of v'^2 approaching endwall, row 5, $Re_{D_{max}}$=30,000, 10,000, and 3000

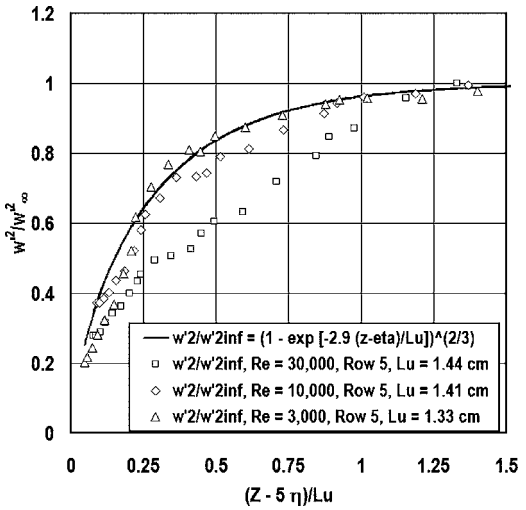

Fig. 22 Wall damping of w'^2 approaching pin, row 5, $Re_{D_{max}}$=30,000, 10,000, and 3000

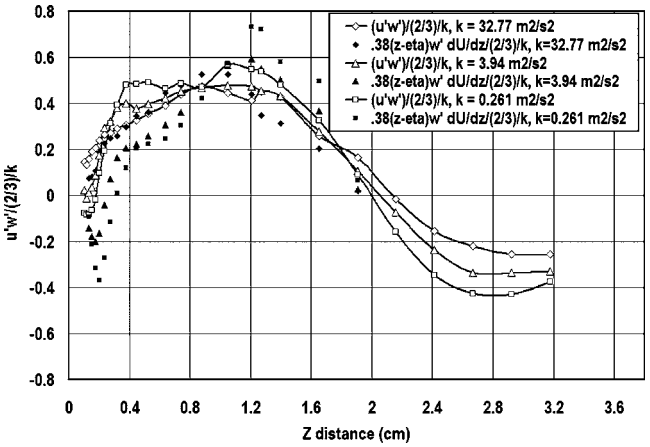

Fig. 23 Comparison of spanwise shear stress, $\overline{u'w'}/(2/3k)^{1/2}$ and simple eddy viscosity model, $w'0.38(z-5\eta)dW/dz$ as a function of Z distance from pin

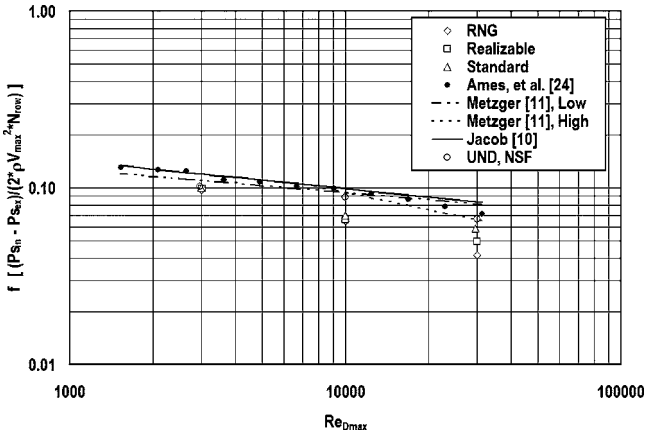

Fig. 24 Comparisons between predictions of flow friction factor, UND data, and correlations

Gradient Transport Models. Most engineering turbulence models are based on the gradient transport assumptions. Gradient transport models suggest that the apparent turbulent shear stress can be modeled with accuracy by an eddy diffusivity for momentum, ν_M, times the local velocity gradient. The simplest eddy viscosity model is the local surface normal velocity, w', times the local mixing length. Far away from the wall the mixing length is expected to be related to the macroscale of turbulence. However, in the near-wall region, where the macroscale of turbulence is significantly greater than the distance to the surface, the mixing length is typically assumed to be proportional to the distance from the wall. Typical constants of proportionality are on the order of 0.4. In Fig. 23, the spanwise apparent shear stress, $\overline{u'w'}$ normalized on $2/3k$ is modeled based on the spanwise normal component of turbulence, w', and the mixing length l ($l=0.38[z-5\eta]$) for row 3 at the three Reynolds numbers. The predicted shear stress is shown with open symbols, while the apparent shear stress estimated by this simple eddy diffusivity assumption is given by solid symbols. The simple model works well away from the pin surface, but begins to overpredict the turbulent shear stress in the near-wall region of the pin. This difference is likely the result of the gradient transport assumption, which assumes turbulent transport can be modeled in terms of a local eddy diffusivity and the local velocity gradient. However, turbulent transport actually occurs across discrete distances often beyond the point where the local velocity gradient is relevant.

Predictions of Flow Friction Factor and Array Average Nusselt Number. Comparisons between measured, correlated, and predicted flow friction factor are displayed in Fig. 24. The experimental data shown in the round symbols can be correlated accurately with Metzger's [11] high- and low Reynolds number correlations for pin fin arrays. However, the CFD calculations significantly underpredict flow friction factor at the higher two Reynolds numbers. Comparisons have shown that the steady symmetrical model predicts separation further downstream than the data suggest. Consequently, pressure recovery has been shown to be overpredicted. The results show that FLUENT's RNG, realizable, and standard k-ε models are consistent at the lower Reynolds number but have significant differences at the higher Reynolds number case. See Ref. [24].

Predictions for average array Nusselt number are shown in Fig. 25 for the three models. The results for the three models are quite consistent but substantially underpredict the Nusselt number. Comparisons indicate that the model underpredicts the influence of turbulence, and the steady symmetrical model fails to accurately represent and predict flow on the backside of the pin. Additionally, the three k-ε models in FLUENT use an enhanced near-wall treatment based on the one-equation model of Wolfstein [20]. This model relies on algebraic equations for mixing length and dissipation. It is likely this model tends to mask differences between different k-ε models. As a result, future work will include calculations using full low Reynolds number turbulence models.

Summary and Conclusions

The objective of the present research has been to investigate the fluid dynamics of pin fin arrays in order to clarify the flow physics with the long-term objective of improving engineering turbulence models. The present paper has documented cross-span velocity, u', w', and shear stress distributions and endwall normal velocity, u', v', and shear stress distributions. Additionally, turbulent power spectra of u', v', and w' have been acquired and have been used to understand the dynamics of turbulence near-pin and endwall surfaces.

This flow has been found to have significant unsteadiness due to shedding off pins. This unsteadiness has been investigated using near-pin surface velocity time records and turbulent spectra. The relative intensity of shedding has been found to increase with Reynolds number. Shedding off pins in row 2 is significantly stronger than shedding from row 1 pins. Additionally, the relative intensity of this shedding has been shown to correlate well with backside heat transfer rates.

Near-pin spanwise velocity distributions show clear evidence of separation in the first two rows. Subsequent rows show very high near-wall turbulence levels, providing evidence of unsteady separation.

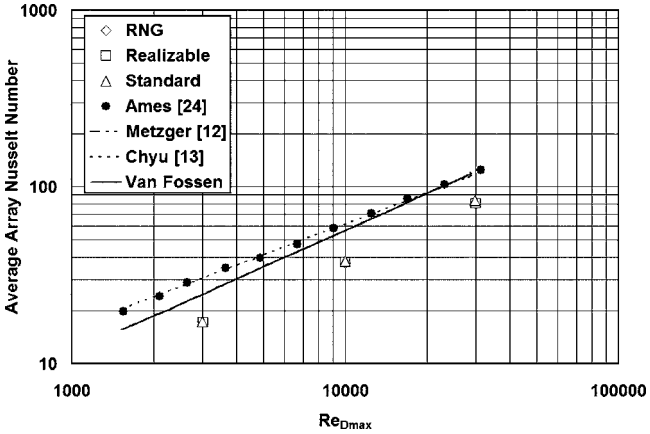

Fig. 25 Comparisons between predictions of average array Nu, UND data, and correlations

Normal x-wire measurements indicate that average values of v'/u' are within 10% of unity. Near the endwall power spectra of v', $E_2(k_1)$ show attenuation of low wave number eddies and v'^2 attenuates as a predictable function of $(Y-5\eta)/Lu$.

Spanwise x-wire measurements show that average values of w'/u' are around 1.35. Near the pin power spectra of $w', E_3(k_1)$ also show attenuation of low wave number eddies. However, although w'^2 is a function of $(Z-5\eta)/Lu$, the form is not as predictable. This difference may be due to the anisotropy of w', the strong production of turbulence by large gradients of dU/dz across the span, and the unsteadiness caused by shedding.

CFD models were found to underpredict heat transfer and pressure drop through arrays. This difficulty was attributed to a combination of the turbulence model, which underpredicted turbulent augmentation, and the steady symmetrical CFD model, which was unable to account for the influence of shedding. Consequently, pin front and backside heat transfer was underpredicted and the level of pressure recovery around the pin was overpredicted, leading to a low estimation of flow friction factor.

Acknowledgment

The present work has been funded through the National Science Foundation. The facility used in this research was developed using funding received by the North Dakota ESPCoR program. Paul Ray and Reuben Gates, while graduate students at UND, were responsible for developing the present UND pin fin heat transfer and flow facility. The authors would also like to thank Matt Morrow for acquiring the midline heat transfer and pressure distributions used in this paper. Additionally, the authors express their appreciation for the current and previous funding and the efforts of prior students.

Nomenclature

A_{min} = minimum array flow path area, m^2
Cp = pressure coefficient, $[Ps(x)\text{-}Ps(0)]/(\rho V_{max}^2/2)$
D = pin or tube diameter, m
$E_1(k_1)$ = one-dimensional energy spectrum function of u', $E_1(k_1)=UE_1(f)/2/\pi$, m^3/s^2
$E_2(k_1)$ = one-dimensional energy spectrum function of v', $E_2(k_1)=UE_2(f)/2/\pi$, m^3/s^2
$E_3(k_1)$ = one-dimensional energy spectrum function of w', $E_3(k_1)=UE_3(f)/2/\pi$, m^3/s^2
f = flow friction factor or pressure loss coefficient, $f=\Delta P/(2\rho V_{max}^2 N)$
f = frequency, $1/s$
h = heat transfer coefficient, $W/m^2/K$
H = channel height, m
k = thermal conductivity, W/m/K
k = turbulent kinetic energy, m^2/s^2
k_1 = wave number, $k_1=2\pi f/U$, m^{-1}
Lu = energy scale, $Lu=1.5|u'|^3/\varepsilon$, m
l = mixing length, m
N = number of array rows
Nu_D = Nusselt number, $Nu=hD/k$
P = pressure, Pa
$Re_{D_{eff}}$ = diameter Reynolds number, based on V_{eff}
$Re_{D_{max}}$ = diameter Reynolds number, based on V_{max}
S = spanwise pin spacing, m
Sh = Stouhal number, $Sh=fD/U$
TRL = turbulence parameter, $TRL=TuRe_D^{5/12}(D/Lu)^{1/3}$
Tu = turbulence level, $Tu=u'/U_\infty$
$U+$ = velocity nondimensionalized on inner variables, $U+=U(Y)/u_\tau$
$U(x)$ = streamwise velocity, m/s
u_τ = shear velocity, $u_\tau=U\cdot(Cf/2)^{1/2}$, m/s
u' = rms streamwise fluctuation velocity, m/s
$\overline{u'w'}$ = apparent turbulent shear stress, m^2/s^2
v' = rms endwall normal fluctuation velocity, m/s
V = normal velocity, m/s
V_{eff} = effective pin approach velocity, m/s
V_{max} = the average velocity through A_{min}, m/s
W = spanwise velocity, m/s
w' = rms spanwise fluctuation velocity, m/s
x = axial distance, m
y = endwall normal distance, m
$Y+$ = dimensionless normal distance from wall in inner variables, $Y+=yu_\tau/\nu$
z = spanwise distance, m

Greek Symbols

ε = turbulent dissipation rate, m^2/s^3
η, eta = Kolmogorov length scale, $\eta=(\nu^3/\varepsilon)^{1/4}$, m
μ = absolute viscosity, Pa s
ν = kinematic viscosity, m^2/s
ρ = fluid density, mass per unit of volume, kg/m^3

References

[1] Metzger, D. E., and Haley, S. W., 1982, "Heat Transfer Experiments and Flow Visualization for Arrays of Short Pin Fins," ASME Paper No. 82-GT-138.
[2] Simoneau, R. J., and Van Fossen, G. J., 1984, "Effect of Location in an Array on Heat Transfer to a Short Cylinder in Crossflow," ASME J. Heat Transfer, **106**, pp. 42–48.
[3] Ames, F. E., Dvorak, L. A., and Morrow, M. J., 2005, "Turbulent Augmentation of Internal Convection of Pins in Staggered Pin Fin Arrays," ASME J. Turbomach., **127**, pp. 183–190.
[4] Baughn, J. W., and Saniei, N., 1990, "Local Heat Transfer Measurements on Arrays of Pin Fins in a Rectangular Duct," *Proceedings of the Ninth International Heat Transfer Conference*, Jerusalem, Hemisphere, New York.
[5] Ames, F. E., and Moffat, R. J., 1990, "Heat Transfer With High Intensity, Large Scale Turbulence: The Flat Plate Turbulent Boundary Layer and the Cylindrical Stagnation Point," Report No. HMT-44, Thermosciences Division of Mechanical Engineering, Stanford University.
[6] Zukauskas, A., and Ziugzda, J., 1985, *Heat Transfer of a Cylinder in Crossflow*, Hemisphere Publishing Corporation, New York.
[7] Hunt, J. C. R., and Graham, J. M. R., 1978, "Free-Stream Turbulence Near Plane Boundaries," J. Fluid Mech., **84**, pp. 205–235.
[8] Thomas, N. H., and Hancock, P. E., 1977, "Grid Turbulence Near a Moving Wall," J. Fluid Mech., **82**, Part 3, pp. 481.
[9] Armstrong, J., and Winstanley, D., 1988, "A Review of Staggered Array Pin Fin Heat Transfer for Turbine Cooling Applications," ASME J. Turbomach., **110**, pp. 94–103.
[10] Jacob, M., 1938, "Heat Transfer and Flow Resistance in Cross Flow of Gases Over Tube Banks," Trans. ASME, **59**, pp. 384–386.
[11] Metzger, D. E., Fan, C. S., and Shepard, W. B., 1982, "Pressure Loss and Heat Transfer Through Multiple Rows of Short Pins," *Heat Transfer 1982*, Hemisphere, Washington, DC, Vol. 3, pp. 137–142.
[12] Metzger, D. E., Shepard, W. B., and Haley, S. W., 1986, "Row Resolved Heat Transfer Variations in Pin Fin Arrays Including Effects of Nonuniform Arrays and Flow Convergence," ASME Paper No. 86-GT-132.
[13] Chyu, M. K., Hsing, Y. C., Shih, T. I.-P., and Natarajan, V., 1998, "Heat Transfer Contributions of Pins and Endwall in Pin-fin Arrays: Effects of Thermal Boundary Conditions Modeling," ASME J. Turbomach., **121**, pp. 257–263.
[14] Miller, R. W., 1996, *Flow Measurement Engineering Handbook*, 3rd ed., McGraw-Hill, New York.
[15] Dvorak, L. A., 2004, "Turbulent Augmentation of Heat Transfer Off Pin and Endwall Surfaces in a Staggered Pin Fin Array," Master's Thesis, Mechanical Engineering Dept., University of North Dakota.
[16] Jorgensen, F. E., 1971, "Directional Sensitivity of Wire and Fiber Film Probes, an Experimental Study," DISA Information, May 1971, No. 11, pp. 31.37.
[17] Hinze, J., 1975, *Turbulence*, 2nd ed., McGraw-Hill, New York.
[18] Moffat, R. J., 1988, "Describing Uncertainties in Experimental Results," Exp. Therm. Fluid Sci., **1**, pp. 3–17.
[19] FLUENT 6.0, 2001, FLUENT 6.0 User's Guide, Fluent, Inc., Lebanon, N.H.
[20] Wolfstein, M., 1969, "The Velocity and Temperature Distribution of One-Dimensional Flow With Turbulence Augmentation and Pressure Gradient," Int. J. Heat Mass Transfer, **12**, 301–318.
[21] Kays, W. M., and Crawford, M. E., 1993, *Convective Heat and Mass Transfer*, 3rd ed., McGraw-Hill, New York.
[22] White, F. M., 1991, *Viscous Fluid Flow*, 2nd ed., McGraw-Hill, New York.
[23] Ames, F. E., 1994, "Experimental Study of Vane Heat Transfer and Aerodynamics at Elevated Levels of Turbulence," NASA CR-4633.
[24] Ames, F. E., Solberg, C. S., Goman, M. D., Curtis, D. J., and Steinbrecker, B. T., 2001, "Experimental Measurements and Computations of Heat Transfer and Friction Factor in a Staggered Pin Fin Array," ASME Paper No. DETC 2001/CIE-21761.

The Effect of Inlet Guide Vanes Wake Impingement on the Flow Structure and Turbulence Around a Rotor Blade

Francesco Soranna
Yi-Chih Chow
Oguz Uzol
Joseph Katz

Department of Mechanical Engineering,
Johns Hopkins University,
Baltimore, MD 21218

The flow structure and turbulence around the leading and trailing edges of a rotor blade operating downstream of a row of inlet guide vanes (IGV) are investigated experimentally. Particle image velocimetry (PIV) measurements are performed in a refractive index matched facility that provides unobstructed view of the entire flow field. Data obtained at several rotor blade phases focus on modification to the flow structure and turbulence in the IGV wake as it propagates along the blade. The phase-averaged velocity distributions demonstrate that wake impingement significantly modifies the wall-parallel velocity component and its gradients along the blade. Due to spatially non-uniform velocity distribution, especially on the suction side, the wake deforms while propagating along the blade, expanding near the leading edge and shrinking near the trailing edge. While being exposed to the nonuniform strain field within the rotor passage, the turbulence within the IGV wake becomes spatially nonuniform and highly anisotropic. Several mechanisms, which are consistent with rapid distortion theory (RDT) and distribution of turbulence production rate, contribute to the observed trends. For example, streamwise (in rotor frame reference) diffusion in the aft part of the rotor passage enhances the streamwise fluctuations. Compression also enhances the turbulence production very near the leading edge. However, along the suction side, rapid changes to the direction of compression and extension cause negative production. The so-called wall blockage effect reduces the wall-normal component. [DOI: 10.1115/1.2098755]

Introduction

The flow within a multistage axial turbomachine is inherently unsteady and turbulent. One of the main causes for unsteadiness is the interaction of wakes shed by upstream rotor and stator blades with the blades downstream. Periodically arriving wakes modify the overall velocity distributions around the blades including the structure of boundary layers. Furthermore, the incoming wakes are chopped by the blades, and then diffuse and deform as they pass through the nonuniform strain field in the blade passage. These unsteady interactions affect the performance of blades, and are likely causes for noise and vibrations. Understanding of these phenomena is essential for the development of physically meaningful tools for predicting and accounting for them during the design process, including the development of realistic turbulence models that can be employed in Navier-Stokes solvers. Consequently, numerous numerical and experimental studies have already focused on blade-wake interactions. The numerical studies have consisted mostly of unsteady RANS simulations (e.g., Rai [1], Ho and Lakshminarayana [2], Valkov and Tan [3], Chen et al. [4], and Gerolymos et al. [5]). The experimental efforts have investigated wake-boundary layer interactions (e.g., Dong and Cumpsty [6], Halstead et al. [7], Schobeiri et al. [8], Shin et al.[9], and Soranna et al. [10]), modification to the wake structure during transport through a rotor passage, i.e., "wake recovery" (e.g., Smith [11], Kerrebrock and Mikolajczak [12], Zaccaria and Lakshminarayana [13], Van Zante et al. [14], Adler and Benyamin [15], Sentker and Riess [16], and Sanders et al. [17]), and flow nonuniformities around the rotor blade caused by wake chopping and shearing (Chow et al. [18] and Uzol et al. [19]).

In spite of all the efforts invested to date, it is hard to find detailed data on the effect of wake impingement on the velocity field around the rotor leading edge, as well as on the effect of the blade on the flow and turbulence within the impinging wake. Due to the inherent difficulties in performing measurements within turbomachines, all of the abovementioned investigations provide incomplete pictures. Some are limited to the flow away from the surface due to optical or access restrictions, while others lack sufficient resolution or converged turbulence statistics. Hobson and Shreeve [20] and Hobson et al. [21] present experimental data, obtained using two-component laser Doppler velocimetry, on the distortion and amplification of turbulence near the leading edge of a compressor cascade. In these studies, the inlet turbulence is isotropic and has a low intensity of about 1.5%, which is not quite representative of the actual flow conditions in a typical multistage turbomachine. However, their results do indicate that the turbulence is amplified near the leading edge and some anisotropy is created within the blade passage. Since the data does not cover the entire flow field around the leading edge, it is difficult to interpret the observed trends, especially the cause-and-effect relationships between the turbulence and the local flow field. Modification of isotropic inlet turbulence within a cascade is also examined by De La Riva et al. [22] using hot wire anemometry. The experimental results are compared successfully with predictions of rapid distortion theory. Some of their observations are relevant to the present study, as discussed later in this paper.

This paper presents and discusses the results of an experimental investigation on the flow structure and turbulence around a rotor blade operating downstream of a row of inlet guide vanes (IGV). We focus on the interaction of the IGV wake with the flow near the blade. High-resolution two-dimensional particle image velocimetry (PIV) measurements are performed in a refractive index

Contributed by the International Gas Turbine Institute (IGTI) of THE AMERICAN SOCIETY OF MECHANICAL ENGINEERS for publication in the ASME JOURNAL OF TURBOMACHINERY. Paper presented at the ASME Turbo Expo 2005: Land, Sea and Air, Reno, NV, June 6-9, 2005, Paper No. GT2005-68801. Manuscript received by IGTI, October 1, 2004; final manuscript received February 1, 2005. IGTI Review Chair: K. C. Hall.

matched facility that provides unobstructed view of the entire flow field. Data are obtained at mid-span, at three different rotor blade phases: the first with the IGV wake located just before impinging on the leading edge; the second with the center of the IGV wake impinging on the leading edge; and the third with the center of the wake intersecting with the rotor blade at about 20% of the rotor chordlength. The measurement domain covers a region from about 10% of the chordlength above the leading edge, up to about mid-chord. However, we also present sample data on the flow and turbulence near the trailing edge in order to elucidate certain trends. The results are presented in two parts: The first concentrates on the phase-dependent variations of the velocity field around the rotor blade due to the impinging wake, and the second focuses on the modification to the flow structure and turbulence within the impinging IGV wake. We show that the wake turbulence becomes highly anisotropic and spatially non-uniform due to straining by the flow field around the blade, and due to streamwise diffusion through the rotor passage.

Experimental Setup and Procedures

Facility. The axial turbomachine test facility enables us to perform PIV measurements at any point within an entire stage including the rotor, stator, gap between them, inflow into the rotor and the wake downstream of the stator. The unobstructed optical access is facilitated using a rotor and IGV rows made of a transparent material (acrylic) that has the same optical index of refraction as that of the working fluid which is a concentrated solution, 62%–64% by weight, of NaI in water.

This fluid has a specific gravity of 1.8, i.e., heavier than water, but has a kinematic viscosity of 1.1×10^{-6} m^2/s, which is very close to that of water. We do not measure the ratio between the index of refraction of the blades and the fluid directly but we add sodium iodide until the illuminating laser sheet is not deflected. Thus the blades become almost invisible, do not obstruct the field of view, and do not alter the direction of the illuminating laser sheet while passing through the blades. The reflection from boundaries is also minimal, enabling us to perform velocity measurements very close to the wall. Information related to use and maintenance of the NaI solution can be found in Uzol et al. [23].

In the present configuration, shown schematically in Fig. 1, the first stage consists of a rotor row followed by a stator row, whereas the second stage consists of a stator (IGV) followed by a rotor. The system is driven by a 25 HP, rim driven motor, which drives the first rotor directly, and is connected to the second rotor through a shaft mounted on precision bearings. A 10 mm long honeycomb with 1.58 mm cell openings is installed downstream of the first stage in order to reduce the effect of wakes and secondary structures generated by the first stage. The gap between the honeycomb and the second stage stator is selected as 22 times the honeycomb openings. Tests have shown that, at this distance, the signatures of individual openings diminish. The IGV has 17 blades, each with a chordlength of 50 mm and span of 44.5 mm. The rotor has 12 blades, each with a chordlength of 50 mm and span of 44.5 mm. All the present measurements are performed at a rotor blade speed of 500 rpm, i.e., the Reynolds number based on the rotor tip speed and chordlength is 3.7×10^5. Some geometrical details are summarized in Table 1. The momentum thickness of the upstream IGV wakes, θ_w, is presented in Table 1. It is measured 20% chord lengths downstream of the IGV trailing edge using data obtained in previous studies. The flow coefficient is estimated from $\varphi=(1/c)\int_0^c(\bar{u}/U_{tip})dy$ using data from a plane located 40% of the chordlength upstream of the chord in the same span. More information about the facility can be found in Uzol et al. [23] and Chow et al. [18].

PIV Setup and Experimental Procedure. Two-dimensional PIV measurements are performed at 50% span within a region that extends from 10% of the chordlength upstream (in the rotor reference frame) of the rotor blade leading edge, up to about mid-chord. The flow and turbulence are measured and analyzed at three different rotor blade phases. The time delay between two consecutive phases is 1.5 ms, which corresponds to 15% and 21% of the rotor and stator blade passing periods, respectively (T_R =10 ms and T_S=7.06 ms).

The light sheet is generated using an Nd-YAG laser and images are recorded by a 2048×2048 pixels^2, Kodak Megaplus ES4.0, digital camera. The flow is seeded using 20% silver coated, hollow glass, spheres with a mean diameter of 13 μm and a specific gravity of 1.6, slightly lower than that of the liquid. At each phase we record 1000 image pairs in order to obtain converged statistics on the turbulence. Data analysis includes image enhancement, removal of blade signature and cross-correlation analysis using in-house developed software and procedures (Roth et al. [24], Roth and Katz [25], and Uzol et al. [23]). The present instantaneous sample area is 15×15 mm^2, and two adjacent, slightly overlapping areas are needed for covering the entire region of interest.

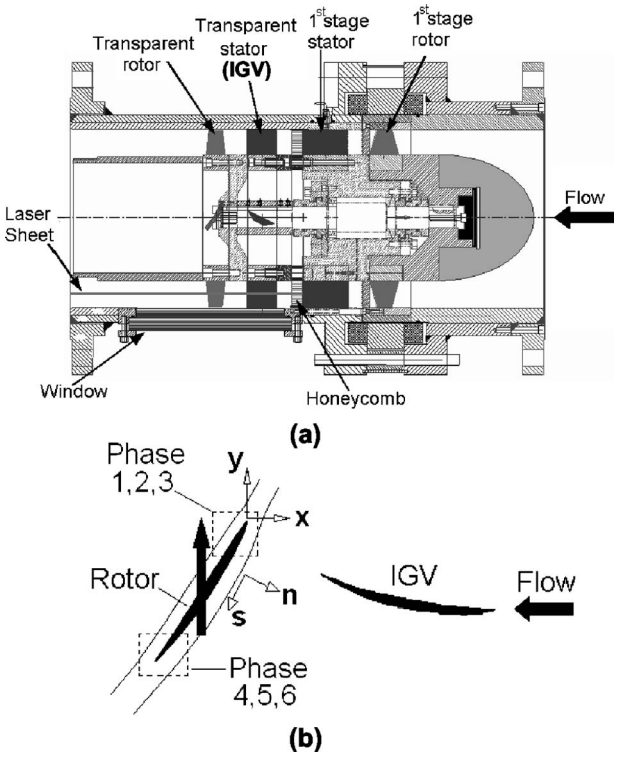

Fig. 1 (*a*) The axial turbomachinery test section. (*b*) Schematic representation of IGV blade and rotor blade. Also indicated: rotor frame coordinates systems (x,y) and (s,n); flow direction and rotor blade displacement direction; area covered by phases 1–6.

Table 1 Geometrical details of the inlet guide vanes and the rotor blades

	IGV	Rotor
No.of blades	17	12
Chord (mm)	50	50
Span (mm)	44.5	44.5
Blade thickness (mm)	8.28	7.37 (hub) 5.62 (tip)
Tip clearence (mm)	0	1.2
Pitch to chord ratio	0.97	1.34
IGV-rotor gap (mm)	40	
Hub to tip ratio	0.708	
φ	0.32	
θ_w/c	0.0133	

With 32×32 pixels^2 interrogation windows, and 50% overlap between windows, each vector map contains 125×125 vectors, and the vector spacing is 117 μm (0.234% of the chordlength). A conservative estimate of the uncertainty in mean displacement in each interrogation window is 0.3 pixels, provided the window contains at least 5–10 particle pairs (Roth et al. [24] and Roth and Katz [25]). For the typical displacement between exposures of 20 pixels, the resulting uncertainty in instantaneous velocity is about 1.5%. Slip due to the difference between the specific gravity of the particle (1.6) and that of the fluid (1.8) may cause an error of less than 0.2%, i.e., much less than other contributors (Sridhar and Katz [26]). Uncertainty related to inflow variations and timing errors is estimated to be less than 0.6%. Additional details about the PIV setup and the data acquisition system can be found in Chow et al. [18] and Uzol et al. [23].

Using the instantaneous measurements, the phase-averaged parameters are calculated as follows

$$\bar{u}_i(x,y,\phi) = \frac{1}{N}\sum_{k=1}^{N}(u_i)_k \tag{1}$$

$$\overline{u_i'u_j'}(x,y,\phi) = \frac{1}{N}\sum_{k=1}^{N}[(u_i)_k-\bar{u}_i][(u_j)_k-\bar{u}_j] \tag{2}$$

$$k(x,y,\phi) = \frac{3}{4}(\overline{u_i'u'}_i) \tag{3}$$

where $N=1000$ is the number of instantaneous vector maps for each phase, x and y are the axial and lateral (almost circumferential) coordinates, respectively, and ϕ is the rotor phase angle. The subscripts i and j take values of 1 and 2, representing the axial (u) and lateral (v, almost circumferential) velocity components, respectively. The definition of the coordinate system used in this study is given in Fig. 1(b) (the positive x axis points upstream). The 3/4 coefficient of k, the "turbulent kinetic energy," accounts for the contribution of the missing out-of-plane velocity component, assuming that it is an average of the available in-plane components. Our recent 3D stereoscopic PIV measurements (Uzol et al. [27]) under the same flow conditions show that within the IGV wake (far from the blade) the out of plane velocity fluctuations are about 10% higher than the average of the in-plane components. Outside of the IGV wake the error is less than 10%. Second order finite differencing is used for calculating the vorticity and the mean strain rate.

Results

Modification of the Velocity Field Around the Rotor Leading Edge. Data are obtained at three phases as the IGV wake is chopped off and sweeps across the rotor blade. Figure 2 presents the distributions of phase-averaged axial, $\bar{u}$, and lateral, v_r, velocity components (the latter in the rotor reference frame) along with the turbulent kinetic energy for the three phases. In phase 1 (top row), the IGV wake center is located at about 15% chord-lengths above the rotor leading edge. In phase 2 (middle row), the IGV wake center is impinging on the leading edge, and in phase 3 (bottom row), the center of the wake intersects with the rotor blade at about 20% of the rotor chordlength. For each phase, two adjacent 15×15 mm^2 sample areas are needed to cover the flow field around the rotor leading edge. The coordinates are fixed in the rotor frame of reference. As a result, the terms "*streamwise*" (denoted as s) and "*normal*" (denoted as n) directions refer to streamlines in the rotor frame of reference (Fig. 1(b)). The rotor leading edge is located at $(x/c,y/c)=(0,0)$, and the field of view extends up to about 40% of the chordlength. The location of the IGV wake in each phase can clearly be identified in the turbulent kinetic energy plots (Fig. 2(c)). In this section, these plots are used only as a reference, in order to relate the phase-dependent variations in the velocity field to the location of the wake. A more detailed discussion on the wake turbulence is presented in the next section.

There is a minimum in axial velocity on the suction side in the vicinity of the leading edge. Even before the wake impinges on the blade, it starts to modify the axial velocity above the leading edge, as is evident from the distortion of the contour lines towards the incoming wake in phase 1. When the center of the wake crosses the leading edge in phase 2, the low axial velocity region expands substantially, due to the axial momentum deficit within the wake. After the wake passes and clears the leading edge region, in phase 3, the low axial momentum region shrinks again. Sweeping of the wake along the suction side of the blade causes substantial changes in distribution of axial velocity. As the wake shifts from phase 1 to 3, the axial velocity decreases, but the wall-normal gradients of axial velocity increase. The latter can be observed from the orientation of the iso-velocity contour lines. The axial velocity contours are almost normal to the blade surface in phase 1, indicating low axial gradients, except for the thin blade boundary layer. Conversely, in phase 3 the contour lines bend upward, indicating an increase in the wall-normal axial velocity gradients.

The relative lateral velocity is also modified by wake passage. The point of minimum relative lateral velocity is located on the pressure side of the blade (as expected), and the effects of wake passage near the leading edge are subtle but noticeable. However, along the blade suction side the changes are substantial. Prior to wake impingement, the lateral velocity accelerates from $s/c=0\%$ to $s/c=2.5\%$. Further along the blade, the flow starts decelerating gradually. As soon as the wake impingement starts (in phase 2), both the acceleration and deceleration regions become significantly smaller, i.e., the streamwise gradients of the relative velocity get much steeper due to the presence of the IGV wake. In phase 3 the acceleration area expands again, but the deceleration region keeps on shrinking, further reducing the high lateral momentum along the suction side.

On the pressure side of the blade, in phase 1, the axial velocity increases up to about 5% of the chord, and then starts decreasing gradually. As the wake sweeps the rotor blade, the point of maximum axial velocity is pushed further below, e.g., from about 15% of the chord in phase 2, to about 25% in phase 3. Furthermore, the magnitude of the axial velocity decreases significantly, and the wall-normal gradients increase. The relative lateral velocity component has a minimum near the leading edge, and in all cases gradually increases below the stagnation point. However, the isovelocity contour lines vary significantly with phase.

Figure 3 presents sample streamwise distributions of axial and relative lateral velocity components along streamlines located 1.5% of the chordlength away from the blade surface. Along the suction side of the blade (Fig. 3(a)), the phase-dependent variations of v_r are much more severe than those of the axial velocity. The maximum relative lateral velocity in phase 3 is about 9% higher than the maximum in phase 1. Phase dependent variations in the distribution of v_r and $\bar{u}$ on both sides of the blade indicate that wake impingement causes substantial changes in the magnitude and distribution of blade loading. The distributions of axial velocity on the suction side show the effect of wake deficit, i.e., a decrease on $-\bar{u}$ within the wake. In phase 2 the axial velocity is lower near the leading edge, and in phase 3, it is lower at $s/c>0.2$, both of them consistent with the location of the wake.

On the pressure side of the blade (Fig. 3(b)), the phase-dependent variations in v_r and $\bar{u}$ are equally severe, but their trends differ. The primary changes in v_r occur below the leading edge, whereas the axial velocity variations extend to the region above the blade. In phase 2, the axial velocity near the leading edge is lower by almost 25% compared to the other phases, consistent with the expected location of wake deficit. Accordingly, in phase 3 the pressure side axial velocity is significantly lower around $s/c\sim0.1$. Further below, the point of maximum axial ve-

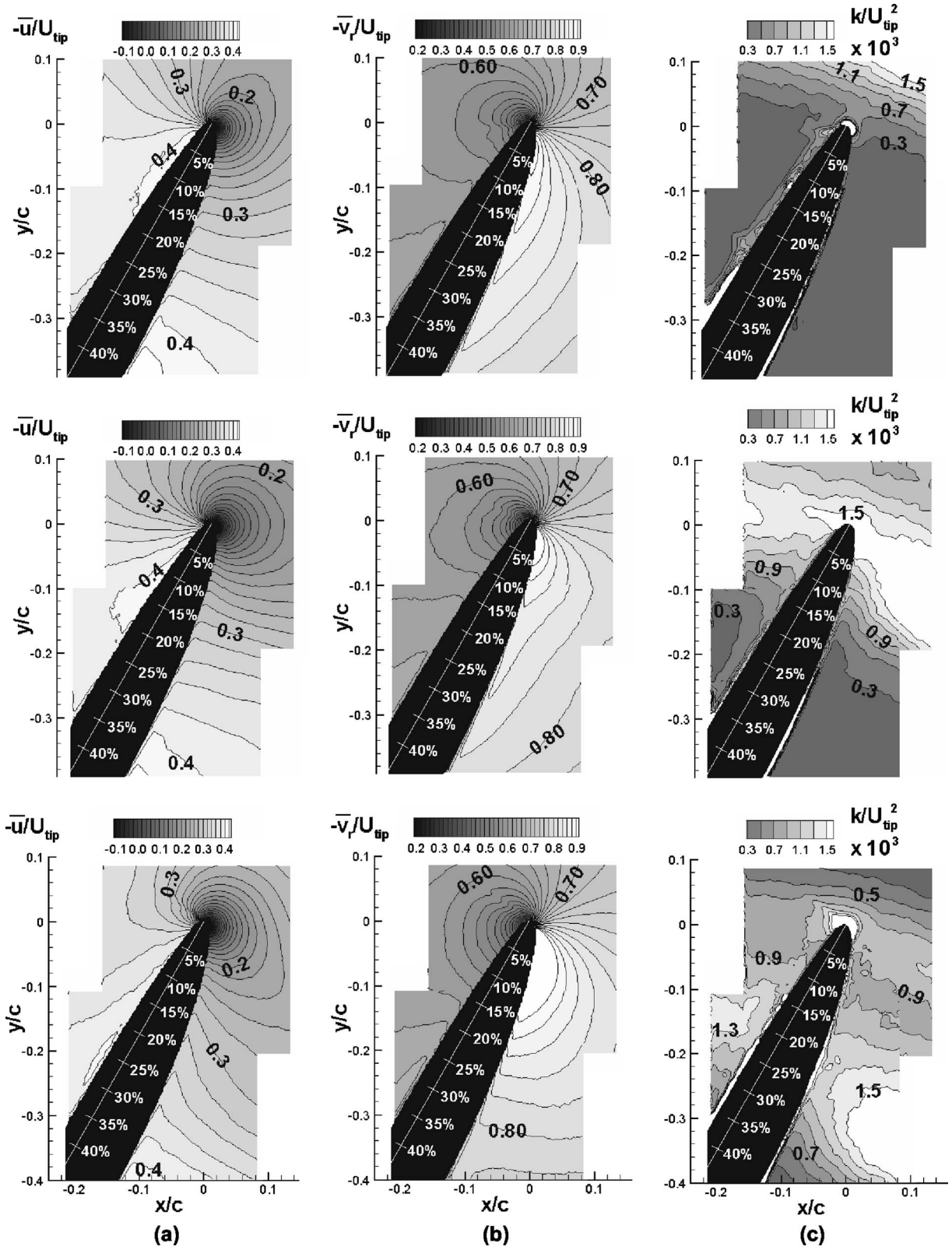

Fig. 2 Phase-averaged (*a*) axial ($-\bar{u}$), (*b*) relative lateral ($-\overline{v_r}$) velocity components, and (*c*) turbulent kinetic energy for three different phases, around the rotor blade leading edge at mid-span. Top row: phase 1 (t/T_S=0.0); middle row: phase 2 (t/T_S =0.213); bottom row: phase 3 (t/T_S=0.426). T_S=7.06 ms is the stator blade passing period. c=50 mm is the rotor blade chord (solid white line). U_{tip}=8 m/s. Contour increments $\Delta\bar{u}=\Delta\overline{v_r}$=0.02 and Δk=0.2.

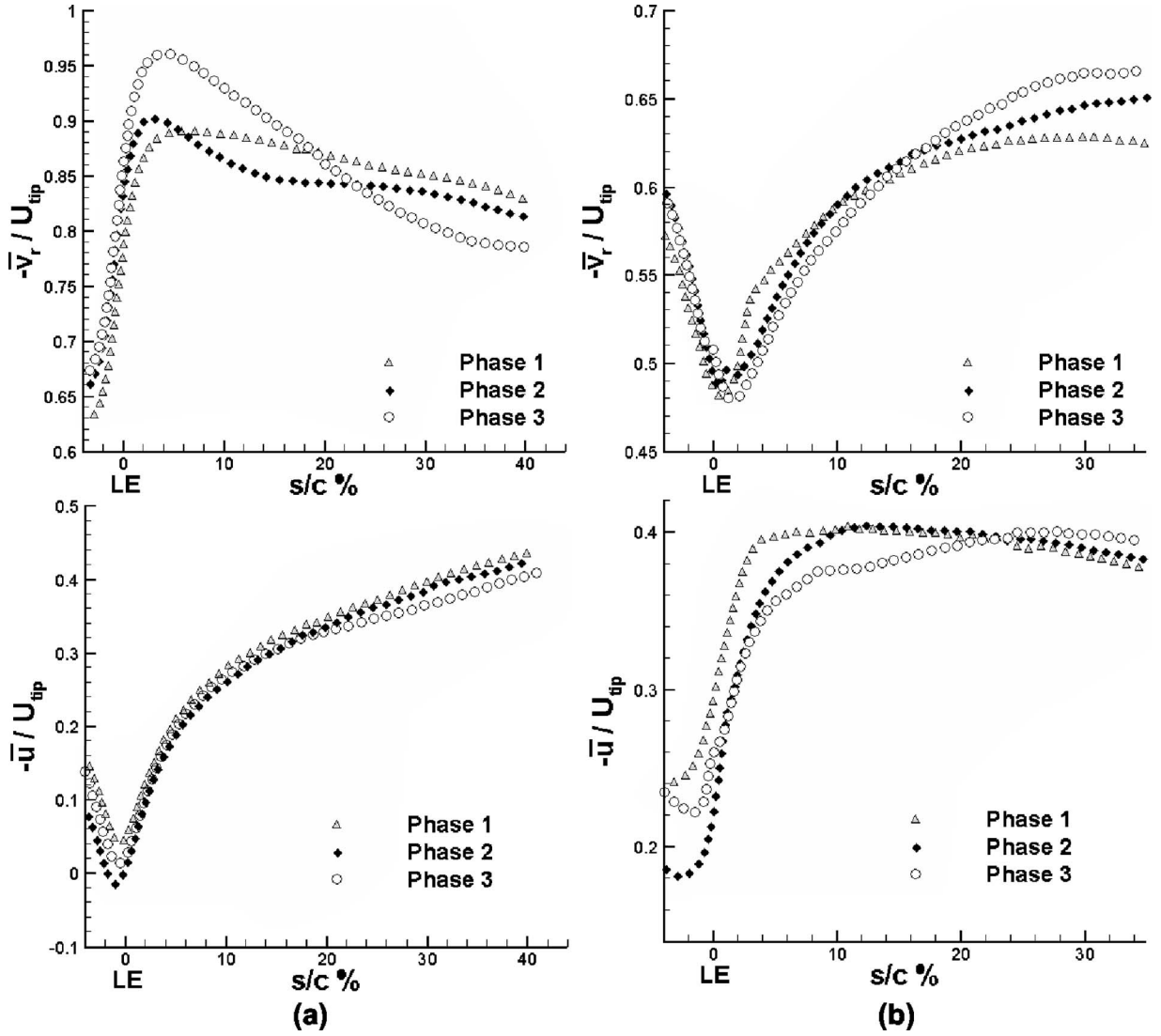

Fig. 3 Streamwise variation of the phase-averaged relative lateral velocity (top row) and axial velocity (bottom row) along the rotor blade (*a*) suction side and (*b*) pressure side, 1.5% chord-lengths away from the surface

locity is also pushed to higher s/c as the wake sweeps along the pressure side. The phase dependent variations in the lateral velocity component along the pressure side occur mostly at $s/c > 0.15$. At $s/c \sim 0.3$, the magnitude of $\bar{v}_r$ in phase 3 is about 8% higher than that in phase 1.

To demonstrate the effect of impingement on blade loading, Figs. 4(*a*) and 5(*a*) show the distributions of $\bar{u}_s$ and $\partial \bar{u}_s / \partial s$ respectively, along the same streamline on the suction side. In phase 3, $\bar{u}_s$ has a minimum just ahead of the wake impingement area. Being near the leading edge, it has a maximum in the middle of the wake. Thus, the flow is decelerating in the $0.05 < s/c < 0.32$ region. However, in later phases, when the wake impinges on the aft parts of the blade (not shown, see Soranna et al. [10]), the maximum in $\bar{u}_s$ occurs behind the wake. The maximum differences in $\bar{u}_s$ between phases 3 and 1 are about 6.5%. In phase 2, when a smaller fraction of the wake impinges, the differences are smaller.

On the pressure side (Figs. 4(*b*) and 5(*b*)) the magnitude of $\bar{u}_s$ vary by 2–5 % between phases. Wake impingement seems to reduce the values of $\partial \bar{u}_s / \partial s$ just below the leading edge. Within the area influenced by the wake, $\bar{u}_s$ increases monotonically, whereas in the region outside of the wake $\bar{u}_s$ peaks at $s/c = 0.24$.

Modification of Mean Vorticity and Turbulence in the Impinging Wake. As the chopped segments of IGV wake propagate through the rotor passage, they are subjected to spatially nonuniform flow and strain fields. Consequently, the shape of the wake is modified, as we intend to show using the mean vorticity distribution, while the turbulence within the wake becomes spatially nonuniform and highly anisotropic. Interpretation of the trends has been quite a challenge due to the presence of several, sometimes conflicting mechanisms that affect the turbulence. As we will demonstrate, nonuniform turbulence production, straining by the flow around the blade, and diffusion through the blade passage modulate each component of the velocity fluctuations in a different manner.

Mean Vorticity Distributions. Transport through the rotor passage exposes the wake segment to a spatially non-uniform velocity distribution. As illustrated in Fig. 6, as the forward part of the wake passes the leading edge on the suction side, the forward part propagates at a high velocity, while its aft part is still located above the leading edge, and as a result still moves at a low velocity (see Fig. 2). Thus, near the leading edge, the wake is stretched in the streamwise direction (in the rotor reference frame), i.e., it

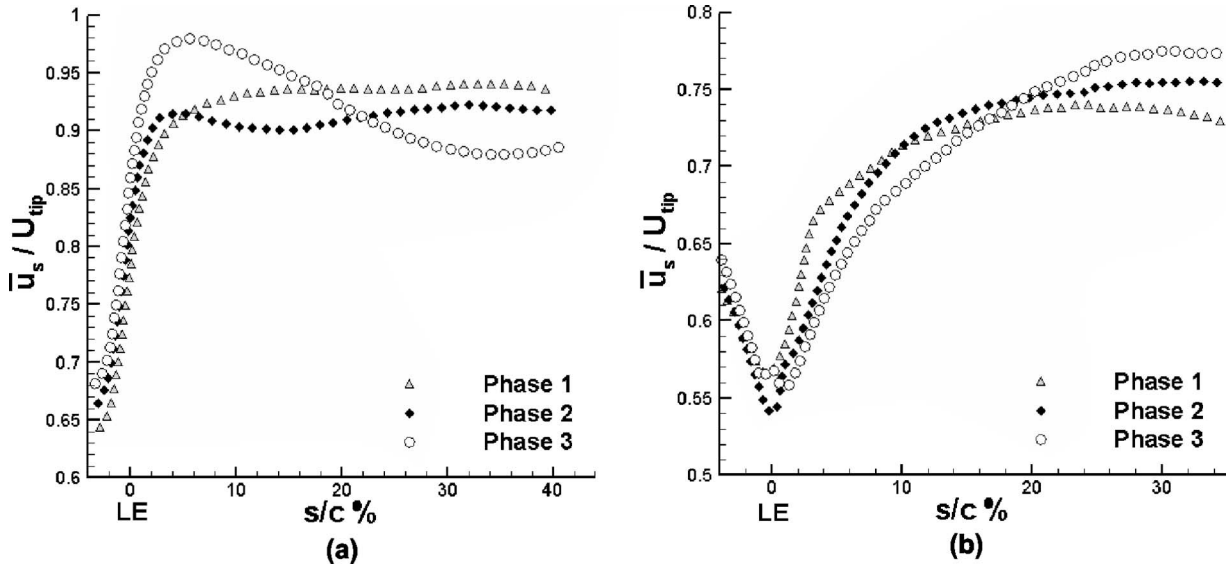

Fig. 4 Streamwise variation of $\overline{u_s}$ along the rotor blade (*a*) suction side and (*b*) pressure side, 1.5% chord-lengths away from the surface

becomes wider. Conversely, near the trailing edge, the wake is exposed to a negative streamwise relative velocity gradient ($\partial u_s / \partial s < 0$), and as a result becomes narrower.

In order to demonstrate the stretching and compression of the wake width, we use the previously discussed data for the flow near the leading edge, and introduce three additional phases that focus on wake-boundary layer interaction near the trailing edge. Details on these latter phases including the velocity distributions within the boundary layer are discussed in Soranna et al. [10], and we will refer to them as phases 4–6. They have been recorded in the same facility and under the same condition (except for the phase). The time separation between these additional phases is 1 ms (10% of the rotor blade passing period), i.e., shorter than the time delay between phases 1–3. Also, only 500 velocity distributions are used for calculating the ensemble-averaged statistics.

Figure 7 shows the distribution of mean radial vorticity $\bar{\omega}$ for phases 1 to 6. The top row (phases 1 to 3) shows the vorticity field around the leading edge, while the bottom row (phases 4 to 6) presents the vorticity field near the trailing edge. All the phases show the elevated vorticity along the rotor boundary layers. The IGV wake is characterized by a layer with negative vorticity followed by an almost parallel layer with positive vorticity. The wake width can be estimated from the distance between the upper edge of the positive vorticity layer and the lower edge of the negative layer. In phase 1 the negative layer is just emerging while the positive layer is still above our field of view. In phase 2 the negative layer is already chopped, and the positive layer starts entering the sample area. In phase 3 the positive layer is being dissected by the leading edge. Between the positive and negative layers there is a region characterized by almost zero vorticity (see illustration in Fig. 6). Several observations can be made regarding the structure of the wake in phase 3 based upon the vorticity distribution:

First, the chopped IGV wake segment on the pressure side is narrower than the segment on the suction side. On the suction side the width is about 50% of the chordlength while on the pressure

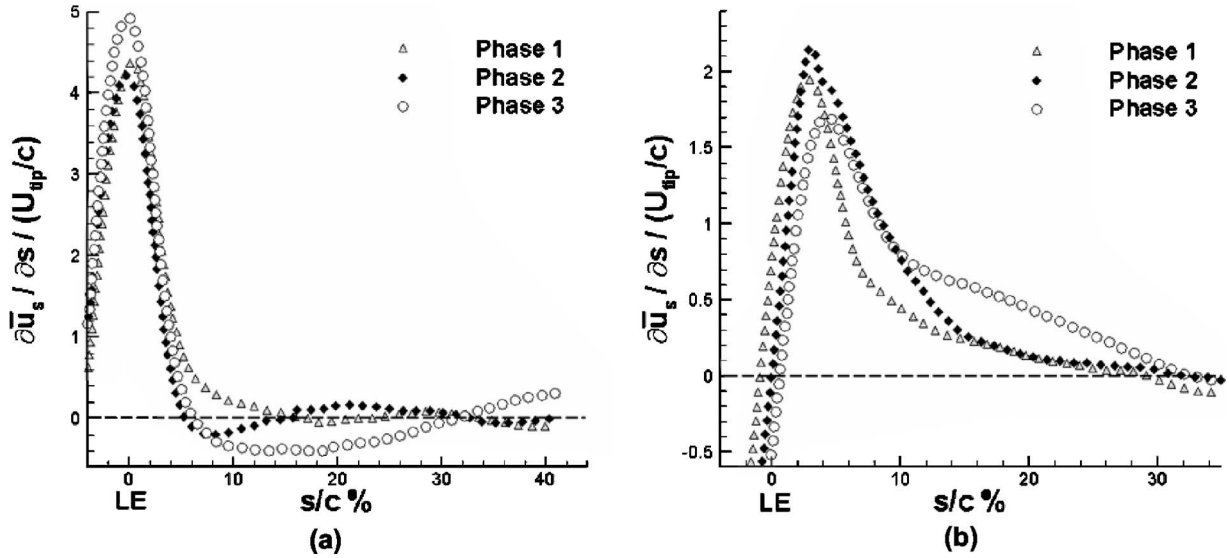

Fig. 5 Streamwise variation of $\partial \overline{u_s} / \partial s$ along the rotor blade (*a*) suction side and (*b*) pressure side, 1.5% chord-lengths away from the surface

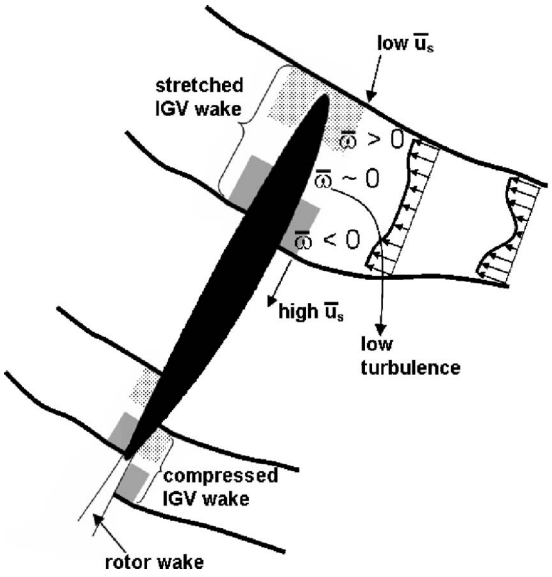

Fig. 6 Representation of the process of extension and compression of the IGV wake as it sweeps the rotor blade

side it is only about 40% of the chordlength. This difference is caused by the higher advection velocity on the suction side. For example, near the leading edge, i.e., at $0<s/c<0.05$, the magnitude of $\overline{v_r}$ on the suction side is almost twice the velocity on the pressure side (Fig. 2). Second, as noted before, both wake segments, but especially the one traveling along the suction side, are extended/stretched in the streamwise direction due to differences in the streamwise velocity between the leading and trailing parts of the wake (Hodson [28]). In phase 3, the trailing positive vorticity layer intersects with the blade at the point of minimum $\overline{v_r}$. This part of the wake is therefore "trapped," while the leading part of the wake, at higher s/c, is accelerated through a region of high lateral momentum. Stretching of the wake increases the spatial separation between the positive and negative vorticity layers, causing the formation of a wide region of very low vorticity between them. Also, the negative layer is clearly wider than the positive layer. Due to the lower advection velocity, the gap between vorticity layers on the pressure side is significantly smaller.

The trends are reversed as the IGV wake approaches the diffusion region near the trailing edge of the blade, which is characterized by decreasing advection velocity. As a result, the trailing part of the IGV wake moves faster than the forward part, decreasing

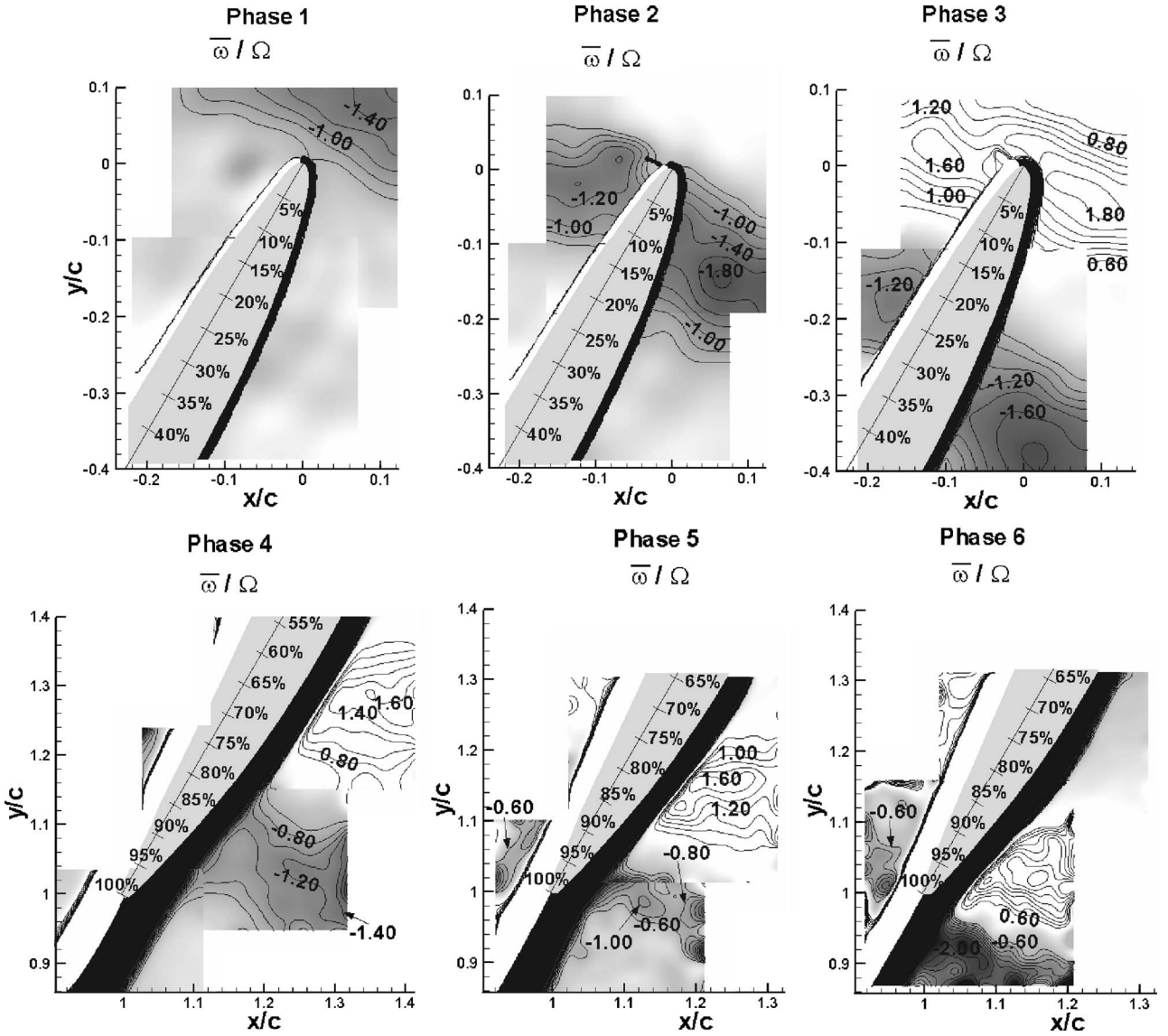

Fig. 7 Distribution of normalized $\bar{\omega}$ for different phases. Top row: phases 1 to 3 (leading edge region). Bottom row: phases 4 to 6 (trailing edge region). Contour increment is 0.2.

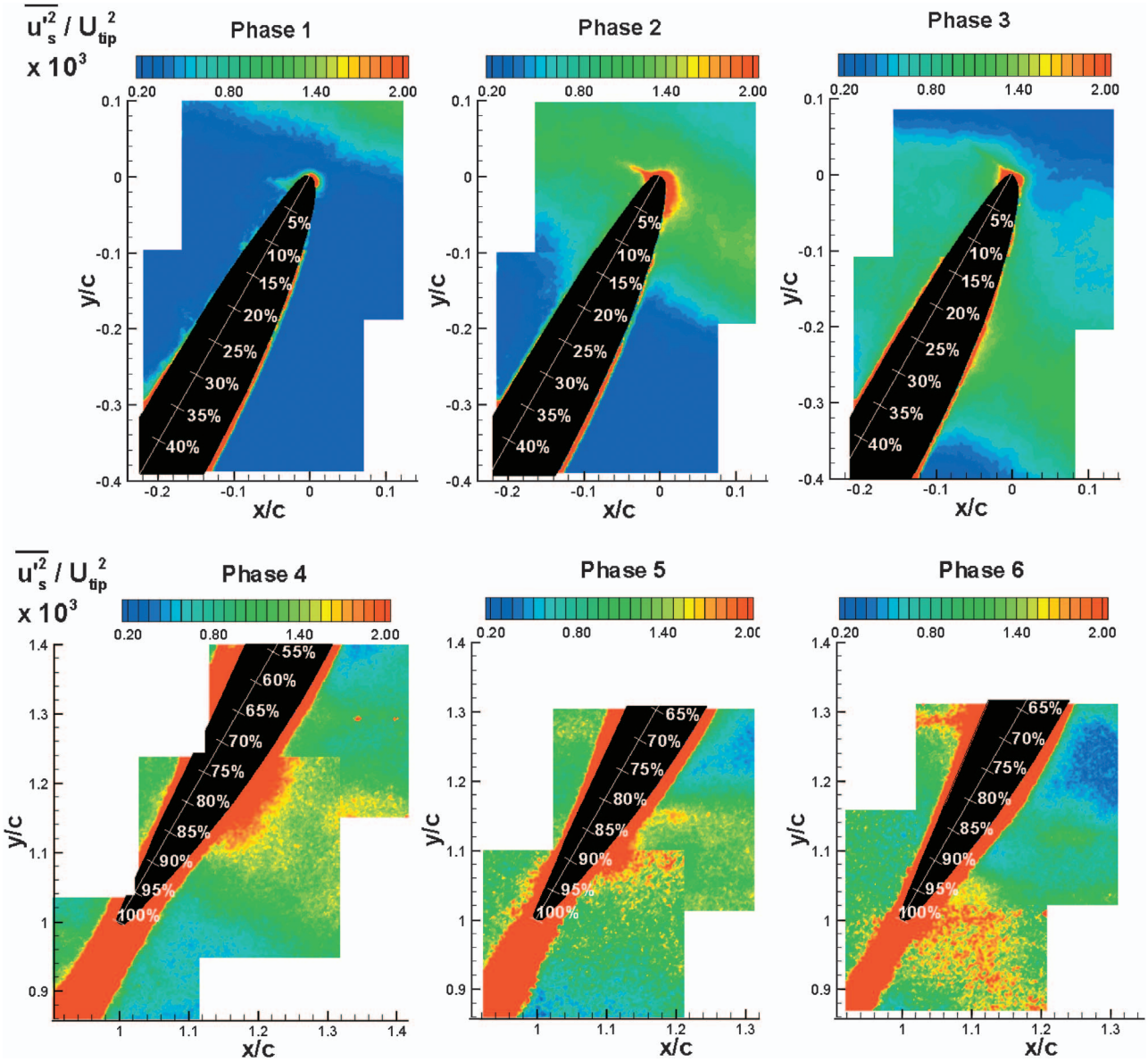

Fig. 8 Distribution of normalized $\overline{u_s'^2}$ for different phases. Top row: phases 1 to 3 (leading edge region). Bottom row: phases 4 to 6 (trailing edge region).

the overall thickness of the wake, the width of the positive and negative vorticity layers, and the gap between them. In phase 6, the wake is impinging near the trailing edge of the blade, and its width decreases to about 25% of the chordlength, i.e., to about half the width near the leading edge. Note also that in phase 6 the difference in advection velocity across the blade causes a phase lag between the wake segments on the pressure and suction sides. Since the other end of the pressure side segment passes by the suction side of the previous blade, the wake segment becomes elongated within the rotor passage, consistent with the observations of Zaccaria and Lakshminarayana [13]. The phase lag also causes differences in axial velocity across the rotor wake below the blade trailing edge. As shown in Chow et al. [18], these differences shear the rotor wake, and generate highly turbulent kinks.

Modifications to the Turbulence Within the IGV Wake. Wake impingement exposes the rotor blade to a band with elevated turbulence that peaks close to the center of the wake, as shown by the distributions of turbulent kinetic energy in Fig. 2(*c*). The IGV wake turbulence becomes highly nonuniform and anisotropic, as a result of exposure to the local, phase-dependent strain field generated by the rotor blade.

In this section we first demonstrate these non-uniformities, and then discuss possible causes for their occurrence. The results are presented in coordinate system (s,n) in which s is aligned with the local phase averaged streamlines in the rotor frame of reference (Fig. 1(*b*)). Figures 8 and 9 show the distribution of streamwise and normal Reynolds stresses, $\overline{u_s'^2}$ and $\overline{v_n'^2}$, respectively, near the leading edge in phases 1–3, and near the trailing edge in phases 4–6.

As we examined these contours we were initially perplexed by what seemed to be inconsistent and sometimes-conflicting trends. Among them, and this is an incomplete list, one can mention the substantially higher velocity fluctuations in phases 4–6 (compared to phases 1–3), the increase of the wall-parallel component and decrease of wall-normal component near the leading edge of the blade and the complex distribution of $\overline{v_n'^2}$ in phase 3. The main

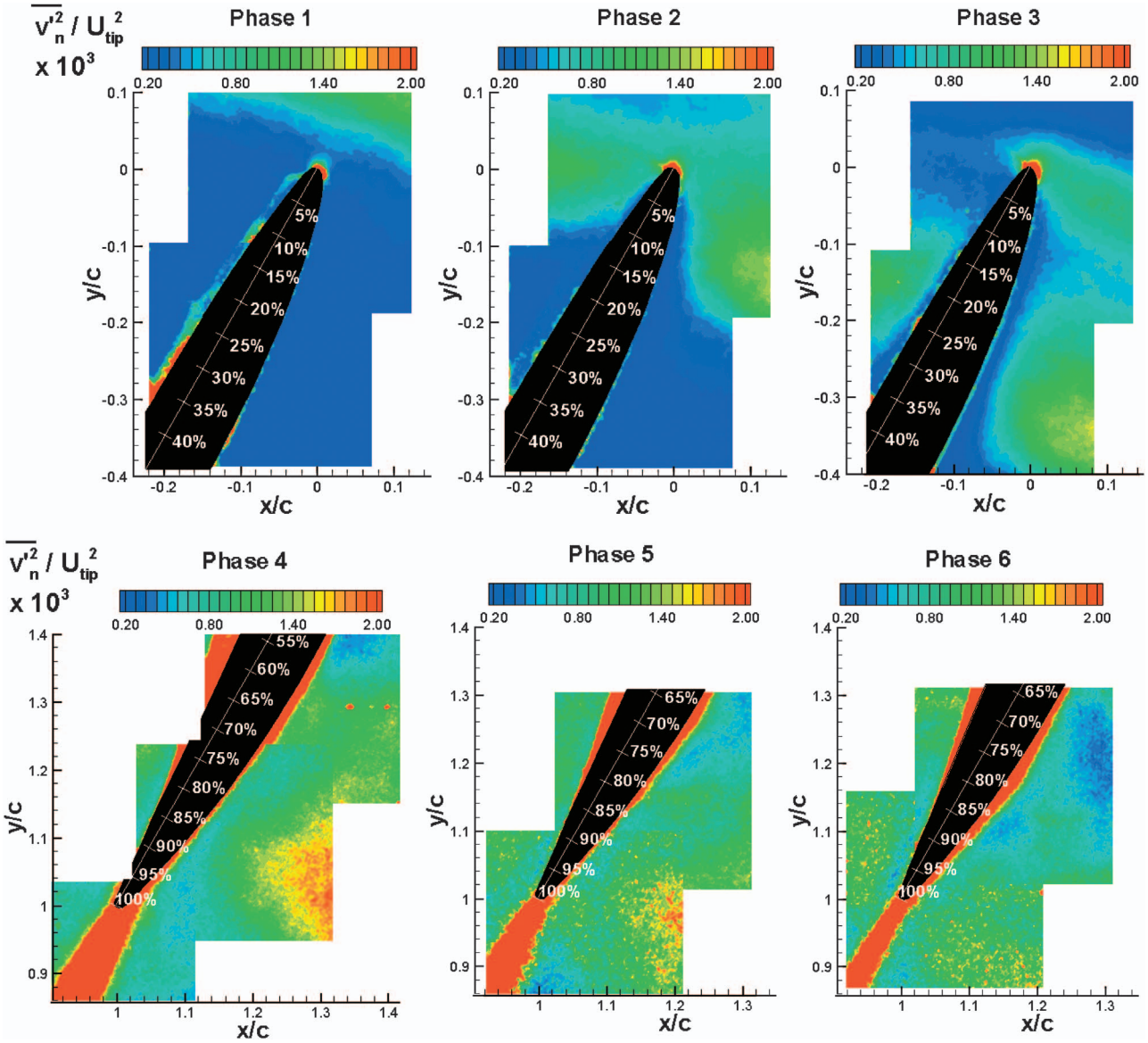

Fig. 9 Distribution of normalized $\overline{v_n'^2}$ for different phases. Top row: phases 1 to 3 (leading edge region). Bottom row: phases 4 to 6 (trailing edge region).

reason for these confusing trends is the simultaneous existence of several mechanisms that alter the turbulence level within the IGV wake. Included are straining and destraining by the mean flow around the blade, diffusion in the blade passage and wall blockage. We will examine the effect of each mechanism separately. In doing so, we will relate the distribution of the Reynolds stresses to the magnitude and orientation of the principal strain field in different regions. Figure 10 is introduced to illustrate the principal strain orientations in these regions, and will be often referred to in the following discussions.

Effect of streamwise diffusion, compression and extension. Axial flow compressors rely on aerodynamic diffusion to achieve pressure rise. The diffusion process substantially alters the turbulence within wake segments traveling through the rotor passage. In a recent paper, De La Riva et al. [22] examine the behavior of initially isotropic grid turbulence flowing through a compressor cascade. They observe that diffusion increases the streamwise velocity fluctuations and suppresses the wall-normal fluctuations. They also show that the evolution of turbulence through the cascade is quantitatively consistent with predictions of rapid distortion theory (RDT, Batchelor [29]). RDT may be applied to the turbulence propagating through the rotor blade passage of a real turbomachine provided the parameter Sk/ε, where S is the strain magnitude and ε is the dissipation rate, is large (k/ε is the time scale of large scale turbulence, the so-called eddy turnover time). The present distributions of normal stresses are consistent with the trends predicted by RDT. For example, starting with phases 4 to 6, $\overline{u_s'^2}$ increases and $\overline{v_n'^2}$ decreases in the diffusion dominated region, in the aft part of the rotor blade passage. This region is characterized by $\partial \overline{u_s}/\partial s < 0$, i.e., the mean flow is compressed in the streamwise direction and extended in the normal direction (region 1 in Fig. 10). According to RDT prediction, such a process increases the streamwise velocity fluctuations, and suppresses the normal fluctuations (e.g., Chen et. al [30]). An increase in streamwise component can also be predicted by examining the relevant production terms in the Reynolds stress transport equations (Pope [31]). In the diffusion region (no. 1), $-\overline{S_{ss}}\,\overline{u_s'^2}$ is positive and large ($\overline{S_{ij}}$ is the phase averaged strain rate), contributing to an increase in streamwise fluctuations, whereas $-\overline{S_{nn}}\,\overline{v_n'^2}$ is negative, indicating a decrease in the wall-normal turbulence level. Away from the wall, in region 1, s and n are almost aligned with the principal

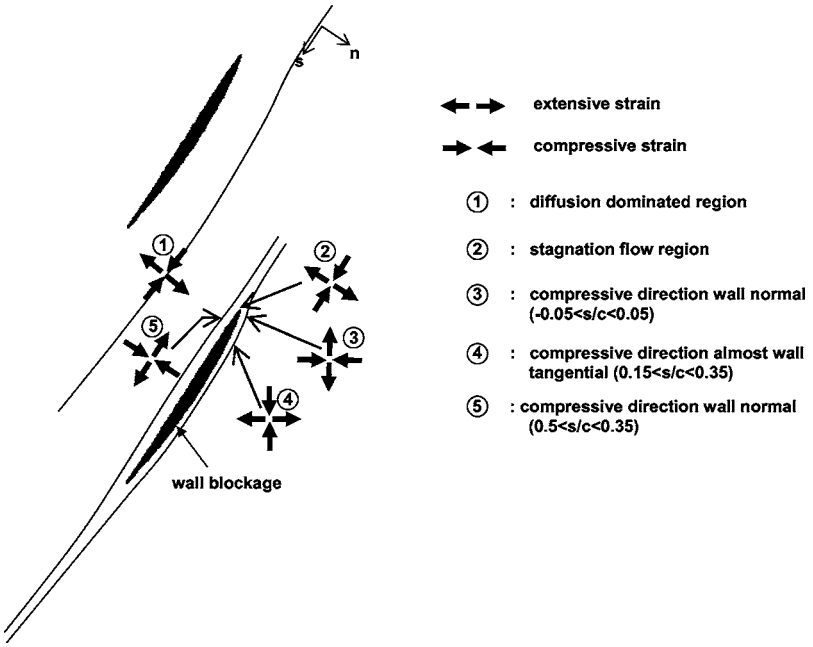

Fig. 10 Representation of the orientation of the principal strain in different regions around the leading edge and within the rotor passage

directions, and the values of $\overline{u_s' v_n'}$ are small. Thus, only normal components contribute to the production.

Due to the diffusion in the previous passage, the IGV wake turbulence arriving in phases 1 and 2 must already have elevated $\overline{u_s'^2}$ and suppressed $\overline{v_n'^2}$. This trend becomes clearly evident by comparing the distributions of $\overline{u_s'^2}$ and $\overline{v_n'^2}$ in phase 2, especially near and to the left of the pressure side of the blade, i.e., within the passage that includes the previous blade. Clearly, $\overline{u_s'^2} > \overline{v_n'^2}$ in regions that are not affected significantly by the strain field generated near the leading edge of the blade (details follow). On the pressure side this trend persists also in phase 3, but the picture becomes more complicated due to leading edge effects.

Effect of straining on the Reynolds stress distributions. Following the logic introduced in the previous section, the streamwise fluctuations should be suppressed in a region with $\overline{S_{ss}} > 0$, i.e., when the streamwise component is stretched. Since the phase averaged flow at midspan is almost two dimensional, axial stretching is accompanied by normal compression, $\overline{S_{nn}} < 0$ (continuity). Thus, in a region with streamwise stretching one should expect to observe a decrease in the streamwise fluctuations, and an increase in the wall-normal turbulence. To demonstrate this trend in the present data, let us focus on the region with elevated wall-normal Reynolds stress in phase 3 that extends to the right of the leading edge, between $s/c = -0.05$ and $s/c = 0.05$ (region 3 in Fig. 10). In the same region the streamwise turbulence intensity is considerably reduced. We conjecture that this phenomenon is caused by enhanced wall-normal turbulence production, which is driven by streamwise stretching and wall-normal compression of the turbulence. In order to support this claim, Fig. 11 shows the distributions of the compressive, $\overline{S_c}$, and extensive, $\overline{S_e}$, mean principal strain rates. In reality they represent the in-plane projection of the eigenvalues of the strain rate tensor. Due to the almost two dimensional nature of the flow at midspan, the compressive and extensive eigenvalues have almost equal magnitude, and opposite signs. The thin lines in each figure indicate the corresponding principal directions of compression and extension. As is evident, the highest strain rates, both compressive and extensive, are distributed around the leading edge. On the suction side, in region 3, the principal direction of compression is, for the most part, horizontal while the direction of extension is vertical. Also note that, in this region, because of the blade geometry, the wall-normal velocities are aligned with the direction of compression, while the wall-parallel fluctuations are aligned with the direction of extension. Thus the compressed, wall-normal fluctuations should increase, while the stretched wall-parallel fluctuations should decrease. In order to further elucidate this point, we project the Reynolds stress tensor onto a coordinate system aligned with principal directions of the strain rate tensor. The distributions of the normal Reynolds stresses, $\overline{u_c'^2}$ and $\overline{u_e'^2}$, in the compressive and extensive principal directions, respectively, are presented in Fig. 12. Clearly, in region 3, $\overline{u_c'^2}$ is significantly larger than $\overline{u_e'^2}$. The turbulence is enhanced along the principal direction of compression, which in this case is normal to the local streamwise direction.

With reference to Fig. 11, one can also see that on the suction side, in the $0.15 < s/c < 0.35$ region (region 4 in Fig. 10), the principal directions of compression and extension are rotated about 90° compared to their orientation to the right of the leading edge. Thus, in this area, the compressive strain rate is almost aligned with the streamwise direction, namely the streamwise velocity fluctuations should increase, and the (stretched) wall-normal fluctuations should be suppressed. Indeed, in this region $\overline{u_s'^2} > \overline{v_n'^2}$. Furthermore, when projected onto the principal directions of strain, Fig. 12 shows that $\overline{u_c'^2}$ is significantly larger than $\overline{u_e'^2}$, i.e., the high normal stresses are clearly aligned with the compressive direction. However, the strain rates in this region are lower than those at the leading edge. Therefore, the effect of straining on turbulence production must also diminish (quantitative results follow, see Fig. 13), and may be even overwhelmed by another mechanism, such as advection of turbulence generated before.

Along the pressure side of the blade (region 5 in Fig. 10), the direction of compression is normal to the wall while the extension is oriented in the streamwise direction. In spite of these trends, the stretched $\overline{u_s'^2}$ is larger than the compressed $\overline{v_n'^2}$, in contrast to the expected local production and/or RDT predictions. To explain this contradiction, note that the strain rates on the pressure side are lower than those on the suction side, i.e., the turbulence production rate is lower. Furthermore, as noted before, the IGV wake segment propagating along the pressure side has already experi-

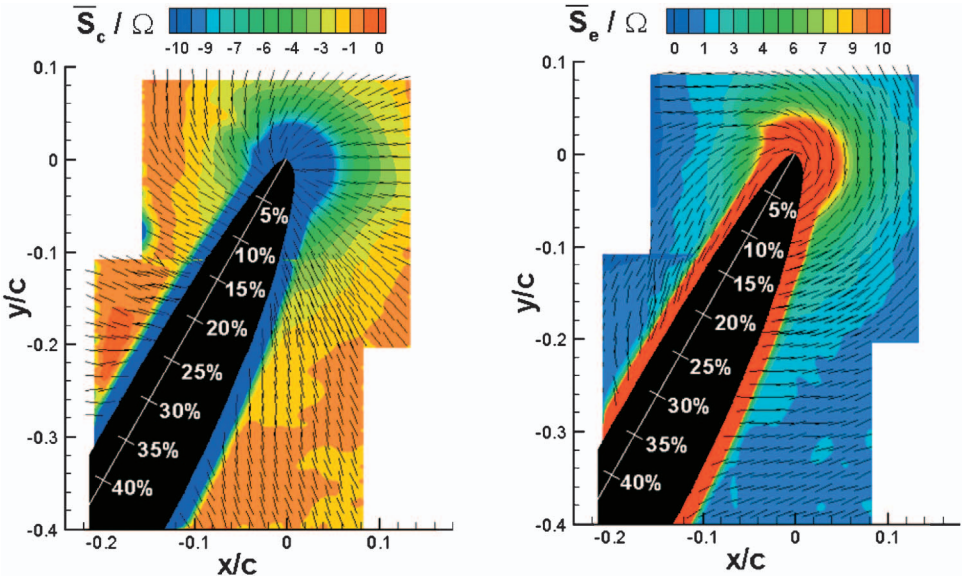

Fig. 11 Compressive and extensive principal strain rates distributions in phase 3. The lines indicate the principal directions of compression and extension.

enced the effects of diffusion (region 1), which enhances the streamwise component and suppresses the normal fluctuations. The local production is too weak to overcome the effects of prior diffusion.

Effects of wall blockage. The turbulence near the blade is additionally modified by the well-known "wall blockage" phenomenon (Perot and Moin [32]), which suppresses the wall-normal turbulence, and increases the wall-parallel (streamwise) fluctuations. This phenomenon has been studied theoretically (Hunt and Graham [33]), experimentally (e.g., Uzkan et al. [34] and Thomas et al. [35]), and numerically (Perot and Moin [32]), typically under simplified conditions of no mean shear. As Perot and Moin [32] show, wall blockage causes intercomponent turbulent kinetic energy transfer from the wall-normal to the wall-parallel component. The main contributor to this effect is the pressure strain term in the Reynolds stress transport equations. De La Riva et al. [22] show that wall blockage affects the distribution of initially isotropic turbulence while passing near the blades of a compressor cascade. Although their setup does not involve passage of an IGV wake, they do demonstrate that this phenomenon is relevant to turbulence within turbomachines. The present distributions in phase 3 clearly demonstrate suppression of the wall-normal component and enhancement of the wall-parallel component in thin layers located near the wall but outside of the boundary layer. This phenomenon persists along both the pressure and suction sides of the blade, especially in the $0.15 < s/c < 0.3$ region. One can also observe the effects of wall blockage on the distributions of near-wall turbulence in phases 4–6, especially along the suction side of the blade.

Effect of production rate. Still focusing on phase 3, one cannot avoid noticing the region with low turbulence between $s/c = 0.05$

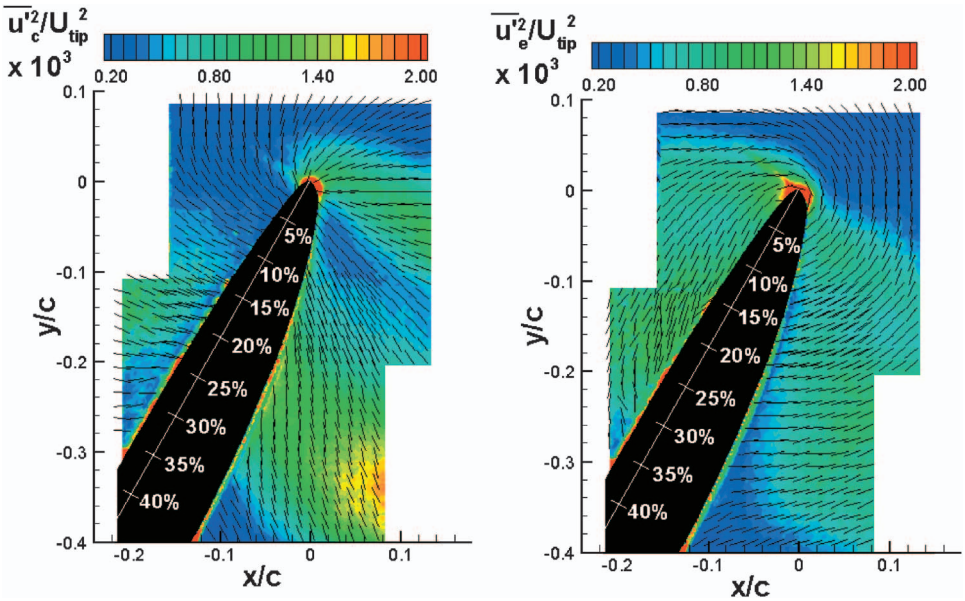

Fig. 12 Distribution of Reynolds stresses locally aligned with the principal directions of compression and extension. The lines indicate the principal directions of compression and extension.

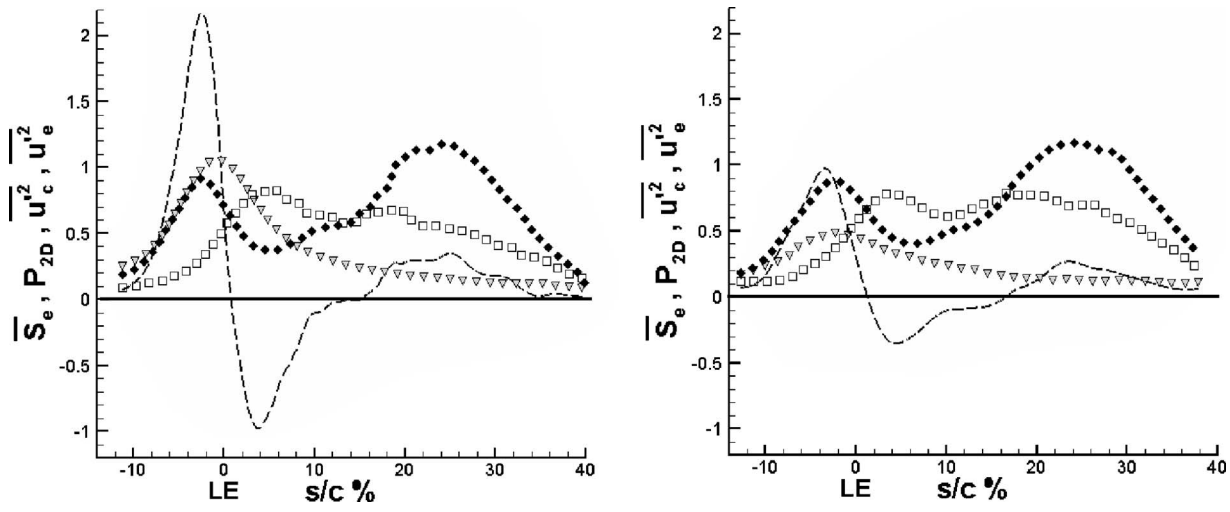

Fig. 13 Streamwise distribution of $\nabla\overline{S_e}/(10\Omega)$, ♦ $(\overline{u_c'^2}/U_{tip}^2)\times10^3$, □ $(\overline{u_e'^2}/U_{tip}^2)\times10^3$, -- $P_{2D}\times10^3/(U_{tip}^3/c)$. Distance from suction surface in chord lengths: (*a*) 3% ; (*b*) 6%. Phase 3.

and $s/c=0.15$, on the suction side of the blade (Figs. 8, 9, and 12). The presence of this region is puzzling considering that this area is located within what we consider to be part of the wake. This low turbulence domain coincides with the low mean vorticity area, in the gap created as the negative vorticity layer propagates at a high streamwise velocity, while the positive layer is almost stuck near the leading edge (Figs. 6 and 7). To explain the decreased turbulence level there, we calculate the distribution of production and show that it is negative, i.e., the local non-equilibrium conditions cause transfer of energy from the turbulence to the mean flow. Since we only have two-dimensional data, we can only calculate the "two-dimensional production" P_{2D} (Chow et al. [36]), keeping in mind that out-of plane terms are missing. However, as long as we confine ourselves to mid-span, where the out-of-plane mean shear is most likely much lower than the in-plane velocity gradients, the results should at least provide the correct trends. For the rotor near-wake region, recent 3D data confirm our assumption (Uzol et al. [27]). In a coordinate system aligned with the principal strain directions

$$P_{2D}=-\overline{S_c}\,\overline{u'^2_c}-\overline{S_e}\,\overline{u'^2_e} \tag{4}$$

Under the assumption of a quasi-two-dimensional flow $\overline{S_c}\approx-\overline{S_e}$, thus

$$P_{2D}\approx\overline{S_e}(\overline{u'^2_c}-\overline{u'^2_e}) \tag{5}$$

The distribution of production, along with the components contributing to it along two streamlines, is presented in Fig. 13. The production can be positive or negative depending on the relative magnitude of $\overline{u_c'^2}$ and $\overline{u_e'^2}$. In equilibrium conditions $\overline{u_c'^2}>\overline{u_e'^2}$, due to the compression. Negative production would occur under non-equilibrium conditions, e.g., when the direction of strain changes rapidly, while the turbulence requires time to respond. In such a case, locally $\overline{u_e'^2}>\overline{u_c'^2}$ and the production becomes negative. In the present flow, the negative production region extends between $s/c=0.01$ and $s/c=0.15$, almost coincident with the low turbulence region in the transition between region 3 and 4 shown in Fig. 10. As is evident, the directions of compression and extension switch by almost 90 deg (Figs. 11 and 12), creating the non-equilibrium conditions.

We conclude the discussion by focusing on the high positive production region located just above the leading edge (region 2 in Fig. 10). Here, Fig. 13(*a*) shows that along the 3% streamline, there is a narrow domain with elevated $\overline{u_c'^2}$, low $\overline{u_e'^2}$ and high S, causing very large production. Along the 6% streamline (Fig. 13(*b*)) the strain is lower, and so is the production. Along the blade, the production becomes positive again only at $s/c>0.15$, i.e., at region 4 (Fig. 10). As noted before the production here is quite low.

Conclusions

This paper presents and discusses the results of an experimental investigation of the flow structure and turbulence around a rotor blade operating downstream of a row of inlet guide vanes (IGV). We focus on the interaction of the IGV wake with the flow near the rotor blade, at midspan. High-resolution 2D PIV data is obtained at several rotor blade phases, three of which focus on the flow near the leading edge, while another series examines the effect of wake impingement on the flow near the trailing edge. The results are presented in two parts: the first concentrates on the phase-dependent variations of the velocity field around the rotor leading edge, and the second focuses on the modification to the flow structure and turbulence within the impinging IGV wake.

Wake impingement causes significant variations in the distribution of $\overline{u_s}$ on both sides of the blade. On the suction side, near the leading edge, the flow tends to decelerate $(\partial\overline{u_s}/\partial s<0)$ within the wake impingement region. On the pressure side, near the leading edge, wake impingement makes the streamwise (in rotor reference frame) velocity gradients milder. Further below, within the area influenced by the wake, $\overline{u_s}$ increases monotonically. Due to the spatially nonuniform velocity distribution, especially on the suction side, the wake deforms while propagating along the blade, expanding near the leading edge and shrinking again to about one half of its maximum width near the trailing edge. This effect is weaker on the pressure side.

While being exposed to the nonuniform strain field within the rotor passage, the turbulence within the impinging IGV wake becomes spatially nonuniform and highly anisotropic. This paper attempts to isolate specific mechanisms that contribute to the observed trends, although in some cases several mechanisms occur simultaneously. The following regions have been identified.

- Diffusion dominated region (no. 1, Fig. 10): Consistent with RDT, due to the deceleration of the flow in the aft part of the rotor passage, the compressed streamwise velocity fluctuations are enhanced, while the stretched wall-normal fluctuations are suppressed. By the time the wake exits the rotor passage (phase 6), away from the wall, the values of $\overline{u_s'^2}$ are 30% larger than those of $\overline{v_n'^2}$. Subsequently, the wall-normal component also increases, but not to the same ex-

tent, presumably due to transfer of energy from the more powerful component to the weaker one (isotropization).
- Stagnation flow region (no. 2): The immediate vicinity of the leading edge is characterized by large positive production associated with the high strain rate, resulting in elevated turbulence level. Enhancement of $\overline{u_s'^2}$ occurs along the compressed streamwise direction, while $\overline{v_n'^2}$, which is aligned with the extensive principal direction, decreases.
- Leading edge region (no. 3): Along the suction side of the blade, away from the immediate vicinity of the stagnation point, the streamwise velocity component is stretched and the wall-normal component is compressed. Thus, consistent with RDT predictions, the stretched wall-parallel fluctuations are considerably lower than the compressed wall-normal fluctuations.
- Negative production region (between no. 3 and no. 4): Here, the wake turbulence is strikingly reduced due to the local nonequilibrium conditions caused by a rapid change in the orientation (almost 90 deg) of the compressive and extensive strains. Consequently, the production rate becomes negative, thus reducing the turbulent kinetic energy.
- Wall blockage region: Near the wall but outside of the boundary layer, the blockage reduces the wall-normal fluctuations.

As is evident from the present observations, the availability of data covering substantial regions around the blade at different phases enables us to explore and understand causes and effects in wake-blade interactions. we hope that the resulting insight will enable us to develop improved tools for predicting the dynamics of turbulence within turbomachines.

Acknowledgment

This project is sponsored in part by ONR under Grant No. N00014-99-1-0965, managed by P. Purtell and in part by AFOSR under Grant No. F49620-01-1-0010, managed by T. Beutner. The ONR program is part of a joint effort involving W. Blake (NSWC/Carderock), H. Atassi (U. of Notre Dame) and Y.T. Lee (NSWC/Carderock). We would like to thank Yury Ronzhes and Stephen King.

Nomenclature

x = axial coordinate
y = lateral (almost circumferential) coordinate
s = streamwise coordinate (rotor frame of reference)
n = wall-normal coordinate (rotor frame of reference)
c = chord length
ϕ = rotor phase angle
N = number of instantaneous vector maps
U_{tip} = rotor blade tip speed
$\overline{u}$ = axial mean velocity
$\overline{v_r}$ = lateral (almost circumferential) mean velocity (in the rotor frame of reference)
$\overline{u_s}$ = streamwise mean velocity
u_s' = streamwise velocity fluctuation
v_n' = wall-normal velocity fluctuation
u_c' = velocity fluctuation along principal direction of compression
u_e' = velocity fluctuation along principal direction of extension
k = turbulent kinetic energy
$\bar{\omega}$ = mean vorticity
$\overline{S_{ij}}$ = mean strain rate tensor
S = strain magnitude
$\overline{S_{ss}}$, $\overline{S_{nn}}$ = streamwise and wall-normal mean strain rate tensor components
$\overline{S_c}$, $\overline{S_e}$ = compressive and extensive principal strain rates
P_{2D} = two-dimensional production rate of turbulent kinetic energy
Ω = rotor angular velocity
θ_w = momentum thickness
φ = flow coefficient

References

[1] Rai, M. M., 1987, "Navier-Stokes Simulation of Rotor/Stator Interaction Using Patched and Overlaid Grids," J. Propul. Power, **3**, pp. 387–396.
[2] Ho, Y. H., and Lakshminarayana, B., 1995, "Computation of Unsteady Viscous Flow Through Turbomachinery Blade Row due to Upstream Rotor Wakes," ASME J. Turbomach., **117**, pp. 541–552.
[3] Valkov, T. V., and Tan, C. S., 1998, "Effect of Upstream Rotor Vortical Disturbances on the Time-Average Performance of Axial Compressor Stators: Part I-Framework of Technical Approach and Wake-Stator Blade Interactions," ASME J. Turbomach., **121**, pp. 377–386.
[4] Chen, T., Vasanthakumar, P., and He, L., 2001, "Analysis of Unsteady Blade Row Interaction Using Nonlinear Harmonic Approach," J. Propul. Power, **17** (3), pp. 651–658.
[5] Gerolymos, G. A., Michon, G. J., and Neubauer, J., 2002, "Analysis and Application of Chorochronic Periodicity in Turbomachinery Rotor/Stator Interaction Computations," J. Propul. Power, **18** (6), pp. 1139–1152.
[6] Dong, Y., and Cumpsty, N. A., 1990, "Compressor Blade Boundary Layers—Part II: Measurements With Incident Wakes," J. Turbomach., **112** (2), pp. 231–240.
[7] Halstead, D. E., Wisler, D. C., Okiishi, T. H., Walker, G. J., Hodson, H. P., and Shin, H. W., 1997, "Boundary Layer Development in Axial Flow Compressors and Turbines—Part I: Composite Picture," J. Turbomach., **119** (1), pp. 114–127.
[8] Schobeiri, M. T., Ozturk, B., and Ashpis, D. E., 2003, "On the Physics of Flow Separation Along the Low Pressure Turbine Blade Under Unsteady Flow Conditions," Proceedings of ASME Turbo Expo 2003, Power for Land, Sea and Air, June 16-19, 2003, Atlanta, GA.
[9] Shin, Y. H., Elder, R. L., and Bennett, I., 2003, "Boundary Layer Measurement on the Blade Surface of a Multi-Stage Axial Flow Compressor," Proceedings of ASME Turbo Expo 2003, Power for Land, Sea and Air, June 16-19, 2003, Atlanta, GA.
[10] Soranna, F., Chow, Y. C., Uzol, O., and Katz, J., 2004, "Rotor Boundary Layer Response to an Impinging Wake," Proceedings of ASME Heat Transfer/Fluids Engineering Summer Conference, Charlotte, NC, July 11-15.
[11] Smith, J. H., Jr., 1966, "Wake Dispersion In Turbomachines," ASME J. Basic Eng., **88D**, pp. 688–690.
[12] Kerrebrock, J. L., and Mikolajczak, A. A., 1970, "Intra-Stator Transport of Rotor Wakes and Its Effect on Compressor Performance," ASME J. Eng. Power, **92**, pp. 359–368.
[13] Zaccaria, M. A., and Lakshminarayana, B., 1995, "Unsteady Flow Field due to Nozzle Wake Interaction With the Rotor in an Axial Flow Turbine—Part 1: Rotor Passage Flow Field," ASME Paper No. 95-GT-295.
[14] Van Zante, D. E., Adamczyk, J. J., Strazisar, A. J., and Okiishi, T. H., 1997, "Wake Recovery Performance Benefit in a High-Speed Axial Compressor," ASME Paper No. 97-GT-535.
[15] Adler, D., and Benyamin, R., 1999, "Experimental Investigation of the Stator Wake Propagation Inside the Flow Passages of an Axial Gas Turbine Rotor," International Journal of Turbo and Jet Engines, **16**, pp. 193–206.
[16] Sentker, A., and Riess, W., 2000, "Experimental Investigation of Turbulent Wake-Blade Interaction in Axial Compressors," Int. J. Heat Fluid Flow, **21**, pp. 285–290.
[17] Sanders, A. J., Papalia, J., and Fleeter, S., 2002, "Multi-Blade Row Interactions in a Transonic Axial Compressor—Part I: Stator Particle Image Velocimetry (PIV) Investigation," ASME J. Turbomach., **124** (1), pp. 10–18.
[18] Chow, Y.-C., Uzol, O., and Katz, J., 2002, "Flow Non-Uniformities and Turbulent "Hot Spots" Due to Wake-Blade and Wake-Wake Interactions in a Multistage Turbomachine," ASME J. Turbomach., **124** (4), pp. 553–563.
[19] Uzol, O., Chow, Y.-C., Katz, J., and Meneveau, C., 2002, "Experimental Investigation of Unsteady Flow Field Within a Two Stage Axial Turbomachine Using Particle Image Velocimetry," ASME J. Turbomach., **124** (4), pp. 542–552.
[20] Hobson, G. V., and Shreeve, R. P., 1993, "Inlet Turbulence Distortion and Viscous Flow Development in a Controlled-Diffusion Compressor Cascade at Very High Incidence," J. Propul. Power, **9** (3), pp. 397–404.
[21] Hobson, G. V., Wakefield, B. E., and Roberts, W. B., 1996, "Turbulence Amplification With Incidence at the Leading Edge of a Compressor Cascade," ASME Paper No. 96-GT-409.
[22] De La Riva, D. H., Devenport, W. J., Chittiappa, M., and Glegg, S. A. L., 2004,"Behavior of Turbulence Flowing Through a Compressor Cascade," AIAA J., **42** (7), pp. 1302–1313.
[23] Uzol, O., Chow, Y. C., Katz, J., and Meneveau, C., 2002, "Unobstructed PIV Measurements Within an Axial Turbo-Pump Using Liquid and Blades With Matched Refractive Indices," Exp. Fluids , **33** (6), pp. 909–919.

[24] Roth, G. I., Mascenik, D. T., and Katz, J., 1999, "Measurements of The Flow Structure and Turbulence Within A Ship Bow Wave," Phys. Fluids, **11**, (11), pp. 3512–3523.
[25] Roth, G. I., and Katz, J., 2001, "Five Techniques for Increasing the Speed and Accuracy of PIV Interrogation," Meas. Sci. Technol. **12**, pp. 238–245.
[26] Sridhar, G., and Katz, J., 1995, "Drag and Lift Forces on Microscopic Bubbles Entrained by a Vortex," Phys. Fluids **7**, pp. 389–399.
[27] Uzol, O., Chow, Y. C., Soranna, F., and Katz, J., 2004, "3D Structure of a Rotor Wake at Mid-Span and Tip Regions," Proceedings of 34th AIAA Fluid Dynamics Conference and Exhibit, June 28-July 1.
[28] Hodson, H. P., 1985, "Measurements of Wake-Generated Unsteadiness in the Rotor Passages of Axial Flow Turbines," J. Eng. Gas Turbines Power, **107**, pp. 467–476.
[29] Batchelor, G. K., and Proudman, I., 1954, "The Effect of Rapid Distortion on a Fluid in Turbulent Motion," Q. J. Mech. Appl. Math., **7** (1), pp. 83–103.
[30] Chen, J., Katz, J., and Meneveau, C., 2004, "Study of Scale-Interactions in Strained and Destrained Turbulence," Proceedings of 2004 ASME Heat Transfer/Fluids Engineering Summer Conference, July 11-15.
[31] Pope, S. B., 2000, *Turbulent Flows*, Cambridge University Press, Cambridge, UK.
[32] Perot, B., and Moin, P., 1995, "Shear-Free Turbulent Boundary Layers. Part 1. Physical Insights Into Near-Wall Turbulence," J. Fluid Mech., **295**, pp. 199–227.
[33] Hunt, J. C. R., and Graham, J. M. R., 1978, "Free-Stream Turbulence Near Plane Boundaries," J. Fluid Mech., **84**, pp. 209–235.
[34] Uzkan, T., and Reynolds, W. C., 1967, "A Shear-Free Turbulent Boundary Layer," J. Fluid Mech., **28**, pp. 803–821.
[35] Thomas, N. H., and Hancock, P. E., 1977, "Grid Turbulence Near a Moving Wall," J. Fluid Mech., **82**, pp. 481–496.
[36] Chow, Y. C., Uzol, O., and Katz, J., 2003, "On the Flow and Turbulence Within the Wake and Boundary Layer of a Rotor Blade Located Downstream of an IGV," Proceedings of ASME Turbo Expo 2003.

Local Heat/Mass Transfer Characteristics on a Rotating Blade With Flat Tip in Low-Speed Annular Cascade—Part I: Near-Tip Surface

Dong-Ho Rhee

Hyung Hee Cho
e-mail: hhcho@yonsei.ac.kr

Department of Mechanical Engineering,
Yonsei University,
Seoul 120-749, Korea

The present study focuses on local heat/mass transfer characteristics on the near-tip region of a rotating blade. To investigate the local heat/mass transfer on the near-tip surface of the rotating turbine blade, detailed measurements of time-averaged mass transfer coefficients on the blade surfaces were conducted using a naphthalene sublimation technique. A low speed wind tunnel with a single stage annular turbine cascade was used. The turbine stage is composed of sixteen guide plates and blades with spacing of 34 mm, and the chord length of the blade is 150 mm. The mean tip clearance is about 2.5% of the blade chord. The tested Reynolds number based on inlet flow velocity and blade chord is 1.5×10^5 and the rotational speed of blade is 255.8 rpm for the design condition. The result at the design condition was compared with the results for the stationary blade to clarify the rotational effect, and the effects of incoming flow incidence angle were examined for incidence angles ranging from −15 to +7 deg. The off-design test condition is obtained by changing the rotational speed maintaining a fixed incoming flow velocity. Complex heat transfer characteristics are observed on the blade surface due to the complicated flow patterns, such as flow acceleration, laminarization, transition, separation bubble and tip leakage flow. The blade rotation causes an increase of the incoming flow turbulence intensity and a reduction of the tip gap flow. At off-design conditions, the heat transfer on the turbine rotor changes significantly due to the flow acceleration/deceleration and the incoming flow angle variation. [DOI: 10.1115/1.2098756]

Introduction

The thermal load on the hot components in a gas turbine engine increases continuously with increasing turbine inlet temperature. As a result, hot components such as the combustor liner and the turbine vane/blade are exposed to severe operating conditions. Especially, the near-tip region and the tip surface of the turbine blade are typical regions that are subjected to the excessive thermal load since the turbine blade tip operates in the transitional environment between the rotating airfoil and the stationary flow path casing, which experiences some of the most extreme fluid-thermal conditions within the turbine [1].

In general, the blade surface, especially the two-dimensional flow region (around the midspan of the blade), has complex and nonuniform heat transfer characteristics related to the flow acceleration, transition and wake. Also, there are additional factors affecting the heat transfer on the blade and shroud such as periodic wakes from upstream vanes and vane/blade interaction due to blade rotation. In addition to the heat transfer characteristics mentioned above, near the tip and on the tip of the blade, extremely high heat transfer rates are observed because of flow acceleration and the thin boundary layer of tip gap flow. The leakage flow through the finite clearance between the tip and casing (shroud) is generated by the pressure difference between the pressure and suction sides of the blade. Also, the leakage flow discharged from the tip gap interacts with the mainstream (hot gases) near the suction side tip of the blade, which may cause excessive heat transfer on the surface. Thus the leakage flow has a strong influence not only on the stage aerodynamic performance but also on the structural durability of the blade as reported by Metzger et al. [2]. Therefore, to improve the reliability and durability of turbine blade, complex cooling techniques have been developed and used on the tip and near-tip regions. However, the region around the blade tip is still one of the weakest regions that need intensive cooling because the tip and near-tip regions are difficult to cool effectively due to the complicated geometry and flow patterns.

To develop the cooling technique and obtain more effective cooling performance, an accurate understanding of heat transfer characteristics is needed and this can be achieved more easily by investigating the heat transfer characteristics on the tip and on the near-tip region at the same time. In addition, various operating conditions should be taken into account for an accurate analysis.

The present study is primarily focused on the effects of blade rotation and off-design condition on both the tip and the near-tip surface heat transfer for the rotating blade under various conditions. This paper (Part I) focuses on local heat transfer characteristics on the blade surface and the local heat transfer on the tip and shroud surfaces is dealt with in Part II (Ref. [3]).

Many researchers have studied the heat transfer characteristics on the vane/blade, especially in the midspan (two-dimensional flow region) [4–8]. Also, the heat transfer on the endwall region has been investigated extensively. Goldstein and Spores [9] measured heat transfer coefficients on the endwall and Hermanson et al. [10] predicted the heat transfer on vane, blade and endwall and compared with experimental results. Recently, Giel et al. [11] presented the local heat transfer information on a highly loaded turbine blade without tip clearance for various mainflow condi-

Contributed by the International Gas Turbine Institute (IGTI) of ASME for publication in the JOURNAL OF TURBOMACHINERY. Manuscript received by IGTI, October 1, 2004; final manuscript received February 1, 2005. IGTI Review Chair: K. C. Hall. Paper presented at the ASME Turbo Expo 2005: Land, Sea, and Air, Reno, NV, June 6 – 9, 2005, Paper No. GT2005-68723.

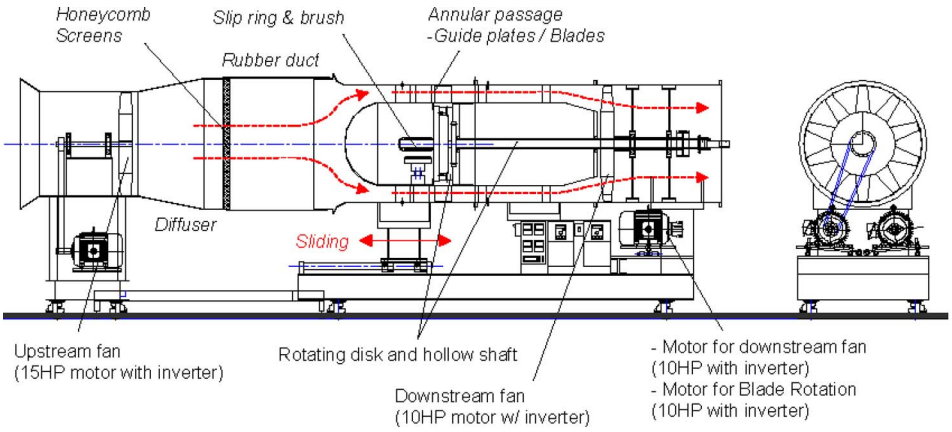

(*a*)

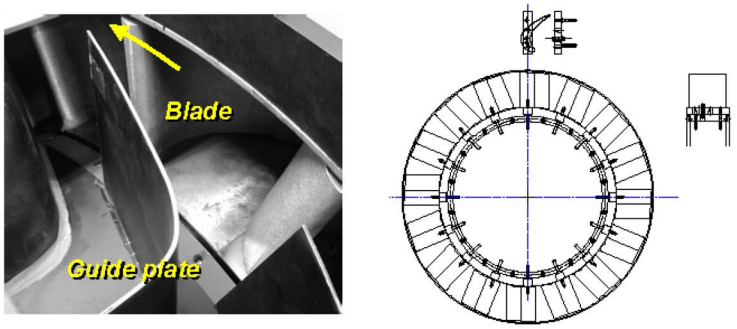

(*b*)

Fig. 1 Experimental apparatus and test section. (*a*) Experimental apparatus; (*b*) test section and rotating disk with blades.

tions in a transonic turbine cascade and reported that the secondary flow significantly increases suction side heat transfer rates near the endwalls.

As mentioned before, the near-tip region has also very complicated heat transfer patterns mainly due to the leakage vortex on the suction side and this causes a relatively high thermal load on the near-tip region. Therefore, several studies on near-tip surface heat transfer have been carried out by some researchers in recent years. Kwak and Han [12] measured detailed heat transfer coefficients on the near-tip surface, tip and shroud in a stationary linear turbine cascade using a transient TLC measurement technique. Jin and Goldstein [13] conducted experiments to investigate the local heat transfer characteristics on the near-tip surface for a low speed stationary linear turbine cascade using a naphthalene sublimation method. In their study, complex distributions of mass transfer coefficients are observed due to the passage and tip leakage vortices. Kwon et al. [14] also reported the effect of tip leakage flow on the blade surface heat transfer.

As reviewed, most of the previous studies have dealt with the tip heat transfer or the blade surface heat transfer separately under limited operating conditions. However, to figure out and understand detailed heat transfer characteristics more precisely, complementary analysis based on the local heat transfer information on the near-tip region, tip and shroud should be done. Therefore, in this study, heat transfer on the tip, shroud and the near-tip surface of the blade is considered together for the rotating blade at various conditions.

In this paper (Part I), the heat/mass transfer characteristics on the blade surface are investigated. First, basic heat transfer characteristics for a stationary blade are examined and the effect of blade rotation is analyzed by comparing the result for a rotating blade with the stationary case. To provide detailed heat transfer information, the effect of off-design condition should be included. In this study, the effect of incidence angles varying from −15 deg to +7 deg is investigated for fixed absolute inlet flow velocity. Detailed heat transfer information on the tip and shroud is presented in Part II.

To measure local heat/mass transfer coefficients on the blade, a naphthalene sublimation method was used. Detailed measurements on the curvilinear surface having various curvature (for example, leading edge region) is possible using this technique and mass transfer coefficient can be converted to heat transfer coefficient using the heat and mass transfer analogy. A comparison with results from heat transfer experiments is presented in this paper.

Experimental Apparatus and Procedures

Experimental Apparatus. Figure 1(*a*) shows the schematic view of the experimental apparatus of the low speed wind tunnel for the annular turbine cascade. The apparatus is composed of three parts: an upstream fan with 15 HP motor, an annular passage with test section (a single stage of turbine) and a downstream fan with 10 HP motor and motor for blade rotation. At the exit of the upstream fan, a diffuser having a honeycomb and screens is installed to ensure uniform incoming flow with low fluctuations. A rubber duct of 1000 mm diameter is used to connect the upstream fan part to the annular passage. A bell mouth and a hemispherical cone are located at the inlet of the passage to induce a developed channel flow. The annular passage has a 1.7-m-long straight section based on the outer casing. The outer and inner diameters of

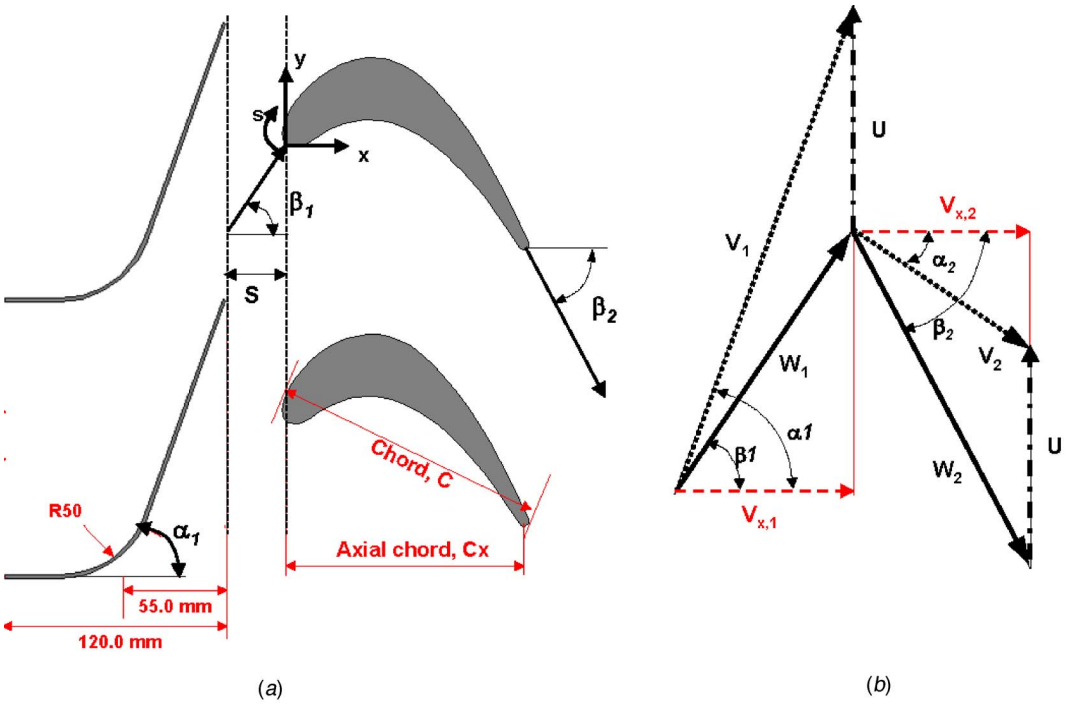

Fig. 2 Guide plate and blade. (*a*) Geometry; (*b*) velocity diagram.

the annular passage are 900 mm and 620 mm, respectively, and the corresponding height of the passage is 130 mm. The annular passage is divided into two parts. As shown in Fig. 1, the front part of the casing can be slid toward the upstream fan to make room for the setup, such as the test blade installation/ dismantlement and the guide plate exchange.

Several windows are made on the outer casing to make it possible to install the shroud test plate for local mass transfer measurements and flow and static pressure measurements. Some curvilinear plates made of acrylic are used for the velocity measurements using hot-wire anemometry.

The test section of a turbine stage is located in the annular passage and a photograph showing the test section is presented in Fig. 1(*b*). To simulate a single turbine stage, the test section is designed to contain a row of sixteen guide plates in front of the rotating disk having sixteen turbine blades. A row of guide plates is located 540 mm downstream from the inlet of the passage and the spacing between the guide plate and blade is 34 mm (S =34 mm). The stationary guide plates were installed on the front part of the casing, and blades were fixed on the rotating disk made of steel. The detailed configurations of the guide plate and blade are presented in the next section.

Two pitot tubes and six *J*-type thermocouples are located 100 mm upstream from the guide inlet to measure the velocity and temperature of the incoming flow. For static pressure and temperature measurements on the rotating blade, pressure transducer (FCO-44, Furness Controls) and *J*-type thermocouples with calibrated IC chips, AD594 (monolithic thermocouple amplifier with cold junction compensation, Analog Devices) are installed in the rotating disk. Twenty-channel slip ring is used to acquire the measured data. The encoder is attached at the end of the rotating axis to measure the rotational speed.

Operation of Apparatus. As mentioned briefly, two fans powered by motors are used to generate the mainflow in the annular passage: upstream fan blows the ambient air into the plenum and the downstream fan draws the flow in the passage. Each motor is controlled by an inverter. The mainflow generates the pressure difference between the pressure and suction sides of the blade, which cause the disk with blades to rotate. In the present study, for the designed flow velocity in the passage, the "free" rotational speed is higher than the "designed" rotational speed (for example, more than 400 rpm while the design condition is 255.8 rpm). Therefore, to meet the design condition, a holding system is required during the experiment. For that reason, an additional induction motor (10 HP) with an inverter is connected to the rotating axis and used to control the rotational speed of the blade. Actually, in this case, regenerative energy comes from the motor because the rotational speed is higher than the synchronous speed in the induction motor. A portion of this energy may be accumulated in the inverter condenser and another portion may be converted into heat emitted through the resistor in the inverter and/or the motor. Thus, the rotating blade (disk) has a fixed/constant rotational speed during the experiments with the induction motor and the inverter. Also, the motor for blade rotation is used to reduce the transient time (starting and shut-down time; less than 30 seconds for a test duration of 60–80 minutes). Thus, the desired conditions were obtained by changing the rotating speed using the motor connected to the rotating axis while maintaining a constant mainflow velocity using two fans. The variation of the rotational speed is maintained within ±0.1 rpm and it was confirmed by the stroboscope.

Guide Plate and Blade Configurations. As mentioned in the previous section, a single stage of turbine is installed in the annular passage. The schematic view of the cross section of the stage at the midspan is shown in Fig. 2.

The guide plates of thickness 1.3 mm are made of steel by laser cutting, and welded to the rolled plate. The number of guide plates is 16 and the axial chord length is 120 mm. Each guide plate has a 70 deg exit angle with a 65-mm-straight section before turning. Since there is a clearance of about 1–2 mm between the tip of the guide plates and the casing, oil-based clay is used to seal the clearance and to prevent the leakage flow through the gap. The geometry of the guide plates is given in Table 1. It is noted that a different guide plate was made and used in the experiments for the

Table 1 Guide plate configurations

Number of guide plates	16
Axial chord length (C_x)	120 mm
Pitch	22.5° (P/C=1.26)
Aspect ratio (l/C)	1.08
Guide plate inlet / exit angle	0°/70°

stationary blade. In that case, the plate is designed to have the exit angle of 56.4 deg, which is the blade inlet angle. The details for the guide plate for the stationary cases are listed in Rhee and Cho [15].

In the present study, the midspan profile of a GE 7FA first stage blade is used for the turbine cascade. Two types of blade are used: one is a dummy to create periodic flow in the annular passage and the other is a test blade for local mass transfer measurements. The dummy blade is manufactured by casting and the test blade is fabricated using a wire-cutting method. Each blade is made of aluminum. Since the inertia of the rotating disk and blades is sufficiently large, the difference of weight between the test blade and dummy blade does not cause additional vibration during the experiments.

The nomenclature and details of the blade geometry are given in Fig. 2 and Table 2. The chord length of blade is 150 mm and the corresponding aspect ratio is 0.87. The pitch of the blade varies from 0.84 to 1.17 with increasing radius. The inlet and exit angles are 56.4 deg and −62.6 deg, respectively, which produce a turning angle of 119.0 deg. Note that the blade has a constant cross section (i.e., blade inlet angle) and consequently the incidence angle changes along the span for a fixed operating condition. The incidence angle variation with rotational speed will be discussed later.

The blade is designed to have a slanted flat tip plane with a 3.8 deg angle to minimize the tip clearance with the annular casing. Hence, the blade has a varying span height, resulting in varying tip clearances along the axial direction. Figure 3 shows the schematic view of the tip clearance and the shapes of the clearance gap between the blade tip and casing (shroud) along the axial direction. The blade has the maximum span of 127 mm on the suction side and the minimum value of 120 mm at the trailing edge. Consequently, the designed gap ranges between 2.2 mm and 5.7 mm, and the pressure side has larger tip clearances than the suction side except in the trailing edge regions ($x/C_x > 0.8$). The mean tip clearance based on measured values of the test blade is about 3.8 mm, which is 2.5% of chord. The mean tip clearance of 2.5% is somewhat larger than a typical value for an industrial gas turbine engine (1%–1.5% of chord) but this tip clearance is reasonable to investigate the leakage flow effects on the local heat/mass transfer characteristics. The uncertainty of tip clearance based on the mean value is thought to be less than

Table 2 Blade configurations

Number of blades		16
Chord length (C)		150 mm
Axial chord (C_x)		131.5 mm
Pitch to chord ratio (p/C)	Hub	0.84
	Mean	1.01 (22.5°)
	Tip	1.17
Aspect ratio (l/C)		0.87
Spacing between vane and blade		34 mm (0.227C)
Radius at mid-span		385 mm
hub/tip radius ratio		0.711
Blade inlet / exit angle		β_1=56.4°/β_2=−62.6°
Turning angle		119.0°
Mean tip clearance (t)		~3.8 mm (t/C=2.5%)

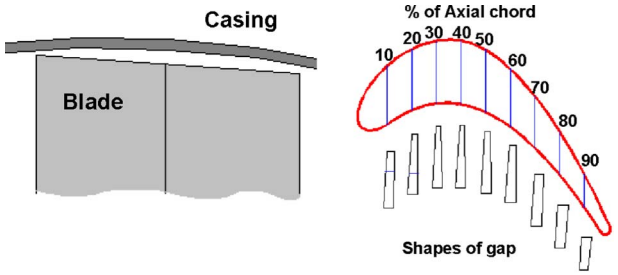

Fig. 3 Schematic view of tip clearance

±1 mm (±26.3%), which results from measurement error, manufacturing error (±0.5 mm), setup, and mechanical vibrations during the experiments.

Static Pressure and Flow Measurements. For static pressure measurements in the rotating rig, two pressure transducers (FCO-44, Furness Controls, Inc.) with different pressure ranges, 25 mmH_2O and 250 mmH_2O, are used. The transducer of low range is used for the measurements of differential pressure of the mainstream at the inlet of the guide plate and the high-range transducer installed in the rotating disk is for the static pressure measurement on the blade surface. The signals from each transducer are transferred to the PC through a data logger (Model No. 34970A, Agilent Technologies, USA) with 22 channel-multiplexer (34901A). The uncertainties of static pressure measurement are estimated as ±4.9% for the 25 mmH_2O pressure transducer and ±5.9% for the 250 mmH_2O pressure transducer.

A constant temperature thermal anemometer (IFA-300 from TSI, Inc.) with single hot-film probe (model 1201-6) is used to measure the boundary layer profile and the velocity and turbulence intensity at the guide exit. The sampling rate was 4000 Hz with a low pass filter of 2000 Hz and 4096 data points are acquired and averaged. To obtain the velocity magnitude distributions at the exit of the guide plate, three sets of measurements were conducted (positioning the probe normal and parallel to the rotating axis and normal to the guide plate exit angle) because the flow is three dimensional. From these results, qualitative flow characteristics can be known although it is hard to know exact velocity magnitude. Also, the experimental and numerical results show reasonable agreement [15]. Turbulence intensity distributions presented in this study are measured when the wire is set to be normal to the guide plate exit angle. The flow angle at the guide exit can be calculated roughly from the data.

Test Parameters and Operating Conditions. In the present study, the effects of blade rotation and incidence angle on local heat transfer were investigated for a rotating blade. Detailed operating conditions for the experiments are described below. It is noted that the operating conditions were set based on the midspan geometry in the present study.

Design Condition. The experiment for the stationary blade was conducted first to investigate the basic heat/mass transfer characteristics on the blade surface and to serve as baseline data for the comparison with the rotating cases. For this experiment, another guide plate with an exit angle equal to the blade inlet angle was installed. The position of the blade was adjusted to obtain uniform inlet velocity distributions since the relative position between the guide plate and blade affects the velocity distributions at the inlet of the blade. The inlet Reynolds number is fixed to $Re_C = 1.5 \times 10^5$.

The experiment with the rotating blade at the design condition was performed at $Re_C = 1.5 \times 10^5$ and the rotational speed of 255.8 rpm (U=10.3 m/s). Detailed conditions for the experiment with rotating blade are listed in Table 3. In the table, some quantities, such as the flow coefficient and the blade loading coefficient, for

Table 3 Design condition for rotating blade (based on mid-span geometry and the inlet Reynolds number)

Inlet flow velocity(V_0)/mean Tu	8.3 m/s/ ~9%
Guide exit flow velocity (V_1)[a]	24.3 m/s
Blade inlet velocity(W_1)/mean Tu	15 m/s/ ~3%
Rotational speed (N)	255.8 rpm
Blade speed (U)	10.3 m/s
Blade exit velocity (W_2)[a]	18.0 m/s
Reynolds number based on W_1 and C(Re_C)	1.5×10^5
Reynolds number based on W_2 and C($Re_{C,exit}$)	1.8×10^5
Flow coefficient (ϕ)	0.805
Blade loading coefficient (ψ)	3.317
Speed work (λ)	0.301
Degree of reaction (R)	0.171
Static pressure reaction ratio ($\Delta P_{s,blade}/\Delta P_{s,stage}$)[b]	0.215

[a]Calculated from inlet to exit area ratio.
[b]Following the equation by Blair [8].

a given condition are also presented. The definitions of these quantities are presented in Ref. [16]. Another parameter, static pressure reaction ratio ($\Delta P_{s,blade}/\Delta P_{s,stage}$) is presented. The static pressure drop across the rotating blade is about 21% of the total pressure drop (i.e., the pressure drop through the stage).

Since the blade has the same blade profile along the span, the blade has a nonzero incidence angle along the span even at the design condition because the guide exit flow angle is fixed at 70 deg over the span. The difference of the blade inlet flow angle along the span is described in Table 4 and shown in Fig. 4. The hub has a positive incidence angle while the incidence angle at the tip is negative. But the difference of incidence angle along the blade span is within the 4.1 deg.

Table 4 Conditions for radial positions at the design condition

Radial position	Hub	Mid-span	Tip
Radius	0.320 m	0.385 m	0.450 m
Blade speed (U)	8.6 m/s	10.3 m/s	12.1 m/s
Relative blade inlet velocity (W_1)	16.5 m/s	15.0 m/s	13.6 m/s
Relative inlet flow angle	59.8°	56.4°	52.3°
Incidence angle	+3.4°	0°	−4.1°

Table 5 Off-design conditions based on the mid-span geometry

Incidence angle	0°	+2.9°	+5°	+7°
N [rpm]	255.8	218.8	188.0	154.5
U [m/s]	10.3	8.8	7.6	6.2
W_1 [m/s]	15.0	16.2	17.3	18.6
Incidence angle	0°	−5°	−10°	−15°
N [rpm]	255.8	307.8	349.5	384.2
U [m/s]	10.3	12.4	14.1	15.5
W_1 [m/s]	15.0	13.3	12.0	11.1

Off-Design Conditions. To investigate the effect of off-design condition on local heat transfer on the blade, the experiments for various incidence angles from −15.0 deg to +7.0 deg were conducted. In the present study, the off-design conditions were obtained by changing rotational speed (i.e., blade speed, U) with fixed inlet flow velocity. For each incidence angle, the rotational speed of the blade is determined from the radius and blade speed at the mid-span as shown in the velocity diagram in Fig. 2(*b*). Note that the relative inlet flow velocity increases with fixed absolute inlet flow velocity as the incidence angle increases. This results in the increase of inlet Reynolds number. For example, at $i=+7$ deg, the relative inlet Reynolds number is more than 20% higher than that at the design condition whereas the value is about 28% lower than the designed value at $i=-15$ deg. In addition, the inlet Reynolds number varies along the span due to the difference of the blade speed. Along the span, the differences in Reynolds numbers are 6%–13% of the values at the midspan for all the tested cases (Fig. 4(*b*)). The static pressure reaction ratio increases with decreasing incidence angle (from 17.8% at $i=7$ deg to 25.4% at $i=-15$ deg).

As mentioned, the incidence angle changes along the span because the blade speed increases with increasing radius. Therefore, the incidence angle at the tip is smaller than that at the midspan, and the difference between the values at the midspan and the tip become larger as the incidence angle decreases. The details of flow conditions with the incidence angles are presented in Table 5 and Fig. 4.

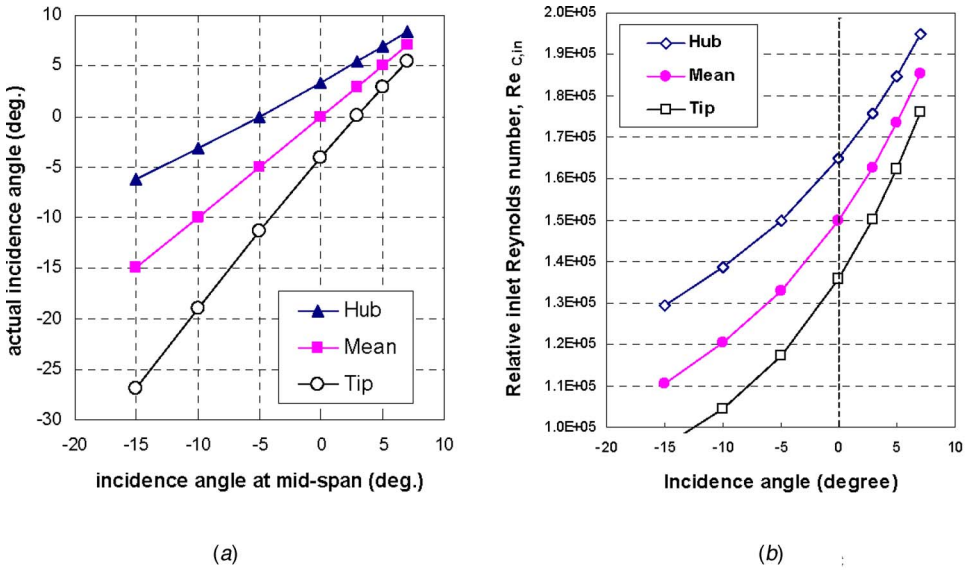

(*a*) (*b*)

Fig. 4 Actual incidence angle and Re_C for various incidence angles. (*a*) Actual incidence angle; (*b*) actual Re_C.

Heat and Mass Transfer Coefficient

Naphthalene Coated Test Blade. Detailed mass transfer measurements were conducted on the blade surface using a naphthalene sublimation method. To coat naphthalene on the test blade, the test blade and four pieces of casting molds were designed and manufactured. The test blade is designed to have a rim of 3 mm along the blade periphery at the tip and the naphthalene-coated surface covers the blade from $z=-0.11C_x$ (15 mm below the midspan) to the near-tip (3 mm below the tip).

Data Reduction. The mass transfer coefficient is obtained from sublimation depth and exposure time. The local mass transfer coefficient is defined as follows

$$h_m = \frac{\dot{m}}{\rho_{v,w} - \rho_{v,\infty}} = \frac{\rho_s \delta y / \delta \tau}{\rho_{v,w}} \tag{1}$$

Since freestream or incoming flow contains no naphthalene, $\rho_{v,\infty}=0$ in the present study. The local sublimation depth (δy) is the difference between total sublimation depth and sublimation depth due to natural convection.

The natural sublimation rate was determined from separate experiments and was estimated as about 10% of total sublimation depth. It is noted that the average of total sublimation depth is less than 0.1 mm and its effect on the blade geometry variation is negligible.

The Sherwood number is expressed as

$$\mathrm{Sh}_C = h_m C / D_{\mathrm{naph}} \tag{2}$$

where D_{naph} is calculated from a correlation equation suggested by Goldstein and Cho [17]. Uncertainty in Sherwood numbers using the method of Kline and McClintock [18] for single sample experiments, considering the measured surface temperature, depth, position and correlation equations, is within ±7.4% in the entire operating range of the measurement, based on a 95% confidence interval.

Mass transfer coefficients can be converted into heat transfer coefficients using the heat and mass transfer analogy. The Prandtl number is 0.71 for air and the Schmidt number is 2.28 for the naphthalene vapor in air at 25 °C. The experiments are conducted at room temperature, and the Lewis number (Pr/Sc) for this study is about 0.31

$$\mathrm{Nu/Sh} = (\mathrm{Pr/Sc})^n \tag{3}$$

The exponent, n, is dependent on the flow regime on the surface. For example, for a laminar flow, n is equal to 0.33 and the conversion equation is Nu=0.675 Sh. In our previous studies of the impinging jet, the exponent of $n=0.4$ has been used and this value has provided reasonable agreement with other studies even though the impinging jet has complex flow patterns such as the stagnation point, flow acceleration, relaminarization and transition. Therefore, in this study, the exponent of $n=0.4$ was used for the comparison of the overall levels and distributions. However, for more accurate comparison, additional work related to the exponent on the different flow regimes should be done.

To measure the local sublimation depth on the curvilinear surface, four-axis measurement system with the LVDT gage was used. Detailed specifications of the LVDT and the measurement system are described by Rhee [19].

Results and Discussion

Inlet Flow and Static Pressure Measurements. In the experiments, the velocity at the inlet of the guide plate (axial velocity, V_0) was fixed at 8.3 m/s, which corresponds to $\mathrm{Re}_C=1.5\times10^5$ at design condition. The flow at the guide plate inlet is fully turbulent and the boundary layer thickness and turbulence intensity are about 10 mm and 9%, respectively. At the guide exit, since the flow is accelerated, the boundary layer thickness is less than 5 mm and the turbulence intensity at midpitch is 3–4%. Measurement results are presented in Ref. [15].

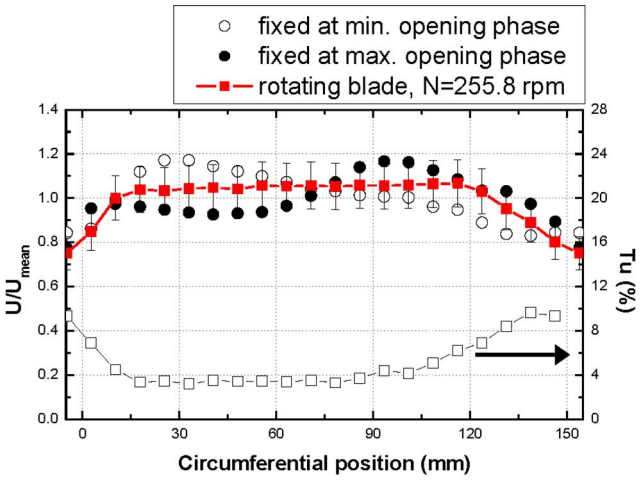

Fig. 5 Circumferential distributions of velocity magnitude at the plane 10 mm downstream of guide exit for rotating blades

Figure 5 shows the distributions of velocity magnitude at midspan on the downstream plane of the guide exit. In this figure, circular symbols indicate the velocity magnitude distributions with a blade fixed at minimum and maximum opening phases while square symbols indicate the results (velocity magnitude and turbulence intensity) with a rotating blade at $N=255.8$ rpm. When the blade is installed and rotates, the upstream flow field is affected periodically since the exit area and static pressure distribution in the downstream region change with blade rotation. The measurement results show that the velocity magnitude oscillates within 10% for the rotating blade (between two different phases). The "roughly calculated" flow angle at the guide exit, not presented in this paper, is slightly lower (difference is within 7 deg) than the design value (70 deg).

To predict the flow characteristics on the blade midspan, the static pressure on the surface was measured and represented in the form of static pressure coefficient. The definition of the static pressure coefficient is as follows

$$C_p = (P_s - P_0)/0.5\rho V_0^2 \tag{4}$$

Figure 6 shows the distributions of time-averaged static pressure coefficients along the blade surface at the midspan. The bold

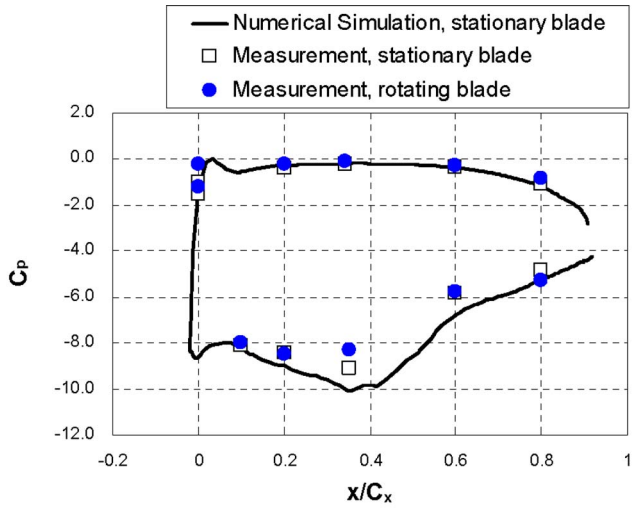

Fig. 6 Static pressure coefficients along the blade at the midspan at $\mathrm{Re}_C=1.5\times10^5$ ($N=255.8$ rpm)

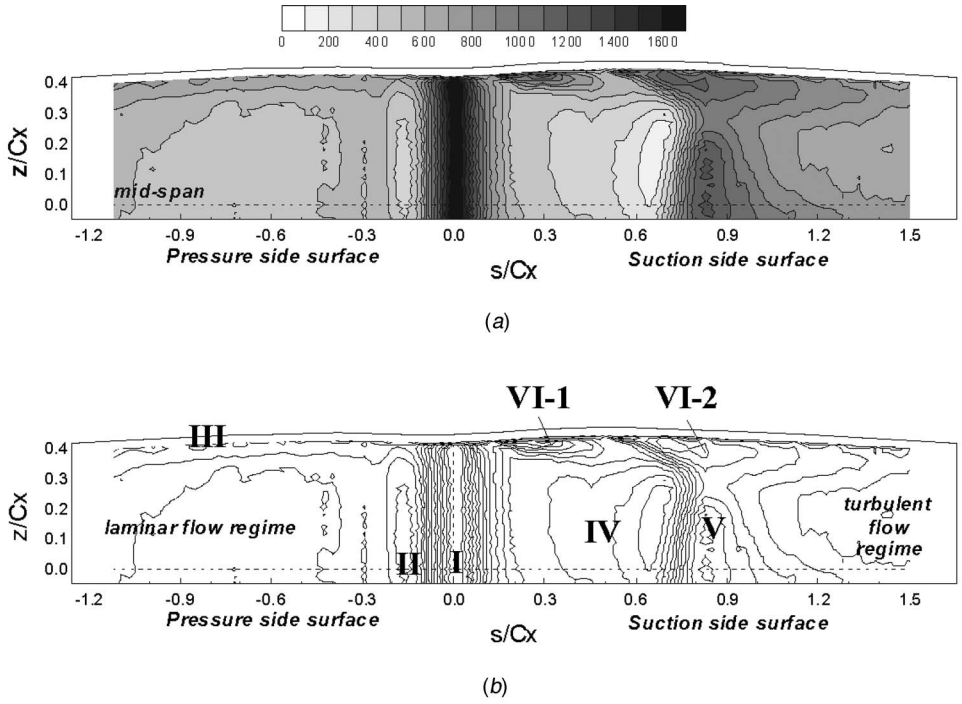

Fig. 7 Local heat/mass transfer characteristics on the blade surface at $Re_C=1.5\times10^5$. (*a*) Mass transfer distribution; (*b*) classification of flow regimes on the surface.

line indicates the result from 3D numerical simulation using FLUENT 6.1 and the open symbols represent the measured result for the stationary blade. The simulation was performed to obtain the steady solutions of turbulent viscous flow field around a stationary case. The RNG k-e turbulence model with nonequilibrium wall function was used. A guide plate and a blade are modeled and a periodic boundary condition was imposed on the sidewalls.

The overall static pressure distribution for the rotating case is quite similar to that of the stationary blade and quite reasonable agreement between the experimental and numerical results was shown.

While C_p values on the pressure side are uniform, on the suction side surface, C_p decreases considerably with flow acceleration. The maximum static pressure difference is observed at $x/C_x\cong0.34$ and then the static pressure recovers forming an adverse pressure gradient. The numerical simulation predicts a minimum value at $x/C_x\cong0.1$ on the pressure side and a laminar separation bubble may be formed near this region. This flow characteristic is reported and well described by Mayle [20] and Chen and Goldstein [4]. Also, the heat transfer pattern due to laminar flow separation is clearly observed in the next section.

It should be noted that the maximum static pressure difference along the blade is formed in the upstream region when compared to an aircraft gas turbine engine blade (for example, Ref. [13]). As a result, the effect of leakage flow at the upstream gap may be stronger than that of an aircraft turbine blade.

Heat/Mass Transfer Measurements on Stationary Blade. Local heat/mass transfer characteristics on the blade surface are presented and then the effects of blade rotation and the incidence angle are examined in this paper.

Basic Heat/Mass Transfer Characteristics. Figure 7 shows the contour plot of Sh_C on the blade surface for the stationary blade at $Re_C=1.5\times10^5$ and the classification of flow regimes on the surface. In the contour plot, the dashed line indicates the midspan of the blade and the outerlines of the contour plot indicate the blade surface. The regions in which mass transfer is not measured including the rim near the tip are blanked in the result. The flow characteristics primarily affecting the local heat transfer on the blade surface and near the tip are classified below.

I. stagnation flow in the leading edge region
II. separation bubble on the pressure side and flow relaminarization
III. flow acceleration near the tip on the pressure side
IV. laminar flow acceleration on the suction side
V. flow transition on the suction side
VI. leakage vortex near the blade tip on the suction side

Complex heat transfer characteristics are found on the blade surface due to these flow patterns. The classification of heat transfer characteristics on the blade surface (Fig. 7(*b*)) is based on the flow characteristics and the result of the present study. In this figure, the Roman numerals correspond to the numerals listed above.

The highest values of Sh are observed along the span at the leading edge (region I in Fig. 7(*b*)) and then Sh decreases as the flow develops on the surface. On the pressure side ($s/C_x\leqslant0.0$), the flow after the stagnation point is expected to be laminar due to the local flow acceleration. Then, the "separated flow transition" occurs in a separated laminar boundary layer at $s/C_x\cong-0.15$, which is indicated as region II in Fig. 7(*b*). The flow may reattach as turbulent flow after the separation bubble in this region. Therefore, a slight increase of heat/mass transfer is observed after a small valley due to the separation. Then, the heat transfer coefficient decreases rapidly with the flow development. In the downstream region ($s/C_x<-0.4$), the heat/mass transfer distributions are quite uniform. This means that the boundary layer after the separation bubble probably undergoes relaminarization. Near the tip on the pressure side, heat/mass transfer enhancement along the tip is found since the near-tip flow is accelerated due to the flow "entrance effect" as mentioned (region III).

Suction side surface has a more complex heat/mass transfer

pattern. In the two-dimensional flow region ($z/C_x \leq 0.3$), after the stagnation point, the laminar boundary layer flow is maintained due to strong acceleration (region IV). Then, at $s/C_x = 0.7-0.8$, the flow transition occurs due to the adverse pressure gradient (region V). This position is also coincident with the geometric throat in the turbine passage. Therefore, relatively high peak values (about 70% of Sh at the stagnation point, $s/C_x = 0.0$) are observed in this region. After the transition, the fully turbulent boundary layer develops and hence the heat/mass transfer coefficient decreases monotonically.

In the near-tip region ($z/C_x \geq 0.3$), the leakage flow from the gap has a dominant effect on the local heat/mass transfer and hence the flow on the surface near the tip is fully turbulent. There are two peaks near the tip on the suction side surface, which are indicated as VI-1 and VI-2 in Fig. 7(*b*). This is because the leakage flow in the tip gap is divided into upstream and downstream tip leakage flows and then these flows develop as two leakage vortices. The behavior of leakage flow mentioned above is described in Rhee and Cho [3,15] and similar heat transfer patterns are also found in Ref. [12]. In the upstream region, a small region of high heat/mass transfer is generated due to the leakage flow from the upstream portion of the gap. But this region is confined to $s/C_x \leq 0.4$. This is possibly because the leakage flow affecting the surface heat transfer is detached from the surface as the flow moves along the surface. This is shown clearly in Part II [3]. Then, a new high heat transfer region due to the downstream leakage vortex begins to appear after a clear demarcation between these two regions (the locally minimum value at $s/C_x = 0.5$ along $z/C_x \cong 0.4$). This leakage vortex impinges on the suction side surface, drawing the mainstream (hot gases) toward the surface. Therefore, relatively high heat/mass transfer regions are formed along the leakage vortex path. The peak value due to this leakage vortex is located at $s/C_x = 0.7$ and the level is about 60% of that at the stagnation point. The effect of the downstream leakage vortex reaches more than 10% of axial chord in the spanwise direction. As s/C_x increases, the level of Sh_C in the near-tip region decreases while the width of the high heat transfer region increases. This means that the leakage vortex becomes larger but weakened. Although the tip leakage vortex becomes weaker, the effect of this vortex is maintained up to the trailing edge of the blade.

It should be noted that the horseshoe and passage vortices are negligible in the present study because the boundary layer thickness is equivalent to the tip clearance (less than 5 mm). The details are presented in Part II [3].

Comparison with Other Studies. Figure 8 presents $Nu/Re_{C,ex}^{0.5}$ along the midspan for the stationary blade in comparison with other studies of mass transfer [5,13,14] and heat transfer experiments [6,7,11]. The data from the mass transfer experiments including the present study are converted to Nusselt numbers using heat and mass transfer analogy. It is noted that the blade geometries of other studies are different from that of the present study and the chord length (axial chord for the comparison with heat transfer experiments) and the exit flow velocity are used for dimensionless numbers to compare the overall distributions.

For the mass transfer experiments (Fig. 8(*a*)), the levels and the heat transfer characteristics are fairly similar although some discrepancies are observed. For example, the values at the stagnation region range within the difference of 10% except the value for high freestream turbulence intensity from Jin and Goldstein [13] and the overall levels of normalized Nusselt numbers on the pressure side and on the laminar flow region of the suction side are in good agreement. Especially, the values on the pressure side due to the laminar separation bubble are quite similar. But, peak values in the region of laminar separation bubble on the pressure side are different and the positions of the additional peaks due to flow transition on the suction side are different due to different incoming flow conditions and blade spacing.

Figure 8(*b*) presents the comparison of heat transfer with the

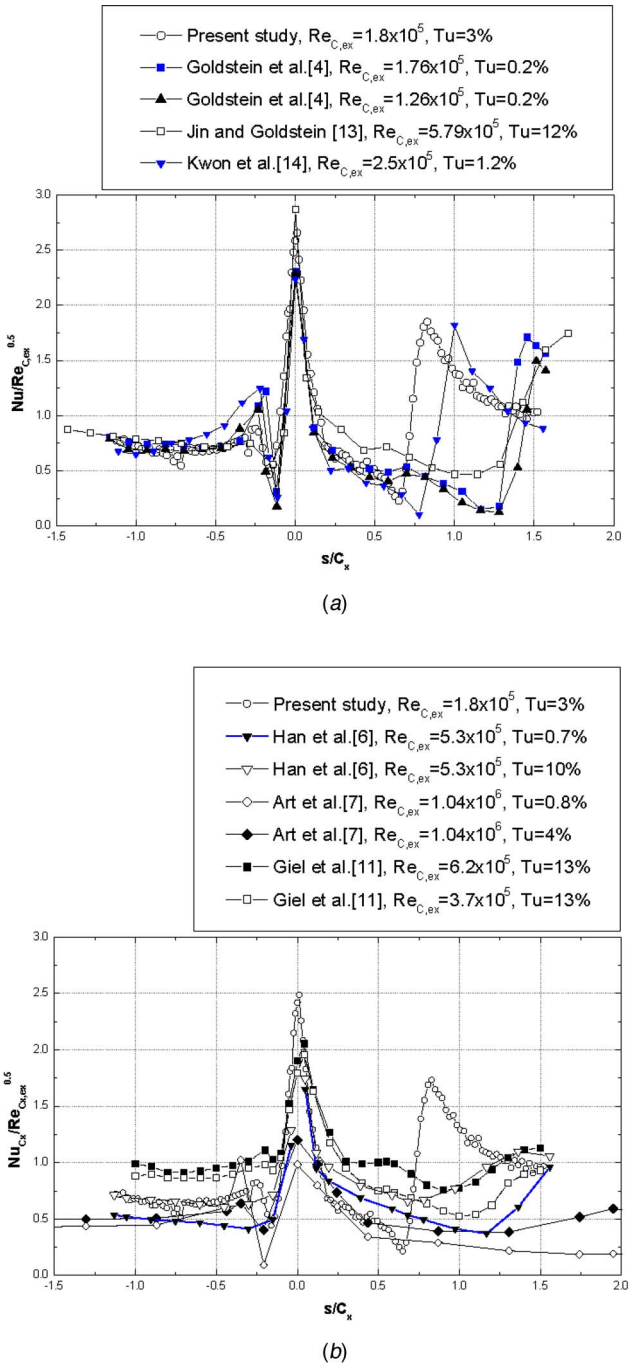

Fig. 8 Comparison of $Nu_C/Re_{C,ex}^{0.5}$ at the mid-span with other studies for stationary blade. (*a*) Mass transfer experiments; (*b*) heat transfer experiments.

data from heat transfer experiments. The levels of the results are similar in the overall region and local valleys on the pressure side are formed at the same positions. However, other results have no or quite small transition regions on the suction side. The possible reason for this difference may be different flow conditions such as high freestream turbulence intensity and high inlet flow Reynolds number.

It should be noted that the levels of the stagnation point heat transfer coefficients for heat transfer experiments are lower than the value for the present study. A conduction error around the leading edge may affect the accuracy of the stagnation point heat transfer because of the steep variation of temperature (i.e., heat

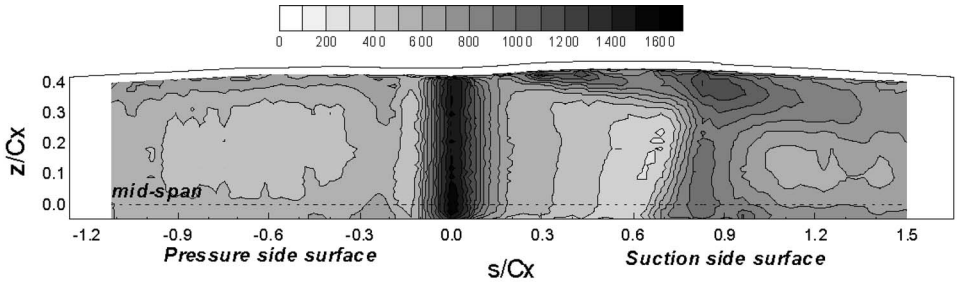

(*a*)

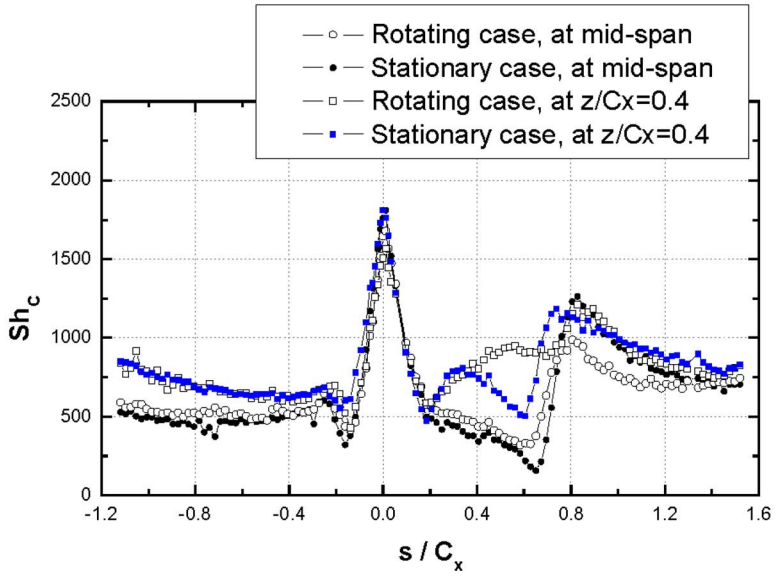

(*b*)

Fig. 9 Local Sh_C distributions on the blade surface at $Re_C=1.5\times10^5$ and $N=255.8$ rpm and its comparison with the stationary case. (a) Contour plot; (b) local distributions.

transfer coefficient). However, for more exact comparison of the stagnation point heat transfer, the effect of the inlet Reynolds number and the leading edge diameter should be considered since the stagnation point heat transfer is strongly dependent on not only the flow conditions but also the leading edge geometry, for example, the inlet Reynolds number and the diameter of the leading edge as mentioned by Giel et al. [11].

Heat/Mass Transfer Measurements on Rotating Blade.

Effect of Blade Rotation. Figure 9 shows the contour plot and the local distributions of Sh_C on the blade surface at $Re_C=1.5\times10^5$ and $N=255.8$ rpm. It is noted that a slight difference in the levels of Sh_C on the surface can be observed in Fig. 9(*b*) when those are compared with the results on the stationary blade. This is because the flow conditions of the incoming flow (i.e., velocity magnitude distributions and turbulence intensity) are not the same as those for the stationary case.

In general, the blade rotation changes the flow characteristics around the blade. Typically, the periodic wake from the upstream vane affects the flow and heat transfer on the blade and consequently the time-averaged turbulent intensity of the flow on the blade surface is increased with blade rotation. In addition, the relative motion between the blade and shroud reduces the amount of tip leakage flow. Therefore, some changes in the size and the position of the classified regions (I to VI in Fig. 7(*b*)) and the level of heat/mass transfer rate are observed although the rotating blade has similar heat transfer characteristics to the stationary case.

On the two-dimensional flow region ($z/C_x<0.3$), the rotation does not have a significant effect on the heat transfer at the stagnation region and on the pressure side surface: separation bubble along the spanwise direction near the leading edge. Only a slight increase of the level of Sh_C is shown on the pressure side due to the wake, which is clearly shown in Fig. 9(*b*). On the suction side, the heat transfer coefficients on the laminar flow region are slightly higher because of the passing wake. While the position of flow transition is not shifted, the peak value of heat/mass transfer coefficient in the transition region is about 20% lower than that for stationary case. This pattern is also found in the previous work done by Goldstein et al. [4]. They mentioned that the turbulent heat transfer after the flow transition on the suction side is reduced when the mainstream turbulence is increased. Thus the blade rotation increases the time-averaged turbulence intensity of the mainstream, and then decreases slightly the heat transfer around the region where the flow transition occurs. Then, the heat transfer coefficient decreases as the turbulent boundary layer develops and has the same value as that for stationary case at the far downstream region ($s/C_x>1.2$).

A noticeable change in heat transfer characteristics is observed in the near-tip region ($z/C_x\geq0.3$). Sh_C values on the pressure side surface are higher than those at the mid-span due to flow acceleration and its level is quite the same as that for the stationary blade (Fig. 9(*b*)). But, it should be noted that the values at the stagnation region are 15% lower than those for the stationary case.

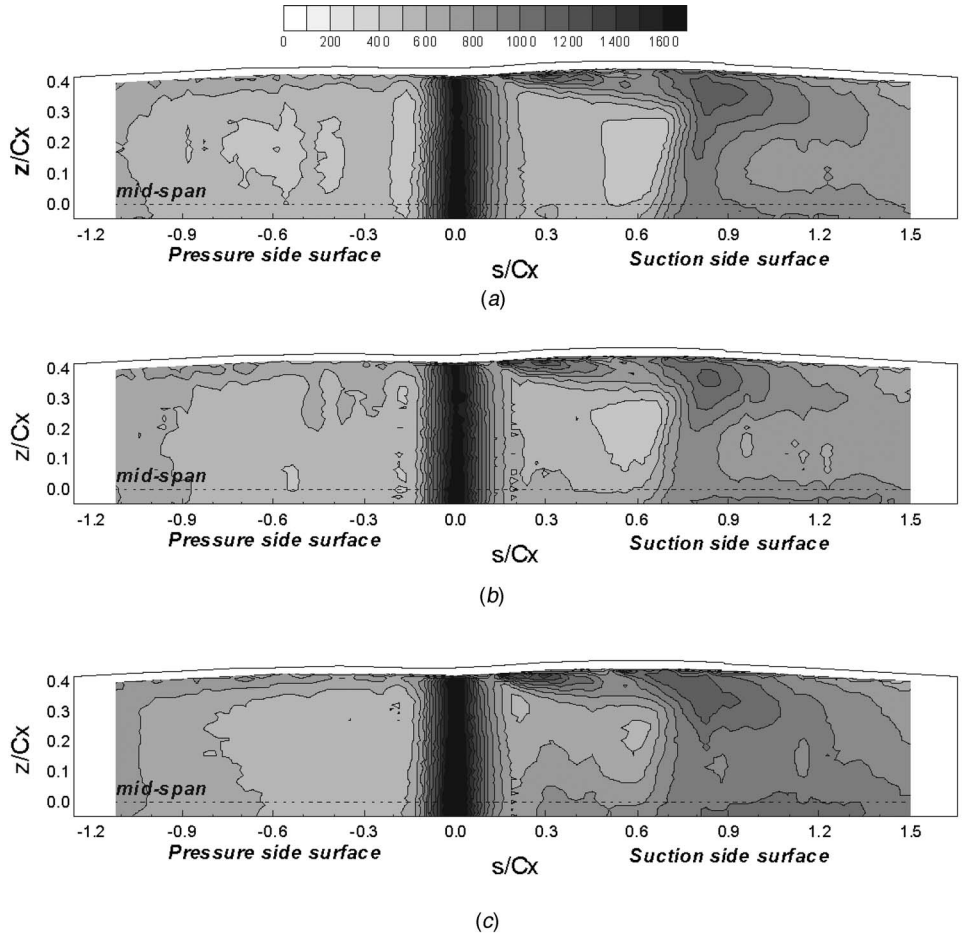

Fig. 10 Contour plots of Sh_C on the surface of blade with positive incidence angles at $Re_{C,ex}=1.8\times10^5$. (*a*) *i*=+2.9 deg (*N*=218.8 rpm); (*b*) *i*=+5 deg (*N*=188.0 rpm); (*c*) *i*=+7 deg (*N*=154.5 rpm).

The primary reason is that the rotating blade has a negative incidence angle near the tip and as a result the Reynolds number of incoming flow near the tip is lower than that at midspan as shown in Fig. 4.

On the near-tip region of the suction side surface, a high heat transfer region due to the upstream tip gap flows is somewhat extended to the downstream side and the region affected by the downstream tip gap flow is enlarged in the spanwise direction and shifted toward the downstream side (the peak value appears at $s/C_x \cong 0.7$), which is clearly shown in Fig. 9(*b*). This is possibly because the downstream leakage vortex is formed near the blade surface with decreased momentum of tip leakage flow. Although the affected region is increased, the peak values at this region are almost the same as those for the stationary blade, and this means that the strength of the vortex is weakened for the rotating blade. Note that the rotating case has a negative incidence angle near the tip because the test condition is set for the mid-span. The negative incidence angle causes more acceleration on the suction side surface, and this makes the locally low heat transfer region with flow laminarization be slightly extended downstream near the tip.

Effect of Incidence Angle. *Positive incidence angle.* Figure 10 shows the contour plots of Sh_C on the blade surface for off-design conditions of positive incidence angles. The Sh_C values at the stagnation region increase with increasing incidence angle because of the increase of the relative inlet Reynolds number. On the pressure side, the separation bubble becomes smaller with increasing incidence angle and is hardly observed when the incidence angle is 7 deg, but the patterns on other regions are similar. Also, in the near-tip region on the pressure side surface, relatively high heat transfer rate is maintained for all the tested conditions. On the suction side, the region of relaminarization becomes smaller and shifted upward as the incidence angle increases. Consequently, the effect of the flow transition is weakened in the two-dimensional flow region and the flow regime on the suction side surface seems to be changed to turbulent flow regime with increasing incidence angle. Near the tip, the positions of the regions affected by the upstream and downstream leakage flows become shifted upstream while the levels are the same.

Figures 11 and 12 show local Sherwood number distributions at the midspan ($z/C_x=0.0$) and near the tip ($z/C_x=0.4$). As shown in Fig. 11, the heat/mass transfer at leading edge increases as the incidence angle increases due to increased relative inlet Reynolds number. On the pressure side surface, the separation bubble on the pressure side disappears and heat/mass transfer coefficients on the downstream region slightly increase with increasing s/C_x for positive incidence angles due to the flow acceleration and this means that the flow on the downstream region might be in a transition or become turbulent with high incidence angle. On the suction side, the effect of transition is quite weak while the values on the relaminarization region are relatively high with positive incidence angles. Near the tip (Fig. 12), the positions of peak values due to leakage flow move upstream with increasing incidence angle while the levels of Sh are almost the same.

Negative incidence angle. Figure 13 shows the contour plots of Sh_C on the blade surface for the rotating blade with negative incidence angles at $Re_{C,ex}=1.8\times10^5$. As the incidence angle de-

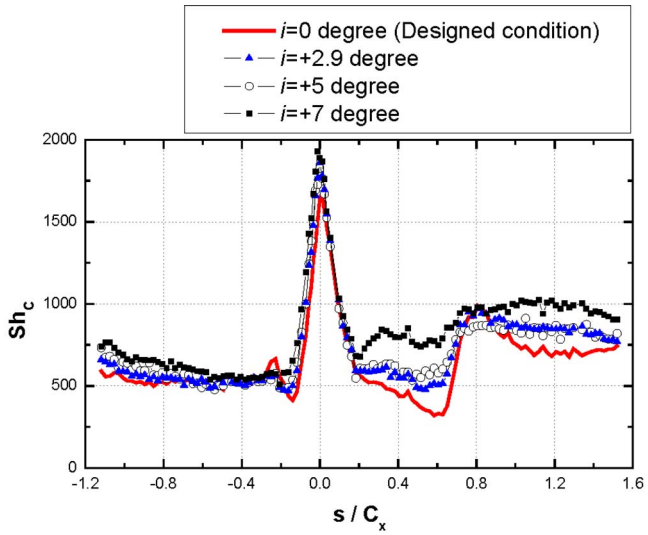

Fig. 11 Local distributions of Sh_C at mid-span for the blade with positive incidence angles at $Re_{C,ex}=1.8\times10^5$

creases, the stagnation region is shifted toward the suction side and the values at this region decrease because the relative inlet Reynolds number is decreased. Also, on the pressure side surface, the size of the separation bubble becomes smaller while the peak after the bubble becomes higher as the incidence angle decreases. The distributions in the near-tip region on the pressure side are hardly affected by the incidence angle like the cases with positive incidence angles.

As expected, some significant changes of the heat transfer on the suction side surface are found with negative incidence angles. First, the heat/mass transfer enhanced region due to the flow transition moves downstream because the local flow acceleration is stronger for smaller incidence angle. Second, the peaks due to the upstream gap flow disappear because a large portion of the tip gap flow becomes shifted downstream as the incidence angle decreases. On the other hand, the interaction between the downstream tip leakage flow and mainstream is promoted due to the accelerated mainflow near the surface and increased flow rate of downstream tip leakage flow. This results in higher heat/mass transfer rate near the tip.

Close examination of Fig. 14 confirms the heat transfer patterns explained above. In Fig. 14, the reduction of the separation bubble size and the increase of the peak are shown clearly with the decreasing incidence angle. For example, this peak value is 70%

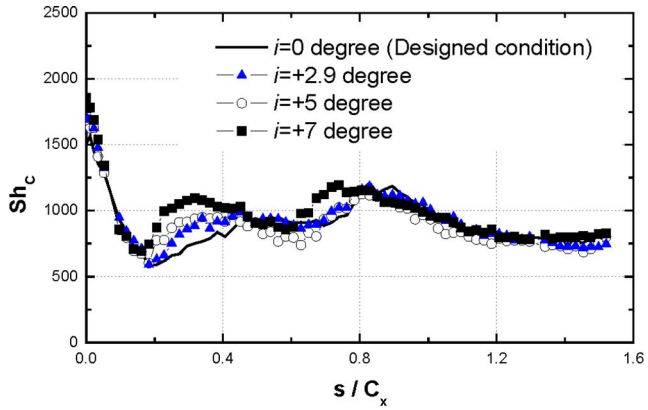

Fig. 12 Local distributions of Sh_C on the suction side surface at $z/C_x=0.4$ for the blade with positive incidence angles at $Re_{C,ex}=1.8\times10^5$

higher than that for the design condition. However, the heat/mass transfer coefficients on the pressure side are almost the same at the downstream region ($s/C_x<-0.3$). This means that the flow regime on the pressure side surface remains unchanged (i.e., laminar flow) in spite of the change of incidence angle. On the suction side, as mentioned, the shift of the transition position for the cases with negative incidence angles is observed in Fig. 14 although the levels of peak values are almost identical.

The most significant effect of the incidence angle variation is found at the near-tip region of the suction surface ($z/C_x=0.4$, Fig. 15). At $z/C_x=0.4$, the level of heat/mass transfer coefficients increases and the region affected by the downstream tip leakage vortex is widened. For example, the peak value for $i=-15$ deg is about 1.3 times as high as that at the design condition and even about 10% higher than the value at the stagnation point. Also, the peak position is shifted a little toward the downstream region with decreasing incidence angle. However, the peak at the upstream region disappears with decreasing incidence angle. This can be easily understood from heat transfer patterns on the tip presented in Part II.

Figure 16 presents the distribution of Sh at the stagnation point with incidence angles. The Sh_C values at the stagnation region increase with increasing incidence angle and this is due to the increase of the relative inlet Reynolds number and its maximum difference is more than 20%.

In general, the heat transfer at the stagnation point of circular cylinder is proportional to $Re^{0.5}$ for a laminar flow and the stagnation point heat transfer is proportional to $Re^{0.52}$ for the impinging jet. Therefore, the values normalized by $Re_C^{0.52}$ are presented together in Fig. 16. The difference is maintained within ±5% and this means that the Sh_C at the stagnation region is more dependent on relative inlet Reynolds number than other flow conditions such as rotational speed or incidence angle.

Figure 17 shows the spanwise averaged Sh on the blade surface at various incidence angles. Noticeable changes are observed around the stagnation region including the pressure side surface and on the suction side surface as clearly shown in local distributions. Thus, the incidence angle of incoming flow affects and changes the heat/mass transfer on the blade surface.

Conclusions

In this paper, the heat/mass transfer characteristics on the blade surface are investigated. First, basic heat transfer characteristics for the stationary blade are examined and the effect of blade rotation is analyzed by comparing the result for rotating blade with the stationary case. Also, the effect of incidence angle is investigated.

The heat/mass transfer characteristics on the blade surface are affected strongly by the local flow characteristics, such as laminarization after flow acceleration, flow transition, separation bubble and tip leakage flow. On the pressure side, local peaks and valley are found due to the stagnation, separation bubble and transition. On the suction side, the heat/mass transfer coefficients decrease due to laminarization and then the heat/mass transfer coefficients increase with flow transition. Near the blade tip, the effects of tip leakage flow are shown in two regions: upstream and downstream regions. The tip leakage flow in the downstream region makes large-scale tip leakage vortex and affects up to 10% of axial chord in the spanwise direction and the peak values due to the tip leakage vortex are 60% of the value at the stagnation point.

The heat/mass transfer characteristics on the rotating blade surface are basically the same as those for the stationary blade. However, the effects of tip leakage vortex on the suction side heat transfer are increased while the heat/mass transfer coefficients on the pressure side surface is almost the same as those for the stationary cases. The peak values due to the transition on the suction side surface are lower than those for the stationary cases because of the elevated turbulence intensity. These are due to the periodic wake and relative motion between blade and shroud.

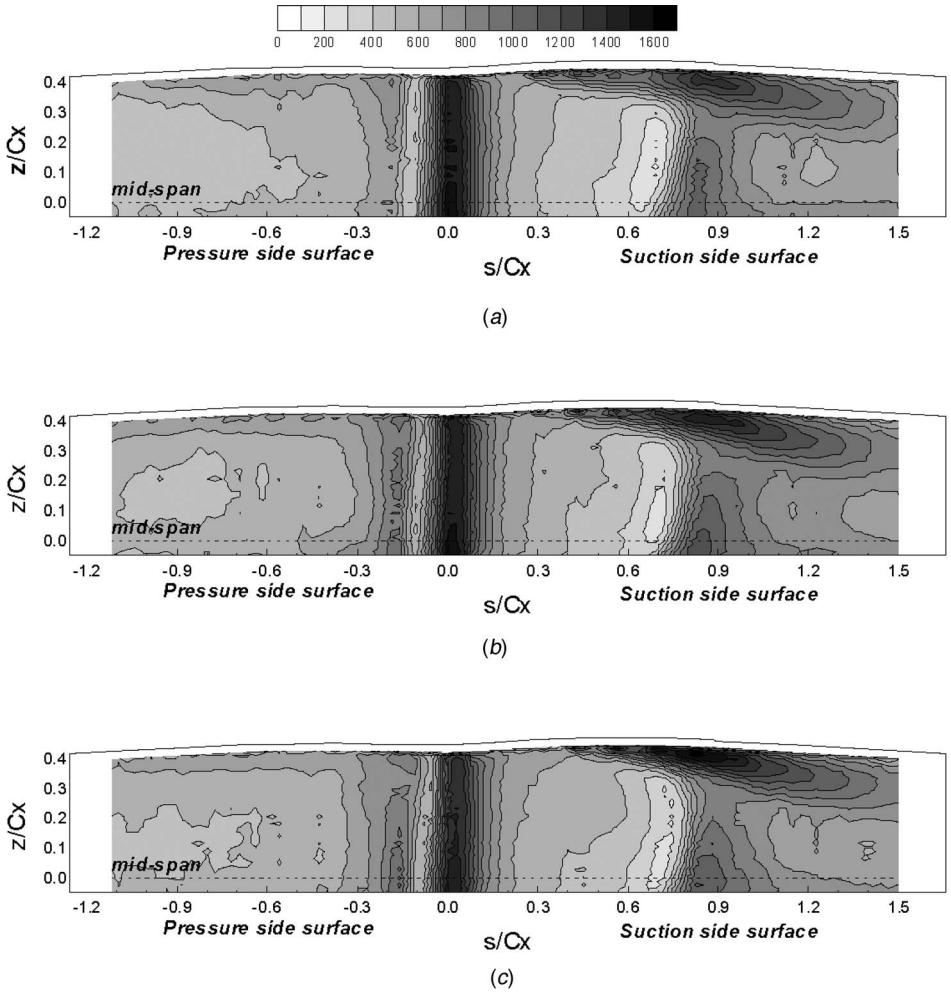

Fig. 13 Contour plots of Sh_C on the surface of blade with negative incidence angles at $Re_{C,ex}=1.8\times10^5$. (*a*) $i=-5$ deg ($N=307.8$ rpm); (*b*) $i=-10$ deg ($N=349.5$ rpm); (*c*) $i=-15$ deg ($N=384.2$ rpm).

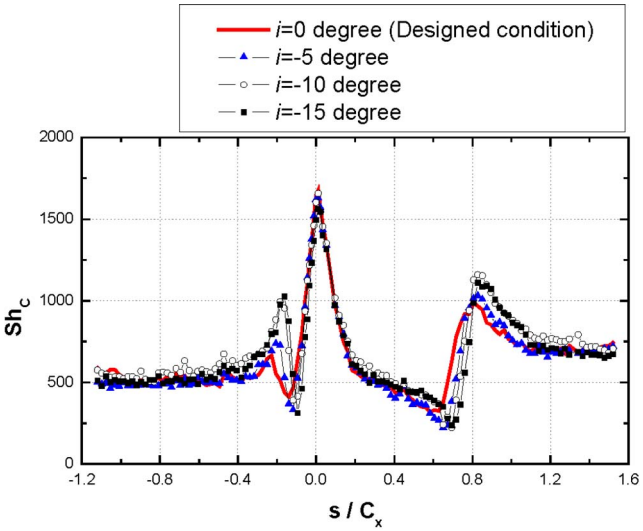

Fig. 14 Local distributions of Sh_C at mid-span for the blade with negative incidence angles at $Re_{C,ex}=1.8\times10^5$

The incidence angle of the incoming flow has a strong influence on the blade surface heat transfer. With the positive incidence angle, the laminar separation bubble on the pressure side surface of the blade disappears and the peak due to the flow transition on

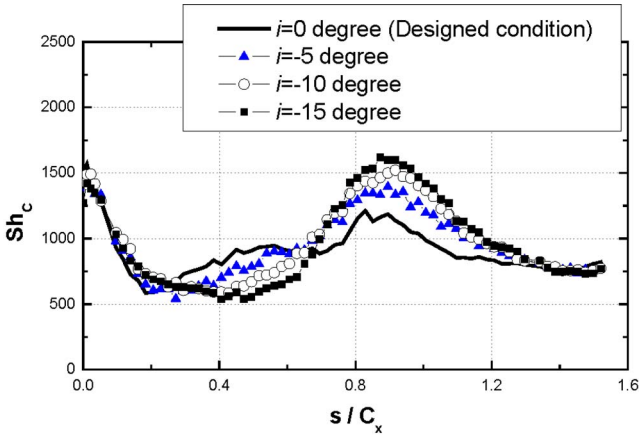

Fig. 15 Local distributions of Sh_C on the suction side surface at $z/C_x=0.4$ for the blade with negative incidence angles at $Re_{C,ex}=1.8\times10^5$

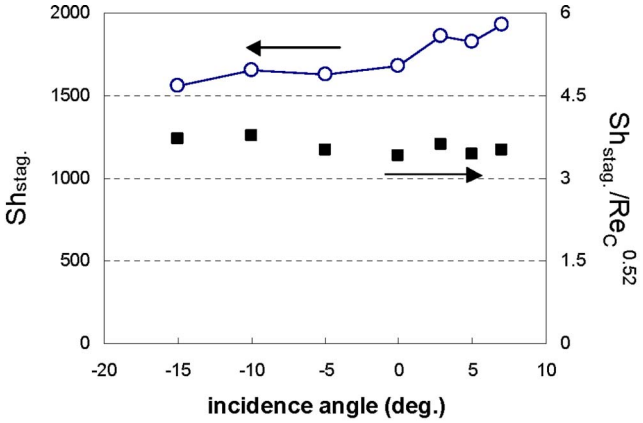

Fig. 16 Sh_C at stagnation point for various incidence angles at $Re_{C,ex}=1.8\times10^5$

the suction surface is shifted toward the tip and the size of the transition region is decreased considerably. In addition, the enhanced region due to the tip leakage vortex is significantly reduced because the leakage flow separates from the blade. As the incidence angle decreases, the position of flow transition becomes shifted downstream and the effects of the tip leakage vortex become stronger because the local flow near the suction surface get accelerated and the tip gap flow is driven downstream. But, the heat/mass transfer on the pressure side is hardly affected.

Acknowledgment

The authors wish to acknowledge support for this study by the Korean Ministry of Science and Technology through the National Research Laboratory program.

Nomenclature

C = blade chord length
C_P = static pressure coefficient
C_x = blade axial chord length
D_{naph} = diffusion coefficient of naphthalene in the air
h_m = local mass transfer coefficient
i = incidence angle
l = blade span
$\dot{m}$ = naphthalene mass transfer per unit time and area
N = rotational speed of blade
Nu_C = Nusselt number
Pr = Prandtl number
p = blade pitch
P_0 = total pressure of incoming flow
P_s = static pressure on the blade surface
R = degree of reaction, $0.5-V_0/2U(\tan\beta_1-\tan\alpha_2)$
Re_C = Reynolds number based on blade chord length and incoming flow velocity
$Re_{C,ex}$ = Reynolds number based on blade chord length and exit flow velocity
S = spacing between guide plate and blade
s = coordinate on blade surface (Fig. 2)
Sc = Schmidt number
Sh_C = Sherwood number based on blade chord length
t = tip clearance
Tu = turbulence intensity of incoming flow
U = blade speed
u = flow velocity at the vane exit
u_{mean} = average flow velocity at the guide plate exit
V_0 = flow velocity at the inlet of guide plate
V_1 = absolute flow velocity at the blade inlet
V_2 = absolute flow velocity at the blade exit
W_1 = relative flow velocity at the blade inlet
W_2 = relative flow velocity at the blade exit
x, y, z, s = coordinate system (Fig. 2)

Greek Symbols

α_1 = guide plate exit angle
α_2 = absolute flow angle at the blade exit
β_1 = blade inlet angle
β_2 = blade exit angle
δz = naphthalene sublimation depth
$\delta\tau$ = test duration
ϕ = flow coefficient, V_0/U
λ = speed work, $1/\psi$
ρ_s = solid naphthalene density
$\rho_{v,w}$ = saturated vapor density of naphthalene
$\rho_{v,\infty}$ = vapor density of naphthalene in the flow
ψ = blade loading coefficient, $2V_0/U(\tan\alpha_1-\tan\alpha_2)$

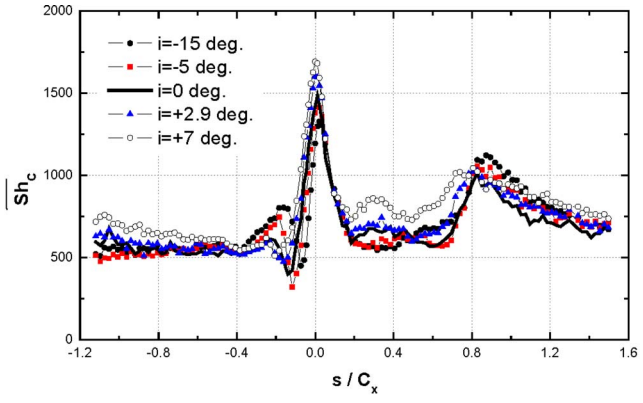

Fig. 17 Spanwise averaged Sh_C on the blade surface for various incidence angles at $Re_{C,ex}=1.8\times10^5$

References

[1] Bunker, R. S., 2001, "A Review of Turbine Blade Tip Heat Transfer," Ann. N.Y. Acad. Sci., **934**, pp. 64–79.
[2] Metzger, D. E., Dunn, M. G., and Hah, C., 1991, "Turbine Tip and Shroud Heat Transfer," J. Turbomach., **113**, pp. 502–507.
[3] Rhee, D. H., and Cho, H. H., 2005, "Local Heat/Mass Transfer Characteristics on Rotating Blade with Flat Tip in a Low Speed Annular Cascade: Part 2—Tip and Shroud," ASME Paper No. GT2005-68724.
[4] Chen, P. H., and Goldstein, R. J., 1992, "Convective Transport Phenomena on the Suction Surface of a Turbine Blade Including the Influence of Secondary Flows Near the Endwall," J. Turbomach., **114**, pp. 776–787.
[5] Goldstein, R. J., Wang, H. P., and Jabbari, M. Y., 1994, "The Influence of Secondary Flows near the Endwall and Boundary Layer Disturbance on Convective Transport from a Turbine Blade," ASME Paper No. 94-GT-165.
[6] Han, J. C., Zhang, L., and Ou, S., 1993, "Influence of Unsteady Wake on Heat Transfer Coefficient From a Gas Turbine Blade," J. Heat Transfer, **115**, pp. 904–911.
[7] Arts, T., Duboue, J.-M., and Rollin, G., 1998, "Aerothermal Performance Measurements and Analysis of a Two-dimensional High Turning Rotor Blade," J. Turbomach., **120**, pp. 494–499.
[8] Blair, M. F., 1994, "An Experimental Study of Heat Transfer in a Large-scale Turbine Rotor Passage," J. Turbomach., **116**, pp. 1–13.
[9] Goldstein, R. J., and Spores, R. A. 1988, "Turbulent Transport on the Endwall in the Region Between Adjacent Turbine Blades," J. Heat Transfer, **110**, pp. 862–869.
[10] Hermanson, K., Kern, S., Picker, G., and Parneix, S., 2003, "Predictions of External Heat Transfer for Turbine Vanes and Blades With Secondary Flowfields," J. Turbomach., **125**, pp. 107–113.
[11] Giel, P. W., Boyle, R. J., and Bunker, R., 2004, "Measurements and Predictions of Heat Transfer on Rotor Blades in a Transonic Turbine Cascade," J. Turbomach., **126**, pp. 122–129.

[12] Kwak, J. S., and Han, J. C., 2003, "Heat Transfer Coefficients on the Squealer Tip and Near Squealer Tip Regions of a Gas Turbine Blade," J. Heat Transfer, **125**, pp. 669–677.
[13] Jin, P., and Goldstein, R. J., 2003, "Local Mass/Heat Transfer on Turbine Blade Near-Tip Surface," J. Turbomach., **125**, pp. 521–528.
[14] Kwon, H. G., Lee, S. W., and Park, B. K., 2002, "Measurements of Heat (Mass) Transfer Coefficient on the Surface of a Turbine Blade with a High Turning Angle Using Naphthalene Sublimation Technique," KSME Journal B, **26**, pp. 1077–1087.
[15] Rhee, D. H., and Cho, H. H., 2005, "Heat/Mass Transfer Characteristics on Stationary Turbine Blade and Shroud in a Low Speed Annular Cascade (I) — Near-Tip Blade Surface," Trans. KSME B, **29**, pp. 485–494.
[16] Bathie, W. W., 1996, *Fundamentals of Gas Turbines*, 2nd ed., John Wiley & Sons, New York.
[17] Goldstein, R. J., and Cho, H. H., 1995, "A Review of Mass Transfer Measurement Using Naphthalene Sublimation," Exp. Therm. Fluid Sci., **10**, pp. 416–434.
[18] Kline, S. J., and McClinetock, F., 1953, "Describing uncertainty in single sample experiments," Mech. Eng. (Am. Soc. Mech. Eng.), **75**, pp. 3–8.
[19] Rhee, D. H., 2004, "Local Heat/Mass Transfer Characteristics on Turbine Rotor and Shroud in a Low Speed Annular Cascade," Ph.D. thesis, Yonsei University.
[20] Mayle, R. E., 1991, "The Role of Laminar-Turbulent Transition in Gas Turbine Engines," J. Turbomach., **113**, pp. 509–537.

Local Heat/Mass Transfer Characteristics on a Rotating Blade With Flat Tip in a Low-Speed Annular Cascade—Part II: Tip and Shroud

Dong-Ho Rhee

Hyung Hee Cho

Department of Mechanical Engineering,
Yonsei University,
Seoul 120-749, Korea

The local heat/mass transfer characteristics on the tip and shroud were investigated using a low speed rotating turbine annular cascade. Time-averaged mass transfer coefficients on the tip and shroud were measured using a naphthalene sublimation technique. A low speed wind tunnel with a single stage turbine annular cascade was used. The turbine stage is composed of sixteen guide plates and blades. The chord length of blade is 150 mm and the mean tip clearance is about 2.5% of the blade chord. The tested Reynolds number based on inlet flow velocity and blade chord is 1.5×10^5 *and the rotational speed of the blade is 255.8 rpm at design condition. The results were compared with the results for a stationary blade and the effects of incidence angle of incoming flow were examined for incidence angles ranging from −15 to +7 deg. The off-design test conditions are obtained by changing the rotational speed with a fixed incoming flow velocity. Flow reattachment on the tip near the pressure side edge dominates the heat transfer on the tip surface. Consequently, the heat/mass transfer coefficients on the blade tip are about 1.7 times as high as those on the blade surface and the shroud. However, the heat transfer on the tip is about 10% lower than that for the stationary case due to reduced leakage flow with the relative motion. The peak regions due to the flow reattachment are reduced and shifted toward the trailing edge and additional peaks are formed near the leading edge region with decreasing incidence angles. But, quite uniform and high values are observed on the tip with positive incidence angles. The time-averaged heat/mass transfer on the shroud surface has a level similar to that of the stationary cases.* [DOI: 10.1115/1.2098767]

Introduction

As the turbine inlet temperature increases, the turbine blade tip region including the shroud becomes one of the weakest regions subject to a severe excessive thermal load since the turbine blade tip operates in the transitional environment between the rotating airfoil and the stationary flow path casing, which experiences the most extreme fluid-thermal conditions within the turbine [1].

The turbine blade has a small tip clearance between the tip and shroud, and the leakage flow through the finite clearance between the tip and casing (shroud) is generated by the pressure difference between the pressure and suction sides of the blade. The flow entering the gap from the pressure side is accelerated and separates at the edge of the tip and then reattaches on the tip surface. Due to these flow characteristics, extremely high heat transfer rates are observed near the tip and on the tip of the blade. Also, the leakage flow discharged from the tip gap interacts with the mainstream (hot gases) near the suction side tip of the blade, which may cause excessive heat transfer on the surface. Thus, the leakage flow has a strong influence not only on the stage aerodynamic performance but also on the structural durability of the blade as reported by Metzger et al. [2]. Therefore, to improve the reliability and durability of turbine blade, complex cooling techniques have been developed and used on the tip and near-tip regions.

To obtain more effective cooling performance, the complete understanding of flow and heat transfer characteristics is required and this can be achieved more easily by investigating the heat transfer characteristics on the tip and on the near-tip region at the same time. In addition, various operating conditions should be taken into account for an accurate analysis.

The flow characteristics around the blade tip (leakage flow) in a turbine have been investigated extensively and the basic tip leakage flow mechanism and the effects on aerodynamics and heat transfer in turbomachinery are well summarized and explained by Lakshminarayana [3]. Recently, with the development of numerical simulation techniques, many numerical studies on the effects of tip geometry have been presented. Ameri and co-workers [4–6] had investigated extensively the effects of tip clearance, tip geometry and casing recess on the flow and heat transfer using a GE-E^3 blade geometry. Yang et al. [7,8], Acharya et al. [9], and Saha et al. [10] also studied the flow and heat transfer characteristics for blades with different leakage reduction strategies including squealer tip and winglet using a commercial code, FLUENT. Tallman and Lakshminarayana [11,12] simulated tip leakage flows in axial flow turbines with various tip clearances and investigated the effects of relative motion of the outer casing numerically for a turbine cascade with a tip clearance height of 1.0% span. They found that the addition of relative motion of the outer casing results in a decrease in the mass flow through the gap. Also, they showed that the majority of the leakage flow exits the gap from

Contributed by the International Gas Turbine Institute (IGTI) of ASME for publication in the JOURNAL OF TURBOMACHINERY. Paper presented at the ASME Turbo Expo 2005: Land, Sea, and Air, Reno, NV, June 6 – 9, 2005, Paper No. GT2005-68724. Manuscript received October 1, 2004; final manuscript received February 1, 2005. IGTI Review Chair: K. C. Hall.

the downstream half of the gap due to the moving casing's shear layer, which is also presented in the work by Metzger et al. [2].

Since the late 1990s, the studies have been performed for the heat transfer on the tip under various conditions. Bunker et al. [13] and Ameri and Bunker [4] investigated tip heat transfer for different tip clearances and tip edge shapes in a linear turbine cascade. Bunker [1] reviewed the studies related to tip heat transfer and suggested guidelines for further studies in this field, such as consideration of blade rotation, shrouded tip geometry and tip cooling. Azad et al. [14,15] and Kwak and Han [16] have studied extensively the GE-E^3 blade tip heat transfer in a stationary linear cascade using a transient liquid crystal technique. They investigated the effects of blade tip clearance (from 1% to 2.5% of blade chord), freestream turbulence intensity (6.1% and 9.7%), tip geometry and film cooling. Saxena et al. [17] investigated the effects of tip geometry and unsteady wake on the tip flow and heat transfer for a blade in a low speed cascade using a steady state HSI-based liquid crystal technique. Jin and Goldstein [18] measured mass transfer coefficients on the flat tip of the blade in a stationary linear cascade using a naphthalene sublimation method. They changed the tip clearance from 0.86% to 6.90% of chord for two different freestream turbulence intensities (0.2% and 12.0%). Papa et al. [19] also investigated the heat transfer characteristics on the squealer tip or the tip with winglet on pressure side at four different tip clearances from 0.6% to 3.6% of chord using a naphthalene sublimation method.

The casing, i.e., the shroud is also one of the hot components that are exposed to extreme thermal loads in a gas turbine engine. However, while the heat transfer characteristics on the blade surface, tip and endwall have been investigated by many researchers, heat transfer on the stationary casing (shroud) has not been focused considering its importance. Metzger et al. [2] measured time-resolved heat flux and compared them with predictions. Kumada et al. [20] investigated the flow patterns in the gap and the heat transfer patterns on the shroud for various conditions in a rotating axial flow turbine. They correlated heat transfer coefficients with tip clearance and Reynolds number and showed that the overall heat transfer coefficients become smaller as the tip clearance increases regardless of rotational speed and the conditions of flow angle. Cho et al. [21] and Rhee et al. [22] presented detailed heat/mass transfer coefficients on the shroud for various tip clearances and different incoming flow turbulence intensities in a linear turbine cascade and recently, Kwak and Han [16] measured and presented local heat transfer coefficients on the shroud for a blade with squealer tip in a stationary linear cascade, and reported that the level of the heat transfer coefficients is about 70% of that on the blade tip. Recently, Thorpe et al. [23,24] measured time-mean and time-resolved heat transfer rate on the shroud in a transonic axial-flow turbine operating at engine representative flow conditions. They found the compressibility effect in the tip gap on the heat transfer on the casing.

Although there are many studies dealing with blade heat transfer, most of the studies have dealt with tip heat transfer or the blade surface heat transfer separately under limited operating conditions. However, to figure out and understand detailed heat transfer characteristics more precisely, complementary analysis based on the local heat transfer information on the near-tip region, tip and shroud should be done. Therefore, in this study, heat transfer distributions on the tip, shroud and the near-tip surface of the blade are considered together for the rotating blade at various conditions.

While Part I deals with the blade surface heat transfer for the rotating blade, the heat/mass transfer characteristics on the tip of the blade and shroud are investigated in this paper (Part II). First, basic heat transfer characteristics on the tip and shroud are examined for the stationary blade and the effect of blade rotation is estimated by comparing the result for the rotating blade with the stationary case. Then, the effect of incidence angles ranging from −15 deg to +7 deg is investigated for a fixed absolute inlet flow velocity. To measure local heat/mass transfer coefficients on the tip and shroud, a naphthalene sublimation method was used.

Experimental Apparatus and Procedure

Experimental Apparatus and Operation. Figure 1(*a*) shows the schematic view of the experimental apparatus of a low speed wind tunnel for the annular turbine cascade. The apparatus is composed of three parts: an upstream fan with 15 HP motor, an annular passage with test section (a single stage of turbine) and a downstream fan with 10 HP motor and motor for blade rotation. The annular passage has a 1.7-m-long straight section based on the outer casing. The outer and inner diameters of the annular passage are 900 mm and 620 mm, respectively, and the corresponding height of the passage is 130 mm. The test section of a turbine stage is located in the annular passage and a photograph showing the test section is presented in Fig. 1(*b*). To simulate a single turbine stage, the test section is designed to contain a row of sixteen guide plates in front of the rotating disk having sixteen turbine blades. The spacing between the guide plate and blade is 34 mm (S=34 mm). The details of experimental apparatus are presented in Part I.

Guide Plate and Blade Configurations. As mentioned in the previous section, a single turbine stage is installed in the annular passage. The schematic view of the cross section of the stage at the mid-span is shown in Fig. 1(*b*).

Sixteen guide plates of thickness 1.3 mm are installed 34 mm upstream of the blades. Each guide plate has a 70 deg exit angle and the axial chord length is 120 mm. As mentioned in Part I, a different guide plate was made and used in the stationary experiments. In that case, the plate is designed to have the exit angle of 56.4 deg, which is the blade inlet angle. The details for the guide plate for stationary cases are listed in Rhee and Cho [25]. The mid-span profile of GE 7FA 1st stage blade is used for the turbine cascade. The chord length of the blade is 150 mm and the inlet and exit angles are 56.4 deg and 62.6 deg, respectively. Note that the blade has a constant cross section (i.e., blade inlet angle) and consequently the incidence angle changes along the span for a fixed operating condition. The mean tip clearance based on measured values of the test blade is about 3.8 mm, which is 2.5% of chord. The nomenclature and details of the blade geometry are given in Fig. 1(*b*) and Table 1.

Operating Conditions

Design Conditions. As explained in Part I, the experiment for the stationary blade was conducted first to investigate the basic heat/mass transfer characteristics on the blade tip and shroud surfaces and to serve as baseline data for comparison with the rotating cases. For this experiment, another guide plate with an exit angle equal to the blade inlet angle was installed and the position of the blade was adjusted to obtain uniform inlet velocity distributions because the relative position between the guide plate and blade affects the velocity distributions at the inlet of the blade. The inlet Reynolds number is fixed to $Re_C = 1.5 \times 10^5$.

The experiment with the rotating blade at the design condition was performed at $Re_C = 1.5 \times 10^5$ and the rotational speed of 255.8 rpm (U=10.3 m/s). Detailed conditions for the experiment with the rotating blade are listed in Table 2. Since the blade has the same blade profile along the span, the blade has a non-zero incidence angle along the span even at the design condition because the guide exit flow angle is fixed at 70 deg over the span. The different blade inlet flow angles along the span are listed in Table 3.

Off-Design Conditions. To investigate the effect of off-design condition on local heat transfer on the blade, the experiments for various incidence angles ranging from −15.0 deg to +7.0 deg were conducted. In the present study, the off-design conditions were obtained by changing rotational speed (i.e., blade speed, U)

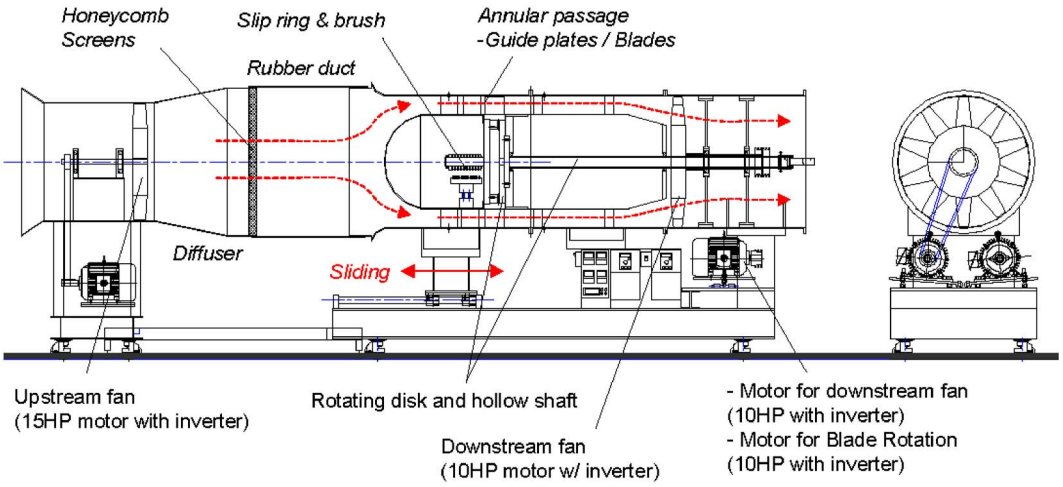

(*a*)

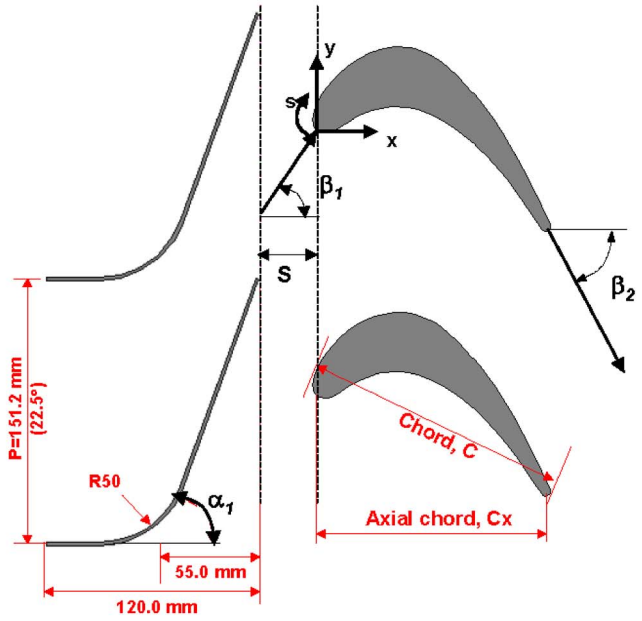

(*b*)

Fig. 1 Schematics of experimental apparatus and test section. (*a*) Experimental apparatus; (*b*) test section

Table 1 Blade configurations

Number of blades	16	
Chord length (C)	150 mm	
Axial chord (C_x)	131.5 mm	
Pitch to chord ratio (p/C)	Hub	0.84
	Mean	1.01 (22.5°)
	Tip	1.17
Aspect ratio (l/C)	0.87	
Spacing between vane and blade	34 mm (0.227C)	
Radius at mid-span	385 mm	
hub/tip radius ratio	0.711	
Blade inlet / exit angle	β_1=56.4° / β_2=−62.6°	
Turning angle	119.0°	
Mean tip clearance (t)	3.8 mm(t/C=2.5%)	

with fixed inlet flow velocity. In addition, the actual incidence angle at the tip is different from that at mid-span because the off-design conditions are based on the mid-span geometry. Tables 4 and 5 present the flow conditions and actual incidence angles at the hub, the mid-span and the tip for various incidence angles.

Table 2 Design conditions for rotating blade (based on mid-span geometry and the inlet Reynolds number)

Inlet flow velocity(V_0)/mean Tu	8.3 m/s/∼9%
Guide exit flow velocity (V_1)[a]	24.3 m/s
Blade inlet velocity(W_1)/mean Tu	15 m/s/∼3%
Rotational speed (N)	255.8 rpm
Blade speed (U)	10.3 m/s
Blade exit velocity (W_2)[a]	18.0 m/s
Re_C	1.5×10^5
$Re_{C,exit}$	1.8×10^5

[a]Calculated from inlet to exit area ratio.

Table 3 Conditions for radial positions at designed condition

Radial position	Hub	Mid-span	Tip
Radius	0.320 m	0.385 m	0.450 m
Blade speed (U)	8.6 m/s	10.3 m/s	12.1 m/s
Relative blade inlet velocity (W_1)	16.5 m/s	15.0 m/s	13.6 m/s
Relative inlet flow angle	59.8°	56.4°	52.3°
Incidence angle (i)	+3.4°	0°	−4.1°

Note that the relative inlet flow velocity (i.e., Re_C) increases for a fixed absolute inlet flow velocity as the incidence angle increases and Re_C also changes along the span due to the variation of blade speed. The variation of Re_C with incidence angle is presented in Part I.

Heat/Mass Transfer Coefficient

Naphthalene Coated Tip and Shroud. Detailed heat/mass transfer measurements on the blade tip and shroud were conducted using a naphthalene sublimation method. To measure the local mass transfer coefficients, test blade tip and shroud with naphthalene-coated surfaces were designed and manufactured. The test blade is made of aluminum, and the shroud is made of steel.

The tip surface of the test blade is designed to have a rim of 5 mm along the periphery to maintain the sharp tip edge and naphthalene is cast within the rim on the tip. The shroud test plate for naphthalene casting also has a rim around the naphthalene coated surface, which covers 1.5 times the pitch in the circumferential direction and 1.2 times the axial chord in the axial direction. The details of the test plates are presented in Ref. [25].

Data Reduction. The mass transfer coefficient is obtained from sublimation depth and exposure time and Sherwood number is used to present the heat transfer results. The Sherwood number is expressed as

$$Sh_C = h_m C / D_{naph} \tag{2}$$

The uncertainty in Sherwood numbers using the method of Kline and McClintock [26] for single sample experiments is within ±7.4% in the entire operating range of the measurement, based on a 95% confidence interval.

To measure local sublimation depth on the curvilinear surface, a four-axis measurement system with a LVDT gage was used. Detailed specifications of the LVDT and the measurement system are described by Rhee [27].

Results and Discussion

Flow and Static Pressure Measurements. The experiments were conducted at $Re_C = 1.5 \times 10^5$. The turbulence intensity of the inlet flow is about 3–4 % in the mid-way and the boundary layer thickness is less than 5 mm. The detailed inlet flow conditions are presented in Part I [28].

To predict the flow characteristics on the shroud, the static pressure was measured on the shroud and represented in the form of static pressure coefficient. The definition of the static pressure coefficient is as follows

$$C_p = (P_s - P_0)/0.5\rho V_0^2 \tag{3}$$

The distribution of C_p at blade mid-span is given in Part I. Figure 2 shows the measured static pressure coefficient distribution on the shroud for the stationary blade at $Re_C = 1.5 \times 10^5$. In this case, the total pressure and the velocity at the inlet of the guide are used to calculate the static pressure coefficient. Small circles in the figure indicate the positions of static pressure taps.

As expected, large difference of static pressure between the pressure and suction sides is shown along the blade periphery. The static pressure decreases rapidly as the flow enters the tip clearance along the pressure side edge due to the flow acceleration (i.e., flow entrance effect). Then the static pressure decreases as the flow develops in the gap passage. In the gap, local peak values of C_p are observed in the middle ($x/C_x \cong 0.4$) with low values at upstream and downstream regions in the gap. This peak is strongly related to the divided tip leakage flows (upstream and downstream leakage flows), and these flow characteristics are confirmed in the local heat/mass transfer results on the shroud (Fig. 3(*b*)) and the blade surface, which is presented in Part I.

Along the suction side edge, the region of the lowest coefficient at the suction side is located at $x/C_x \cong 0.15$, which corresponds to $s/C_x = 0.3-0.4$. This is presumably related to the flow acceleration and the upstream tip leakage flow, which is mentioned in Part I [28]. The high heat transfer on the blade surface in this region ($s/C_x = 0.3-0.4$ near the tip) is due to this flow characteristic.

Table 4 Off-design conditions based on the mid-span geometry

Incidence angle	−15°	−10°	−5°	0°
N[rpm]	384.2	349.5	307.8	255.8
U[m/s]	15.5	14.1	12.4	10.3
W_1[m/s]	11.1	12.0	13.3	15.0
Incidence angle	0°	+2.9°	+5°	+7°
N[rpm]	255.8	218.8	188.0	154.5
U[m/s]	10.3	8.8	7.6	6.2
W_1[m/s]	15.0	16.2	17.3	18.6

Table 5 Actual incidence angle along the span

Incidence angle at mid-span (deg)	Actual incidence angle (deg)		
	Hub	Mean	Tip (i_t)
−15.0	−6.3	−15.0	−26.9
−10.0	−3.2	−10.0	−19.0
−5.0	0.0	−5.0	−11.4
0.0	3.4	0.0	−4.1
2.9	5.4	2.9	0.0
5.0	6.9	5.0	2.8
7.0	8.4	7.0	5.5

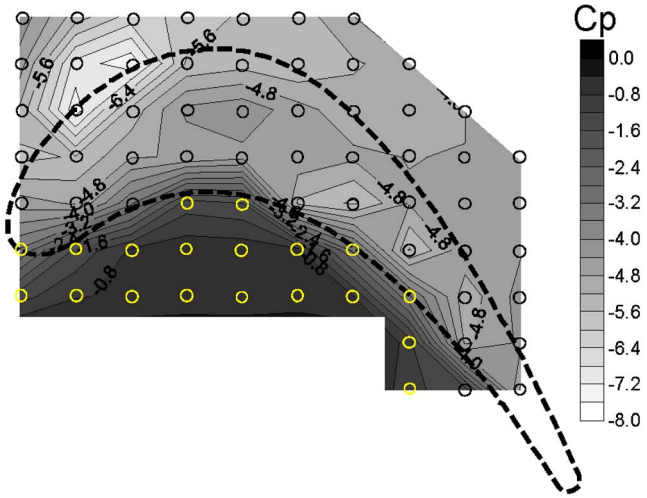

Fig. 2 Distribution of static pressure coefficient on the shroud surface for stationary blade

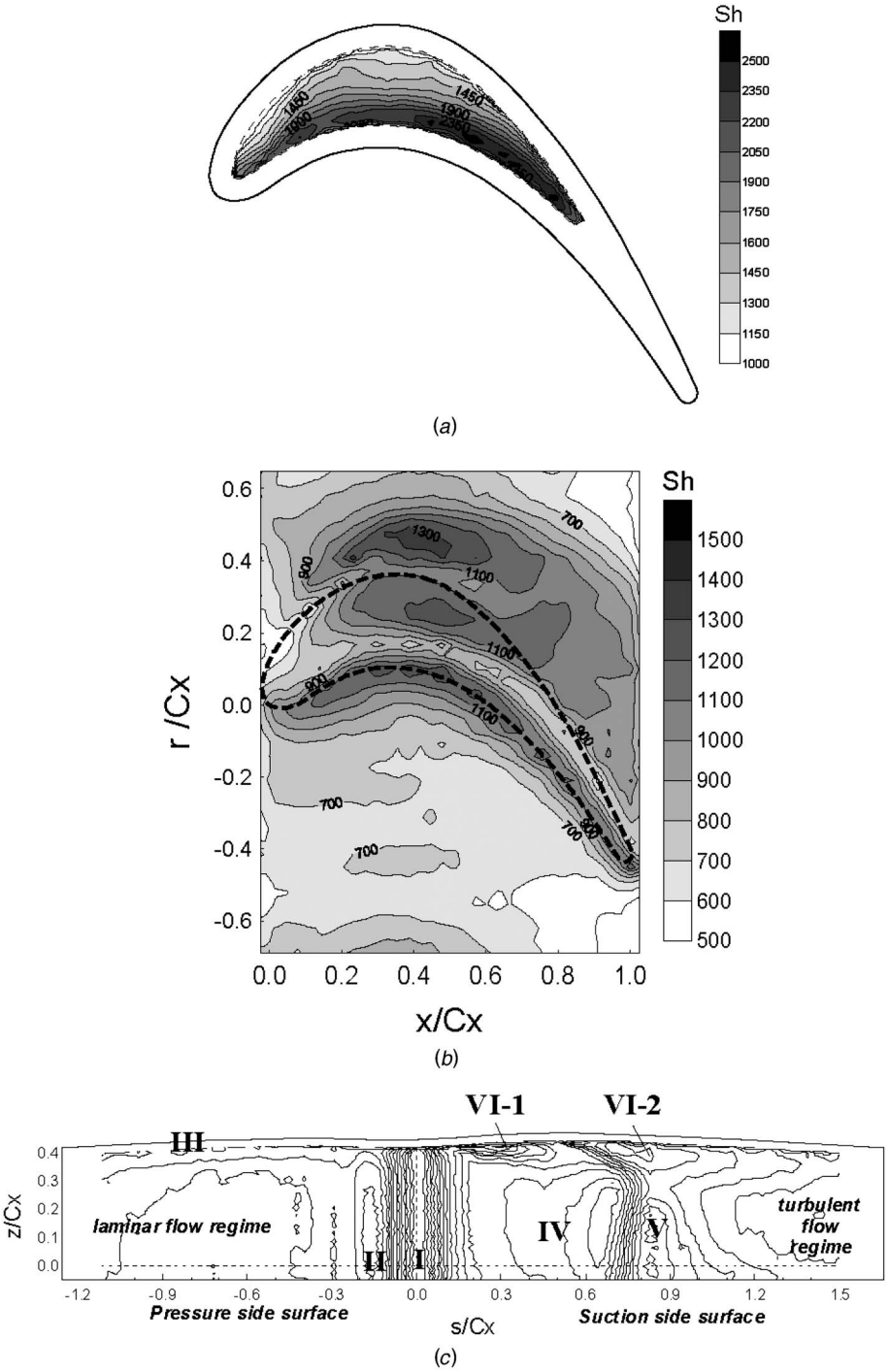

Fig. 3 Contour plots of Sh_C on the tip and shroud surface at $Re_C=1.5\times10^5$. (*a*) On the tip; (*b*) on the shroud; (*c*) on the blade surface [28].

Heat/Mass Transfer Measurements on the Tip and Shroud for Stationary Blade

Heat/Mass Transfer on the Tip. Figures 3(*a*) and 4(*a*) present the local distributions of Sh_C on the flat tip for the stationary blade at $Re_C=1.5\times10^5$. In the figure, the outer line and the blanked region represent the blade profile and the aluminum rim, respectively.

In the tip gap, the flow reattachment after the separation at the pressure side edge of the blade dominates the heat transfer on the tip. Therefore, the heat transfer pattern on the tip is simple: peak values at the reattachment region and then monotonic decrease with flow development. However, the level of heat/mass transfer coefficients is much higher than that on the surface and shroud (about 1.5–1.7 times higher in average value). This explains why the blade tip region is so weak and has to be cooled intensively.

In the upstream region, the region of high heat transfer is formed close to the pressure side edge along the pressure side. But, the tip gap flow tends to be shifted toward the downstream region because the gap entering flow has an axial momentum like the mainstream and relatively low transfer coefficients are observed near the suction side edge in the upstream region. This low transfer region is in accordance with the "sweet spot" reported by

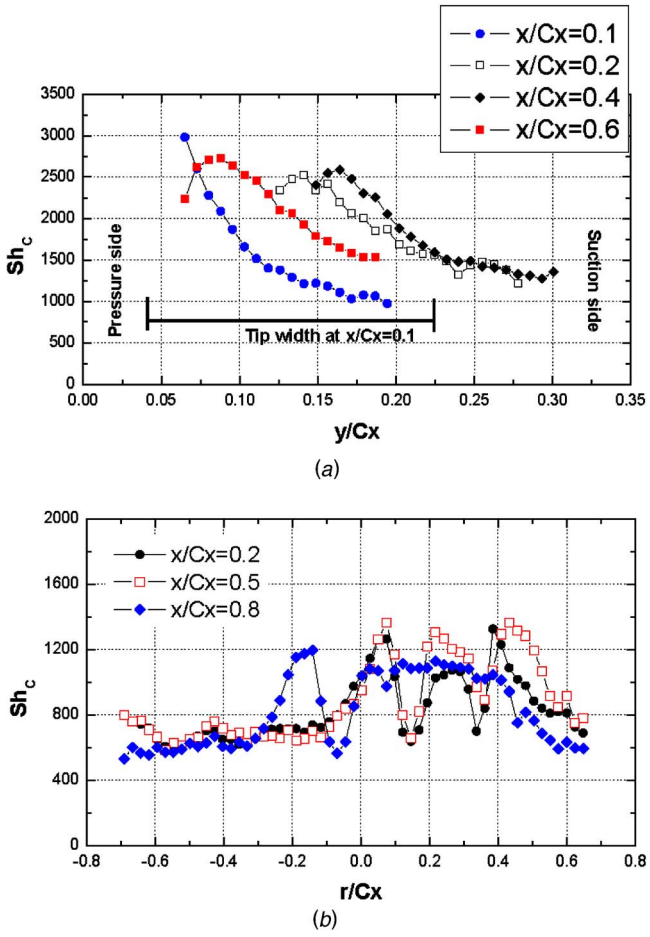

Fig. 4 Pitchwise distributions of Sh_C on the tip and shroud for stationary blade at $Re_C=1.5\times10^5$. (*a*) $i=0$ deg ($i_t=-4.1$ deg); (*b*) $i=+2.9$ deg ($i_t=0$ deg).

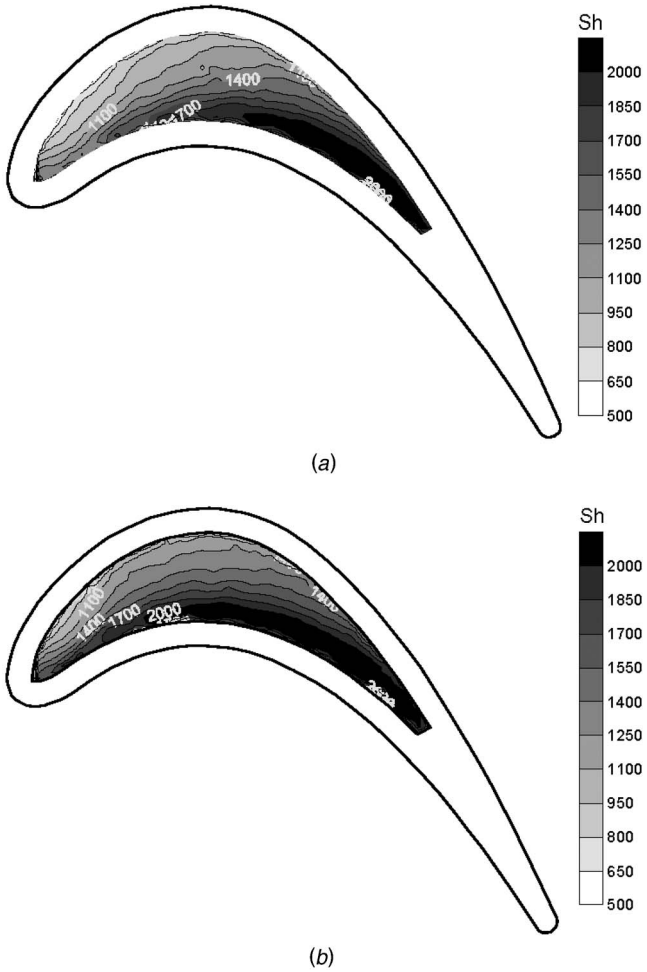

Fig. 5 Contour plots of Sh_C on the flat tip of blade for rotating blade. (*a*) $i=0$ deg ($i_t=4.1$ deg); (*b*) $i=2.9$ deg ($i_t=0$ deg).

Bunker et al. [13]. On the contrary, in the downstream region, as shown evidently in Fig. 3(*a*), local peaks near the pressure side are located in the gap (approximately $0.06C_x$ from the pressure side edge) because a large portion of the flow near the tip enters the gap in this region. This results in a relatively large recirculation bubble at the edge. It is noted that the low heat transfer region due to the flow recirculation at the pressure side edge is not shown clearly because most of this region is coincident with the aluminum rim on the tip.

Heat/Mass Transfer on the Shroud. Local heat/mass transfer distributions on the shroud are shown in Figs. 3(*b*) and 4(*b*). Like the blade surface, the shroud has complex heat transfer characteristics. The heat transfer on the shroud can be classified by the flow patterns, such as flow acceleration, laminarization, transition to turbulence and leakage vortex.

As expected, locally high heat/mass transfer coefficients are observed along the pressure side because of the flow acceleration with thin boundary layer thickness (flow entrance effect). This high heat transfer region corresponds to region III in the blade surface heat transfer (indicated in Fig. 3(*c*)). After the flow enters the tip gap, local valleys of heat/mass transfer are formed in the gap along the pressure side edge. Those regions are coincident with the peaks on the blade tip (Fig. 3(*a*)) exactly. This means that the separation bubble on the blade tip partly blocks the gap and then promotes the acceleration of the gap flow near the shroud. As a result, the flow experiences the relaminarization along the separation bubble on the tip. Then, local peak values are shown in the middle of the gap because of the flow transition, which is clearly shown in Fig. 4(*b*). The flow characteristics described above are also reported by Moore and Tilton [29]. Their visualization result presents quite similar patterns of flow acceleration and transition. However, in the heat transfer studies [9,16], heat transfer characteristics related to flow relaminarization and/or transition in the gap are not reported. This is possibly because these characteristics are dependent on the flow conditions, such as Reynolds number and turbulence intensity.

An additional high heat transfer region is formed outside the suction side edge. This is presumably due to the upstream tip

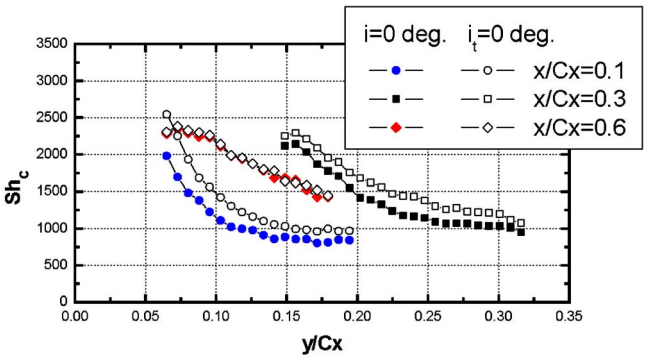

Fig. 6 Local distributions of Sh on the tip for the rotating blade at design condition ($i=0$ deg, $i_t=-4.1$ deg)

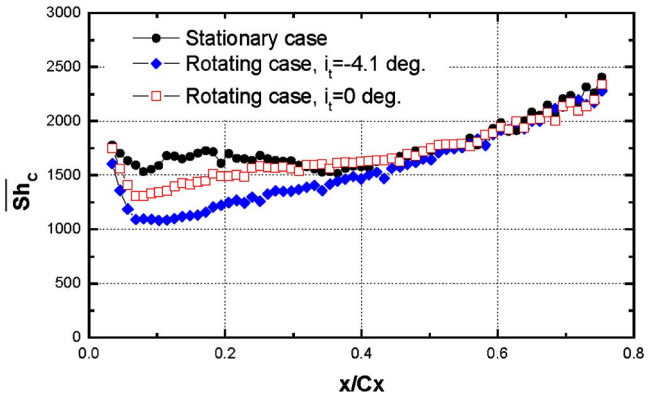

Fig. 7 Pitchwise averaged Sh_C on the tip for the rotating blade at $Re_{C,in}=1.5\times10^5$ and $N=255.8$ rpm

leakage flow. The upstream tip leakage vortex increases the blade surface heat transfer (indicated as region VI-1 in Fig. 3), then it detaches from the surface and increases the heat transfer significantly on the shroud presumably due to the flow impingement and entrainment of mainflow by the leakage vortex. At first, this leakage vortex flows along the suction side edge and then is expected to separate from the blade surface and then be weakened as the flow moves on to the downstream side because the peak values are located apart from the suction side edge of the blade.

The existence of local minimum values between the peaks due to the flow transition and upstream tip leakage vortex reveals that the upstream leakage vortex disturbs the discharge of the downstream tip leakage flow to some extent and the effect of the downstream tip leakage flow is confined to the downstream region. Therefore, the effects of the downstream tip leakage flow on the shroud outside the gap are not as significant as those of the upstream leakage flow although its effect on the blade surface is apparent (VI-2 in Fig. 3(*c*)).

Note that the effect of horseshoe and passage vortices is not observed on the shroud. This is because of the thin boundary layer and large spacing between the blades. Therefore, as mentioned briefly in Part I, the effect of these secondary flows on the blade surface is also negligible.

Heat/Mass Transfer Measurements on the Tip and Shroud for Rotating Blade

Comparison with Stationary Blade. Heat transfer patterns on the tip of the rotating blade are presented in Figs. 5 and 6. Because the incidence angle at the tip is negative for the design condition, another result at $i_t=0$ deg is presented together in these figures. As expected in the results on the blade surface (Part I), for rotating blade cases, the high heat/mass transfer region is shifted toward the downstream side and heat/mass transfer at the upstream region is lower than that in the downstream region.

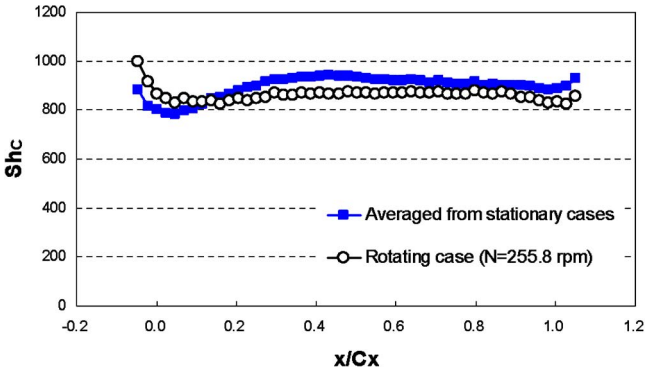

Fig. 8 Streamwise distribution of pitchwise-averaged Sh_C on the shroud for the rotating blade at design condition ($i=0$ deg)

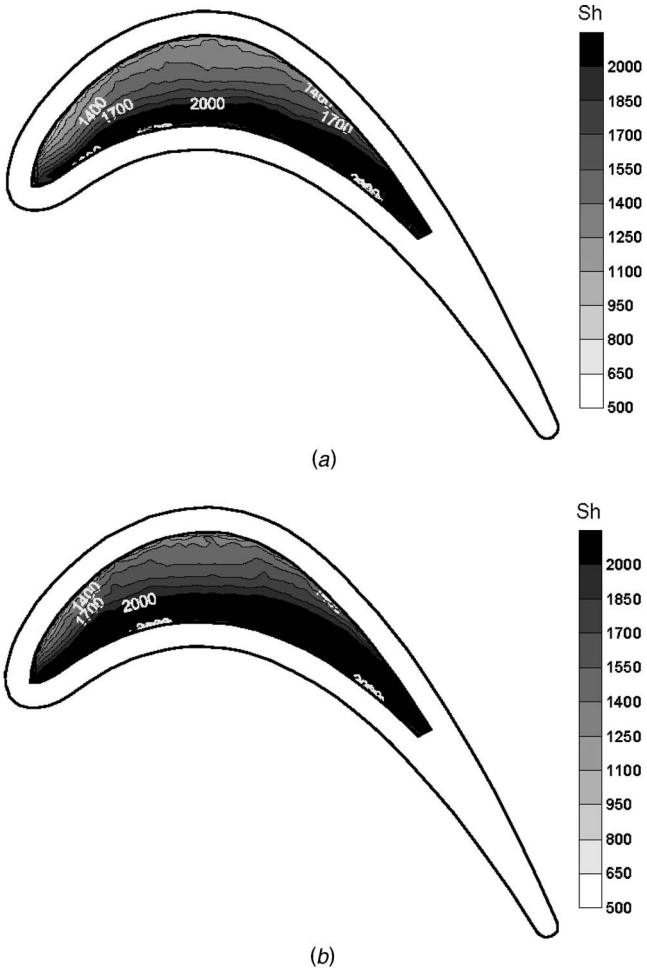

Fig. 9 Contour plots of Sh_C on the flat tip of blade with positive incidence angles at $Re_{C,ex}=1.8\times10^5$. (*a*) $i=+5$ deg ($i_t=+2.8$ deg); (*b*) $i=+7$ deg ($i_t=+5.5$ deg).

When the result for the design condition (Fig. 5(*a*)) is compared with the stationary cases (Figs. 3(*a*) and 4(*a*)), the heat/mass transfer coefficients are quite lower than those for the stationary case primarily because the rotating blade has a negative incidence angle at the tip (about −4.1 deg) and the rotation reduces the flow rate of tip gap flow making thicker boundary layer near the shroud surface. If the incidence angle is zero at the tip as shown in Figs. 5 and 6, the heat/mass transfer coefficients on the tip are slightly increased because the flow rate of gap entering flow increases. However, even when the incidence angle is zero at the tip, this case has about 20% lower values at the upstream region than the stationary case due to the relative motion between the blade and shroud. This means that not only the incidence angle but also the blade rotation plays an important role in determining the local heat/mass transfer at the upstream region on the tip.

The pitchwise averaged Sh_C distributions on the tip are shown in Fig. 7. As mentioned, the rotating case has lower heat transfer coefficients in the upstream region than the stationary case. For example, at $i_t=-4.1$ deg (i.e., incidence angle at the mid-span is zero), the level is only 60% of that of the stationary case. However, in the downstream region, all of the cases have almost the same values. This means that the heat transfer in the downstream region is not significantly affected by the flow conditions such as

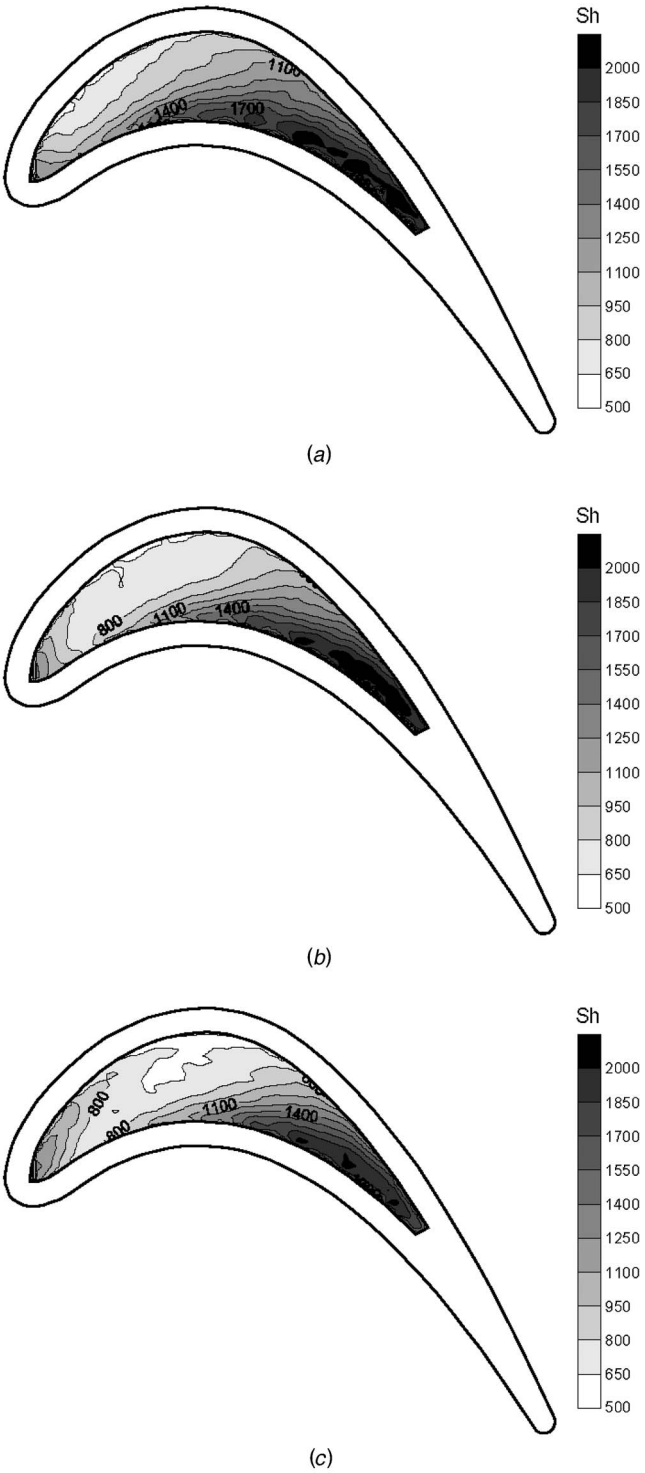

Fig. 10 Contour plots of Sh_C on the flat tip of blade with negative incidence angles at $Re_{C,ex}=1.8\times10^5$. (*a*) $i=-5$ deg ($i_t=-11.4$ deg); (*b*) $i=-10$ deg ($i_t=-19.0$ deg); (*c*) $i=-15$ deg ($i_t=-26.9$ deg).

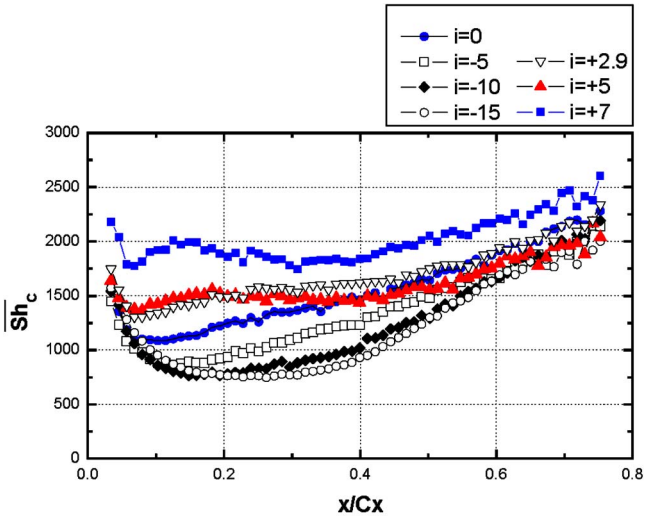

Fig. 11 Pitchwise averaged Sh_C on the tip of blade with various incidence angles at $Re_{C,ex}=1.8\times10^5$

the incidence angle. The main reason is possibly that most of the leakage flow exits the gap from the downstream half of the gap due to the moving casing's shear layer [2,12].

Figure 8 shows the pitchwise-averaged Sh_C on the shroud for the rotating blade at $N=255.8$ rpm and $Re_C=1.5\times10^5$. Although the distributions of time-averaged heat/mass transfer coefficients on the shroud are similar to those for the stationary cases, the level is slightly lower (less than 10%) than that for stationary cases because the tip gap flow is reduced with blade rotation. However, the local heat/mass transfer at the inlet region is higher than that for the stationary cases. This may be related to the elevated turbulence intensity of the mainstream for the rotating case.

Effect of Incidence Angle. On the whole, the effect of rotation on the shroud heat transfer seems not to be significant under the operating conditions in the present study. Hence only the tip heat transfer is considered to examine the effect of incidence angle.

Positive incidence angle. Figure 9 shows the contour plots of Sh_C on the tip for the rotating blade with two different positive incidence angles at $Re_{C,ex}=1.8\times10^5$. As described in the previous section, the flow rate of the gap entering flow increases as the incidence angle increases, and this results in the increase of heat transfer rate in the overall region. The "sweet spot" in the upstream region also disappears because the near-tip flow entering the gap has a higher incoming flow angle.

Negative incidence angle. While the results at positive incidence angles show similar patterns to those for the stationary case and the design condition, the results at negative incidence angles show different patterns. Contour plots of Sh_C on the tip are pre-

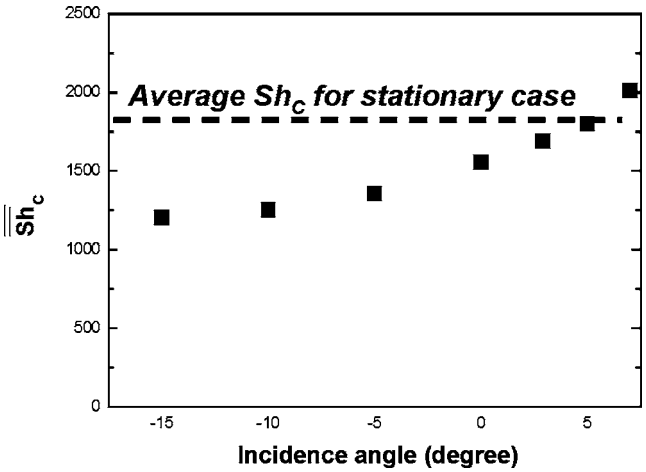

Fig. 12 Area averaged Sh_C on the tip of blade with various incidence angles at $Re_{C,ex}=1.8\times10^5$

sented in Fig. 10 for the rotating blade with negative incidence angles at $Re_{C,ex}=1.8\times10^5$. As the incidence angle decreases from 0 deg to −15 deg the heat/mass transfer enhanced region due to flow reattachment, moves downstream and a region of high heat/mass transfer at the leading edge region appears and becomes enlarged. The reason is that the freestream approaching the blade contacts the leading edge and the suction side edge rather than the pressure side with lower incidence angle due to the "aggressive" turning angle of the blade. Between these two high heat/mass transfer regions, relatively low heat/mass transfer coefficients are observed. But, in the downstream region, heat transfer is not affected by the incidence angle variation because the effect of flow reattachment is dominant. Therefore, it can be inferred that the heat transfer on the upstream region of the tip is strongly influenced by the local flow angle near the tip region while the downstream region is hardly affected.

Average heat/mass transfer. Figure 11 shows the streamwise distributions of the pitchwise averaged Sh_C on the tip for various conditions. Near the leading edge, the averaged heat/mass transfer coefficients are almost the same as each other. But, as the flow moves downstream, the difference between the values for the cases increases rapidly. The distributions for the case of positive incidence angles are quite uniform while the cases with negative incidence angles have quite low values in the upstream region ($0.1\leqslant x/C_x\leqslant0.4$). For the lowest value ($i=-15$ deg) heat/mass transfer is less than 50% of that for the highest value ($i=7$ deg), which means that the blade tip may experience abrupt change of local heat transfer rate in start-up and shut-down process.

In the downstream region ($x/C_x\geqslant0.6$), the values converge into a line. This means that the heat transfer near the trailing edge is not sensitive to the mainflow conditions. Another interesting feature is that the Sh_C values in the downstream region are higher than those in any other regions and this means that this region needs to be cooled more intensively.

Total averaged Sh_C distributions in Fig. 12 also show the same trend with the incidence angle variation. Due to the relative motion between the blade and shroud, the averaged Sh_C on the tip is lower than that for the stationary case even when the incidence angle at the tip is positive ($i_t=2.8$ deg).

Conclusions

In this paper, the heat/mass transfer characteristics on the blade tip and shroud surface are investigated. After the basic heat transfer characteristics for the stationary blade are examined, the effects of blade rotation and incidence angle are investigated.

The tip gap flow due to the pressure difference between the pressure and suction sides induces very high heat/mass transfer rate on the tip. The heat/mass transfer coefficients on the blade tip are about 1.5–1.7 times higher than those on the surface or the shroud due to the flow reattachment after the separation. After the flow reattaches on the tip surface, it develops as new turbulent boundary layer and then the Sh_C decreases monotonically in the pitchwise direction. The shroud has complex heat/mass transfer characteristics because it has complex flow patterns, such as flow acceleration, relaminarization, transition and tip leakage vortex. But, the level of heat/mass transfer coefficients is only 60–70 % of that on the tip.

When the blade rotates, the heat/mass transfer enhanced region on the tip is shifted toward the downstream side and the level of heat/mass transfer coefficients at the upstream region of the tip is slightly decreased due to the reduced tip gap flow with rotation. On the shroud surface, while the distributions of time-averaged heat/mass transfer coefficients are similar to those for the stationary cases, the level is slightly lower (less than 10%) than that for stationary cases. Thus the blade rotation causes some differences in the heat transfer on the surface, tip and shroud due to the reduced tip leakage flow.

The incidence angle of the incoming flow has a strong influence on the blade tip heat transfer. With a positive incidence angle, more uniform and higher heat transfer rates are observed on the tip due to the increased tip gap flow and high flow angle. The enhanced region moves downstream and the low heat transfer region, so-called "sweet spot" is enlarged as the incidence angle decreases. An additional enhanced region appears and becomes enlarged at the leading edge region.

Acknowledgment

The authors wish to acknowledge support for this study by the Korean Ministry of Science and Technology through the National Research Laboratory program.

Nomenclature

C = blade chord length
C_P = static pressure coefficient
C_x = blade axial chord length
D_{naph} = diffusion coefficient of naphthalene in the air
h_m = local mass transfer coefficient
i = incidence angle
l = blade span
N = rotational speed of blade
p = blade pitch
P_0 = total pressure of incoming flow
P_s = static pressure on the shroud
Re_C = Reynolds number based on blade chord length and incoming flow velocity
$Re_{C,ex}$ = Reynolds number based on blade chord length and exit flow velocity
S = spacing between guide plate and blade
Sc = Schmidt number
$\underline{Sh}_C$ = Sherwood number based on blade chord length
$\overline{Sh}_C$ = pitchwise averaged Sherwood number
t = tip clearance
Tu = turbulence intensity of incoming flow
U = blade speed
V_0 = flow velocity at the inlet of guide plate
V_1 = absolute flow velocity at the blade inlet
W_1 = relative flow velocity at the blade inlet
W_2 = relative flow velocity at the blade exit
x,y,z,s = coordinate system (Fig. 1)

Greek Symbols

β_1 = blade inlet angle
β_2 = blade exit angle

References

[1] Bunker, R. S., 2001, "A Review of Turbine Blade Tip Heat Transfer," Ann. N.Y. Acad. Sci., **934**, pp. 64–79.
[2] Metzger, D. E., Dunn, M. G., and Hah, C., 1991, "Turbine Tip and Shroud Heat Transfer," J. Turbomach., **113**, pp. 502–507.
[3] Lakshminarayana, B., 1996, *Fluid Dynamics and Heat Transfer of Turbomachinery*, John Wiley and Sons, New York.
[4] Ameri, A. A., Steinthorsson, E., and Rigby, D. L., 1999, "Effects of Tip Clearance and Casing Recess on Heat Transfer and Stage Efficiency in Axial Turbines," J. Turbomach., **121**, pp. 683–693.
[5] Ameri, A. A., and Bunker, R. S., 2000, "Heat Transfer and Flow on the First Stage Blade Tip of a Power Generation Gas Turbine—Part II: Simulation Results," J. Turbomach., **122**, pp. 272–277.
[6] Ameri, A. A., 2001, "Heat Transfer and Flow on the Blade Tip of a Gas Turbine Equipped with a Mean-Camberline Strip," J. Turbomach., **123**, pp. 704–708.
[7] Yang, H., Acharya, S., Ekkad, S. V., Prakash, C., and Bunker, R. S., 2002, "Flow and Heat Transfer Predictions for a Flat-Tip Turbine Blade," ASME Paper No. GT2002-30190.
[8] Yang, H., Acharya, S., Ekkad, S. V., Prakash, C., and Bunker, R. S., 2002, "Numerical Simulation of Flow and Heat Transfer Past a Turbine Blade With a Squealer-Tip," ASME Paper No. GT2002-30193.
[9] Acharya, S., Yang, H., Ekkad, S. V., Prakash, C., and Bunker, R. S., 2003, "Numerical Study of Flow and Heat Transfer on a Blade Tip With Different Leakage Reduction Strategies," ASME Paper No. GT2003-38617.
[10] Saha, A. K., Acharya, S., Prakash, C., and Bunker, R. S., 2003, "Blade Tip

Leakage Flow and Heat Transfer With Pressure Side Winglet," ASME Paper No. GT2003-38620.
[11] Tallman, J., and Lakshminarayana, B., 2001, "Numerical Simulation of Tip Leakage Flows in Axial Flow Turbines, With Emphasis on Flow Physics—Part I: Effect of Tip Clearance Height," J. Turbomach., **123**, pp. 314–323.
[12] Tallman, J., and Lakshminarayana, B., 2001, "Numerical Simulation of Tip Leakage Flows in Axial Flow Turbines, With Emphasis on Flow Physics—Part II: Effect of Outer Casing Relative Motion," J. Turbomach., **123**, pp. 324–333.
[13] Bunker, R. S., Bailey, J. C., and Ameri, A. A., 2000, "Heat Transfer and Flow on the First Stage Blade Tip of a Power Generation Gas Turbine—Part 1: Experimental Results," ASME J. Turbomach., **122**, pp. 263–271.
[14] Azad, Gm S., Han, Je-Chin, Teng, S., and Boyle, R. J. 2000, "Heat Transfer and Pressure Distributions on a Gas Turbine Blade Tip," J. Turbomach., **122**, pp. 717–724.
[15] Azad, Gm S., Han, Je-Chin, and Boyle, R. J. 2000, "Heat Transfer and Flow on the Squealer Tip of a Gas Turbine Blade," J. Turbomach., **122**, pp. 725–732.
[16] Kwak, J. S., and Han, J. C., 2003, "Heat Transfer Coefficients on the Squealer Tip and Near Squealer Tip Regions of a Gas Turbine Blade," J. Heat Transfer, **125**, pp. 669–677.
[17] Saxena, V., Nasir, H., and Ekkad, S. V., 2003, "Effect of Blade Tip Geometry on Tip Flow and Heat Transfer for a Blade in a Low Speed Cascade," J. Turbomach., **126**, pp. 130–138.
[18] Jin, P., and Goldstein, R. J., 2002, "Local Mass/Heat Transfer on a Turbine Blade Tip," 9th International Symposium on Transport Phenomena and Dynamics of Rotating Machinery, Paper No. HT-ABS-012.
[19] Papa, M., Goldstein, R. J., and Gori, F., 2003, "Effects of Tip Geometry and Tip Clearance on the Mass/Heat Transfer From a Large-Scale Gas Turbine Blade," J. Turbomach., **125**, pp. 90–96.
[20] Kumada, M., Iwata, S., Obata, M., and Watanabe, O., 1994, "Tip Clearance Effect on Heat Transfer and Leakage Flows on the Shroud-Wall Surface in an Axial Flow Turbine," J. Turbomach., **116**, pp. 39–45.
[21] Cho, H. H., Rhee, D. H., and Choi, J. H., 2001, "Heat/Mass Transfer Characteristics on Turbine Shroud with Blade Tip Clearance," Ann. N.Y. Acad. Sci., **934**, pp. 281–288.
[22] Rhee, D. H., Choi, J. H., and Cho, H. H., 2001, "Effect of Blade Tip Clearance on Turbine Shroud Heat/Mass Transfer," ASME Paper No. 2001-GT-158.
[23] Thorpe, S. J., Yoshino, S., Ainsworth, R. W., and Harvey, N. W., 2004, "An Investigation of the Heat Transfer and Static Pressure on the Over-Tip Casing Wall of an Axial Turbine Operating at Engine Representative Flow Conditions. (I) Time-Mean Results," Int. J. Heat Fluid Flow, **25**, pp. 933–944.
[24] Thorpe, S. J., Yoshino, S., Ainsworth, R. W., and Harvey, N. W., 2004, "An Investigation of the Heat Transfer and Static Pressure on the Over-Tip Casing Wall of an Axial Turbine Operating at Engine Representative Flow Conditions. (II) Time-Mean Results," Int. J. Heat Fluid Flow, **25**, pp. 945–960.
[25] Rhee, D. H., and Cho, H. H., 2005, "Heat/Mass Transfer Characteristics on Stationary Turbine Blade and Shroud in a Low Speed Annular Cascade (I) — Near-Tip Blade Surface," Trans. KSME B, **29**, pp. 485–494.
[26] Kline, S. J., and McClinetock, F., 1953, "Describing Uncertainty in Single Sample Experiments," Mech. Eng. (Am. Soc. Mech. Eng.), **75**, pp. 3–8.
[27] Rhee, D. H., 2004, "Local Heat/Mass Transfer Characteristics on Turbine Rotor and Shroud in a Low Speed Annular Cascade," Ph.D. thesis, Yonsei University.
[28] Rhee, D. H., and Cho, H. H., 2006, "Local Heat/Mass Transfer Characteristics on Rotating Blade With Flat Tip in a Low Speed Annular Cascade—Part I: Near-Tip Surface," J. Turbomach., **128**, pp. 96–109.
[29] Moore, J., and Tilton, J. S., 1988, "Tip Leakage Flow in a Linear Turbine Cascade," ASME J. Turbomach., **110**, pp. 18–26.

Averaging Nonuniform Flow for a Purpose

N. A. Cumpsty
Rolls-Royce plc,
Derby, UK

J. H. Horlock
Whittle Laboratory,
.Cambridge, UK

Averaging nonuniform flow is important for the analysis of measurements in turbomachinery and gas turbines; more recently an important need for averaging arises with results of computational fluid dynamics (CFD). In this paper we show that there is a method for averaging which is "correct," in the sense of preserving the essential features of the nonuniform flow, but that the type of averaging which is appropriate depends on the application considered. The crucial feature is the decision to retain or conserve those quantities which are most important in the case considered. Examples are given to demonstrate the appropriate methods to average nonuniform flows in the accounting for turbomachinery blade row performance, production of thrust in a nozzle, and mass flow capacity in a choked turbine. It is also shown that the numerical differences for different types of averaging are, in many cases, remarkably small. [DOI: 10.1115/1.2098807]

1 Introduction

In this paper we revisit an old problem with the aim of clarifying the principles and simplifying application. It is a principal aim of this paper to make the topic seem simple by explaining clearly how averaging is best done. To this end we restrict ourselves to the type of flow found in a gas turbine or turbomachine and to ideal gases, those for which the specific enthalpy is a function of temperature only. Another aim of the paper is to take away the apparent arbitrariness of the treatments in the past. Different schemes for averaging have been proposed, but it seemed to be a matter of opinion or convenience which was used. We will show that the appropriate method of averaging depends on the situation or use to be made of the average and from this it follows that there is a "correct" method of averaging for each situation. We set up a hypothetical uniform flow which is appropriately equivalent to the nonuniform flow—that is, equivalent in the quantities which are most important for the case considered. For example, when considering nonuniform flow into a compressor we imagine a uniform flow which would require the same work input to raise its pressure to some arbitrary level as the work to raise the nonuniform flow to the same pressure. From this uniform flow the appropriate average properties, like average pressure and temperature, may be found. Although we show that there is an appropriate average for particular circumstances, it will, however, be shown that quantitatively the various averages differ very little for flows likely to occur in gas turbines.

All internal flows are, to some extent, nonuniform, though the area of nonuniformity may be restricted to the boundary layers on the internal walls. Very often there are much more extensive nonuniformities, as for example downstream of a fan, compressor, combustor, or turbine. Sometimes there are strong nonuniformities in the flow entering an engine, normally in that case because of flow separation in the intake. In all cases our assessments of component performance (pressure ratio and component efficiency) are based on single values of pressure and temperature at inlet and outlet. Moreover the analysis of the thermodynamic cycle normally uses single values for pressure and temperature at different stations in the engine. The way that the nonuniform flow is represented by single values of temperature and pressure is, therefore, of considerable importance.

There have been a number of articles on averaging, of which the most extensive is the AGARD report of the Panel Working Group by Pianko and Wazelt [1]. More recently the book by Greitzer et al. [2] considers averaging. Pianko and Wazelt refer back to Traupel [3] and to Livesey and Hugh [4]. Many of the conclusions of Pianko and Wazelt are consistent with our own, and we agree with their statement "no uniform flow exists which simultaneously matches all the significant stream fluxes, aerothemodynamic and gemometric parameters of a nonuniform flow." But we did not find their work easy to understand, or their reasons for any particular system of averaging as clear as one might wish. Moreover, in the past the various averaging methods have been treated as alternatives, with different persuasions leading to their adoption. It is the assertion of this paper that the choice of averaging system is not arbitrary, nor is that system unique, for the system of averaging needs to vary with the flow process being considered

In this paper we, therefore, attempt a simpler representation which is intended to make the principles and process transparent. The general approach we will adopt is to consider two uniform streams of perfect gas, one with mass flow rate $\dot{m}_a$, temperature T_a and pressure P_a; the other with mass flow rate $\dot{m}_b$, temperature T_b, and pressure P_b. (Most often the mass flow rates of the two streams are taken here as equal.) Once the underlying philosophy has been clearly shown the generalization to continuously nonuniform distributions of pressure and temperature is straightforward.

The temperatures and pressures that are of most concern for gas turbines are the stagnation or total values and for brevity these will be denoted by T and P; the corresponding static temperature and pressure will be denoted by t and p. The emphasis in this paper is simplicity, so the main part will be presented for a perfect gas, that is an ideal gas for which c_p is constant, $\gamma = c_p/c_v$ is also constant, and $c_p = \gamma R/(\gamma - 1)$. Where it is appropriate, at the exit of the combustor, the effect of fuel-air ratio and temperature on c_p will be touched on. The wider treatment of more general ideal gases, where $c_p = c_p(T)$, may be obtained easily, though the treatment then normally requires numerical methods. The treatment of reacting gases, or mixtures of vapor and liquid, is more difficult and is not considered here.

It remains true today that with experimental data in engines there is frequently little scope to average the data in any way more than a crude area average. Very often the biggest inaccuracy or uncertainty comes from the assumptions necessary to extrapolate the measurements to the walls. The advent of two- and three-dimensional CFD, however, has lead to a new need for averaging output, and in this case there is ample opportunity to select the correct averaging technique, since, in principle, all the variables of the flow are available in greater density of coverage than is common with experiment.

Contributed by the International Gas Turbine Institute (IGTI) of ASME for publication in the JOURNAL OF TURBOMACHINERY. Manuscript received October 1, 2004; final manuscript received February 1, 2005. IGTI Review Chair: K. C. Hall. Paper presented at the ASME Turbo Expo 2005: Land, Sea, and Air, Reno, NV, June 6–9, 2005, Paper No. GT2005-68081.

Four different cases of averaging of stagnation quantities are considered here. In the first three cases the way that the average pressure is found differs but the flux of stagnation enthalpy is matched for the nonuniform flow and the average flow so that the average temperature in all cases is the mass-average stagnation temperature, denoted by T^m. The last case, the flow into a choked nozzle, is rather different and in this case the temperature is averaged differently. The four cases considered are as follows:

(1) *Flow where the flux of enthalpy and availability are of concern*. In this situation the fluxes of availability and enthalpy for the nonuniform flow are equal to those of the uniform average flow. The mass-average enthalpy and availability give the mass-average entropy and from these one can determine a derived pressure P^d and derived temperature T^d. Put another way, the average pressure and temperature are chosen to give fluxes of mass, enthalpy, and availability for the uniform flow which are equal to those of the nonuniform flow. This approach will be referred to as an **availability average** and the resulting derived pressure will be denoted P^{dB};

(2) *Flow into a compressor or turbine* where the interest is in the work input or output, the pressure ratio across it and the efficiency. The derived average pressure in this case will be referred to as the **work-average** stagnation pressure and denoted by P^{dw};

(3) *Flow leaving the outlet guide vanes of a fan or LP turbine*, so that the component downstream is the propelling nozzle of a jet engine. In this case the average stagnation pressure is that which gives the same gross thrust as the nonuniform pressure. The derived **thrust-average** stagnation pressure is denoted by P^{dt};

(4) *Flow into a choked nozzle, such as the first row of a high-pressure turbine*, where the quantity of concern is the mass flow capacity of the nozzle. In this case the stagnation pressure is effectively uniform (since the flow velocities in a combustor are low) but the stagnation temperature may vary by a large amount, typically by a factor of about two. In this case the average stagnation temperature is the **nozzle average** denoted by T^{dn}.

2 Extensive Properties and Flux

In flow devices like gas turbines, compressors etc. we are normally concerned with flux of matter, enthalpy and entropy. The flux of enthalpy $\int H d\dot{m}$ is important because the difference between inlet and outlet is equal to the sum of the heat and work. The flux of entropy $\int s d\dot{m}$ is important because it provides a measure of the losses which occur. It is well known that for a perfect gas

$$s - s_{\text{ref}} = c_p \ln(T/T_{\text{ref}}) - R \ln(P/P_{\text{ref}}) = R \ln[(T/T_{\text{ref}})^{\gamma/(\gamma-1)}/(P/P_{\text{ref}})]$$

where T_{ref} and P_{ref} denote reference conditions. In the interests of brevity, T_{ref} and P_{ref} will normally be omitted from expressions for entropy as written in this paper. Both enthalpy and entropy are extensive properties—those that define a property per unit mass. Another extensive quantity of obvious application to flow machines is the availability, $B=H-T_0 s$, where the temperature of the environment is T_0, taken to be constant. It follows that the flux of availability is given by

$$\int B d\dot{m} = \int H d\dot{m} - T_0 \int s d\dot{m}$$

Where it is possible to define a flux it is very straightforward to define useful and meaningful averages, usually referred to as mass averages. For the specific cases of enthalpy and entropy we obtain

$$\dot{m} s^m = \int s d\dot{m} \quad \text{and} \quad \dot{m} H^m = \int H d\dot{m}.$$

Just as entropy and enthalpy lend themselves to mass averages derived from the flux, so too does the availability,

$$\dot{m} B^m = \int B d\dot{m}.$$

In contrast to enthalpy and entropy, pressure and temperature are not extensive but intensive properties and it is, for example, meaningless to talk of the flux of pressure. For many gases, and all the gases that will be considered here, the enthalpy may be related to the temperature by $H=c_p T$, where c_p is either constant or a function of temperature alone. If the gas is effectively perfect, that is $c_p=$const, the expression for the flux of enthalpy may be rewritten as

$$\dot{m} T^m = \int T d\dot{m}.$$

Thus, although the temperature is an intensive property, the linear relationship between enthalpy and temperature for a perfect gas makes the mass average of temperature convenient and useful. The same is not true for pressure and most of the present paper is concerned with the way in which pressure should be averaged. Although it is without formal justification it is common to use a mass-average stagnation pressure, defined by

$$\dot{m} P^m = \int P d\dot{m}.$$

and where helpful this will be compared with the more appropriately defined averages.

3 The Averaged State and Derived Properties

It has normally been assumed, either explicitly or tentatively, that there must be a "correct" method of averaging which will be universally valid: Unfortunately this does not seem to be the case. Whenever a two- or three-dimensional flow is simplified down to an equivalent one-dimensional flow, information is necessarily discarded. The manner in which this should be discarded depends on the purpose for which the average is being created—*there is an appropriate method for each application whose use is not a matter of choice or preference*.

For a pure substance, such as air or combustion products of a particular chemical composition, all the gas properties may be obtained if two independent properties are known, the two-property rule. So if, for example the enthalpy and entropy are known it is possible to find temperature, pressure, density and so on. Different authors have explored the possible base variables, see for example, Traupel [3] and Livesey and Hugh [4]. Here we take stagnation enthalpy and entropy as our base properties which we mass average so that we may obtain derived average pressure P^d and temperature T^d from them. Thus

$$P^d = P(H^m, s^m) \quad \text{and} \quad T^d = T(H^m, s^m)$$

in terms of mass average enthalpy and entropy. For the special case of the perfect gas the derived stagnation temperature is equal to the mass average temperature

$$T^d = T^m$$

4 Area Averaging

The appropriate average for the static pressure is derived from the net force on an area A, that is

$$F = A p^A = \int p dA,$$

where A is the cross-sectional area and p^A is the area-average static pressure. This may be generalized to the area average of a flux of momentum. There is, however, no foundation for averaging stagnation pressure, temperature, enthalpy or entropy on the basis of the area: The procedures for stagnation enthalpy or stagnation pressure

$$AH^A = \int HdA \quad \text{or} \quad AP^A = \int PdA,$$

are without rational basis.

Notwithstanding the emphatic statement above, area averaging is widely used for a practical reason—it is very often the best and only procedure available for averaging the readings of a limited number of pressure probes and thermocouples buried in an engine. As will be shown with a numerical example in the context of the flow out of a fan, the area average will agree surprisingly well with the more rational averages in many practical cases; where it becomes noticeably inaccurate is when there is a region of separated fluid which occupies a significant cross-sectional area but passes very little mass flow. This was illustrated in the case of loss in a compressor blade row by Cumpsty [5] and examples are given for set profiles in Greitzer et al. [2].

5 Mixed Out Averaging

One of the approaches to averaging a nonuniform flow is to imagine the flow undergoing a hypothetical process downstream of the plane under consideration so that the flow mixes out to a uniform condition. Being hypothetical, this may be undertaken under different assumptions and the two most common are constant static pressure or constant flow area. Even though the process normally takes a long distance in the flow direction, it is normal to ignore the friction on the endwalls. This is the approach of Dzung [6] which was extended by Prasad [7] in a recent paper. The approach may be defended on the grounds that it is definite and prescribed, there being nothing arbitrary about it beyond the specification of constant area or uniform static pressure. However, it is not normally a very useful approach, since few devices have sufficient distance downstream to make this process even vaguely realistic. But the mixed-out average may be useful for the case of wakes in the blade-to-blade surface, downstream of well designed blades (that is unseparated blades with thin wakes), an approach described by Amecke [8]. The reason that this is useful is that the wakes normally mix out in a distance comparable with the pitch or chord of the blades and so a nearly uniform downstream condition is a good approximation for cascade testing. (The approach also has application for mixers and similar devices, where active steps are taken to produce rapid mixing and adequate length is allowed for this.) Even for the blade-to-blade flow it is probable that in most turbomachines the next blade row downstream will be encountered before the flow is anywhere near mixed out to uniform. The mixed-out average is generally pessimistic, since it presumes that wholly irreversible processes are responsible for modifying the flow towards uniform, whereas the processes in the following blade row may be better approximated as reversible.

6 Availability Averaging

Availability averaging provides a convenient place to consider averaging from a simple, but rigorous, point of view. We will consider the condition for a uniform flow with a derived average value of T and P which produces fluxes of enthalpy and availability equal to those of the nonuniform flow. From the definition of availability, $B=H-T_0s$, it follows that an equal flux of availability and enthalpy implies an equal flux of entropy: it would be equally valid to refer to this as entropy averaging.

Consider the case shown in Fig. 1, with the flow divided into two uniform streams, one at temperature and pressure T_a and P_a, the other at T_b and P_b.

For convenience assume $\dot{m}_a=\dot{m}_b$ so that conservation of enthalpy can be written in terms of the mass average, H^m, as

$$\dot{m}H_a + \dot{m}H_b = 2\dot{m}H^m$$

or

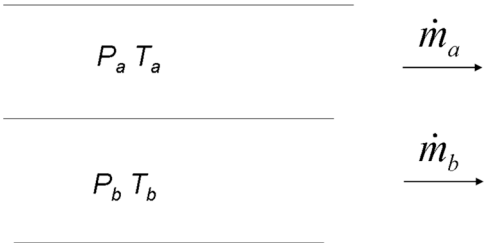

Fig. 1 Two streams of perfect gas

$$\dot{m}T_a + \dot{m}T_b = 2\dot{m}T^m$$

for a perfect gas, for which $T^d=T^m$.

Conservation of availability, equating the fluxes for the nonuniform flow and the equivalent uniform stream, leads to

$$\dot{m}B_a + \dot{m}B_b = 2\dot{m}B^m,$$

which, given the equality of enthalpy flux, produces a relation in terms of entropy

$$\dot{m}s_a + \dot{m}s_b = 2\dot{m}s^m.$$

Since $s=c_p \ln T - R \ln P = R\gamma/(\gamma-1)\ln T - R \ln P$, the equating of availability and entropy flux leads to

$$\gamma/(\gamma-1)\ln T_a + \gamma/(\gamma-1)\ln T_b - \ln P_a - \ln P_b = 2\gamma/(\gamma-1)\ln T^d - 2 \ln P^d,$$

where the superscript d denotes the derived values from entropy. Replacing the derived temperature with the mass average, $T^d=T^m$, produces the derived pressure, which is equal to the availability-averaged pressure,

$$P^{dB} = \exp\{1/2 \ln(P_aP_b) - \gamma/2(\gamma-1)\ln(T_aT_b) + \gamma/(\gamma-1)\ln(T^m)\}.$$

This method provides a rigorous definition for the average pressure, since it conserves the flux of enthalpy and availability, but it has some limitations. Consider the case when $P_a=P_b=P$, but $T_a > T_b$. Given that $T^d=T^m=(T_a+T_b)/2$, the expression for derived pressure may be written

$$P^{dB} = \exp\{\ln P - \gamma/2(\gamma-1)\ln(T_aT_b) + \gamma/(\gamma-1)\ln[(T_a+T_b)/2]\}.$$

Since $(T_a+T_b)/2 > \sqrt{T_aT_b}$ it follows that $P^{dB} > P$ whenever the temperature is nonuniform. This can demonstrated very easily for the simple case of two streams given above. Consider two equal mass flows of air, each at a pressure of 1 bar, with $T_a=1200$ K and $T_b=1000$ K. In this case the derived pressure $P^{dB}=1.015$ bar, 1.5% above the pressure physically experienced.

The above treatment has considered two streams, each uniform. This can be generalized to a flow with continuously varying stagnation temperature T and pressure P. The conservation of enthalpy leads to the mass-average temperature, $\dot{m}T^m=\int T d\dot{m}$, while the conservation of entropy gives

$$\dot{m}s^m = \int (c_p \ln T - R \ln P) d\dot{m}.$$

The mass average entropy can be written

$$s^m = c_p \ln T^m - R \ln P^{dB}$$

so that the derived pressure is the entropy-average pressure given by

$$\ln P^{dB} = \frac{1}{\dot{m}} \int \ln P d\dot{m} - \frac{\gamma}{(\gamma-1)\dot{m}} \int \ln T/T^m d\dot{m} \qquad (1)$$

(see also Livesey and Hugh [4]). This equation in terms of integrals shows what could be seen above by considering the two streams: if the temperature is not uniform but the pressure is uniform, the derived pressure will greater than the uniform pressure.

The creation of a derived pressure higher than the actual one is a consequence of the assumption of equal fluxes of availability for the uniform and nonuniform streams. When the availability approach is used, a difference in temperature represents a hypothetical opportunity for work creation (with a reversible heat engine). If a uniform flow with equal enthalpy and availability flux is defined the pressure of the uniform flow must be higher than that of the nonuniform flow to compensate for the removed ability to produce work from the temperature difference. The algebra associated with this is relegated to Appendix A.

The use of an averaging treatment which equates flux of enthalpy and availability has been given some emphasis here even though it is not a widely used choice. It was initially proposed by Traupel [9] for the analysis of complete internal combustion plants (both naturally aspirated and turbocharged) and subsequently applied to an industrial gas turbine by Horlock [10]. The local values of H^m and B^m are obtained upstream and downstream of components and these give the actual work outputs and the maximum possible work outputs from each component between inlet and outlet states. The overall rational efficiency of the plant is then obtained as the sum of the work outputs from all the components divided by the exergy of the fuel supplied (see Kotas, [11]). The location and magnitude of all the irreversibilities may also be obtained. Availability (and enthalpy) averaging is, therefore, attractively rigorous to the thermodynamicist, but the availability approach for analyzing gas turbines has not been extensively adopted; one difficulty is the absence of a universally agreed definition of component performance (see Horlock, [10]) and the failure of these to fit easily into the expression for overall plant performance. Without the adoption of availability analysis for the gas turbine the use of availability averaging is not the most suitable, as made evident by the average pressure exceeding the individual stream pressures when the temperature is not uniform.

Based on the use of entropy, an averaging system has been proposed by the Engineering Sciences Data Unit (ESDU) described in Refs. [12,13]. The ESDU system uses a correct expression for an equality in entropy flux for the nonuniform flow and the flux of average flow based on derived pressure and temperature

$$\ln P^d - \frac{\gamma}{\gamma-1}\ln T^d = \frac{1}{\dot{m}}\int \ln P d\dot{m} - \frac{\gamma}{\gamma-1}\frac{1}{\dot{m}}\int \ln T d\dot{m} \quad (2)$$

However, in the ESDU system the derived pressure is obtained by equating the first term of each side of Eq. (2), while the derived average temperature is obtained by equating the second term on each side of the equation, which has no logical justification. This, being mathematically incorrect, leads in general to incorrect averages for both stagnation pressure and stagnation temperature.

7 Work Averaging Into and Out of Turbomachines

This is one of the most important applications of averaging and the expression we will obtain was given by Pianko and Wazelt [1], though without much explanation. *What we wish to find is average stagnation pressure and temperature that will give the correct work input or output when the flow leaves an ideal compressor or turbine at a uniform outlet pressure* P_2. The average temperature is the mass average, but the average pressure needs to be considered more carefully.

As for the availability averaging, we first consider two streams, Fig. 1, with pressure and temperature P_a, T_a and P_b, T_b, entering a turbomachine. The average inlet pressure will be referred to as the work-average, P^{dw}. The mass-average inlet stagnation temperature, for equal mass flows in each stream, is

$$T^m = \tfrac{1}{2}(T_a + T_b).$$

Consider a reversible and adiabatic compressor, in which the total power input is given by

Table 1 Alternative averages of pressure

Temperature variation at inlet	Pressure variation at inlet	P^{dw} work average Eq. (3)	P^{dB} Availability average, Eq. (1)	P^m mass-average
1-2-1	1-2-1	1.469	1.576	1.5
uniform	1-2-1	1.463	1.472	1.5
1-2-1	uniform	1	1.079	1
uniform	1-1.1-1	1.0495	1.0496	1.05

$$\dot{W}/\dot{m} = c_p(T_{a2} - T_a) + c_p(T_{b2} - T_b)$$
$$= c_p T_a[(P_2/P_a)^{(\gamma-1)\gamma} - 1] + c_p T_b[(P_2/P_b)^{(\gamma-1)\gamma} - 1].$$

The appropriate derived average inlet pressure P^{dw} will be the value which requires the same power input to raise the total flow to a uniform outlet pressure P_2, namely,

$$\dot{W}/\dot{m} = 2c_p T^m[(P_2/P^{dw})^{(\gamma-1)\gamma} - 1].$$

Equating these two expressions for the power leads to

$$T_a(P_2/P_a)^{(\gamma-1)\gamma} + T_b(P_2/P_b)^{(\gamma-1)\gamma} = 2T^m[(P_2/P^{dw})^{(\gamma-1)\gamma}$$

or

$$P^{dw} = \left[\frac{2T^m}{T_a/P_a^{(\gamma-1)\gamma} + T_b/P_b^{(\gamma-1)\gamma}}\right]^{\gamma/\gamma-1}$$
$$= \left[\frac{T_a + T_b}{T_a/P_a^{(\gamma-1)\gamma} + T_b/P_b^{(\gamma-1)\gamma}}\right]^{\gamma/\gamma-1}.$$

This expression for the average pressure has the advantage that when $P_a = P_b = P$ the average pressure is equal to P, even when $T_a \neq T_b$.

For a flow with a continuous variation in pressure and temperature, the average is written

$$P^{dw} = \left[\frac{\int T d\dot{m}}{\int (T/P^{\gamma-1/\gamma}) d\dot{m}}\right]^{\gamma/\gamma-1} \quad (3)$$

which is an equation given by Pianko and Wazelt [1] in Sec. 3.2.7.2. Equation (3) shows very clearly that when the pressure is uniform the average pressure is equal to that pressure, unlike the availability average, Eq. (1) even for non-uniform temperature.

Table 1 shows some numerical values associated with this work averaging and compares this with other types of average. The work-average pressure, denoted P^{dw}, is obtained from Eq. (3) and the availability-average pressure, P^{dB} is obtained from Eq. (1); also shown is the mass-average pressure, P^m, which, though often used, is without rational basis. The temperature for all cases is averaged on a mass-weighted basis (i.e., a mass-average temperature). The results in Table 1 were calculated when the stagnation temperature and pressure were specified to vary linearly (i.e., constant gradient) with mass flow fraction, being symmetric about the center of the passage. The pressure and temperature are nondimensionalized, since for perfect gases it is only ratios which matter: the expression 1-2-1, for example, means that the value is 1 near the wall, rises to 2 at the center and falls again to 1 at the other wall. It will be noted that a range of stagnation pressure or stagnation temperature of 2:1 is large.

With the pressure variation of 2:1 there is considerable difference between the averages. If the performance of a turbine or compressor is of concern, then the work-average pressure is the correct value and in the case of nonuniform temperature the mass average would overestimate the pressure by about 2%, while the availability derived value would overestimate the average pressure by a little over 5% in this case and by only 0.2% if the

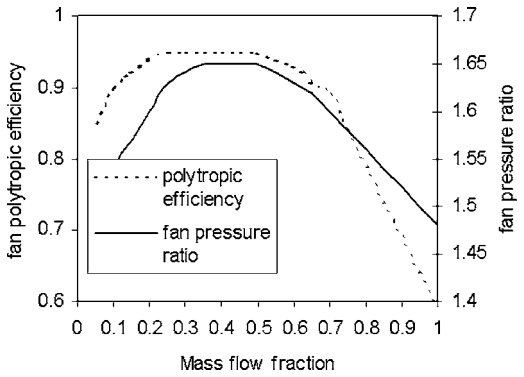

Fig. 2 Hypothetical fan profile of pressure ratio and polytropic efficiency

temperature were uniform. The derived pressure based on availability, P^{dB}, shows the peculiarity of having values that exceed the actual pressure when the temperature is nonuniform, as noted above.

It is noteworthy that as the magnitude of the stagnation pressure is reduced (down to a maximum of 10% of the mean) in Table 1 the various average pressures become more nearly equal. Indeed it can be shown algebraically, see Appendix B, that in the limit as the amplitude tends to zero, the work-average and the availability derived average tend to a mass average value. It is for this reason that for typical low-speed aerodynamic tests the use of a mass-average pressure distribution downstream of, for example, a cascade of blades is quite satisfactory, since the dynamic head is small compared with the absolute ambient pressure.

Availability averaging and work averaging have many features in common. Both give the same pressure *ratio* across a compressor or turbine with a given downstream condition, see Appendix C. They, therefore, give equal work input or output. Availability averaging gives the correct flux in availability (and entropy) but therefore an average pressure greater than the real one, whereas work averaging gives the correct pressure but an incorrect entropy flux. As will be shown in Sec. 10, however, the numerical discrepancies are small even when the degree of nonuniformity is large.

8 Averaging the Flow Into a Propelling Nozzle

The bypass flow downstream of a fan is accelerated in a nozzle and expanded to the atmospheric pressure. The primary concern in this case is the thrust produced, which is equivalent here to the mass average of the jet velocity. In assessing the potential thrust-producing capability of the flow entering the nozzle we can imagine the nozzle to be ideal, which is to say reversible and adiabatic. We can also assume that each streamtube expands independently without interaction with the rest of the flow down to atmospheric pressure p_a. For two streams, each of mass flow rate $\dot{m}/2$ entering the nozzle with pressure and temperature P_a, T_a and P_b, T_b the gross thrust is given by

$$F_g = (m/2)\sqrt{2c_pT_a\left(1-\left(\frac{p_a}{P_a}\right)^{\gamma-1/\gamma}\right)} + (m/2)\sqrt{2c_pT_b\left(1-\left(\frac{p_a}{P_b}\right)^{\gamma-1/\gamma}\right)}.$$

The appropriate equivalent thrust-average pressure, P^{dt}, is, taking the average temperature to be the mass average,

$$F_g = m\sqrt{2c_pT^m\left(1-\left(\frac{p_a}{P^{dt}}\right)^{\gamma-1/\gamma}\right)}$$

and the derived thrust average pressure may be obtained after equating the two expressions for gross thrust.

Table 2 Average fan pressure ratio

$(fpr)^{dt}$	$(fpr)^{m}$	$(fpr)^{dw}$
1.585	1.5875	1.586

Generalizing this to the case when temperature and pressure vary continuously leads to

$$\frac{P^{dt}}{p_a} = \left\{1-\left(\frac{1}{\dot{m}}\int\sqrt{\frac{T}{T^m}\left(1-\left(\frac{p_a}{P}\right)^{\gamma-1/\gamma}\right)}d\dot{m}\right)^2\right\}^{-\gamma/\gamma-1} \quad (4)$$

The pressure P which appears inside the integral is, in the case of a fan, equal to the fan pressure ratio multiplied by the ram pressure, so this stagnation pressure is a function of flight Mach number and intake pressure recovery.

A numerical example was carried out to investigate the significance of averaging on the basis of Eq. (4). A flow was specified which is similar to that which might exist downstream of the bypass outlet guide vanes of a civil engine fan; this is shown in Fig. 2, with the abscissa denoting the fraction of mass flow across the annulus and the fan stagnation pressure ratio and polytropic efficiency as ordinates. The flow is assumed to have no swirl and no radial component of velocity. In the averaging carried out the flow is specified by streamtubes, each carrying equal mass flow rates, with the pressure rise and efficiency across the fan specified for each streamtube. For the purpose of this exercies the pressure ratio of the fan is multiplied by the ram pressure ratio, 1.6038, associated with flight at Mach 0.85.

The average pressure from Eq. (4) can be turned to a thrust-average fan pressure ratio, $(fpr)^{dt}$. This is compared in Table 2 with the mass-average fan pressure ratio, $(fpr)^{m}$ and the work-average pressure ratio, Eq. (3), written $(fpr)^{dw}$.

The remarkable feature of the comparison in Table 2 is the similarity in the values of average pressure. Even though the thrust-average fan pressure ratio is correct in terms of the goal of the fan, the work-average pressure ratio is less than 0.1% higher. This difference in pressure ratio results in a thrust difference of 0.28%, which borders on the significant. However, the results do show that the optimization of a fan pressure versus span within normally acceptable limits will not result in significant variations in thrust.

Very frequently the performance of fans is assessed from a number of probes in the duct which give an approximation to an area average. This is without any theoretical justification, but it is the best that can be accomplished. The simulated fan data of Fig. 2 can be used to generate area-average pressures $(fpr)^{A}$. To do this the flow is again assumed free of swirl and to have no radial component. Then it is necessary to assume a flow Mach number at a point in the stream to arrive at flow areas corresponding to the streamtubes used in the simulation: three cases were calculated, setting the Mach number to 0.6, 0.5, and 0.4 at the position of peak stagnation pressure. The results are shown in Table 3.

It can be seen that the area-average pressure ratios of Table 3 also agree closely with the thrust-average and other averages in Table 2. Only when the bypass flow was close to separation (the velocity going to zero over part of the duct) as it was for the $M_{\text{peak}}=0.4$ case, did the area average start to deviate by more than one percent. The conclusion must, therefore, be that the method of averaging the flow upstream of a propelling nozzle is not

Table 3 Area average fan pressure ratio

$M_{\text{peak}}=0.6$	$M_{\text{peak}}=0.5$	$M_{\text{peak}}=0.4$
$(fpr)^{A}=1.581$	$(fpr)^{A}=1.577$	$(fpr)^{A}1.551$

significant—what will be far more important is the method used to extrapolate the measured or calculated data to the walls of the duct.

9 Averaging Flow Into a Choked Turbine Nozzle Row

One of the key parameters in analyzing engine performance to derive turbine pressure ratio and efficiency is the mass flow rate through the turbine nozzles, the HP turbine nozzles in particular. What is the capacity of the nozzle? The nozzles are choked, or nearly choked, so the critical dimension required is the effective area of the nozzle throat, A. The area may be measured directly, but this is not normally of sufficient accuracy. The effective area can be obtained by carrying out tests to measure mass flow as a function of pressure ratio with a facility that provides nominally uniform inlet flow. The effective area may also be derived from CFD. But no matter how accurate the measurement the question arises, what happens when the flow into the nozzle is not uniform?

When the HP turbine nozzle is downstream of a combustor the inlet stagnation pressure is nearly uniform, since the Mach numbers in the combustor itself are low. The inlet stagnation temperature, however, can vary by about 2:1 in a civil engine and by far more than this in an advanced military engine. Since the pressure is nearly uniform it seems logical to take the average pressure to be the actual stagnation pressure, but a logical method should be found for averaging the temperature so that the nozzle flow capacity with nonuniform flow is correctly deduced from any measurements with uniform inflow. It is normally assumed that the mass average of stagnation temperature is appropriate, but this case demonstrates that it is wrong to assume this and an appropriate average of temperature ought to be used. Fundamentally it is important to go back to ask what are the key quantities which ought to be conserved: in the case of the choked nozzle it is the nondimensional mass flow through a choked throat.

It is best to begin with a nondimensional expression for the mass flow rate through a throat area A, written here as

$$\frac{\dot{m}\sqrt{c_pT}}{AP} = f(M,\gamma).$$

For the choked flow at the throat, when $M=1$, $f=f(\gamma)$ only. At the high temperatures out of a combustor c_p is a function of static temperature and fuel-air ratio, but for simplicity here it will be taken as constant. Again assume two equal mass flows, $\dot{m}/2$, with equal stagnation pressure but with temperatures T_a and T_b. The two streams are assumed to pass independently through the nozzle without interacting or mixing, and at the choked section they occupy areas A_a and A_b, respectively. If $f(\gamma)$ is the same for each of the streams then

$$\frac{\dot{m}\sqrt{c_pT_a}}{2A_aP} = \frac{\dot{m}\sqrt{c_pT_b}}{2A_bP} = f(\gamma).$$

Let A be the total area at the choking surface, $A=A_a+A_b$. If the nozzle is to pass a choking mass flow $\dot{m}$, with an average temperature T^{dn}, then

$$\frac{\dot{m}\sqrt{c_PT^{dn}}}{AP} = f(\gamma)$$

and it follows that

$$T^{dn} = (\sqrt{T_a}/2 + \sqrt{T_b}/2)^2. \tag{5}$$

It should be noted that the averaged temperature T^{dn} is not now the mass-averaged temperature, so that the enthalpy and entropy flux it gives are not the same as the total enthalpy and entropy flux of the two flows a and b. As noted before, an average requires some information to be given up—in this case conservation of enthalpy and availability (or entropy) are lost, but mass flow capacity through the choked nozzle is preserved.

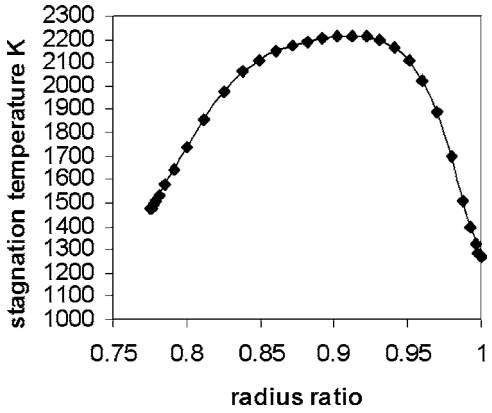

Fig. 3 Circumferential average temperature out of a combustor

An alternative approach is to use mass-average temperature T^{ma} and allow the area A' required to pass the mass flow to be different from the actual area A. It may be shown that

$$A'/A = (T_a^{1/2} + T_b^{1/2})/[2(T_a + T_b)]^{1/2}.$$

Although this alternative approach is correct in accounting for the temperature variation in terms of effective area, it detracts from the thrust of this paper, which is to find appropriate averages for the property that varies, which in this case is temperature.

The result for two equal mass flows, Eq. (5), may be generalized to the continuous distribution of temperature so that

$$T^{dn} = \left(\frac{1}{\dot{m}}\int \sqrt{T}d\dot{m}\right)^2 \tag{6}$$

If the properties of the gas, c_p and γ, vary, the corresponding integral can be written

$$T^{dn} = \left(\frac{f(\bar{\gamma})}{\dot{m}\bar{c}_p}\int \frac{\sqrt{c_pT}}{f(\gamma)}d\dot{m}\right)^2 \tag{7}$$

where $\bar{c}_p$ is a mass average. Using the gas constant R with $\bar{c}_p$ yields an average $\bar{\gamma}$. The process involved in arriving at Eqs. (6) and (7) can be thought of as an area average of the nondimensional flow capacity at the throat of the nozzle.

Figure 3 shows a radial temperature profile which is similar to that leaving the combustor of a modern civil aircraft engine which meets current emission standards with a comfortable margin. The distribution in Fig. 3 represents an area average of the circumferential variation in temperature at each radius and the true extent of nonuniformity is larger than shown in Fig. 3. (The area average is not the proper method for averaging circumferential variations but represents the consequence of practical limitations.) Because the temperature rise relative to compressor delivery depends on the local amount of fuel burned, the fuel-air ratio can be deduced from this temperature distribution upstream of the first row of rotor blades. The inlet stagnation pressure was assumed uniform, consistent with the low Mach numbers inside the combustor. The nozzle-average temperature T^{dn} was evaluated in two ways: the simplest using Eq. (6) with gas properties held constant; the more complete approach with all the properties allowed to vary, as in Eq. (7). (See Table 4.)

In this case the mass-average stagnation temperature is not the appropriate average to use, since the flux of enthalpy is *not* the quantity relevant to the mass-flow capacity of the nozzle. The differences between appropriate averages in temperature and the mass average, about 10 K, may appear small compared to the absolute magnitudes. However, this error could lead to errors in turbine efficiency derived from engine measurements of around

Table 4 Evaluation of average entry temperature to a nozzle row (Mass average temperature T^m=1960.8 K)

Variation in	Temperature only	Temperature, c_p and γ
Nozzle av. temp T^{dn}	1950.7 K	1951.6 K

one percent. The error would be still larger if the circumferential variation were included.

10 A Further Numerical Example

It was noted in Secs. 7 and 8 that the averages converge on the mass-average pressure when the variation in pressure is small; this is demonstrated in the limit in Appendix B. The following numerical example gives further illustration of the surprising extent to which an equivalence valid in the limit as the variation goes to zero gives good estimates for quite large levels of variation.

In the example here the flow was assumed to vary sinusoidally across a passage, with the stagnation temperature given by

$$T = T_{\text{wall}}[1 + \Delta_T \sin(\pi \dot{m}/\dot{m}_{\text{total}})].$$

where Δ_T denotes the amplitude of the variation in temperature as a fraction of T_{wall}. An equivalent form is used for the stagnation pressure,

$$P = P_{\text{wall}}[1 + \Delta_P \sin(\pi \dot{m}/\dot{m}_{\text{total}})].$$

The temperature was averaged on the basis of mass average, while for the pressure the work average (Eq. (3)), the availability average (Eq. (1)) and the mass average were obtained and expressed as ratios. In addition a thrust average was obtained for the pressure where it was assumed that there was a ram pressure ratio of 1.60. The ratios of average pressure are shown in Fig. 4 when the pressure varied and ratios of average pressure when temperature is varied are shown in Fig. 5. In these graphs it is worth drawing attention to the very large scale needed to show the variations. These results support the impression already given: the difference between the averages are small compared with uncertainties arising from measurement errors or uncertainty in CFD.

11 Averaging of Static Quantities

As already stated, the requirements for averaging static quantities are rather different from the stagnation ones. Certain useful and general statements can be made. The first is that in deciding which system of averaging should be used thought needs to be given to the requirements and application of the average, just as was stressed with averaging of stagnation quanitities. The second

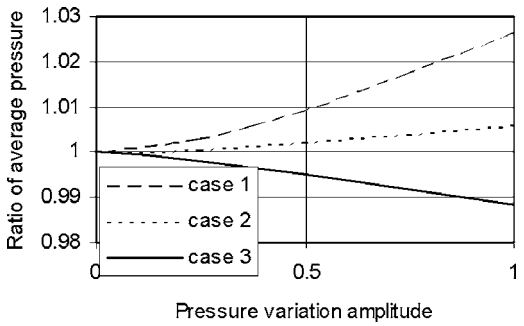

Fig. 4 Comparison of averaged pressures for sinusoidal variation in stagnation pressure. Temperature uniform. Case 1—*mass average/work average*, Case 2—*availability average/work average*, and Case 3—*thrust average/work average*.

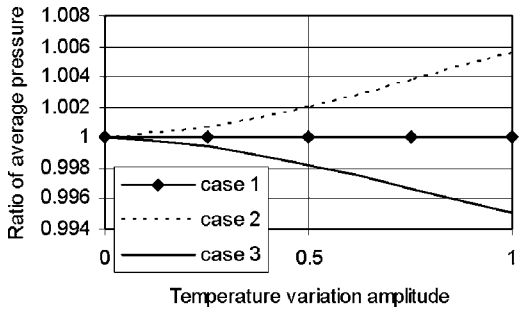

Fig. 5 Comparison of averaged pressures for sinusoidal variation in stagnation temperature. Pressure uniform. Case 1—*mass average/work average*, Case 2—*availability average/work average*, and Case 3—*thrust average/work average*.

is that averages based on flux are appropriate for extensive properties but not intensive ones. As noted before, a mass average of static pressure is not a meaningful quantity.

In considering the performance of turbomachines an efficiency is sometimes expressed in terms of the total-to-static conditions, meaning that at inlet the stagnation conditions are used, while at exit the static conditions are used. It is then tempting to think that a similar averaging approach may be used for the exit static as the inlet stagnation conditions. Moreover, since as shown in Sec. 10, the mass-average stagnation pressure agrees numerically very closely with the work-average, it might appear legitimate to use the mass-average static pressure at exit. This, however, is not the case. If static conditions are to be used at exit they should be defined where the static pressure is uniform, as in a large plenum or in the open atmosphere. If the static pressure downstream of a turbomachine is not uniform, averaging is not the correct way to arrive at a single value; preferably the outlet station should be moved to where the static pressure is uniform, but otherwise the static pressure at a particular position (for example, at the outer casing) should be used. An example of the effects of nonuniform static pressure is given in Greitzer et al. [2]. Nonuniform static pressure is clear evidence that the flow is being turned or accelerated, and such regions do not lend themselves to providing a good reference condition downstream of a turbine or compressor.

Certain processes of concern to the gas turbine and turbomachinery community depend on static temperature: for example, evaporation and condensation of vapors, chemical reaction equilibrium and rate, infrared radiation. Since enthalpy is related to temperature it is tempting to again carry out a mass-average of temperature, this time the static temperature. However, for the examples given above, the phenomena of concern are linked to temperature in a highly nonlinear manner. The correct basis for averaging should be arrived at with consideration of the physical process of interest and a mass average of flux of static temperature (or flux of static enthalpy) is not going to provide a suitable representative value, for example, for condensation/evaporation, chemical reaction or infrared radiation.

12 Conclusions

(1) The averaging of stagnation pressure and stagnation temperature should be based on a clear view of the purpose for which the averages are intended. The procedure is then neither arbitrary nor optional.

(2) Normally the appropriate average for stagnation temperature is the mass-average, since this gives the correct value of enthalpy flux, according to ideal-gas assumptions. This is *not* the case when the *flow capacity* of a nozzle is required, and in this case an average based on the square root of temperature is appropriate.

(3) For flow entering a compressor or turbine the average of stagnation pressure should be that based on uniform conditions

giving work input/output from an ideal compressor or turbine equal to the work with the nonuniform pressure. (The expression for this had been given by Pianko and Wazelt.)

(4) The appropriate average pressure for a flow entering a propelling nozzle is based on an expansion in an ideal nozzle so that the same gross thrust (average jet velocity) is produced by both the average pressure and the nonuniform pressure. The same type of approach may be adapted to other flows where averaging is required.

(5) An average based on setting up a uniform flow with enthalpy flux and availabilty flux equal to those of the nonuniform flow, and deriving the average pressure and temperature from this uniform flow, gives the mass-average for the stagnation temperature and the availability-average for the stagnation pressure. This average is also equivalent to that based on flux of enthalpy and entropy. This average is not, in general, very suitable for use in turbomachines or engines where conventional definitions of pressure ratio and efficiency are being used, but is appropriate when availability accounting is being applied to these devices.

(6) It is common in practice to adopt a mass-average of the stagnation pressure. This is an approach which cannot, in general, be justified rigorously. However, if the variation in stagnation pressure is small compared to the absolute pressure, the work-average and the availability-average pressure are both very similar to the mass-average value. It can be shown that in the limit as the pressure variation tends to zero, the work- and the availability-averages tend to the mass-average.

(7) The practicalities of engine or turbomachine operation often mean that the best average that can be carried out from measurements is an area average from a rake or traverses of pressure and temperature, with no opportunity for carrying out rigorously based averaging systems. This gives a fairly crude area average of pressure and temperature. The largest variation or uncertainty in the average then tends to come from practical issues like the system used to extrapolate data from the probe nearest to the wall to the wall itself.

(8) Provided that the flow does not contain major separations, the average of stagnation pressure based on area-average, mass-average, availability-average, thrust-average, or the work-average all agree remarkably closely. Measurement errors, or inaccuracy in CFD, are likely to be more important than differences in the scheme of averaging adopted.

Acknowledgment

The authors would like to thank Rolls-Royce for permission to publish this paper and for having caused them to become involved in the issues. They would also like to express their thanks to Dr. L. H. Smith, consultant to General Electric Aircraft Engines, for sharing unpublished notes and offering helpful comments and advice; to Professor E. M. Greitzer and Dr. C. S. Tan of the Gas Turbine Laboratory, M.I.T., for many suggestions which have improved the paper; and to Professor J. B. Young of Cambridge University whose ideas played a significant role in initiating the study some years ago. The consideration of flows in choked turbine nozzles was greatly assisted by John Northall of Rolls-Royce, who has considered related issues using CFD.

Nomenclature

B = availability, $B=H-T_0 s$, based on stagnation quantities
c_p, c_v = specific heat capacities
F_g = gross thrust
H = stagnation enthalpy
$\dot{m}$ = mass flow rate ($\dot{m}=\int \rho \mathbf{V}.\mathbf{n}dA$, where symbols have their usual meaning
P, p = stagnation (total) pressure, static pressure
p_a = ambient static pressure
R = gas constant
s = entropy
T, t = stagnation (total) temperature, static temperature
$\dot{W}$ = power
γ = ratio of specific heat capacities

Superscripts

A = area average
d = derived average properties (T or P) from other thermodynamic properties
dB = derived average properties from enthalpy and availability (entropy) fluxes
dn = average based on nozzle flow capacity
dt = derived average properties from consideration of thrust
dw = derived average properties from enthalpy flux and work consideration
m = mass average

Appendix A: The Raised Pressure Associated With Availability Averaging

Consider two streams of equal mass flow, one at temperature T_{a1} the other at T_{b1}. The pressures are equal for both at P_1. The average temperature is $T^{m1}=(T_{a1}+T_{b1})/2$. The derived pressure, obtained from conservation of enthalpy and availability flux is given by

$$\ln P^{dB} = \ln P_1 + \frac{\gamma}{\gamma-1}\left(\ln T^{m1} - \frac{1}{2}\ln T_{a1}T_{b1}\right)$$

which leads to

$$\ln(P^{dB1}/P_1) = \frac{\gamma}{\gamma-1}\ln\frac{(T_{a1}+T_{b1})/2}{\sqrt{T_{a1}T_{b1}}}$$

and then to

$$\frac{P^{dB1}}{P_1} = \left(\frac{T_{a1}+T_{b1}}{2\sqrt{T_{a1}T_{b1}}}\right)^{\gamma/\gamma-1}.$$

Suppose that the flow at this average temperature and pressure were expanded to pressure P_2 in an isentropic turbine. The work output would be given by

$$W = c_p(T^{m1}-T_2) = c_p T^{m1}(1-(P_2/P^{dB})^{\gamma-1/\gamma}).$$

But $P_2/P^{dB1}=(P_2/P_1)(P_1/P^{dB1})$, so that

$$W = c_p T^{m1}\left(1-\left(\frac{P_2}{P_1}\frac{P_1}{P^{dB}}\right)^{\gamma-1/\gamma}\right) = c_p T^{m1}\left(1-\left(\frac{P_2}{P_1}\right)^{\gamma-1/\gamma}\frac{2\sqrt{T_{a1}T_{b1}}}{T_{a1}+T_{b1}}\right).$$

Now consider the two separate streams expanding through the turbine to the same downstream pressure. The turbine work is given by

$$W_t = c_p\frac{T_{a1}+T_{b1}}{2}\left(1-\left(\frac{P_2}{P_1}\right)^{\gamma-1/\gamma}\right)$$

and the two streams leave at temperatures

$$T_{a2}=T_{a1}(P_2/P_1)^{\gamma-1/\gamma} \quad \text{and} \quad T_{b2}=T_{b1}(P_2/P_1)^{\gamma-1/\gamma}.$$

Because the two streams have different temperatures there can be ideal heat engines between them exchanging heat and producing work. Since this will be reversible there will be no creation of entropy and the mean exit temperature can then be shown to be given by

$$T^{m2}=\sqrt{T_{a2}T_{b2}}$$

and the work from the external engine is

$$W_e = \frac{c_p}{2}(T_{a2} - T_{m2}) + \frac{c_p}{2}(T_{b2} - T_{m2}) = \frac{c_p}{2}(T_{a2} + T_{b2}) - c_p\sqrt{T_{a2}T_{b2}}.$$

The combined work from the turbine and the external heat engine is given by

$$W_t + W_e = c_p \frac{T_{a1} + T_{b1}}{2}\left(1 - \left(\frac{P_2}{P_1}\right)^{\gamma-1/\gamma}\right) + \frac{c_p}{2}(T_{a2} + T_{b2}) - c_p\sqrt{T_{a2}T_{b2}}$$
$$= c_p T^m\left(1 - \frac{\sqrt{T_{a1}T_{b1}}}{T^m}\left(\frac{P_2}{P_1}\right)^{\gamma-1/\gamma}\right).$$

This is the same expression as that obtained by expanding the derived pressure P^{dB1} down to pressure P_2 in a reversible turbine. It serves to illustrate the special nature of the processes implied by the entropy average which leads to the derived pressure, processes which are not achievable in any practical device.

Appendix B: Convergence of Work-Average and Mass-Average Pressure

Mass averaging, strictly mass-flux averaging, is so widespread that it is worth showing how the work-average converges to this when the variation in the pressure about the mean is small. For convenience here take the temperature to be uniform, with uniform c_p and γ. It is also convenient to write the pressure in the form $P = P_{\text{ref}} + P'$ with the work-average as $P^w = P_{\text{ref}} + P'_{\text{av}}$ where P_{ref} is any pressure within the range of values of P. The average value that is being sought is P'_{av}, which could be viewed as the average gauge pressure, the pressure relative to atmosphere that might be measured in a laboratory experiment, for example. It is assumed that P'/P_{ref}, and therefore, $P'_{\text{av}}/P_{\text{ref}}$, is much less than unity. If the temperature is uniform equation (3) may be written

$$\left(\frac{1}{P_{\text{ref}} + P'_{\text{av}}}\right)^{\gamma-1/\gamma} = \frac{1}{\dot{m}}\int\left(\frac{1}{P_{\text{ref}} + P'}\right)^{\gamma-1/\gamma} d\dot{m}$$

which may be expanded by the binomial theorem to give

$$\dot{m}\frac{1}{(P'_{\text{ref}})^{\gamma-1/\gamma}}\left(1 - \frac{\gamma-1}{\gamma}\frac{P'_{\text{av}}}{P_{\text{ref}}}\right) = \frac{1}{(P'_{\text{ref}})^{\gamma-1/\gamma}}\int\left(1 - \frac{\gamma-1}{\gamma}\frac{P'}{P_{\text{ref}}}\right)d\dot{m}$$

neglecting second order terms, leading to

$$\frac{P'_{\text{av}}}{P_{\text{ref}}} = \int \frac{P'}{P_{\text{ref}}} d\dot{m}.$$

This confirms that when the variation in pressure about any reference or mean value (such as ambient pressure) is small the work average tends to the mass average. It may similarly be shown that other forms of average, such as the entropy-average or availability-average likewise tends to a mass average in the limit of small variations.

Appendix C: Pressure Ratio Based on Availability-Average and Work-Average Pressures

Consider the example outlined in Sec. 6 on availability averaging and Sec. 7 on work averaging. The process described in Sec. 7 is shown on T-s diagrams in Fig. 6 when treated by availability averaging and by work averaging. It is assumed that each stream behaves independently as it is compressed from its inlet stagnation pressure, P_{a1} and P_{b1}, to the uniform outlet pressure P. For compression in a reversible adiabatic compressor,

$$T_{a1}/P_{a1}^{(\gamma-1)/\gamma} = T_{a2}/P^{(\gamma-1)/\gamma},$$

$$T_{b1}/P_{b1}^{(\gamma-1)/\gamma} = T_{b2}/P^{(\gamma-1)/\gamma}$$

Then for **work averaging** from Sec. 7

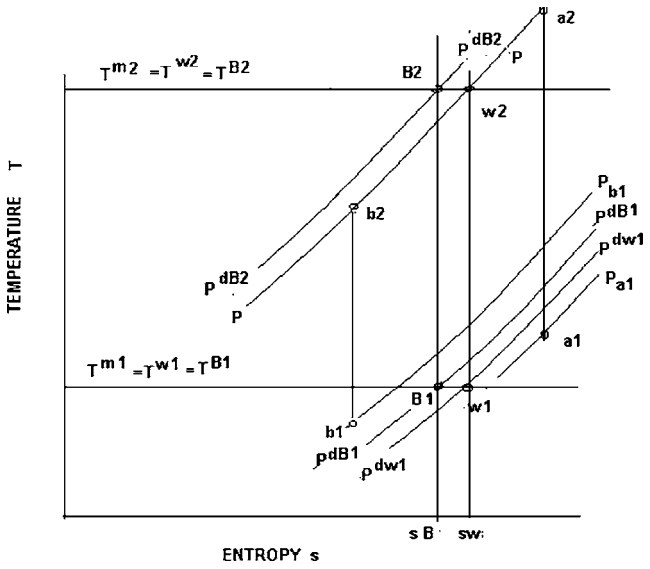

Fig. 6 Temperature-entropy diagrams showing a comparison between availability averaging and work averaging for two streams entering at P_{a1}, T_{a1} and P_{b1}, T_{b1}; leaving at P_{a2}, T_{a2} and P_{b2}, T_{b2}. Availability-average state points marked as $B1$ and $B2$, work-average state points marked as $w1$ and $w2$.

$$P^{dw1} = \left[\frac{2T^{m1}}{T_{a1}/P_{a1}^{(\gamma-1)/\gamma} + T_{b1}/P_{b1}^{(\gamma-1)/\gamma}}\right]^{\gamma/\gamma-1} = \left[\frac{2T^{m1}}{T_{a2}/P^{(\gamma-1)/\gamma} + T_{b2}/P^{(\gamma-1)/\gamma}}\right]^{\gamma/\gamma-1}$$

so the pressure ratio is

$$r^{dw} = P/P^{dw1} = \left[\frac{T_{a2} + T_{b2}}{2T^{m1}}\right]^{\gamma/\gamma-1} = (T^{m2}/T^{m1})^{\gamma/\gamma-1}$$

For **availability averaging**, from Sec. 6, at entry to the adiabatic reversible compressor

$$\gamma/(\gamma-1)\ln T_{a1} + \gamma/(\gamma-1)\ln T_{b1} - \ln P_{a1} - \ln P_{b1} = 2\gamma/(\gamma-1)\ln T^{dB1} - 2\ln P^{dB1}$$

and likewise at exit. Since the entropy average here also implies the enthalpy average, for a perfect gas the entropy-average temperature is the mass-average temperature. Hence for the two streams at inlet and exit

$$2\ln P^{dB1} = 2\gamma/(\gamma-1)\ln T^{m1} - \gamma/(\gamma-1)\ln(T_{a1}/P_{a1}^{\gamma/\gamma-1}) - \gamma/(\gamma-1)\ln(T_{b1}/P_{b1}^{\gamma/\gamma-1})$$

$$2\ln P^{dB2} = 2\gamma/(\gamma-1)\ln T^{m2} - \gamma/(\gamma-1)\ln(T_{a2}/P^{\gamma/\gamma-1}) - \gamma/(\gamma-1)\ln(T_{b2}/P^{\gamma/\gamma-1})$$

Hence, by subtraction,

$$\ln P^{dB2} - \ln P^{dB1} = \gamma/(\gamma-1)\ln T^{m2} - \gamma/(\gamma-1)\ln T^{m1}$$

so that the pressure ratio based on entropy-averages is given by

$$r^{dB} = P^{dB2}/P^{dB1} = (T^{m2}/T^{m1})^{\gamma/(\gamma-1)}$$

which is equal to the pressure ratio based on work-average pressures, r^{dw} derived above.

References

[1] Pianko, M., and Wazelt, F., 1982, "Propulsion and Energetics Panel Working Group 14 on Suitable Averaging Techniques in Non-Uniform Internal Flows," AGARD Advisory Report No 182, Advisory Group for Aerospace Research and Development, Neuilly Sur Seine, France.

[2] Greitzer, E. M., Tan, C. S., and Graf, M., 2004, *Internal Flow Concepts and Applications*, Cambridge University Press, Cambridge, MA.
[3] Traupel, W., 1978, *Thermal Turbomachines*, Vol 1, 3rd ed., Springer-Verlag, Berlin.
[4] Livesey, J. L., and Hugh, T., 1966, "Suitable Mean Values in One-Dimensional Gas Dynamics," J. Mech. Eng. Sci., **8**, pp. 374–383.
[5] Cumpsty, N. A., 2004, *Compressor Aerodynamics*, Krieger, Malabar, FL.
[6] Dzung, L. S., 1971, *Konsistente Mittelwerte in der Theorie der Turbomaschinen fuer kompressible Medien*, BBC-Mitteilungen, Bd58, pp. 485–492.
[7] Prasad, A., 2004, "Calculation of the Mixed-out State in Turbomachine Flows," Paper presented at the ASME/IGTI Turbo Expo, Vienna. Paper GT2004–54021.
[8] Amecke, J., 1967, "Evaluation of Wake Measurements in Two-dimensional Cascades," AVA-Report 67A49.
[9] Traupel, W., 1957, "Reciprocating Engine and Turbine in Internal Combustion Engineering," Proc. CIMAC (Int. Cong. Combustion Engineering) **37**.
[10] Horlock, J. H., 1992, "The Rational Efficiency of Power Plants and Their Components," ASME J. Eng. Gas Turbines Power, **114**(4), pp. 603–611.
[11] Kotas, T., 1985, *The Exergy Method of Thermal Plant Analysis*, Butterworths, London.
[12] ESDU Data Item No 95011, *One-Dimensional Representation of Steady, Spatially Nonuniform Flow. An Equivalent Mean-value Set for Compressible Flow. Part 1 Implementation for an Ideal Calorically-Perfect Gas*, ESDU International, issued 1995 and with amendments 1998.
[13] ESDU Data Item No 97029, *One-Dimensional Representation of Steady, Spatially Nonuniform Flow. An Equivalent Mean-value Set for Compressible Flow. Part 2 Implementation for an Ideal Thermally-Perfect Gas*, ESDU International, issued 1998.

Long-to-Short Length-Scale Transition: A Stall Inception Phenomenon in an Axial Compressor With Inlet Distortion

Feng Lin
Applied Research Center,
Indiana Institute of Technology,
Fort Wayne, IN 46803
e-mail: flin@indianatech.edu

Meilin Li

Jingyi Chen

Institute of Engineering Thermophysics,
Chinese Academy of Sciences,
Beijing, People's Republic of China

A theoretical and experimental study of stall inception processes in a three-stage low-speed axial flow compressor with inlet distortion is presented in this paper. Since inlet distortion provides asymmetric flows imposing onto the compressor, the main goal of this research is to unveil the mechanism of how such flows initiate long and/or short length-scale disturbances and how the compression system reacts to those disturbances. It is found that the initial disturbances are always triggered by the distorted flows, yet the growth of such disturbances depends on system dynamics. While in many cases the stall precursors were the short length-scale spikes, there were some cases where the compressor instability was triggered after the disturbances going through a long-to-short length-scale transition. A Moore-Greitzer-based (system scale) model was proposed to qualitatively explain this phenomenon. It was found that, when the compressor operated in a region where the nonlinearity of the characteristics dominated, long length-scale disturbances induced by the inlet distortion would evolve into short length-scale disturbances before they disappeared or triggered stall. However, the model was not able to predict the fact that many disturbances that were triggered by the distorted sector(s) were completely damped out in the undistorted sector(s). It is thus suggested that in future research of compressor instability, one should consider the flows in blade passage scale, the dynamics in system scale, and their interaction simultaneously. [DOI: 10.1115/1.2098808]

Introduction

Rotating stall and surge are the two major instability phenomena that limit the performance of axial flow compressors. Despite numerous research efforts over the past five decades, the ability to predict the stall/surge margin, and further to suppress such instability in modern high-performance compressors, still remains on the wish list of compressor design engineers. One of the main reasons for it is that rotating stall and surge are not only related to local flow structure inside the blade passages, but also to the system dynamics that include the compressor as a whole and its up- and downstream components [1,2]. The inherited unsteady blade passage flows (even when the system is steady on average), the nonlinearity of the system dynamics, and the interaction among them complicate this instability problem.

In the past decade, under the "umbrella" of active stall control technology, the interaction between the local flow and the system dynamics has been studied through investigating stall triggering mechanism. Researchers studied the stall precursors and how the system reacts to them. Stall precursors are the flow disturbances from which stall cells evolve. While the initiation of stall precursors is strongly related to local flow structure, their evolution, i.e., their growth or decay over time, is governed by the system dynamics. It was found that there were two basic types of stall precursors, long-length-scale "modes" and short-length-scale "spikes" [3,4]. Camp and Day [5] introduced a critical angle of incidence to describe the different response of compressors to modes and spikes showing clearly the importance of interaction between the system and the local blade flow.

Intuitively, it was commonly assumed that the stall precursors would continuously evolve into full stall once it emerged. Hence, early detection of stall precursors was believed to be beneficial to active stall control because it might give more time for actuators to react. With active stall control as a goal in mind, several signal-processing methods were developed for early stall precursor detection [6–8]. Recently, the development of wavelet transform has made it possible to not only detect the emergence of flow disturbances but also track their evolution process thereafter. After careful configuration, Lin et al. [9] developed a wavelet analysis tool, specifically targeting the signal analysis of stall inception processes. With the help of this wavelet tool, in a recent study of the stall inception process in a three-stage, low-speed compressor [10], it was found that the spike disturbances evolved *intermittently*, rather than continuously, to full stall. Spike disturbances were first found to emerge at a location related to structural asymmetry in stationary frame when another asymmetry in rotating frame swept by. Then, the disturbances decayed rapidly (usually in less than one rotor revolution) once they propagated out of their birth spots. The full stall was triggered only by one such spike disturbance emerging a few rotor revolutions prior to stall onset. Inoue et al. [11] and Leinhos et al. [12] also applied wavelet to study stall inception processes in their experiments.

These previous findings inspired the authors to pursue the relation between structure/flow asymmetries of compressors and system instability, i.e., rotating stall. Since steady circumferential inlet distortion provides a practical scenario of stationary flow asymmetry to compressor, it is interesting to investigate the stall inception process with inlet distortion, observe how the modal and/or spike disturbances are generated, and understand how the system reacts to those disturbances.

Traditionally, the purpose of inlet distortion research is to predict the flow instability in the inlet with the distorted incoming flow as the upstream boundary and the compressor (actuator disk) as the downstream boundary condition. Multiple segment parallel compressor model [13], actuator disks [14], perturbation analysis

Contributed by the International Gas Turbine Institute (IGTI) of ASME for publication in the JOURNAL OF TURBOMACHINERY. Manuscript received by the IGTI, October 1, 2004; final manuscript received February 1, 2005. IGTI Review Chair: K. C. Hall. Paper presented at the ASME Turbo Expo 2005: Land, Sea, and Air, Reno, NV, June 6–9, 2005, Paper No. GT2005-68656.

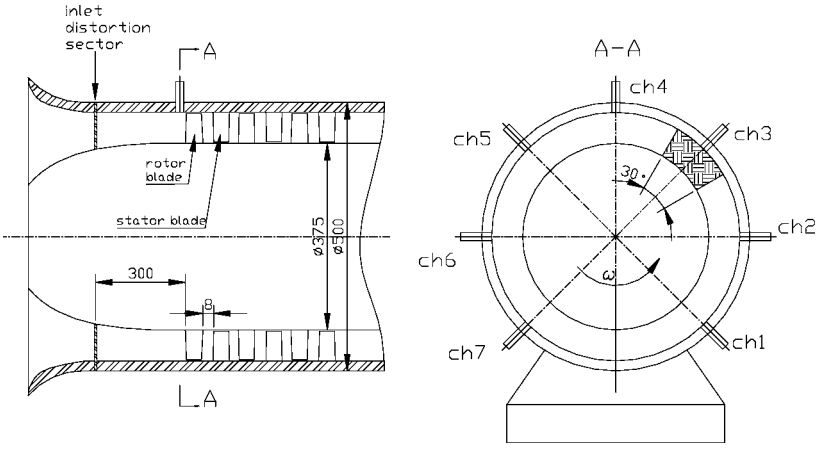

Fig. 1 The test compressor and probe locations

[15], and distortion-induced swirling flows [16] are typical examples of inlet distortion models. Hynes and Greitzer [17] proposed a linear stability analysis to axial compression systems with inlet distortion. Hynes and Greitzer's analysis consists of two steps: first solving steady solutions of the system with finite-strength distortions as the background flows, regardless of whether they are physically stable or not; then, imposing an infinitesimal flow disturbance onto the steady background flows and analyzing the eigenvalues of such a disturbance for each spatial Fourier mode. With this model as the theoretical foundation, Spakovszky et al. [18] actively stabilized a high-speed stage with both radial and circumferential distortions.

The philosophy and methodology of this paper are different. The condition under which the inlet flow and/or compressor system lose stability is not the major focus. Instead, inlet distortion is used as a practical example to illustrate how structure/flow asymmetry may trigger flow disturbances, and how those disturbances develop thereafter. In other words, the focus of this research is the stall triggering mechanism when inlet distortion is the major triggering force. Understanding such a mechanism is crucial to active stall control because the success of such control eventually relies on the ability to detect and actively suppress those flow disturbances before they grow. Moreover, as demonstrated in this paper, with the presence of inlet distortion the stall triggering mechanism involves unknown dynamic interaction between the local blade passage flow and the compressor as a whole, which calls for further research in this direction.

This paper is organized as follows. After introducing the test facility and the signal-processing methods, a model that is capable of simulating the unsteady stall inception processes is presented. The test results are then presented with side-by-side comparison with the model simulation. Discussions and conclusions end the paper.

Table 1 Specifications of the three-stage low-speed axial compressor

Rotational speed (rpm)	2400	Mass flow rate (kg/s)	2.6
Pressure coefficient	2.32	Rotor tip clearance (% of tip chord)	3.4
Outer diameter (mm)	500	Hub-tip ratio	0.75
Rotor-stator axial gap (mm)	8	Stage axial gap (mm)	8
Rotor blade number	60	Stator blade number	60
Rotor aspect ratio	1.86	Stator aspect ratio	1.86
Rotor midspan chord length (mm)	33.3	Stator midspan chord length (mm)	33.3
Rotor midspan stagger angle (deg)	44	Stator midspan stagger angle (deg)	23

Experimental Setup

Figure 1 depicts the test compressor and the locations of seven dynamic pressure probes. The seven pressure sensors are high-response, Kulite transducers (sensors 1 to 7). These sensors are spaced 45 deg apart between each sensor pair and 90 deg apart between sensor 1 and 7, because the rig support stand is located between sensors 1 and 7. The sampling rate is 79,167 Hz. The Kulite transducers all have a rated pressure of 34.475 kPa (5 PSI) and a sensitivity of 3.75 mV/kPa. The transducer's zero-pressure output is less than ±5% of full scale. The overall compressor performance in terms of total-to-static pressure rise coefficient and flow coefficient is measured with eight on-casing static pressure taps around the annulus in both the inlet and the outlet of the compressor.

The key geometry data of the test compressor are listed in Table 1.

The distortion screens and their locations in the annulus are illustrated in Fig. 2. Note that the 90-deg distortion screen did not completely cover the whole section of the annulus. It was designed like this due to the structure limitation in this particular test rig. However, this moon-shape design introduced radial distortion and further complicated the test results. Nevertheless, its major effect was still circumferential, so its results were still analyzed and compared to our model simulations. Also, due to the limitation of time and funding, the effects of different levels of distortion were not investigated at this point. More distortion plates/screens are designed and will be tested in the near future. For now,

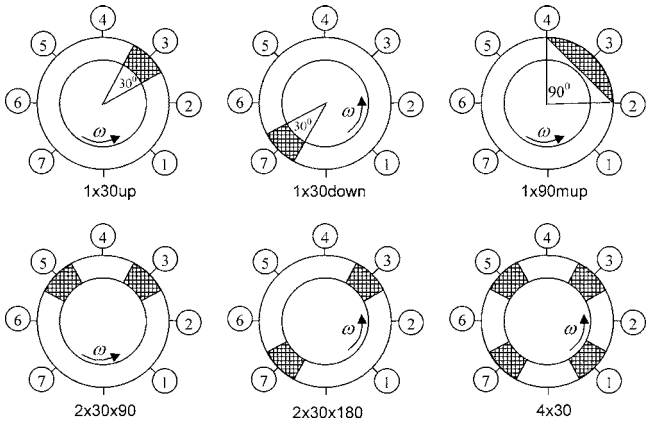

Fig. 2 Tested distortion cases. The numbers indicate the locations of the pressure sensors.

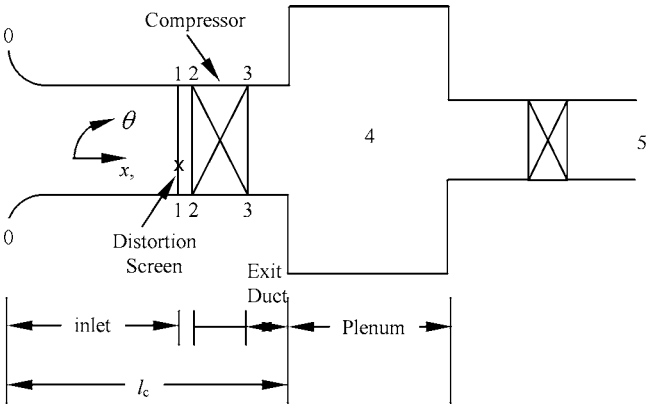

Fig. 3 The lumped system model with inlet distortion

because our major purpose is to demonstrate the existence of the interaction between the blade passage flow and the system dynamics, we do not include the level of distortion as one of the test parameters.

Signal Processing Methods

Realizing that stall inception processes are highly unsteady and the disturbances may root into blade passage flows, we choose signal-processing methods that carefully preserve the original information, instead of filtering the raw data. One of the best candidates is wavelet transform. We will use the method developed in Lin et al. [10] and, whenever necessary, combine it with direct observation of raw data.

Lumped System Model With Inlet Distortion

Similar to the idea of the Hynes-Greitzer (HG) model, consider a lumped compression system model as illustrated in Fig. 3. However, unlike the HG model, which splits the model into two parts, distorted steady background flow and its linear stability analysis, we directly model the distorted unsteady flow through the system and thus make it possible to track the stall inception processes.

Models of Inlet Duct and Distortion Screen. For the inlet duct before the distortion screen, since it is a straight duct, applying the unsteady 1D Euler equation to the axial direction yields

$$\frac{\partial U}{\partial t} = -\frac{1}{\rho}\frac{\partial P_T}{\partial x}$$

Therefore, integrating it along the inlet length before distortion screen, we obtain

$$P_{T1} - P_{T0} = -\rho l_I \frac{\partial U}{\partial t}$$

When flow passes the distortion screen, the total pressure drop is assumed to be proportional to the dynamic pressure of the flow. That is

$$P_{T2} - P_{T1} = -K_L(\theta)\rho U^2$$

where $K_L(\theta)$ is the dimensionless loss coefficients that define the distortion map. The unsteady effect in this section of inlet is neglected because the length from the screen to the first rotor is short compared to the other characteristic lengths in the system. It is worthy to note that this model differs from the model of Hynes and Greitzer [17] in that the interaction between the compressor and the distortion screen is accounted for in the system in this model. The Hynes-Greitzer model assumed the incoming flow is distorted due to a divided plenum as the source of the incoming flow, which imposed a fixed total pressure distortion map onto the compressor regardless of how compressor would have reacted to the distorted incoming flow.

Table 2 Values of dimensionless parameters

λ_r^*	l_c^*	B
0.8	6.71	0.1

System Model. By summing up the total-to-static pressure rise from inlet to plenum, we obtain

$$\psi = \psi_c(\phi) - l_c^*\frac{\partial \phi}{\partial t^*} - \lambda_r^*\frac{\partial \phi}{\partial \theta} - K_L(\theta)\phi^2 \tag{1}$$

The procedures to arrive at this equation are very similar to those of the Moore-Greitzer model [2], except for the models for the inlet duct and the distortion screen. Equation (1) is only the first part of the system model. The second part considers the dynamics of flow cumulated inside the plenum. Following Greitzer's original derivation [19], it is straightforward to obtain the following equation:

$$4l_c^* B^2 \frac{d\psi}{dt^*} = \Phi - \sqrt{\gamma\psi} \tag{2}$$

where B is the Greitzer's B parameter and γ is the throttle coefficient. The greater value it is, the larger opening the throttle has. Φ, defined as $1/2\pi\int_0^{2\pi}\phi\, d\theta$, is the averaged velocity at each time instant.

Equations (1) and (2) contain two unknowns, ϕ and ψ. Solving these two equations simultaneously will give the unsteady response of the compression system to the distortion screen, whose total pressure distortion map is specified with the loss coefficient $K_L(\theta)$.

Results

In the following subsections, in order to unveil the dynamic mechanisms underlining the observed phenomena, the experimental results and the simulation results will be presented side-by-side together, whenever possible.

Steady Undistorted and Distorted Compressor Characteristics. Table 2 lists the corresponding dimensionless parameters used in the model. The value of λ_r^* was corrected from its pure geometry value after considering the unsteady "gap" effect discussed in Longley [20]. l_c^* is a sum of geometric parameters and the corrected λ_r^*. The value for the Greitzer's B parameter is chosen somewhat arbitrarily as long as it is low enough to ensure rotating stall is the only instability mode of the model.

The axisymmetric characteristic $\psi_c(\phi)$ is obtained by fitting the experimental compressor characteristic without distortion. The following fifth order polynomial is obtained as a result of the curve fitting

$$\psi_c(\phi) = 0.5995 + 54.0763\phi^2 - 167.0889\phi^3 + 157.9917\phi^4 - 51.8844\phi^5 \tag{3}$$

which is shown in Fig. 4 as a dotted line.

Chen [21] used a commercial computational fluid dynamics (CFD) package and simulated the flows around distortion screens with and without a downstream rotor. Within the operation range covered by that simulation, the loss coefficients remain roughly constant regardless of the unsteadiness in the flow. Therefore, the loss coefficient K_L for the distortion screen is chosen and fixed at 1.6, based on the simulation results of Chen [21].

The model is validated with steady compressor performance. Figure 4 depicts the experimental and simulation results for case 1×90 as an example. In order to emulate the experimental process, for each distortion case, we first obtained a stable solution of the system while the throttle was set far away from the stall boundary. Then, we closed the throttle a little (i.e., reducing the value of throttle coefficient γ) and ran the model for a period of

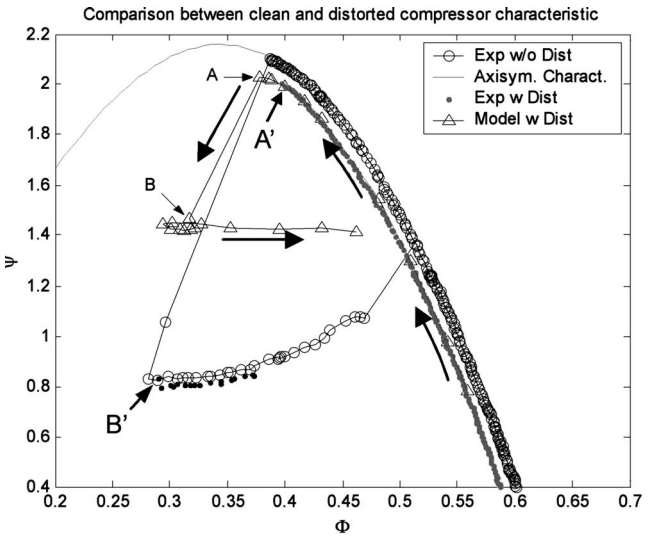

Fig. 4 Test results of steady clean and distorted compressor characteristics (case 90mup in Fig. 2)

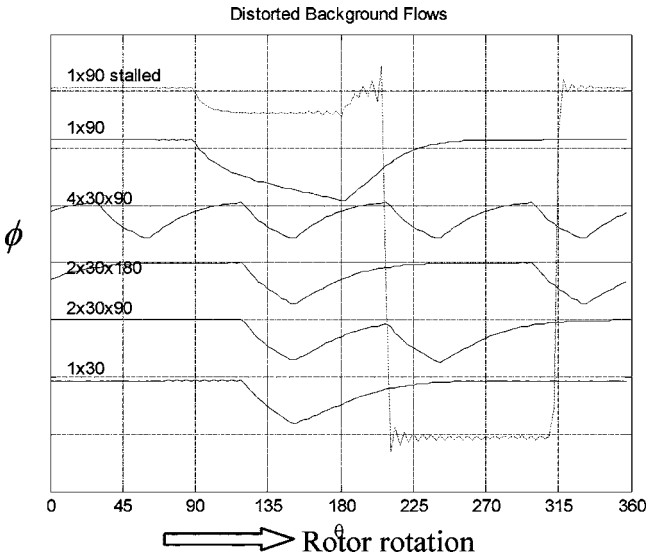

Fig. 6 Simulated distorted background flows

time long enough to reach a new, stable solution while using the previous one as the initial condition. By gradually closing the throttle in this way until rotating stall occurs and then gradually opening it back up, we obtain the simulated compressor characteristics with distortion, such as the one shown in Fig. 4. Before the system stalls, the model provides very good agreement with the experimental results. As the system is throttled close to the instability boundary, the system becomes sensitive to throttle movement. While the model cannot quantitatively predict the stall boundary, nor the stalled pressure rise, the model qualitatively matches with the experimental results, including the hysteresis associated with rotating stall.

Although we assume the flow without distortion to be axisymmetric, the flow in this test compressor is actually not. In an early study [10], it was found that there was an asymmetry located in the vicinity of probe 7. Its physical cause is still not clear. This can also be confirmed by the fact that in current experiments the compressor performs completely different when the same 1×30 distortion screen was placed in two different annular locations. Figure 5 depicts the steady stall limits for all tested distortion cases listed in Fig. 2. As seen in Fig. 5, the compressor's stall limit with case 1×30down (i.e., a 1×30 screen located in front of probe 7)

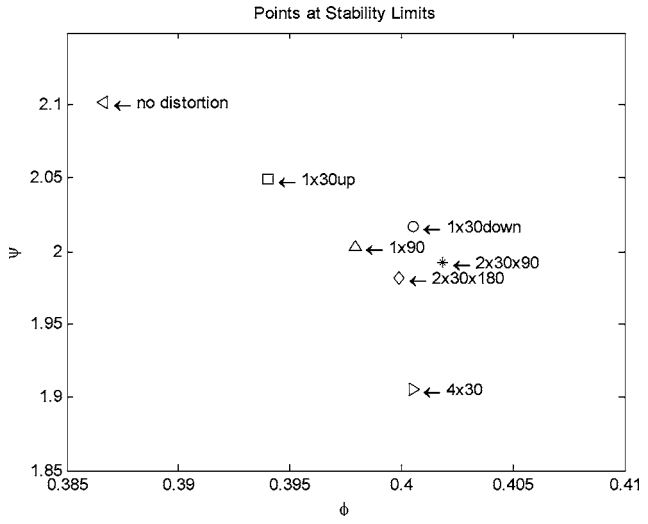

Fig. 5 Test results of steady stall limits with distortion

occurs at a lower pressure coefficient and higher flow rate than that of case 1×30up (the same screen placed in front of probe 2). Later, we will demonstrate that the unsteady stall inception processes for these two cases are also significantly different from each other.

Because we have no choice but to use the undistorted flow compressor characteristic, as if it was axisymmetric, to obtain $\psi_c(\phi)$ for our model, it is not a surprise that we cannot predict the instability boundary as well as the stalled pressure rises. However, the model is still valid because it qualitatively predicts the system behavior, which suits our purpose at present.

The distortion screens impose strong asymmetric incoming flows onto the compressor. Before it stalls, the compressor tolerates the distortion and operates in distorted background flows that will soon be demonstrated as the sources of unsteady disturbances. Unlike the stall cells, the distorted background flow does not rotate. Figure 6 depicts simulated distorted background flows for all tested distortion cases when the system was just about to become unstable (point A in Fig. 4 and equivalent points for other cases). A stalled flow distribution for case 1×90 is also plotted for comparison (point B in Fig. 4). The y axis of this figure is the dimensionless flow velocity ϕ.

The simulation indicates that when the flows are stable, the compressor rotor expands the distorted sectors wider than the angles covered by distortion screens. Longley [20] obtained similar results and showed that they agreed with measured circumferential variation in flow coefficient, $\phi(\theta)$. However, in this paper we cannot provide such measurement due to the limit capability of our measurement tools. Because this compressor is subject to structural asymmetry even without inlet distortion, and we cannot include such an asymmetry in the model, we are not sure how far away these predicted distorted background flows would be from the actual ones in the tests. Nevertheless, we are confident that the results in Fig. 6 should be qualitatively true because the annular averaged compressor characteristics matches with measured results qualitatively, such as the one shown in Fig. 4.

Unsteady Stall Inception Processes

Long-to-Short Scale Transition. To illustrate the typical features of unsteady stall inception processes, consider such a process with 1×90 distortion (case 90mup) as an example.

The compressor was throttled from point A′ at Fig. 4 to point B′. Figure 7 depicts a segment of the original data series (a), the corresponding wavelet spectrum (b) and global-averaged wavelet

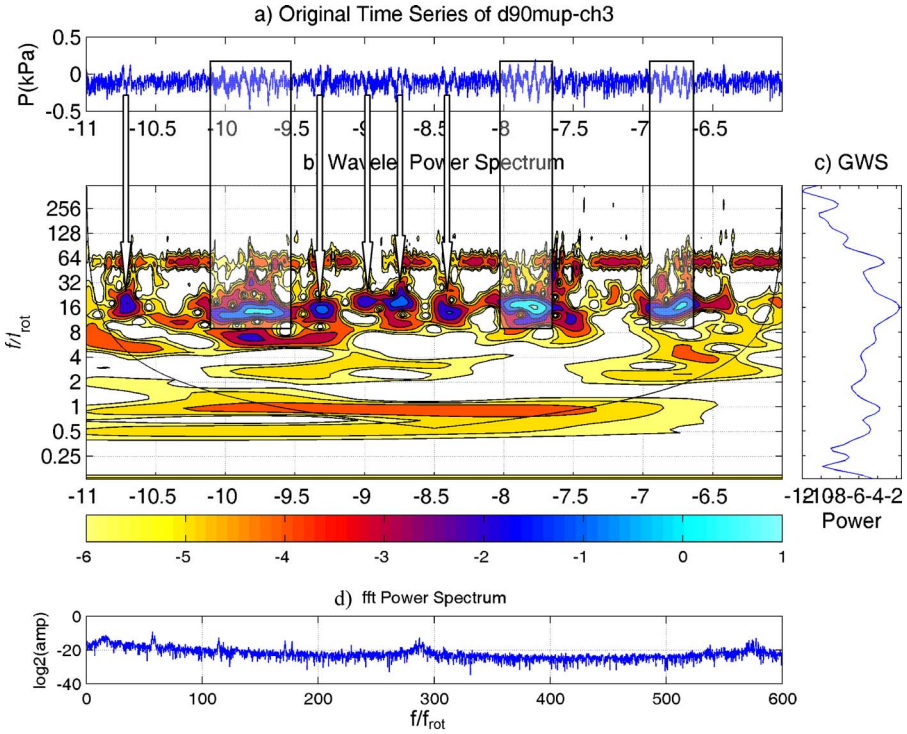

Fig. 7 (a) A segment of time series for pressure for case 90mup; (b) The wavelet spectrum of the data in (a); (c) The global wavelet spectrum for the same data; (d) The Fourier power spectrum. The horizontal axes in (a) and (b) are time axis in rotor revolutions before stall onset. f/f_{rot} means the frequency as multiples of the rotor rotating frequency.

spectrum [abbreviated as GWS, (c)], and finally the Fourier-based power spectrum (d) for probe 3. The color scheme in Fig. 7(*b*) is for the amplitude of the wavelet components. The absolute values of these wavelet components are not of concern; it is the relative comparison among these values that is important to us. The data segment was taken from −11 rotor revolutions (i.e., 11 revolutions prior to stall onset) to −5 rotor revolutions. By comparing the original time series (a) with the wavelet spectrum (b), one can see wherever there were irregular signals (i.e., disturbances) in the original data; correspondingly, there were strong energy spots appearing in the frequency band between 8 and 32 times of rotor frequency. Three boxes and several arrows were placed to indicate such correspondences. This feature will later be used to examine how disturbances travel from one probe to another. The GWS and the Fourier power spectrum do not provide much helpful information about unsteady processes and thus will be discarded later.

We now take a close look at the data segment between −10.6 to −8.8 rotor revolutions. In Fig. 8, the original signals from all seven probes are placed side-by-side, together with the seven bands of wavelet spectra. The signal from probe 2 is placed at both the bottom and top to represent the cyclic placement of the probes. One can clearly see from this figure that a disturbance was first captured by probe 2 and traveled around the compressor annulus from probe to probe. When it first emerged at probe 2, it stretched from −10.4 to −9.8 rotor revolutions, which is approximately 60% of the annulus. So, it is a long length-scale disturbance (abbreviated as LLSD in Fig. 8). But, its length scale rapidly shrank and it split into two spikes as it traveled from probe to probe. One disappeared before reaching probe 7 and the other one passed probe 7 but did not reach probe 1. As for the one that arrived at probe 7, its length scale was about 3 blade pitches. We refer to this phenomenon as a "long-to-short scale transition." Throughout the entire stall inception process, the disturbances came and went until the last one that triggered the full stall. The intermittent growth pattern was qualitatively similar to the stall inception without inlet distortion as studied in Lin et al. [10]. The initial disturbance might be long in length scale, such as the ones shown in Fig. 8, or short such as the ones marked with arrows in Fig. 7. If it was a long length-scale one, it transited into a short one before it decayed or grew. If it was short to start with, it decayed or grew without significant length-scale transition.

As a matter of fact, this is not the first time that such scale transition in prestall flow disturbances was found. Day et al. [22] observed that, with the presence of inlet distortion, the instability did not happen until after a short length-scale disturbance (not short enough to be called a spike) was formed, while the stall inception process did start with a long length-scale (modal) wave. A similar phenomenon was observed in experiments by others such as Longley, according to Day et al. [22].

It is intuitive to recognize that the distortion screen triggered the initial disturbances because the blade loading condition within the distortion sector is much more severe than those without distortion. As the disturbances propagated into the clean sectors, they damped out rapidly. Jahnen et al. [23] observed the same phenomenon and stated that full stall "occurs only when the damping of the disturbance in the undistorted sector is insufficient to prevail its growth." However, what is not intuitive is the length-scale transition phenomenon that we discovered in our tests with the help of the wavelet tool. To understand the underlining mechanism for length-scale transition, we use our model, Eqs. (1) and (2), to simulate the stall inception process as the compressor is throttled from point A (γ=0.750) to point B (γ=0.729) in Fig. 4. The simulation results are depicted in Figs. 9–11.

Figure 9 is the time traces of eight equally-spacing virtual velocity probes. The distortion screen is placed at the region starting from probe 2 and ending at probe 4. The rotor rotates from probe 1 towards probe 8. While all probes sense modal waves within the first eight rotor revolutions, length-scale transition can be clearly seen in time traces of probes 4, 5, and 6. In order to better illustrate the length-scale transition, a velocity contour for the first 8

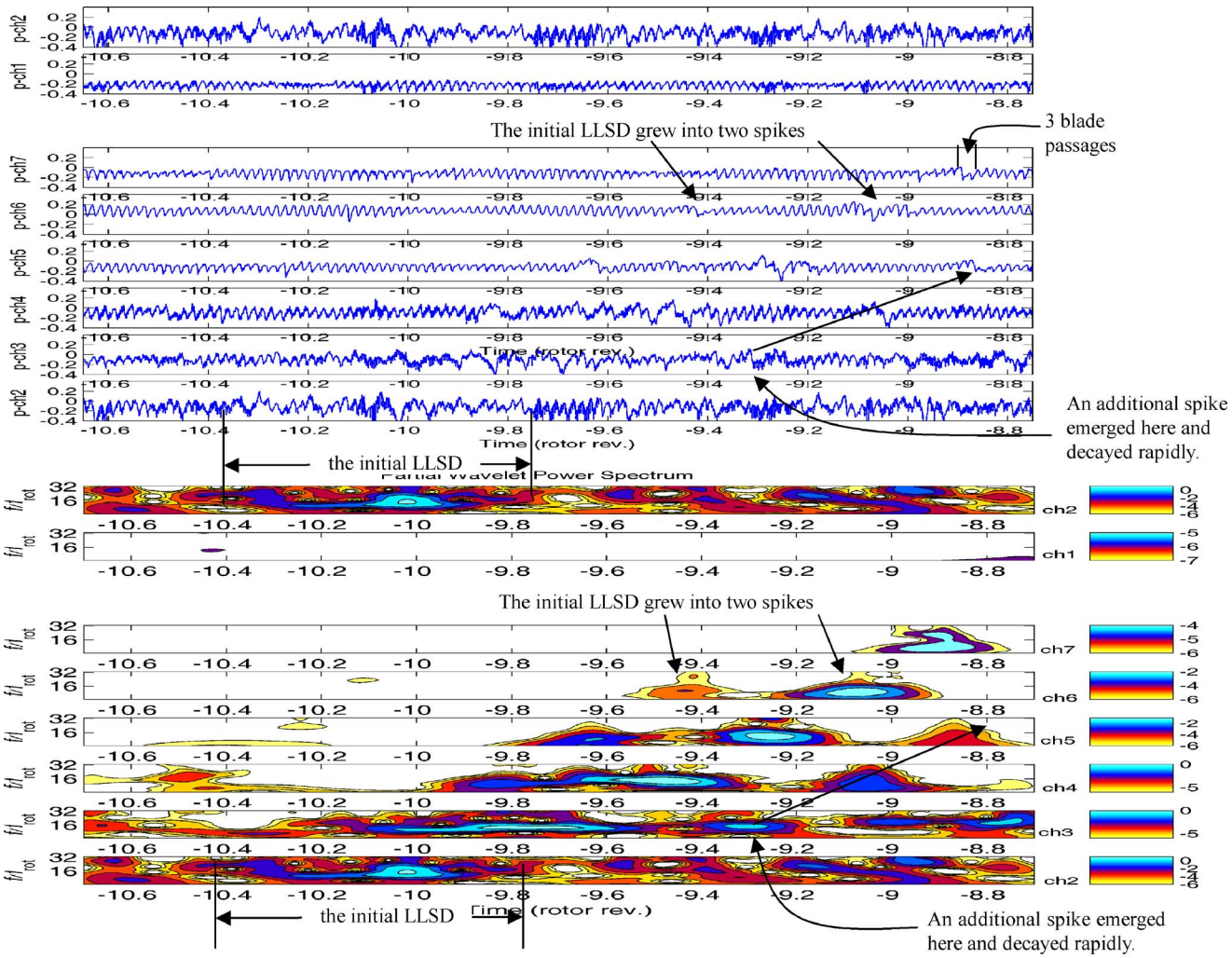

Fig. 8 Segments of time series from all seven pressure sensors and their wavelet spectra placed side-by-side

rotor revolutions is plotted in Fig. 10, along with the eight time traces of the virtual probes. According to Fig. 6, the distorted background flow starts at 90 deg (probe 1), reaches its minimum velocity at 180 deg (probe 4), and recovers at about 225 deg (probe 5). This is the initial condition at time zero (point A in Fig. 4). Right after the throttle is set to the value for point B in Fig. 4, a long length-scale disturbance emerges out of the distorted background flow and propagates along the direction of rotor rotation with a speed slower than rotor rotation. This long length-scale disturbance does not last long. By the time it reaches probe 5, its length scale is significantly shorter. Within 3 rotor revolutions of time, it shrinks and disappears before it even reaches probe 6. Another long length-scale disturbance is born immediately after the disappearance of the first one. This second one follows the same pattern of scale transition, only that it lasts a little longer and reaches a little farther, causing a "spike" in probe 6. Followed by its own length-scale transition, the third long length-scale disturbance eventually triggers the full stall. (The full stall is out of the range of Fig. 10, but can be seen in Fig. 9.)

It is worthy to note that, according to simulation, the disturbance that emerges out of the distorted background flow should propagate in the direction of rotor rotation. Thus, in the test, the first probe to be able to detect the significant rotating disturbance should be probe 4, not probe 2. This discrepancy between the test and the simulation is attributed to the moon-shape design of this 90-deg distortion screen. This deficiency will be fixed in future

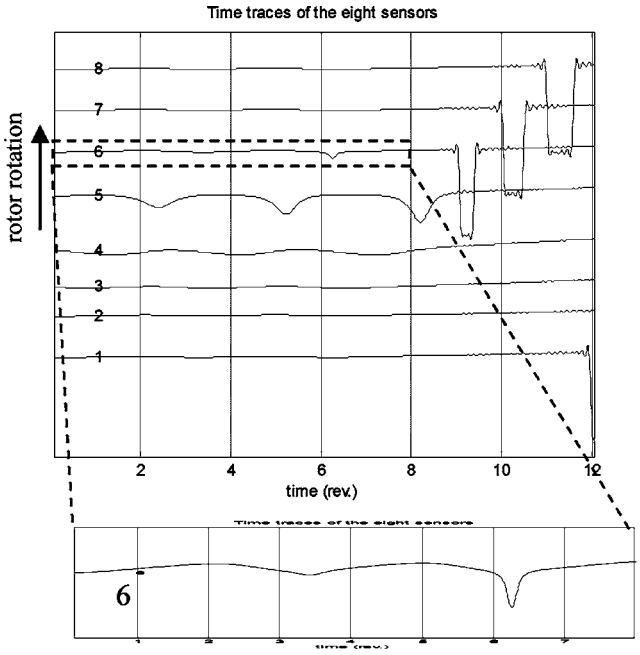

Fig. 9 Simulated time traces of eight virtual velocity probes

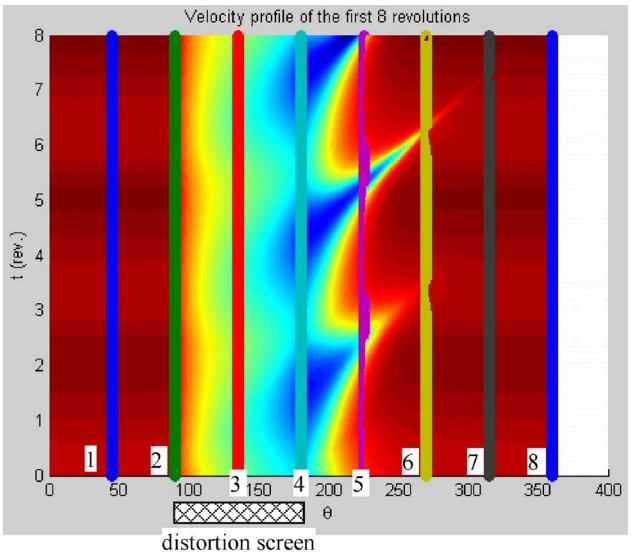

Fig. 10 Simulated velocity contours

research. Nevertheless, the dynamics of the unsteady growth of the disturbance is qualitatively captured by the model, indicating that the circumferential distortion dominated the stall inception process.

Such a growth pattern for the long length-scale disturbances can neither be predicted by linear stability models, nor by nonlinear models that contain only the first few spatial modes. Figure 11 is the simulated time history of the first five spatial Fourier modes for the disturbance alone. The fact that these modes do not grow monotonously indicates that the system's dynamics is not linear at all. As a consequence of such nonlinearity, the interaction among the spatial modes is very strong. As a matter of fact, the energy of a long length-scale disturbance concentrates on the first few spatial modes, while that of a short length-scale one spreads out to a wide range of spatial modes. Hence, the length-scale transition corresponds to the energy transfer from lower order modes to higher order modes. The nonlinear terms in the compressor characteristics, Eq. (3), are responsible for such energy transfer among spatial modes. As an illustrative example, consider a pure sine wave with a length scale of 2π, that is, $\phi(\theta)=\sin(\theta)$. Then

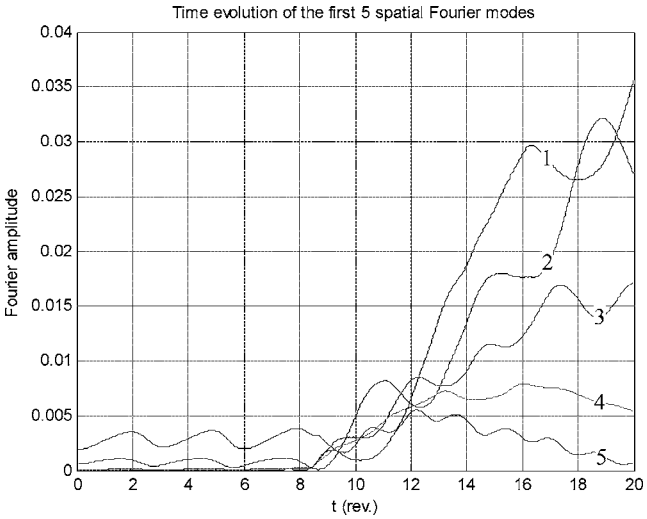

Fig. 11 Simulated growth of the first five spatial Fourier modes

$$\phi^5(\theta)=\frac{5}{4}\sin(\theta)-\frac{3}{4}\sin(3\theta)+\frac{1}{4}\sin(5\theta)$$

This means the fifth-order term in Eq. (3) has the potential to spread the energy of the first spatial mode to the third and the fifth modes. Such nonlinear interaction among modes happens recursively as time goes on, causing the length-scale transition as evidenced in both the experiments (Fig. 8) and the simulations (Figs. 9–11).

According to the above argument, the length-scale transition could only happen if the nonlinear terms of the compressor characteristic dominate. In other words, it could only happen when the system is operating near the peak of the characteristic. Another necessary condition for the scale transition is that the initial disturbance should be in long length scale. If the disturbances emerge as a short length-scale spike, then it would still evolve as a spike because nonlinear terms of the characteristic cannot do the opposite: concentrating the already widely spread energy back into the first few modes. While in simulation, the distorted background flow always acts as the source for long length-scale disturbances, in reality the compressor may subject both long and short length-scale disturbances because of the complexity of the flows in nature, such as the example given in Figs. 7 and 8. Our model cannot fully capture the origins of those disturbances, but it did capture the growth pattern of the disturbances qualitatively.

The Role of Compressor's Own Structural Asymmetry. In an earlier study of this test compressor, it was found that there was a structural asymmetry located in the vicinity of probe 7, while the physical cause for it is still not clear. The interaction between this "built-in" asymmetry and the "external asymmetry" introduced by inlet distortion screens becomes interesting. A 30-deg distortion screen is placed first at the circumferential location of probe 3 (case 1×30up), 180 deg away from probe 7, then at the location of probe 7 overlapping with the structural asymmetry (case 1×30down). It had been already demonstrated in Fig. 5 that the steady performances for these two cases were quite different. Case 1×30down had much lower limit in pressure rise than case 1×30up. The comparison of the unsteady stall inception processes for these two cases is given as below.

Wherever the distortion screen was placed, the location became a source of initial disturbance. For case 1×30up, this 30-deg screen intermittently initiated short length-scale disturbances (SLSD, or spikes) throughout the entire stall inception process. For convenience, we define the edge of the screen through which the rotor sweeps into the distorted sector as the "leading edge," and the one through which the rotor sweeps out as the "trailing edge." Then, the SLSD was always first detected by the probe located at or closest to the "trailing edge" (i.e., probe 4 in this case). Figure 12 depicts a segment of data for this case. There were two spikes generated in this data segment. Both were first detected by probe 4. While the second one disappeared after passing through probe 1 (225 deg of rotation), the first one survived more than one revolution. When it struck the screen once more, it was enhanced and such enhancement was again detected by probe 4. The probes located at the leading edge and in the middle of the distorted sector were relatively quiet. This scenario continued until one of such spikes triggered the full stall.

In contrast to what happened in case 1×30up, the initial disturbances for case 1×30down were long length-scale ones. Every time the rotor struck the distorted sector, a long length-scale disturbance emerged and was detected first by probe 1, the closest probe to the trailing edge of the distortion screen. It then rapidly split into two short ones before disappearing within less than one rotor revolution. Figure 13 depicts a typical example. Compared to Fig. 12, it is clear that in this case, long-to-short scale transition plays an important role in stall triggering mechanism.

As a comparison, Fig. 14 is a simulation result for 1×30 cases. Since our model does not contain an element to simulate the built-in structural asymmetry of the compressor, there is no dif-

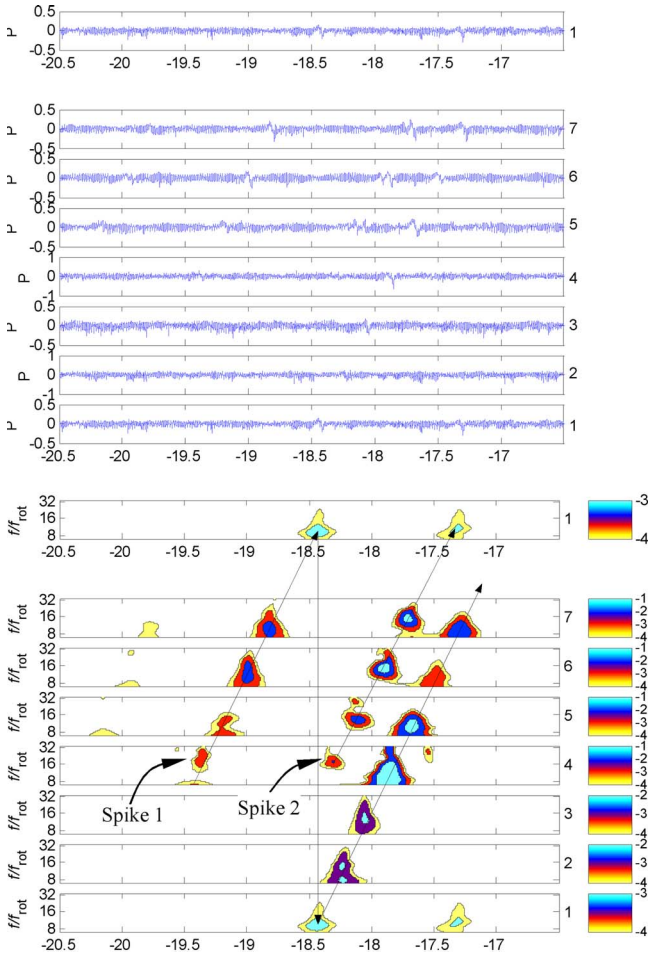

Fig. 12 Test data and wavelet spectra of case 1×30up

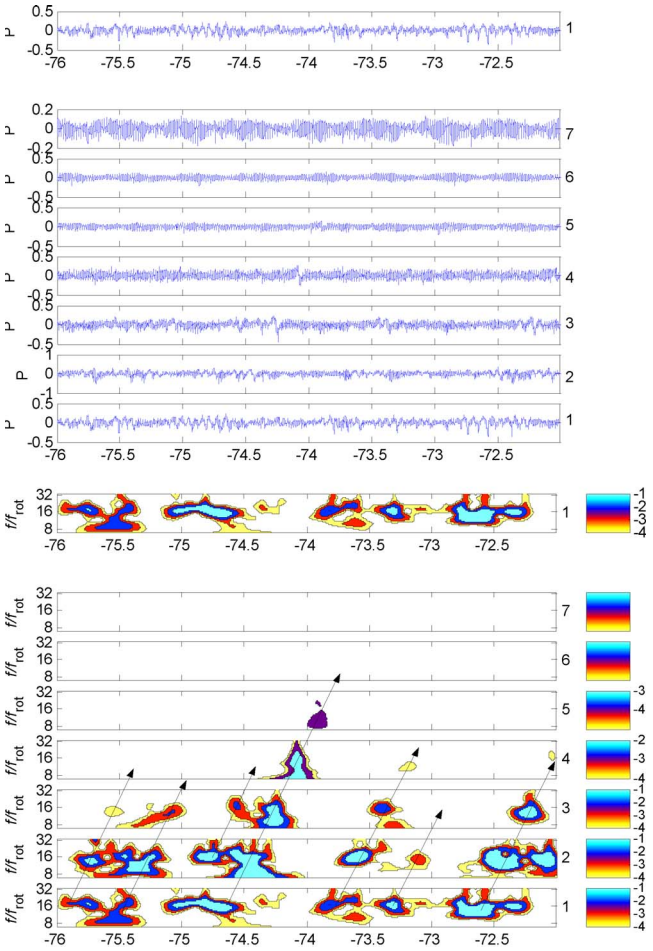

Fig. 13 Test data and wavelet spectra of case 1×30down

ference between 1×30up and 1×30down in simulation. A disturbance grows out the distorted background flow, traveling in the direction of rotor rotation so that it is first detected by the probes on the trailing edge side. The length scale of this disturbance is the same order as the scale of the distorted background flow. It then goes through a length-scale transition to trigger the full stall.

The Effects of Multiple Distortion Screens. Up to this point, both the test data and the simulation results indicated that distortion screens initialized rotating disturbances, and that the growth of these rotating disturbances was dominated by the nonlinearity of the system. The long-to-short scale transition is an evidence of existence for such nonlinearity. To further elaborate these points, we tested and simulated cases with more than one distortion screen in the annulus.

Although in cases 2×30×180 and 4×30 all the screens were placed axisymmetrically, in reality the flow is still not symmetric due to the fact that the compressor by itself is not symmetric. Therefore, in our test results no symmetry should be expected. Since we found that case 1×30down produced stronger initial disturbance due to the overlapping of the inlet distorted sector and the structural asymmetry, we would expect that for both cases of 2×30×180 and 4×30, the rotating disturbances should be detected first by the probes located closest to the trailing edge of the dominating distorted sector. This means that for 2×30×180, we would expect most of the rotating disturbances emerged at probe 1. For 4×30, the same thing is true except probe 1 is now located behind a distorted sector, which usually is quiet according to previous test and simulation results. So, we would expect most likely probe 2 might be the first one to detect the emergence of the disturbances, if there were any. Moreover, we expect that the additional distortion screens would enhance the rotating disturbances that pass by those screens. These expectations are verified with test results.

In Figs. 15 and 16, each figure depicts one example for each case, respectively. Figure 15 depicts the wavelet spectra for a segment of data from −10.5 to −0.5 revolutions prior to stall onset. As expected, probe 1 was the first to detect the emergence of one or two spike disturbances every rotor revolution. Most of these disturbances decayed even before they reached probe 3. For those that reached probe 4, they got enhanced at probe 4, just as we expected as well. The full stall was triggered by one of these disturbances.

As for case 4×30, probe 2 detected the emergence of most disturbances as expected (Fig. 16). When those disturbances started to propagate, they were enhanced after making themselves pass through the rest of the distortion screens. Such enhancement was detected in probes 4 and 6, clearly demonstrated in Fig. 16.

For case 2×30×90, the scenarios get more complicated. Each distortion screen initializes a spike disturbance, but whether it would be one prevailing over the other or they both grow depends on the throttle position. According to model simulation, there are three possible scenarios in this case. Scenario 1 is depicted in Fig. 17, obtained with a γ value of 0.0655, less than but very close to the critical value (γ_c=0.0656) for the stability limit. In this scenario, the first spike prevails over the second one and grows into the full stall cell, while the second one decays rapidly. When the throttle closes a little further (γ=0.0650), we obtain scenario 2, in which the second spike dominates and the first one decays (Fig.

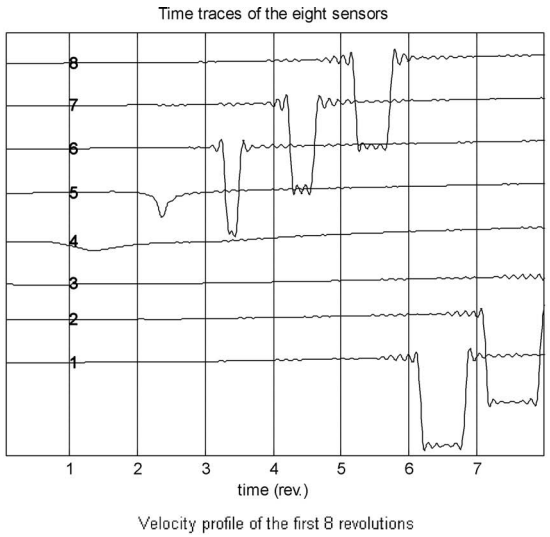

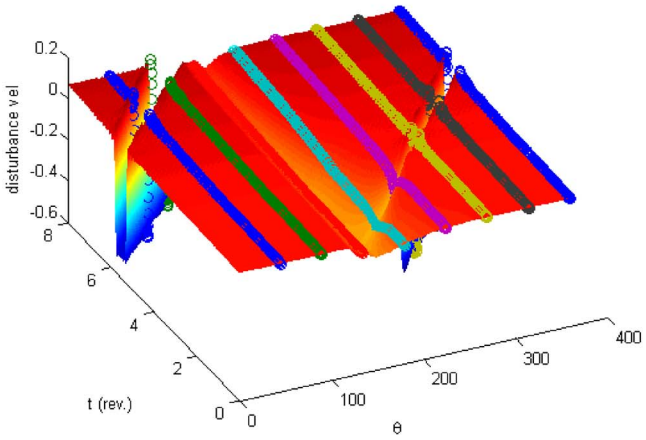

Fig. 14 Simulated results for case 1×30

18). Scenario 3 occurs when the throttle is closed even deeper into the unstable region (γ=0.060), both spikes grow, and eventually there are two full stall cells (Fig. 19).

The actual test results were quite similar to scenarios 1 and 2. Sometimes, a disturbance emerged on probe 6 (Fig. 20(*a*)), yet sometimes its first appearance was on probe 4 (Fig. 20(*b*)). Both probes 4 and 6 were located at the trailing edges of the distortion

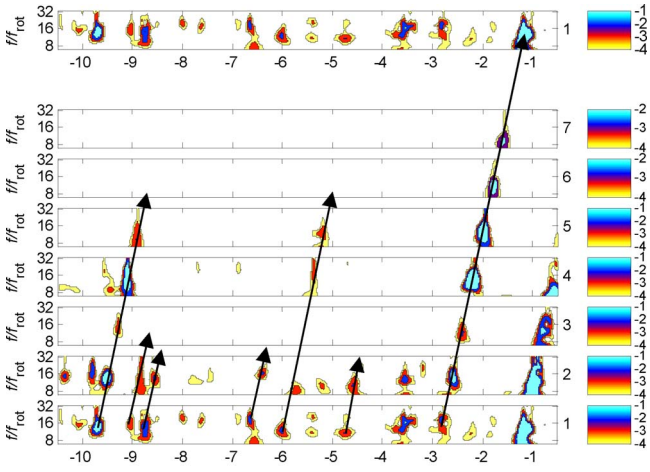

Fig. 15 Wavelet spectra of test results case for 2×30×180

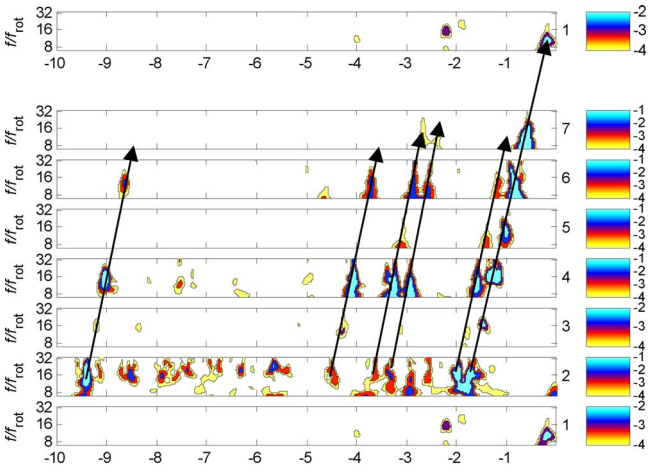

Fig. 16 Wavelet spectra of test results of case 4×30

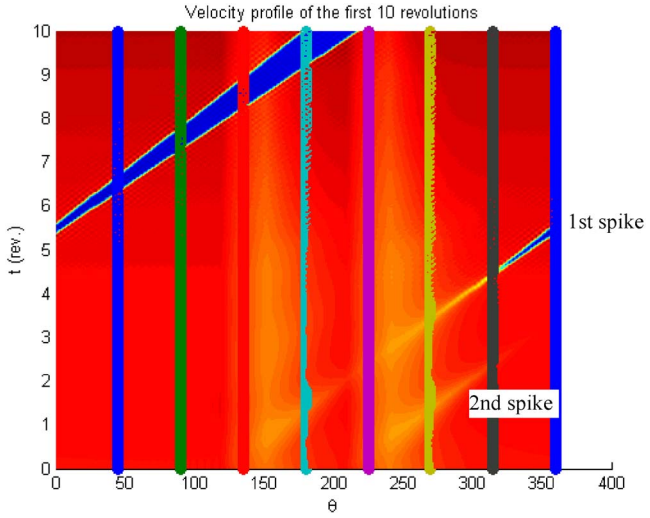

Fig. 17 Simulated scenario 1 for case 2×30×90

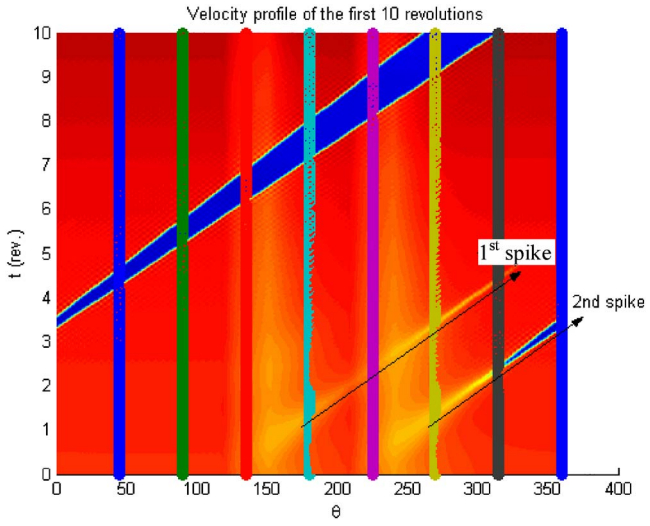

Fig. 18 Simulated scenario 2 for case 2×30×90

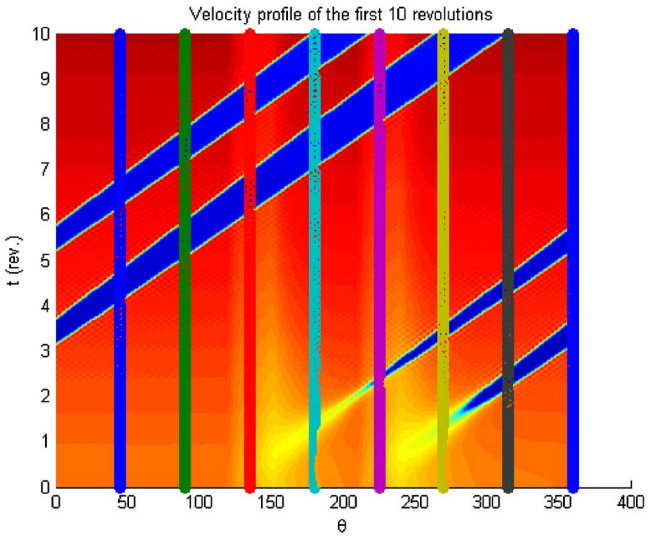

Fig. 19 Simulated scenario 3 for case 2×30×90

screens. The full stall was triggered by a long length-scale disturbance emerged on probe 6 after a length-scale transition.

Conclusions and Discussions

The unsteady stall inception processes of a total of six cases of inlet distortion were tested and simulated in this paper. From the analysis of test data, the results first confirm some of the observations by other researchers in literature (such as Jahnen et al. [23]), which are

(1) The distorted sectors are the sources of the initial disturbances, and
(2) The disturbances generated due to the existence of the distorted sectors may decay or grow in the undistorted sectors, depending on whether the damping in the undistorted sector is sufficient to prevail over the growth of the disturbances or not, which usually happen within one rotor revolution.

At the same time, the new findings of this research are:

(3) If the initial disturbance is of long length scale and the compressor dynamics is dominated by its nonlinear characteristic, the instability is indeed triggered by spikes that evolved from long length-scale disturbance, and
(4) In case of pure circumferential distortions, the emergence of the rotating disturbances is first detected by the probes located at or outside yet closest to the trailing edge of the distortion sectors.

The corresponding model simulation is able to qualitatively capture the conclusions (1), (3), and (4) but not (2).

Intuitively, from the flow physics point of view, it is not hard to explain conclusions (1) and (2). The distorted sectors represent higher aerodynamic loads to the rotor blade, so these sectors with higher loads naturally become the sources of disturbances. Once the disturbances emerge and travel out of the distorted sectors and enter into the undistorted sectors, they have a tendency to decay because the aerodynamic loads of the rotor blades are significantly reduced. In other words, the undistorted sectors tend to damp out the disturbances. Therefore, the overall stability depends on whether the damping is strong enough or not. However, the intuitive flow physics cannot convincingly explain conclusions (3) and (4). The length scale transition is certainly not intuitive from the flow physics point of view. At the same time, if the aerodynamic loading is the key factor for the emergence of rotating disturbances, one may expect the disturbances to first be detected by the probe located at the location where the heaviest aerodynamic loads are. But, our test results did not support this argument.

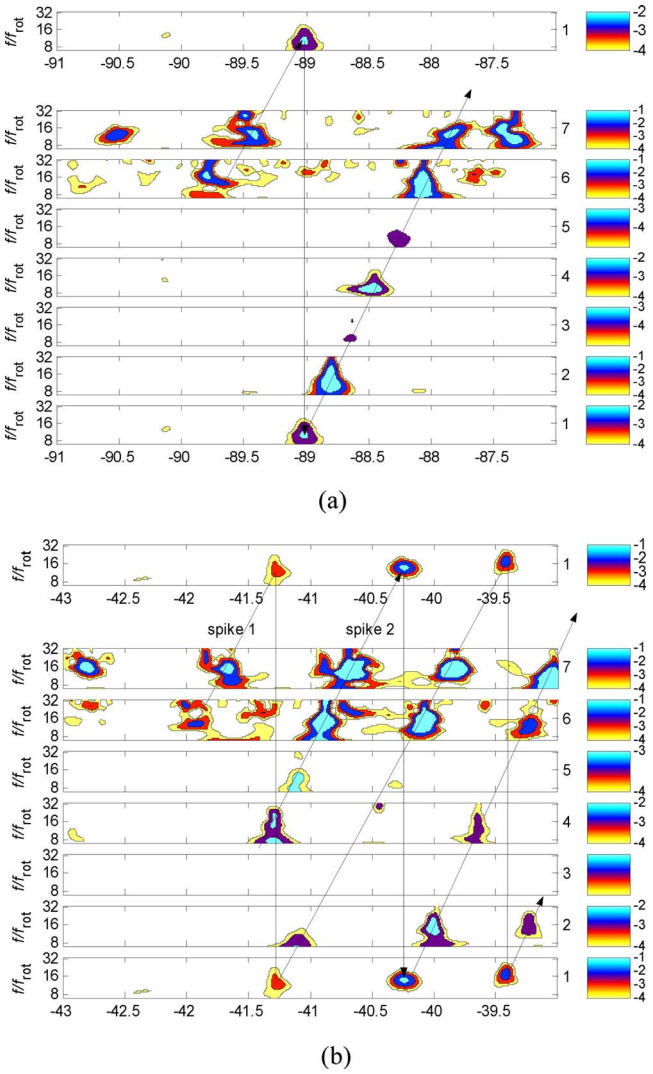

Fig. 20 Wavelet spectra of test results for case 2×30×90

On the other hand, from the point of view of system dynamics (i.e., analysis based on the system model), the behaviors such as conclusions (1), (3), and (4) are easily understandable. The distorted background flows are the initial conditions for system evolution; hence, they are naturally the sources of the rotating disturbance. The length-scale transition is the result of energy redistribution among the spatial Fourier modes due to the nonlinearity of the system. The propagation direction of the rotating disturbance is also a natural result of system dynamics, as shown in all of the figures for simulation results in this paper, so it is not surprising that they are detected only after they leave the distorted sector. However, the system model the way it is right now cannot explain conclusion (2). The model considers the aerodynamic loading upon the whole system by using the compressor characteristic, but does not contain any information about the aerodynamic loading in blade passage scale. Thus, the model cannot simulate the damping effect that the undistorted sectors may present to the rotating disturbance. According to the model, once they emerged, the rotating disturbances travel around the annulus as if there was no difference between distorted and undistorted sectors. As a consequence, the time scale for the disturbances to grow or decay is always more than one rotor revolution.

The inability to predict the time scale of the growth or decay of rotating disturbance indicates that the model in its current form neglects very important information of compressor aerodynamics,

especially the circumferentially nonasymmetric aerodynamic loads of rotor blades. In order to model such aerodynamic loads, one has to model the blade passage flows of the compressor. However, the system scale model does provide some crucial insights about this complicated instability problem that are difficult to grasp in pure flow physics. Hence, it is suggested that the integration between the blade passage flows and the system dynamics should be considered in developing new models for compressor instability with inlet distortion. The findings of this paper may also stimulate new strategy of active stall control. The ability of pinpointing the exact location and time of the emergence of rotating disturbances makes it possible to eliminate them right at their birthplace. Meanwhile, the new understanding of the interaction between system dynamics and blade passage flow would provide a foundation for new controller design and implementation.

Acknowledgment

The support of the National Science Foundation of China through Grant 50176050 is gratefully acknowledged.

Nomenclature

B = Greitzer's B parameter
f = pressure signal frequency
f_{rot} = rotor's rotating frequency
K_L = coefficient of distortion screen
l_c = time lag for the entire compressor system
l_I = inlet length
P_{c} = compressor characteristic
P_T = total pressure
P = static pressure
U = axial flow velocity
ρ = air density
γ = throttle coefficient
λ_r = time lag of rotors
ψ = pressure coefficient
ϕ = flow velocity coefficient

Superscripts

* = dimensionless quantities

References

[1] Greitzer, E. M., and Strand, T., 1978, "Asymmetric Swirling Flows in Turbomachine Annuli," ASME J. Eng. Power, **100**, pp. 618–629.
[2] Moore, F. K., and Greitzer, E. M., 1986, "A Theory of Post-stall Transients in Axial Compression Systems: Part I," ASME J. Eng. Gas Turbines Power, **108**, pp. 68–76.
[3] Garnier, V. H., Epstein, A. H., and Greitzer, E. M., 1991, "Rotating Waves as a Stall Inception Indication in Axial Compressors," ASME J. Turbomach., **113**, pp. 290–302.
[4] Day, I. J., 1993, "Stall Inception in Axial Flow Compressors," ASME J. Turbomach., **115**, pp. 1–9.
[5] Camp, T. R., and Day, I. J., 1999, "A Study of Spike and Modal Stall Phenomena in a Low-Speed Axial Compressor," ASME J. Turbomach., **120**, pp. 393–401.
[6] Tryfonidis, M., Etchevers, O., Paduano, J. D., Epstein, A. H., and Hendricks, G. J., 1995, "Pre-Stall Behavior of Several High-Speed Compressors," ASME J. Turbomach., **117**, No. 1, pp. 62–80.
[7] Bright M. M., Qammar, H. K., Weigh, H. J., and Paduano, J. D., 1997, "Stall Precursor Identification in High-Speed Compressor Stages Using Chaotic Time Series Analysis Methods," ASME J. Turbomach., **119**, pp. 491–498.
[8] Lin, F., 1998, "Use of Symbolic Time Series Analysis for Stall Precursor Detection," The 34th AIAA/ASME/SAE/ASEE Joint Propulsion Conference, Cleveland, OH, July, Paper No. AIAA-98–3310.
[9] Lin, F., Chen, J., and Li, M., 2002a, "Practical Issues of Wavelet Analysis of Unsteady Tip Flows in Compressors," AIAA/ASME/SAE/ASEE Joint Propulsion Conference, Indianapolis, IN, July, Paper No. AIAA-2002-4082.
[10] Lin, F., Chen, J., and Li, M., 2004, "Wavelet Analysis of Rotor-Tip Disturbances in an Axial-Flow Compressor," AIAA J. Propul. Power, **20**, No. 2, pp. 319–334.
[11] Inoue, M., Kuroumaru, M., Yashida, S., and Furukawa, M., 2001, "Short- and Long-Scale Disturbances Leading to Rotating Stall in an Axial Compressor Stage With Different Stator/Rotor Gaps," ASME Paper No. 2001-GT-341.
[12] Leinhos, D. C., Schmid, N. R., and Fottner, L., 2001, "The Influence of Transient Inlet Distortions on the Instability Inception of a Low Pressure Compressor in a Turbofan Engine," ASME J. Turbomach., **123**, pp. 1–8.
[13] Mazzawy, R. S., 1977, "Multiple Segment Parallel Compressor Model for Circumferential Flow Distortion," ASME J. Eng. Power, pp. 288–297.
[14] Hawthorne, W. R., Mitchell, N. A., McCune, J. E., and Tan, C. S., 1978, "Nonaxisymmetric Flow through Annular Actuator Disks: Inlet Distortion Problem," ASME J. Eng. Power, **100**, pp. 604–617.
[15] Stenning, A. H., 1980, "Inlet Distortion Effects in Axial Compressors," ASME J. Fluids Eng., Vol. **102**, pp. 7–13.
[16] Tan, C. S., and Greitzer, E. M., 1986, "Nonaxisymmetric Compressible Swirling Flow in Turbomachine Annuli," AIAA J., **24**, No. 1, pp. 92–100.
[17] Hynes, T. P., and Greitzer, E. M., 1987, "A Method for Assessing Effects of Inlet Flow Distortion on Compressor Stability," ASME J. Turbomach., **109**, pp. 371–379.
[18] Spakovszky, Z. S., van Schalkwyk, C. M., Weigl, H. J., Paduano, J. D., Suder, K. L., and Bright, M. M., 1999, "Rotating Stall Control in a High-Speed Stage With Inlet Distortion: Part I and II," ASME J. Turbomach., **121**, pp. 510–524.
[19] Greitzer, E. M., 1976, "Surge and Rotating Stall in Axial Flow Compressors, Part I and II," ASME J. Eng. Power, **98**, pp. 190–217.
[20] Longley, J. P., 1990, "Measured and Predicted Effects of Inlet Distortion on Axial Compressors," ASME Paper No. 90–GT-214.
[21] Chen, T., 2004, "Relationship between the Axial Compressor With Inlet Distortion and Stall Margin," Masters Thesis, Institute of Thermophysics, Chinese Academy of Sciences (in Chinese).
[22] Day, I. J., Breuer, T., Escuret, J., Cherrett, M., and Wilson, A., 1999, "Stall Inception and the Prospects for Active Control in Four High-speed Compressors," ASME J. Turbomach., **121**, pp. 18–27.
[23] Jahnen, W., Peters, T., and Fottner, L., 1999, "Stall Inception in a 5-Stage HP-Compressor With Increased Load Due to Inlet Distortion," ASME Paper No. 99-GT-440.

Modeling of Film Cooling—Part I: Experimental Study of Flow Structure

Stefan Bernsdorf

Martin G. Rose

Reza S. Abhari

Institute of Energy Technologies,
Department of Mechanical Engineering,
Swiss Federal Institute of Technology - ETHZ,
CH-8092 Zurich, Switzerland

This paper, which is Part I of a two part paper, reports on experimental data taken in a steady flow, flat plate wind tunnel at ETH Zürich, while Part II utilizes this data for calibration and validation purpose of a film cooling model embedded in a 3D CFD code. The facility simulates the film cooling row flow field on the pressure side of a turbine blade. Engine representative nondimensionals are achieved, providing a faithful model at larger scale. Heating the freestream air and strongly cooling the coolant gives the required density ratio between coolant and freestream. The three dimensional velocities are recorded using nonintrusive PIV; seeding is provided for both air streams. Two different cylindrical hole geometries are studied, with different angles. Blowing ratio is varied over a range to simulate pressure side film cooling. The three dimensional flow structures are revealed. [DOI: 10.1115/1.2098768]

Keywords: film cooling, flow structure, density ratio, blowing ratio, PIV

Introduction

The main interest in the improvement of the film cooling, next to the reason of increase of efficiency, is the enhancement of the lifetime of a turbine blade. This results directly in a significant reduction of engine cost and is therefore a strong argument for the industry to engage in film cooling research.

A new experimental facility has been constructed at ETH Zurich. It has two main goals. First, to determine a better understanding of the physics involved in film cooling and the influence of the numerous flow parameters. Enhanced understanding will facilitate cooling development and design innovation. Secondly, the experimental results obtained with this facility are used to calibrate the Burdet-filmcooling model that has recently been implemented into the LSM-internal flow solver MULTI3, as presented in Part II of this paper [1].

The concept of the test rig presented here was to create a facility where steady and unsteady film cooling can be quantified regarding both the flow and thermal properties. This leads to a continuously running closed-loop wind tunnel, as detailed flow measurements are not feasible in a transient facility. Measurement techniques decided on in the early concept phase were particle image velocimetry PIV for flow measurements and double sided thin film heat flux gauges for surface heat flux measurement. Probe measurements with fast and slow temperature and pressure sensors was another desired feature.

As designed, a large range of independent flow parameters can be adjusted in this unique facility. Geometrical, flow and thermal conditions all cover the typical conditions of a turbine pressure side to great extent. In detail: the exchangeable cooling hole geometry is scaled up to 5 mm diameter, while relative dimensions like spacing and hole length are preserved. Arrangement of the holes in single and double arrays is possible. The holes can be cylindrical or shaped, with streamwise angle in the range from 20 deg to 90 deg and any lateral angle. This paper presents the results of two geometrical cases with a single array of 7 holes of constant diameter, length and spacing. The variation is in the streamwise angle between 30 deg and 50 deg.

The governing flow conditions are Mach number M, density ratio DR, blowing ratio BR, or momentum flux ratio IR. Additionally, the turbulence intensity Tu and the momentum thickness θ have a significant influence on the film cooling behavior. This paper presents the results of steady film cooling with variation in BR and DR.

Thermal management allows the independent adjustment of three temperature levels. The main flow is heated (120 °C max.), the secondary flow is cooled (−50 °C min) and the test surface is temperature controlled (15 °C to 30 °C) by internal cooling, effectively creating an isothermal boundary condition. This paper presents flow results only. Thermal results will be presented at a later stage.

Previous Research

Many studies have focused on film cooling in the past decades. A lot of different approaches were taken, utilising different experimental facilities, a variety of measurement techniques, geometrical and functional differences in the test section and different flow regimes. The effects of geometrical, thermal, and flow parameters were studied, and models have been established. Numerical modelling of film cooling has been conducted and the results compared to data obtained from corresponding experiments.

Two general setups of test rigs are used for film cooling research. The transient technique utilizes a blow-down facility, as done by numerous investigators like Abhari, Abhari et al., Dunn, Eads, Giang, Guenette et al., and Teekaram et al. [2–9]. The obvious advantage for heat transfer measurements is the possibility to adjust temperatures of both solids and fluids without having to take serious measures to counter wall conduction errors in the short duration of measurement. Furthermore, surface heat flux measurements are tremendously facilitated, as a single time resolved temperature allows the assessment of the heat flux. Steady test facilities, as used by Goldstein et al., Ligrani et al., and Pietrzyk et al. [10–13], allow for longer measurement times, as is necessary for some measurements techniques involving lasers or a mass/heat transfer analogy.

Different types of test sections are used. The geometrically simple form of a flat plate with one or more film holes often offers

Contributed by the International Gas Turbine Institute (IGTI) of ASME for publication in the JOURNAL OF TURBOMACHINERY. Manuscript received by IGTI, October 1, 2004; final revision, February 1, 2005. IGTI Review Chair: K. C. Hall. Paper presented at the ASME Turbo Expo 2005, Land, Sea, and Air, Reno, NV, June 6 - 9, 2005, Paper No. GT2005-68783.

a sufficient approximation of the reality for a lot of research interests (e.g., Cho et al. [14], Forth et al. [15], and Giang [7]). Linear cascades of airfoils with film holes are utilized on a more complex level (e.g., Popp et al. [16] and Smith et al. [17]) and also research with full-scale rotating rigs is conducted (e.g. Dunn [5] and Dunn et al. [18]).

The influence of the density ratio was recognized as one of the major influences on the mixing and thus on the general film cooling performance. The experimental modeling of the higher density of the coolant flow is either achieved with cryogenic cooling or with the use of a foreign gas.

Steady flow regimes for both main and coolant flow are widely used to study film cooling. Giang [7] points out, that the efficiency of the cooling depends strongly on the mixing process between coolant flow and main flow, which in turn depends on other conditions. Studies have been done to investigate the possible factors that could influence the cooling performance. For instance, Goldstein et al. [19] investigated the geometrical effects of the cooling holes; Forth et al. [15] studied the effects of density and temperature ratios between the primary and secondary flows; Bons et al. [20] studied freestream turbulence effects, etc.

A wide variety of measurement techniques have been used in film cooling research. A general distinction has to be made between flow measurements and heat transfer measurements, as well as between steady and time resolved measurement capability.

Noninvasive techniques like PIV (e.g., Gogineni et al. [21]) have become an attractive tool for flow measurements in recent years, as these techniques have become established and commercially available. The classic flow measurement methods utilizing pitot-static probes and hot wires (e.g. Rockwell [22]) have the advantage of simplicity, high accuracy and easily quantifiable errors. Therefore they are still widely used as a supportive or sole flow measurement system. Nonquantitative techniques like shadowgraph (e.g., Smith et al. [17], Ligrani et al. [12]) or different types of flow visualisation are also utilized, as the flow field is often of secondary interest, next to heat transfer information, to the researchers.

Heat transfer measurements have been conducted with liquid crystals (e.g., Ekkad et al. [23] and Honami et al. [24]) infrared cameras (e.g., Ligrani et al. [12]) and with thin film gauges (e.g., Abhari et al. [3,4], Dunn et al. [5,18], Epstein et al. [25], and Guenette et al. [8]).

Liquid crystals give a reasonable time-resolution and information on the entire covered surface. Two of the bigger problems of this technique are that optical access is necessary, and sensitivity of the crystals only extends over a small temperature range. Utilisation of an infrared camera again requires optical access. Data of the entire surface can be measured at once. Calibration poses some difficulties here. Thin film gauges give highly time resolved data at discrete locations. No optical access is required, but the influence of the gauges on the heat flux, through creating a thermal discontinuity, must be considered.

Naphthalene sublimation is used in mass transfer-analogues heat flux measurement (e.g., Cho [14] and Goldstein [26]). Time averaged surface data of the convective component of the heat transfer is obtained without wall conduction and radiation errors. The drawback is the change of the surface shape over time, even though minute, and with that an influence on the mass transfer.

Computational modelling of film cooling is another area of research effort. Based on the fluid dynamic problem of jets in cross flow (e.g., Le Grivèe [27]), 2D models for the mixing have been established, successively incorporating the trajectory angle and the density ratio (e.g., Abhari [2]). This model is used quasisteady in unsteady flow calculations.

During recent years a film cooling project was established at ETH Zurich. Complimentary experimental investigation and CFD modelling were built up in parallel. A 3D model for each cooling jet is implemented into an existing CFD code. Burdet et al. [1] presents the first results in Part II of this paper.

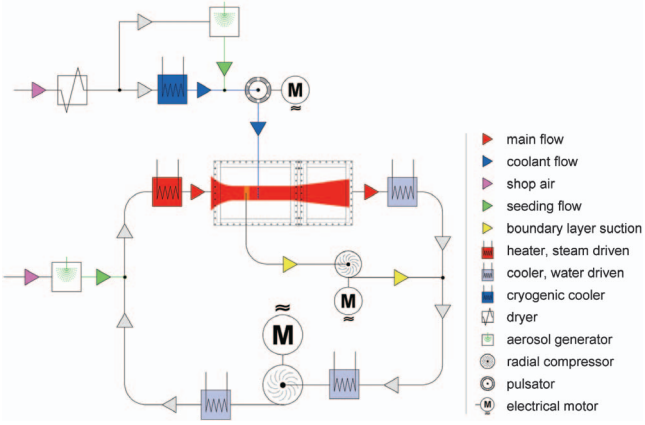

Fig. 1 Schematic of test rig

Introduction to Test Facility

The film cooling test rig, as shown in Fig. 1, is based on a former supersonic calibration facility. It consists of four major sections supported by a custom made monitoring system. The rig is designed to be operated with different measurement techniques. At present a stereoscopic PIV system is implemented.

The rigs operating range is given in Table 1 together with the respective range in real pressure side film cooling.

Mainflow. A centrifugal compressor of 297 mm diameter, driven by a 470 kW electrical motor, creates the main flow in the experimental closed loop facility. The impeller is taken from an ABB VTC 254 turbo charger. The gearbox and periphery are custom made for the application. The pressure in the system is self-adjusting by a small blow out valve. The resulting pressure level in the test section is around the ambient pressure level.

Temperature is controlled with a water-cooled heat exchanger downstream of the compressor, while a second cooler is installed just upstream of the impeller intake for its protection against overheating. That configuration allows a temperature range from 18 °C to 40 °C in the freestream. A steam-air heat exchanger is installed upstream of the test section to raise the main flow temperature up to 120 °C. This 200 kW heat exchanger is fed by 7 bar saturated steam from the house heating system. The heater is controlled with a feedback control loop. The heat is extracted from the main flow downstream of the test section by a water-cooled heat exchanger.

The pipe work containing the main flow is suspended from the ceiling to allow thermal expansion of the steel piping. Additionally, a compensator replaces a section of the pipe to allow angular and lateral displacement of the pipe without causing damage. The hot section of the test rig, between the steam heater and the water cooler, is wrapped in 30 mm thermal insulation sheets and the test section is thermally decoupled from the ambient by ceramic insulators.

The rotational speed of the impeller determines the pressure ratio and with that the resulting mass flow rate in the system. At its maximum speed of 30,000 rpm the compressor can deliver up

Table 1 Capabilities of new test facility

	Typical conditions pressure side film cooling	Capabilities new test rig
DR	1–1.8	1–1.6
BR	0.8–4	0.5–3
IR	0.9–2	0.1–5
M	0.3–0.8	0.1–0.64

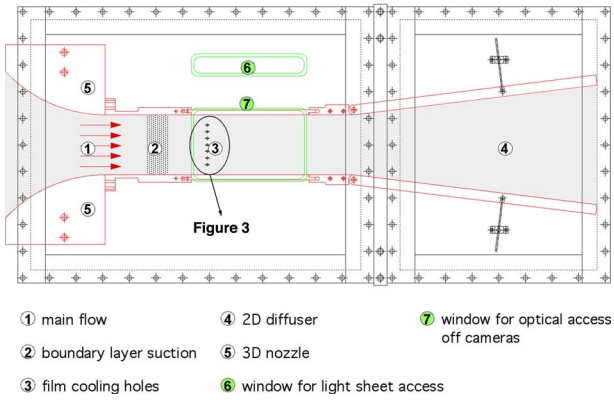

Fig. 2 Sketch of test section

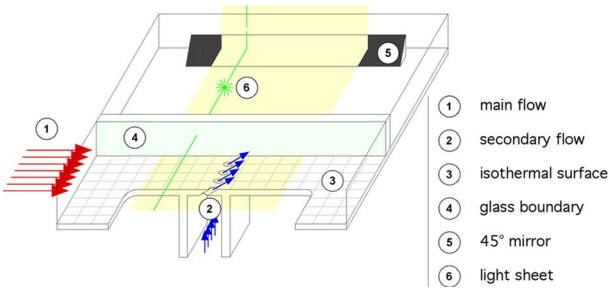

Fig. 4 Schematic of injection arrangement

to 4 kg/s. At present, the maximum mass-flow rate required is at about 1.5 kg/s, for a freestream Mach number of $M=0.5$.

The boundary layer thickness of the main flow is controlled by a suction arrangement. A centrifugal blower drives the boundary layer suction, extracting through 327 discrete holes of 1.2 mm diameter stacked in 11 arrays over an area of 60×180 mm. The extracted air is fed back into the loop far downstream of the cooler. The maximum capacity of the suction is about 50 g/s and is adjusted with a hand valve.

Oil aerosol is blown from the seeding generator into the main flow upstream of the heater during PIV measurements.

Cooling flow. The secondary flow is delivered by the shop air system with a maximum of 75 g/s. First a drier lowers the dew point of the air to −70 °C. Two cylinders filled with water absorbing solid particles are alternately drying the air and recuperating inside that drier. Next in line is a fast acting self-controlling pressure control valve, followed by a massflow measurement section. Downstream is a single cycle cooler, capable of reducing the temperature down to −63 °C at cooler exit. The 12 m piping connecting the cooler and the primary wind tunnel is wrapped in 40 mm insulation. A seeding generator containing 5 arrays of Laskin nozzles adds an oil aerosol 1.5 m upstream of the injection location.

Test section. The test section has a rectangular flow path of 40×181 mm cross section. A schematic is shown in Fig. 2. A 3D nozzle accelerates the flow coming from the settling chamber. The area of main interest is the injection site of the secondary flow in a range from $5d$ upstream to $35d$ downstream of the origin of coordinates (see Fig. 3). 15 mm glass walls on three sides provide optical access. The top and the bottom wall allow access of the light sheet. The light sheet is introduced to the system from the front, via the top window and a 45 deg mirror (see Fig. 4). The two cameras look into the test section through the front window.

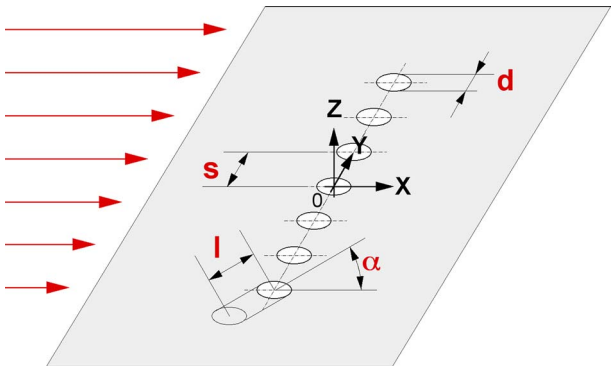

Fig. 3 Definition of coordinates and dimensions

Downstream of the injection site is a 2D diffusor to recover some of the dynamic pressure.

The definition of the coordinate system and of the relevant geometrical parameters is illustrated in Fig. 3.

The origin of the coordinate system as used in all results presented is in the center of the middle hole, irrespective of geometry. The two different geometries presented in this paper are defined in Table 2.

PIV system. the PIV system utilized in this project is a commercially available stereoscopic system. Two CCD cameras with a resolution of 1280×1024 pixel and a dynamic range of 12 bit are mounted on a two-axis high accuracy traverse system, as shown in Fig. 5. The double pulsed Nd:YAG laser with 120 mJ power per pulse is mounted on an additional third traverse axis. The light sheet optics, which is connected directly with the laser, creates a light sheet in *XY* orientation with variable thickness. The path of the lightsheet inside the test section is illustrated in Fig. 4.

The cameras and the laser head are mounted on a massive cast iron table, as shown in relation to the test section in Fig. 5. Simultaneous traversing of the laser in vertical direction (Z_{laser} in Fig. 5) with traversing of the cameras in horizontal direction (Z_{cameras} in Fig. 5) allows the scanning of the flow volume in Z direction without the need of recalibration for every light sheet position.

The system also consists of two linked computers. The first computer is a specialized device containing the frame-grabber cards and the unit to synchronize the cameras and the laser. It also functions as a data buffer between the second computer and the cameras. The second computer is a standard PC with vast amount of hard disk to store the results. This computer runs the PIV software package, which controls the first computer, organizes the data and finally processes it.

Measurement Procedure

The conduction of a measurement series consists of two main parts. First the flow parameters are adjusted with the aid of the real-time monitoring system. 40 primary data channels (pressure, temperature, frequency, and mass flow) are acquired directly from their corresponding sensors. These are written to file together with 10 derived flow parameters. The most relevant parameters like main flow Mach number, blowing ratio and density ratio are shown online, thus allowing their fast and accurate adjustment. The warm up of the entire system can take up to three hours, depending mainly on the density ratio chosen.

Secondly the flow velocities are measured using the PIV system. This includes a whole series of steps, starting with the setup

Table 2 Definition of geometry

Geometry	d	$\text{No.}_{\text{holes}}$	s/d	l/d	α
i	5 mm	7	4	2.8	30 deg
ii	5 mm	7	4	2.8	50 deg

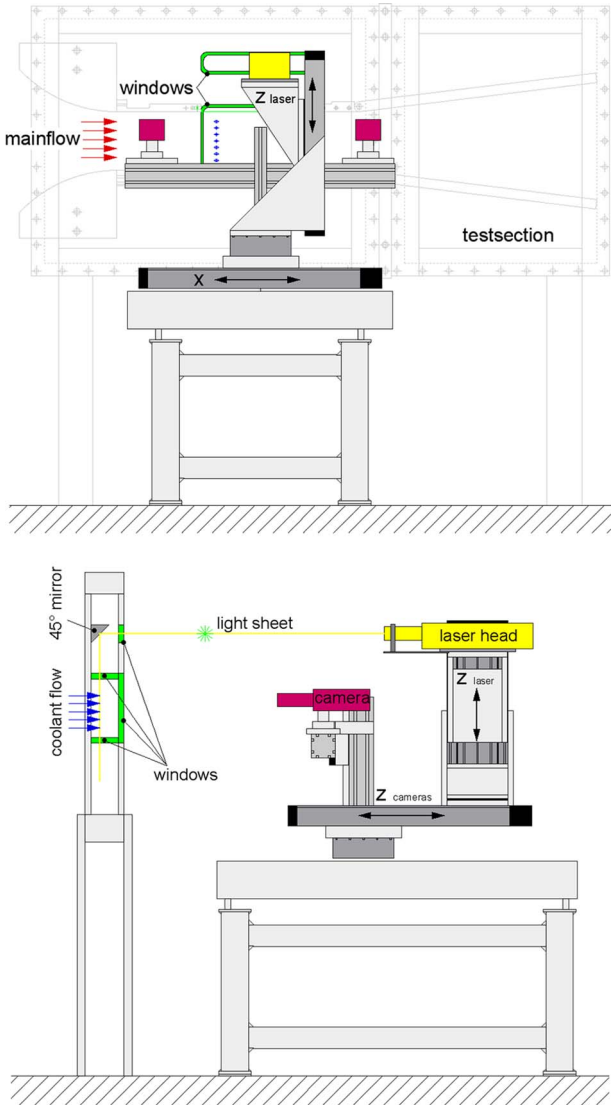

Fig. 5 Mounting of PIV system

of the cameras and the laser, going on to the calibration and error assessment, over to the actual measurement and ends with the data processing.

The PIV system is used with two cameras at different angles to the test surface. Double pictures separated by a time step of 2.5 μs are taken throughout all experiments. The field of view of a camera is around 45 mm $\times$ 36 mm. The corresponding displacement between the two frames of a seeding particle travelling with the freestream main flow velocity of 110 m/s is close to 8 pixels.

The setup is the critical step in the PIV measurement, determining the quality and reliability of the final results. The cameras are adjusted so they look at the same area of the flow. Then they are focused and the light sheet is adjusted to be parallel to the *XY* coordinates of the flow and to have a defined thickness of 1 mm. The three traverse axes are adjusted to be parallel to the *X*, *Y*, and *Z* axis, respectively.

The calibration is performed with the aid of a single layer calibration target, consisting of a flat black plate with white points. The target is placed into the test section parallel to the *XY* plane. The points are arranged in a 2D array of constant spacing and have three different sizes. The difference in size defines the center of the target and the orientation. Both cameras take pictures of that target in five defined distances orthogonal to the target. The PIV software detects the points and determines a linear transformation matrix for each camera. This matrix allows the transformation of the pictures taken in the respective orientation of each camera into the flow coordinate system. Furthermore, the two matrices allow the transformation of the two 2D vector fields, derived from each camera, into one vector field in *XY* plane with 3D flow vectors.

Table 3 Parameters of experiments

Case	α	*M*	*BR*	*DR*	*IR*
1	30 deg	0.297	0.994	1.000	0.987
2	30 deg	0.306	0.994	1.511	0.654
3	30 deg	0.298	2.003	1.000	4.012
4	30 deg	0.304	2.042	1.585	2.631
5	30 deg	0.298	2.692	1.000	7.245
6	30 deg	0.308	2.692	1.602	4.524
7	50 deg	0.296	1.006	0.994	1.017
8	50 deg	0.296	2.001	0.993	4.037
9	50 deg	0.304	1.007	1.462	0.693
10	50 deg	0.308	2.012	1.530	2.686

Establishing the measurement accuracy (from raw picture to a 3D-vector field) is done with the aid of two simple experiments. Sandpaper is placed onto the test surface and lit in a diffuse way. The cameras are then traversed relative to the sandpaper while taking the double picture. The software is set in a way that the displacement between the double pictures corresponds to a velocity of 100 m/s in one direction and 0 m/s in the two other directions, thus creating a virtual and defined velocity field. The results show that the error for the *U* and the *V* component is of the order of 1% of the virtual freestream velocity (U=100 m/s) while the error for the *W* component was about 5%.

In order to reduce the effect of reflection from the background 30 double frames are shot for each condition. A mean pixel value of those 30 double frames is determined after the measurement. The mean pixel is subtracted from every double frame, thus eliminating the background reflection.

The final cross-correlation on every single frame is performed with 32 $\times$ 32 pixel interrogation windows to obtain a vector field. Further features used in the correlation are 50% overlap of the areas, a one-step iterative refinement of the interrogation area with deforming windows, high accuracy sub-pixel refinement and a peak validation with a ratio between the minimum peak height and the peak 2 of 1.1. A local moving average validation over 3 $\times$ 3 vectors with an acceptance factor of 0.1 is chosen as local neighborhood validation. A Gaussian weighting function is applied to each interrogation area to deal with the particles at the border of the interrogation area. A detailed description of the options used can be found in the software manual [28].

The mean vector field over all 30 samples is determined for each camera in the next step. The 3D conversion is done with the two mean vector fields, thus giving a 2D plane in *XY* orientation with averaged 3D velocity information.

The flow field is scanned in *Z* direction in increments of 1 mm to 3 mm. All resulting planes are combined in a flow volume containing the three component flow vectors as well as a number of derivatives like flow angle, vorticity and shear stress. The flow volume consists of 10 to 12 planes with 79 $\times$ 63 vectors, giving a total number of roughly 50,000 to 60,000 data points.

Flow Conditions

All results presented here are averaged over 20 to 30 double frames. The respective experiments were performed under steady flow conditions. The flow conditions of the different experiments are defined by the main flow Mach number *M*, the density ratio *DR*, the blowing ratio *BR*, the momentum flux ratio IR, and the stream-wise flowangle α. The main flow boundary layer is defined by the momentum thickness θ and the shape factor *H*. An overview is given in Table 3.

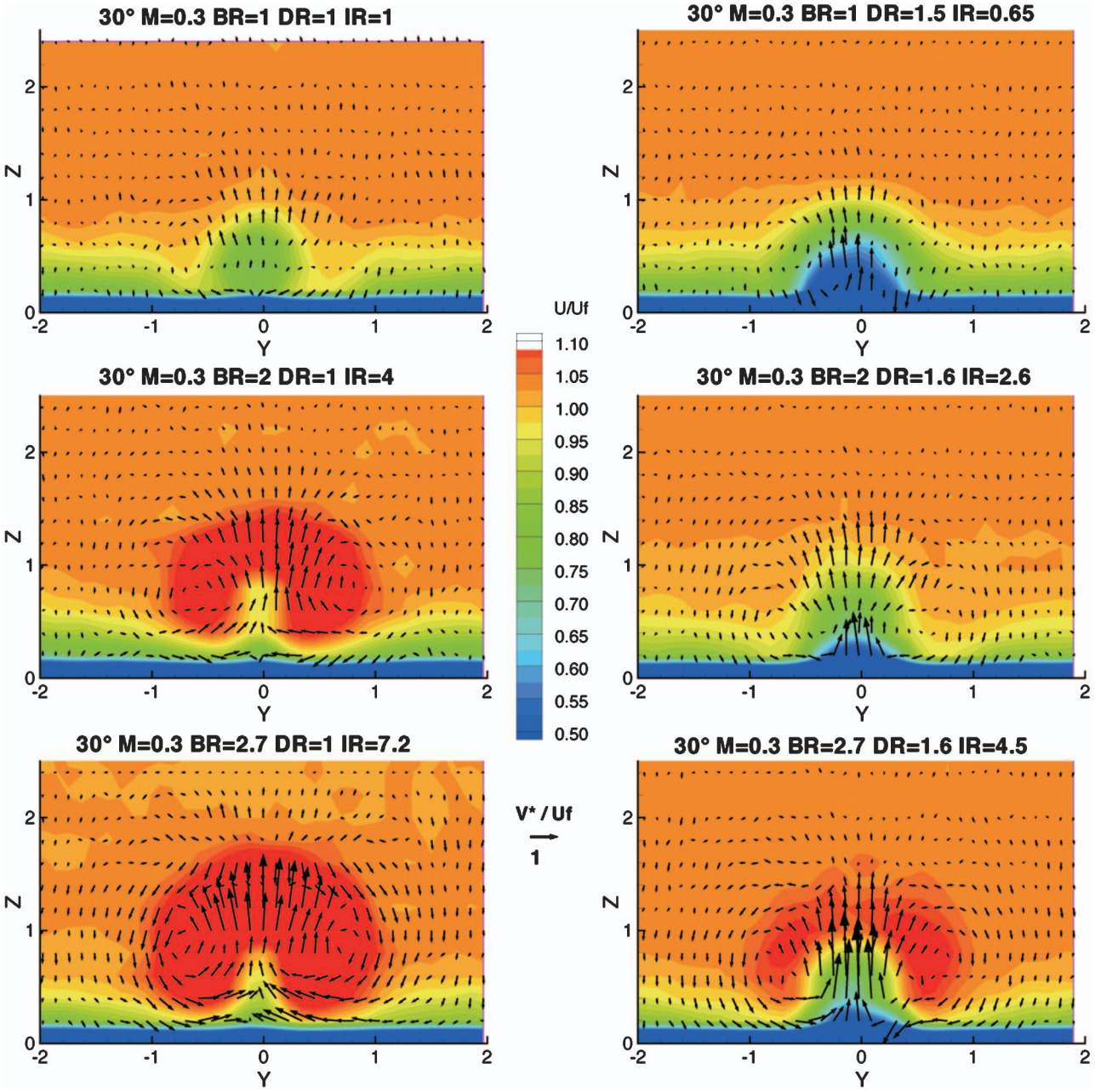

Fig. 6 Influence of BR and DR on axial velocity at $X=4$

The parameters are defined globally. The momentum thickness was quantified before the PIV measurement campaign with a three hole pneumatic probe. The momentum thickness, nondimensionalized by the hole diameter, has a constant value of $\theta=0.051$, with a shape factor of $H=2.3$. The velocity profiles show good correspondence to the 1/7-power approximation for turbulent boundary layers.

The density of the main flow is derived from the pressure and temperature taken just upstream of the cooling holes. The velocity of the main flow is derived from its directly measured mass flow rate, the cross section of main flow area and the aforementioned density. The density of the coolant flow is derived from the pressure and temperature taken in the plenum upstream of the cooling holes. The velocity of the coolant flow is derived from its directly measured mass flow rate, the total cross section of all cooling holes and the aforementioned density. With that the above-stated parameters *BR*, *DR*, and *IR* are defined. The main flow Mach number is derived from the velocity and the speed of sound, derived from the main flow temperature.

Results

This section presents the most interesting results of the flow measurements. Velocities are non-dimensionalized with the freestream axial velocity component. Streamlines, if given in a 2D plot represent the projection of the 3D streamlines into that plane. They are all started at the centerline of the cooling hole.

First the influence of *BR*, *DR*, and α on the flow structure is shown. Secondly, one parameter combination is analyzed in more detail.

Figure 6 gives a comparison of flow structure for varying *BR* and *DR* with constant $\alpha=30$ deg. Each row has a constant *BR*

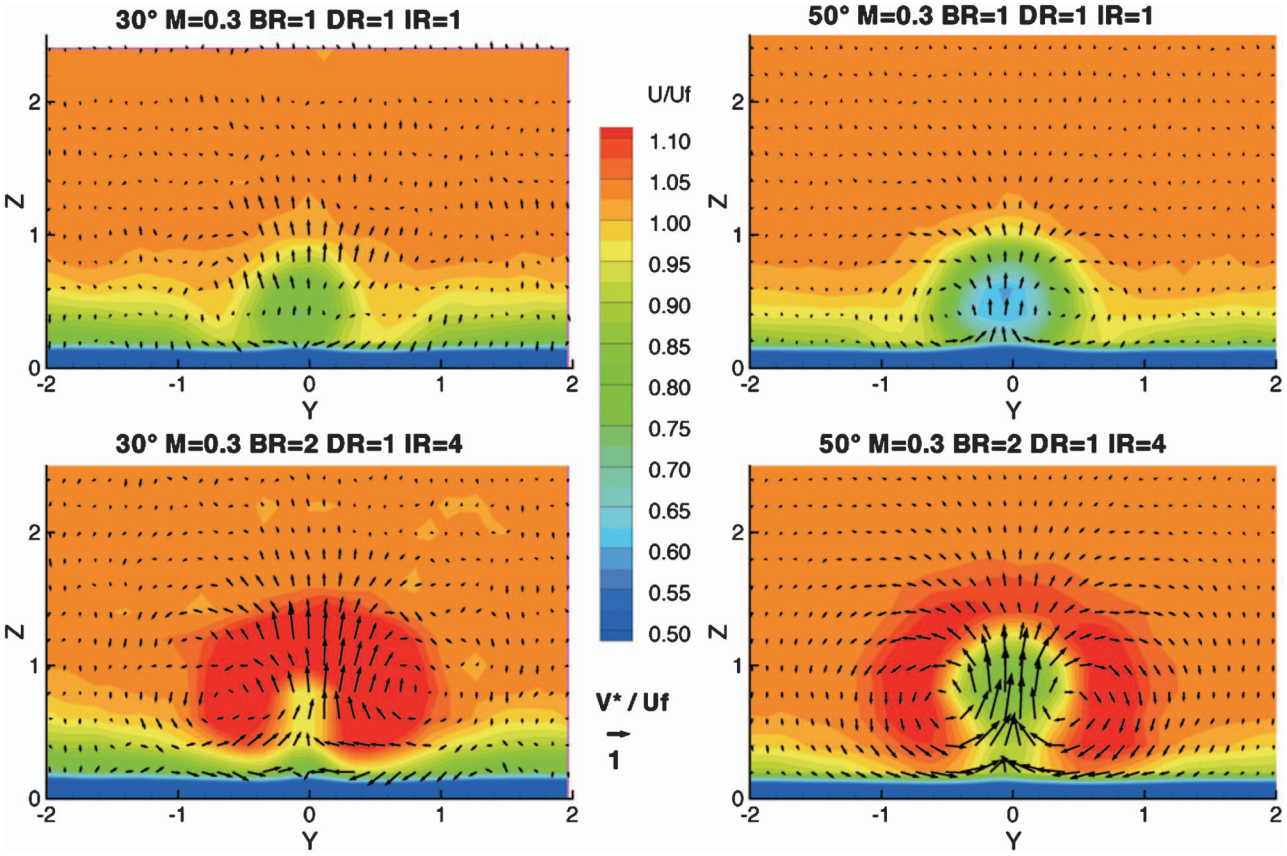

Fig. 7 Influence of α and *BR* on axial velocity at $X=4$

whilst both columns have constant DR. The planes are representing the flow at $X=4$, showing the axial velocity component in color and the flow vectors.

As expected, increase in *BR* results in increase in the axial flow component. Notable is the decrease of boundary layer thickness with increasing *BR*. This decrease of thickness will be associated with increases in heat transfer coefficient. The pictures seem to indicate that the increased entrainment of main flow into the centre of the jet originates at least partly from the boundary layer region. Increase in *DR* means reduced *IR* for constant *BR*. Therefore, the direct comparison of plots from left to right show a weaker jet for higher *DR*/lower *IR*. Furthermore, the respective centre of the kidney vortices is at a lower level above the surface. It should be noted that the high *DR* cases entrain more low velocity fluid into the centre of the jets than the corresponding low *DR* cases.

Figure 7 shows the comparison of flow structure for varying α and *BR*. The left column shows the flow at $X=4$ for $\alpha=30$ deg with increasing *BR*, while the right column shows the same for $\alpha=50$ deg. Again, the plots give the axial velocity component in color as well as the flow vectors.

Comparing the left with the right column, it can be observed that the respective centre of the kidney vortices are generally at lower level and closer to the centerline $Y=0$ for the cases with higher stream wise hole angle. As expected, the center of the jets are at a higher level for $\alpha=50$ deg.

The previously noted thinning of the boundary layer is much stronger for the steeper hole angle α.

Figure 8 shows the center line plots ($Y=0$) for four different flow conditions, all with $\alpha=50$ deg. The color represents the axial velocity component. 20 streamlines are inserted into each plot to give a better representation of the flow path. The streamlines are analyzed in greater detail in Fig. 9. The plots are arranged from top to bottom with increasing *IR*.

Figure 9 shows the penetration of the different jets into the freestream as function of the momentum flux ratio *IR*. A streamline emerges from the center of the cooling hole, assuming that the streamline follows the hole exit angle between $Z=0$ and Z

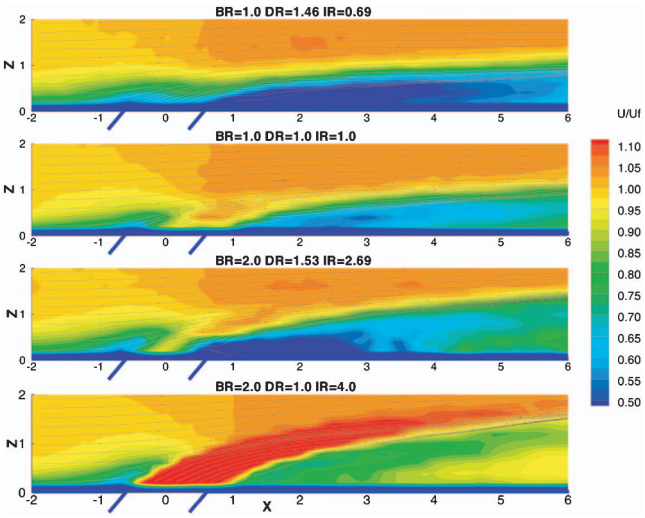

Fig. 8 Influence of *IR* on centerline axial velocity

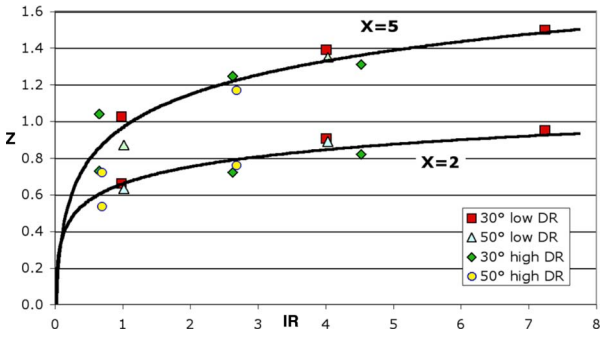

Fig. 9 Penetration of jet into freestream

=0.2. The intersection between that streamline and the two axial positions of interest, $X=2$ and $X=5$ lead to the plot below.

Surprisingly, the hole exit angle has a weak effect on the trajectory, and in some cases the penetration for 30 deg is even higher than for 50 deg. At low *IR* the hole angle has a stronger effect on the trajectory than at high *IR*. In general the data collapses towards a logarithmic trendline. These results might be a function of the streamlines chosen to define the trajectory.

Figures 10 and 11 show plots parallel to the surface *XY* at three different heights from top to bottom. The holes are represented by ellipses of low eccentricity, showing the correct outline. The left column shows the stream wise vorticity ω_x. The right column gives the vorticity normal to the surface ω_z. The third vortical component ω_y is not shown here, as it is comparably insignificant. Vorticity is nondimensionalized with the freestream velocity and the hole diameter in all plots.

Figure 10 shows the low *BR*, *DR*, and *IR* case for $\alpha=50$ deg. We can see the streamwise vorticity ω_x associated with the boundary layer inside the cooling hole "**A**". We also see the trailing limbs of the kidney vortices fed by this vorticity. In Fig. 10, $Z=0.2$, streamwise vorticity, the vortices appear to attenuate rapidly with downstream distance; but this is due to the jet penetrating further into the mainstream flow. In $Z=0.6$, the signal of the kidney vorticity gets stronger "**B**". However, by $Z=1.0$, the vorticity values are much weaker, the jet does not penetrate this far. In Fig. 10 the normal vorticity reveals the dominant shear around the jet, positive on one side and negative on the other. At $Z=0.2$ the

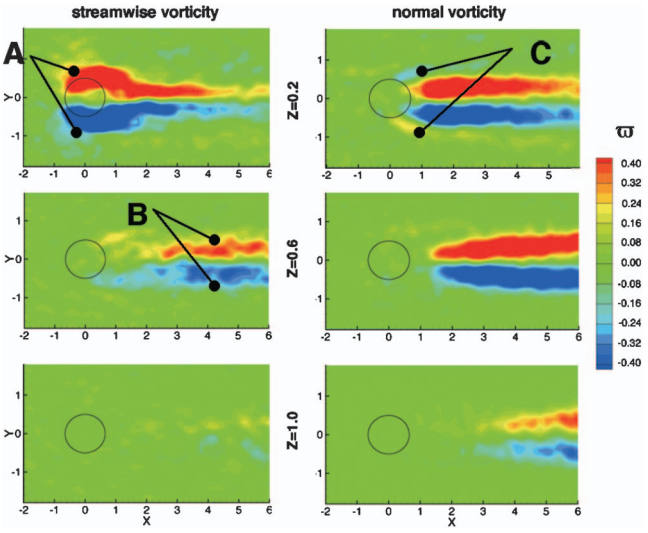

Fig. 10 $\alpha=50$ deg, *BR*=1, *DR*=1, and *IR*=1

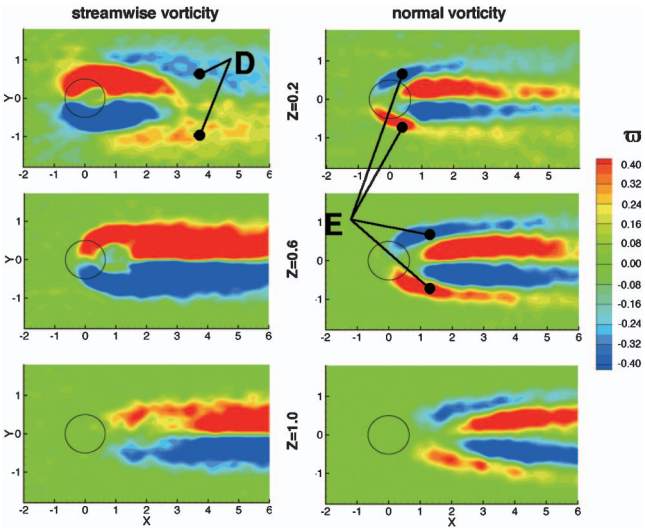

Fig. 11 $\alpha=50$ deg, *BR*=2, *DR*=1, and *IR*=4

normal vorticity shows two weak regions of opposite sign "**C**". It is possible that these are artifacts from the much weaker horseshoe vortex system around the coolant jet.

In Fig. 11 we can see a significant change due to the increase of blowing ratio. Penetration is much stronger and the vorticity is of a significantly greater magnitude. For the streamwise vorticity ω_x, near the wall at $Z=0.2$ evidence of a rather diffuse region of vorticity "**D**" of the reverse sign of the kidney vortices can be seen. This is interpreted as being vorticity due to the horseshoe vortex, which has been transported by unsteady flow structures and is rapidly mixing. At $Z=0.6$ and 1.0 we see the strong kidney vortex pair.

In Fig. 11 the normal vorticity ω_z shows four distinct regions. The central two are associated with the viscous mixing of the jet, as seen in Fig. 10 at lower blowing ratio. The outer two "**E**" are also associated with the mixing of the jet. These appear to attenuate rapidly at all heights through the boundary layer. The reason we see this effect for higher blowing ratio is the higher velocity of the jet than its surrounding.

Figures 12 and 13 each show an isocontour plot, where the iso-surface represents $U/U_f=0.95$. Effectively, the entrainment of high velocity fluid into the center of the jet is represented here. Both figures are based on results from geometry with $\alpha=50$ deg. Figure 12 shows the case with *BR*=1, *DR*=1, and *IR*=1. Figure 13 shows the case with *BR*=2, *DR*=1, and *IR*=4.

Figures 12 and 13 show, very graphically, the change of flow structure as blowing ratio is increased. From inflow to outflow one can see the isosurface drops to get nearer to the wall. This, as was previously suggested, is due to the jets entrainment of the inlet boundary layer. The effect is much stronger at higher blowing

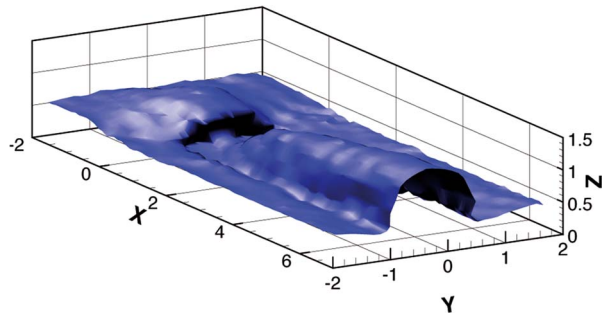

Fig. 12 50 deg, *BR*=1, *DR*=1, and *IR*=1; iso-plane $U/U_f=0.95$

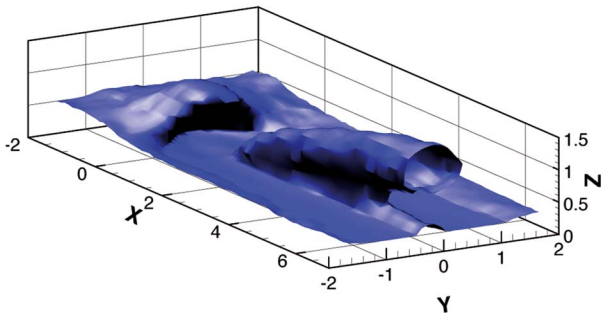

Fig. 13 50 deg, *BR*=2, *DR*=1, and *IR*=4; iso-plane U/U_f=0.95

rate. In front of the hole the isosurface lifts because the pressure rises here due to the blockage of the jet. At the higher blowing rate in Fig. 13 the jet forms a clear "lifted off" free jet above the wall. The distortion of the jet into the kidney shape can also be seen. On the centerline of the jet the isosurface lifts. This will reduce shear and heat transfer in this small region.

Conclusions

3D PIV has been used to study the complex 3D flow field associated with steady film cooling. This study has included a range of parameters: hole angle, blowing ratio, density ratio, and momentum flux ratio. The results revealed the classical phenomena of the formation of the kidney vortex pair and jet lift off at higher momentum flux ratios.

The center line trajectory of the coolant collapses well for momentum flux ratios. The high resolution of the 3D PIV allows visibility of some detailed flow physics. The PIV data shows us that the incoming flat plate boundary layer is thinned by the entrainment of the coolant jets. This effect gets stronger as blowing ratio, density ratio and hole angle are increased. This can be expected to increase mean heat transfer coefficients. The measured vorticity components reveal the expected signature of the kidney vortices and also suggest artefacts from horseshoe vortex activity and unsteady vortex shedding from the sides of the jet. These mechanisms will augment mixing and may reduce the film cooling effectiveness.

We now have a large body of experimental data characterizing steady film cooling to provide empirical input for film cooling modelling. The next steps are unsteady flow measurements and heat transfer measurements of forced unsteady cooling jets, simulating blade row interaction.

Acknowledgment

The authors would like to acknowledge the support of this project by GE Aircraft Engines through their university strategic alliance program. Specifically the technical interaction with André Burdet, Dr. Robert Bergholz, and Dr. Frederick Buck has been very helpful in the formulation of this project. The facility would not have been built without Hans Suter, Thomas Kuenzle, Peter Lehner, and Christoph Raeber.

Nomenclature

X = axial (streamwise) coordinate
Y = lateral coordinate
Z = vertical coordinate
U, V, W = mean velocity components
V^* = velocity magnitude YZ plane $=(V^2+W^2)^{1/2}$
ρ = density
P = static pressure
T = total temperature
d = hole diameter
s = pitch distance between two holes
l = length of the hole pipe
α = streamwise injection angle
DR = density ratio $=\rho_c/\rho_f$
BR = blowing ratio $=\rho_c U_c/\rho_f U_f$
IR = momentum flux ratio $=BR^2/DR$
ω_X = streamwise vorticity $=\partial W/\partial Y-\partial V/\partial Z$
ω_Y = crosswise vorticity $=\partial U/\partial Z-\partial W/\partial X$
ω_Z = normal vorticity $=\partial V/\partial X-\partial U/\partial Y$
ϖ = nondimensional vorticity $=\omega d/U_f$
Tu = turbulence intensity $=U'/U_\infty$
δ^* = displacement thickness $=\int(1-U/U_f)dx$
θ = momentum thickness $=\int U/U_f(1-U/U_f)dx$
H = shape factor $=\delta^*/\theta$

Subscripts

c = coolant fluid
f = freestream fluid

Superscripts

$'$ = instantaneous value
∞ = time-averaged value

References

[1] Burdet, A., and Abhari, R. S., The Modelling of Film Cooling - Part II: Model for Use in 3D CFD, ASME Paper No. GT2005-68780.
[2] Abhari, R. S., 1996, "Impact of Rotor-Stator Interaction on Turbine Blade Film Cooling," J. Turbomach., **118**, pp. 123–133.
[3] Abhari, R. S., and Epstein, A. H., 1994, "An experimental Study of Film Cooling in a Rotating Transonic Turbine," J. Turbomach., **116**, pp. 63–70.
[4] Abhari, R. S., Guenette, G. R., Epstein, A. H., and Giles, M. B., 1992, "Comparison of Time-Resolved Turbine Rotor Blade Heat Transfer Measurements and Numerical Calculations," J. Turbomach., **114**, pp. 818–827.
[5] Dunn, M. G., 1990, "Phase and Time Resolved Measurements of Unsteady Heat Transfer and Pressure in a Full-Stage Rotating Turbine," J. Turbomach., **112**, pp. 531–538.
[6] Eads, T. A., 1992, "Shock Tube Study of the Effects of Large Density Differences and Blowing Ratio on Heat Transfer to a Film-Cooled Flat Plate," MSc, Wright-Patterson AFB, Ohio School of Engineering.
[7] Giang, T. T. L., 1999, "Effects of Unsteady Cooling Flow on Heat Transfer to a Film-Cooled Flat Plate," MSc, The Ohio State University, Columbus.
[8] Guenette, G. R., Epstein, A. H., Giles, M. B., and Haimes, R., 1989, "Fully scale Transonic Turbine Rotor Heat Transfer Measurements," J. Turbomach., **111**, pp. 1–7.
[9] Teekaram, A. J. H., Forth, C. J. P., and Jones, T. V., 1989, "The Use of Foreign Gas to Simulate the Effects of Density Ratios in Film Cooling," ASME J. Turbomach., **111**(1), pp. 57–62.
[10] Goldstein, R. J., and Jin, P., "Film Cooling Downstream of a Row of Discrete Holes with Compound Angle," Proceedings of the ASME Turbo Expo 2000.
[11] Ligrani, P. M., and Bell, C. M., 2001, "Film Cooling Subject to Bulk Flow Pulsations: Effects of Density Ratio, Hole Length-to-Diameter Ratio, and Pulsation Frequency," Int. J. Heat Mass Transfer, **44**(10), pp. 2005–2009.
[12] Ligrani, P. M., Saumweber, C., Schulz, S., and Wittig, S., 2001, "Shock Wave - Film Cooling Interactions in Transonic Flows," ASME J. Turbomach., **123**(4), pp. 788–797.
[13] Pietrzyk, J. R., Bogard, B. G., and Crawford, M. E., 1989, "Experimental Study of the Interaction of Dense Jets With a Crossflow for Gas Turbine Applications," 89-1, Turbulence and Turbine Cooling Research Laboratory, Mechanical Engineering Department, The University of Texas at Austin, Austin, TX.
[14] Cho, H. H., and Goldstein, R. J., 1995, "Heat (Mass) Transfer and Film-Cooling Effectiveness With Injection through Discrete Holes on the Exposed Surface," ASME J. Turbomach., **117**(3), pp. 451–460.
[15] Forth, C. J. P., Loftus, P. J., and Jones, T. V., 1985, "Effect of Density Ratio on the Film-Cooling of a Flat Plate," AGARD Conf. Proc., CP **390**, pp. 113-143.
[16] Popp, O., Smith, D. E., Bubb, J. V., Grabowski, H. C., Diller, T. E., Schetz, J. A., and Ng, W. F., "An Investigation of Heat Transfer in a Film Cooled Transonic Turbine Cascade, Part I: Steady Heat Transfer," Proceedings of the ASME Turbo Expo 2000.
[17] Smith, D. E., Bubb, J. V., Popp, O., Grabowski, H. C., Diller, T. E., Schetz, J. A., and Ng, W. F., "An Investigation of Heat Transfer in a Film Cooled Transonic Turbine Cascade, Part II: Unsteady Heat Transfer," Proceedings of the ASME Turbo Expo 2000.
[18] Dunn, M. G., and Hause, A., 1982, "Measurement of Heat Flux and Pressure in a Turbine Stage," J. Eng. Power, **104**, pp. 215–223.
[19] Goldstein, R. J., Eckert, E. R. G., and Burggraf, F., 1974, "Effects of Hole Geometry and Density on 3-Dimensional Film Cooling," Int. J. Heat Mass Transfer, **17**(5), pp. 595–607.
[20] Bons, J. P., MacArthur, C. D., and Rivir, R. B., 1996, "The Effect of High Freestream Turbulence on Film Cooling Effectiveness," ASME J. Turbomach., **118**(4), pp. 814–825.

[21] Gogineni, S., Goss, L., Pestian, D., and Rivir, R., 1998, "Two-Colour Digital PIV Employing a Single CCD Camera," Exp. Fluids, **25**(4), pp. 320–328.
[22] Rockwell, R. K., 1989, "Transient Heat Transfer Measurements on a Flat Plate in Turbulent Flow Using an Electrical Analog," MSc, Air Force Institute of Technology, Wright-Patterson Air Force Base, OH.
[23] Ekkad, S. V., Zapata, D., and Han, J. C., 1997, "Heat Transfer Coefficients Over a Flat Surface With Air and CO2 Injection Through Compound Angle Holes Using a Transient Liquid Crystal Image Method," ASME J. Turbomach., **119**(3), pp. 580–586.
[24] Honami, S., Shizawa, T., and Uchiyama, A., 1994, "Behaviour of the Laterally Injected Jet in Film-Cooling - Measurements of Surface-Temperature and Velocity / Temperature Field Within the Jet," ASME J. Turbomach., **116**(1), pp. 106–112.
[25] Epstein, A. H., Guenette, G. R., Norton, R. J. G., and Yuzhang, C., 1986, "High Frequency Response Heat Flux Gauge for Metal Blading," Rev. Sci. Instrum., **57**(4), pp. 639–649.
[26] Goldstein, R. J., and Cho, H. H., 1995, "A Review of Mass-Transfer Measurements Using Naphthalene Sublimation," Exp. Therm. Fluid Sci., **10**(4), pp. 416–434.
[27] Le Grivèe, E., 1978, "Mixing Process Induced by the Vorticity Associated With the Penetration of a Jet Into a Cross Flow," J. Eng. Power, **100**.
[28] 2002, "Flow Manager Software and Introduction to PIV Instrumentation," Dantec Dynamics A/S.

The Influence of Turbulence on Wake Dispersion and Blade Row Interaction in an Axial Compressor

Alan D. Henderson
e-mail: Alan.Henderson@utas.edu.au

Gregory J. Walker
e-mail: greg.walker@utas.edu.au

School of Engineering,
University of Tasmania,
Hobart 7001, Australia

Jeremy D. Hughes
Rolls-Royce plc,
Derby DE24 8BJ, UK
e-mail: jeremy.hughes@rolls-royce.com

The influence of free-stream turbulence on wake dispersion and boundary layer transition processes has been studied in a 1.5-stage axial compressor. An inlet grid was used to produce turbulence characteristics typical of an embedded stage in a multistage machine. The grid turbulence strongly enhanced the dispersion of inlet guide vane (IGV) wakes. This modified the interaction of IGV and rotor wakes, leading to a significant decrease in periodic unsteadiness experienced by the downstream stator. These observations have important implications for the prediction of clocking effects in multistage machines. Boundary layer transition characteristics on the outlet stator were studied with a surface hot-film array. Observations with grid turbulence were compared with those for the natural low turbulence inflow to the machine. The transition behavior under low turbulence inflow conditions with the stator blade element immersed in the dispersed IGV wakes closely resembled the behavior with elevated grid turbulence. It is concluded that with appropriate alignment, the blade element behavior in a 1.5-stage axial machine can reliably indicate the blade element behavior of an embedded row in a multistage machine. [DOI: 10.1115/1.2098809]

Introduction

The high level of turbulence and unsteadiness inside multistage axial compressors strongly influences the boundary layer transition from laminar to turbulent flow on blade surfaces. This is important as boundary layer behavior influences both individual blade performance and overall compressor performance. The subject of transitional flow in turbomachinery has attracted a large amount of research attention, and is well summarized in the reviews of Mayle [1] and Walker [2].

The unsteadiness experienced by an embedded blade row in an axial machine is partly due to unsteady pressure fields arising from the relative motion of adjacent upstream and downstream rows. Pressure fluctuations can also arise from moving shock waves in high speed machines. The embedded blade also experiences vortical disturbances produced by the relative motion of wakes convected from blade rows further upstream. The latter disturbances are modified by the process of wake dispersion in which wakes from one row are chopped and rotated in passing through the row immediately downstream.

The wake dispersion process causes pitchwise-periodic variations in time-mean flow, periodic disturbance level and random turbulent fluctuations. With identical blade numbers in rotor or stator row pairs of neighboring stages, altering their relative circumferential alignment can then produce variations in performance of the downstream row. This process, called "indexing" or "clocking," has been suggested as a method of improving axial turbomachine efficiency and influencing noise generation.

Blade wake dispersion and clocking effects in a 1.5-stage axial compressor were extensively studied by Walker et al. [3,4]. They found that IGV clocking significantly influenced the extent and nature of boundary layer transition on the downstream stator. They also found that the amplitude of periodic fluctuations in stator losses was greatly changed, although the time mean loss values varied by only a small amount. More recently Mailach and Vogeler [5] measured unsteady pressure distribution on rotor and stator blades in a low-speed four stage axial compressor. They found that unsteady pressure profiles were nearly independent of the convected wake through the passage; this was partially due to the low Mach number of the research compressor. The position of the upstream wakes significantly influenced the magnitude of the unsteady pressure fluctuations.

Other recent work on clocking effects has focused on axial turbines. Hummel [6] measured significant changes in shock strength with clocking inside a transonic turbine. Tiedemann and Kost [7] found that impinging nozzle guide vane wakes on the downstream stator resulted in decreased periodic fluctuations and variation in stator incidence. These investigations, and also those of Reinmöller et al. [8], Haldeman et al. [9], and Jouini et al. [10], suggest that some efficiency improvements are achievable from clocking; but the complexity of the flow phenomena involved makes it difficult to draw general conclusions.

The process of wake dispersion and interaction in turbines differs significantly from that in compressors. The higher loading of turbine blades causes the chopped upstream wake segments to undergo increased rotation and distortion as seen in Stieger and Hodson [11]. This results in greater spreading of wake fluid over the turbine blade surface, and greater dispersion at the outflow. The other fundamental difference is in the direction of the relative jet associated with upstream wakes. In turbines, the convection of wake fluid relative to the local freestream (or "wake jet") pushes fluid towards the suction surface of downstream blades; in compressors, the wake jet is away from the suction surface.

Low-speed single-stage research compressors are commonly used for making detailed studies of many flow phenomena. Their simple construction and low cost make them particularly useful for the detailed and sensitive flow measurements required in evaluating design concepts or validating computational fluid dynamics (CFD) codes. Wisler et al. [12] give numerous examples of how cost-effective low-speed testing has aided the design of axial turbines and compressors. Although the flow is very differ-

Contributed by the International Gas Turbine Institute (IGTI) of THE AMERICAN SOCIETY OF MECHANICAL ENGINEERS for publication in the ASME JOURNAL OF TURBOMACHINERY. Paper presented at the ASME Turbo Expo 2005: Land, Sea, and Air, Reno, NV, June 6–9, 2005, Paper No. GT2005-68432. Manuscript received by IGTI, October 1, 2004; final revision February 1, 2005. IGTI Review Chair: K. C. Hall.

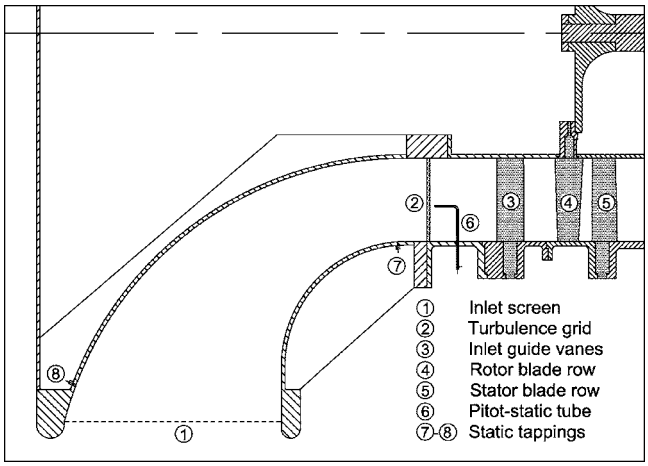

Fig. 1 University of Tasmania research compressor facility

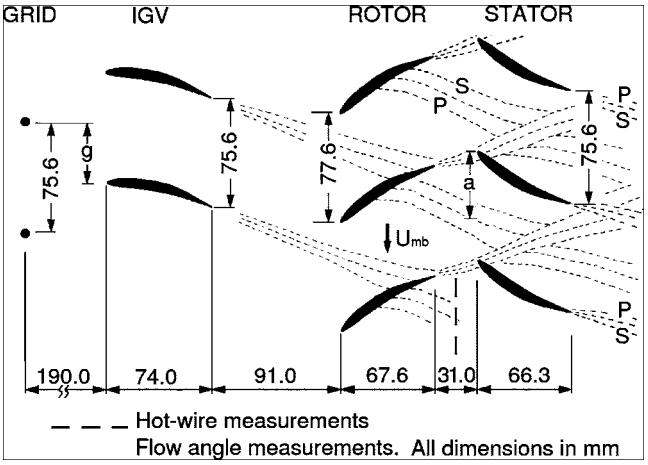

Fig. 2 Cross section of the research compressor showing the mid-passage turbulence grid and blade row configuration and a typical instantaneous wake dispersion pattern: *S*=suction surface, *P*=pressure surface

ent from multistage compressors, most basic flow phenomena are similar in nature. It is possible to make the flow inside single-stage compressors more representative of multistage machines, as demonstrated by Place et al. [13]. They modified a single-stage axial compressor by installing a turbulence generating grid to raise the level of background turbulence, fitting teeth to the upstream hub and casing to thicken wall boundary layers, and installing a screen downstream of the stator to simulate the potential field resulting from downstream rows. Of these changes, raising the background turbulence level would most greatly influence the boundary layer transition on the blades of an embedded row.

The current research investigates how increased free-stream turbulence level influences wake dispersion and clocking effects in a 1.5-stage axial compressor. Measurements taken with the original low-turbulence inflow configuration are compared to those at high turbulence, the latter achieved using a turbulence grid. Surface hot-film measurements on an outlet stator blade indicate how the boundary layer transition behavior is altered. Significant conclusions are drawn about the influence of free-stream turbulence on wake dispersion and interaction processes, and the ability of 1.5-stage machines to simulate the performance of an embedded blade row in a multistage machine.

Experimental Detail

Research Compressor. Air enters the compressor radially through a cylindrical inlet 2.13 m in diameter and 0.61 m wide. The flow then passes through a 6.25:1 contraction, where it turned 90 deg to the axial direction. The compressor has three blade rows: Inlet guide vanes (IGV), rotor, and stator as shown in Figs. 1 and 2. The stationary blade rows both have 38 blades and the rotor has 37 blades, giving space/chord ratios of 0.99 and 1.02, respectively. The blade profiles were based on a British C4 section with a constant chord length of 76.2 mm and an aspect ratio of 3.0. The blade profiles were stacked about a radial axis to achieve free-vortex flow and 50% reaction at mid-span position at design flow conditions.

The test section annulus is constant in area with hub and casing diameters of 0.69 and 1.14 m, respectively. The flow passes through an annular diffuser before discharging through a cylindrical throttle at exit. The throttle can be automatically adjusted to achieve the desired flow coefficient. The rotor is directly coupled to a 30 kW DC motor via a long shaft. The speed is controlled by an analogue feedback loop with a computer controlled reference voltage. The speed control for a fixed set point was within ±0.2 rpm.

Instruments are inserted into the test section through an axial slot in the casing wall. A probe traversing rig allows accurate positioning in axial and radial directions. The IGV and stator blade rows are held in movable rings which allow circumferential traversing over 2 blade pitches via stepper drives. This enables the stationary blade rows to be aligned circumferentially (clocked) relative to each other and the fixed turbulence grid as indicated by the variables (a) and (g) shown in Fig. 2. It also permits relative circumferential traverses to be conducted with circumferentially fixed probes.

The background turbulence level of the research compressor was raised using a turbulence generating grid similar to that of Place et al. [13], who mainly focused on measuring machine performance and turbulence characteristics. The turbulence grid was installed immediately downstream of the inlet contraction to allow mixing of rod wakes prior to the compressor stage. The grid consisted of 38 radial rods, each spanning between rings fixed to the hub and casing. The number of rods was made equal to the number of blades in the stationary rows so that every blade in a stationary row would experience the same disturbance field. Measurements (not presented here) showed that the rod wakes had not quite mixed at the IGV row. For that reason the IGV was aligned with the grid to achieve the most uniform stator inlet flow. This corresponded to placing the IGV row in the minimum grid turbulence location ($g/S=0.5$). The rod diameter of 7.94 mm was chosen to achieve 4% turbulence intensity at inlet to the stator row, which is typical of the background turbulence intensity in multistage axial compressors. The pressure loss of the grid was sufficiently small to allow the same set of test flow coefficients as in the no-grid case. The calculated turbulence intensity was based on data for grids and screens given by Roach [14] with decay computed along the time-mean flow path from the grid to stator inlet at mid-span.

Scope of Investigation. Data were obtained for three compressor flow coefficients ($\phi=V_a/U_{mb}$): 0.600, 0.675, and 0.840. These corresponded to high, medium, and low load cases as detailed in Table 1. Compressor load was controlled by adjusting the variable

Table 1 Measured stator inlet incidences for low and high turbulence cases

Loading	ϕ (V_a/U_{mb})	Re_1	i (Low Tu)	i (High Tu)
High	0.600	110000	2.9 deg	3.0 deg
Medium	0.675	117000	−0.4 deg	0.1 deg
Low	0.840	130000	−6.9 deg	−7.3 deg

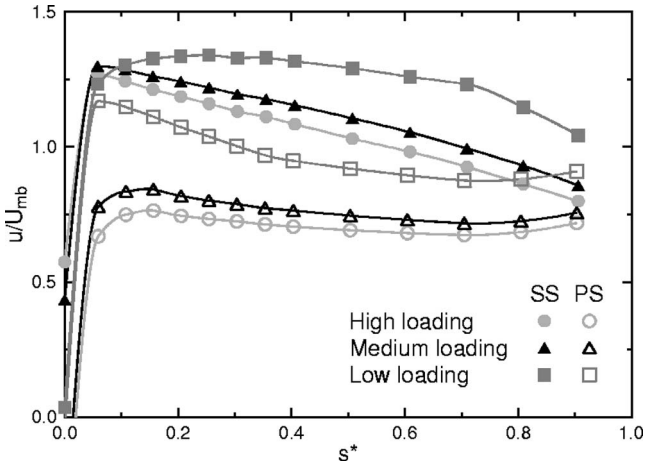

Fig. 3 Measured stator blade surface velocity distribution for the the three load cases without turbulence grid (from Walker et al. [4]): *SS*=suction surface; *PS*=pressure surface

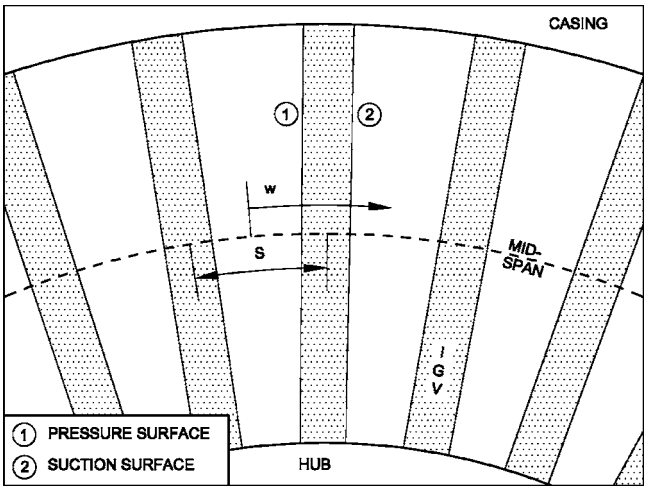

Fig. 4 View looking upstream showing path of probe traverse relative to inlet guide vanes. The origin for circumferential position (*w*) is arbitrary.

throttle until the desired flow coefficient was achieved. These three load cases, used in the previous investigations of Walker et al. [3,4], correspond to near stall (high load), design (medium load), and maximum flow (low load). Measurements were obtained before and after installation of the turbulence generating grid to allow direct comparison for these cases. All measurements were performed at mid-span position at a constant Reynolds number (Re_{ref}=120,000), which corresponds to a rotor speed of approximately 500 rpm in normal laboratory conditions. The stator inlet Reynolds number (Re_1) for each compressor varies with the flow coefficient as shown in Table 1.

In earlier studies [3,4] prior to installation of the turbulence grid, the mean axial velocity at inlet (V_a) was measured by a pitot-static tube located upstream from the test section. As the close proximity of the grid would have interfered with this reference, an alternative method was required. This was achieved by installing static ring tappings on the compressor inlet contraction, indicated by (7) and (8) in Fig. 1. The contraction pressure differential was calibrated against the existing reference prior to installation of the grid. This ensured that the flow coefficient in each test case would remain the same after the turbulence grid was installed.

The surface pressure distributions for the three load cases prior to installation of the turbulence grid are shown in Fig. 3 (from Walker et al. [4]). These were obtained from static pressure tappings on the stator surface. The high and medium load cases show that peak suction velocity occurs within 5% chord from the leading edge, followed by a near linear deceleration over the remaining surface. The low load case shows a more gradual acceleration to a plateau at 30% chord. A slight discontinuity at 70% chord indicates the presence of a separation bubble. Further description of these distributions is given in Walker et al. [4].

It should also be noted that these surface pressure distributions were made with a larger rotor-stator axial gap (80.7 mm). However, the suction surface velocities were re-measured with the smaller axial gap used in the present investigation (31.0 mm), and only minor differences were noted.

Measurement Techniques. Measurements of the stator inlet flow field were performed in the axial gap between the rotor and stator blade rows using a single wire Dantec 55P05 probe with sensor aligned in the radial direction. The circumferential traverses were completed by changing the relative positions of the IGV and probe over one blade pitch as illustrated in Fig. 4. The results for the low turbulence case were obtained by moving the IGV row relative to a fixed probe position. However in the high turbulence case, the IGV was fixed to avoid the slight clocking effect between the grid and the IGV, as noted earlier. In this case the probe was fixed between two stator blades using a mounting bracket spanning between the trailing edges of two neighboring blades, and the stator row and probe clocked over one blade pitch. The hot-wire probe traverses were performed in 32 circumferential steps across one blade passage.

One stator blade was instrumented with an array of 61 hot-film sensors positioned at mid-span as detailed in the previous investigations of Walker et al. [4]. Not all sensors were used in each test case.

Both the hot-wire and hot-film instruments were operated using TSI IFA100 constant temperature anemometers. In each test the offset and gain settings were optimized to maximize the signal range for input to the data acquisition card. The frequency response were estimated from square wave tests to be greater than 70 and 30 kHz, respectively. All signals were low pass filtered at 20 kHz. The data sampling rate was 50 kHz to avoid aliasing of the signal.

All data were acquired by computer using an United Electronic Industries WIN30DS simultaneous sample and hold card. The sampling process was triggered once per revolution by a pulse from an encoder attached to the rotor shaft. Each data set consisted of 512 data traces, each containing 1024 samples. An individual trace corresponded to approximately 6 rotor blade passing periods.

The hot-wire probe was calibrated using an in situ method developed by Solomon [15]. In this method a local velocity coefficient u/U_{mb} was measured with a pre-calibrated three hole probe over a range of rotor speeds. A direct calibration was made by replacing the three hole probe with the hot-wire probe and repeating the process. Solomon [15] also investigated calibrating the probe in a different wind tunnel and then re-assembling it in the compressor for measurement. However, this was found to introduce large errors caused by changes in lead contact resistances. The in situ method eliminated this requirement and was found to be fast and repeatable.

Data Processing Techniques

Unsteady Flow Field. The hot-wire traces were processed using the ensemble-averaging technique detailed in Evans [16]. Walker et al. [3,4] later adapted and refined this method in their research. A brief summary of their method follows.

Instantaneous velocity is commonly expressed in terms of a time-mean $\bar{u}$ and associated fluctuating component u'. The flow

under examination has strong periodic events and can also be defined in terms of an ensemble-averaged velocity $\langle u \rangle$ and fluctuating component u''. This may be expressed as

$$u = \bar{u} + u' = \langle u \rangle + u'' \tag{1}$$

The ensemble-averaged velocity field observed by a stationary probe downstream of the rotor is circumferentially periodic with a wavelength equal to the IGV pitch. It retains this periodicity through the stator due to the equal numbers of IGV and stator blades. The periodic disturbance level or "unsteadiness" must be evaluated over an integral number of blade-passing periods. This is expressed by

$$\tilde{T}u = (\langle u \rangle - \bar{u})_{\text{rms}}/U \tag{2}$$

The random unsteadiness or turbulence level is given by

$$Tu = u''_{\text{rms}}/U \tag{3}$$

The total disturbance level is given by

$$Tu_D = u'_{\text{rms}}/U \tag{4}$$

Assuming the periodic and random turbulence levels are statistically independent they may be related by

$$Tu_D^2 = \tilde{T}u^2 + Tu^2 \tag{5}$$

Stator Blade Intermittency. Measurements from the array of hot-film sensors were processed to calculate the quasi-shear stress, defined as

$$\tau_q = \left(\frac{E^2 - E_o^2}{E_o^2} \right)^3 \tag{6}$$

which is known to be proportional to the wall shear stress τ_w. This technique was originally developed by Hodson et al. [17], and was used in the extensive investigations of Halstead et al. [18,19]. The data were further processed to determine the turbulent intermittency γ using a method described in Solomon [15]. This method uses a hybrid probability distribution function combined with a peak valley counting algorithm. Intermittency records from individual traces were finally combined to evaluate the temporal variation of ensemble average intermittency $\langle \gamma \rangle$. Walker et al. [4] presented results of both ensemble-averaged quasi-shear stress and ensemble-averaged intermittency, and found the latter provided a more useful description of the state of the boundary layer.

Integral Length Scale. The length scale of free-stream turbulence is known to influence the boundary layer transition process, as discussed by Mayle [1]. Camp and Shin [20] present a method for calculating the integral length scale from single hot-wire traces in an axial turbomachine. The method was slightly adapted by Hughes [21] to allow longer traces to be constructed by joining together shorter traces. A power spectrum analysis of an individual trace will show large spikes at frequencies corresponding to the rotor blade passing frequency and the associated harmonics. These spikes represent periodic events, which lead to oscillations in the autocorrelation function. The spikes are removed from the power spectrum, the signal reconstructed, and then autocorrelated. The integral length scale is given by

$$\Lambda = \bar{u} \int_0^\infty \text{ACF}(\tau) d(\tau) \tag{7}$$

where $\text{ACF}(\tau)$ is the autocorrelation function of the signal $u(t)$ for a given phase shift τ. In practice, the upper limit of integration is usually taken as the first zero of the autocorrelation function.

Observations and Discussion

Stator Inlet Flow Angle. A United Sensor CA120 cobra type three-hole probe was used to measure the stator inlet flow angle at mid-span position. The flow angle was measured at 32 circumferential positions over a blade pitch and then averaged. The stator incidence i shown in Table 1 is the flow angle relative to the design blade inlet angle. The results show that incidence changes between the low and high turbulence cases were no greater than 0.5 deg. Small changes are not unexpected, considering the increased turbulence level may have altered the IGV and rotor deviations, and the grid may have slightly altered the annulus wall boundary layer development and axial velocity profiles.

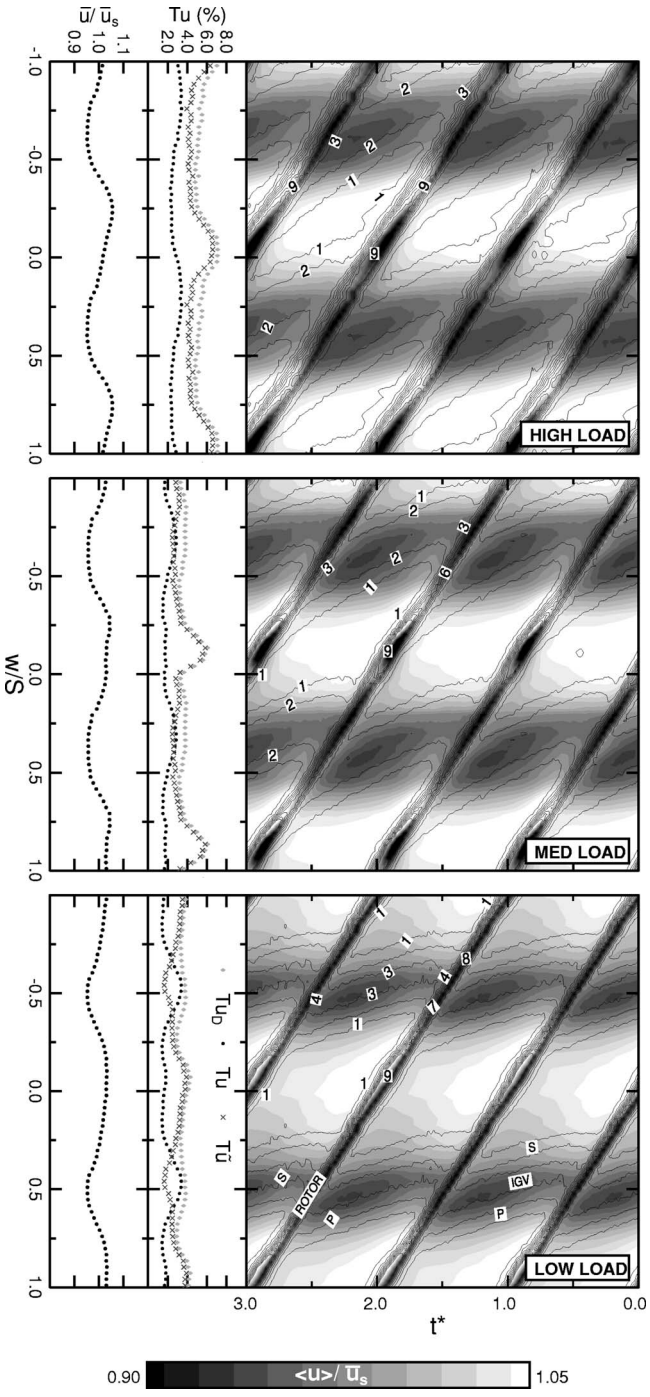

Fig. 5 Stator inlet flow field for low turbulence case (without grid). The line contours show ensemble-averaged disturbance level $\langle Tu \rangle$ in 1% intervals. The color contours show ensemble-averaged velocity $\langle u \rangle / \bar{u}_s$.

Stator Inlet Flow Field. Figures 5 and 6 show the processed

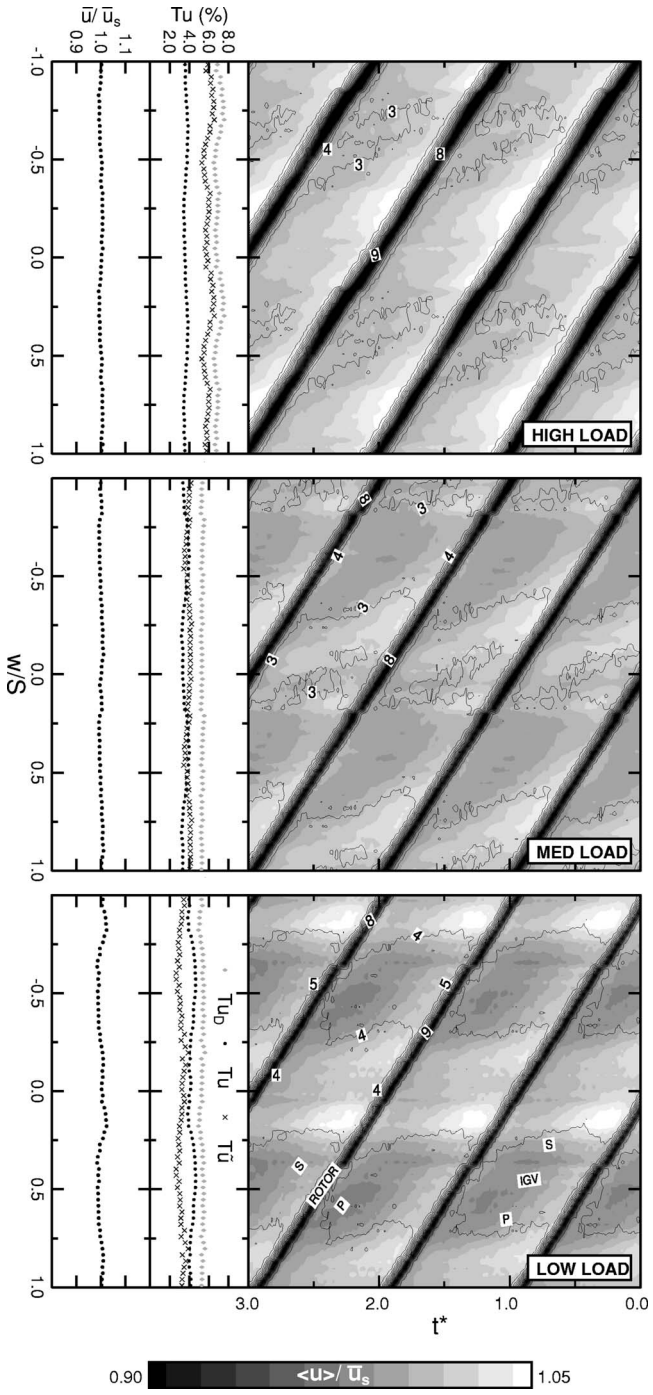

Fig. 6 Stator inlet flow field for high turbulence case (with grid). The line contours show ensemble-averaged disturbance level $\langle Tu \rangle$ in 1% intervals. The color contours show ensemble-averaged velocity $\langle u \rangle / \bar{u}_s$.

hot-wire results at inlet to the stator row for the three load cases at both high and low turbulence. The results have been replotted over a second passage by assuming the flow to be periodic in the pitchwise direction. Each plot represents the instantaneous view of the unsteady flow field on a cylindrical surface at mid-span radius, that would result from the flow being convected unaltered from the measuring station with zero whirl. The horizontal axis shows time nondimensionalized by rotor passing period ($t^* = t/T$). This convention shows the earliest measurements on the right ($t^* = 0$).

Table 2 Turbulence properties for the high turbulence case

Loading	ϕ (V_a/U_{mb})	Tu_D (%)	Tu (%)	Λ/c (%)
High	0.600	6.9	3.6	5.4
Medium	0.675	5.3	3.6	6.4
Low	0.840	5.3	4.2	8.3

The rotor wakes are clearly defined by bands of high turbulence level running diagonally across the plots. These are diagonal due to the changing probe position relative to the fixed rotor position where triggering starts. The rotor wakes increase in thickness as compressor loading is increased. The IGV wakes are shown by the horizontal segments with slightly higher than average turbulence level in the passage. This contrasts with the dispersion pattern shown in Fig. 2 because the whirl component of velocity has not been included. The IGV wake segments resulting from rotor blade chopping are increasingly rotated as the rotor blade loading increases. The IGV wakes are hardly visible in the high turbulence case, indicating that the elevated free-stream turbulence has accelerated their mixing out.

The line graphs on the left hand side of Figs. 5 and 6 show time-mean values of turbulence intensity components and velocity against circumferential position. Apparent turbulence level Tu_D is shown together with the periodic component $\tilde{T}u$ and random component Tu. Large levels of periodic unsteadiness are observed in low turbulence case, with periodic accumulations of low energy rotor wake fluid on the suction side of the IGV wake street; this is indicated by increased apparent and periodic turbulence levels. The positions of the IGV wakes correspond to elevated random turbulence and minimum velocity. The circumferential distribution of all parameters is essentially uniform in the high turbulence cases, with the random disturbance level approximating that within the IGV wake street in the low turbulence cases.

Stator Inlet Turbulence Properties. Circumferential averaged turbulence properties at the stator inlet for the high turbulence case are presented in Table 2. Turbulence intensity is observed to be a strong function of blade loading, as found by Camp and Shin [20]. Increased loading results in thicker rotor wakes and higher total disturbance level.

The integral length scale at the stator inlet will be influenced by four main sources of turbulence: inlet disturbances, grid turbulence, and the IGV and rotor blade wakes. Fluctuations in the velocity signal due to random turbulence in the rotor wake will still be present, even though the periodic fluctuations were removed. Turbulence from the rotor wakes should have an integral length scale of approximately 2% chord, as measured by Camp and Shin [20]. As the integral length scale increases with distance from the source of turbulence (Roach [14]), the turbulence from the grid and IGV blade wakes should have significantly larger integral length scales than the rotor wakes. The rotor wake fluid periodically crosses the measurement point and lowers the time-mean integral length scale.

The grid elements and IGV blades, being circumferentially fixed, will cause circumferential variations in integral length scale relative to the stator blades as shown for the low load case in Fig. 7. Similar pitchwise variations at low loading were observed by Camp and Shin [20]. The integral length scale for the other load cases in the present investigation (not shown) had significantly less pitchwise variation.

The trend of integral length scale increasing with flow coefficient indicated in Table 2, is opposite to that observed by Camp and Shin [20]. It is thought that lower rotor loading in the present study reduced the IGV wake dispersion, and produced more extensive regions of flow with larger integral length scale from the

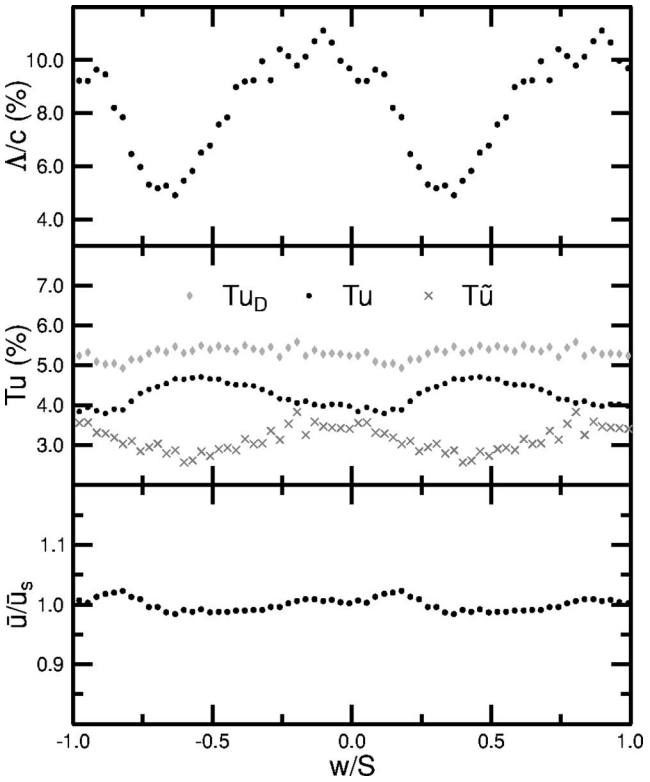

Fig. 7 Circumferential variation of turbulence properties at stator inlet for low loading (high turbulence case)

inlet or turbulence grid. Conversely, higher rotor loading spreads the IGV wakes over a larger pitchwise distance, contributing to a smaller average length scale.

Stator Blade Surface Intermittency Distribution. The processed results of ensemble-average turbulent intermittency on the stator blade are presented in Figs. 8–10. Each figure shows three contour plots at a particular compressor load. The data are displayed in the conventional *s-t* diagram format. The horizontal axis denotes dimensionless surface distance (s^*) and the vertical axis indicates dimensionless time (t^*).

Clocking Effects at Low Turbulence. The top two plots in each figure show the effect of clocking on the stator surface intermittency distribution for the low free-stream turbulence case without the grid (from measurements of Hughes [21]). The high and medium loading cases show wake-induced turbulent strips on both suction and pressure surfaces starting near the leading edge and extending downstream. These strips are immediately followed by regions of calmed flow, which are most clearly observable on the suction surface. Transition between these regions occurs further along each surface. These general features are consistent with those described in Halstead et al. [18,19]. Similar measurements made with the larger axial gap, previously mentioned, are presented and discussed in Walker et al. [4].

Clocking the IGV blade row has a strong influence on the transition between the wake-induced strips. In the high and medium load cases, aligning the IGV wake on the stator blade row ($a/S=0.0$) results in the suction surface transition moving closer toward the leading edge due to the effects of the IGV wake turbulence. With the IGV wakes in the stator passage ($a/S=0.5$), however, the stator blade element is exposed to pockets of low free-stream turbulence level (less than 1%) from the inlet, and transition onset between the wake-induced strips is considerably delayed.

Suction surface transition is least influenced by clocking for the low load case. Here transition occurs through a rearward separation bubble and is not significantly altered by the free-stream turbulence level. However, the pressure surface transition is strongly influence by clocking due to the presence of a leading edge separation bubble. The separation is largely suppressed by the effects of high free-stream turbulence when the stator blade is immersed in the IGV wake street ($a/S=0.0$). In this case there is nearly steady transition at the leading edge. With the IGV wakes in the stator passage ($a/S=0.5$), the later transition in the leading edge bubble allows the development of wake induced transition strips followed by marked calming effects.

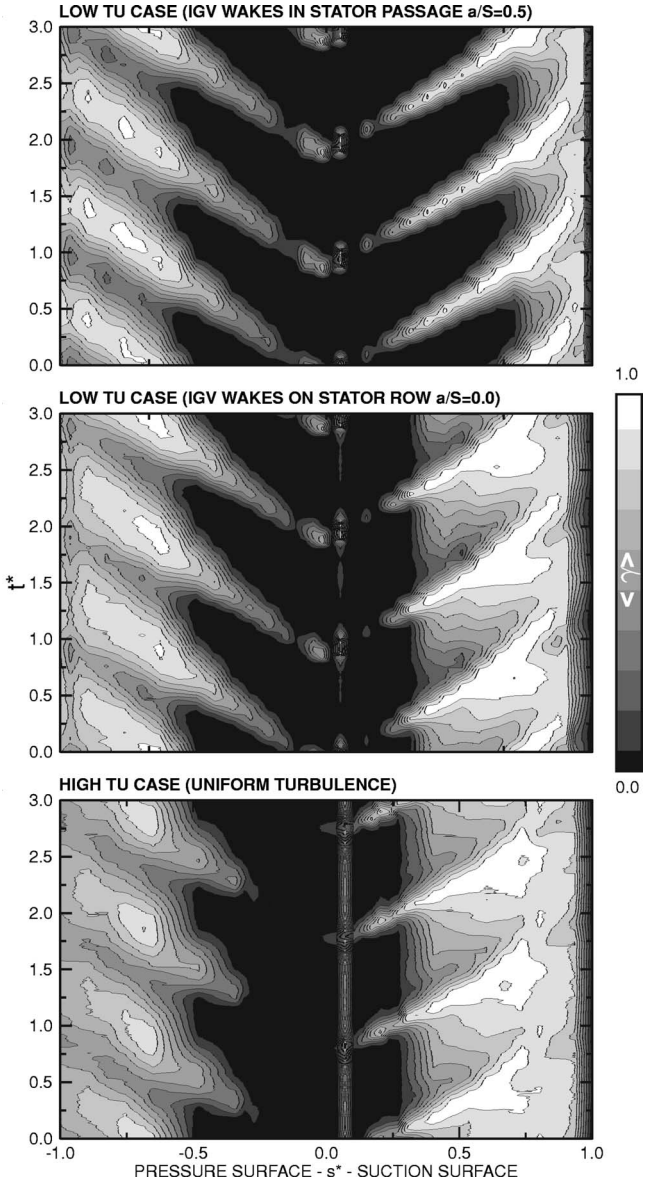

Fig. 8 Stator surface intermittency for high load cases

The intermittency detected at the leading edge of some test cases could be due to genuine turbulent flow, which then decays naturally. Alternately, it may be a false indication of turbulent flow due to the rotor wake fluid interacting with the thin shear layer or to unsteady flow associated with wake chopping. It is unlikely leading edge separation occurs in the medium and high load cases due to the smooth leading edge curvature.

Effect of Increased Turbulence. The bottom plot on each figure shows the intermittency distribution at high turbulence with the grid installed. Although the turbulence profile at inlet was more

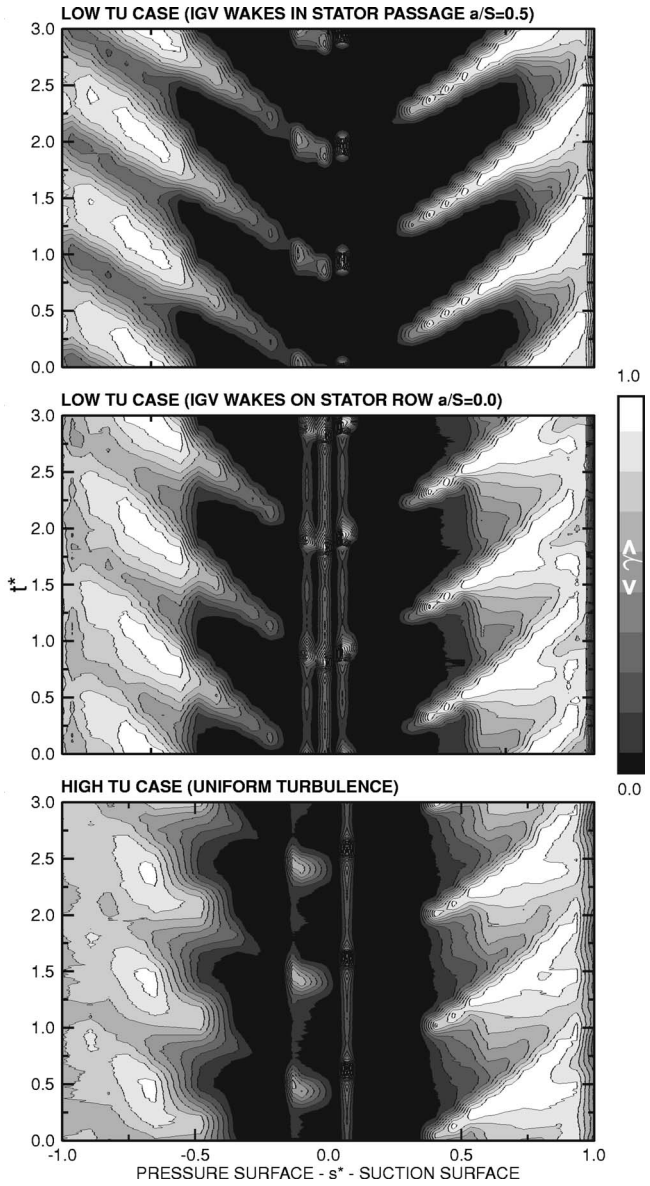

Fig. 9 Stator surface intermittency for medium load cases

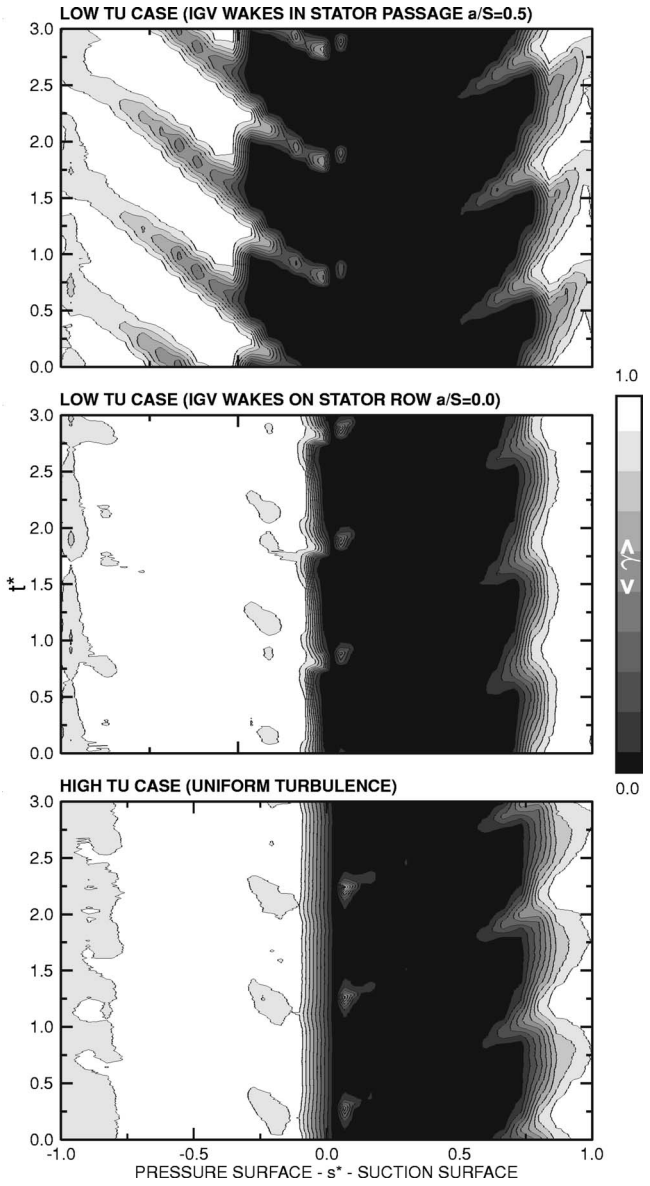

Fig. 10 Stator surface intermittency for low load cases

uniform, as shown in the previous section, the IGV wake street was deliberately placed in the stator passage ($a/S=0.5$) to ensure that the stator row was exposed to turbulence generated from the grid, rather than from IGV wake street.

The general features of the intermittency distributions for each load case closely resemble the low turbulence no-grid case with the IGV wake street on the stator row ($a/S=0.0$). At medium and high loads the suction surface transition between the rotor wake-induced turbulence strips moves closer toward the leading edge. The regions of calmed flow following the turbulence strip are also more sharply defined. The differences in intermittency distributions due to the grid installation are considered primarily due to the altered free-stream turbulence properties, as the associated incidence changes were relatively small (see Table 1). Other minor differences, particularly near the leading edge on the pressure surface, are attributed to a different selection of hot-film sensors used in each investigation.

Concluding Discussion

The use of single-stage axial machines in simulating the behavior of an embedded blade row in a multistage axial turbomachine has previously been questioned in the literature due to the lack of a uniform high turbulence environment. The present study has compared the transitional behavior on the outlet stator of 1.5-stage axial compressor under the natural low turbulence inflow conditions with that under artificially generated high turbulence conditions characteristic of multistage operation. The blade element behavior under the uniform high turbulence conditions differed insignificantly from that of the low turbulence inflow case where the blade element was immersed in the IGV wake street. It is concluded that a 1.5-stage machine can be used in this manner to simulate the transitional flow behavior on an embedded blade row without artificially increasing the inlet turbulence.

The turbulence grid was shown to significantly influence the wake dispersion and the IGV wake/rotor wake interaction processes in the present study. The IGV wake fluid was more widely diffused by the grid turbulence resulting in reduced values of IGV wake velocity defect. The unsteadiness seen by the downstream stator row was greatly reduced because of the smaller accumulation of low energy rotor wake fluid on the suction surface of the IGV wake street. These observations have significant implications for the modeling of clocking effects in multistage axial machines.

In particular, the modeling of wake dispersion from blade rows further upstream must take due account of free-stream turbulence effects on wake diffusion in order to obtain reliable predictions of performance changes and unsteadiness variations due to blade row clocking.

Acknowledgment

The financial support of Rolls-Royce plc is gratefully acknowledged.

Nomenclature

- a = circumferential distance of stator blade leading edge from center of IGV wake street at mid-span
- c = blade chord
- g = circumferential distance of IGV blade leading edge from center of grid wake street at mid-span
- i = blade incidence
- s = surface distance
- s^* = dimensionless surface distance $= s/s_{\max}$
- $s_{\max}$ = surface distance from leading edge to trailing edge
- t = time
- t^* = dimensionless time $= t/T$
- u = streamwise velocity
- w = circumferential distance
- E = anemometer output voltage
- E_0 = anemometer output voltage at zero flow
- Re = compressor inlet Reynolds Number $= V_a.c/\nu$
- $\mathrm{Re}_{\mathrm{ref}}$ = reference Reynolds Number $= U_{mb}.c/\nu$
- Re_1 = stator inlet Reynolds Number $= V_1.c/\nu$
- S = blade pitch
- T = rotor passing period
- Tu_D = total disturbance level
- $\tilde{T}u$ = periodic disturbance level
- Tu = random disturbance level (turbulence)
- U = local free-stream velocity
- U_{mb} = mid-span rotor blade speed
- V_a = mean axial velocity at compressor inlet
- V_1 = velocity at stator inlet
- γ = turbulent intermittency
- Λ = integral length scale
- ν = kinematic viscosity
- ϕ = flow coefficient $= V_a/U_{mb}$
- τ_q = quasi-wall shear stress
- τ_w = wall shear stress

Superscripts and Subscripts

- $\langle\ \rangle$ = ensemble (phase lock) average
- s = pitchwise average
- $-$ = time mean
- $'$ = instantaneous fluctuation from time-mean
- $''$ = instantaneous fluctuation from ensemble mean

References

[1] Mayle, R. E., 1991, "The Role of Laminar-Turbulent Transition in Gas Turbine Engines," ASME J. Turbomach., **113**, pp. 509–537.

[2] Walker, G. J., 1993, "The Role of Laminar-Turbulent Transition in Gas Turbine Engines—A Discussion," ASME J. Turbomach., **117**, pp. 207–217.

[3] Walker, G. J., Hughes, J. D., Köhler, I., and Solomon, W. J., 1998, "The Influence of Wake-Wake Interactions on Loss Fluctuations of a Downstream Axial Compressor Blade Row," ASME J. Turbomach., **120**, pp. 695–704.

[4] Walker, G. J., Hughes, J. D., and Solomon, W. J., 1999, "Periodic Transition on an Axial Compressor Stator—Incidence and Clocking Effects. Part I—Experimental Data, Part II—Transition Onset Predictions," ASME J. Turbomach., **121**, pp. 398–415.

[5] Mailach, R., and Vogeler, K., 2004, "Rotor-Stator Interactions in a Four-Stage Low Speed Axial Compressor—Part 1: Unsteady Profile Pressures and the Effect of Clocking," ASME Paper GT2004-53098.

[6] Hummel, F., 2002, "Wake-Wake Interaction and its Potential for Clocking in a Transonic High-Pressure Turbine," ASME J. Turbomach., **124**(1), pp. 69–76.

[7] Tiedemann, M., and Kost, F., 2001, "Some Aspects of Wake-Wake Interactions Regarding Turbine Stator Clocking," ASME J. Turbomach., **123**(3), pp. 526–533.

[8] Reinmöller, U., Stephan, B., Schmidt, S., and Niehuis, R., 2002, "Clocking Effects in a 1.5 Stage Axial Turbine-Steady and Unsteady Experimental Investigations Supported by Numerical Simulations," ASME J. Turbomach., **124**(1), pp. 52–60.

[9] Haldeman, C., Dunn, M., Barter, J., Green, B., and Bergholtz, R., 2004, "Experimental Investigation of Vane Clocking in a One and 1/2 Stage High Pressure Turbine," ASME Paper GT2004–53477.

[10] Jouini, D. B. M., Little, D., Bancalari, E., Dunn, M., Haldeman, C., and Johnson, P. D., 2003, "Experimental Investigation of Airfoil Wake Clocking Impacts on Aerodynamic Performance in a Two Stage Turbine Test Rig," ASME Paper GT-2003–38872.

[11] Stieger, R. D., and Hodson, H. P., 2004, "The Unsteady Development of a Turbulent Wake Through a Downstream Low-Pressure Turbine Blade Passage," ASME Paper GT2004–53061.

[12] Wisler, D. C., Halstead, D. E., and Beacher, B. F., 1999, "Improving Compressor and Turbine Performance Through Cost-Effective Low-Speed Testing," ISOBE Paper 99–7073.

[13] Place, J. M. M., Howard, M. A., and Cumpsty, N. A., 1996, "Simulating the Multistage Environment for Single-Stage Compressor Experiments," ASME J. Turbomach., **118**, pp. 706–716.

[14] Roach, P. E., 1987, "The Generation of Nearly Isotropic Turbulence by Means of Grids," Int. J. Heat Fluid Flow, **8**(2), pp. 82–92.

[15] Solomon, W. J., 1996, "Unsteady Boundary Layer Transition on Axial Compressor Blades," Ph.D. thesis, University of Tasmania.

[16] Evans, R. L., 1975, "Turbulence and Unsteadiness Measurements Downstream of a Moving Blade Row," ASME J. Eng. Power, **122**, pp. 131–139.

[17] Hodson, H. P., Huntsman, I., and Steele, A. B., 1994, "An Investigation of Boundary Layer Development in a Multistage LP Turbine," ASME J. Eng. Power, **116**, July, 375–383.

[18] Halstead, D. E., Wisler, D. C., Okiishi, T. H., Walker, G. J., Hodson, H. P., and Shin, H., 1997, "Boundary Layer Development in Axial Compressors and Turbines: Part 1 of 4—Composite Picture," ASME J. Turbomach., **119**(1), pp. 114–127.

[19] Halstead, D. E., Wisler, D. C., Okiishi, T. H., Walker, G. J., Hodson, H. P., and Shin, H., 1997, "Boundary Layer Development in Axial Compressors and Turbines: Part 2 of 4—Compressors," ASME J. Turbomach., **119**(3), pp. 426–444.

[20] Camp, T. R., and Shin, H. W., 1995, "Turbulence Intensity and Length Scale Measurements in Multistage Compressors," ASME J. Turbomach., **117**, pp. 38–46.

[21] Hughes, J. D., 2001, "Unsteady Aerodynamics of Axial Compressors," Ph.D. thesis, University of Tasmania.

Heat Transfer on Internal Surfaces of a Duct Subjected to Impingement of a Jet Array with Varying Jet Hole-Size and Spacing

U. Uysal
Department of Mechanical Engineering,
Sakarya University,
54187 Sakarya, Turkey

P.-W. Li

M. K. Chyu
e-mail: mkchyu@engr.pitt.edu

Department of Mechanical Engineering,
University of Pittsburgh,
Pittsburgh, PA 15261

F. J. Cunha
Pratt and Whitney,
United Technologies,
East Hartford, CT 06108

One significant issue concerning the impingement heat transfer with a jet array is related to the so-called "crossflow," where a local jet performance is influenced by the convection of the confluence from the impingement of the jet/jets placed upstream. As a result, the heat transfer coefficient may vary along the streamwise direction and creates more or less nonuniform cooling over the component, which is undesirable from both the performance and durability standpoints. Described in this paper is an experimental investigation of the heat transfer coefficient on surfaces impinged by an array of six inline circular jets with their diameters increased monotically along the streamwise direction. The local heat transfer distributions on both the target surface and jet-issuing plate are measured using a transient liquid crystal technique. By varying the jet hole-size in a systematic manner, the actual distribution of jet flow rate and momentum within a jet array may be optimally metered and controlled against crossflow. The effects on the heat transfer coefficient distribution due to variations of jet-to-target distance and interjet spacing are investigated. The varying-diameter results are compared with those from a corresponding array of uniform jet diameter. [DOI: 10.1115/1.2101859]

Introduction

The continuing pursuit of high inlet temperature in gas turbines requires highly sophisticated cooling techniques to maintain the metal temperatures below acceptable limits. Jet impingement is one of the most effective means for cooling of turbine components and is a subject of intense study in the thermal and fluid literature [1–4]. A great portion of previous studies have focused on the heat transfer characteristics on a target surface impinged by either a single jet or a jet array. The case with jet array is more relevant to turbine cooling applications. However, due mainly to interaction among jets in the array, the transport phenomena associated with an array are far more complex than that of a single jet.

One significant issue pertaining to array jet impingement is the so-called "crossflow," where a local jet performance is convectively influenced by the flow in cross direction that comes from confluence of the impingement of upstream jet/jets. Even with identical jet-hole geometry and interjet spacing across the entire array, the heat transfer coefficient on the surface subjected to direct impingement (target wall) varies significantly along the crossflow direction. In some cases, the maximum local heat transfer coefficient could be an order of magnitude higher than that of the minima. This nonuniform cooling phenomenon is undesirable from both the turbine performance and durability standpoints.

Crossflow effects have been recognized as an important issue in the turbine heat transfer community since the 1970s [5–13]. However, the information available to date remains rather spotty and incomprehensive. Most of the pervious studies were directed to modifying the inadequacy of existing correlations of two-dimensional arrays for prediction of internal cooling performance in turbine airfoils or combustor liners. This is due primarily to the fact that crossflow tends to deflect jet axis, reducing or increasing heat transfer and shifting stagnation point downstream. As the crossflow effect can be cumulative, the change in magnitude and displacement of the maximum heat transfer associated with an impinged stagnation point also increases with the streamwise direction. Many studies also reported that the effect of crossflow decreases as the jet-to-target space increases. However, such a claim is by no means universal and may be reversed for different flow and geometrical conditions.

Based on the observations aforementioned and collective information revealed from the relevant literature, two dimensionless parameters stand out as the most dominant variables in the system, i.e., $M=(\rho u)_j/(\rho u)_m$, the mass velocity ratio between the jet and the crossflow, and H/D, the distance between the jet and the target plate, normalized by the jet diameter. Therefore, it is anticipated that, for a given H/D, the crossflow effect can be tempered, or even controlled, with an increase in M toward downstream. The way how M should be varied is basically an optimization issue and should depend on the value of H/D, as well as on other geometric parameters, e.g., jet array spacing and flow conditions. With this notion in mind, this study is an attempt to explore such effects by varying the jet hole-size in a monotonically increasing manner along the streamwise direction.

The evidence of variations in jet hole-size and interjet spacing on the heat transfer over a target plate was first reported in a recent study by Gao et al. [13]. They used a two-dimensional array consisting of eight jet rows with linearly stretched spacing along both streamwise and spanwise directions. The operating range of M is well below one, signifying strong crossflow dominance in their systems. Their results indicated that the existing correlations by Kercher and Tabakoff [5] and Florschutz et al. [9] overpredict the effect of crossflow on local heat transfer and underpredict the heat transfer coefficients when the crossflow is strong.

Contributed by the International Gas Turbine Institute (IGTI) of ASME for publication in the JOURNAL OF TURBOMACHINERY. Manuscript received by IGTI, October 1, 2004; final manuscript received February 1, 2005. IGTI Review Chair: K. C. Hall. Paper presented at the ASME Turbo Expo 2005: Land, Sea, and Air, Reno, NV, June 6–9, 2005, Paper No. GT2005-68106.

To facilitate a more controlled investigation, the present study implements a one-dimensional, rather than two-dimensional, jet array. Hence the spent-air from a jet or jets upstream, which accounts for the magnitude of crossflow at a given streamwise location, can be accurately estimated. As jet impingement is known to induce significant heat transfer nonuniformity with sharp gradients, it is desirable to obtain detailed local heat transfer distributions over the domain of interest. Similar to some recent studies [11–13], this is achieved by making use of the transient liquid crystal technique based on a custom-developed image acquisition system [14].

The heat transfer measurement was made on both the impinged target surface and the jet-issuing plate, or simply the jet plate. Heat transfer on the jet plate could play a significant role for its contribution toward the overall heat transfer in the cooling channel. According to Van Treuren et al. [11], such contribution can amount to 40% of the target plate heat transfer for large H/D and Reynolds number. On the other hand, the convective transport near the jet plate may be affected as the channel sidewalls interfere with the jet flow and causes a postimpingement flow uplift or upwash [7,15]. This phenomenon may be more pronounced when H/D is small. To the authors' knowledge, no detailed local heat transfer information on the jet plate is available in the open literature to date.

Experimental Setup and Data Reduction

To model the general structure of an internal cooling passage, the test section is a rectangular channel made of clear Plexiglas of 12.7 mm thick. The channel consists of two main plates: a target plate and a jet plate, opposite to each other, as shown in Fig. 1. Both plates are of the same wet area, 470 mm by 50.8 mm. The jet plate is patterned with multiple jet nozzles and spaced in various distances. To simulate the crossflow, the channel has one end closed, and the other end is open for spent-air discharge. There are six inline, circular jets placed on the jet plate and their diameters vary in an increasing manner: 3.2, 4.8, 6.4, 7.9, 9.5, and 12.7 mm along the streamwise direction toward discharge exit. The interjet pitch is kept at either 6.5 or 7.5 times the *upstream* jet diameter, i.e., $S=6.5D_{j,up}$, and $7.5D_{j,up}$ so the physical distances between any two neighboring jets are different. As a baseline for comparison, a jet plate of uniform jet size, $D=7.9$ mm, which gives the total jet flow area equal to that of the nonuniform jet array, is also established. In this case, the interjet spacing is 7.5 times the jet diameter, making the case. Another important geometric parameter is the gap between jet plate and target plate, which ranges from 6.4 to 19.1 mm. Table 1 lists the local values of H/D for both the uniform and varying jet-hole cases. The jets are labeled from 1 to 6 following the streamwise direction, i.e., jet 1 being the upstream-most jet [top in Fig. 1(*a*)]. Note that the magnitude of H/D varies by a factor of 4 for the cases with nonuniform jet holes. Also given in Table 1 are streamwise locations of the jet centers and their actual hole sizes.

Figure 2 illustrates the overall experimental setup. Compressed air is metered with standard ASME orifices, for which the readings from pressure differential across the orifice are converted to mass flow rates via a calibrated data acquisition system with sampling rate of 5 Hz and recorded by a computer. The temperature variation among the jets at a given instant is virtually nonexistent.

The measurement of local heat transfer coefficient is by employing the liquid crystal technique, in conjunction with the solution of one-dimensional transient heat conduction in a semi-infinite solid. Under a convection boundary condition at its surface, the temperature on the surface of a semi-infinite solid, T_w, can be expressed by

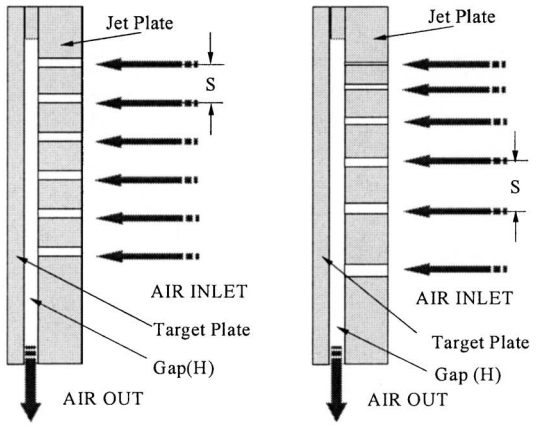

(a) Channels- (Left: uniform jets, Right: Varying jets)

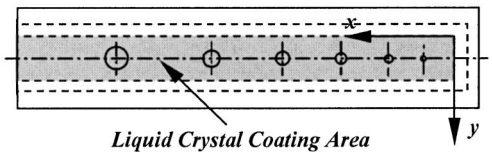

(b) Jet plate with varying jet diameter and inter-jet spacing

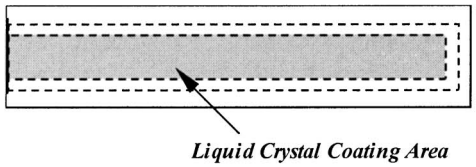

(c) Target plate (470mm x 51mm)

Fig. 1 Test model

$$\frac{T_w - T_i}{T_r - T_i} = 1 - \exp\left(\frac{h^2 \alpha t}{k^2}\right) erfc\left(\frac{h\sqrt{\alpha t}}{k}\right) \tag{1}$$

where T_i is the initial temperature of the solid; T_r is the reference temperature for the convection system, which is chosen as the jet temperature, T_j; h is the convective heat transfer coefficient based on T_w and T_r (or T_j); and k and α are the thermal conductivity and diffusivity of the solid, respectively. From the fundamental standpoint, a more rigorous choice of reference temperature under the jet impingement situation is the recovery temperature or adiabatic-wall temperature [6–8]. However, an estimate based on the current flow conditions reveals that this will only make nominal influence on heat transfer coefficient, less than 2%. In reality, it is much more advantageous for turbine designers to base h on a single-valued reference temperature, such as that in the jet plenum or at jet inlet. In the present study, both jet plenum and jet inlet temperatures are measured using a number of miniature thermocouples and both temperatures are virtually identical.

A key feature of the present experiment is measuring the time lap during which the liquid-crystal coated surface is experienced from the beginning of the transient test to the appearance of maximum intensity. In general, thermochromic liquid crystal reflects white light with maximum intensity near the spectrum of green color. As the state of maximum intensity can be calibrated against

Table 1 Local *H*/*D* values at impinging jet locations

	Uniform jet-hole size D=7.94 mm				Nonuniform jet-hole size				
Jet	Jet-center location x(mm)	H=6.4 mm	H=12.7 mm	H=19.1 mm	Jet-center location x(mm)	Jet diameter D(mm)	H=6.4 mm	H=12.7 mm	H=19.1 mm
1	36.2	0.8	1.6	2.4	36.2	3.2	2.0	4.0	6.0
2	87.8	0.8	1.6	2.4	67.1	4.8	1.3	2.7	4.0
3	139.4	0.8	1.6	2.4	108.4	6.4	1.0	2.0	3.0
4	191.0	0.8	1.6	2.4	160.0	7.9	0.8	1.6	2.4
5	242.6	0.8	1.6	2.4	221.7	9.5	0.7	1.3	2.0
6	294.2	0.8	1.6	2.4	304.2	12.7	0.5	1.0	1.5

temperature prior to actual tests, a specific correspondence between time, t, to reach the maximum intensity state and T_w can be established. With such data available for each pixel over the designated viewing domain, the distribution of local heat transfer coefficient, h, can be determined through a computer-aided solution for Eq. (1). While there are different versions of transient liquid crystal methods, the technique overall is well developed and details are available in the open literature, such as [11–14].

Results and Discussion

The experiments span over five different Reynolds numbers, 1.4×10^4, 2.2×10^4, 2.8×10^4, 3.4×10^4 and 4.0×10^4, based on the jet mean velocity and a jet hydraulic diameter, D_h. For the case with varying jet-hole size, the jet hydraulic diameter is an average of the six participating jets, defined as

$$D_h = \frac{\sum_1^6 D_i^2}{\sum_1^6 D_i} \tag{2}$$

Using the hole-size data listed in Table 1 leads to D_h=8.73 mm, which is about 10% higher than that of the uniform hole case.

Table 2 shows the comparative magnitude of mass (volume) flow rate discharged from each jet and its estimated ratio to the crossflow rate at the location of impingement. Most evident is the severe nonuniformity or redistribution of the total flow rate among the six participating jets for the varying diameter case. The difference between the largest jet (sixth, downstream-most) and the smallest jet (first) is almost twentyfold. This redistribution also makes the jet-to-cross flow rate ratios (G) consistently higher than the corresponding values of uniform jet-diameter case, by about two to three times. While these effects are expected to influence the overall convective transport in the system, more significantly, this also implies that the current approach may be a viable means for optimizing the jet-impingement cooling performance. As mentioned earlier, to demonstrate the latter aspect is one of the main scopes of this study.

The uncertainty analysis with a 95% confidence level in the measured parameters is based on the method of Kline and McClintock [16]. The local heat transfer coefficient, h, measured in the present liquid-crystal-based system, depends strongly on the temperatures of test surface, inlet, and exit. The uncertainties of these temperature readings are about ±0.2°C, which correspond to 0.5%, 0.3% and 0.7% at these key locations, respectively. Other factors contributing to the uncertainty of h are errors in the temperature-color calibration of liquid crystal, the lap-time for the

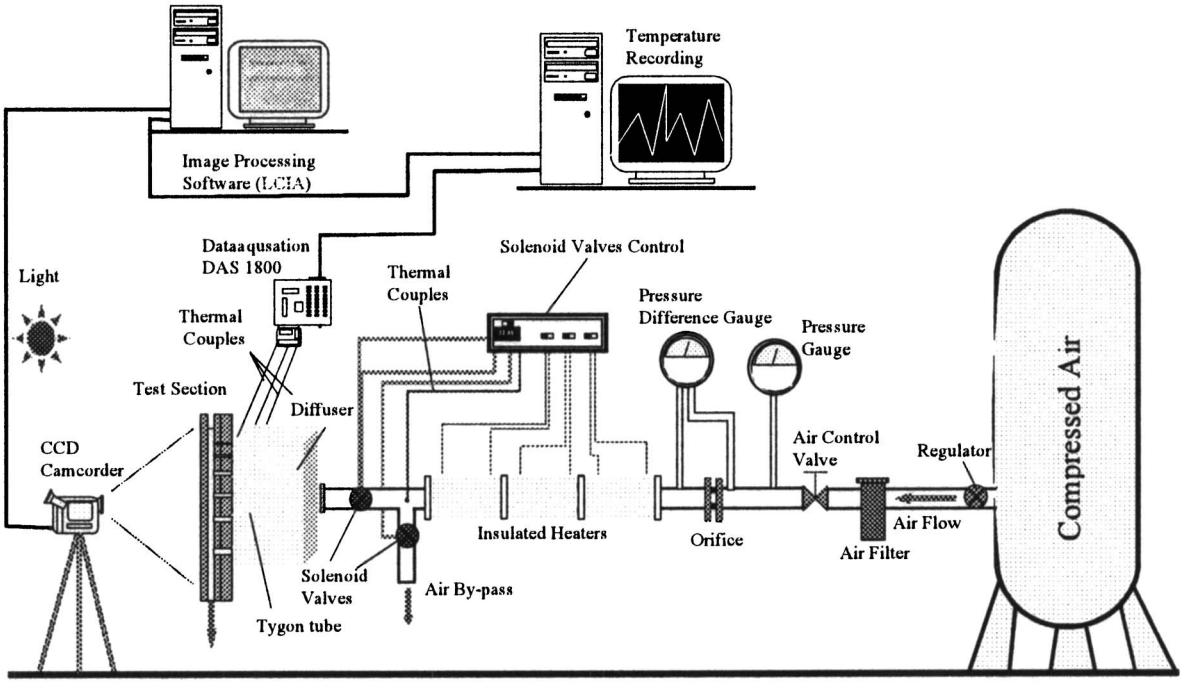

Fig. 2 Experimental setup

Table 2 Jet flow rate

Jet	Uniform diameter D=7.9 mm: Jet-center x(mm)	Jet flow rate (%)	Jet-to-cross flow rate ratio (G)	Varying diameter D_h=8.7 mm: Jet-center x(mm)	Jet flow rate (%)	Jet-to-cross flow rate ratio (G)
1	36.2	16.7	NA	36.2	2.6	NA
2	87.8	16.7	1.00	67.1	5.8	2.25
3	139.4	16.7	0.50	108.4	10.4	1.23
4	191.0	16.7	0.33	160.0	16.2	0.86
5	242.6	16.7	0.25	221.7	23.4	0.67
6	294.2	16.7	0.20	304.2	41.6	0.71

liquid crystal reaching the designated color, and the thermal diffusivity of the substrate. The errors in these three parameters are estimated at 0.5%, 0.4%, and 1%, respectively. Another major error contributing to the uncertainty is the error in measuring the flow rate or Reynolds number in the air supply system, which is about 4%. Combining all these errors leads to the overall 7% uncertainty for the magnitude of local heat transfer coefficient.

Local Heat Transfer Coefficient on Target Plate. The local heat transfer coefficient and Nusselt number for both target plate and jet plate are discussed first for nonuniform jet array and then for uniform jet array in this section. Figure 3 displays contour images of the local heat transfer coefficient, which show the heat-transfer-enhanced area from the impingement of jets with varying diameter. Figure 4 illustrates the effects of jet-to-target distance on the heat transfer over the target surface. The specific data shown in Fig. 4 are the spanwise-averaged, streamwise-resolved Nusselt numbers at Re=22,000 for all three jet-to-target spacing, i.e., H =6.4, 12.7, and 19.1 mm. The corresponding values of H/D_h are 0.73, 1.45, and 2.18, respectively. Both figures reveal that heat transfer coefficient on the target plate shows multiple peak values at locations corresponding to direct jet impingement or the stagnation point. The level of these peaks rises toward downstream as the jet diameter, as well as the jet-flow rate, increases. This is in a sharp contrast to the general trend associated with a uniform jet-hole array, where the local heat transfer decreases with the streamwise coordinate, due to increasing crossflow effects [9–13]. Apparently, the effect of increased jet flow rate and momentum

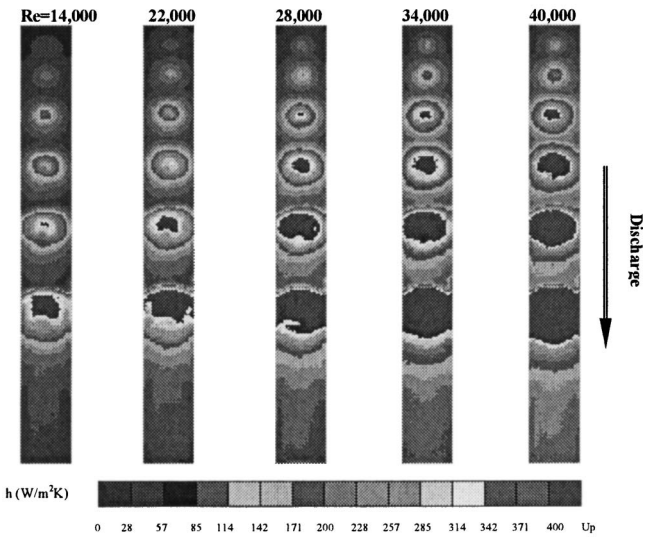

Fig. 3 Images of local heat transfer coefficients on target plate (S=6.5$D_{j\text{-}up}$, H/D_h=1.45, H=12.7 mm)

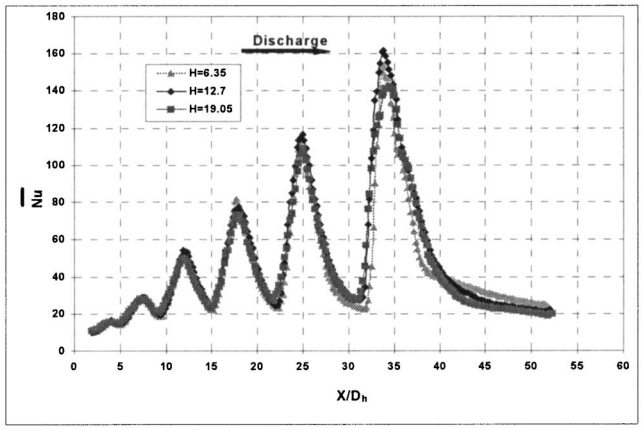

Fig. 4 Spanwise-average Nusselt number for target plate (Re =22,000, S=6.5$D_{j\text{-}up}$)

overwhelms confluence of the cross-flow from upstream.

Further examining the data in Fig. 4 shows that the influence of jet-to-target spacing (H or H/D_h) on the heat transfer over the target surface is rather moderate. No apparent downstream-shift of peak heat transfer induced by crossflow is observed. However, the figure reveals a trend that the highest impingement heat transfer underneath the downstream-most jet occurs at the intermediate jet-to-target spacing, i.e., H=12.7 mm or H/D_h=1.45. Several earlier studies [9,11] for rather narrow jet-to-target spacing, $H/D \sim 1$, indicated that crossflow can, in fact, increase the heat transfer as it convects more coolant from upstream. On the other hand, it is also understandable that when spacing H is overly wide, the jet may become too weak to penetrate through crossflow and thus the heat transfer coefficient on the impinged surface decreases. Therefore, H/D_h=1.45 represents an optimal heat transfer condition for the present test range, resulting from these two competing effects. Figure 5 shows the effects of Reynolds number on the heat transfer over target surface with this optimal spacing. An increment in Reynolds number elevates the level of heat transfer, most notably at the locations under direct impingement. This is consistent with the general finding in the jet impingement heat transfer literature.

One way to reason the insignificant influence of crossflow on the target-surface heat transfer can be made by examining the general features of momentum transport in the system. Figure 6 shows the estimated velocity ratio between the jet flow and cross-

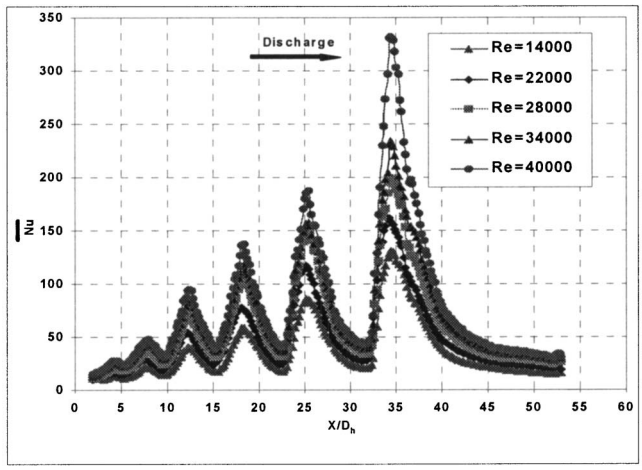

Fig. 5 Effect of Reynolds number on target plate heat transfer (S=6.5$D_{j\text{-}up}$, H/D_h=1.45, H=12.7 mm)

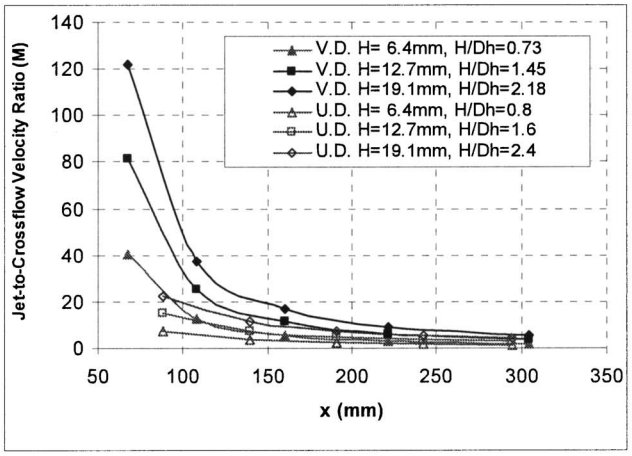

(a)

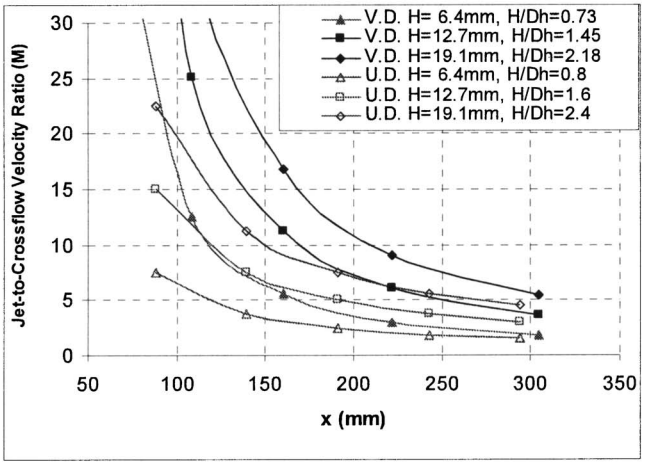

(b)

Fig. 6 Jet-to-crossflow velocity ratio

flow for all six participating jets in both varying-diameter (V.D.) and uniform-diameter (U.D.) arrays, though the current focus lies on the former geometry. The symbols in the figure mark actual impingement locations corresponding to the center of a jet, from the second jet to the sixth jet. The first jet data are absent as there is virtually no crossflow associated. Earlier studies [6,7] have reported that crossflow imposes no effect on jet deflection and stagnation point heat transfer when $M > 8$. This is based on the results from measurements of surface heat transfer and flow visualization for single jets and with relatively wide jet-to-target spaces, $H/D \sim 3-12$. The present data shown in Fig. 6 clearly indicate that the magnitudes of M for the most part of the varying-diameter cases far exceed this criterion.

According to Fig. 6(*b*), a close-up view of M distribution, only the last two jets, especially for the narrowest channel ($H = 6.4$ mm, $H/D_h = 0.73$), may be subject to the crossflow effect. However, such lower values in M may be compensated by the excessive cooling mass injected by these downstream jets. As shown in Fig. 7, the last two jets in the varying diameter case together contribute nearly 65% of the total flow rate injected into the system. Because of channel confinement and potential interference with the side walls, such massive jet-flow addition likely induces stronger and more complex secondary flows in the jet vicinity than its single-jet-in-crossflow counterpart. Therefore, the nature of jet-crossflow interaction under the current condition

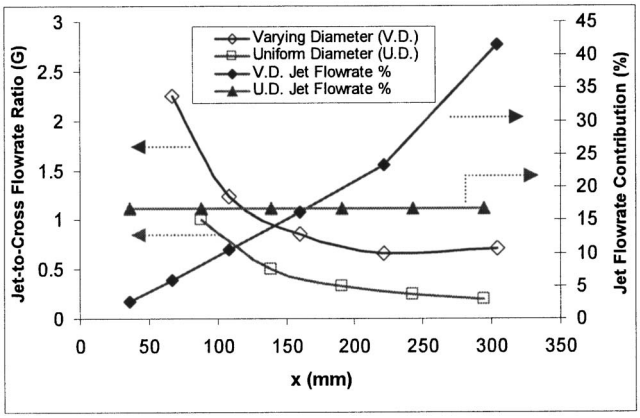

Fig. 7 Jet-to-crossflow flow rate ratio and individual jet flow rate contribution

could be very different than that observed in the earlier studies. Further examining Figs. 6 and 7 reveals that, for a given total flow rate over a jet array, the case with varying diameter consistently produces significantly higher jet-to-crossflow velocity and flow rate ratios. These higher ratios alleviate the level of influence by the crossflow.

Local Heat Transfer Coefficient on Jet Plate. Contour images of the local heat transfer coefficient on the jet plate for $2650 < \mathrm{Re} < 6900$ are shown in Fig. 8. Exhibited in Fig. 9 is the spanwise-averaged, streamwise-resolved Nusselt number on the jet plate at $\mathrm{Re} = 4000$ for three different jet-to-target spaces. One notable finding from these figures is that the magnitudes of heat transfer on jet plate are about only one-third to one-half the corresponding values on the target plate. This level of heat transfer is in good agreement with that reported by Van Treuren et al. for cases with relatively large jet-to-target spacing and high Reynolds number [11]. As suggested by earlier studies on jet-flow visualization and numerical simulation [7,15], one of the dominating features of convective transport adjacent to the jet plate is the "up-wash" of the jets after impingement on the target plate. This is evidenced by the fact that the border area, not the center area, in Fig. 8 has higher heat transfer coefficient. This phenomenon becomes more significant toward downstream, as the jet-diameter as

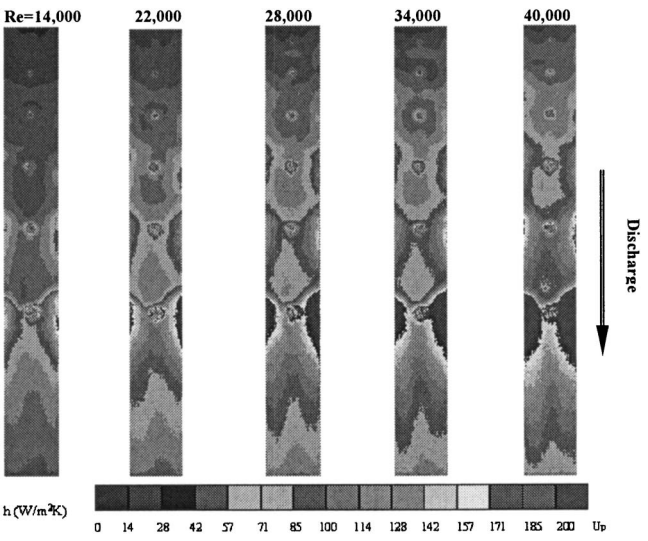

Fig. 8 Images of the local heat transfer coefficients on jet plate ($S = 6.5D_{j\text{-}up}$, $H/D_h = 1.45$ or $H = 12.7$ mm)

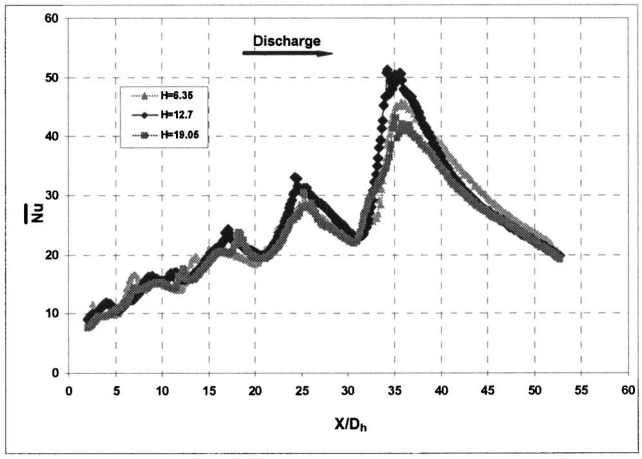

Fig. 9 Spanwise-average Nusselt number for jet plate (Re =22,000, $S=6.5D_{j\text{-}up}$)

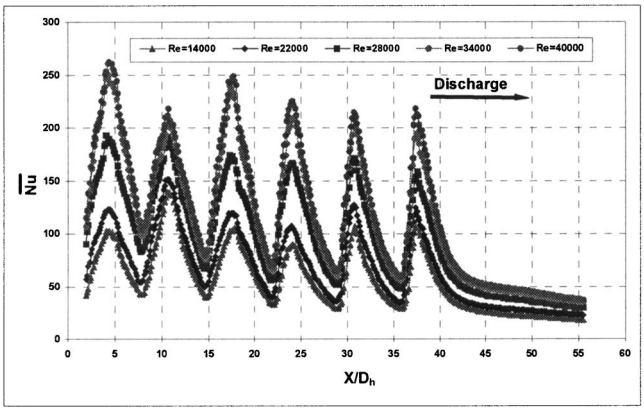

Fig. 11 Span-average Nusselt number on target plate with uniform jet diameter ($S=6.5D_h$, $H/D_h=1.6$, or $H=12.7$ mm)

well as the flow rate added to the channel increase.

Another important observation is that the heat transfer on the jet plate appears to be more sensitive to the crossflow than that on the target plate. Clearly displayed in Fig. 9, the peak of the Nusselt number, which signifies a locally most intensified up-wash, for the two downstream most jets occurs at different locations as the jet-to-target spacing varies. The peak shifts toward downstream with a decrease in H or H/D_h. This is a common indicator of crossflow effect prevailing in the region. Apparently, the postimpingement up-wash does not inherit the same level of momentum as that of the freshly issued jet before reaching the target plate. The influence of crossflow between the target wall and the jet plate marks one of the major differences in transport phenomena between these two major surfaces. Similar to the target plate, the maximum spanwise-average heat transfer coefficient on jet plate exists when $H/D_h=1.45$ ($H=12.7$ mm). Figure 10 shows the effects of Reynolds number with the jet-to-target spacing fixed at this optimal value. The level of heat transfer coefficient rises with Reynolds number and the locations of peak Nu appear to be insensitive to the Reynolds number.

Heat Transfer with Uniform Jet Diameter and Spacing. While it is recognized that the specific geometry for the varying-diameter jet array discussed above is by no means optimal in heat transfer, similar measurement was made for an array with uniform jet diameter as a baseline for comparison. The jet diameter in this case is $D=7.9$ mm, which gives the same overall flow cross-sectional area as that of the varying diameter case, and the interjet spacing is $S/D=7.5$. The jet-to-target space is set at $H=12.7$ mm, which gives the highest heat transfer for the varying-diameter case, and the interjet spacing is $S/D=7.5$. The jet-to-target space is set at $H=12.7$ mm, which gives the highest heat transfer for the varying-diameter case. Figures 11 and 12 show the spanwise-averaged, streamwise-resolved Nusselt number on the target plate and jet plate, respectively. Similar to the varying-diameter case, the jet plate heat transfer coefficient accounts for about one-third to one-half the target plate's counterpart. Relatively speaking, the heat transfer coefficient with uniform jet-size is more uniform spatially than that with nonuniform diameters.

Effect of Interjet Spacing. A comparison of Figs. 5 and 10–12 reveals that varying the jet diameter alone can reverse the trend of local heat transfer distribution of the baseline case with uniform jet cross section. This also implies that the varying-diameter approach may be promising in gaining more magnitude and uniformity in overall heat transfer, provided that the combined jet-size variation and interjet spacing can be optimized. The present data suggest that to reach such optimal conditions, the extent of variation in jet diameter needs to be less severe and the interjet spacing may be rearranged in different fashions.

To illustrate the effects of interjet spacing, Fig. 13 shows the difference in average heat transfer coefficient between two comparative cases: $S=6.5D_{j\text{-}up}$ and $7.5D_{j\text{-}up}$. Partly because such a streamwise-pitch variation is somewhat small, the overall change in heat transfer between these two cases is rather moderate. However, it is clear that the effect is significantly greater on the target plate than on the jet plate. It is also evident that, for medium and large jet-to-target spacing, i.e., $H=12.7$ mm and $H=19.1$ mm, the

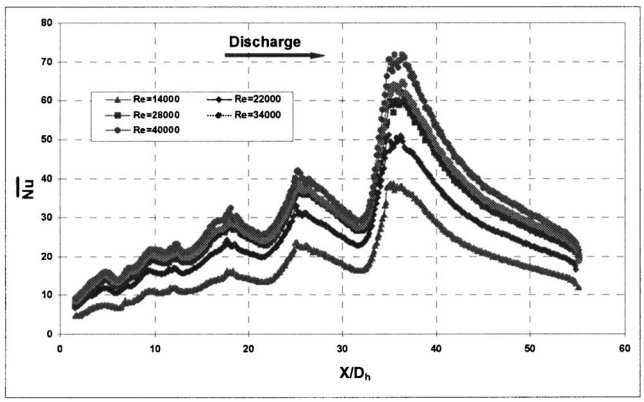

Fig. 10 Effects of Reynolds number effects on jet plate heat transfer ($S=6.5D_{j\text{-}up}$, $H/D_h=1.45$, or $H=12.7$ mm)

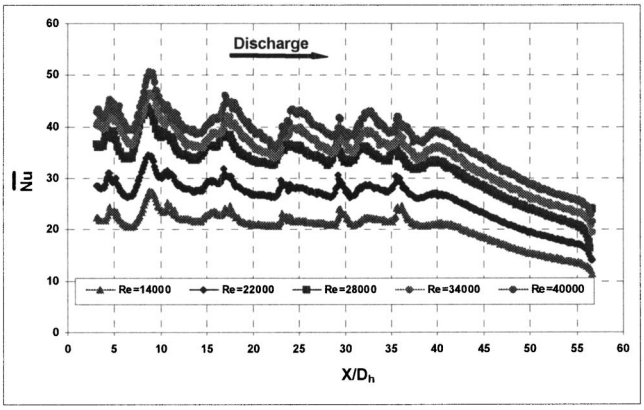

Fig. 12 Span-average Nusselt number on jet plate with uniform jet diameter ($S=6.5D_h$, $H/D_h=1.6$, or $H=12.7$ mm)

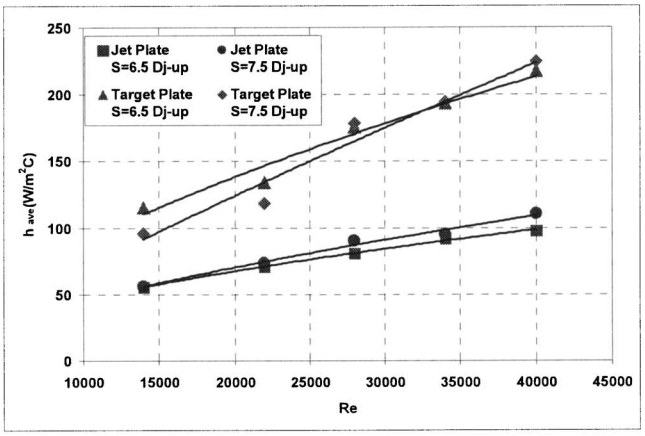

(a) H/D_h=0.73, H=6.4mm

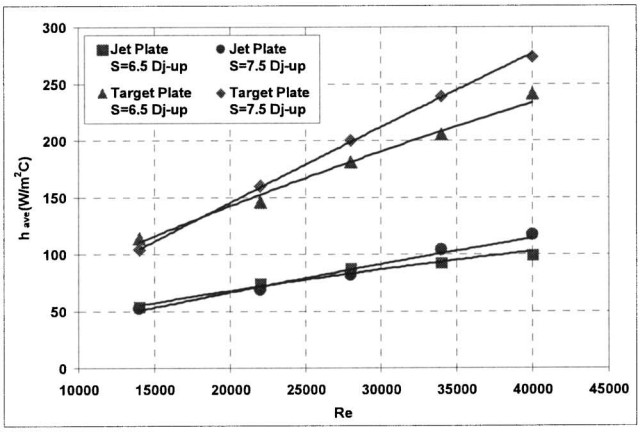

(b) H/D_h=1.45, H=12.7mm

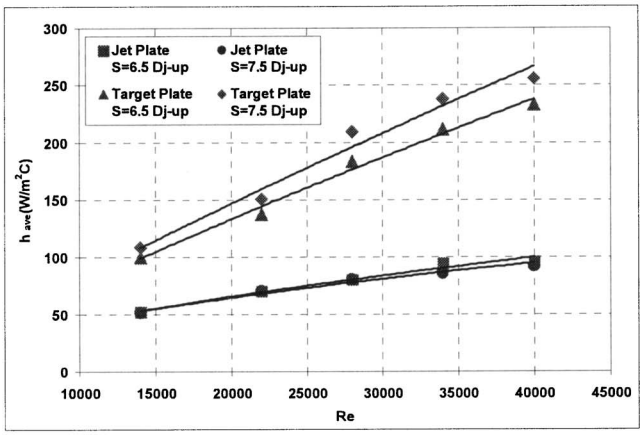

(c) H/D_h=2.18, H=19.1mm

Fig. 13 Area-average heat transfer coefficient and effect of interjet spacing

heat transfer coefficient for $S=7.5D_{j\text{-}up}$ is consistently higher than that of $S=6.5D_{j\text{-}up}$. While this trend may be applicable only to limited situations, it is speculated that the merging interaction of two neighboring jets in the present study might suppress the enhancement of heat transfer.

Conclusions

The present heat transfer experiment on internal surfaces of a rectangular channel subject to impingement of a jet array of varying diameters has drawn conclusions as follows.

1. The varying-jet-diameter approach significantly alters the nature of momentum transport in the system, as compared to the uniform jet-diameter case. Most notable is the elevated values in jet-velocity-to-crossflow ratio. As a result, the heat transfer on the target plate shows little influence of crossflow. In fact, key heat transfer features in the impinged region directly underneath a jet bear strong resemblance to that of a single jet. This implies that direct interaction among neighboring jets in the array is weak.
2. Heat transfer characteristics on the jet-issuing plate are very different from that on the target plate. The influence of crossflow is rather evident. The transport phenomena near the jet plate, as a result of side-wall interference, are dominated by the up-wash of postimpingement jet flow. The momentum of the up-wash is considerably smaller than that of the primary jet. The peak of heat transfer, which typically locates near the streamwise-center of an impinging jet, is shifted notably toward downstream. The shift is more significant as the jet-to-target space decreases, signifying stronger crossflow influence. Overall, the average heat transfer on the jet plate is approximately one-third to one-half the corresponding values on the target plate.
3. The space separating the jet and the target plates is expected to affect the strength of crossflow. Among the three different jet-to-target spacing, i.e., H/D_h=0.73, 1.45, and 2.18, the case with intermediate space H/D_h=1.45 (H=12.7 mm) always yields the highest heat transfer on both target plate and jet plate. However, the differences in heat transfer among these three cases are rather moderate. When the jet-to-target space is narrow, the jet fails in developing sufficient level of turbulence for heat transfer enhancement at the impingement. On the other hand, jet flow with very large jet-to-target spacing dissipates excessively and cannot penetrate the crossflow, resulting in lower heat transfer at the impingement.
4. Overall, the present study has demonstrated that varying-diameter is a promising means to alleviate and control the influence of crossflow in a jet array. While to provide new design guidelines for jet impingement cooling is not within the scope of this work, the jet heat transfer enhancement may be accomplished by optimizing the combined effect of participating geometric parameters, such as jet-size variation, jet-to-target spacing, and interjet spacing. Further investigation on this subject is recommended.

Nomenclature

D = jet diameter, m
D_h = average jet diameter (m) defined in Eq. (2)
G = mass flowrate ratio between local jet and crossflow
h = local heat transfer coefficient, W/m^2-K
h_{ave} = area-average heat transfer coefficient, W/m^2-K
H = jet-to-target space, m
k = thermal conductivity, W/m-K
M = mean velocity ratio between jet and cross flow
$\underline{\mathrm{Nu}}$ = local Nusselt number, hD_h/k
$\overline{\mathrm{Nu}}$ = span-average Nusselt number
Re = Reynolds number, uD_h/ν
S = streamwise distance between two jets, m
t = lap time for test, s
T = temperature, C or K
u = flow velocity, m/s
α = thermal diffusivity, m^2/s

ν = kinematic viscosity of fluid, m^2/s

Subscript

ave = average over entire array
j = jet
j-up = jet of upstream
w = on the wall
m = main stream

References

[1] Martin, H., 1977, "Heat and Mass Transfer Between Impinging Gas Jets and Solid Surfaces," Adv. Heat Transfer, **13**, pp. 1–60.
[2] Obot, N. T., Mujumdar, A. S., and Douglas, W. J. M., 1982, "Effect of Semi-Confinement on Impingement Heat Transfer," *Proc. 7th Int. Heat Transfer Conf.*, Munich, September 6–10, Vol. 3, pp. 395–400.
[3] Jambunathan, K., Lai, E., Moss, M. A., and Button, B. L., 1992, "A Review of Heat Transfer Data for Single Circular Jet Impingement," Int. J. Heat Fluid Flow, **13**(2), pp. 106–115.
[4] Bizzak, D. J., and Chyu, M. K., 1995, "Use of a Laser-Induced Fluorescence Thermal Imaging System for Local Jet Impingement Heat Transfer Measurement," Int. J. Heat Mass Transfer, **38**(2), pp. 267–274.
[5] Kercher, D. M., and Tabakoff, W., 1970, "Heat Transfer by a Square Array of Round Air Jets Impinging Perpendicular to a Flat Surface including the Effect of Spent Air," J. Eng. Power, **92**, pp. 73–82.
[6] Sparrow, E. M., Goldstein, R. J., and Rouf, 1975, "Effect of Nozzle-Surface Separation Distance on Impingement Heat Transfer for a Jet in a Crossflow," ASME J. Heat Transfer, **97**, pp. 528–533.
[7] Bouchez, J. P., and Goldstein, R. J., 1975, "Impingement Cooling from a Circular Jet in a Crossflow," Int. J. Heat Mass Transfer, **18**, pp. 719–730.
[8] Behbahani, A. I., and Goldstein, R. J., 1983, "Local Heat Transfer to Staggered Arrays of Impinging Circular Air Jets," J. Eng. Power, **105**, pp. 354–360.
[9] Florschuetz, L. W., Berry, R. A., and Metzger, D. E., 1980, "Periodic Streamwise Variations of Heat Transfer Coefficients for Inline and Staggered Arrays of Circular Jets with Crossflow of Spent Air," ASME J. Heat Transfer, **102**, pp. 132–137.
[10] Hollworth, B. R., and Cole, G. H., 1987, "Heat Transfer to Arrays of Impinging Jets in Crossflow," ASME J. Turbomach., **109**, pp. 564–571.
[11] Van Treuren, K. W., Wang, Z., Ireland, P. T., and Jones, T. V., 1993, "Detailed Measurements of Local Heat Transfer Coefficient and Adiabatic Wall Temperature Beneath an Array of Impinging Jets," ASME J. Turbomach., **16**, pp. 369–371.
[12] Hung, Y., Ekkad, S. V., and Han, J-C., 1998, "Detailed Heat Transfer Distributions under an Array of Orthogonal Impinging Jets," J. Thermophys. Heat Transfer, **12**, pp. 73–79.
[13] Gao, L., Ekkad, S. V., and Bunker, R. S., 2003, "Impingement Heat Transfer under Linearly Stretched Arrays of Holes," ASME Paper No. GT2003-38178.
[14] Chyu, M. K., Ding, H., Downs, J. P., and Soechting, F. O., 1998, "Determination of Local Heat Transfer Coefficient Based on Bulk Mean Temperature Using a Transient Liquid Crystals Techniques," Exp. Therm. Fluid Sci., **18**, pp. 142–149.
[15] Zecchi, S., and Bacci, A., 2004, "Numerical Analysis of Crossflow and Single Jet Impinging on a Heated Surface with Shaped Groove," ASME Paper No. GT2004-53549.
[16] Kline, S. J., and McClintock, F. A., 1953, "Describing Uncertainties in Single-Sample Experiments," Mech. Eng. (Am. Soc. Mech. Eng.), **75**, pp. 3–8.

Effects of Reynolds Number and Freestream Turbulence on Turbine Tip Clearance Flow

Takayuki Matsunuma
National Institute of Advanced Industrial Science and Technology,
1-2-1 Namiki, Tsukuba,
Ibaraki 305-8564, Japan

Tip clearance losses represent a major efficiency penalty of turbine blades. This paper describes the effect of tip clearance on the aerodynamic characteristics of an unshrouded axial-flow turbine cascade under very low Reynolds number conditions. The Reynolds number based on the true chord length and exit velocity of the turbine cascade was varied from 4.4×10^4 to 26.6×10^4 by changing the velocity of fluid flow. The freestream turbulence intensity was varied between 0.5% and 4.1% by modifying turbulence generation sheet settings. Three-dimensional flow fields at the exit of the turbine cascade were measured both with and without tip clearance using a five-hole pressure probe. Tip leakage flow generated a large high total pressure loss region. Variations in the Reynolds number and freestream turbulence intensity changed the distributions of three-dimensional flow, but had no effect on the mass-averaged tip clearance loss of the turbine cascade. [DOI: 10.1115/1.2103091]

Introduction

The clearance between the blade tips and casing endwall in a turbine induces leakage flow, which arises due to the pressure difference between the pressure surface and the suction surface of the blade. The leakage flow emerging from the clearance interacts with the passage flow and rolls up into a vortex known as the "tip leakage vortex." Although the size of the clearance is typically about one percent of the blade height, the leakage flow through this small clearance has a significant effect on the aerodynamics of the turbine. For example, the tip clearance loss of a turbine blade can account for as much as one-third of the total losses (Booth [1]). The loss of performance due to the tip clearance flow has therefore been intensively studied for many years. Booth [1] and more recently Sjolander [2] presented comprehensive reviews of the various effects of tip clearance flow. Bindon [3], Dishart and Moore [4], Yaras and Sjolander [5], and Heyes and Hodson [6] made detailed measurements of the tip clearance flow. Moreover, Heyes et al. [7] and Morphis and Bindon [8] investigated the effect of tip geometry. Concurrently, many efforts focusing on loss prediction methods have been continuing over a long period [9–15].

Almost all experiments on and predictions of tip clearance flow have neglected the relative motion between the blade tips and the casing endwall of actual gas turbines. The effect of this relative motion has been experimentally investigated by Yaras and Sjolander [16]. Tallman and Lakshminarayana [17] numerically simulated the effects of the casing relative motion. The findings of these researchers showed that the relative motion in a turbine reduces the leakage flow and affects the pressure difference across the blade tip by forming a scraping vortex; however, the relative motion does not greatly affect the general flow pattern over the tip.

Moreover, low Reynolds number flows have become increasingly important with the new generation of small gas turbines (Bons et al. [18]). Blade Reynolds numbers for the turbine stage of such gas turbines can drop to below 10^5. For example, the Reynolds numbers of the turbine cascades of 300 kW industrial ceramic gas turbines (Arakawa et al. [19]), which are two-stage axial-flow turbines with unshrouded rotor blades, are approximately 6×10^4 because of the increased viscosity caused by high turbine inlet temperatures and miniaturization of the cascade. These Reynolds numbers are considerably smaller than the Reynolds numbers of conventional gas turbines. At these low Reynolds numbers, the boundary layer is dominated by laminar flow and is susceptible to flow separation and strong secondary vortices that develop into increased loss, leading to reduced performance (e.g., Curtis et al. [20], Murawski et al. [21], Lou and Hourmouziadis [22], Howell et al. [23], Volino and Hultgren [24], and Van Treuren et al. [25]). Figure 1 shows the effect of the Reynolds number on the mass-averaged total pressure loss of a turbine cascade without tip clearance (Matsunuma et al. [26]). The loss at the low Reynolds number is nearly double that at the high Reynolds number. This increase is due to the increase in the profile loss and the secondary loss. At higher Reynolds numbers, the measured data agree with the curve of the −0.2 power of the Reynolds number, as shown by the blue line in the figure. This result conforms with the well-known fact that the losses in a turbine vary according to the −0.2 power of the Reynolds number (Fielding [27]). However, the curve of the −0.2 power law does not match that of the measured data at lower Reynolds numbers. At lower Reynolds numbers, the curve of the −0.35 power of the Reynolds number (the green line in the figure) fits more closely than the curve of the −0.2 power law. This indicates that the increase in loss (or the fall in performance) at lower Reynolds numbers can be greater than that predicted by the conventional law of the −0.2 power of Reynolds number.

In the Ainley-Mathieson loss prediction model [9], the tip clearance loss varies according to the −0.2 power of the Reynolds number. However, other loss predictions neglect the effect of the Reynolds number on the tip clearance loss because of the obscure effect of the Reynolds number. A recent book concerning the fluid dynamics of turbomachinery (Lakshminarayana [28]) reports that the tip clearance loss depends on the Reynolds number and the freestream turbulence intensity. However, the book does not demonstrate the effects of these parameters in concrete form.

This paper therefore describes a study to investigate the effect of tip clearance on the loss and flowfield of a turbine cascade at low Reynolds numbers.

Contributed by the International Gas Turbine Institute (IGTI) of ASME for publication in the JOURNAL OF TURBOMACHINERY. Manuscript received by IGTI, October 1, 2004; final manuscript received February 1, 2005. IGTI Review Chair: K. C. Hall. Paper presented at the ASME Turbo Expo 2005: Land, Sea and Air, Reno, NV, June 6 - 9, 2005, Paper No. GT2005-68009.

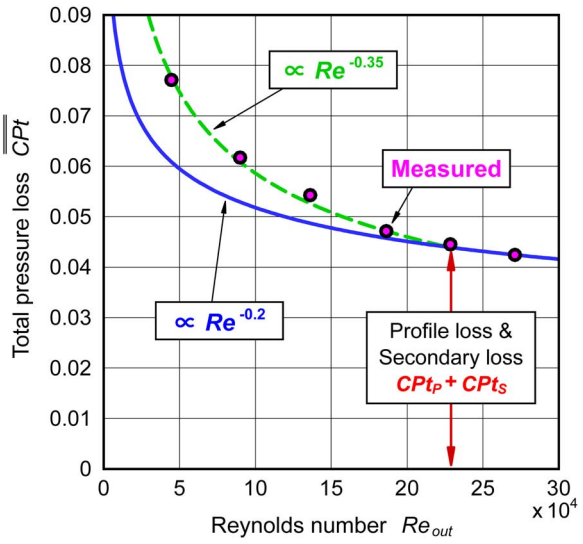

Fig. 1 Total pressure loss (zero clearance)

Experimental Facility and Method

Annular Wind Tunnel and Turbine Cascade. Figure 2 shows the annular turbine wind tunnel used in this experiment. This wind tunnel is an air-suction type, open-circuit facility with a low-turbulence inlet flow. The total length of the wind tunnel is approximately 3.8 m. The outer and inner annular wall diameters of the test section are 500 and 350 mm, respectively. An axial-flow turbine nozzle cascade designed using a free vortex method to attain radial equilibrium was installed in the test section. The geometry and specifications of the turbine cascade are shown in Fig. 3 and Table 1. Figure 4 shows the design velocity and pressure distributions on the surface at the turbine cascade midpan. It should be noted that the turbine cascade is a stationary blade row with axial inflow and the loading on this blade surface is more front-loaded than that of rotor blades, as shown in Fig. 4(*b*). Although the relative motion between the blade tip and the casing endwall was not modeled in this experiment, the author considers that the effect of the relative motion on the flow field is likely to be insignificant even under low Reynolds number conditions.

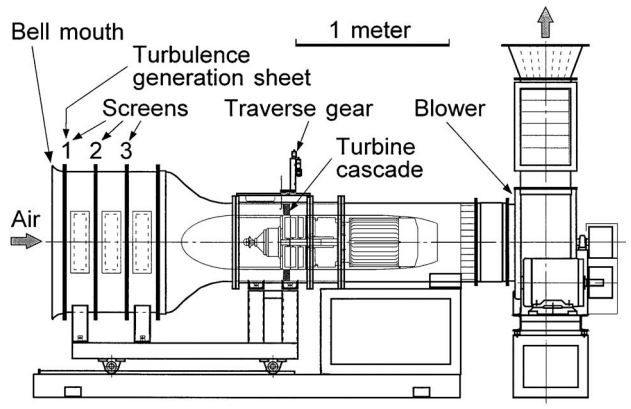

Fig. 2 Annular turbine wind tunnel

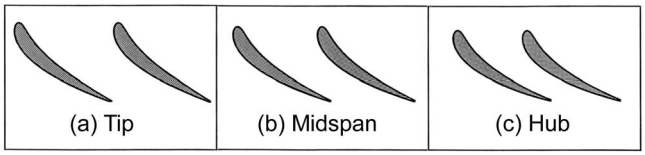

Fig. 3 Geometry of turbine cascade

Table 1 Specifications of turbine cascade

		Tip	Midspan	Hub
Number of blades	N		28	
Chord	C	69.2 mm	67.6 mm	66.2 mm
Axial chord	C_{ax}	45.3 mm	42.8 mm	40.2 mm
Blade span	H		75.0 mm	
Blade pitch	S	56.1 mm	47.7 mm	39.3 mm
Aspect ratio	H/C	1.08	1.11	1.13
Pitch / chord ratio	S/C	0.81	0.71	0.59
Solidity	C/S	1.23	1.42	1.68
Inlet blade angle	α_{in}	0.0 deg	0.0 deg	0.0 deg
Exit blade angle	α_{out}	63.9 deg	67.4 deg	71.1 deg
Stagger angle	ξ	49.3 deg	51.0 deg	52.8 deg
Inner diameter	D_H		350 mm	
Outer diameter	D_T		500 mm	
Hub / tip ratio	D_H/D_T		0.7	
Tip clearance	k	0.5 mm (with tip clearance) 0.0 mm (without tip clearance)		

Experimental Instruments and Method. The inlet flow condition of the turbine cascade was measured using a three-hole pressure probe, with a 2.1 mm head width and a 0.7 mm head height, at the axial position of $z/C_{ax}=-0.706$, 30 mm upstream from the leading edge at midspan. The number of spanwise measurement points was 73. The turbulence characteristics of the inlet flow were obtained using a single-element, hot-wire anemometer (model 0248R-T5, Kanomax Japan Inc., Osaka, Japan). The measurement uncertainty of the boundary layer displacement thickness and the momentum thickness at the inlet was estimated to be 0.03 mm (0.04% of the blade span).

The wake traverse of the turbine cascade was carried out at a distance of 6.6 mm axially from the trailing edge at midspan, i.e., $z/C_{ax}=1.156$, as shown in Fig. 5. The distributions of total pressure, velocity, flow angle, etc., were obtained using a miniature five-hole pressure probe with a head diameter of 2.1 mm. The total number of measurement points was 819 (21 spanwise $\times$ 39 pitchwise locations). The traverse mechanisms had resolutions of 0.004 mm in the spanwise direction and 0.0036 deg in the pitchwise direction. The uncertainties of the passage mass-averaged total pressure loss coefficient and flow angle were estimated to be 0.0012 and 0.060 deg, respectively.

The pressure probes were calibrated in a probe calibration wind tunnel. The range of the calibration angle was ±30 deg. One pressure transducer (model PDCR23D, Scanivalve Corp., Liberty Lake, WA) with a fluid switch was used to measure all pressure values both in the calibration and in the experiment in order to minimize measurement errors.

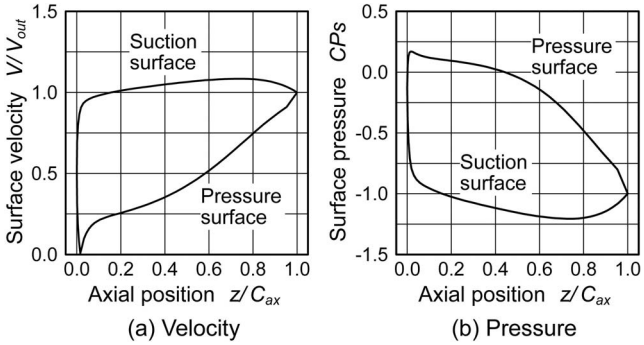

Fig. 4 Design velocity and pressure distributions on surface at turbine cascade midspan

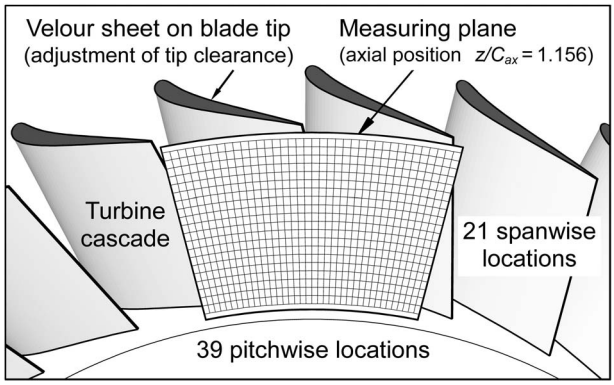

Fig. 5 Measurement locations

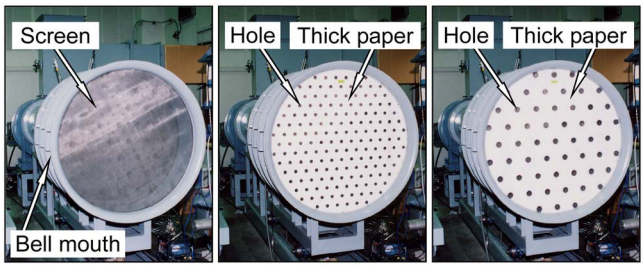

Fig. 6 Adjustment of freestream turbulence intensity

Experimental Conditions. Originally, the turbine cascade fixed on the inner annular wall of the test section had a tip clearance of 0.5 mm (0.67% span) between the blade tip and the outer annular wall (namely, the "with tip clearance" case). A velour sheet tape was attached to the tip of the blade for obviation of the tip clearance ("without tip clearance" case).

The Reynolds number based on the true chord length and exit velocity of the turbine cascade Re_{out} was varied from 4.4×10^4 to 26.6×10^4 by changing the axial flow velocity at the test section, approximately from 4 to 24 m/s. The flow in this experiment was regarded as incompressible because the Mach number based on the exit velocity was very low, at M_{out}=0.028–0.177.

The wind tunnel had a low freestream turbulence intensity with a value of 0.5% at the inlet of the test section. The freestream inlet turbulence intensity Tu_{in} was varied from 0.5% to 4.1% using turbulence-generating sheets (Fig. 6) to produce a high inlet turbulence intensity that was more representative of that in a real turbine, rather than the low inlet turbulence obtained in typical wind tunnels. As shown in Fig. 6, these sheets were made of 1 mm-thick paper in which several holes were punched at equally spaced intervals, placed on a screen in the bell-mouth section. Table 2 shows the turbulence intensities and integral length scales at the midspan of the turbine inlet measured by the single-element, hot-wire anemometer. The turbulence length scale was determined from a time trace of the instantaneous streamwise velocity. The averaged turbulence length scale was approximately 90 mm for low turbulence intensity and 10 mm for high turbulence intensity, which resembles the values obtained in the other wind tunnels (Ames [29], and Boyle et al. [30]).

Results and Discussion

Inlet Flow Conditions

Effect of Reynolds Number. Figure 7 shows the spanwise distributions of inlet velocity, total pressure loss, and turbulence intensity at three Reynolds numbers ($Re_{out}=26.6\times10^4$, 13.4×10^4, and 4.4×10^4) for the lowest free-stream turbulence intensity Tu_{in}=0.5%. The velocity distribution of the freestream (spanwise distance y/H=0.1 to 0.9) had an almost constant value; i.e., no

Table 2 Turbulence intensities and length scales at midspan of turbine inlet (axial position $z/C_{ax}=-0.706$)

Reynolds number Re_{out}	Turbulence intensity Tu_{in}(%)			Integral length scale of turbulence L_c(mm)		
	Setting No. 1	Setting No. 2	Setting No. 3	Setting No. 1	Setting No. 2	Setting No. 3
4.3×10^4	0.5	0.9	2.8	67.4	16.9	10.9
8.9×10^4	0.5	1.1	3.6	74.0	12.1	8.4
13.4×10^4	0.5	1.3	4.1	82.9	10.2	8.4
18.0×10^4	0.5			98.6		
22.2×10^4	0.5			98.0		
26.7×10^4	0.5			102.5		
Average	0.5	1.1	3.5	87.2	13.1	9.2

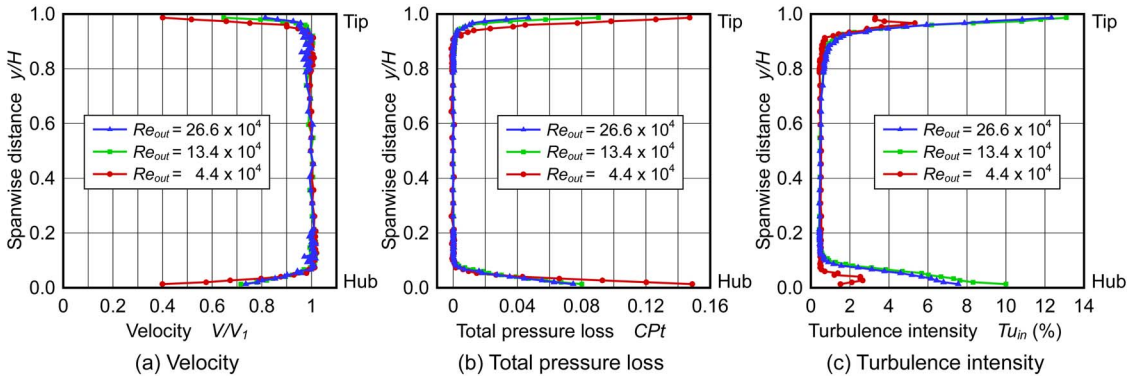

Fig. 7 Spanwise distributions of inlet velocity, total pressure loss, and turbulence intensity at three Reynolds numbers (freestream turbulence intensity Tu_{in}=0.5%, axial position $z/C_{ax}=-0.706=-0.706$)

Table 3 Effect of Reynolds number on inlet boundary layers ($Tu_{in}=0.5\%$)

Re_{out}	Tip boundary layer $\delta_1/H(\%)$	Tip boundary layer $\delta_2/H(\%)$	Tip boundary layer H_{12}	Hub boundary layer $\delta_1/H(\%)$	Hub boundary layer $\delta_2/H(\%)$	Hub boundary layer H_{12}
4.3×10^4	2.36	1.09	2.17	2.23	0.99	2.24
8.9×10^4	1.63	0.78	2.09	1.56	0.75	2.08
13.4×10^4	1.41	0.72	1.97	1.67	0.98	1.71
18.0×10^4	1.35	0.77	1.76	1.67	1.00	1.67
22.2×10^4	1.21	0.68	1.78	1.66	1.01	1.65
26.7×10^4	1.22	0.72	1.69	1.66	0.99	1.68

velocity gradient. The total pressure loss and turbulence intensity distribution of the freestream was also uniform and independent of the Reynolds number. The boundary layer thickness was approximately 8% of the blade span at both the tip and hub endwalls. In the boundary layer regions, the velocity deficit in Fig. 7(*a*) and total pressure loss in Fig. 7(*b*) increase as the Reynolds number decreases.

The effect of the Reynolds number on the inlet boundary layers is summarized in Table 3. The boundary layer momentum thickness δ_1 and displacement thickness δ_2, which are normalized by the blade span H, increase as the Reynolds number decreases. The shape factor $H_{12}(=\delta_1/\delta_2)$ at both endwalls is approximately 1.7 in the highest Reynolds number condition ($Re_{out}=26.6\times10^4$) and 2.2 in the lowest Reynolds number condition ($Re_{out}=4.4\times10^4$). In general, the shape factor is $H_{12}=2.6$ in the laminar boundary layer and $H_{12}=1.4$ in the turbulent boundary layer under a no-pressure-gradient condition (Schlichting [31]). Therefore, the boundary layer is considered to be a near-turbulent regime at the high Reynolds number and near-laminar regime at the low Reynolds number.

In Fig. 7(*c*), the turbulence intensity near the tip and hub endwalls decreases suddenly as the Reynolds number decreases, from 10%–13% at the high and middle Reynolds number ($Re_{out}=26.6\times10^4$ and 13.4×10^4) to 2%–5% at the low Reynolds number ($Re_{out}=4.4\times10^4$), which is associated with the transformation of the inlet boundary layer from the turbulent regime to the laminar regime.

Effect of Freestream Turbulence Intensity. Figure 8 shows the spanwise distributions of inlet velocity, total pressure loss, and turbulence intensity at three freestream turbulence intensities ($Tu_{in}=0.5\%$, 1.3%, and 4.1%) at $Re_{out}=13.4\times10^4$, which corresponds to the middle Reynolds number in this study. The distributions of velocity and total pressure loss in Figs. 8(*a*) and 8(*b*) are uniform in the freestream region. The distributions of the turbulence intensity at the freestream region in Fig. 8(*c*) are almost constant, although a deviation of ±0.28% is observed in the high freestream turbulence intensity condition $Tu_{in}=4.1\%$ (the red line in Fig. 8(*c*)).

The effect of freestream turbulence intensity on the inlet boundary layers is summarized in Table 4. The boundary layer momentum thickness δ_1 and displacement thickness δ_2 increase slightly as the freestream turbulence intensity increases. The shape factor H_{12} decreases as the freestream turbulence intensity increases, which means that the boundary layer at a high freestream turbulence intensity is closer to the turbulent regime than that at a low freestream turbulence intensity. The effect of the freestream turbulence intensity is relatively smaller than that of the Reynolds number.

Total Pressure Loss Distributions

Effect of Reynolds Number. Figure 9 shows the effect of the Reynolds number on total pressure loss distributions at the exit of the turbine cascade. The upper figures (Fig. 9(*a*)) show the high Reynolds number condition ($Re_{out}=26.6\times10^4$) and the lower figures (Fig. 9(*b*)) show the low Reynolds number condition ($Re_{out}=4.4\times10^4$). The freestream turbulence intensity for both Rey-

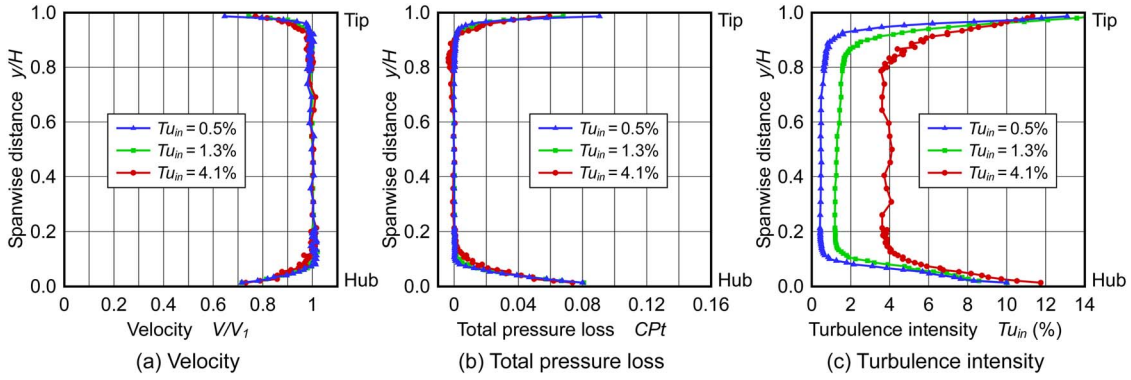

Fig. 8 Spanwise distributions of inlet velocity, total pressure loss, and turbulence intensity at three freestream turbulence intensities (Reynolds number $Re_{out}=13.4\times10^4$, axial position $z/C_{ax}=-0.706=-0.706$)

Table 4 Effect of freestream turbulence intensity on inlet boundary layers ($Re_{out}=13.4\times10^4$)

Tu_{in}	Tip boundary layer $\delta_1/H(\%)$	Tip boundary layer $\delta_2/H(\%)$	Tip boundary layer H_{12}	Hub boundary layer $\delta_1/H(\%)$	Hub boundary layer $\delta_2/H(\%)$	Hub boundary layer H_{12}
0.5%	1.41	0.72	1.97	1.67	0.98	1.71
1.3%	1.32	0.74	1.78	1.75	1.05	1.67
4.1%	1.58	1.00	1.59	1.93	1.24	1.55

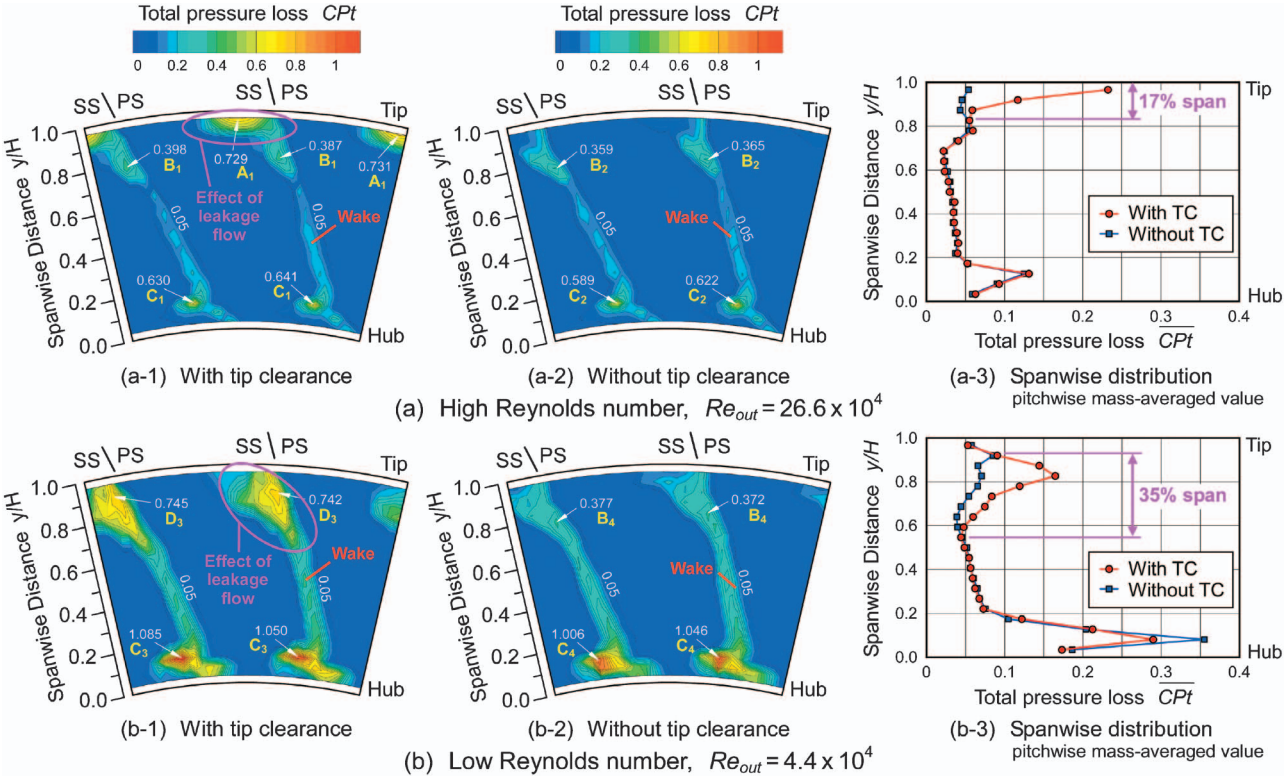

Fig. 9 (Color) Effect of Reynolds number on total pressure loss distributions at exit of turbine cascade (Tu_{in}=0.5%)

nolds numbers is fixed at Tu_{in}=0.5%. The left-hand figures (Figs. 9(*a*-1) and 9(*b*-1)) show the distributions with tip clearance, the central figures (Figs. 9(*a*-2) and 9(*b*-2)) show the distributions without tip clearance, and the right-hand figures (Figs. 9(*a*-3) and 9(*b*-3)) show the spanwise distributions with and without tip clearance. The spanwise distributions were obtained by calculating the pitchwise mass-averaged values of the total pressure loss at each spanwise position.

First, the tip clearance effect at a high Reynolds number is discussed with reference to Fig. 9(*a*). In Fig. 9(*a*-1) with tip clearance, two regions of high total pressure loss exist near the tip endwall (spanwise distance y/H=0.92–1.00, indicated by "A") and behind the trailing-edge suction side (SS) (spanwise distance y/H=0.68–0.29, indicated by "B"). In a comparison between Figs. 9(*a*-1) and 9(*a*-2), high-loss region "A" is clearly observed only in Fig. 9(*a*-1) with tip clearance, because the region is caused by the leakage vortex through the tip clearance. On the other hand, high-loss region "B" is observed in both Figs. 9(*a*-1) and 9(*a*-2), since a passage vortex sweeps up the inlet endwall boundary layer fluid on the suction surface. The tip leakage vortex produces larger total pressure loss than the tip-side passage vortex. The maximum peak value of high-loss region A_1 due to the tip leakage vortex is approximately double the maximum peak value of high-loss region B_1 due to the tip-side passage vortex. Although high-loss region "C," which is caused by the secondary flow, exists near the hub endwall, the tip clearance flow has no effect on the loss distribution around the region. These loss distributions are similar to those of previous experimental studies in high Reynolds number conditions (e.g., Dishart and Moore 4). Figure 9(*a*-3) clearly demonstrates that the tip clearance flow affects only the tip-side area (y/H=0.83–1.00, 17% of the blade span).

Second, the effect of the Reynolds number is discussed by means of a comparison between Figs. 9(*a*) and 9(*b*). Figure 9(*b*-1) shows the total pressure distribution at the lowest Reynolds number $Re_{out}=4.4\times10^4$ with tip clearance. The high-loss region indicated by "D" spreads widely on the suction side between the spanwise distance y/H=0.58 and the tip endwall (y/H=1.00). Although the high-loss regions near the tip endwall at a high Reynolds number separate into two parts, namely, regions "A" and "B" in Fig. 9(*a*-1), those at a low Reynolds number join together in region "D" in Fig. 9(*b*-1). This is because the tip-side passage vortex increases dramatically as the Reynolds number decreases, and the passage vortex and the tip leakage vortex strongly interact with each other and merge into a combined high-loss region. The high-loss region near the hub endwall, region "C," is also affected by the decrease of the Reynolds number. Region C_3 in Fig. 9(*b*-1) with tip clearance is located at a slightly higher spanwise position than region C_4 in Fig. 9(*b*-2) without tip clearance, because the tip clearance flow induces upward flow in the freestream region and affects the whole flow field, as mentioned later in Fig. 14(*b*-1). Figure 9(*b*-3) shows that the high-loss region due to the tip clearance spreads widely along the suction side from the tip endwall to the midspan direction between y/H=0.58 and y/H=0.93 (35% of the blade span). The effect of the tip clearance on the loss distributions at a high Reynolds number is limited near the tip endwall, whereas that at a low Reynolds number appears in the whole flow field.

Effect of Freestream Turbulence Intensity. Figure 10 shows the effect of the freestream turbulence intensity on total pressure loss distributions at the exit of the turbine cascade. The upper figures (Fig. 10(*a*)) show the low freestream turbulence intensity condition (Tu_{in}=0.5%) and the lower figures (Fig. 10(*b*)) show the high freestream turbulence intensity condition (Tu_{in}=4.1%). The Reynolds number for both turbulence intensity conditions is fixed at $Re_{out}=13.4\times10^4$, which corresponds to the middle Reynolds number in this study.

The effect of the freestream turbulence intensity is discussed by means of a comparison between Figs. 10(*a*) and 10(*b*). The high-loss region of the tip clearance flow at a higher freestream turbulence intensity in Fig. 10(*b*-1) is more concentrated in the tip

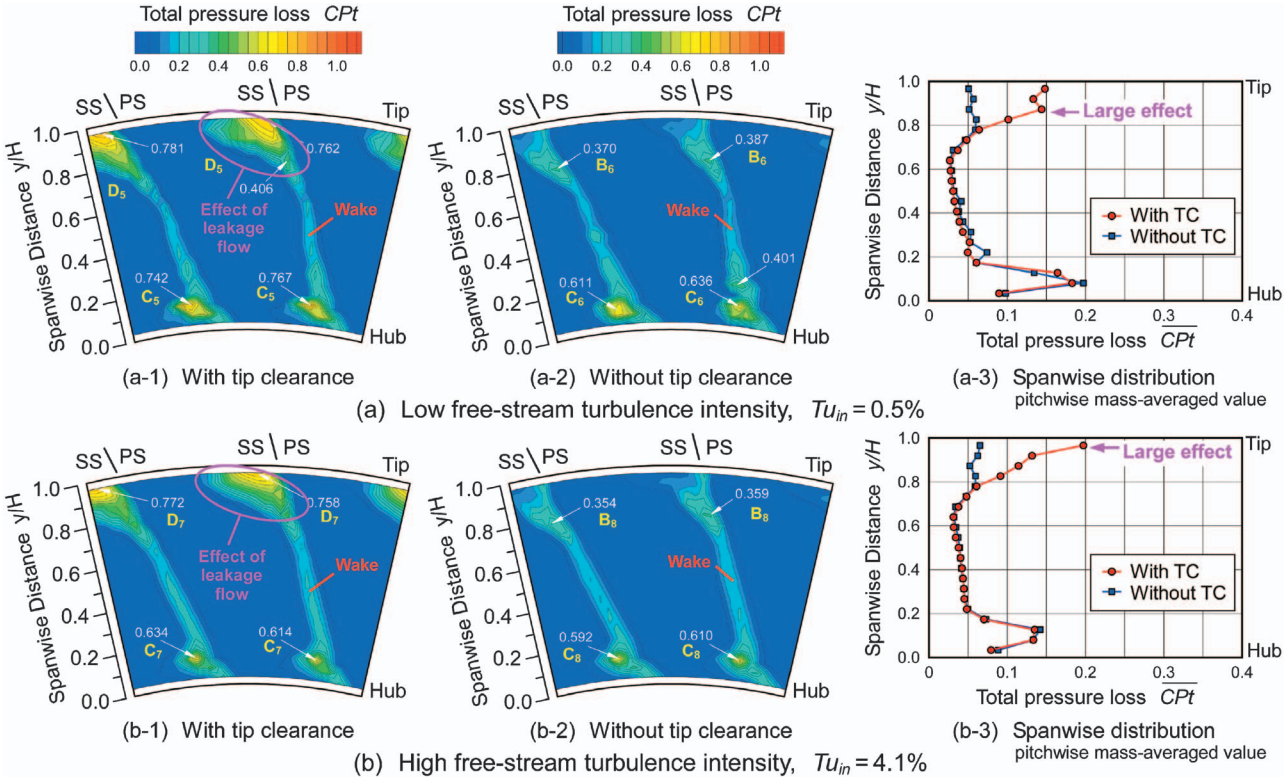

Fig. 10 (Color) Effect of freestream turbulence intensity on total pressure loss distributions at exit of turbine cascade ($Re_{out}=13.4\times10^4$)

region than that at a lower free-stream turbulence intensity in Fig. 10(*a*-1). In Fig. 10(*a*-1) at $Tu_{in}=0.5\%$ with tip clearance, a high total pressure loss region exists on the trailing-edge suction side near the tip endwall (spanwise distance $y/H=0.68$–1.00, indicated by "D_5"). On the other hand, in Fig. 10(*b*-1) at $Tu_{in}=4.1\%$, the high-loss region, indicated by "D_7," spreads on the suction side between the spanwise distance $y/H=0.74$ and the tip endwall ($y/H=1.00$). This is because the high freestream turbulence intensity weakens the passage vortices at the tip and hub endwalls and reduces the effect of rolling up the inlet boundary layer on the suction surface. In the spanwise distributions in Figs. 10(*a*-3) and 10(*b*-3), the maximum difference between the cases with and without tip clearance is observed around $y/H=0.87$ at $Tu_{in}=0.5\%$, whereas the maximum difference is observed near the tip endwall $y/H=0.97$ at $Tu_{in}=4.1\%$.

The effect of the freestream turbulence intensity shown in Fig. 10 is less conspicuous than the effect of the Reynolds number shown in Fig. 9.

Tip Clearance Loss (Mass-Averaged Value)

Mass-Averaged Total Pressure Loss. Figure 11 shows the mass-averaged total pressure loss at the exit of the turbine cascade, CPt_{out}. These values were obtained by calculating the pitchwise and spanwise mass-averaged values of total pressure loss in Figs. 9 and 10. The red lines indicate the condition with tip clearance and the blue lines indicate that without tip clearance. The exit loss CPt_{out} increases dramatically as the Reynolds number decreases. This increase in loss is caused by the increased profile loss (loss associated with the boundary layer, separation, and wake) and the increased secondary loss (loss associated with the secondary vortex), which are produced by the thickened and laminarized boundary layer accompanying the decrease in the Reynolds number.

Measured Tip Clearance Loss. Figure 12 shows the tip clearance loss CPt_{TC}. These values were obtained by calculating the difference between the exit losses with and without tip clearance in Fig. 11. The average of the tip clearance loss is 0.0153 and the deviation is only ±0.0004, which corresponds to ±2.6% of the averaged value. The Reynolds number and freestream turbulence intensity have no effect on the tip clearance loss (mass-averaged value). This result contrasts remarkably with the sudden increase in the profile loss and the secondary loss accompanying the decrease in the Reynolds number.

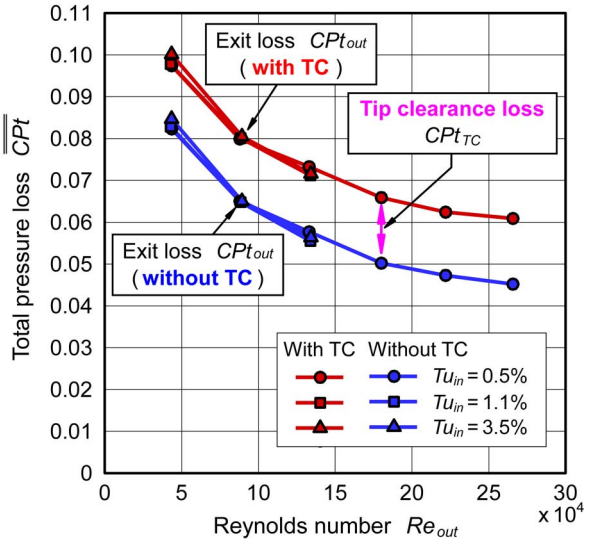

Fig. 11 Mass-averaged exit loss

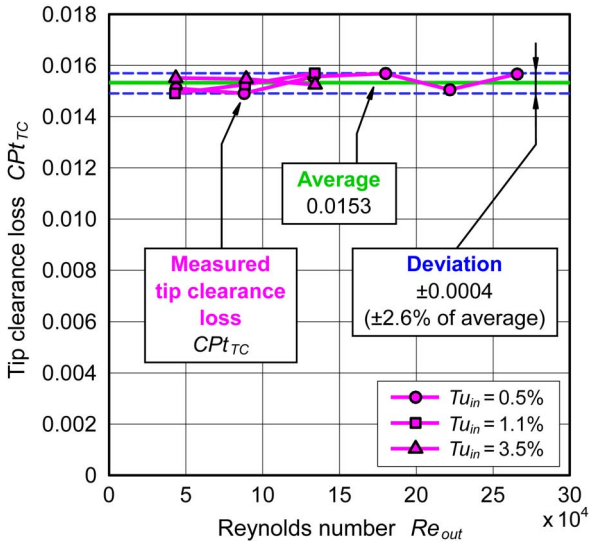

Fig. 12 Measured tip clearance loss

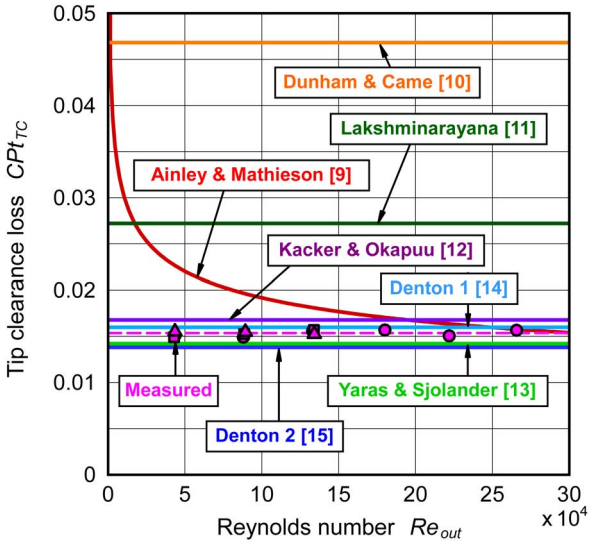

Fig. 13 Measured and predicted tip clearance losses

Comparison between Measured and Predicted Tip Clearance Losses. Numerous efforts over a long period have focused on the prediction of tip clearance loss, in order to clarify the effects of tip clearance in turbines. Table 5 shows various correlations of the tip clearance loss. These prediction methods are empirical correlations based on many turbine rig tests. The parameters for the correlations are the size of the tip clearance and blade properties such as chord length, blade height, lift coefficient, flow angle, and so on.

Figure 13 shows a comparison between the measured and pre-

Table 5 Various correlations of tip clearance loss

Prediction method	Tip clearance loss CPt_{TC}
Ainley and Mathieson [9]	$0.5\left(\frac{k}{h}\right)\left(\frac{c}{s}\right)^2 C_L^2\left(\frac{\cos^2\alpha_2}{\cos^3\alpha_m}\right)\left(\frac{\mathrm{Re}}{2\times 10^5}\right)^{-0.2}$
Dunham and Came [10]	$0.47\left(\frac{c}{h}\right)\left(\frac{k}{c}\right)^{0.78}\left(\frac{c}{s}\right)^2 C_L^2\left(\frac{\cos^2\alpha_2}{\cos^3\alpha_m}\right)$
Lakshminarayana [11]	$\Delta\eta = 0.7\left(\frac{k}{h}\right)\left(\frac{\psi}{\cos\alpha_m}\right)\left[1+10\sqrt{\left(\frac{k}{c}\right)\left(\frac{\varphi}{\psi}\right)\left(\frac{1}{\cos\alpha_m}\right)}\right]$
Kacker and Okapuu [12]	$\frac{\Delta\eta}{n_{\text{without TC}}} = 0.93\left(\frac{k}{h}\right)\left(\frac{1}{\cos\alpha_2}\right)\left(\frac{R_{\text{tip}}}{R_{\text{mean}}}\right)$
Yaras and Sjolander [13]	$2K_E C_D\left(\frac{k}{h}\right)\left(\frac{c}{s}\right) C_L^{1.5}\left(\frac{\cos^2\alpha_2}{\cos^3\alpha_m}\right)$
Denton 1 [14]	$2C_D\left(\frac{k}{h}\right)\left(\frac{c}{s}\right)\left(\frac{1}{\cos\alpha_2}\right)\int_0^1\left(\frac{V_s}{V_2}\right)^3\left(1-\frac{V_p}{V_s}\right)\sqrt{\left[1-\left(\frac{V_p}{V_s}\right)^2\right]}\frac{dz}{c}$
Denton 2 [15]	$\frac{\Delta\eta}{\eta_{\text{without TC}}} = 0.6\left(\frac{k}{h}\right)\left(\frac{c}{s}\right)\left(\frac{1}{\cos\alpha_2}\right)$

Note: c: chord length C_D: discharge coefficient
C_L: lift coefficient h: blade height
K_E: constant related to loading distribution
k: tip clearance R: radius s: pitch
V_2: exit velocity V_p: surface velocity on pressure side
V_s: surface velocity on suction side α_2: exit flow angle
α_m: mean flow angle $\Delta\eta$: efficiency drop η: efficiency
ϕ: flow coefficient ψ: blade loading coefficient

Table 6 Predicted values of tip clearance loss

Correlation	CPt_{TC}	Correlation	CP_{TC}
Measurement	0.0153 (0%)	Kacker and Okapuu [12]	0.0170 (+11.1%)
Ainley and Mathieson [9]	0.0167 at $Re=2\times10^5$	Yaras and Sjolander [13]	0.0140 (−8.5%)
Dunham and Came [10]	0.0468 (+205.9%)	Denton 1 [14]	0.0164 (+7.2%)
Lakshminarayana [11]	0.0272 (+77.8%)	Denton 2 [15]	0.0139 (−9.2%)

dicted tip clearance losses. Table 6 summarizes the comparison between the measurement and predictions.

The correlation presented by Ainley and Mathieson [9] in 1951 is the most famous correlation, which is widely utilized in the design procedure for turbines even in the present day. The prediction of the Ainley-Mathieson correlation, indicated by the red line in Fig. 10, has good agreement with the measured data at higher Reynolds numbers over 2×10^5, although it overpredicts the tip clearance loss at lower Reynolds numbers. This is caused by the dependence of the tip clearance loss of the Ainley-Mathieson correlation upon the −0.2 power law of the Reynolds number.

Dunham and Came [10] presented a revised correlation of the Ainley-Mathieson correlation in 1970. The Dunham-Came correlation removed the Reynolds number dependence of the tip clearance loss from the Ainley-Mathieson correlation, because the effect of the Reynolds number on the tip clearance flow was uncertain. The predicted tip clearance loss of the Dunham-Came correlation (orange line) is three times larger than the measured value. The overprediction of the Dunham-Came correlation was also described by Yaras and Sjolander [13].

Lakshminarayana [11] provided a correlation based on a potential vortex model in 1970. The predicted value (dark green line) is 1.8 times larger than the measured value. Similar overpredictions of the correlation were observed by Booth [1], who explained that the overprediction was caused by the fact that the correlation was derived from compressor data, not turbine data.

Kacker and Okapuu [12] presented a further revised correlation of the Ainley-Mathieson and Dunham-Came correlations in 1982. The difference between the predicted value (0.0170, purple line) and the measured value (0.0153) is +0.0017, which corresponds to +11.1% of the measured value. This difference is within the error range of 15% described by Kacker and Okapuu themselves.

In 1992, Yaras and Sjolander [13] reviewed the previous correlations of tip clearance loss and provided an improved prediction method that is consistent with detailed experimental observations. The Yaras-Sjolander correlation (light green line) agrees well with the measurements. The value of 0.0140 predicted from the Yaras-Sjolander correlation has a small difference of −0.0013(−8.5%) from the measured data.

Denton [14] gave a comprehensive lecture on loss mechanisms in turbomachinery in 1993. The difference between the predicted value (0.0164, light blue line) and the measured value (0.0153) is only +0.0011(+7.2%). The simplest correlation by Denton [15] predicted a value of 0.0139 (dark blue line), which is 0.0014 (9.2%) smaller than the measured value.

Recent prediction methods of tip clearance loss by Yaras and Sjolander [13] and Denton [14,15] give satisfactory agreement of within ±10% with the measured data in this study.

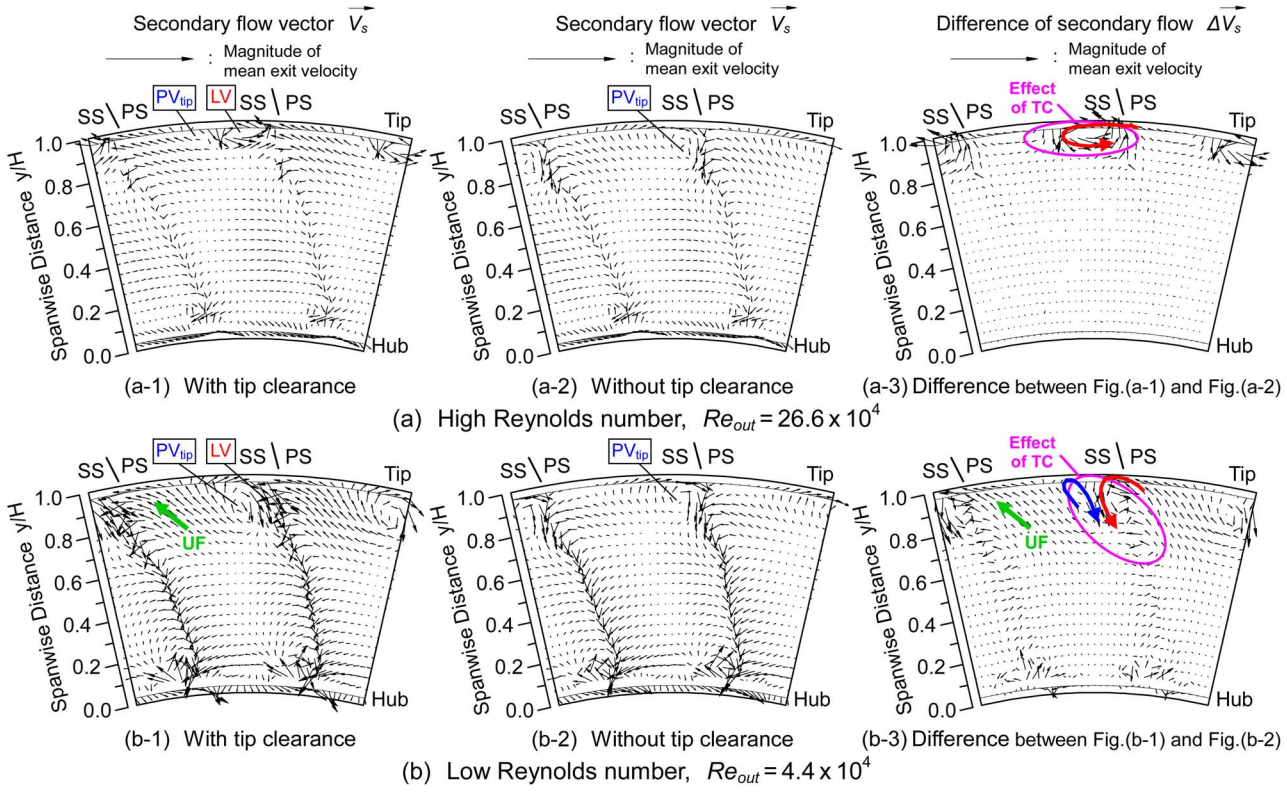

Fig. 14 Effect of Reynolds number on secondary flow vector distributions at exit of turbine cascade ($Tu_{in}=0.5\%$)

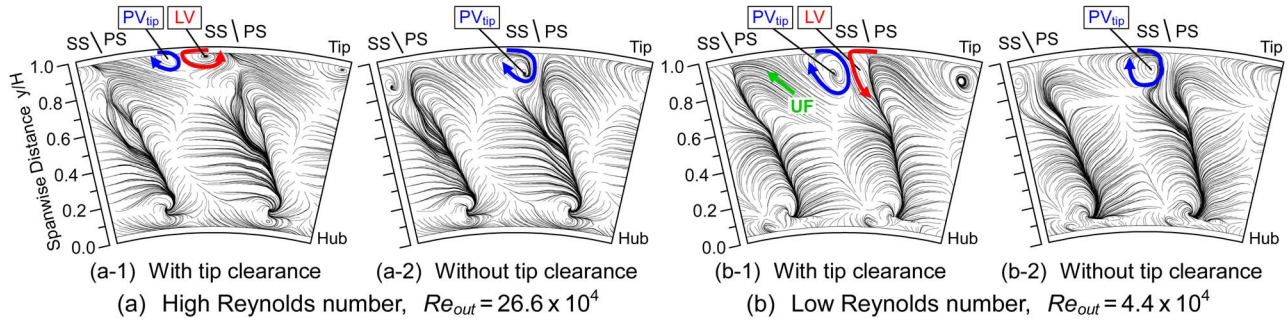

Fig. 15 Effect of Reynolds number on trace of secondary flow (Tu_{in}=0.5%)

Fluid Mechanisms of Three-Dimensional Flow

Effect of Reynolds Number. Figure 14 shows the effect of the Reynolds number on secondary flow vector distributions at the exit of the turbine cascade. The secondary flow vector is defined as a local velocity component normal to the design average streamwise direction (67.4 deg). The upper figures (Fig. 14(*a*)) show the high Reynolds number condition ($Re_{out}=26.6\times10^4$) and the lower figures (Fig. 14(*b*)) show the low Reynolds number condition ($Re_{out}=4.4\times10^4$). The left-hand figures (Figs. 14(*a*-1) and 14(*b*-1)) show the distributions with tip clearance, the central figures (Figs. 14(*a*-2) and 14(*b*-2)) show the distributions without tip clearance, and the right-hand figures (Figs. 14(*a*-3) and 14(*b*-3)) show the difference between the distributions with and without tip clearance. Figure 15 shows the traces of the secondary flow vectors in Fig. 14.

The tip clearance effect at a high Reynolds number is discussed next with reference to Figs. 14(*a*) and 15(*a*). In the "without tip clearance" cases shown in Figs. 14(*a*-2) and 15(*a*-2), a clockwise passage vortex (indicated by "PV_{tip}") exists near the tip endwall of the suction surface. In the "with tip clearance" cases shown in Figs. 14(*a*-1) and 15(*a*-1), a counterclockwise leakage vortex (indicated by "LV") exists close to the tip endwall. The passage vortex in Figs. 14(*a*-1) and 15(*a*-1) is weakened by the leakage vortex and shifts to a position distant from the suction side. The difference of the velocity vectors shown in Fig. 14(*a*-3) also clearly demonstrates the influence of the tip leakage vortex.

The effect of the Reynolds number is now discussed by means of a comparison between (*a*) and (*b*) in Figs. 14 and 15. In Figs. 14(*a*-2) and 14(*b*-2) without tip clearance, the passage vortex strengthens as the Reynolds number decreases, because of the thick boundary layer thickness in the low Reynolds number condition. In Figs. 14(*a*-1) and 14(*b*-1) with tip clearance, the leakage vortex is swept up on the suction surface due to the strengthening of the passage vortex as the Reynolds number decreases. At a high Reynolds number, as mentioned above, the tip-side passage vortex is weakened by the leakage vortex. At a low Reynolds number, however, the passage vortex is strengthened by the leakage vortex, because of the strong interaction between the passage vortex and leakage vortex (the blue and red lines in Fig. 14(*b*-3)).

At the low Reynolds number shown in Fig. 14(b-1), the leakage vortex induces upward flow in the freestream region near the tip endwall pressure side (indicated by "UF" in Fig. 14(*b*-1)). The upward flow causes the upward shift of the region of the hub-side passage vortex. Although the tip clearance flow at a high Reynolds number affects only the vicinity of the tip region in Fig. 14(*a*-3), the tip clearance flow at a low Reynolds number affects the whole flow field in Fig. 14(*b*-3).

Figure 16 shows the effect of the Reynolds number on axial vorticity distributions at the exit of the turbine cascade. In this figure, the black line contours of the total pressure loss are superimposed on the color flood contours of the axial vorticity. The tip leakage vortex "LV" (counter-clockwise rotation) and the tip-side passage vortex "PV_{tip}" (clockwise rotation) have positive and negative vorticity, respectively. Figures 16(*a*-3) and 16(*b*-3) show enlarged views near the tip endwall with tip clearance, of the square regions in Figs. 16(*a*-1) and 16(*b*-1). The secondary flow vectors in Fig. 14 are also superimposed in the figures. The core of the high total pressure loss exists in the region of tip leakage vortex at both high and low Reynolds numbers.

Effect of Freestream Turbulence Intensity. Figure 17 shows the effect of the freestream turbulence intensity on the traces of the secondary flow vectors. The tip-side passage vortex and tip leakage vortex at the higher freestream turbulence intensity shown in Fig. 17(*b*-1) are more concentrated in the tip region than those at the lower freestream turbulence intensity shown in Fig. 17(*a*-1). This is because the passage vortices near the tip and hub endwalls are weakened as a result of the high freestream turbulence.

Flow Angle

Spanwise Distributions of Flow Angle. Figure 18 shows the spanwise distributions of the flow angle at the exit of the turbine cascade. These values were obtained by calculating the pitchwise mass-averaged values at each spanwise position. The tip leakage vortex generates a low-flow-angle region (an underturning region) near the tip. The decrease in the flow angle due to the tip clearance becomes larger as the Reynolds number decreases. This is because the leakage vortex is swept up on the suction surface due to the strengthened passage vortex at a low Reynolds number.

Mass-Averaged Flow Angle. Figure 19 shows the mass-averaged flow angle at the exit of the turbine cascade. These values were obtained by calculating the pitchwise and spanwise mass-averaged values of flow angle distributions. At a higher Reynolds number without tip clearance, the exit flow angle closes toward the design value, 67.4 deg. The existence of tip clearance causes a decrease in the exit flow angle. The exit flow angle decreases steadily as the Reynolds number decreases. This decrease in flow angle is caused by the increased boundary layer, separation, and secondary flows as the Reynolds number decreases.

Tip Clearance Effect on Mass-Averaged Flow Angle. Figure 20 shows the decrease in flow angle due to the existence of the tip clearance, which is defined as the difference of the mass-averaged flow angle between the cases with and without tip clearance in Fig. 19. The decrease in the flow angle predicted by Ainley and Mathieson [9] is also shown as the green dashed line in Fig. 20.

The decrease in flow angle at the higher Reynolds number is very close to the predicted value of Ainley and Mathieson's correlation. The decrease in flow angle at lower Reynolds numbers is larger than that at higher Reynolds numbers. This is because of the strong interaction between the passage vortex and the leakage vortex and the sweeping up of the low-energy fluid on the blade

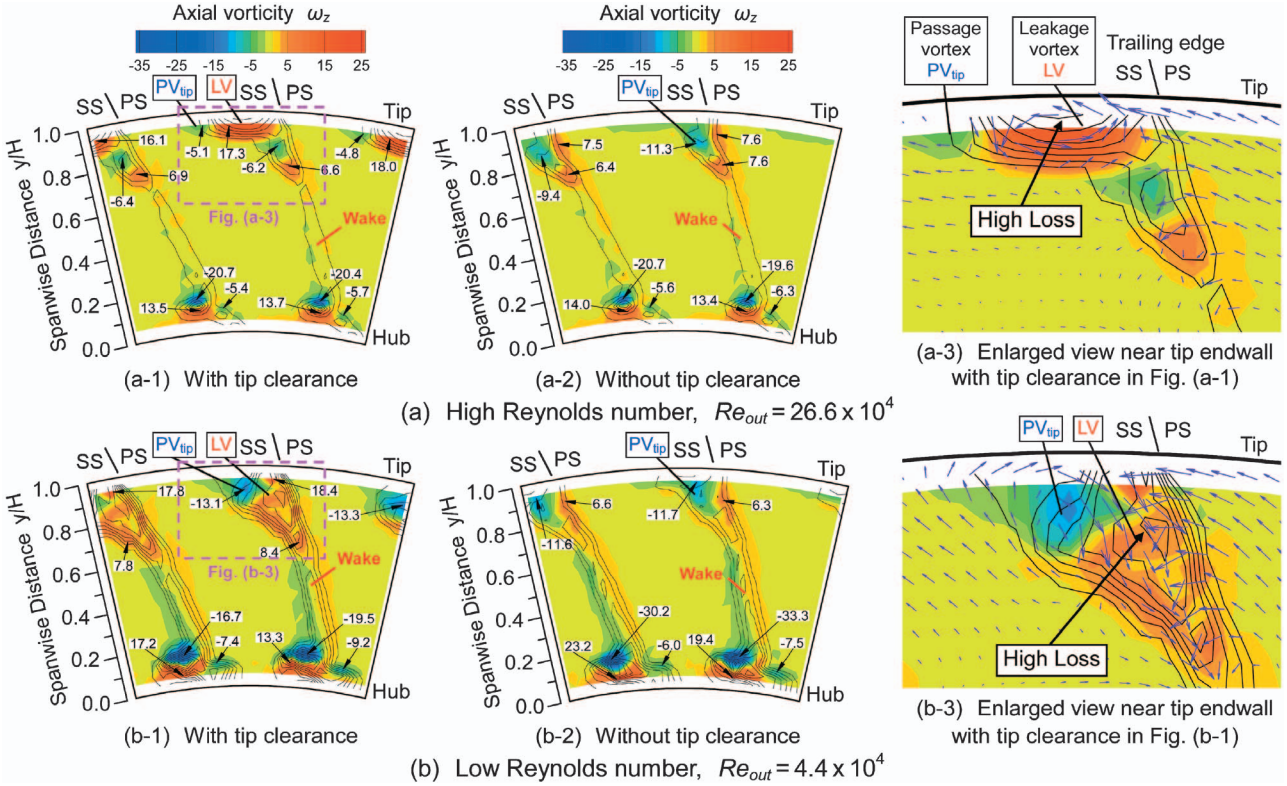

Fig. 16 (Color) Effect of Reynolds number on axial vorticity distributions at exit of turbine cascade (Tu_{in}=0.5%): line contours of total pressure loss superimposed on flood contours of axial vorticity

suction surface. This fact contrasts with the finding that the mass-averaged tip clearance loss remains constant at various Reynolds numbers (Fig. 12).

The increase in freestream turbulence intensity from 0.5% to 1.3% results in the improvement of the decrease in flow angle. This is because the higher turbulence intensity induces the transition of the boundary layer on the endwalls. The boundary layer transition weakens the growth of the tip-side passage vortex and reduces the interaction between the passage vortex and the tip clearance vortex. However, the increase in freestream turbulence intensity from 1.3% to 4.1% produces almost no improvement of the decrease in the flow angle. The reason for this may be that the increase in free-stream turbulence intensity does not induce a change in the boundary layer at relatively higher turbulence intensity conditions.

It is important to accurately predict the decrease in the exit flow angle in order to design a high-performance turbine operating at low Reynolds numbers, because the decreased flow angle causes a mismatch of the incidence angle of the downstream blade row and a reduction in the turbine efficiency. In this turbine, for example, a 1 deg decrease in the exit flow angle causes a decrease of approximately 5 deg in the incidence angle of the downstream turbine cascade.

Conclusions

This paper describes the effect of tip clearance on the aerodynamic characteristics of a turbine cascade under very low Reynolds number conditions, $Re_{out}=4.4\times10^4\sim26.6\times10^4$. The freestream turbulence intensity was varied between 0.5% and 4.1%. Three-dimensional flow fields at the exit of the turbine cascade were measured both with and without tip clearance using a five-hole pressure probe.

1. Tip leakage flow generated a large high total pressure loss region. The distributions of loss and three-dimensional flow were strongly affected by the Reynolds number. The tip leakage vortex remained near the tip endwall region at higher Reynolds numbers. At lower Reynolds numbers,

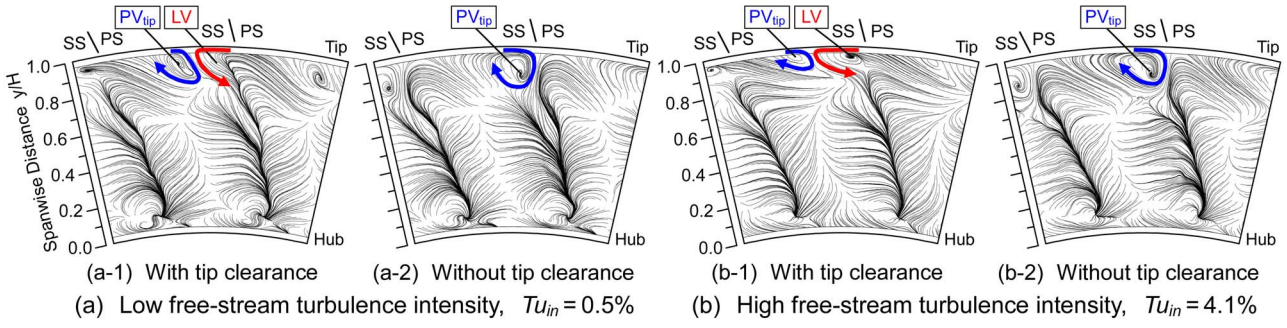

Fig. 17 Effect of freestream turbulence intensity on trace of secondary flow ($Re_{out}=13.4\times10^4$)

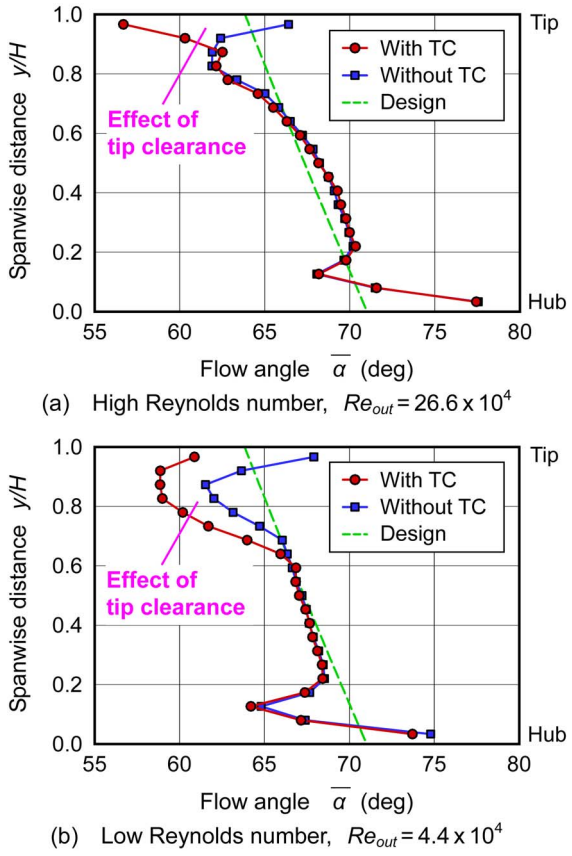

Fig. 18 Effect of Reynolds number on spanwise distributions of flow angle (Tu_{in}=0.5%)

however, the leakage vortex spread toward the midpassage and affected a wide area of the passage because of the strong interaction between the leakage vortex and the tip-side passage vortex.

2. The tip clearance loss (the mass-averaged loss that was generated by the tip clearance flow) remained almost constant for various Reynolds numbers and freestream turbulence intensities. This result was in contrast to the sudden increase in the profile loss and the secondary loss at low Reynolds numbers.
3. The tip clearance losses predicted by the existing models were compared with the measured loss. Recent models gave satisfactory results within ±10% of the loss measured in this study.
4. The decrease in the mass-averaged exit flow angle due to the tip clearance showed a gradual increase as the Reynolds number decreased. This is because of the strong interaction between the leakage vortex and the passage vortex at low Reynolds numbers.

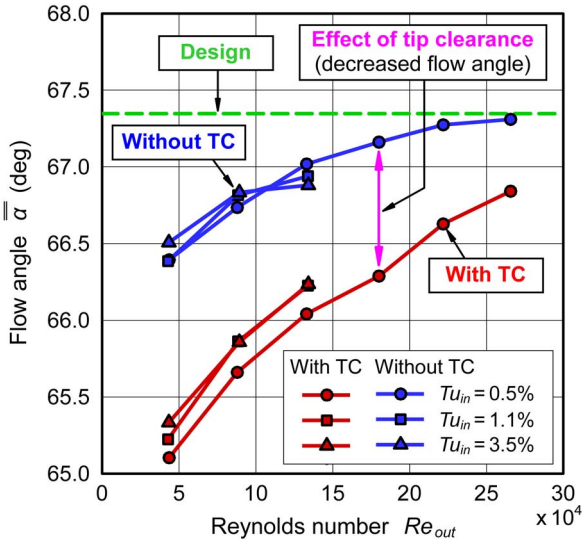

Fig. 19 Mass-averaged exit flow angle

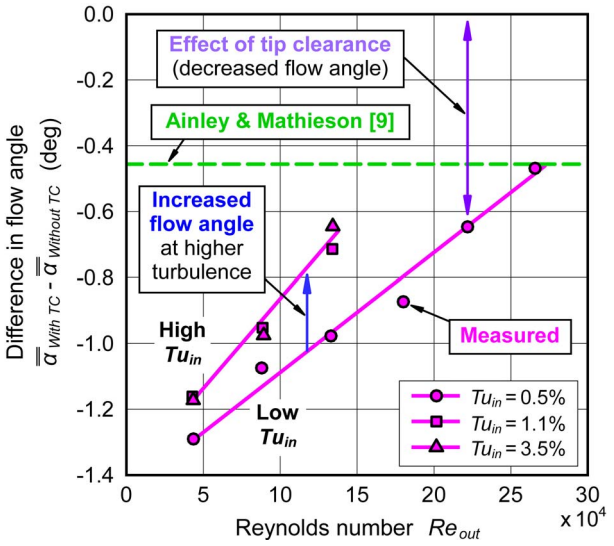

Fig. 20 Decrease in exit flow angle due to tip clearance

Acknowledgment

This study was supported by a grant from the "Micro Gas Turbine/Solid Oxide Fuel Cell Hybrid Cycle for Distributed Energy System" research project of the Department of Core Research for Evolutional Science and Technology (CREST) of the Japan Science and Technology Agency (JST). The author would like to thank Professor Haruo Yoshiki of the University of Tokyo, and Dr. Yasukata Tsutsui and Dr. Hiro Yoshida of the National Institute of Advanced Industrial Science and Technology, for their help during the course of this work.

Nomenclature

C = chord length
C_{ax} = axial chord length
CPs = static pressure $CPs=(Ps-Ps_{in,midspan})/\frac{1}{2}\rho\overline{\overline{V_{out}}}^2$
CPt = total pressure loss $CPt=(Pt_{in,midspan}-Pt)/\frac{1}{2}\rho\overline{\overline{V_{out}}}^2$
H = blade span
H_{12} = shape factor ($=\delta_1/\delta_2$)
k = tip clearance
LE = leading edge
L_z = integral length scale of turbulence
PS = pressure surface side
Ps = static pressure
Pt = total pressure
r = radial distance
Re = Reynolds number
SS = suction surface side
TE = trailing edge
Tu = turbulence intensity
S = blade pitch

V = velocity
V_s = secondary flow vector
y = spanwise distance from hub endwall
z = axial distance from leading edge at midspan
α = flow angle measured from axial direction
δ_1 = boundary layer displacement thickness
δ_2 = boundary layer momentum thickness
η = isentropic efficiency
θ = tangential (pitchwise) distance
ω_z = axial vorticity (positive value indicates counter-clockwise rotation)

$$\omega_z = (\partial(rV_\theta)/r\partial r - \partial V_r/r\partial\theta)C_{\text{midspan}}/\bar{\bar{V}}_z$$

Subscripts

hub = blade hub side
in = blade inlet
out = blade exit
tip = blade tip side
TC = tip clearance
– = pitchwise mass-averaged value
= = pitchwise and spanwise mass-averaged value

References

[1] Booth, T. C., 1985, "Importance of Tip Clearance Flows in Turbine Design," VKI Lecture Series 1985–05, *Tip Clearance Effects in Axial Turbomachines*, von Karman Institute for Fluid Dynamics, Belgium, pp. 1–34.
[2] Sjolander, S. A., 1997, "Overview of Tip-Clearance Effects in Axial Turbines," VKI Lecture Series 1997–01, *Secondary and Tip-Clearance Flows in Axial Turbines*, von Karman Institute for Fluid Dynamics, pp. 1–29.
[3] Bindon, J. P., 1989, "The Measurement and Formation of Tip Clearance Loss," ASME J. Turbomach., **111**, pp. 257–263.
[4] Dishart, P. T., and Moore, J., 1990, "Tip Leakage Losses in a Linear Turbine Cascade," ASME J. Turbomach., **112**, pp. 599–608.
[5] Yaras, M., and Sjolander, S. A., 1990, "Development of the Tip-Leakage Flow Downstream of a Planar Cascade of Turbine Blades: Vorticity Field," ASME J. Turbomach., **112**, pp. 609–617.
[6] Heyes, F. J. G., and Hodson, H. P., 1993, "Measurement and Prediction of Tip Clearance Flow in Linear Turbine Cascade," ASME J. Turbomach., **115**, pp. 376–382.
[7] Heyes, F. J. G., Hodson, H. P., and Dailey, G. M., 1992, "The Effect of Blade Tip Geometry on the Tip Leakage Flow in Axial Turbine Cascades," ASME J. Turbomach., **114**, pp. 643–651.
[8] Morphis, G., and Bindon, J. P., 1994, "The Performance of a Low Speed One and Half Stage Axial Turbine with Varying Rotor Tip Clearance and Tip Gap Geometry," ASME Paper No. 94-GT-481.
[9] Ainley, D. G., and Mathieson, G. C. R., 1951, "A Method of Performance Estimation for Axial-Flow Turbines," A.R.C. Technical Report R&M, No. 2974, British Aeronautical Research Council.
[10] Dunham, J., and Came, P. M., 1970, "Improvements to the Ainley-Mathieson Method of Turbine Performance Prediction," ASME J. Eng. Power, **92**, pp. 252–256.
[11] Lakshminarayana, B., 1970, "Methods of Predicting the Tip Clearance Effects in Axial Flow Turbomachinery," ASME J. Basic Eng., pp. 467–482.
[12] Kacker, S. C., and Okapuu, U., 1982, "A Mean Line Prediction Method for Axial Flow Turbine Efficiency," ASME J. Eng. Power, **104**, pp. 111–119.
[13] Yaras, M. I., and Sjolander, S. A., 1992, "Prediction of Tip-Leakage Losses in Axial Turbines," ASME J. Turbomach., **114**, pp. 204–210.
[14] Denton, J. D., 1993, "Loss Mechanisms in Turbomachines," ASME J. Turbomach., **115**, pp. 621–656.
[15] Denton, J. D., 2004, "Axial Turbine Aerodynamic Design," *Cambridge Turbomacninery Course*, Whittle Laboratory, University of Cambridge, U.K.
[16] Yaras, M. I., and Sjolander, S. A., 1992, "Effects of Siulated Rotation on Tip Leakage in a Planar Cascade of Turbine Blades, ASME J. Turbomach., **114**, pp. 652–667.
[17] Tallman, J., and Lakshminarayana, B., 2001, "Methods for Desensitizing Tip Clearance Effects in Turbines," ASME Paper No. 2001-GT-486.
[18] Bons, J. P., Sondergaard, R., and Rivir, R. B., 2002, "The Fluid Dynamics of LPT Blade Separation Control Using Pulsed Jets," ASME J. Turbomach., **124**, pp. 77–85.
[19] Arakawa, H., Suzuki, T., Saito, K., Tamura, S., and Kishi, S., 1997, "Research and Development of 300 kW Class Ceramic Gas Turbine Project in Japan," ASME Paper No. 97-GT-87.
[20] Curtis, E. M., Hodson, H. P., Banieghbal, M. R., Denton, J. D., and Howell, R. J., 1997, "Development of Blade Profiles for Low Pressure Turbine Applications," ASME J. Turbomach., **119**, pp. 531–538.
[21] Murawski, C. G., Sondergaard, R., River, R. B., Vafai, K., Simon, T. W., and Volino, R. J., 1997, "Experimental Study of the Unsteady Aerodynamics in a Linear Cascade with Low Reynolds Number Low Pressure Turbine Blades," ASME Paper No. 97-GT-95.
[22] Lou, W., and Hourmouziadis, J., 2000, "Separation Bubbles Under Steady and Periodic-Unsteady Main Flow Conditions," ASME J. Turbomach., **122**, pp. 634–643.
[23] Howell, R. J., Ramesh, O. N., Hodson, H. P., Harvey, N. W., and Schulte, V., 2001, "High Lift and Aft-Loaded Profiles for Low-Pressure Turbines," ASME J. Turbomach., **123**, pp. 181–188.
[24] Volino, R. J., and Hultgren, L. S., 2001, "Measurements in Separated and Transitional Boundary Layers Under Low-Pressure Turbine Airfoil Conditions," ASME J. Turbomach., **123**, pp. 189–197.
[25] Van Treuren, K. W., Simon, T., von Koller, M., Byerley, A. R., Baughn, J. W., and Rivir, R., 2002, "Measurements in a Turbine Cascade Flow under Ultra low Reynolds Number Conditions," ASME J. Turbomach., **124**, pp. 100–106.
[26] Matsunuma, T., Abe, H., and Tsutsui, Y., 1999, "Influence of Turbulence Intensity on Annular Turbine Stator Aerodynamics at Low Reynolds Numbers," ASME Paper No. 99-GT-151.
[27] Fielding, L., 2000, *Turbine Design*, ASME Press, New York, pp. 27–28.
[28] Lakshminarayana, B., 1996, *Fluid Dynamics and Heat Transfer of Turbomachinery*, Wiley, New York.
[29] Ames, F. E., 1997, "The Influence of Large-Scale, High-Intensity Turbulence on Vane Heat Transfer," ASME J. Turbomach., **119**, pp. 23–30.
[30] Boyle, R. J., Lucci, B. L., Verhoff, V. G., Camperchioli, W. P., and La, H., 1998, "Aerodynamics of a Transiting Turbine Stator Over a Range of Reynolds Numbers," ASME Paper No. 98-GT-285.
[31] Schlichting, H., 1979, *Boundary Layer Theory*, McGraw-Hill, New York, pp. 453–455.

Investigation of Vortex Shedding and Wake-Wake Interaction in a Transonic Turbine Stage Using Laser-Doppler-Velocimetry and Particle-Image-Velocimetry

E. Göttlich
e-mail: emil.goettlich@tugraz.at

J. Woisetschläger

P. Pieringer

B. Hampel

F. Heitmeir

Institute for Thermal Turbomachinery
and Machine Dynamics,
Graz University of Technology,
Graz, Styria A-8010, Austria

The current paper presents a time-resolved experimental flow investigation in a highly loaded transonic gas turbine stage operating continuously under engine representative conditions. The measurement was performed with a two-component laser-doppler-velocimeter (LDV) and a three-component stereoscopic particle-image-velocimeter (3C-PIV). Unsteady velocity data were obtained in axis perpendicular planes (LDV) and tangential planes (3C-PIV) between stator and rotor as well as downstream of the rotor. The results of the time-resolved investigation at several radii show the vortex shedding process from the trailing edges of nozzle guide vanes and rotor blades. This vortex shedding was found to be phase locked to higher harmonics of the blade passing frequency. Pressure waves evoked by reflection of the trailing edge shocks of the vanes on the passing rotor blades interact with the boundary layers on the rear suction side of the vanes and on the rotor blade surfaces while running upstream and downstream the flow. They are responsible for this phase-locking phenomenon of the shedding vortices. At midspan, the vortices shedding from stator and rotor blades were also observed by PIV. The in-plane vorticity distribution was used to discuss the wake-wake interaction indicating that wake segments from the nozzle guide vanes were chopped by the rotor blades. These chopped segments are still visible in the distributions as a pair of counter rotating vortices. The nozzle wake segments are transported through the rotor passages by the flow, influencing the vortex street of the rotor blades as they pass by with the higher velocity of the main flow. A comparison with a numerical simulation is also given.
[DOI: 10.1115/1.2103092]

Introduction

The unsteady flow in turbomachines is characterized by the interaction between stationary and rotating blade rows and their wakes. The wake flow moves downstream and influences pressure distribution, heat transfer, and boundary layer transition on succeeding blades. One source of loss is generated by wake mixing.

Much research work has been performed to investigate these wakes including the vortex shedding process and loss generation in nonrotating cascades, e.g., [1,2]. Recent research deals with the wake flow in rotating machines. The retroaction of rotor blades on the vortex shedding frequencies of the upstream vanes has been investigated by [3,4] with phase locking of the vortex shedding to higher harmonics of the blade passing frequency observed by the authors.

Less literature is available dealing with wake-wake interaction, e.g., [5]. The vortex streets of the nozzle guide vanes are chopped by the rotor blades into individual segments which subsequently pass through the rotor passages independent from each other. They interact with the vortices shed from the rotor blades as they pass by with the higher velocity of the main flow. A modulation and destabilization of the rotor vortex streets was shown in [6].

The current paper focuses on the vortex shedding and the wake-wake interaction of a highly loaded transonic gas turbine stage which operates under engine representative conditions in the continuously running cold-flow test facility of the institute.

The flow investigation was performed with nonintrusive optical measurement techniques like laser-doppler-velocimetry (LDV) and particle-image-velocimetry (PIV). The LDV data were recorded under the same conditions already published in [7]. This set of time-resolved flow data for single positions in the fluid flow together with the stage geometry is available for download at the institute's home page. Additionally, PIV measurements were performed in tangential planes at midspan between stator and rotor as well as downstream the rotor to get instantaneous velocity measurements of the whole flow field, thus enabling the determination of the vortex streets and their interaction mechanisms.

Experimental Facility and Instrumentation

Test Facility. The transonic test turbine of the Institute for Thermal Turbomachinery and Machine Dynamics (Styria, Austria) is a continuously operating cold-flow open-circuit facility which allows the testing of turbine stages with a diameter up to 800 mm in full flow similarity (corrected speed and pressure ratio) due to its modular design. Pressurized air is delivered by a separate 3 MW compressor station. The shaft power of the test stage drives a three stage radial brake compressor. This brake compressor delivers additional air mixed to the flow from the compressor station and increases the overall mass flow. The air temperature in the mixing chamber (turbine stage inlet) can be adjusted by coolers between 40°C to 185°C. The maximum shaft speed of the test rig is limited to 11 550 rpm. Depending on the stage characteristic a maximum coupling power of 2.8 MW at a total mass flow of

Contributed by the International Gas Turbine Institute (IGTI) of ASME for publication in the JOURNAL OF TURBOMACHINERY. Manuscript received October 1, 2004; final manuscript received February 1, 2005. IGTI Review Chair: K. C. Hall. Paper presented at the ASME Turbo Expo 2005: Land, Sea, and Air, Reno, NV, June 6 - 9, 2005, Paper No. GT2005-68579.

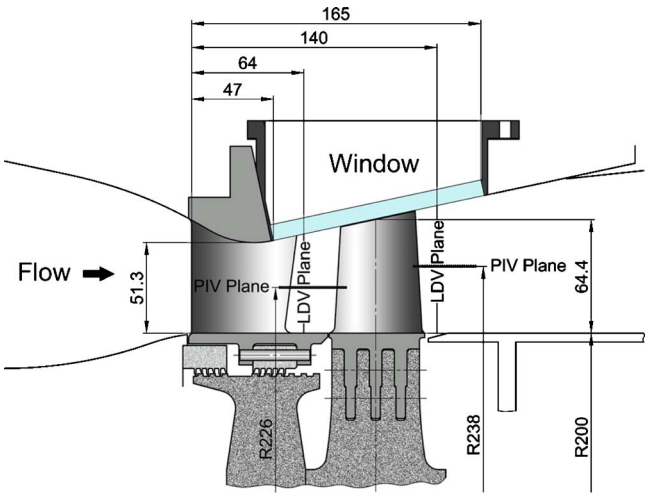

Fig. 1 Meridional flow path and measurement planes

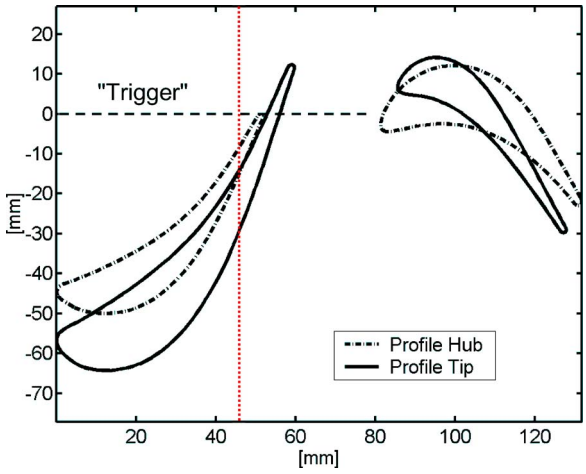

Fig. 2 Profiles at trigger zero position

22 kg/s can be reached. Detailed information on the design and construction of the facility can be found in [8], on the operation in [9].

Turbine Stage Tested. The meridional section of the turbine stage is given in Fig. 1. The convergent-divergent meridional flow path in the stator region is required to accelerate the flow to supersonic velocity and is obtained by a strong contraction of the shroud contour while the hub diameter is kept constant. The hub contour is cylindrical while the shroud contour is conical in the rotor section.

The optical access for LDV and PIV measurements is realized with different glass windows. The measurement planes between stator and rotor as well as in the downstream section of the rotor are shown in Fig. 1. Some important operating conditions for this investigation and the geometrical data of the stage are given in Table 1.

There are 24 nozzle guide vanes and 36 rotor blades, so the blade ratio between guide vanes and rotor blades is 2:3, a ratio which eases computational fluid dynamics (CFD) modeling of this test stage.

In Fig. 2 the vertical dotted line indicates the beginning of a gap of 0.8 mm between the nozzle guide vane tip and the outer shroud contour (between 46 mm and the trailing edge of the vanes). This gap is necessary to rotate the stator ring and the guide vane casing during test run to change the relative position between vane and measurement system. The gap between rotor blade tip and shroud is 1 mm.

The nozzle guide vanes, the rotor blades, and the endwalls were covered with a high-temperature flat black paint to reduce surface reflections. To allow a rotor-phase-resolved analysis of the measured velocities in the positions traversed, a reference signal provided by the monitoring system of the turbine was used to trigger the data sampling (uncertainty: blade pitch/300, a phase delay depending on speed was accounted for).

Droplets of DEHS oil (Di-Ethyl-Hexyl-Sebacin-Esther) with a nominal diameter 0.7 μm were added by PALLAS AGF 5.0D seeding generator 30 cm upstream of the stator blades as seeding material for the optical measurements. These particles guarantee sufficiently high particle response at transonic flow conditions. (In the region of the trailing edge shocks a smearing effect of 0.5 mm due to seeding particle inertia was estimated).

Laser Doppler Velocimetry (LDV). The optical velocity measurement of the flow at different radii was performed by a two-dimensional LDV system (DANTEC FiberFlow with two burst spectrum analyzer (BSA) processors) fed by a 6 W argon-ion laser (COHERENT). Optical access was realized through a small plan-parallel glass window of 9 mm thickness and 120×23 mm surface dimension. An antireflection coating was applied. The main optical parameters of the LDV system are presented in Table 2.

Four laser beams were emitted by the optical probe head into the measurement volume. Light scattered by the tracer particles passing through the probe volume was collected in back-scatter mode. Velocity data were recorded by point wise detection along radial lines in two axis-perpendicular planes (see Fig. 1, 0.12 mm probe volume diameter and 2.6 mm length in radial direction). The LDV system was mounted on a lightweight traverse in order to adjust the radial position of the probe head. The position in circumferential direction was changed by turning the nozzle guide vane casing. After the turning to a new position the flow was allowed to settle.

Figure 3 shows the LDV measurement locations in two radial planes $B1$ and $C1$. The z axis is equal to the machine axis, the x

Table 1 Stage geometrical data and operating conditions

Number of nozzle guide vanes	24
Number of rotor blades	36
Nozzle chord (midspan) [mm]	78.9
Nozzle axial chord (midspan) [mm]	56.1
Geometric turning angle nozzle [deg]	70
Blade chord (midspan) [mm]	55.9
Blade axial chord (midspan) [mm]	46.8
Geometric turning angle blade [deg]	107
Nozzle aspect ratio (exit height / chord)	0.70
Blade aspect ratio (exit height / chord)	1.24
Rotor tip clearance / span [%]	1.4
Vane-blade spacing	47
Pressure ratio $p_{tot,in}/p_{out}$	3.50
Rotational speed [rpm]	10,600
Inlet total temperature $T_{tot,in}$ [K]	403
Reynolds number nozzle guide vane exit	$2.57 \cdot 10^6$
Reynolds number rotor blade exit	$1.69 \cdot 10^6$
Blade exit Mach number	0.46
Loading factor $\Delta h/u^2$	1.51

Table 2 Optical beam system

Velocity component	u	v
Focal length [mm]	400	400
Wavelength [nm]	514.5	488
Beam spacing [mm]	38	38
Beam diameter [mm]	2.2	2.2
Focal spot diameter [μm]	119.1	112.9
Number of fringes	21	21

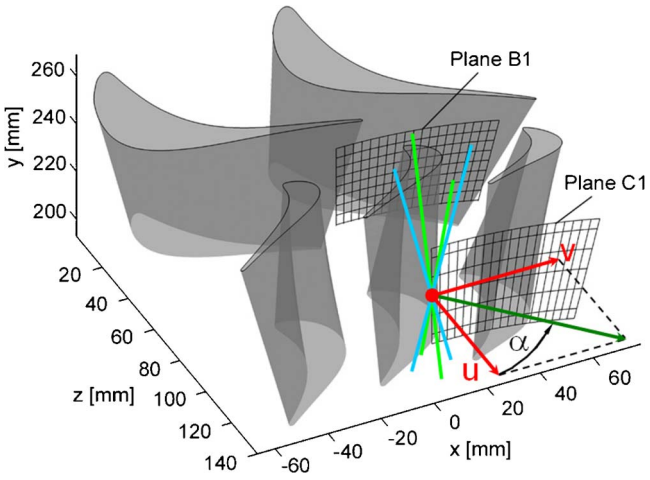

Fig. 3 LDV measurement locations

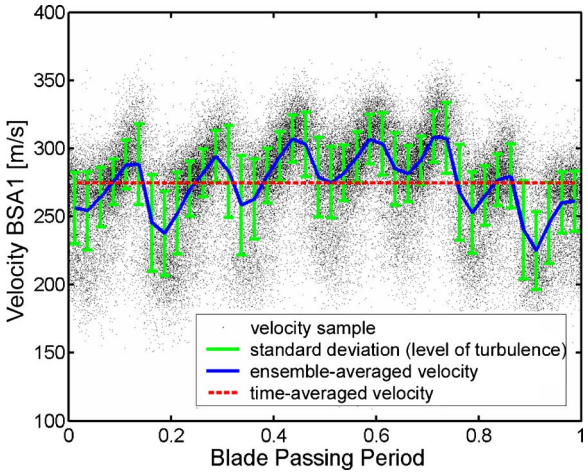

Fig. 4 Velocity decomposition for phase averaged data

axis is in tangential and the y axis in radial direction. Zero position for the z axis is the stator leading edge, for the y axis the rotor axis center and for the x axis the zero position is identical with the trigger zero position (see Fig. 2).

LDV measurements were performed between 30% and 85% relative span in $B1$ and 25% to 80% relative span in $C1$ since laser reflections from the hub and the window prevented valid burst detection closer to the endwalls. The grid behind the rotor is more wide meshed since time for measurement was limited due to the contamination of the window by seeding oil in this position.

The LDV system acquired a velocity sample each time a seeding particle crossed the LDV probe volume. A reference signal of the monitoring system of the turbine was used to sort the recorded velocity samples by the actual rotor position. Since a two-dimensional LDV was applied, only the velocities in two different directions (i.e., axial and circumferential direction for plane $C1$) were detected. In plane $B1$ the LDV head was turned by 24 deg to keep the velocity components below the maximum detectable velocity of the applied optical beam system. In each measurement position approximately 80,000 velocity bursts were collected. They were sorted with the help of the trigger signal provided by the shaft monitoring system to the proper rotor position. All data recorded were then mapped into one 10 deg section, i.e., into one blade passing period (time for one rotor blade to move for one pitch). As a result the data represent the average value over 36 rotor blade channels.

Such a velocity recording for a single position and one component (BSA 1) is given in Fig. 4, with black dots indicating the single samples. The blade passing period was divided into 40 evaluation windows, which means that the averaged velocity samples were assigned to 40 different stator-rotor positions per rotor blade pitch.

The velocity was ensemble averaged at each evaluation window by means of a linear regression method presented in [10]. The instantaneous velocity vector $\mathbf{V}_{k,i}$ was decomposed as follows:

$$\mathbf{V}_{k,i} = \overline{\mathbf{V}}_k + \mathbf{V}'_k = \overline{\overline{\mathbf{V}}}_k + \tilde{\mathbf{V}}_k + \mathbf{V}'_k \tag{1}$$

The last term represents an unresolved fluctuating component after ensemble averaging and may contain coherent structures that are not a harmonic of blade passing. Here it is used to quantify the level of turbulence in each evaluation window by determination of variance and standard deviation.

With 40 evaluation windows the number of velocity samples per window was still high enough to allow mean value and level of turbulence to be calculated with the following uncertainty. For a confidence level of 95% an uncertainty of 3.5 m/s inside and 0.9 m/s outside the rotor wake for the ensemble averaged velocity as well as 11 m/s inside and 2.5 m/s outside the rotor wake for the unresolved velocity was calculated.

Particle Image Velocimetry (PIV). A stereoscopic particle image velocimeter DANTEC FlowMap 1500 together with two DANTEC 80C60 HiSense cameras (1280×1024 pixel) and a NEW WAVE Gemini double cavity Nd:YAG laser (120 mJ/pulse) was used to measure the time-resolved velocity distribution of the whole flow field simultaneously enabling the determination of vortex structures.

A special light-sheet optics consisting of a spherical lens (600 mm focal length), a cylindrical lens (−10 mm focal length), and a prism was used to illuminate the seeding particles in a plane section of the flow. Optical access for the cameras was realized through a large plane-concave glass window of 13 mm thickness and 120×70 mm surface dimension. Again, an antireflection coating was applied. The general arrangement of the components is given in Fig. 5, the overlapping field of view of both cameras is shown in Fig. 6 for the different measurement planes (1–4).

For each camera the two images of one PIV recording during the two laser pulses (time between pulses 1 μs downstream of the stator, 1.5 μs downstream of the rotor) were evaluated using a cross-correlation technique resulting in a vector field of particle displacements within the interrogation areas between the pulses (interrogation area size 64×64 pixel with 50% overlap, resulting in a map of 38×31 vectors). Finally, a range validation, a correlation peak ratio validation, and a moving average validation were applied to reject invalid vectors [11].

To relate the single displacements in the recordings to physical

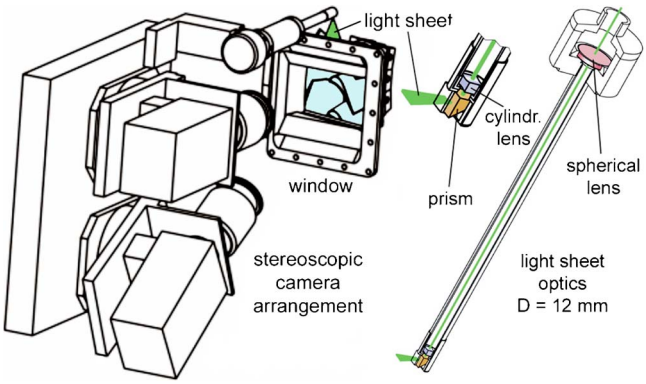

Fig. 5 General arrangement of PIV system

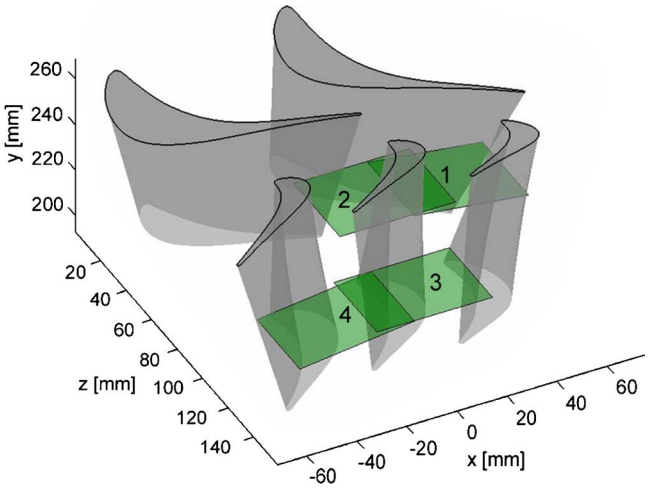

Fig. 6 PIV measurement locations

length and combine them into a three-dimensional vector field a calibration through the curved window was performed using a special calibration target (100×100 mm white plate with a square grid of black dots, dot spacing 2.5 mm, dot size 1.5 mm). This calibration procedure resulted in a polynomial function relating the single displacements recorded by the two cameras into three-dimensional velocity vectors for the overlapping field of view of both cameras (47.5×37.5 for planes 1 and 2, 47.5×35 for planes 3 and 4).

The signals of the shaft monitoring system were used to trigger the PIV recordings. Measurements in four different planes at R226 mm and at R238 mm were recorded downstream of the stator and downstream of the rotor, respectively, see Fig. 6. These measurement planes were realized by rotating the stator and/or adjusting a trigger delay in the acquisition software of the PIV system, while the positions of the cameras and the light sheet optics were fixed in the laboratory frame. For each measurement plane, sets of 180 PIV recordings at six different stator-rotor positions were stored. From these 180 three-dimensional vector fields a mean vector field, flow angles, and vorticity were calculated. For observation of coherent structures in the flow (e.g., shedding vortices) the vorticity distribution was calculated from the in-plane components of velocity

$$\omega_z = \frac{\partial v}{\partial x} - \frac{\partial u}{\partial y} \tag{2}$$

In this formula u and v are the in-plane velocity components, x and y represent the in-plane coordinates, and ω_z is the vorticity with the z direction perpendicular to the measurement plane.

For final evaluation and data presentation all results were transformed into a nozzle guide vane position indicated in Fig. 6 and added continuously over several nozzle guide vane pitches. Note that in two neighboring 15 deg sectors (corresponds to one vane pitch) the same flow effects occur with a time difference of a half blade passing period (t/τ=0.5) due to the vane blade ratio of 2:3. Therefore the results have to be phase corrected for every other 15 deg sector by three stator-rotor positions out of six.

A measurement uncertainty of 6 m/s inside and 1 m/s outside the wake was calculated using a confidence level of 95% (100 valid vectors, variance 30 and 5 m/s, respectively). Probably the uncertainty is much smaller due to a preaveraging over approximately ten seeding particles within the interrogation areas.

Unsteady Three-Dimensional CFD Simulation

The numerical code applied was developed at the Institute [12] and solves the Reynolds-averaged Navier-Stokes equations using a time-iterative characteristic method based on the finite-volume discretization. Turbulence is modeled by the one-equation model of Spalart and Allmaras. To gain a stable and accurate procedure the code uses a decomposition of the conservative inviscid fluxes leading to a set of wave-type equations. Using this characteristic form of the flow equations the computational efforts caused by multiple matrix manipulations of conservative flow solvers can be avoided, thus leading to a reduction in computer time. Discretization in time is done by a second-order approximation of the time evolution, which is solved in an implicit way. To cope with pitch ratio unequal one, the code uses phase lagged boundary conditions. To further reduce calculation effort and time, pressure-gradient-sensitive wall functions were applied [12].

A multiblock grid consisting of ten blocks and a total count of about 1,000,000 cells was used for the numerical calculation. The tip clearance between rotor blade and outer casing is meshed by (only) 16 cells, though the use of wall functions still allows a good spatial resolution there. The fillets at the stator hub and tip and at the rotor hub are modeled as well. The channel is meshed by 72 cells from hub to outer casing [12].

Results and Discussion

Phase-Locking of Vortex Shedding. In the actual paper time-space plots of the LDV results are used to show the phase locking of the vortex shedding process in the investigated turbine stage. In Fig. 7 the turbulent kinetic energy k in the midsection of measurement planes $B1$ and $C1$ is shown over three blade passing periods. On the left, the profiles of vanes and blades at midspan are shown for two different moments in time (t/τ=0 and t/τ=0.5) together with the measurement planes $B1$ and $C1$. To calculate the equa-

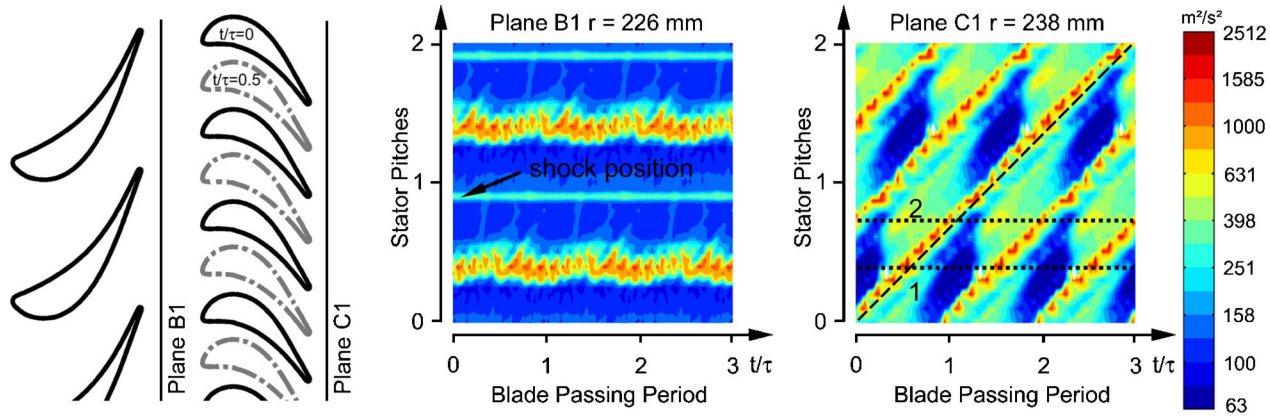

Fig. 7 Time-space plots of turbulent kinetic energy in plane B1 and C1 at midspan measured by LDV

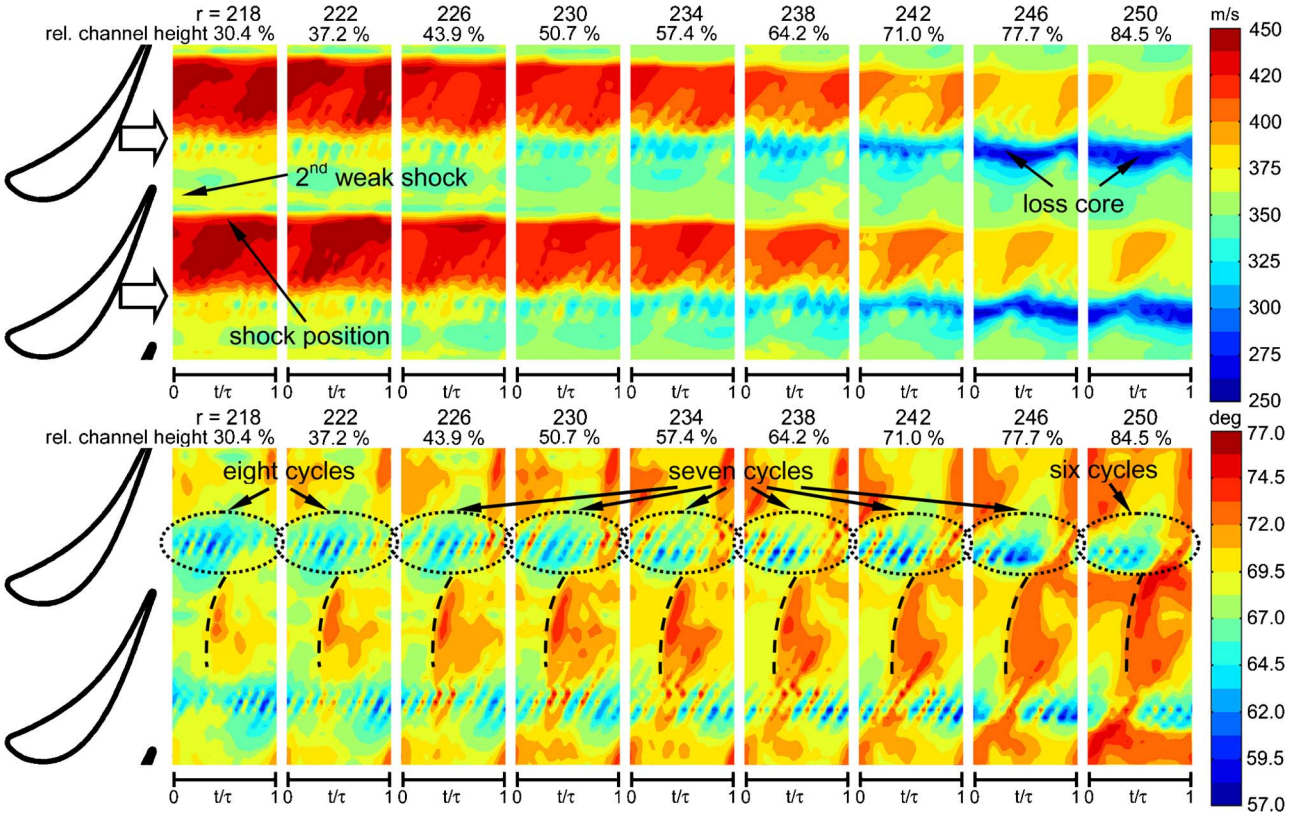

Fig. 8 Time-space plots of velocity and yaw angle in plane B1 at different radii measured by LDV

tion for the turbulent kinetic energy from two-component LDV measurements, the following assumption was used (evenly distributed level of turbulence):

$$k = 0.75(\overline{u'^2} + \overline{v'^2}) \tag{3}$$

Due to the vane-blade ratio of 2:3 and the used axis scales effects related to the moving rotor blades appear as structures under 45 deg like the wake flow indicated by a dashed line, where structures from the stationary guide vanes become visible as horizontal contours. A horizontal section through the plot indicates the history of turbulent kinetic energy at a point of the circumferential line. At the position indicated by a dotted line marked "1" only a low turbulent kinetic energy can be observed besides the rotor wakes within the blade passing cycle. In contrast a higher turbulence occurs between the rotor wakes at position "2." This higher level of turbulence is evoked by the chopped nozzle wake segments which pass the measurement plane at this circumferential position. The knowledge of this position is important for airfoil clocking investigations.

Additionally, information of the effects over the blade height is essential to get more insight to the unsteady flow through this investigated transonic turbine stage. So in the following pictures a separate time-space plot for each circumferential line of the measurement grid is given, see Figs. 8 and 9.

The LDV system acquires the velocity bursts randomly over a high number of rotor revolutions. If the vortex shedding from the blades is not phase locked to the rotor blade movement, the wake structure in the time-space plot will appear as a continuous stripe of higher turbulent kinetic energy. Examination of Fig. 7 shows diagonal structures of discrete spots of higher turbulence over the blade passing period representing the shed vortices from the rotor blade trailing edge. This means that the vortex shedding frequency is phase locked to higher harmonics of the blade passing frequency (6.37 kHz). In the present case seven vortices shed from the trailing edge within one blade passing period, therefore the vortex shedding is locked to the sixth harmonic ($7 \times 6.37 = 44.59$ kHz) of the blade passing frequency.

This observation is confirmed by [4] where the authors investigated the same turbine stage with laser vibrometers to get spectra of the density fluctuations in the flow over a broad range of operating conditions. At lower speeds for example 8300 and 9660 rpm the vortex shedding is locked to the eighth and seventh higher harmonic of the blade passing frequency, respectively. Examination of the vortex shedding process at the trailing edges of the nozzle guide vanes the same effects can be found (Fig. 7).

Again the shedding frequency is phase locked to the sixth harmonic of the blade passing frequency. This can also be seen in Fig. 4 where the curve of the ensemble averaged velocity shows seven pronounced velocity changes during one blade passing period. This decomposition represents the velocity component measured by BSA1 in a point in the nozzle wake.

Figure 8 gives the time-space plots of velocity (top) and yaw angle (bottom) for LDV-measurement plane *B*1 at the different radii measured. In these plots the relative position of the vane profiles at midspan can be seen on the left. The sharp velocity decrease across the shock can be observed slightly upstream the trailing edge. A second weak shock begins to form at the trailing edge at smaller radii. At the outer measurement positions the influence of the losses caused by the upper passage vortex can be seen, which accumulates low momentum fluid on the suction side wake flow. Indicated by white arrows are the vortex streets in the nozzle wakes showing a variation of shedding frequency along the blade height.

In the yaw angle distributions over the blade passing cycle (Fig. 8, lower diagrams) the number of phase-locked vortex shedding sequences can be identified very clearly by counting pairs of areas with very low and very high angle values. Whereas the vortex shedding is phase locked to the sixth harmonic at midspan, eight

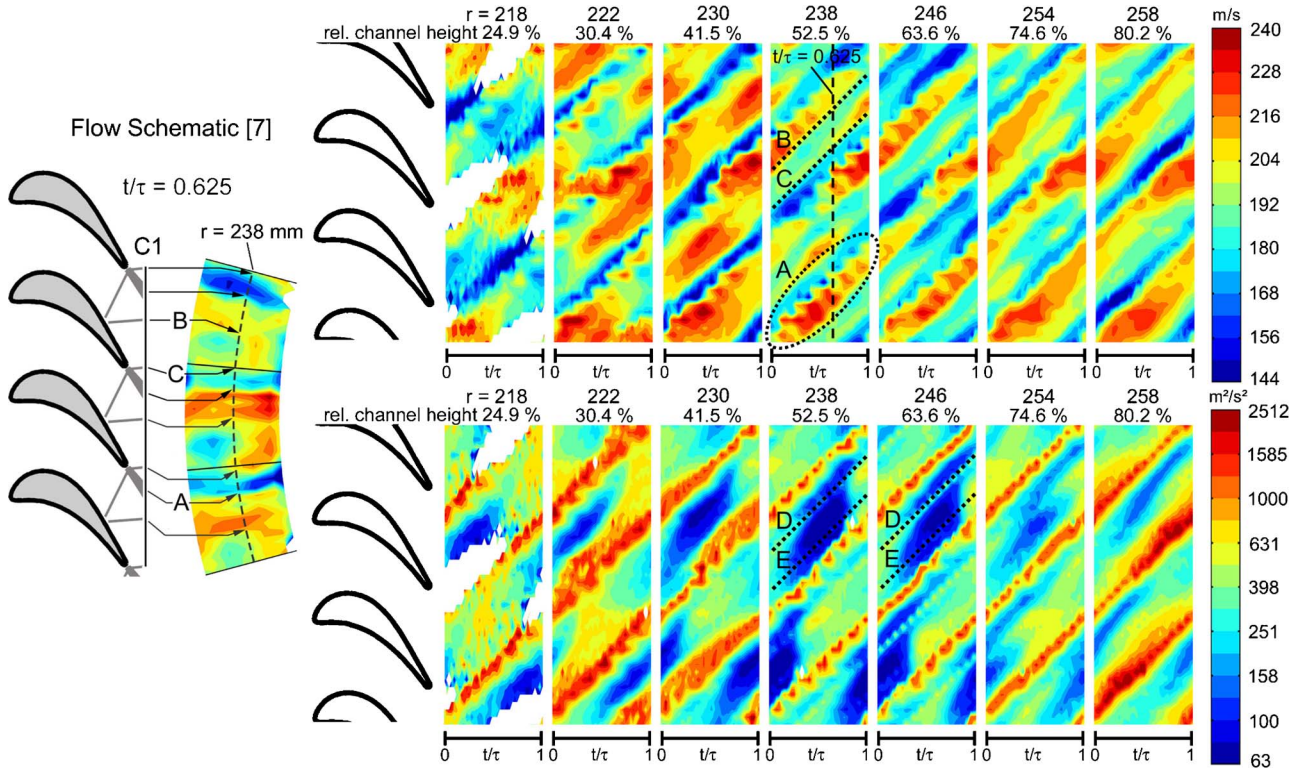

Fig. 9 Time-space plots of velocity and turbulent kinetic energy in plane C1 at different radii measured by LDV

structures indicate the shedding vortices at $r=218$ and 222 mm. There, the phase is locked to the seventh harmonic of the blade passing frequency. On the outer line only six shedding sequences can be observed in the yaw angle distribution. For that reason the vortex shedding is phase locked to the fifth higher harmonic of the blade passing frequency there. A variation of vortex shedding frequency over the blade height was also detected in the CFD results [12].

Figure 9 gives the time-space plots of velocity (top) and turbulent kinetic energy (bottom) for LDV-measurement plane *C*1 at the different radii measured. Again, the relative position of the blade profiles at midspan can be seen on the left. At $r=238$ mm the seven shedding cycles indicate the locking to the sixth harmonic (marked with "*A*," compare also with the (TKE) plot). The dotted diagonal lines mark the trailing edge shocks on pressure side ("*B*") and suction side ("*C*"). The first one is reflected on the rear part of the neighboring blade's suction side. These oscillating shocks are also visible in the turbulent kinetic energy plots below (marked with "*D*" and "*E*"). On higher and lower radii the phase-locking effect gets more and more smeared. A detection of the shedding vortices within these plots is no more evident with the applied spatial measurement resolution there. It seems that the smaller distances to the hub passage vortex and the tip clearance vortex are responsible for this smearing of the time-space plots.

Triggering Mechanism of Vortex Shedding. The unsteady CFD simulation is used to explain the triggering of the vortex shedding, see Fig. 10.

The vane suction side shock extends across the interface between stator and rotor towards the axial direction (see Fig. 10, thick line at $t/\tau=0.14$). This shock is periodically reflected at the surface of the passing rotor blades. Reflected pressure waves move upstream toward the vane suction side (Fig. 10, dashed lines) and impinge on the trailing edges (see Fig. 10, $t/\tau=0.14$). There, it enforces a vortex separation (Fig. 10, arrow). From then on the wake is shedding undisturbed, until the next reflected shock wave triggers it again.

So, the pressure wave is reflected on the vane suction side after traveling upstream, and then starts to move downstream through the rotor passages to the trailing edge influencing the boundary layers and the vortex shedding in a similar way there.

The upstream running pressure waves can also be found in the measurement results of LDV and PIV. If such a wave travels through the measurement position it decreases the axial velocity component, thus increasing the yaw angle. The pressure waves are indicated in Fig. 8 (lower image) with dashed lines. An increase of their strength with increasing radius can be detected over the investigated blade height.

In the PIV results (Fig. 11) a fluctuation of the flow velocity

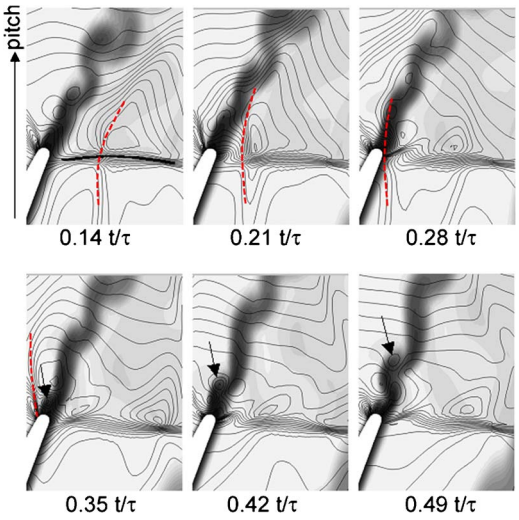

Fig. 10 Nozzle wake at 50% span, lines indicate isobars, gray-scale indicate entropy

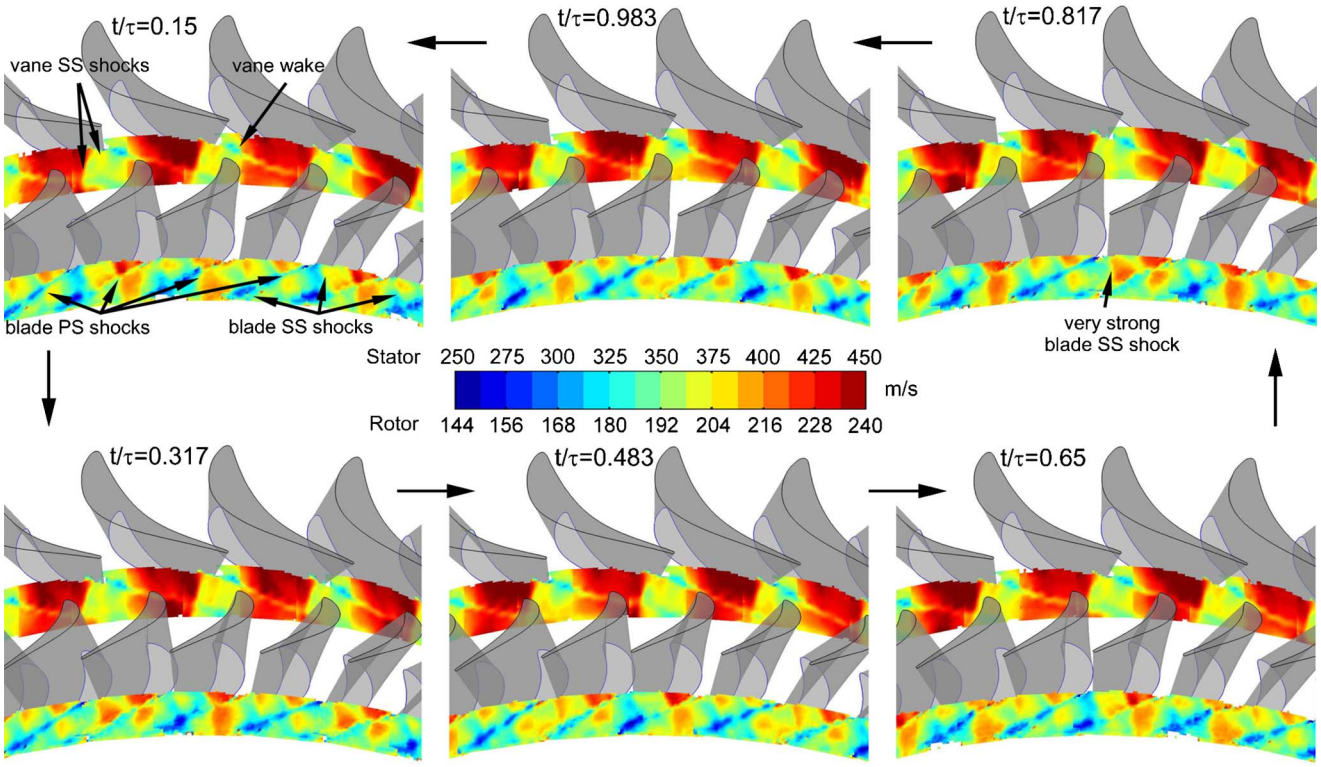

Fig. 11 Time-resolved stereoscopic PIV results showing velocity distributions at midspan

upstream of the vane suction side shock can be observed. The arrows between the pictures indicate the direction of frame order of the six stator-rotor positions. Comparison of the velocity in the vane exit flow with the yaw angle distribution of Fig. 12 shows a relation between the upstream propagating pressure waves and these fluctuations. Again, the pressure waves are highlighted with dotted lines. At $t/\tau=0.15$ a wave coming from blade 2 is ready to impinge onto the vane suction side. A second one coming from blade 1 becomes visible in the measurement area (indicated with "*A*"). This matches very well with the CFD simulation shown in

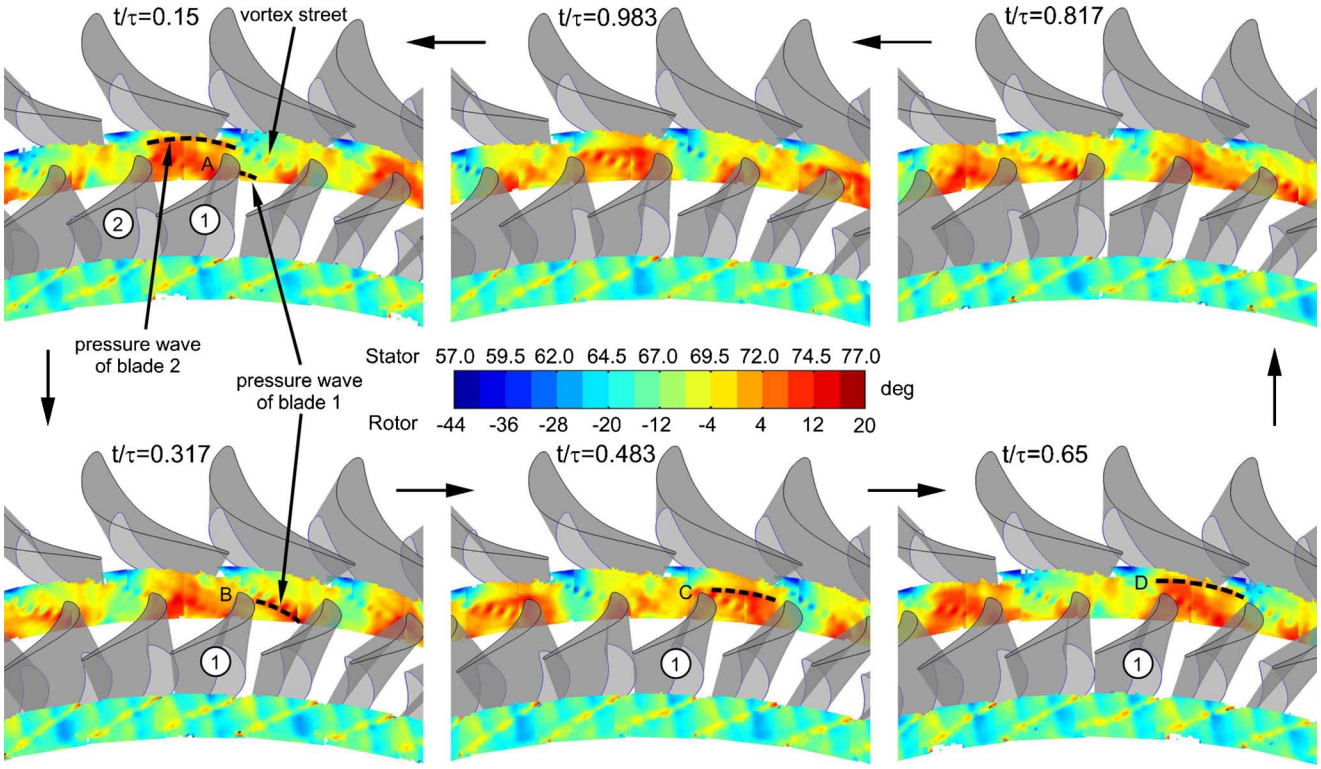

Fig. 12 Time-resolved stereoscopic PIV results showing yaw angle distributions at midspan

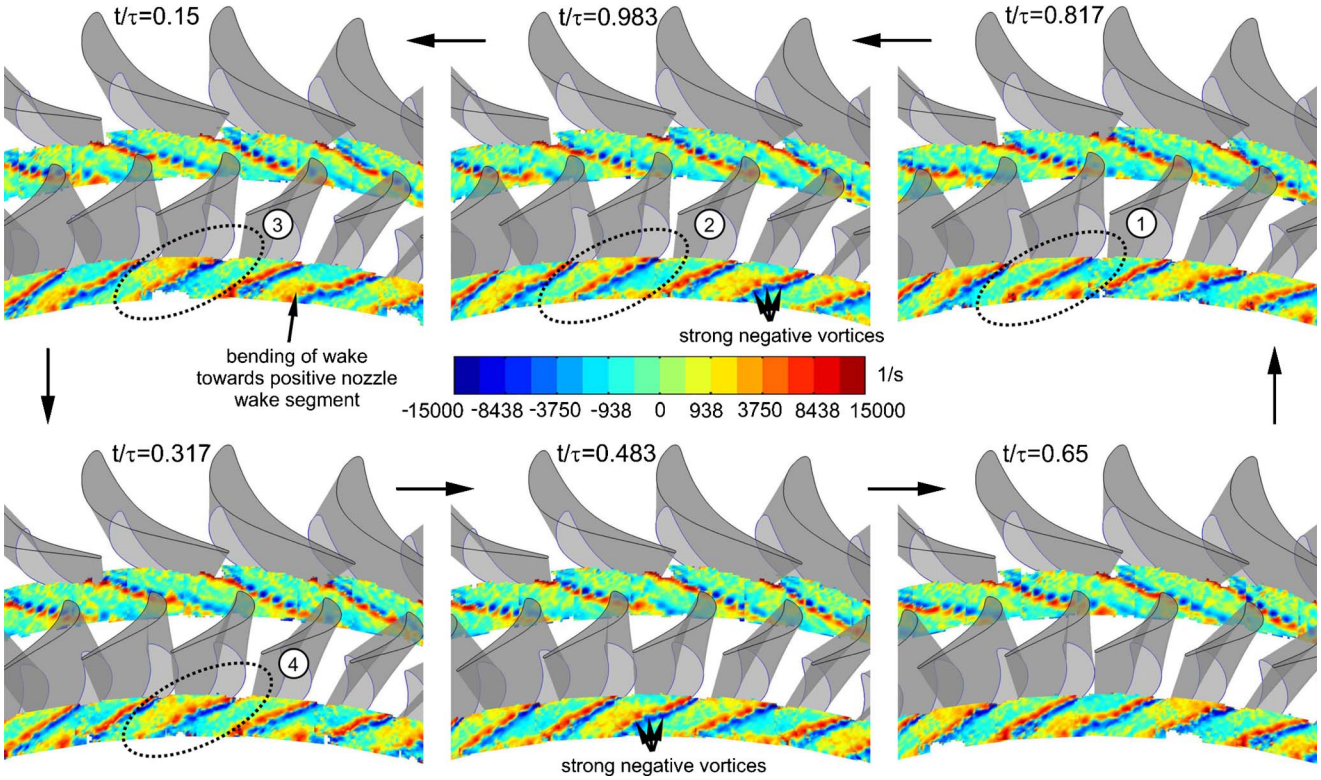

Fig. 13 Time-resolved stereoscopic PIV results showing vorticity distributions at midspan

Fig. 10. During further movement of the rotor the pressure wave propagates upstream ("*B*" and "*C*") and start to hit the next vane (see "*D*"). Due to the vane-blade ratio of 2:3 every half blade passing period two neighboring blades are hit by a pressure wave, thus the vortex shedding is phase lagged by $t/\tau=0.5$. It seems that the running pressure waves decreases the axial velocity component by pressing back the fluid and accelerates the flow in circumferential direction like in a convergent-divergent channel. Thus an increase in overall velocity can be seen in the nozzle exit whenever a pressure wave travels upstream.

The downstream traveling pressure waves cannot be detected in the PIV results easily, but a strong modulation of the rotor blade trailing edge shocks during the blade passing cycle caused by the inhomogeneous rotor inflow can be observed (see Fig. 11).

Wake-Wake Interaction. The vorticity calculated with the measured in-plane velocity components (PIV) or the axial and tangential velocity components in a cylindrical section at midspan (CFD) is used to investigate the wake-wake interaction in this transonic turbine stage.

Without the described phase locking of the vortex shedding the PIV results would not show any pronounced vortex structures in the wake since they were gained by averaging over 180 PIV recordings at the same stator-rotor position. This averaging and the lower spatial resolution cause smaller vorticity values in comparison to the results of the numerical simulation.

The measured vorticity distribution in Fig. 13 and the calculated one in Fig. 14 use nonlinear colorbars $\{\text{sign}(\omega_z) \times \text{sqrt}[\text{abs}(\omega_z)]\}$ to visualize the chopped nozzle wake segments in the rotor passages and in the rotor exit flow.

In these figures the vortex shedding takes place clockwise (negative) from the pressure side and counter-clockwise (positive) from the suction side of the vanes. The pressure side vortices are much stronger due to the thinner boundary layer thickness, leading to a stronger velocity gradient normal to the wall. However, in both cases, measurement and calculation, they seem to decay faster in comparison with the suction side vortices.

The time-resolved flow field downstream of the rotor is much more complex because of the time-periodic nozzle wake passing. The nozzle wake is chopped by the rotor leading edges. These segments are transported through the rotor passages independent from each other [13]. Similar to the investigations in [6], the vortex shedding is smoother (less pronounced) from the rotor trailing edges than from the vane (Fig. 13). The wake flow interferes with the trailing edge shocks acting as instability for the shedding vortices.

Further examination of Figs. 13 and 14 show a modulation of the strength of the shedding vortices from the rotor trailing edges over the blade passing cycle. Looking for instance at the encircled areas marked with numbers "1" to "4" one can see an increase in the strength of the shedding vortices. Interesting is the fact that at the start of this raise in strength ($t/\tau=0.817$) the trailing edge shock at the blade suction side has reached its maximum, see Fig. 11. It seems reasonable that the modulating of the vortex shedding is caused by the trailing edge shocks due to stator-rotor interaction.

In the rotor exit flow the two counter-rotating parts of the chopped nozzle segments can be observed in the PIV results as well as in the calculation. It was found that the rotor vortex street has the strong tendency to bend against the direction of rotation whenever a positive turning nozzle wake segment passes by. Additionally, these positive turning segments seem to increase the negative turning vortices in the wake flow, see Fig. 13. This is also predicted in [6] that vortices rotating in the opposite direction increase their strength. A destabilization of vortex shedding by this effect has to be investigated separately.

Conclusions

The paper shows novel results of detailed flow measurements and a CFD simulation of a highly loaded transonic single stage axial turbine regarding vortex shedding and wake-wake interaction.

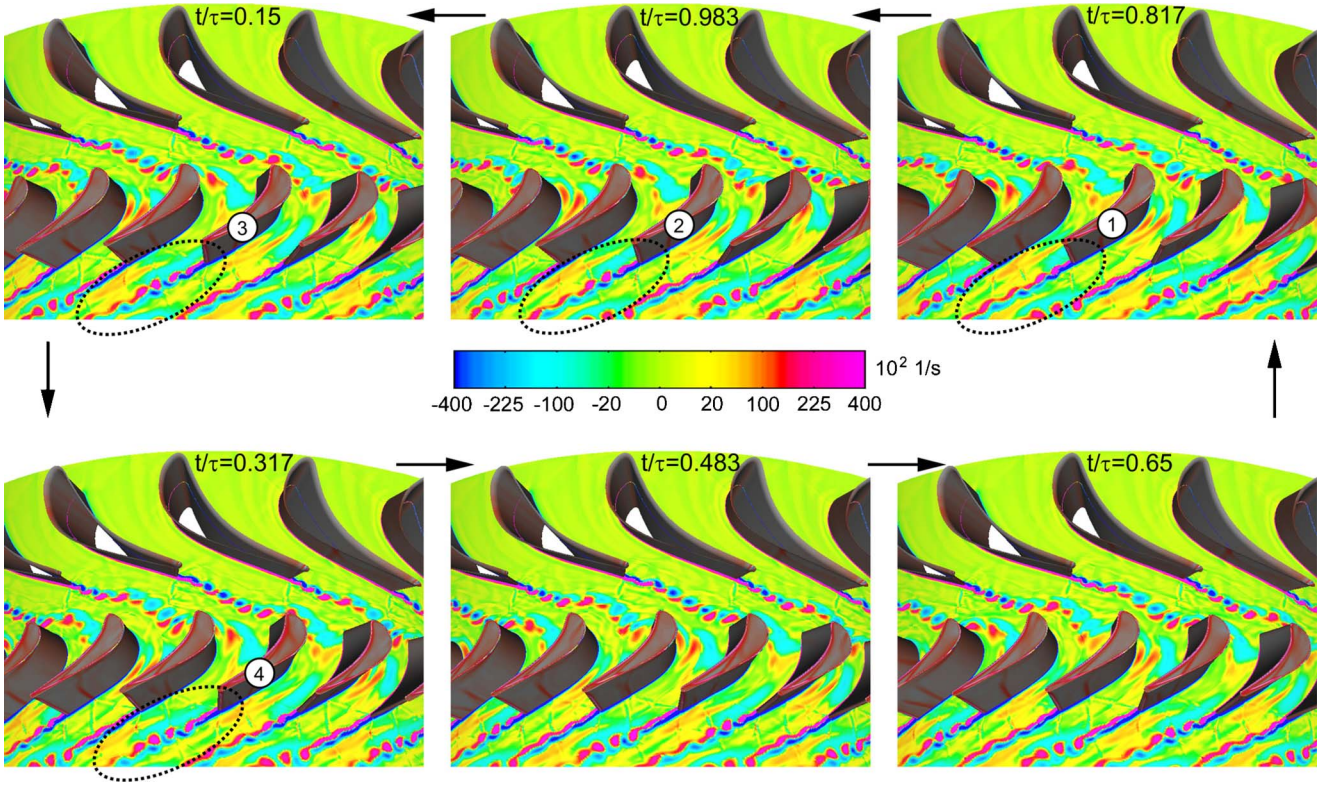

Fig. 14 Unsteady CFD results showing vorticity distributions at midspan

Turbulent kinetic energy gained by time-resolved LDV measurements was used to show the phase locking of the shedding vortices to the rotor position. The reason for the phase-locking effect is the reflection of the vane trailing edge shocks on the passing rotor blades. Traveling upstream these pressure waves enforce a vortex separation whenever they impinge at the rear part of the vane suction side and interact with the boundary layer there. Also, the investigation shows a variation of vortex shedding frequency over the blade height due to the prevailing velocities.

Additionally, stereoscopic PIV measurements and a CFD simulation were used to determine the vorticity of the shedding vortices and to show the modulation in strength. Consequences of wake-wake interaction on those effects are also shown. The measurement results as well as the CFD calculations highlight the same phenomena.

The time-resolved LDV data are available as download at the institute's home page and can be used for CFD verification.

Acknowledgment

This work was made possible by the Austrian Science Fund (FWF) and the Austrian Ministry for Education, Science and Culture (BMBWK) within Grant No. Y57-TEC "Non-Intrusive Measurement of Turbulence in Turbomachinery." The support of Dr. H. P. Pirker in operation of the 3 MW compressor station is also gratefully acknowledged. The authors would also like to thank R. Pecnik for preparing the representation of the CFD results. Graz University of Technology is a member of the thematic network "PIV-NET" funded by the European Union.

Nomenclature

t = time, s
PS = pressure surface
SS = suction surface
p = absolute pressure, bar
r = radial position, m
T = absolute temperature, K
x, y, z = Cartesian coordinates, m
u, v, w = velocity components, m/s
$\mathbf{V}$ = velocity vector, m/s
k = turbulent kinetic energy, m^2/s^2

Greek

τ = rotor blade passing period, s
ω = vorticity, 1/s
α = yaw angle, deg

Subscripts

i = instantaneous
k = burst spectrum analyzer (BSA)
tot = total
in = at inlet
out = at outlet
z = according to z direction

Superscripts

$-$ = ensemble-averaged properties
$=$ = time-averaged properties
$\sim$ = periodic quantity
$'$ = unresolved fluctuating quantity

References

[1] Cicatelli, G., and Sieverding, C. H., 1995, "A Review of the Research on Unsteady Turbine Blade Wake Characteristics," AGARD PEP *85th Symposium on Loss Mechanisms and Unsteady Flows in Turbomachines*, Derby, 8–12 May, VKI RP 1996-59, von Karman Institute, Rhode Saint Senèse, Belgium.

[2] Carscallen, W. E., Currie, T. C., Hogg, S. I., and Gostelow, J. P, 1999, "Measurement and Computation of Energy Separation in a Vortical Wake Flow of a Turbine Nozzle Cascade," ASME J. Turbomach., **121**, pp. 703–708.

[3] Sondak, D. L., and Dorney, D. J., 1999, "Simulation of Vortex Shedding in a Turbine Stage," ASME J. Turbomach., **121**, pp. 428–435.

[4] Woisetschläger, J., Lang, H., Hampel, B., and Göttlich, E., 2002, "Influence of Blade Passing on the Stator Wake in a Transonic Turbine Stage by Particle Image Velocimetry and Laser Vibrometry," IMechE J. Power and Energy, **217** Part A, pp. 385–391.

[5] Tiedemann M., and Kost F., 2001, "Some Aspects of Wake-Wake Interactions Regarding Turbine Stator Clocking," ASME J. Turbomach., **123**, pp. 526–533.
[6] Hummel F., 2002, "Wake-Wake Interaction and its Potential for Clocking in a Transonic High-Pressure Turbine," ASME J. Turbomach., **124**, pp. 69–76.
[7] Göttlich, E., Neumayer, F., Woisetschläger, J., Sanz, W., and Heitmeir, F., 2004, "Investigation of Stator-Rotor Interaction in a Transonic Turbine Stage Using Laser Doppler Velocimetry and Pneumatic Probes," ASME J. Turbomach., **126**, pp. 297–305.
[8] Erhard, J., and Gehrer, A., 2000, "Design and Construction of a Transonic Test Turbine Facility," ASME Paper No. 2000-GT-480.
[9] Neumayer, F., Kulhanek, G., Pirker, H. P., Jericha, H., Seyr, A., and Sanz, W., 2001, "Operational Behavior of a Complex Transonic Test Turbine Facility," ASME Paper No. 2001-GT-489.
[10] Glas, W., Forstner, M., Kuhn, K., and Jaberg, H., 2000, "Smoothing and Statistical Evaluation of LDV Data of Turbulent Flows in Reciprocating Machinery," Exp. Fluids, **29**, pp. 411–417.
[11] Lang, H., Mørck, T., and Woisetschläger, J., 2002, "Stereoscopic Particle Image Velocimetry in a Transonic Turbine Stage," Exp. Fluids, **32**, pp. 700–709.
[12] Pieringer, P., Göttlich, E., Woisetschläger, J., Sanz, W., and Heitmeir, F., 2005, "Numerical Investigation of the Unsteady Flow through a Transonic Turbine Stage Using an Innovative Flow Solver," accepted for 6th European Conference on Turbomachinery, Lille, France, pp. 339–352.
[13] Hodson, H. P., Dawes, W. N., 1998, "On the Interpretation of Measured Profile Losses in Unsteady Wake-Turbine Blade Interaction Studies," ASME J. Turbomach., **120**, pp. 276–284.

Diego Lelli
e-mail: d.lelli@surrey.ac.uk

John W. Chew
e-mail: j.chew@surrey.ac.uk

Fluids Research Centre,
University of Surrey,
Guildford GU2 7XH, UK

Paul Cooper
ALSTOM Power Limited,
Newbold Road,
Rugby Warwickshire, CV2 12NH, UK

Combined Three-Dimensional Fluid Dynamics and Mechanical Modeling of Brush Seals

Development and application of a combined 3D computational fluid dynamics (CFD) and 3D bristle bending model for brush seals is described. The CFD model is created using commercial CFD mesh generation and solver software. A small gap is assumed between all bristles in the CFD model so as to avoid meshing problems at contact points and allow for imperfections in bristle geometry. The mechanical model is based on linear beam bending theory and allows large numbers of bristles to be modelled with arbitrary bristle-to-bristle contact and imported from the CFD solution. Deformed geometries may be exported directly to the mesh generation software, allowing iterative solution of the coupled aerodynamic/mechanical problem. [DOI: 10.1115/1.2103093]

1 Introduction

Brush seals are a relatively new type of aerodynamic seal for turbomachinery applications. They have found increasing industrial use in gas turbine aero and power generation engines over the last decade.

A brush seal is a set of fine diameter fibers densely packed between retaining and backing plates. There are three main components: bristle pack, front plate, and backing plate (Fig. 1). It is convenient to divide the bristle pack into two regions: the overhanging region, as indicated, and the outer portion. The backing plate is positioned downstream of the bristles to provide mechanical support for the bristles under the differential pressure loads. The inherent flexibility enables the seal to survive large rotor excursions, resulting from vibration, thermal, and centrifugal growth, and rotor imbalance or eccentricity during normal operation, without sustaining appreciable permanent damage.

Several workers have confirmed that the leakage of brush seals is considerably less (ranging from 3 to 20 times) than that of labyrinth seals when tested at the same conditions (see, for example, [1–7]). In addition to significant leakage reduction, the flexible brush seals maintain stable leakage performance for longer service while labyrinth seals suffer permanent performance degradation due to transient rotor excursions. The main advantage of a brush seal is the achieved minimum clearance between the rotor surface and bristle tips. The brush seal fits the rotor surface with a very small clearance or in interference; therefore it is referred to as a contact seal. When contact occurs, the only flow path through the seal is via voids among bristles in the overhanging region. Another characteristic feature of a brush seal is that the bristles are inclined in the direction of rotor rotation with a typical lay angle of 45 deg to the radial direction. The flexible bristle bundle tolerates rotor excursions with less wear compared to other sealing applications. The flexible bristles also close the clearance as they wear out or after transient rotor excursion by changing their lay angle due to inward radial flow in the bristle pack from the radial pressure gradient. This dynamic behavior of a brush seal, called blowdown, maintains a good leakage performance. A good brush seal bibliography is given in the literature [6].

Flow analysis of the brush seal, which is of interest in this study, is a key element of research into seal behavior. The flow and pressure fields in close vicinity of the bristle pack and within the bristle matrix affect the seal dynamics and performance. In their multiple brush seals tests, O'Neill et al. [8] reported bristle instability caused by the momentum of the leakage flow hitting the bristle pack. The bristle pack forms a complex porous structure blocking the flow path.

There are two main issues arising from the balance of forces on the bristles. One is that the bristles get packed tighter as pressure load pushes them against the backing plate while the inward radial flow tends to move the bristle tips toward the rotor surface (i.e., blow down). Blow down tends to close the clearance with the rotor surface, yet it increases the bristle tip wear. The other issue is the bristle stiffening effects when the aerodynamic forces cannot overcome the internal friction within the bristle pack and with the backing ring.

This is called bristle hangup. After transient rotor excursions or bristle wear, the clearance should close to maintain the minimum leakage, but may not due to "hangup" at high pressure loadings. This introduces a hysteresis issue for increasing versus decreasing pressure loading during operation. Additionally, swirl in the flow approaching the seal can produce other aerodynamic forces on bristles at the upstream face. The flow within the bristle pack is the driving mechanism of the seal dynamics; therefore, a clear flow representation is required.

The aim of the present work is to study the brush seal with a computational fluid dynamics (CFD) analysis, considering the full three-dimensional (3D) flow among the bristles, and a mechanical model predicting the 3D bending behavior of bristles. The modeling approach is also described in Sec. 2 with results presented in Sec. 3. Conclusions and future work are described in Sec. 4.

2 Mathematical Modeling

2.1 Overview. In the present work, the capability to calculate brush seal behavior is developed by combining 3D, detailed CFD, flow modeling with a 3D mechanical model. The method used involves iterations between CFD and mechanical models. The three main components of the iterations are as follows:

1. Geometry definition and MESHING.
2. CFD solution for the 3D flow through the bristles.
3. Mechanical solution to obtain bristle displacements.

The iterative procedure is illustrated in Fig. 2. After the CFD calculation is carried out, the aerodynamic forces on the bristles are available. These are given as input to the mechanical model, together with the "old" bristles' configuration and a new deformed geometry is calculated. Importing the new geometry to the mesh

Contributed by the International Gas Turbine Institute (IGTI) of ASME for publication in the JOURNAL OF TURBOMACHINERY. Manuscript received October 1, 2004; final manuscript received February 1, 2005. IGTI Review Chair: K. C. Hall. Paper presented at the ASME Turbo Expo 2005: Land, Sea, and Air, Reno, NV, June 6 - 9, 2005, Paper No. GT2005-68973.

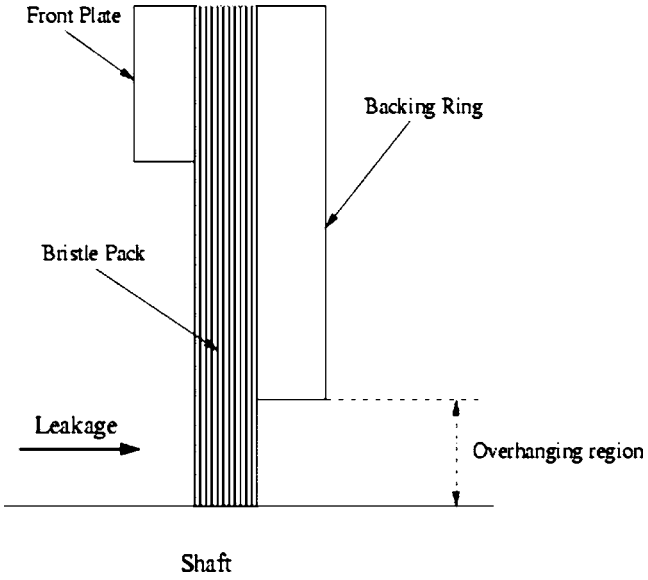

Fig. 1 Schematic of a brush seal

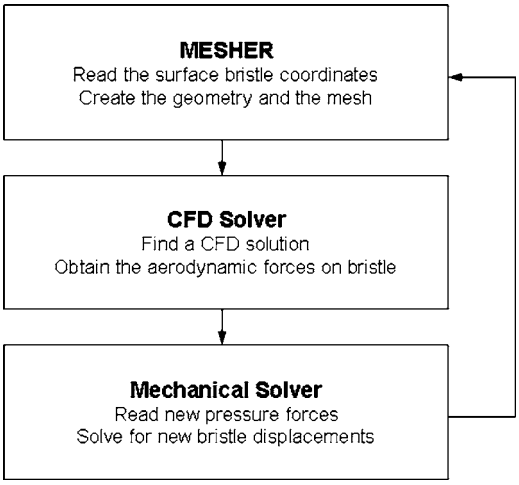

Fig. 2 Fluid-structure iteration procedure

generator, it is possible to then obtain a new grid to use in the next CFD simulation. The procedure described above should be continued until convergence in the deformation is found.

In order to test the iterative procedure, a simple brush seal configuration, was set up including a row of just five bristles, as shown in Fig. 3. In this test case, both the mechanical and fluid dynamics models assumed periodicity in the circumferential direction. The iterative procedure is described and illustrated below using this simple example. Further results for a simple geometry and a real seal geometry are then given in Sec. 3.

2.2 Mechanical Model. SUBSIS (an acronym of Surrey University brush seal iterative simulator) was used in this study. This is an iterative code developed to predict the bending behavior of bristles in a brush seal. The 3D method, on which the code is based, allows a large number of bristles to be considered with arbitrary imposed aerodynamic forces. The problem is discretized by splitting the bristles into a number of elements, and all forces are effectively then applied at points on the bristles. Provided enough elements are used, accurate solutions will be produced. Bristle-to-bristle interaction and shaft and backing ring contacts are taken into account, as well as arbitrary initial bristle packing and lay angles. Aerodynamic loads are applied on bristle rows to calculate deflection in axial, circumferential, and radial directions. However, the model currently neglects friction at the backing plate and between the bristle rows. Brush seals are known to exhibit strong pressure-friction coupling resulting in bristle stiffening, so this will have to be addressed in future work to fully exploit the model.

The so-called 3D-splay and inclined 3D-prop effects are included in the model. The 3D-splay effect is illustrated by considering rotor incursions into a perfectly packed periodic brush seal (i.e., hexagonal packing with no initial clearance between bristles and the backing ring). This must cause displacements in the axial direction, as the volume of the pack cannot be reduced further. The inclined 3D-prop effect arises from the reaction force, acting on a bristle, at the backing ring edge and implies that the bristles are bent toward the rotor. It should also be noted that the mechanical model uses linear beam theory and the principle of superposition to get the deflection of a given point along the bristle; this allows faster computation but could involve inaccuracies for large deflections. Formally, the linear approximation is valid when the square of the derivative of bristle deflection with respect to distance along the bristle is small compared to unity. Further infor-

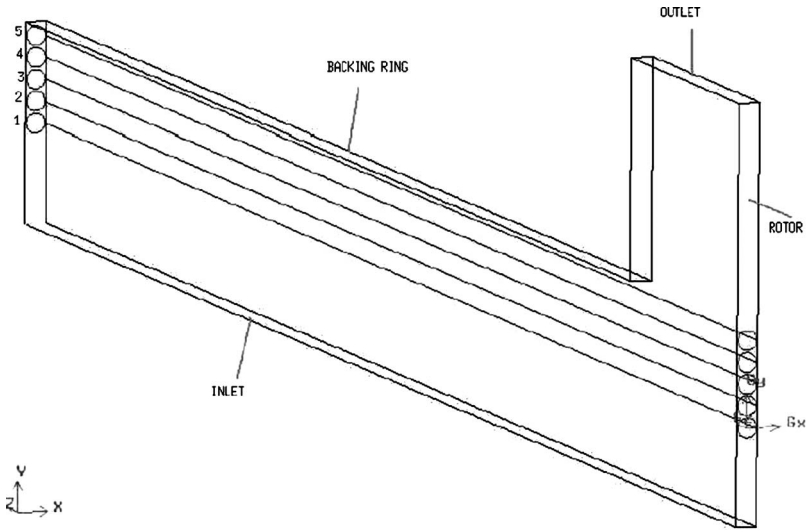

Fig. 3 Simple brush seal used in the present work showing the bristle numbers

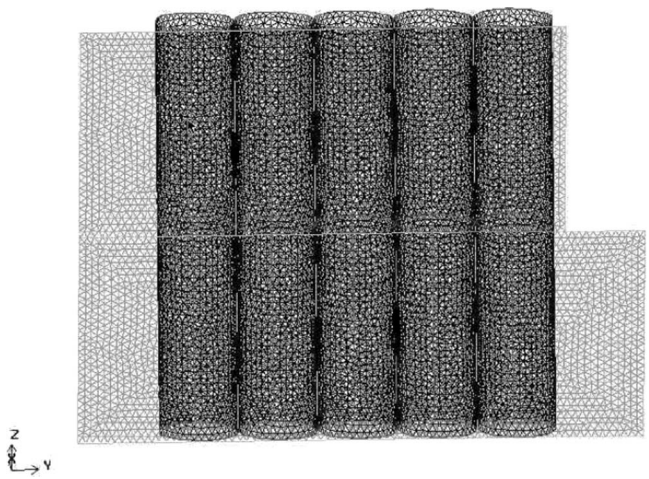

Fig. 4 Mesh detail in the backing-ring end region (coarser mesh) for a deformed configuration; the figure shows the small gaps between the bristles

mation on the code is given by Guardino and Chew [11]. Validity of the present calculations is discussed further in Sec. 3.2.2

2.3 Meshing. The brush seal geometry contains very high aspect ratio ($L/\delta \cong 1200$) channels, between the bristles. This leads to some difficulty in keeping the mesh fine enough to capture the flow in the small gaps between bristles while economizing on mesh points in regions less affected by high gradients. Further problems arise when considering the deformed geometry as it is then not possible to perform a simple projection of a face mesh along a straight line.

The mesh generator used in the present work is GAMBIT [13]. The geometry output from the mechanical model gives a series of vertex coordinates for each bristle. In producing this geometry the bristle diameter is assumed to be slightly smaller (typically 1.52 μm for a 76 μm bristle diameter) than the actual diameter assumed in the bending calculation. This avoids contact between bristles in the CFD model, and may be justified by considering that the bristles will not be perfectly smooth and some leakage will occur in practice, due to geometry imperfections. The vertex data can be read into the mesh generator.

Current meshes use a mix of hexahedral and tetrahedral cells. Results from two meshes will be presented here. The coarser mesh is shown in Fig. 4 and has ~800 000 cells. The finer mesh has ~1 700 000 cells. Considering all the meshes used here the maximum element skewness was 0.4 and the maximum aspect ratio 18.

2.4 CFD Solution. The flow through the bristle pack has been calculated with the FLUENT [12] CFD package, using a laminar model. The assumption of laminar flow is justified by the low Reynolds number of the flow in the gaps between the bristles. For example, with a gap size of 5 μm, velocity of 100 m/s, pressure of 2×10^5 Pa, and temperature of 300 K, the Reynolds number is about 67. Total pressure was specified at the inlet, static pressure was specified at the outlet, and no-slip conditions applied on all walls. For the axial inflow cases the flow angle was specified as axial, otherwise the inlet "swirl" velocity was specified. An implicit steady 3D solver, with a second-order upwind differencing scheme, with the "SIMPLE" pressure-velocity coupling algorithm, was used to obtain the fluid dynamics field. Once the CFD solution was obtained, a UDF (i.e., user defined function [12]) was used to calculate the aerodynamic forces on the bristles; more details about this procedure will be given in Sec. 2.5.

2.5 Coupling Procedure. As described in Sec. 2.1 above, the iterative solution procedure involves successive runs of the CFD solver, the mesh generator, and the mechanical model. In the first step, the CFD solution for the initial configuration, with the undeformed bristles, is performed. The aerodynamic forces are obtained by running a user defined function (UDF) in the CFD program. This function is programmed in the "C" computing language and calculates the aerodynamic forces on the bristles from the flow solution. The output from the UDF is a distribution of force per length along the bristles. For the mechanical problem the bristle bending problem is discretized by defining a number of elements along the length of each bristle and approximating all forces on the bristle to point forces acting on the elements' nodes. The forces on these nodes are obtained by integrating the force distribution over the areas corresponding to the mechanical model element. To get the discrete force distribution, the surface of the bristles is split into 19 elements with a finer element size where the gradients are expected to be the largest, and coarser elsewhere.

The integration to get the forces acting on the mechanical model nodes is done using a "C" program that takes the discrete force distribution as input and returns a file, containing the forces that can be used as the input file for the mechanical model. The integration process is completely automatic.

The deflected configuration is then calculated and output to files, each storing the points of a bristle. These files are then used as input for the meshing software. The geometry definition and the meshing procedure are automated using a "journal file" (see Ref. [13]). Analogous procedures are also possible for other commercial mesh generators. To keep this meshing procedure completely automatic, the following approach was adopted:

- Definition of a volume containing the finer and unstructured part of the mesh, but large enough to contain the deflected bristles.
- Bristles' radius reduction to avoid bristle intersections as explained in Sec. 2.3.

Table 1 Brush seal parameters used in the calculations

Packing type		Rectangular
Total number of bristles		5
Lay angle	Φ	0°
Bristle length	L	9.30 mm
Height of bristle overhang	H	1.40 mm
Bristle diameter	D	0.076 mm
Young's modulus	E	2.25×10^{11} N/m^2
Minimum initial clearance between bristles	δ	0.0076 mm
Number of bristle elements	K	20
Initial rotor interference	Z_{rotor}	0.00 mm
Pressure load	ΔP	1.00 bar

3 Results

3.1 Simplified Geometry. The iterative coupling procedure was first used to predict the 3D bending behavior of bristles in the simple brush seal shown in Fig. 3. The parameters employed in this work are as summarized in Table 1 unless otherwise stated. The Young's modulus used is for a cobalt-based alloy known as Haynes-25 (see Ref. [14]). Incompressible flow and an axially directed inflow is assumed in this simplified model. Each iterative calculation in the mechanical model has been continued until the displacement residual was much smaller than the deflection.

The axial aerodynamic forces per unit length acting on each of the five bristles and the pressure field on the periodic plane of the incompressible CFD solution are shown in Figs. 5 and 6. Note that the bristle numbering starts with the most upstream bristle, and that these results are for an undisturbed pack. Strong variations in aerodynamic force (associated with strong flow variations) occur on the downstream bristles near the backing ring edge position which almost divides the bristle pack into two separate regions. In this case, convergence of the coupled procedure was rapid, and the aerodynamic forces changed by no more than about

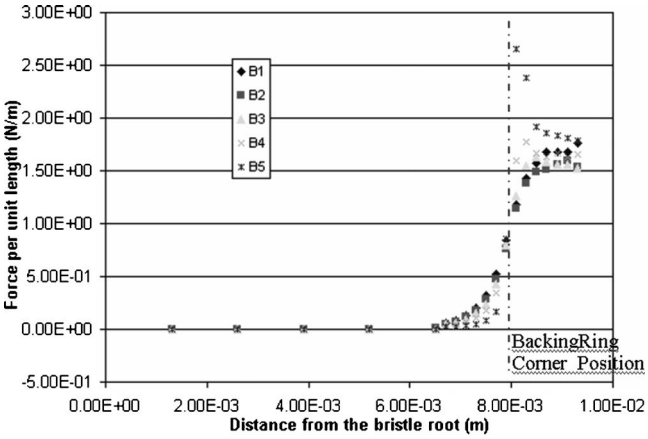

Fig. 5 Forces per unit length on the five bristles. $\Delta P = 1$ bar.

10% from the initial undisturbed geometry calculation.

As shown by the pressure contours in Fig. 6 and velocity vectors in Fig. 7, the strongest flow occurs near the backing ring edge. In this region, there is a strong flow directed down the backing plate and along the bristles. This is due to the comparatively weak resistance to flow in this direction compared to that normal to the bristles. Not surprisingly, the peak aerodynamic forces occur on the downstream bristle near the backing ring edge. The strong velocities near the backing ring corner in Fig. 7 may explain the negative relative pressures in Fig. 6. Note that assuming a pressure load of 10^5 Pa distributed evenly over the five bristles in the region overhanging the backing ring would give a uniform aerodynamic force on each bristle of 1.52 N/m. It is interesting to note that values are slightly greater than this in Fig. 5. A thorough investigation of this effect would require study of the influence of outlet boundary conditions (including their influence on convergence of the CFD solution), and this has not been undertaken here. Some reversed flow at the (nominal) outlet boundary was observed in this solution.

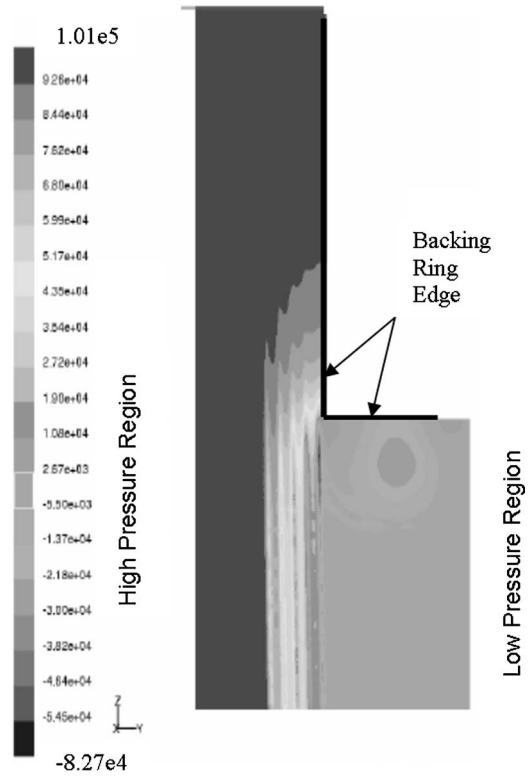

Fig. 6 Relative pressure (Pa) contours on the periodic plane in the backing ring corner region

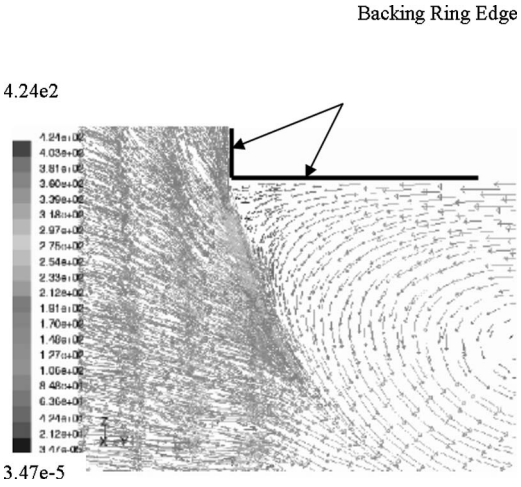

Fig. 7 Velocity vectors colored by the velocity magnitude (m/s)

The bristle positions, shown in Fig. 8, did not change substantially after the first iteration. Thus for this case a good solution could be obtained without iteration. The deflections show the expected behavior. The downstream bristle (five) pivots at the backing ring edge and the pack compresses, taking up the initial gaps allocated between the bristles.

A simple mesh dependency test was conducted for the CFD model. For the same conditions on a deformed geometry, two calculations, on meshes of ~800 000(coarser) cells and ~1 700 000(finer) cells, were carried out. Very small changes were found, and so the coarser mesh was used for these simulations.

3.2 Real Geometry.

3.2.1 Seal Specifications. A real brush seal has been investigated using the coupled model. Table 2 summarizes the seal geometry, where the lay angle is defined as the angle formed by the bristle centerline and the radial direction (at the bristle tip). The seal configuration is one from an experimental study at Oxford University reported by Owen et al. [9]. To obtain periodic surfaces along the circumferential direction (**x** *axis* in the model) in the CFD model, the geometry has been cut with two planes containing bristle centerlines. This gives a model containing five complete bristles and ten half bristles. As the periodic planes cut through the bristles, the "thickness" of the CFD domain is just over one bristle diameter as it includes the clearance between the bristles.

The CFD mesh generation was guided by results for the simple geometry. Use of wedge shaped elements, rather than the purely tetrahedral elements used for the simple geometry, allowed economies to be made on the number of cells. The final mesh included 700 000 cells. The flow model in this case is compressible.

In the mechanical model, two rows of bristles are included to simplify the periodic boundary condition, so 20 complete bristles were included.

3.2.2 Axial Inlet Flow. In this section, results for the real seal geometry with axial inlet flow are presented, with pressure differences across the seal of 4, 7, and 12 bar. A converged fully coupled solution has been completed only for the 4 bar pressure difference case. In this case the bristle deflections changed little after the first iteration (as was found for the simplified geometry considered above). For the remaining cases, bristle deflections were more severe and the automatic mesh generation failed. For

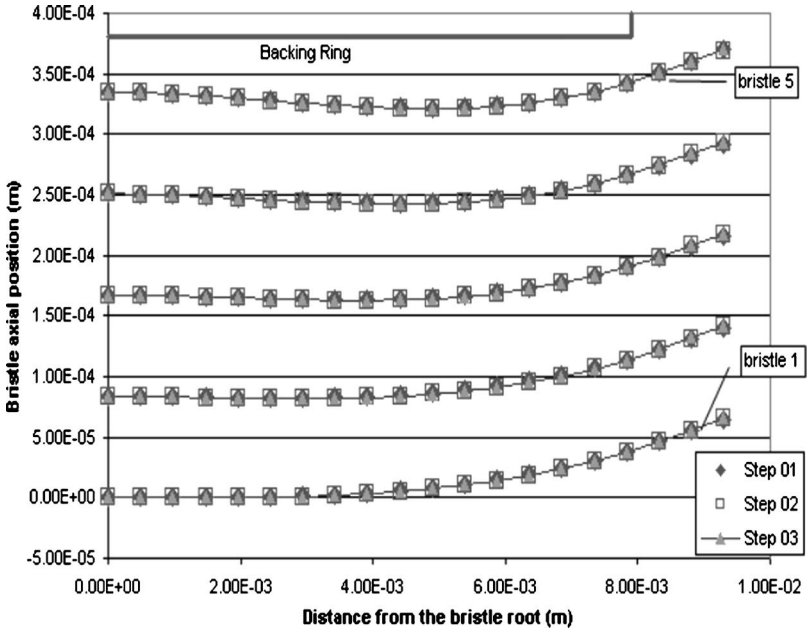

Fig. 8 Bristle centerline positions in the axial radial plane in the three iterative steps; the position of the BR is shown on top of the graph

these cases a combined (rather than fully coupled) analysis was undertaken. In the combined model aerodynamic forces calculated for the undisturbed bristle pack were used in the mechanical model without iteration. As will be shown below the combined model yielded very encouraging results.

From the CFD results, the static pressure distributions near the overhanging region on the middle circumferential plane for the ΔP 4 and 12 bar cases are shown in Fig. 9. Note that, with the assumed hexagonal packing arrangement, this plane cuts through just five bristles. It is clear from the pressure field that the region near the bristle roots is quiescent. The strongest flow develops close to the backing ring corner region, as for the simplified geometry. In this case with the nonzero lay angle, the gradient in the radial pressure creates a *blow-down* force on the bristles, pressing the bristle tips into the rotor.

Aerodynamic forces on the bristles are extracted from the CFD solution and are presented in Fig. 10 for the $\Delta P = 12$ bar case. These graphs show the forces per unit length used to get the point forces for the mechanical model. $B10$ is the downstream bristle in these graphs. Axial forces are positive in the streamwise direction. Radial forces are positive when directed away from the rotor. Circumferential forces are positive when directed in the usual direction of rotor rotation. It is clear that the maximum forces occur on the downstream bristle. The aerodynamic blow-down force is strongest near the backing ring edge, as expected from the pressure distribution.

Table 2 Brush seal parameters

Packing type		Hexagonal
Total number of bristles		10
Lay angle	Φ	40 deg
Bristle length	L	13.35 mm
Height of bristle overhang	H	1.00 mm
Bristle diameter	D	0.100 mm
Young's modulus	E	2.25×10^{11} N/m^2
Minimum initial clearance between bristles	δ	0.004 mm
Number of bristle elements	K	20
Initial rotor interference	Z_{rotor}	0.00 mm

Figure 11 shows the axial deflections for the bristle centerlines at different pressure loadings. These show the expected trends. The aerodynamic blow-down results in a reactive force on the rotor. Although friction is neglected in the initial estimate of the shaft reaction, it is straightforward to correct this calculated reaction to allow for friction between bristle tips and rotor, and then estimate the rotor torque. The essential point is that the component of reaction normal to the bristle is given by the frictionless solution and this must remain the same in the case with rotor/bristle tip friction. This procedure does not, of course, take account of friction with the backing ring and between bristles which can also be important. Results from this calculation, using a friction coefficient of 0.3, chosen in the middle of the range given by Aksit [15], are shown in Fig. 12, which also includes Oxford University's experimental data. The experimental data was obtained from transient "run-down" experiments which showed significant variations in torque (see for example, Wood et al. [10]). The experimental results in Fig. 12 are the maximum values reported. Given the uncertainties, the agreement with the present model is considered very good. Leakage flow rates were also compared with experimental data and were found to be about half the measured values. This suggests that the perfect packing and interbristle clearance assumed in the analysis may not be fully representative. Further discussion of this is given in Sec. 3.2.4.

The deflections considered here are well within the range of validity of the linear bending theory (see, for example, Stango et al. [16]). However the model does not include "liftoff" of bristles from the shaft surface due to axial bending. This effect will be of order d/L times the axial deflection. However here it is appropriate to replace the full bristle length L by the length of the bristle overhanging the backing ring. This gives a possible liftoff of about 10 μm. In practice this may be countered by the blow-down effects due to the forces in the radial and circumferential directions. Note also that the mechanical model does allow liftoff or blowdown due to forces in the radial and circumferential directions.

3.2.3 Swirling Inlet Flow. The model used above was extended to include the effect of inlet swirl. Results were obtained

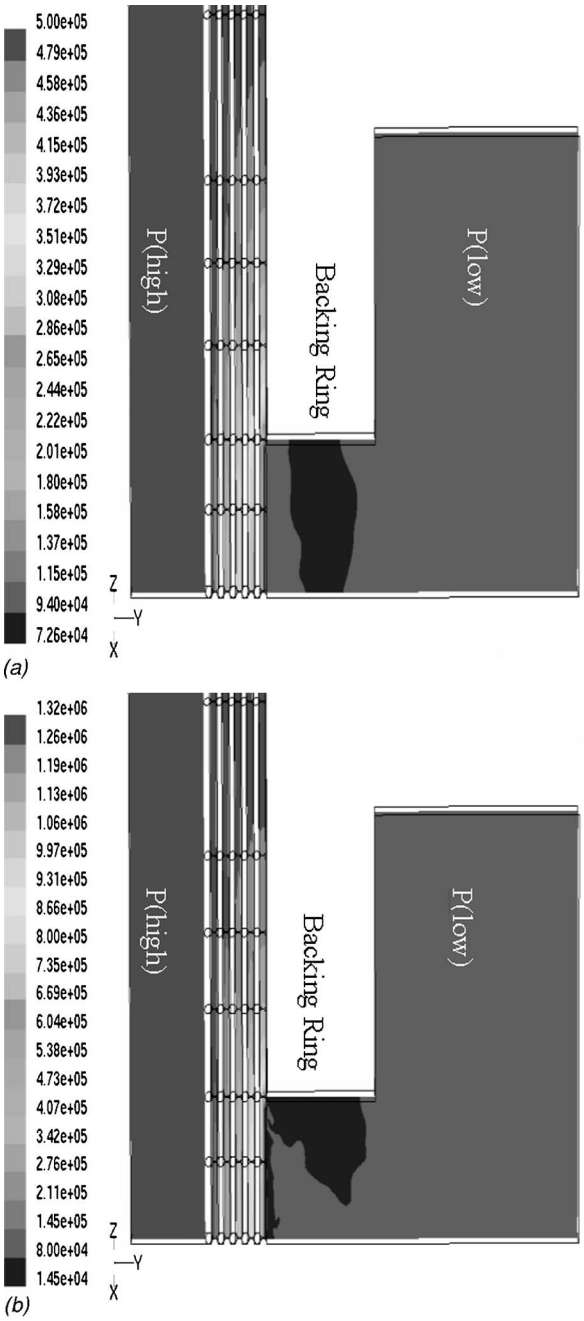

Fig. 9 Contours of static pressure (Pa) near the overhanging region (a) 4 bar (b) 12 bar

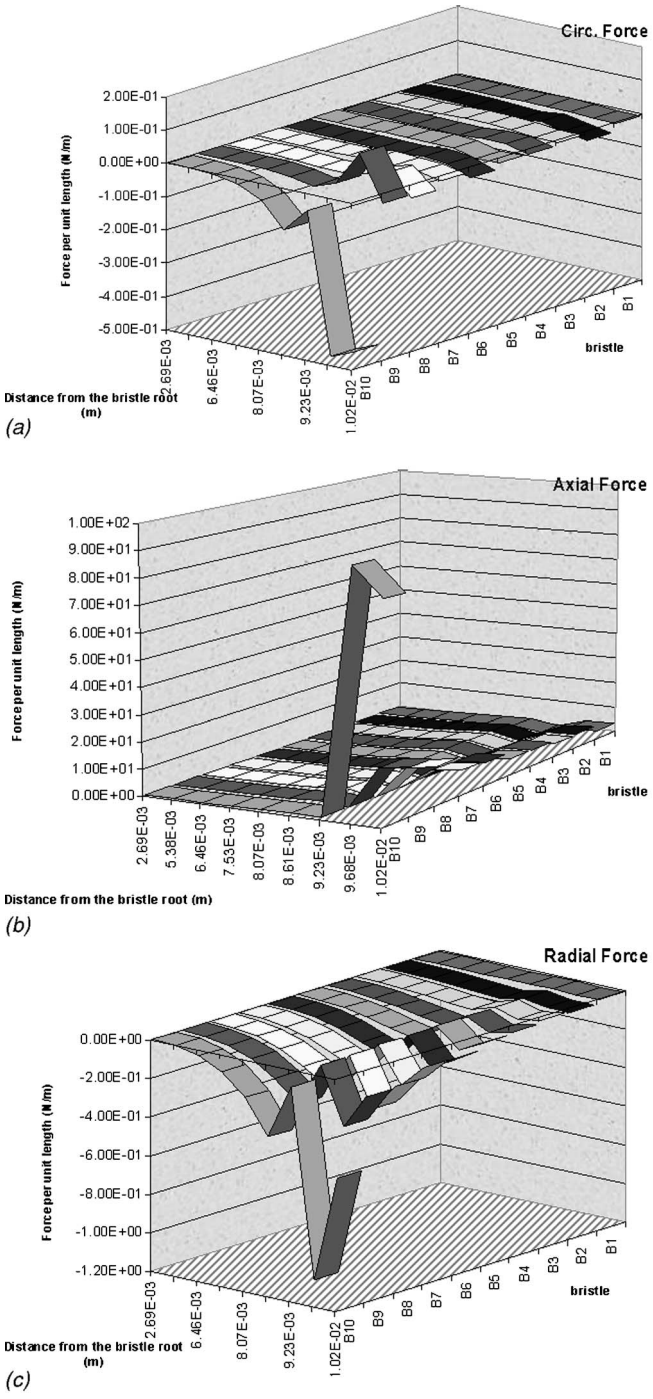

Fig. 10 Aerodynamic forces from the CFD calculation with $\Delta P = 12$ bar (a) circumferential forces (b) axial forces (c) radial forces

for the 4 bar pressure loading case with inlet swirl velocities of 50 and 150 m/s. In both cases, the inlet swirl resulted in some relatively small additional aerodynamic forces on the upstream bristle row, but had little effect on the forces on other bristles or on the calculated bristle deflections.

3.2.4 Large Pack Effects. A preliminary analysis has been carried out investigating bristle movements in a larger bristle pack. The procedure involved the CFD forces from one row only being repeated over the pack number of rows. This simulation was aimed at testing if, with a larger bristle pack, the aerodynamic forces applied could cause any asymmetry in the seal. This actually happened for the case studied (the ΔP 12 bar, case of Sec. 3.2.2), and is shown in Fig. 13, where slipping lines appeared in the middle of the pack. These results are for a pack with ten bristle rows in both the axial and circumferential directions with circumferential periodicity assumed. The results indicate that for a more detailed analysis of the seal, this model should include enough rows to capture the asymmetric behavior which could not be revealed if considering too few bristles. Such effects might also contribute to the underprediction of seal leakage referred to in Sec. 3.2.2, and might lead to more significant effects of inlet swirl than were described above.

4 Conclusions

Coupled 3D CFD and mechanical simulations for a brush seal have been demonstrated. Progress has been made on automating a

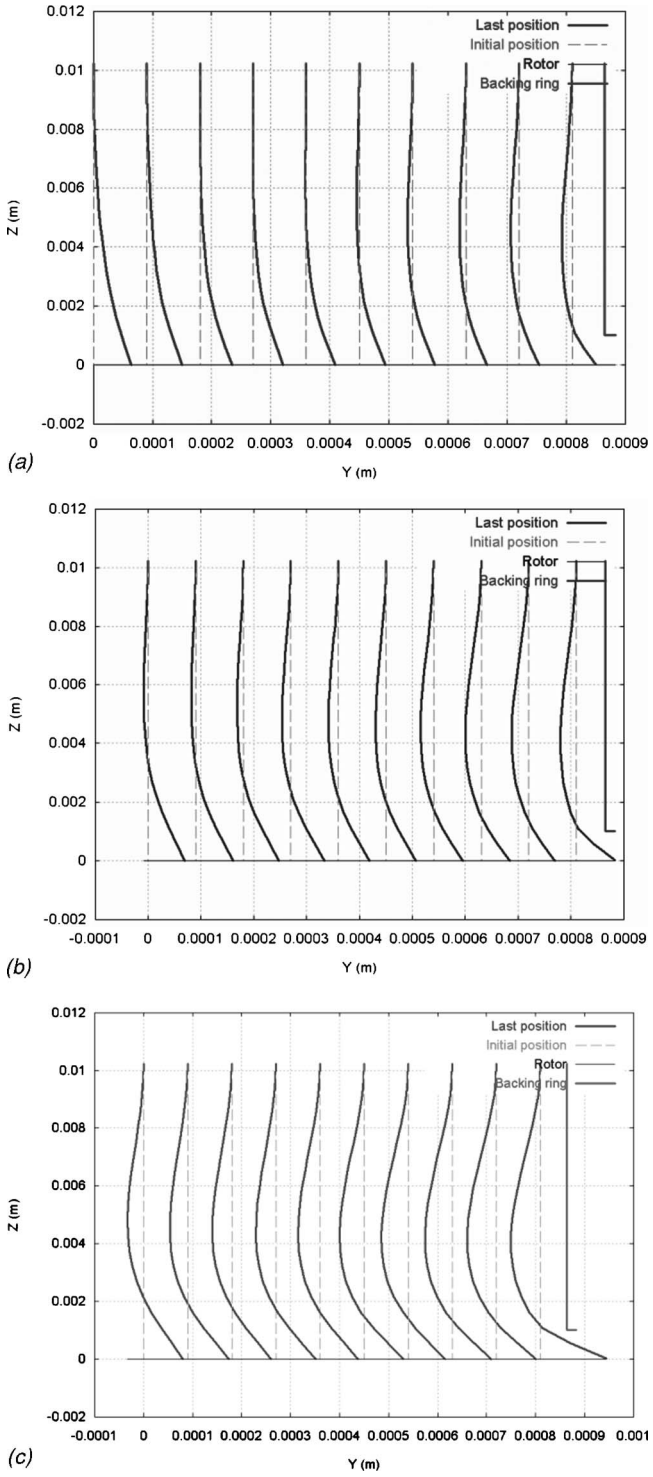

Fig. 11 Bristle deflections in the axial-radial plane (a) 4 bar (b) 7 bar (c) 12 bar

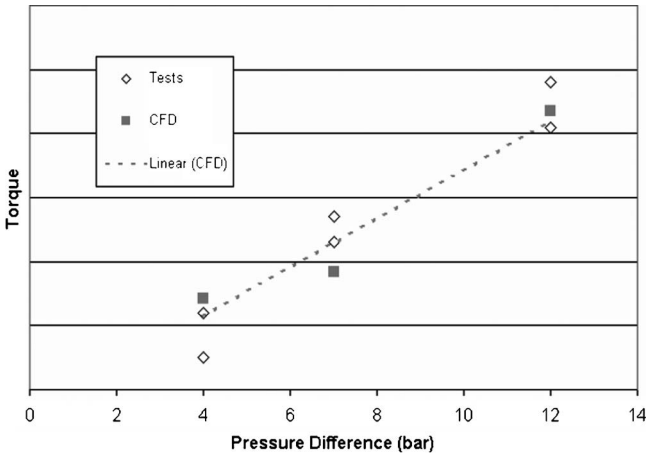

Fig. 12 Variation of torque with pressure difference across seal

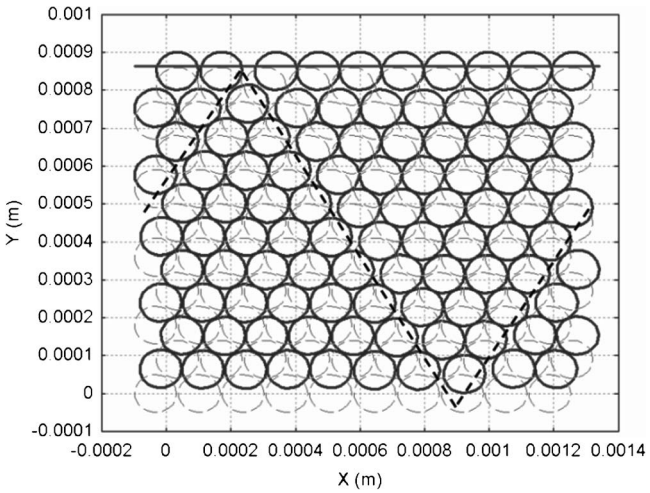

Fig. 13 Large pack bristle tips. The dashed lines indicate the slipping planes in the pack; ---- initial position;—last position,—backing ring.

fully coupled procedure, with CFD mesh generation for the deformed geometries being the main difficulty. The results obtained give insight into brush seal behaviour and there is considerable scope for further development and exploitation of the method, particularly as the available computing power continues to improve.

Torque predictions from the model are in good agreement with experimental data. Leakage flows appear to be underpredicted, but these will be sensitive to the packing and inter-bristle clearance assumed in the model. For practical application, calibration of the model to match measured leakage rates could be undertaken.

The mechanical model indicates that asymmetric deformations are likely, and such effects will have to be included in a fully representative model.

Acknowledgment

Financial support for this work from ALSTOM Power Limited is gratefully acknowledged. The authors also wish to thank colleagues at ALSTOM, the University of Surrey, and the University of Oxford for their technical input. This includes the brush seal test data referred to in this report which was generated at the University of Oxford.

Nomenclature

BR = Backing ring
D = Diameter of bristle
d = Bristle deflection
d^* = Normalized bristle deflection ($=d/D$)
H = Backing ring overhang height
K = Number of bristle elements
L = Actual bristle length

R = Total reaction force
UDF = User defined function
x, y, z = Circumferential, axial, radial direction respectively

Greek

μ = Friction coefficient
δ = Initial gap clearance between bristle and backing ring
Φ = Lay angle (=0 deg for radially aligned bristle)
ΔP = Pressure difference across seal

Subscripts

ax = Axial
circ, c = Circumferential
n = Normal to the bristle surface
rotor, r = Rotor surface

References

[1] Ferguson, J. G., 1988, "Brushes as High Performance Gas Turbine Seals," ASME Paper No. 88-GT-182.
[2] Chupp, R. E., and Dowler, C. A., 1993, "Performance Characteristics of Brush Seals for Limited-Life Engines," ASME J. Eng. Gas Turbines Power, **115**, pp. 390–396.
[3] Chupp, R. E., and Nelson, P., 1993, "Evaluation of Brush Seals for Limited-Life Engines," AIAA J. **9**(1), pp. 113–118.
[4] Carlile, J. A., Hendricks, R. C., and Yoder, D. A., 1993, "Brush Seal Leakage Performance With Gaseous Working Fluids at Static and Low Rotor Speed Conditions," ASME J. Eng. Gas Turbines Power, **115**, pp. 397–403.
[5] Gorelov, G. M., Rezinik, V. E., and Tsibizov, V. I., 1988, "Experimental Study of Brush Seal Flow Characteristics and Comparison With a Labyrinth Seal," Izvestitiya VUZ, Aviatsionnaya Tekhnika, **31**(4), pp. 43–46 (Allerton Press).
[6] Chupp, R. E., Aksit, M. F., Ghasripoor, F., Turnquist, N. A., and Demiroglu, M., 2001, "Advanced Seals for Industrial Turbine Applications," AIAA Paper No. 2001-3626.
[7] Dinc, S., et al., 2002, "Fundamental Design Issues of Brush Seals for Industrial Applications," ASME J. Turbomach., **124**, pp. 293–300.
[8] O'Neill, A. T., Hogg, S. I., Withers, P. A., Turner, M. T., and Jones, T. V., 1997, "Multiple Brush Seals in Series," ASME Paper No. 97-GT-194.
[9] Owen, A., K., Jones, T. V., Guo, S., M., and Hogg, S., 2003, An Experimental and Theoretical Study of Brush Seal and Shaft Thermal Interaction," ASME Paper No. GT2003-38276.
[10] Wood P. E., and Jones T. V., 1997, "A Test Facility for the Measurement of Torques at the Shaft to Seal Interface in Brush Seal," ASME Paper No. 97-GT-184.
[11] Guardino, C., and Chew, J. W., 2004, "Numerical Simulation of 3D Bristle Bending in Brush Seals," ASME Paper No. GT2004-53176.
[12] Fluent 6.1 Documentation, FLUENT Package, Fluent Inc., Lebanon, NH.
[13] Gambit 2.1.2 Documentation, FLUENT Package, Fluent Inc., Lebanon, NH.
[14] http://www.alloywire.com/haynes25.htm
[15] Aksit, M. F., 2003, "Analysis of Brush Seal Bristle Stresses With Pressure-Friction Coupling," ASME Paper No. GT2003-38276.
[16] Stango, R. J., Zhao, H., and Shia, C. Y., 2003, "Analysis of Contact Mechanics for Rotor-Britle Interference of Brush Seal," ASME J. Tribol., **125**, pp. 414–421.

Film Cooling Effectiveness and Heat Transfer on the Trailing Edge Cutback of Gas Turbine Airfoils With Various Internal Cooling Designs

P. Martini

A. Schulz

H.-J. Bauer

Lehrstuhl und Institut für Thermische Strömungsmaschinen, Universität Karlsruhe (TH), Kaiserstr. 12, 76128 Karlsruhe, Germany

The present study deals with trailing edge film cooling on the pressure side cutback of gas turbine airfoils. Before being ejected tangentially onto the inclined cut-back surface the coolant air passes a partly converging passage that is equipped with turbulators such as pin fins and ribs. The experiments are conducted in a generic setup and cover a broad variety of internal cooling designs. A subsonic atmospheric open-loop wind tunnel is utilized for the tests. The test conditions are characterized by a constant Reynolds number of $Re_{hg}=250\,000$*, a turbulence intensity of* $Tu_{hg}=7\%$*, and a hot gas temperature of* $T_{hg}=500$ K. *Due to the ambient temperature of the coolant, engine realistic density ratios between coolant and hot gas can be realized. Blowing ratios cover a range of* $0.20<M<1.25$. *The experimental data to be presented include discharge coefficients, adiabatic film cooling effectiveness, and heat transfer coefficients in the near slot region* $(x/H<15)$. *The results clearly demonstrate the strong influence of the internal cooling design and the relatively thick pressure side lip* $(t/H=1)$ *on film cooling performance downstream of the ejection slot.* [DOI: 10.1115/1.2103094]

Introduction

The thermodynamic cycle efficiency of gas turbines is closely linked to the peak temperature of the working fluid. Advanced gas turbines are operated at peak temperatures that are well beyond the maximum allowable metal temperatures. Currently, temperatures of up to 2000 K are attained at the combustor exit. As a consequence, all hot gas-ducting elements of a gas turbine have to be cooled intensively by compressed air. Since the coolant does not participate in the whole cycle, cooling inherently is a loss. One major developmental effort therefore is to further reduce the required amount of coolant, i.e., to optimize cooling techniques. For thermally high loaded blades and vanes, generally a combination of film cooling and internal convective cooling is utilized to guarantee wall temperatures within the limits of the blade material.

An adequate cooling of the blade's trailing edge is challenging due to geometric constraints in combination with aerodynamic demands. From an aerodynamic point of view the trailing edge should be designed as thin as possible, which is in conflict with the cooling design and structural integrity. State-of-the-art cooling concepts often use a pressure side cutback where the pressure side wall of the trailing edge is shortened with respect to the suction side. Cooling air is ejected through a spanwise slot onto the cutback surface. In order to ensure the structural integrity of the trailing edge, arrays of ribs or pin fins in the coolant passage connect the pressure side and the suction side walls. Additionally, they act as turbulators promoting the internal convective heat transfer in the coolant passage and controlling the blade's coolant mass flux.

Figure 1 shows a cross-sectional view of a turbine blade with trailing edge cutback (in this example, the slot is laterally disrupted by stiffening lands). The film formed by the slot may be of a complex, three-dimensional structure, especially when turbulators are located close to the ejection slot, i.e., the lip overhang is short. Furthermore, as the lip thickness in such configurations typically is in the order of the slot height, the mixing process in the near slot region may be additionally affected by flow instabilities like vortex shedding.

There only exist a few studies dealing with trailing edge cooling by means of a pressure side cutback. Taslim et al. [1] investigate the film cooling effectiveness downstream of trailing edge slots that are spanwise disrupted by wooden lands. They consider the impact of lip thickness, density ratio, slot width, and ejection angle. In accordance to other sources ([2–5]), they identify the ratio of lip thickness to slot height being a key parameter for film cooling on cut-back surfaces. It is observed that the effectiveness is virtually insensitive to a variation of the density ratio and slot width for a given blowing ratio. Uzol et al. [6] and Uzol and Camci [7] investigate the discharge behavior of different trailing edge slots at varying length of the cutback surface in a scaled up subsonic cascade. (PIV) as well as traverses of the total pressure in the wake indicate that trailing edges with cutback induce smaller aerodynamic losses than those without cutback. Holloway et al. [8,9] numerically investigate a trailing edge slot, spanwise disrupted by lands, for realistic turbine conditions. Their (URaNS) calculations reveal periodic vortex shedding from the lip ($t/H=0.9$). This vortex shedding might be involved in the relatively fast decay of film cooling effectiveness for slots with larger t/H. Martini et al. [10] investigate a trailing edge slot equipped with an internal rib array featuring a small lateral pitch of $s/H=2$. For this highly obstructed slot they observe a grouping of two coolant jets each (sometimes three coolant jets), which is attributed to the Coanda effect. The grouping allows hot gas entrainment in the near slot region. For some blowing ratios, a permanent and random regrouping process is observed leading to an unstable nature

Contributed by the International Gas Turbine Institute (IGTI) of ASME for publication in the JOURNAL OF TURBOMACHINERY. Manuscript received October 1, 2004; final manuscript received February 1, 2005. IGTI Review Chair: K. C. Hall. Paper presented at the ASME Turbo Expo 2005: Land, Sea, and Air, Reno, NV, June 6-9, 2005, Paper No. GT2005-68083.

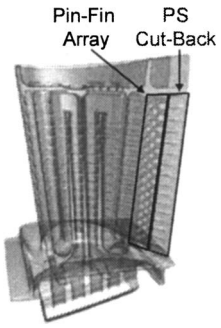

Fig. 1 Cross-sectional view of a turbine blade with pressure side cutback

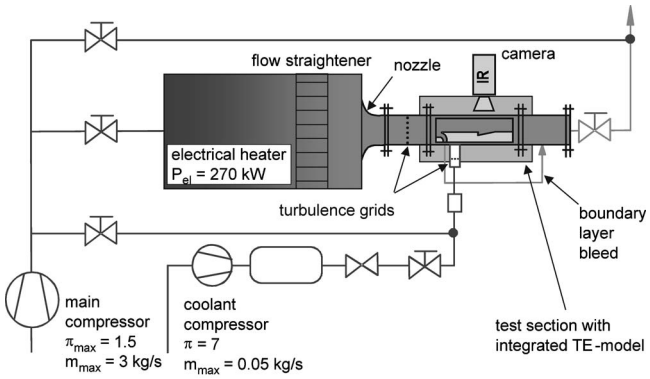

Fig. 2 Schematic view of the atmospheric test facility

of the adiabatic wall temperatures on the cutback surface. A similar phenomenon is also reported by Nina and Whitelaw [11].

As stated earlier, the number of publications directly focusing on pressure side trailing edge film cooling is quite limited. Nevertheless, there has been extensive research in the field of film cooling by wall jets emerging from unobstructed as well as obstructed slots. Goldstein [12] gives a detailed review on the most relevant work, done before 1971. The effect of the upstream boundary layer on film cooling performance is investigated by Kacker and Whitelaw [13]. In accordance with other sources, they find only a weak influence of the upstream aerodynamic boundary layer thickness on film cooling effectiveness. Marek and Takina [14] investigate the influence of main flow turbulence intensity on film cooling effectiveness. For a thin-lipped clean slot, they observe a significant decrease in film cooling effectiveness as Tu_{hg} is increased. Sturgess [15,16] investigates film cooling for practical combustor slots that are supported by circular metering ports. The importance of a lip overhang to achieve a uniform cooling film at the slot exit is emphasized. If lip overhang is not considered properly, hot gas entrainment may lead to a significant reduction in film cooling effectiveness when compared to the ideal clean slot. A geometrical parameter is derived to classify practical cooling slots with respect to their film cooling performance.

The majority of studies focus on film cooling effectiveness, assuming that heat transfer remains relatively unchanged by the injection. However, this assumption has shown to be valid only further downstream of the slot. In the near slot region, the heat transfer is found to be strongly affected by the coolant flow (see, e.g., [17–19]).

To the knowledge of the authors, there is no detailed data available in the open literature on film cooling performance in the near slot region of practical trailing edge slots, equipped with arrays of ribs or pin fins. Hence, the scope of the present work is to provide a complete set of experimental data describing the overall cooling performance (i.e., effectiveness and heat transfer) including the discharge behavior obtained for internal cooling designs that are relevant in modern trailing edge cooling concepts.

Test Setup and Operating Conditions

The experimental work is conducted in the subsonic test facility (Fig. 2) of the Institut für Thermische StrömungsMaschinen, Baden Würtlemberg Germany. The open wind tunnel is connected to a radial compressor providing a maximum mass flow of 3 kg/s. The air is heated in a temperature controlled electrical heater consisting of 18 heating cartridges with a total power of 270 kW. Using coolant air at ambient temperature allows for the investigation of film cooling at an engine realistic density ratio. After heating, the air passes a system of mixers, flow straighteners, and a high contraction nozzle to achieve a homogenous temperature and velocity field at the entrance of the hot wind tunnel. The tunnel dimensions are 105 mm in height at a lateral width of 220 mm. A grid of square bars is inserted upstream of the trailing edge model to obtain an elevated level of turbulence for the film cooling experiments ($Tu_{hg}=7\%$). A variable boundary layer bleed is utilized upstream of the trailing edge model. This guarantees an engine realistic boundary layer thickness of the main flow at the ejection slot plane.

The test section is characterized by its excellent optical accessibility. Three circular sapphire windows in the top wall of the tunnel allow for infrared thermography of the test surface. A large quartz window on one of the sidewalls provides additional optical access. The other sidewall is equipped with a traversing mechanism carrying a Pitot probe for detecting the total pressure and temperature profiles at various streamwise and lateral positions in the test section. The static pressure is measured by according wall pressure tabs. The coolant air is supplied by a second compressor and metered by a hot film air mass flux sensor. After passing a diffuser and a flow straightener, the coolant enters a rectangular high aspect ratio duct of 180 mm width and 15 mm height. Similar to the main flow, a turbulence grid of square bars is inserted into the duct, providing the desired level of turbulence at the inlet into the coolant cavity ($Tu_c=5\%$).

A cross-sectional view of the enlarged trailing edge model is shown in Fig. 3. The modular design allows for the investigation of trailing edge slots with various internal turbulator arrangements. $G1$ is a double in-line rib array used in (LP) turbines whereas $G2a$ is an equilaterally staggered array of cylindrical pins, which is predominantly found in (HP) turbines. The array consists of six rows where the last row of pins is located in the $L2$ region. Alternatively, a five-row configuration is tested ($G2b$) with the last row being removed to allow for a more uniform coolant flow at the slot exit.

An aluminium nose section ($L0=92$ mm) is used to separate the upstream near wall main flow. A wedge shaped ($\alpha=10$ deg) base plate made from steel serves as a support frame for the different test plates. The pressure side equivalent ($L1/L2$) aligns flush with the nose section. It is bolted to the base plate covering the coolant cavity. To guarantee an engine realistic Biot number, the pressure side equivalent wall ($L1/L2$) and the turbulators are machined from high quality steel with $\lambda=14$ W/(mK). As the turbulators are normally cast, large fillet radii between the pins and the endwalls are unavoidable. To consider their potential impact on the film mixing process, the turbulators in $L2$ are equipped with fillets of $R_f/D=R_f/H=0.5$. Table 1 shows the key dimensions for the trailing edge cooling configurations, investigated in the present work.

For the determination of film cooling effectiveness and heat transfer coefficients in the $L3$ region, two different test plates are utilized. The first one consists of Tecapeek, a high temperature resistant plastic material featuring an extremely low thermal conductivity ($\lambda=0.25$ W/(mK)). This plate covers the $L3$ region but

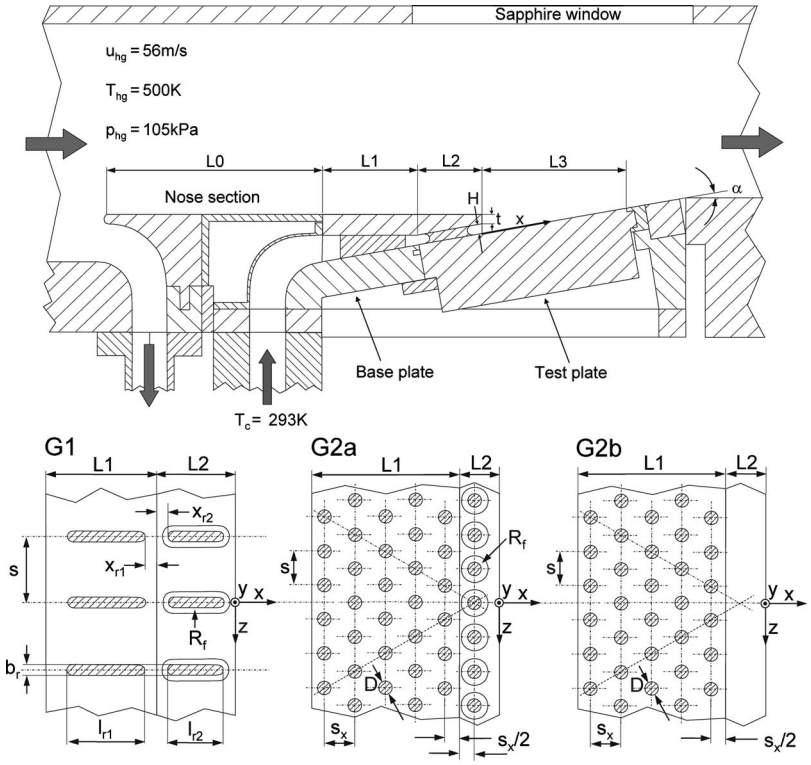

Fig. 3 Cross-sectional view of the trailing edge model and internal cooling design (key dimensions see Table 1)

also extends approximately 30 mm into the *L*2 region leading to almost adiabatic conditions on the suction side equivalent wall.

A second test plate made from Titanium (TiAl6V4) is used for the heat transfer experiments. It extends over the *L*3 region and is heated from the back by a temperature controlled cylindrical heater of 1.5 kW electric power. The heater is embedded into a solid copper block to ensure a uniform heat load on the backside of the test plate. Throughout the heat transfer tests, a temperature controlled guiding segment heats the suction side equivalent of *L*2 to keep the step in surface temperature between *L*2 and *L*3 as low as possible.

Table 2 lists the experimental test conditions. The hot gas velocity is set to 56 m/s(Re_{hg}=250,000). Traverses of the main flow velocity directly upstream of the ejection slot reveal the 1/7 power law characteristic of a turbulent boundary layer with $\delta/H \approx 1$. The main flow temperature is T_{hg}=500 K. Depending on the coolant mass flow rate, the reference coolant temperature T_c (measured at the slot exit) varies between 295 and 330 K. The density ratio ρ_c/ρ_{hg} is between 1.5 and 1.7 and covers an engine realistic range. Blowing ratios M from 0.2 up to 1.25 are tested where M is defined as a slot averaged value

$$M = \frac{\overline{(\rho_c \cdot u_c)}_{slot}}{\rho_{hg} \cdot u_{hg}} = \frac{m_c}{A_{slot} \cdot \rho_{hg} \cdot u_{hg}} \quad (1)$$

Table 1 Key dimensions of the internal cooling design (see also Fig. 3)

	*G*1	*G*2*a*	*G*2*b*
s/H[−]	4/6/8/10	2/2.5/3	2/2.5/3
b_r[mm]	4		
D[mm]		4/4.8/6	4/4.8/6
H[mm]	4	4/4.8/6	4/4.8/6
$L1$[mm]	40	52	52
$L2$[mm]	28	12/14.4/18	12/14.4/18
$L3$[mm]	60	60	60
l_{r1}[mm]	28		
l_{r2}[mm]	20		
R_f/H[−]	0.5	0.5	
s[mm]	16/24/32/40	12	12
s_x[mm]		10.39	10.39
t/H[−]	1	1	1
x_{r1}[mm]	4		
x_{r2}[mm]	4		

Measuring Technique and Data Processing

An infrared scanner (THERMOVISION 900 by AGEMA) is applied to detect the surface temperature mappings of the film cooled cut-back surface. The system features an excellent spatial resolution of 136×272 pixels at 0.36 mm^2 per pixel. The frame rate is 15 Hz. Potential scattering effects are eliminated by averaging 32 single frames. The surface of the test plate is coated by a special black paint with a well-defined emissivity of ε=0.95 that remains constant over a wide range of viewing angles. The infrared images are calibrated against the temperature readings of six NiCr-Ni thermocouples which are embedded flush to the *L*3 surface and recorded simultaneously.

Details of this in situ calibration can be taken from [20].

Table 2 Experimental test conditions

Main flow conditions	Coolant flow conditions
Re_{hg}=250 000	$T_{c,L2exit}$=295–330 K
Ma_{hg}=0.125	$T_{c,L1inlet}$=293 K
u_{hg}=56 m/s	Tu_c=5%
Tu_{hg}=7%	M=0.2–1.25
T_{hg}=500 K	ρ_c/ρ_{hg}=1.5–1.7
p_{hg}=105 k Pa	
$\delta/H \approx 1$ ($L2$ exit)	

The adiabatic film cooling effectiveness η_{aw} and the isoenergetic heat transfer coefficient h_f are derived by using the principle of superposition of film cooling [23]. It is based on the assumption that momentum and energy transport are decoupled. For a given temperature difference between the main flow and the wall (T_{hg}-T_w), the principle of superposition results in the well-known linear relationship between the surface heat flux (q_{conv}) and the nondimensional coolant temperature θ

$$\frac{q_{\text{conv}}}{(T_{hg}-T_w)} = h_f(1-\eta_{aw}\theta) \tag{2}$$

with

$$\theta = \frac{T_{hg}-T_c}{T_{hg}-T_w} \tag{3}$$

By means of two experiments at different θ but unchanged flow conditions (accomplished by varying the wall temperature), the linear relationship in Eq. (2) can be extrapolated to determine the adiabatic film cooling effectiveness and the isoenergetic heat transfer coefficient

$$\eta_{aw} = \frac{T_{hg}-T_{aw}}{T_{hg}-T_c} = \frac{1}{\theta_1}\left(1-\frac{q_{\text{conv},1}}{h_f(T_{hg}-T_{w,1})}\right) \tag{4}$$

$$h_f = \frac{q_{\text{conv}}}{T_{aw}-T_w} = \frac{1}{\theta_2-\theta_1}\left(\frac{\theta_2\cdot q_{\text{conv},1}}{T_{hg}-T_{w,1}} - \frac{\theta_1\cdot q_{\text{conv},2}}{T_{hg}-T_{w,2}}\right) \tag{5}$$

In Eqs. (4) and (5), the index "1" represents the first (near adiabatic) test whereas "2" denotes the second (heat flux) experiment. As Tecapeek is not perfectly insulating there is still a slight convective surface heat flux ($q_{\text{conv},1}$) in the near adiabatic experiment. Consequently, for both experiments a subsequent heat flux analysis of the solid test plate is performed to reveal the local heat flux in the $L3$ region ($q_{\text{conv},1}$ and $q_{\text{conv},2}$). The simulation is based on the finite volume approach and considers the different thermal conductivities of the test plate materials. The symmetry of the temperature mappings suggest to consider just one slice of the test plate with a spanwise extension of a single pitch, s. The calibrated temperatures detected by the scanner are used as the thermal boundary condition on the film cooled surface of the test plate. The temperature on the back surface is gained from several thermocouples. With respect to the heat flux experiment, the back of the test plate is almost isothermal due to the high thermal conductivity of the copper body. The remaining surfaces are treated as adiabatic (symmetric).

The discharge behavior of the cooling slots is defined by the discharge coefficient (C_D) that relates the measured coolant mass flux to the ideal mass flux resulting from an isentropic expansion from p_{1t} (mass flow averaged total pressure upstream of the turbulators) to p_2 (static pressure at the ejection slot plane) in a nozzle with the same exit area A_{slot}.

$$C_D = \frac{m_{c,\text{real}}}{m_{c,\text{ideal}}} = \frac{m_{c,\text{real}}}{p_{1t}\left(\frac{p_2}{p_{1t}}\right)^{\kappa+1/2\kappa} A_{\text{slot}}\sqrt{\frac{2\kappa}{(\kappa-1)RT_{1t}}\left[\left(\frac{p_{1t}}{p_2}\right)^{\kappa-1/\kappa}-1\right]}} \tag{6}$$

Experimental Uncertainties

The experimental uncertainties for the film cooling experiments are derived by the method proposed by Kline and McClintock [21]. The uncertainty is 1.5% for the main flow Reynolds number (Re_{hg}) and 2.5% for the blowing ratio (M). The analysis reveals an uncertainty interval of 3.4% for the discharge coefficients (C_D). The mean uncertainty for the adiabatic film cooling effectiveness is 2.6% for blowing ratios $M=0.35$ and above, whereas it increases up to 4.5% for the lowest blowing ratio tested ($M=0.20$). Finally, a one-dimensional heat flux analysis reveals a mean uncertainty of 11.2% for the isoenergetic heat transfer coefficients (h_f) when the blowing ratio is $M=0.35$ and above. However, for the lowest blowing ratio of $M=0.20$, the uncertainty can attain values of up to 19%.

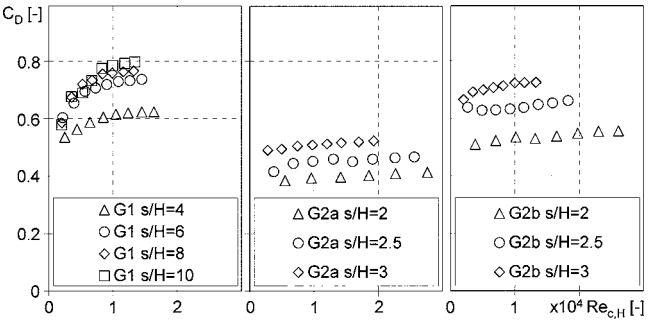

Fig. 4 Discharge coefficient of the trailing edge slots

Results

Discharge Coefficients. Figure 4 shows the discharge coefficients for the different trailing edge slots. In all cases, the discharge coefficients increase with the coolant Reynolds number $\text{Re}_{c,H}$. For the pin fin arrays, however, this effect seems to be less pronounced. Furthermore, the results clearly indicate the influence of the s/H ratio on C_D, which can be attributed to the altered internal blockage of the slot.

Defining an alternative discharge coefficient C_D^* with an effective minimum throat area A_{throat} instead of the overall slot area A_{slot} (see Eq. (6)), the effect of internal blockage is taken into account. Figure 5 demonstrates the data collapse for the different s/H ratios if C_D^* is used. Furthermore, very similar levels of C_D^* can be stated for all trailing edge cooling slots.

Adiabatic Film Cooling Effectiveness. Figure 6 shows for one representative aspect ratio of each slot design the local distribution of η_{aw} on the trailing edge cut-back surface. The results clearly indicate the different film cooling behavior of the pin fin arrays compared to the double in-line rib array. For all blowing ratios tested, the film cooling effectiveness downstream the pin fin arrays ($G2a, G2b$) is laterally uniform. In case of $G2a$ this can be attributed to the high turbulence of the flow emerging from the slot, which intensifies the lateral spreading of the coolant. For the configuration without $L2$ pins ($G2b$), there is an additional effect caused by the lip overhang. It allows for a more uniform coolant film at the slot exit. This leads to enhanced film cooling effectiveness compared to the pin fin array with $L2$ pins ($G2a$). For blowing ratios $M>0.35$, the in-line rib array ($G1$) shows significant nonuniformities of adiabatic film cooling effectiveness in lateral direction. For $M<0.65$ the film cooling effectiveness on the cut-

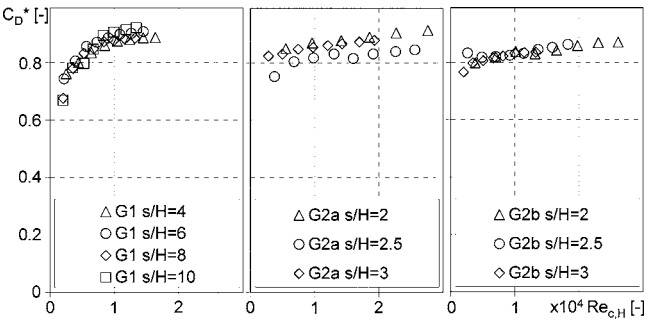

Fig. 5 Discharge coefficients C_D^* of the trailing edge slots based on A_{throat}

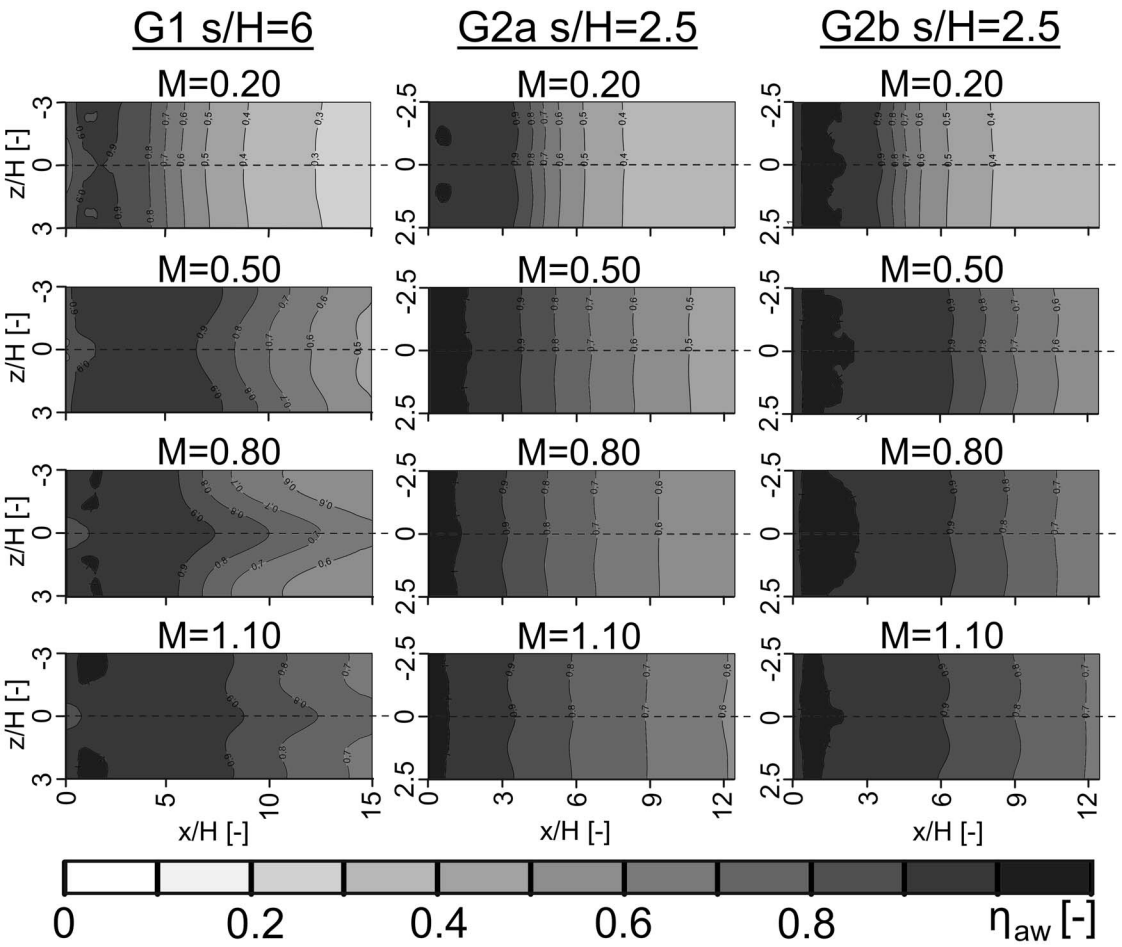

Fig. 6 Local distribution of adiabatic film cooling effectiveness downstream of the slot

back surface is maximum in the undisturbed region between the ribs. However, as M is increased, the peak effectiveness shifts from between the ribs to the region directly downstream of the ribs. The nonuniform lateral distribution of η_{aw} is most significant for $M=0.80$.

The previous phenomenon is found for the rib arrays ($G1$) exclusively and might be a result of vortex shedding from the relatively thick lip ($t/H=1$). In [9], it is found to be particular intense for mass velocity ratios around unity. Defining a blowing ratio M_{eff} that is based on the open area between the $L2$ turbulators (A_{throat}) and not on the overall slot area ($A_{\text{slot}}=S\times H$), the effective mass velocity ratio at the slot exit between the turbulators can be determined by Eq. (7). Depending on s/H, the blowing ratio M that results in $M_{\text{eff}}=1$ ranges from $M=0.70$ for $s/H=4$ to $M=0.87$ for $s/H=10$.

$$M_{\text{eff}}=\frac{m_c}{A_{\text{throat}}\cdot\rho_{hg}\cdot u_{hg}} \tag{7}$$

For $M\approx 0.8$ (i.e., $M_{\text{eff}}\approx 1$ between the ribs), the characteristic peaks of film cooling effectiveness in the wake of the ribs might be explained in the following way. In the slot exit region that is not directly influenced by the presence of the ribs, an intensive vortex shedding develops. On the other hand, vortex shedding should be attenuated in the turbulent wake of the ribs where the coolant velocity (i.e., M_{eff}) is lower.

In Fig. 7, the laterally averaged film cooling effectiveness is plotted versus x/H for three representative cooling configurations and blowing ratios M between 0.20 and 1.25. For all internal cooling designs tested, the film cooling effectiveness at the slot

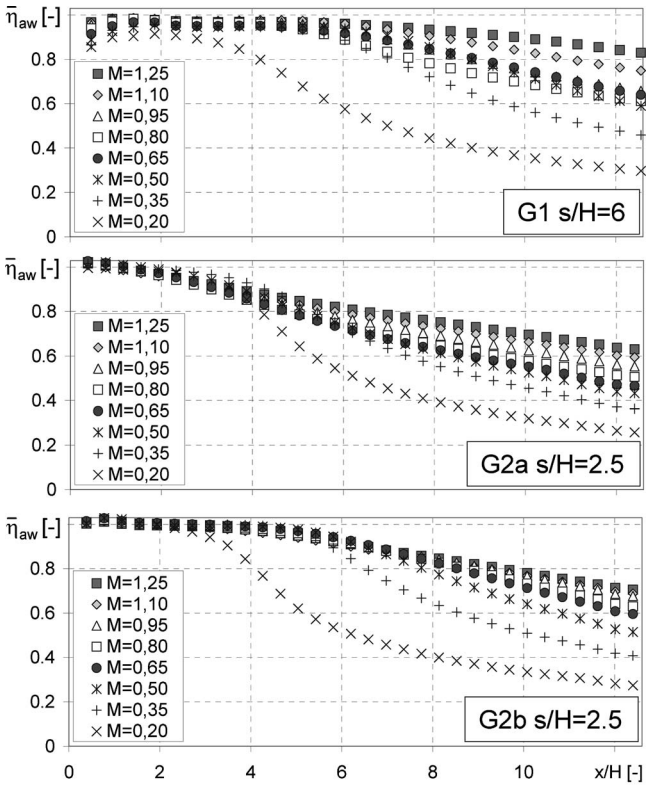

Fig. 7 Laterally averaged adiabatic film cooling effectiveness

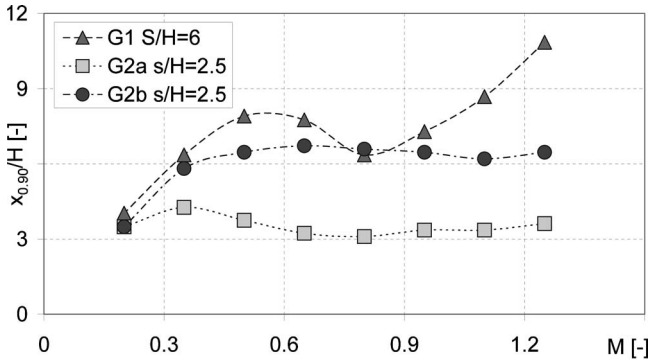

Fig. 8 Variation of the effective core region with the blowing ratio

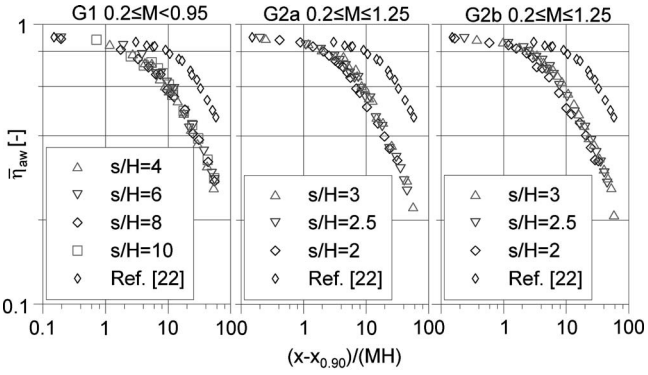

Fig. 9 Decay of adiabatic film cooling effectiveness downstream of the effective core region ($x_{0.90}$)

exit is practically unity for the entire range of blowing ratios. However, Fig. 7 clearly shows that the extension of the region where $\eta_{aw} \approx 1$ (the core region), is a function of the internal slot design and significantly varies for the different configurations.

In contrast to $G2$a, where η_{aw} starts to decay immediately downstream of the slot, the two other configurations ($G1$, $G2$b) show an extended core region for all blowing ratios except for the lowest one ($M=0.20$). Figure 7 also reveals that the double in-line rib array ($G1$), which comes close to a clean slot especially for large s/H ratios, shows the highest levels of $\bar{\eta}_{aw}$. Interestingly, for $G1$, a decrease of the laterally averaged film cooling effectiveness downstream of the core region is observed as M is increased from 0.5 to 0.80.

Figure 8 illustrates the influence of internal slot design and blowing ratio on the extension of the effective core region ($x_{0.90}$) for the three representative configurations of Fig. 7. In the present case, the effective core region is arbitrarily defined as the distance from the slot exit to the point where the laterally averaged film cooling effectiveness falls below a level of $\eta_{aw}=0.90$.

As indicated by Fig. 8, the extension of the effective core region depends on the blowing ratio as well as the internal slot design. Focusing the view on the long rib configuration ($G1$), the highest levels of $x_{0.90}/H$ can be stated. The overall maximum ($x_{0.90}/H \approx 11$) is reached for $G1$ at $M=1.25$. Starting from a blowing ratio of $M=0.20$, where the results for all configurations almost fall on top of each other, the core length of the in-line rib array increases almost linearly with the blowing ratio. However, this trend is reversed for intermediate blowing ratios between $M=0.5$ and 0.8. Here, the extension of the core region decreases, featuring a local minimum ($x_{0.90}/H \approx 6.5$) for a blowing ratio of $M=0.8$. Changing M in both directions from that point leads to increasing values of $x_{0.90}/H$ (which means increasing effectiveness on the cutback). However, for low coolant mass flow rates the core length decreases again and $x_{0.90}$ must be zero for $M=0$.

As stated earlier, the local minimum of $x_{0.90}/H$ for $G1$ can be best explained by the influence of vortex shedding from the pressure side lip. The results for the double in-line rib array in Fig. 8 support the findings in [9] where the effect of vortex shedding on the mixing is most intensive for blowing ratios around unity. Since the internal obstruction caused by the long ribs is relatively low, it is assumed that the qualitative behavior shown by $G1$ in Fig. 8 is quite similar to that obtained for the clean slot without turbulators.

In contrast to the double in-line rib arrays, the highly obstructed slots with pin fin arrays ($G2$) show a completely different behavior of $x_{0.90}/H$. It seems that the turbulence generated by the pin fins does not allow for an increase of the effective core region for blowing ratios beyond $M=0.50$. Due to the immediate decay of adiabatic film cooling effectiveness, the pin fin array with the turbulators being located close to the slot exit ($G2$a) marks a lower limit of $x_{0.90}/H$ in Fig. 8. At the same time, $G2$a shows the weakest dependency of $x_{0.90}/H$ on the blowing ratio.

Increasing the lip overhang, as established by $G2$b, leads to significantly improved levels of $x_{0.90}/H$, which are comparable to $G1$ for low and intermediate blowing ratios.

Figure 9 shows the decay of laterally averaged film cooling effectiveness downstream of $x_{0.90}$ plotted versus a nondimensional distance in a log-log scale. By using the parameter $[(x\text{-}x_{0.90})/(MH)]$ the experimental data obtained for the different s/H ratios tested for each cooling configuration ($G1$, $G2$a, $G2$b) almost fall to a single line. For the pin fin arrays ($G2$a and $G2$b), the parameter $(x\text{-}x_{0.90})/(MH)$ can be successfully applied for the whole range of blowing ratios tested. In case of the double in-line rib arrays ($G1$), however, this parameter correlates the decay behavior only for $M<0.95$.

Independent of the s/H ratio, the results for all three trailing edge configurations ($G1$, $G2$a, $G2$b) in Fig. 9 are quite close to each other. This suggests that the influence of the internal cooling design on the decay of film cooling effectiveness downstream of the core region is relatively weak. Hence, by presenting the results for adiabatic film cooling effectiveness in terms of Figs. 8 and 9 it seems possible to confine the main influence of the internal cooling design on its effect to the extension of the core region.

This might be an indication that further downstream, the turbulence generated by the pressure side lip is dominating the film mixing process. However, this statement only relies on the present experimental findings and further investigations seem to be necessary to verify it.

To quantify the main effect of lip thickness on the decay of η_{aw}, the present results are compared to a correlation for an ideal slot (i.e., clean thin-lipped slot) with $\alpha=10$ deg as proposed by Mukherjee [22]. He subdivides the cooling film downstream of the slot into three characteristic regions. The core region is followed by a zone called transition region where the velocity profiles of the coolant are similar to a wall jet. Further downstream, the flow near the wall behaves like a turbulent boundary layer.

The correlation from 22 is evaluated for various blowing ratios and the results are plotted in Fig. 9. The use of the parameter $(x\text{-}x_{0.90})/(MH)$ is confirmed since the data gained from the correlation also fall to a single line. The start of the turbulent boundary layer region for the ideal slot (Ref. [22]) can be identified at $(x\text{-}x_{0.90})/(MH) \approx 15$ followed by a monotonic decay of η_{aw} in the log-log scale of Fig. 9. Comparing the data for the ideal slot with the experimental ones from the present work, the drawbacks in terms of film cooling effectiveness are clearly visible. Interestingly, the decay of film cooling effectiveness downstream of the thick-lipped trailing edge slots is quite similar to that predicted for the ideal thin-lipped slot in the turbulent boundary layer region but starts significantly earlier. One possible explanation for this

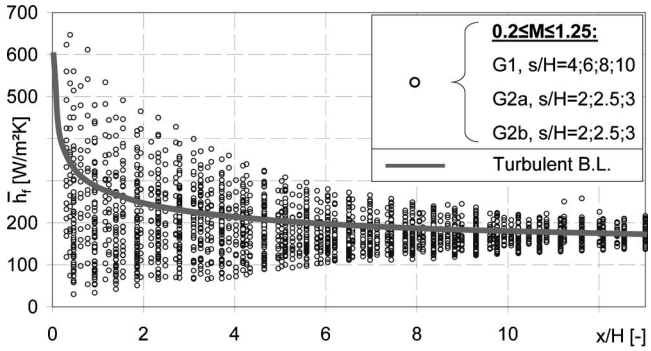

Fig. 10 Laterally averaged heat transfer coefficients downstream of the slot exit and heat transfer for the turbulent boundary layer on a flat plate

behavior might be that due to an intensified mixing of coolant and the hot gas the start of the turbulent boundary layer region is shifted toward the slot exit. This might also explain the rapid approach of the heat transfer coefficients in the $L3$ region to levels predicted for the turbulent boundary layer flow over a flat plate.

Heat Transfer Coefficients. The previous statement is strikingly confirmed by Fig. 10. The circular marks in this figure represent the entire (laterally averaged) heat transfer results on the cut-back surface obtained for all trailing edge slots and blowing ratios tested.

The thick red line in Fig. 10 marks the result from a correlation for turbulent boundary layer heat transfer on a flat plate multiplied by a factor of 1.18.

$$h = 1.18 \cdot [0.0287 \cdot \mathrm{Pr}^{-0.4} \cdot \mathrm{Re}_{hg,x}^{-0.2} \cdot \rho_{hg} \cdot \mathrm{cp}_{hg} \cdot u_{hg}] \tag{8}$$

This factor accounts for the effect of an elevated level of free stream turbulence ($\mathrm{Tu}_{hg}=7\%$) on heat transfer as suggested by Blair [24].

Taking the experimental results from Fig. 10, it can be stated that the heat transfer coefficients downstream of the ejection slot approach the turbulent boundary layer heat transfer within a downstream distance of approximately ten slot heights. Within this region, h_f is predominantly affected by the coolant flow (i.e., the coolant Reynolds number and the internal cooling design) whereas downstream of $x/H=10$, the heat transfer coefficients are mainly driven by the external flow.

Figure 11 shows the local distributions of h_f for three representative cooling designs and various blowing ratios. Also with respect to h_f, the double in-line rib array ($G1$) significantly deviates from what is observed for the pin fin arrays ($G2$a, b). For $G1$, Fig. 11 indicates strong variations of the heat transfer coefficient in lateral direction immediately downstream of the ejection slot ($x/H<3$). Due to the turbulence production of the $L2$ ribs, relatively high levels of heat transfer can be stated in the wake area. On the other hand, in the near slot region lateral to the wakes, zones of significantly reduced convective heat transfer become visible for all blowing ratios.

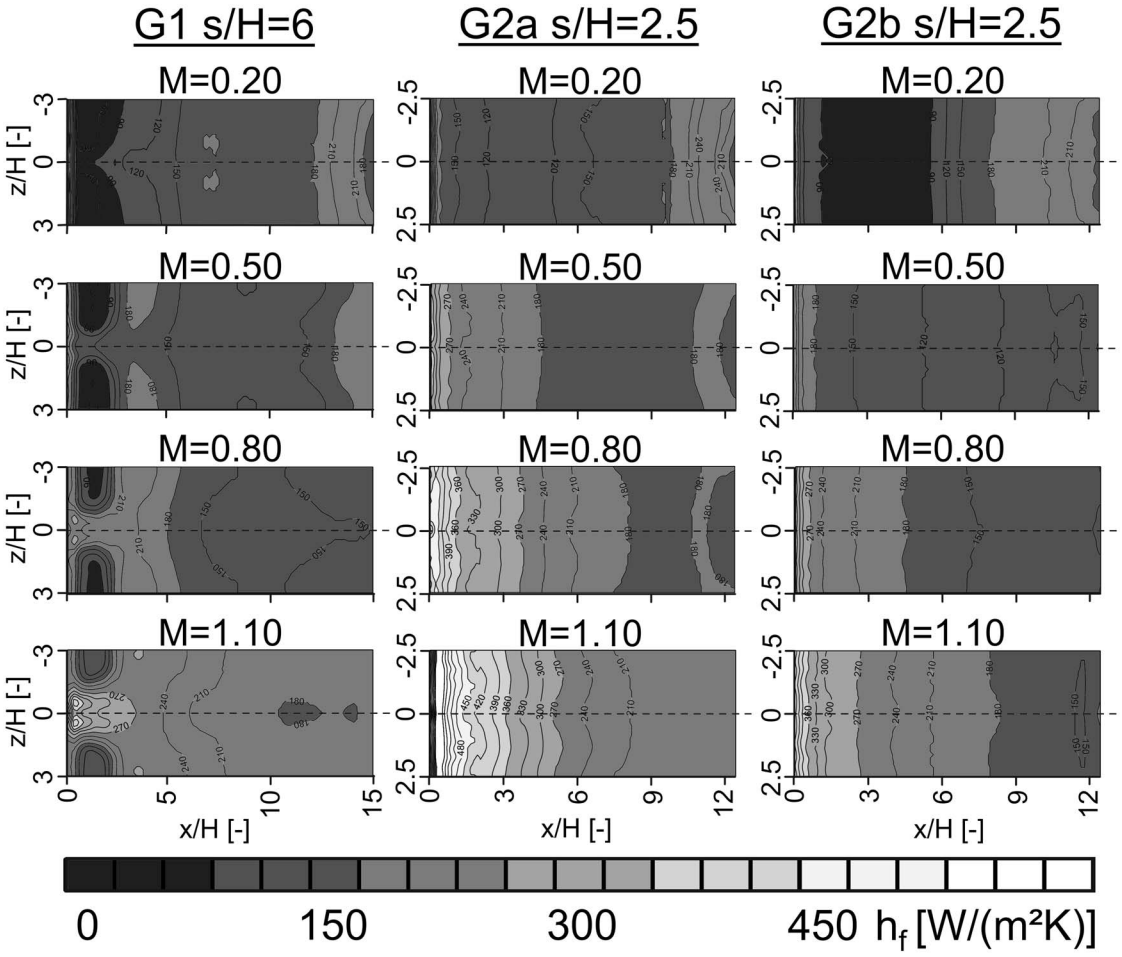

Fig. 11 Local distribution of heat transfer coefficients downstream of the slot

There exist two complementary explanations for these low levels of heat transfer in the undisturbed region immediately downstream of the slot. It is known that the stepwise increase of the flow area at the slot exit impresses an adverse pressure gradient to the coolant flow in the near slot region. Especially for lower blowing ratios, where the momentum of the coolant flow is small compared to the main flow, the zones of lower heat transfer might be the result of a local recirculation bubble.

The phenomenon of a recirculation bubble directly downstream of $2d$ slots with finite lip thickness is also reported by other authors like Bittlinger et al. [25] and Burns and Stollery [26]. In the present case, the existence of a separation bubble is confirmed by additional measurements of the wall static pressure along the trailing edge cutback and by numerical studies focusing on the prediction of film cooling performance on the trailing edge cutback [27] (see also Fig. 14).

However, there exists a complementary explanation for the low rates of heat transfer observed for the in-line rib configuration ($G1$) directly downstream of the ejection slot. Supplementary heat transfer measurements in the last internal region ($L2$) reveal significantly lower heat transfer coefficients between the ribs than expected for a turbulent duct flow. Most likely, this can be attributed to relaminarization caused by the strong acceleration in the convergent upstream section of the coolant cavity ($L1$). So, the low rates of heat transfer experimentally found downstream of the slot exit of $G1$ could be also regarded as a direct continuation of the internal heat transfer levels. Further downstream ($x/H>3$), a laminar/turbulent transition might explain the local maximum of heat transfer observed in Fig. 10. Finally, also a combination of both effects might cause the observed phenomenon of low heat transfer rates in the near slot region for G1.

Figure 11 also indicates that heat transfer downstream of the two pin fin arrays ($G2$a, b) is laterally much more uniform in the near slot region than it is observed for the double in-line rib array ($G1$). This may be again explained by the intensive lateral mixing caused by the turbulence production of the pin fin arrays. Furthermore, compared to the double in line rib array, the heat transfer in the near slot region downstream of the pin fin arrays is substantially higher. This is especially true for $G2$a (with $L2$ pins) where the maximum values of h_f are observed. However, it is also $G2$a that produces maximum pressure losses and lowest levels of η_{aw} of all trailing edge slots investigated.

Figure 12 shows the laterally averaged heat transfer coefficient versus x/H for the three representative trailing edge cooling slots for all blowing ratios tested. Focusing the view on $G1$, $s/H=6$, the low heat transfer coefficients in the near slot region are clearly visible. As indicated earlier, heat transfer downstream of the slot exit rapidly attains a level predicted for a turbulent boundary layer flow on a flat plate. Depending on the blowing ratio (i.e., the coolant Reynolds number) which affects heat transfer in the near slot region, the heat transfer coefficients either increase or decrease in downstream direction in order to approach the levels predicted by Eq. (8). A comparison of the three trailing edge slots in Figure 12 reveals that the main differences of heat transfer are limited to a region of four to five slot heights downstream of the slot exit. Nevertheless, the influence of the blowing ratio on h_f extends further downstream. Figure 12 also clearly shows that the assumption of heat transfer coefficients being unchanged by the coolant injection does not hold for the important near slot region $x/H<10$.

The influence of the s/H ratio on the heat transfer coefficient on the trailing edge cutback ($L3$) turns out to be relatively low. Typically, the area averaged heat transfer does not vary by more than 10%–15% for the different s/H ratios. This statement is confirmed by Fig. 13, where the Stanton numbers defined by Eq. (9) are plotted versus the coolant Reynolds number $\mathrm{Re}_{c,x}$ at $x/H=4$.

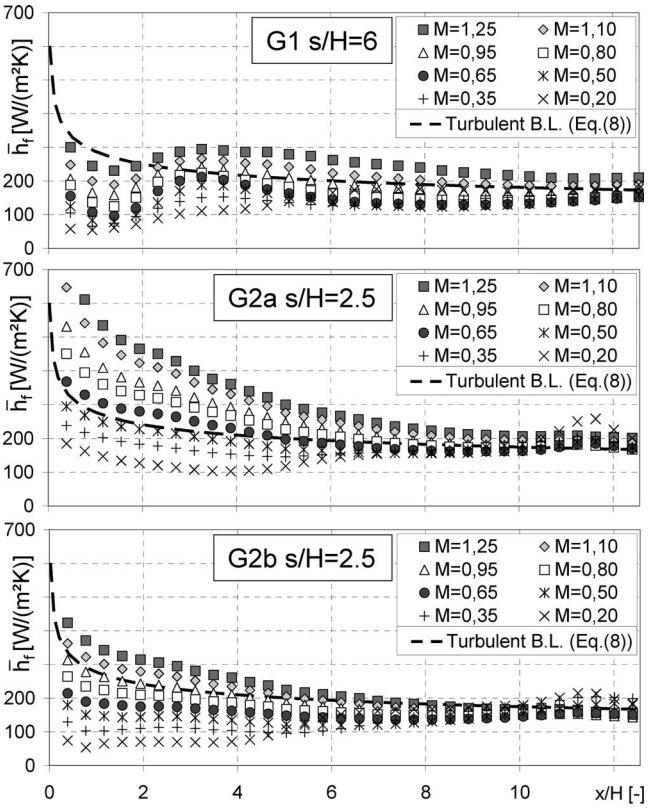

Fig. 12 Laterally averaged heat transfer coefficients

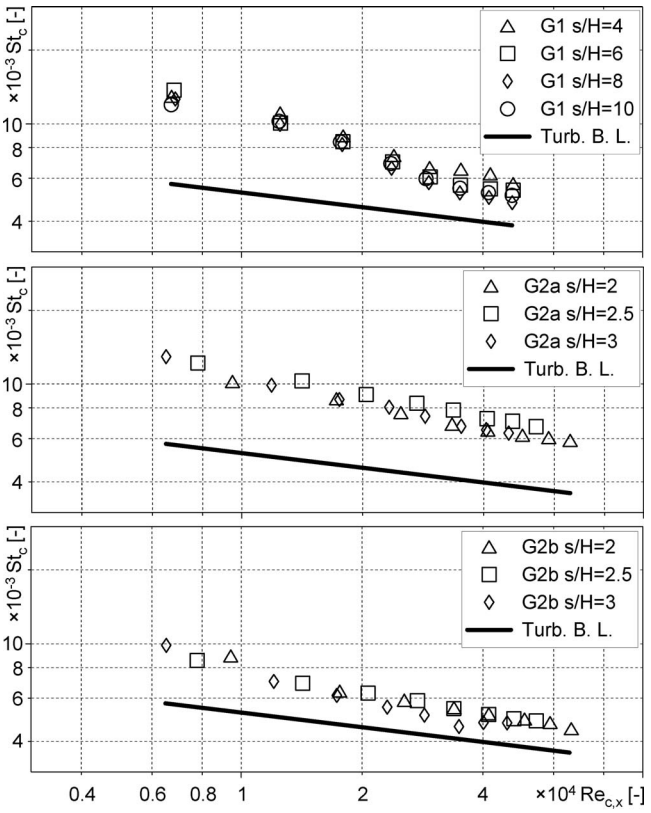

Fig. 13 Variation of St_c with $\mathrm{Re}_{c,x}$ for different trailing edge slots at $x/H=4$ and for the flat plate

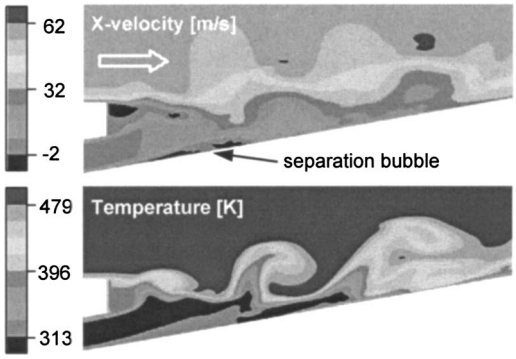

Fig. 14 Prediction of the instantaneous velocity and temperature field on the cut-back (*G*1, *s*/*H*=6, *M*=0.50) in a plane between two ribs (*z*/*H*=3)

$$\mathrm{St}_c = \frac{\bar{h}_f}{\rho_c \cdot cp_c \cdot u_c} = \frac{\bar{h}_f \cdot A_{\mathrm{slot}}}{m_c \cdot cp_c} \tag{9}$$

For reasons of comparison, Fig. 13 also includes the correlation for flat plate turbulent boundary layer heat transfer (based on the coolant flow conditions) that is given is by Eq. (10)

$$\mathrm{St} = 0.0287 \cdot \mathrm{Pr}^{-0.4} \cdot \mathrm{Re}_{c,x}^{-0.2} \tag{10}$$

As illustrated by Fig. 13 the heat transfer for all trailing edge slots at $x/H=4$ is found to be substantially higher than the Stanton numbers predicted by Eq. (10). However, the decay of St_c with $\mathrm{Re}_{x,c}$ observed for both pin fin arrays (*G*2*a*, *G*2*b*) is quite similar to the correlation. This is an indication for the turbulent state of the boundary layer ($\mathrm{St}_c \sim \mathrm{Re}_{c,x}^{-0.2}$). The Stanton numbers for the double in line rib array (*G*1) show a stronger decay with $\mathrm{Re}_{x,c}$ at $x/H=4$ than is expected for a fully turbulent boundary layer. Bearing in mind that the boundary layer at the slot exit of *G*1 is still affected by the coolant flow acceleration in *L*1 the stronger decay might be explained by a transitional state of the boundary layer in that region.

Summary and Conclusions

A comprehensive experimental study is conducted to investigate film cooling performance downstream of various trailing edge cooling slots. The key results can be summarized as follows:

The discharge coefficients of the trailing edge cooling slots tend to increase with the coolant Reynolds number. They are obviously influenced by the presence of internal obstructions like ribs or pin fin arrays. However, defining a discharge coefficient that is based on the minimum throat area inside the coolant cavity, leads to very similar levels for all configurations tested.

The film cooling effectiveness is significantly affected by the internal slot design and the relatively thick lip, which may give rise to vortex shedding (especially in case of *G*1). Although the measuring technique applied here does not allow for a direct identification of this high-frequency phenomenon, several observations lead to the conclusion that flow instabilities generated in the wake of the lip might be involved in the relatively fast decay of film cooling effectiveness along the trailing edge cutback.

This statement is not only confirmed by the work of others but also supported by extensive numerical studies performed by Martini et al. that are reported in a parallel publication [27]. So, without going into the details here, the numerical results in Fig. 14 are only intended to provide an idea of the unsteady flow situation on the trailing edge cutback, affecting the film mixing process in case of *G*1.

The experimental results indicate that the extension of the core region where η_{aw} is close to unity is strongly influenced by the internal cooling design, whereas the decay of η_{aw} downstream of the core region is similar for all trailing edge cooling slots. This suggests that the mixing generated by the lip ($t/H=1$ for all slots) dominates in that region. The decay of η_{aw} is almost the same as it is observed for a clean thin lipped slot in the turbulent boundary layer region which might be an indication for an upstream shift of the turbulent boundary layer region closer to the slot exit. However, further investigations seem to be necessary to verify this.

The heat transfer coefficients downstream of all trailing edge slots show a rapid approach to the level predicted for a turbulent boundary layer on a flat plate without coolant injection (typically within ten slot heights). The experiments reveal that the internal design mainly affects the region $x/H<5$ whereas the influence of the blowing ratio (i.e., the coolant Reynolds number) extends further downstream.

Directly downstream of the slot exit, the double in line rib array (*G*1) shows very low levels of heat transfer in the region that is not affected by the turbulating ribs. This is most likely the result of a local separation bubble. Additionally, the strong flow acceleration in the convergent part of the coolant cavity could also be responsible for low heat transfer in that region.

Although the present study confirms the assumption of a relatively rapid approach to a level without injection, it is also clear that in the important near slot region ($x/H<10$) the heat transfer coefficients substantially deviate from the predictions of a flat plate turbulent boundary layer.

It is important to take all these effects into account for the layout of a trailing edge cooling system using a pressure side cutback. So, the present study might be considered as a contribution to avoid mispredictions of the wall temperature in one of the most critical regions of the turbine blade.

Acknowledgment

The reported work was performed within a research project that is part of the European project "AITEB—Aerothermal Investigation of Turbine Endwalls and Blades" (5FP, G4RD-CT-1999-00055). The permission for the publication is gratefully acknowledged by the authors.

Nomenclature

A_{slot} = overall slot area ($A_{\mathrm{slot}}=S\times H$) ($\mathrm{m}^2$)
A_{throat} = minimum throat area in the cavity (m^2)
Bi = Biot number ($\mathrm{Bi}=h_f t_{\mathrm{wall}}/\lambda_{\mathrm{wall}}$)
C_D = discharge coefficient (Eq. (6))
C_D^* = discharge coefficient based on A_{throat}
c_p = specific heat at constant pressure, J/(kg K)
D = pin diameter (m)
H = slot height at L2 exit (m)
h_f = heat transfer coefficient ($h_f=q_{\mathrm{conv}}/(T_{\mathrm{aw}}-T_{\mathrm{w}})$), ($\mathrm{W}/(\mathrm{m}^2\,\mathrm{K})$)
M = blowing ratio [$M=m_c/(A_{\mathrm{slot}}\rho_{\mathrm{hg}}u_{\mathrm{hg}})$]
Ma_{hg} = hot gas Mach number
m_c = coolant mass flow rate (kg/s)
M_{eff} = effective blowing ratio based on A_{throat}
p_{1t} = total pressure of coolant upstream of L1 (Pa)
p_2 = static pressure at the slot exit (Pa)
p_{hg} = static pressure of hot gas (Pa)
Pr = Prandtl number ($\mathrm{Pr}=\mu c_p/\lambda$)
q_{conv} = convective heat flux (W/m^2)
R = ideal gas constant [$R=287.22$ J/(kg K)] (J/(kg K))
$\mathrm{Re}_{c,H}$ = coolant Reynolds number [$\mathrm{Re}_{c,H}=m_c H/(A_{\mathrm{throat}}\mu_c)$]
Re_{hg} = hot gas Reynolds number ($\mathrm{Re}_{\mathrm{hg}}=\mathrm{u}_{\mathrm{hg}}\rho_{\mathrm{hg}}(\mathrm{L0}+L1+L2)/\mu_{\mathrm{hg}}$)
s = lateral pitch between two ribs or pins (m)
S = overall coolant slot width (m)
St_c = Stanton number (Eq. (9))

t = lip thickness (m)
T_{1t} = total coolant temperature upstream of $L1$ (K)
T_{aw} = adiabatic wall temperature (K)
T_c = coolant temperature at the slot exit (K)
T_{hg} = static temperature of hot gas (K)
Tu_c = coolant turbulence intensity
Tu_{hg} = hot gas turbulence intensity
T_w = wall temperature (K)
u_c = coolant velocity at the slot exit (m/s)
u_{hg} = hot gas velocity at the slot exit (m/s)
x = streamwise distribution downstream of slot exit (m)
$x_{0.90}$ = effective core region where $\eta_{\mathrm{aw}} \geqq 0.90$ (m)
y = coordinate normal to the cutback (L3) (m)
z = spanwise coordinate (m)

Greek

θ = nondimensional temperature ratio (Eq. (3))
α = trailing edge wedge angle ($\alpha = 10°$) (deg)
δ = boundary layer thickness (m)
ε = emissivity
η_{aw} = adiabatic film cooling effectiveness (Eq. (4))
κ = ratio of specific heats
λ = thermal conductivity (W/(m K))
μ = dynamic viscosity (Pa s)
ν = kinematic viscosity (m^2/s)
ρ = density (kg/m^3)

References

[1] Taslim, M. E., Spring, S. D., and Mehlmann, B. P., 1990, "An Experimental Investigation of Film Cooling Effectiveness for Slots of Various Exit Geometries," AIAA Paper No. AIAA-90-2266.
[2] Sivasegaram, S., and Whitelaw, J. H., 1969, "Film Cooling Slots: The Importance of Lip Thickness and Injection Angle," J. Mech. Eng. Sci., **11**, (1), pp. 22–27.
[3] Burns, W. K., and Stollery J. L., 1968, "The Influence of Foreign Gas Injection and Slot Geometry on Film Cooling Effectiveness," Int. J. Heat Mass Transfer, **12**, pp. 935–951.
[4] Pai, B. R., and Whitelaw, J. H., 1971, "The Prediction of Wall Temperature in the Presence of Film Cooling," Int. J. Heat Mass Transfer, **14**, pp. 409–426.
[5] Kacker, S. C., and Whitelaw, J. H., 1969, "An Experimental Investigation of Slot Lip Thickness on the Impervious Wall Effectiveness of the Uniform Density, Two-Dimensional Wall Jet," Int. J. Heat Mass Transfer, **12**, pp. 1196–1201.
[6] Uzol, O., Camci, C., and Glezer, B., 2001, "Aerodynamic Loss Characteristics of a Turbine Blade with Trailing Edge Coolant Ejection—Part 1: Effect of Cut-Back Length, Spanwise Rib Spacing, Free-Stream Reynolds Number, and Chordwise Rib Length on Discharge Coefficients," ASME J. Turbomach., **123**, pp. 238–248.
[7] Uzol, O., and Camci, C., 2001, "Aerodynamic Loss Characteristics of a Turbine Blade with Trailing Edge Coolant Ejection—Part 2: External Aerodynamics, Total Pressure Losses, and Predictions," ASME J. Turbomach., **123**, pp. 249–257.
[8] Holloway, D. S., Leylek, J. H., and Buck F. A., 2002, "Pressure Side Bleed Film Cooling. Part 1: Steady Framework For Experimental and Computational Results," ASME Paper No. GT-2002-30471.
[9] Holloway, D. S., Leylek, J. H., and Buck F. A., 2002, "Pressure Side Bleed Film Cooling. Part 2: Unsteady Framework For Experimental and Computational Results," ASME Paper No. GT-2002-30472.
[10] Martini, P., and Schulz, A., 2004, "Experimental and Numerical Investigation of Trailing Edge Film Cooling by Circular Wall Jets Ejected from a Slot with Internal Rib Arrays, ASME J. Turbomach., **126**, pp. 229–236.
[11] Nina, M. N. R., and Whitelaw, J. H., 1971, "The Effectiveness of Film Cooling With Three-Dimensional Slot Geometries," ASME Paper No. 71-GT-11.
[12] Goldstein, R. J., 1971, "Film Cooling," Adv. Heat Transfer, **7**, pp. 321–379.
[13] Kacker, S. C., and Whitelaw, J. H., 1967, "The Dependence of the Impervious Wall Effectiveness of a Two-Dimensional Wall Jet on the Thickness of the Upper Lip Boundary Layer," Int. J. Heat Mass Transfer, **10**, pp. 1623–1624.
[14] Marek, C. J., and Takina, R., 1975, "Effect of Free Stream Turbulence on Film Cooling," NASA TN D-7958.
[15] Sturgess, G. J., 1985, "Design of Combustor Cooling Slots for High Film Effectiveness—Part 1: General Film Development," ASME Paper No. 85-GT-35.
[16] Sturgess, G. J., 1985, "Design of Combustor Cooling Slots for High Film Effectiveness—Part 2: Film Initial Region," ASME Paper No. 85-GT-36.
[17] Seban, R. A., 1960, "Heat Transfer and Effectiveness for a Turbulent Boundary Layer with Tangential Fluid Injection," ASME J. Heat Transfer, **82**, pp. 303–312.
[18] Seban, R. A., and Back, L. H., 1962, "Effectiveness and Heat Transfer for a Turbulent Boundary Layer with Tangential Injection and Variable Free-Stream Velocity," ASME J. Heat Transfer, **84**, pp. 235–244.
[19] Metzger, D. E., Baltzer, R. T., Takeuchi, D. I., and Kuenstler, P. A., 1972, "Heat Transfer to Film Cooled Combustion Chamber Liners," ASME Paper No. 72-WA/HT-32.
[20] Martiny, M., et al., 1996, "In Situ Calibration for Quantitative Infrared Thermography," QIRT 96, Eurotherm Seminar, No. 50, Stuttgart, Germany, Sept. 2–5.
[21] Kline, S. J., and McClintock, F. A., 1953 "Describing Uncertainties in Single-Sample Experiments," Mech. Eng. (Am. Soc. Mech. Eng.), **75**, pp. 3–8.
[22] Mukherjee, D. K., 1976, "Film Cooling with Injection Through Slots," ASME J. Eng. Power, **98**, pp. 556–559.
[23] Gritsch, M., Baldauf, S., Martiny, M., Schulz, A., and Wittig, S., 1999, "The Superposition Approach to Local Heat Transfer Coefficients in High Density Ratio Film Cooling Flows," ASME Paper No. 99-GT-168.
[24] Blair, M. F., 1983, "Influence of Free-Stream Turbulence on Turbulent Boundary Layer Heat Transfer and Mean Profile Development. Part 1: Experimental Data," ASME J. Heat Transfer, **105**, 33–47.
[25] Bittlinger, G., Schulz, A., and Wittig, S., 1994, "Film Cooling Effectiveness and Heat Transfer Coefficients for Slot Injection at High Blowing Ratios," ASME Paper No. 94-GT-182.
[26] Burns, W. K., and Stollery J. L., 1968, "The Influence of Foreign Gas Injection and Slot Geometry on Film Cooling Effectiveness," Int. J. Heat Mass Transfer, **12**, 935–951.
[27] Martini, P., Schulz, A., Bauer, H.-J., and Whitney, C. F., 2005, "Detached Eddy Simulation of Film Cooling Performance on the Trailing Edge Cut-Back of Gas Turbine Airfoils," ASME Paper No. GT2005-68084.

Journal of Turbomachinery

Technical Brief

Predicting Blade Stress Levels Directly From Reduced-Order Vibration Models of Mistuned Bladed Disks

Sang-Ho Lim

Christophe Pierre[1]
e-mail: Pierre@umich.edu

Matthew P. Castanier

Department of Mechanical Engineering,
The University of Michigan,
Ann Arbor, MI 48109-2125

The forced vibration response of bladed disks can increase dramatically due to blade mistuning, which can cause major durability and reliability problems in turbine engines. To predict the mistuned forced response efficiently, several reduced-order modeling techniques have been developed. However, for mistuned bladed disks, increases in blade amplitude levels do not always correlate well with increases in blade stress levels. The stress levels may be computed by postprocessing the reduced-order model results with finite element analysis, but this is cumbersome and expensive. In this work, three indicators that can be calculated directly from reduced-order models are proposed as a way to estimate blade stress levels in a straightforward, systematic, and inexpensive manner. It is shown that these indicators can be used to predict stress values with good accuracy relative to finite element results, even for a case in which the displacement and stress levels show different frequency response trends. [DOI: 10.1115/1.2098754]

1 Introduction

It is well known that the forced vibration amplitudes of bladed disks can increase dramatically due to small, random discrepancies among the blades, which are referred to as mistuning. As a result, blade mistuning can lead to significant durability and reliability problems in turbine engines. In order to analyze bladed disk designs and assess the effects of mistuning, a finite element model (FEM) is typically employed. From a finite element vibration analysis, the displacement and the stress state can be obtained at all degrees of freedom (DOF) and finite elements. However, industrial bladed disk FEMs usually feature very large numbers of DOF, and thus traditional finite element analysis (FEA) can be prohibitively expensive. To address this issue, a variety of techniques [1–6] have been developed for constructing and analyzing FEM-based reduced-order models (ROMs). Although such ROMs can be used to solve the vibration response quickly and accurately relative to FEA, they are typically formulated in terms of modal and physical displacement variables for the bladed disk, whereas the primary variable of interest for durability and reliability studies is stress. To calculate blade and/or disk stress levels, the displacements predicted by the ROM analysis can be projected back to finite element coordinates and then post-processed via FEA [4]. However, it may be cumbersome and expensive to translate the ROM output to the FEM input format and then calculate the stress field with FEA, especially if this process needs to be repeated many times for a Monte Carlo simulation. In order to take full advantage of a highly efficient reduced-order modeling technique, it would be better to be able to predict the increase in stress levels due to mistuning directly from the ROM.

In structural dynamic problems, changes in vibratory stress levels can usually be approximated based on changes in the corresponding displacement levels, as long as the shape of the vibration response does not change significantly over a frequency range of interest. However, bladed disk structures feature frequency regions of high modal density, and in these regions blade mistuning can greatly alter the system mode shapes, from an extended pattern for a tuned system to a localized pattern for a mistuned system. Nevertheless, for the resonant response of both tuned and mistuned bladed disks, the displacement shape of each blade often resembles that of a tuned cantilevered-blade mode (the mode of a single blade cantilevered at its interface with the disk). Indeed, if the blade motion is dominated by a single cantilevered-blade mode throughout the frequency range of interest, then blade displacements may be used to describe stress levels. However, if there is more than one dominant cantilevered-blade mode, which occurs when blade modes have close natural frequencies, then blade stress trends may not match blade displacement trends. Also, blade mistuning is usually modeled as a variation of blade stiffness. Therefore, even if two blades have the same displacements, they may experience different levels of stress. In general, some care must be taken to relate blade displacement results to stress levels.

In this work, three indicators are proposed as ROM-based measures of the level of blade stress in a mistuned bladed disk. These indicators are defined using (1) the Euclidean norm of blade displacements, (2) the modal amplitude of a cantilevered blade, and (3) the strain energy in a blade. All three indicators can be calculated directly from the ROM results, without requiring an expensive finite element stress analysis for the mistuned bladed disk. In the following sections, these indicators are formulated, and then their accuracy is examined and validated by comparing their stress predictions to the largest Von Mises stresses in the blades calculated from a much more costly finite element analysis.

2 Stress Indicators

If a tuned blade is modeled as a single-DOF lumped parameter model with a mass (m_b) and a spring (k_b), the stress level is

[1]To whom correspondence should be addressed.

Contributed by the International Gas Turbine Institute of ASME for publication in the JOURNAL OF TURBOMACHINERY. Manuscript received February 23, 2005; final manuscript received August 1, 2005. Review conducted by D. Wisler.

proportional to $k_b|x|$, where $|x|$ is the amplitude of the spring deformation. Then, the ratio of the stress level of a mistuned blade to that of a tuned, cantilevered blade at its resonance becomes $(1+\delta)|x|/|x_{cb}|$, where δ is a nondimensional blade-stiffness mistuning value, and $|x_{cb}|$ is the amplitude of the resonant response of a tuned, cantilevered blade. That is, the stress ratio is the product of $1+\delta$ and the displacement ratio, $|x|/|x_{cb}|$. If this stress ratio and the stress level of a cantilevered blade are known, then the stress level of any blade can be calculated.

However, when using a finite element model, the elastic deformation induced by the motion of the disk is included in the blade motion, and thus the stress state for a blade in a bladed disk assembly can be different from that for a cantilevered blade. Still, if the blade vibration is dominated by motion corresponding to a single mode of a tuned cantilevered blade, then the level of the largest stress in a blade—which is perhaps most meaningful in terms of design safety—can be approximated by assuming that the disk-induced motion is negligible, which is often the case for blade-dominated system modes. In this work, based upon this assumption, three indicators are proposed that represent the largest stress in a blade when normalized by the largest stress in a cantilevered blade at the resonance condition corresponding to the dominant cantilevered-blade mode. Therefore, each indicator is referred to as a normalized stress indicator (NSI). Each NSI is defined such that it can be calculated directly from the displacements obtained from a ROM analysis.

The first normalized stress indicator is formulated in terms of the Euclidean norm of the physical blade displacement vector

$$\mathrm{NSI} = (1+\delta)u_m/u_{cb} \tag{1}$$

where u_m is the Euclidean displacement norm for a blade in the mistuned bladed disk, and u_{cb} is the Euclidean displacement norm for the resonant response of a tuned cantilevered blade. Here, δ is the modal stiffness mistuning value for the dominant cantilevered-blade mode.

The second normalized stress indicator is formulated in terms of modal amplitudes

$$\mathrm{NSI} = (1+\delta)a_m/a_{cb} \tag{2}$$

where a_m is the dominant modal amplitude of a mistuned blade when the vibration response is described in tuned cantilevered-blade modal coordinates, and a_{cb} is the modal amplitude for the resonant response of a tuned cantilevered blade. Note that a_m and a_{cb} correspond to the same cantilevered-blade mode. However, this formulation does not require that cantilevered-blade modes be used as basis vectors in the ROM, because the system motion can be projected onto these modes to retrieve a_m. Furthermore, a coordinate transformation between ROM modal coordinates and cantilevered-blade modal coordinates can be calculated a priori to make this an extremely inexpensive indicator to compute.

The third normalized stress indicator is formulated in terms of blade strain energy. For a single-DOF lumped parameter model, the ratio of the strain energy in a mistuned blade to that in a tuned, cantilevered blade at its resonance becomes $(1+\delta)(|x|/|x_{cb}|)^2$. Therefore, using the strain energy in a blade, an analogous indicator is proposed

$$\mathrm{NSI} = \sqrt{(1+\delta)E_m/E_{cb}} \tag{3}$$

where E_m is the peak strain energy of a blade in the bladed disk during one period of oscillation, and E_{cb} is the peak strain energy during one period of oscillation for the resonant response of a tuned cantilevered blade.

Although disk-induced motion is usually small, the physical displacements of blades are determined by the disk-induced rigid body and elastic motion as well as by the cantilevered-blade motion. Only the disk-induced elastic motion and the cantilevered-blade motion affect the blade stress level. However, the NSI proposed in Eq. (1) is affected by the rigid body motion. Nevertheless, this does not imply that this NSI is less accurate than the other two, because none of the proposed NSIs accounts for the disk-induced elastic motion appropriately. Also note that, even if the disk-induced elastic motion may affect considerably the stress level locally near the blade root, the change in total blade strain energy due to this motion may be very small.

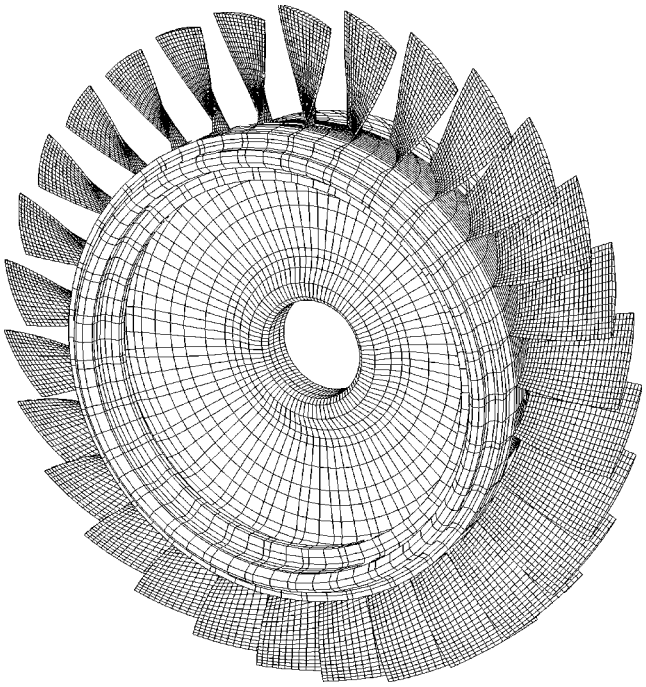

Fig. 1 Finite element mesh for an industrial rotor

In order to test the three proposed indicators, the FEM of an industrial rotor with 29 blades shown in Fig. 1 was used. (This rotor model was also studied in previous work by the authors [4,6].) Blade mistuning was implemented by varying Young's modulus in the finite elements of the blades, and 50 randomly mistuned systems were obtained. Each mistuned system was tested in two excitation frequency regions: 9–11 kHz and 26–29 kHz. The second flexural bending (2F) mode of a cantilevered blade is the dominant blade motion in 9–11 kHz, and the third flexural bending (3F) mode is dominant in 26–29 kHz. For external forcing, engine order excitations were considered by applying a unit force normal to the blade surface on one of the nodes at each blade tip. Engine order 1 and 3 were used for 9–11 kHz and 26–29 kHz, respectively. For each mistuned system and frequency region, a resonant frequency at which the largest Euclidean blade displacement norm occurs was identified. At that frequency, the response data for the 29 blades obtained from the FEA were collected. Thus, for each frequency region, 1450 sets of blade response data were obtained, and the Euclidean blade displacement norm, the amplitude of the 2F or 3F cantilevered-blade mode, and the peak blade strain energy during a period of oscillation were calculated for each data set. Also, the largest peak Von Mises stress in each blade during a period of oscillation was calculated using the complex stress state for the finite element centers obtained from the FEA. The results for the 2F and 3F regions are shown in Figs. 2 and 3, respectively.

In these figures, the "normalized largest stress" is defined as the ratio of the largest Von Mises stress of a blade in a mistuned system to that of a tuned, cantilevered blade. If the NSIs were to measure the normalized largest stress exactly, then all the data points should appear on the lines of unit slope in Figs. 2 and 3. However, as mentioned above, the disk-induced component of blade motion is not accounted for by the NSIs. Therefore, not all the data points fall on the lines, although they are located close to them. In Fig. 2, although all indicators underestimate the stress

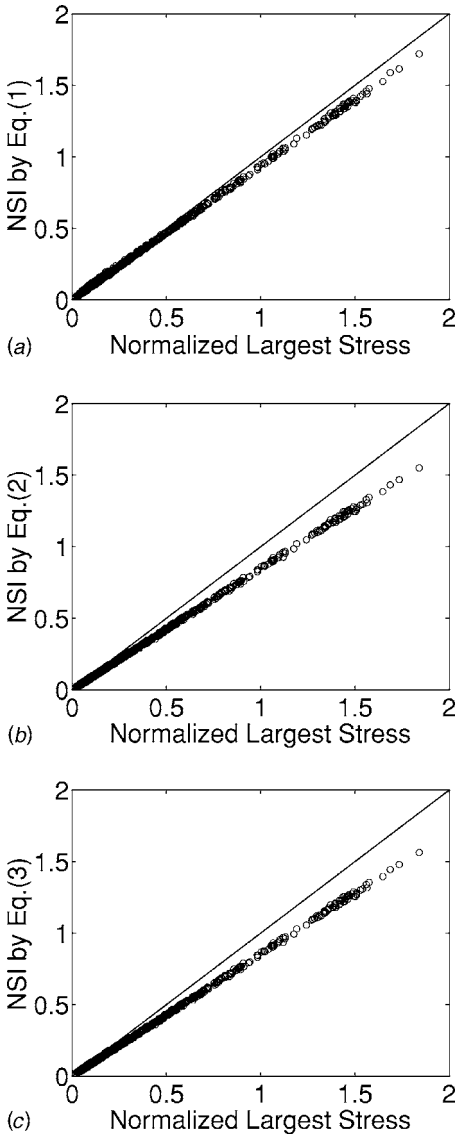

Fig. 2 Performance of normalized stress indicators in the 2nd flexural mode region; (*a*) using Euclidean norm, (*b*) using modal displacement, (*c*) using strain energy

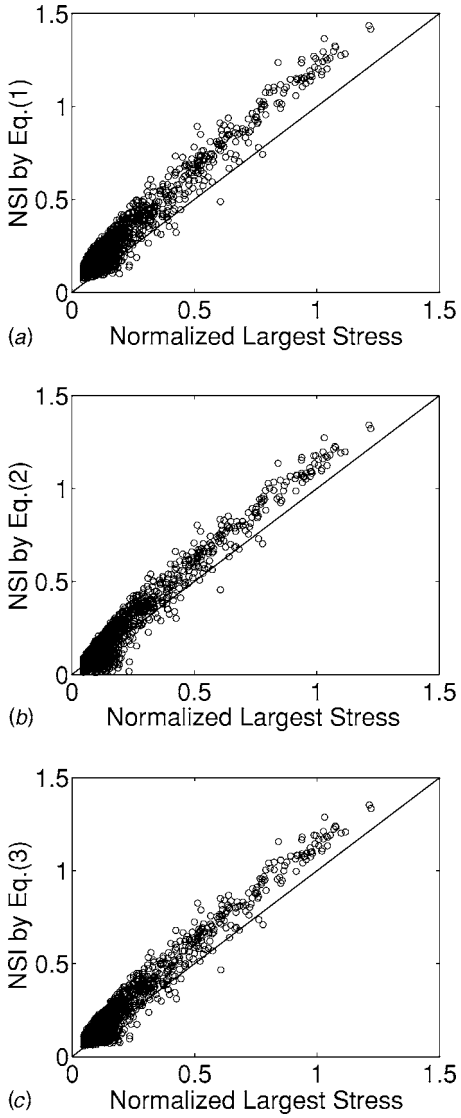

Fig. 3 Performance of normalized stress indicators in the 3rd flexural mode region; (*a*) using Euclidean norm, (*b*) using modal displacement, (*c*) using strain energy

level, the NSI based on the Euclidean norm is seen to be a better stress approximation than the other two indicators. This is because disk-induced elastic motion increases the stress level for the 2F mode region, and the rigid body motion also increases the level of the NSI using the Euclidean norm. The data points in Fig. 3 are considerably more scattered than in Fig. 2, especially for small NSI values, but the general trend is that the NSIs overestimate the blade stress level slightly. This means that disk-induced elastic motion generally tends to decrease the stress level in the 3F region. Hence, it can be seen that the results of the NSI based on the Euclidean norm are worse. Finally, Figs. 2 and 3 show that the NSIs based on modal displacement and on blade strain energy produce almost the same results, which means that the blade strain energy is determined mostly by the dominant cantilevered-blade mode.

All three of the proposed indicators show good agreement with the normalized largest Von Mises stress. However, it should be noted that the NSIs of Eqs. (1) and (3) require the recovery of all the physical blade displacements in finite element coordinates. In contrast, the NSI of Eq. (2) is based on modal displacements, and therefore it is the least expensive to obtain.

3 Estimation of Blade Stress Level

Now, suppose that the NSI value of a blade can be calculated and that the largest stress for the cantilevered-blade response is known. Then, the largest stress in the blade can be approximated as the product of the NSI value and the cantilevered-blade stress. In this section, two cases of blade stress estimation are studied using the same model as in the previous section. The mistuning values are those given in Table 2 in the authors' previous work [6] that was obtained by a random number generator. In the first case considered, a single cantilevered-blade mode is dominant over the frequency range of interest. In the second case, two blade-dominated mode families are so close that the dominant cantilevered-blade mode for each blade can be different and change throughout the investigated frequency region.

In order to calculate the NSI value, the dominant cantilevered-blade mode needs to be known. Usually, within a given blade-dominated mode family, blade motion is governed by a single cantilevered-blade mode. However, if more than one blade-dominated mode family is present in the motion of a mistuned system, the modal displacements of the corresponding cantilevered-blade modes need to be calculated for each blade at

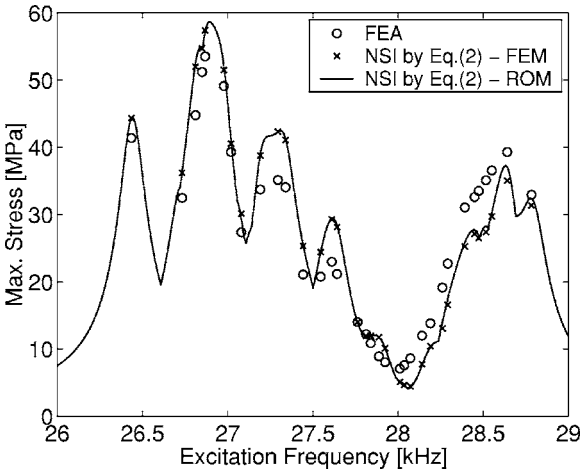

Fig. 4 Mistuned forced response in the frequency range 26–29 kHz, where the 7th cantilevered-blade mode is dominan

every frequency, in order to determine which mode is dominant. That is, even if the stress measures defined in Eqs. (1) or (3) are used, the modal displacements still need to be calculated. This encourages again the use of Eq. (2) as a stress indicator. Therefore, the estimation of blade stress in this study was performed using only the cantilevered-blade modal amplitude stress indicator, Eq. (2).

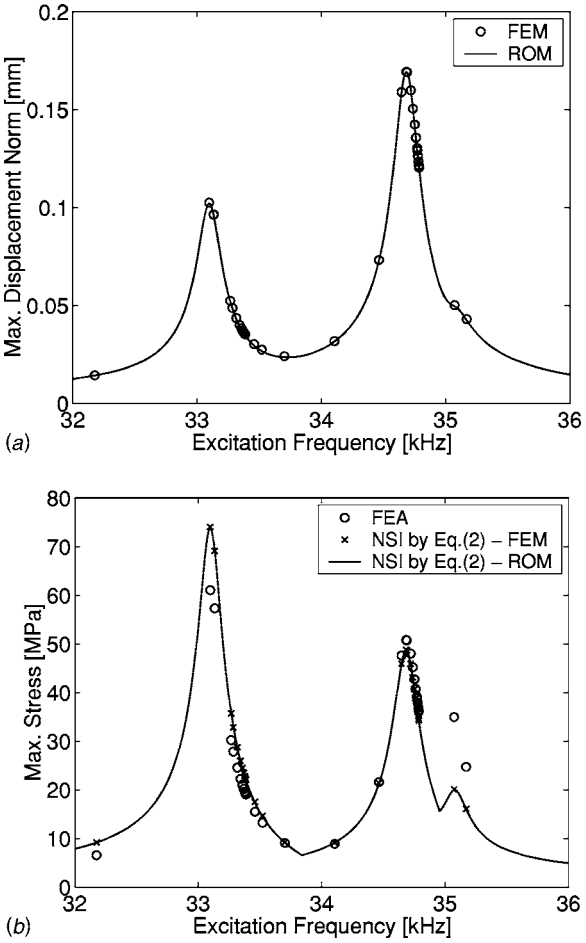

Fig. 5 Tuned forced response in the frequency range 32–36 kHz, where the 8th and 9th cantilevered-blade modes are dominant; (*a*) Euclidean displacement norm, (*b*) Von Mises stress

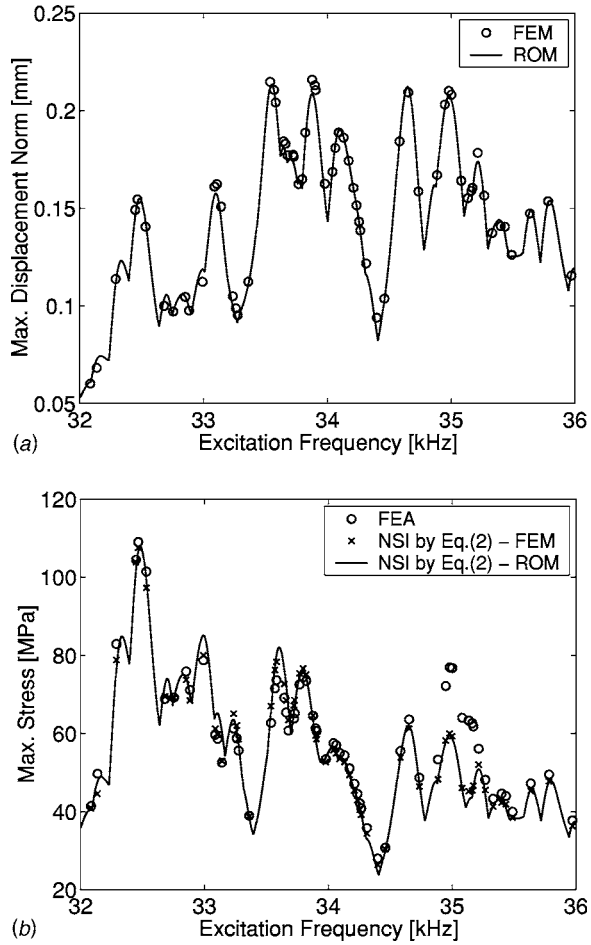

Fig. 6 Mistuned forced response in the frequency range 32–36 kHz, where the 8th and 9th cantilevered-blade modes are dominant; (*a*) Euclidean displacement norm, (*b*) Von Mises stress

The first case considered concerns the frequency range 26–29 kHz, in which, as mentioned earlier, the 3F blade mode is dominant. From the FEA, stresses and displacements were obtained by applying engine order 3 excitation. Since the FEA stress calculation is computationally expensive, it was performed only at the natural frequencies of the mistuned bladed disk, and the NSI values were calculated from Eq. (2) based on these FEA results. In addition, a 34-DOF ROM was built using the component mode mistuning method [6] and NSI values were again calculated, but this time based on the ROM results and at all excitation frequencies in the 26-29 kHz range. At each frequency, the largest Von Mises stresses for the 29 blades were calculated from the FEA results or estimated from the NSI values, and the largest value among all blades was taken, thus providing the maximum stress envelope in terms of frequency. Figure 4 compares the results from the FEA and those by the NSIs. It can be seen that the results obtained with the FEM-based NSI and by the ROM-based NSI match very well, and that they are in good agreement with the direct FEA stress calculation across the frequency range.

The second case features two close blade-dominated mode families in the 32–36 kHz range, dominated by the third torsion (3T) and the second stripe (2S) cantilevered-blade modes. For this frequency region, a larger ROM with 66 DOF was constructed, which included modes from both families. Engine order 5 excitation was applied. At every frequency, a dominant cantilevered-

blade mode was determined for each blade, and then the NSI value and the estimated stress were obtained according to this dominant mode. In addition, the Euclidean blade displacement norm was calculated for each blade via FEA or ROM, and the maximum norm among all blades was selected. The results obtained for the tuned bladed disk are shown in Fig. 5: the Euclidean blade displacement norm is depicted in Fig. 5(*a*) and the maximum stress in Fig. 5(*b*), in terms of the excitation frequency. Observe the three resonant peaks in the investigated frequency region, as shown in Fig. 5(*b*), although the smallest peak barely appears in Fig. 5(*a*). The motion of the bladed-disk assembly is dominated by the 3T blade mode at the first peak around 33.1 kHz, and by the 2S blade mode at the second peak around 34.7 kHz. However, at the third peak around 35.1 kHz, the motion is dominated by disk rather than blade motion, contrary to the other two peaks. Therefore, the third peak in Fig. 5(*a*) is small. Also, it is seen that the stress results obtained with the NSI do not approximate well the FEA stress calculation around the third peak, as shown in Fig. 5(*b*). This is because at the third peak the blade stress level is affected greatly by the disk-induced elastic motion. Also, comparing Figs. 5(*a*) and 5(*b*), observe that the trend of the displacement results is qualitatively different from that of the stress results. That is, although the 3T blade mode gives smaller maximum displacements than the 2S mode, the maximum stress for the 3T mode is higher than for the 2S mode.

Results were also obtained for the mistuned system, and they are depicted in Fig. 6. Note again that the trend of the displacement results is considerably different from that of the stress results. It can also be seen in Fig. 6(*b*) that the NSI results are in very good agreement with the FEA results, except around 35.1 kHz which corresponds to the third peak in Fig. 5(*b*). Since the tuned-system mode corresponding to the third peak features small blade motion, this mode is not altered as much by blade mistuning as the other blade-dominated modes. Therefore, even for the mistuned system, the motion corresponding to this mode occurs around 35.1 kHz.

4 Conclusions

Three normalized stress indicators were proposed as approximate measures of the largest blade stress level in a mistuned bladed disk. These stress measures were defined using the Euclidean blade displacement norm, the amplitude of a dominant cantilevered-blade mode, and the strain energy in a blade. All three can be calculated efficiently from results obtained with a reduced-order model, without having to resort to expensive finite element stress calculations for the mistuned bladed disk. The three NSIs were tested using the finite element model of an industrial rotor. All three indicators showed good accuracy relative to finite element results. However, the computational cost of the NSI based on the amplitude of a dominant cantilevered-blade mode is significantly lower than the other two, especially when more than one dominant blade mode is present in a frequency range.

It was demonstrated with a case study that, when more than one blade-dominated mode family is present in the frequency region of interest, blade displacement amplitudes can feature trends that are qualitatively different from those of stress levels. This suggests that using raw displacement results from reduced-order models can lead to erroneous predictions for stress. Instead, stress indicators, such as those proposed in this work, should be calculated to assess bladed disk designs.

Acknowledgment

This work was supported by the GUIde Consortium on blade durability.

References

[1] Castanier, M. P., Óttarsson, G., and Pierre, C., 1997, "A Reduced-Order Modeling Technique for Mistuned Bladed Disks," ASME J. Vibr. Acoust., **119**(3), pp. 439-447.

[2] Yang, M.-T., and Griffin, J. H., 1997, "A Reduced Order Approach for the Vibration of Mistuned Bladed Disk Assemblies," ASME J. Eng. Gas Turbines Power, **119**(1), pp. 161-167.

[3] Yang, M.-T., and Griffin, J. H., 2001, "A Reduced Order Model of Mistuning Using a Subset of Nominal System Modes," ASME J. Eng. Gas Turbines Power, **123**(4), pp. 893-900.

[4] Bladh, R., Castanier, M. P., Pierre, C., and Kruse, M. J., 2002, "Dynamic Response Predictions for a Mistuned Industrial Turbomachinery Rotor Using Reduced Order Modeling," ASME J. Eng. Gas Turbines Power, **124**(2), pp. 311-324.

[5] Petrov, E. P., Sanliturk, K. Y., and Ewins, D. J., 2002, "A New Method for Dynamic Analysis of Mistuned Bladed Disks Based on the Exact Relationship Between Tuned and Mistuned Systems," ASME J. Eng. Gas Turbines Power, **124**(3), pp. 586-597.

[6] Lim, S., Bladh, R., Castanier, M. P., and Pierre, C., 2003, "A Compact, Generalized Component Mode Mistuning Representation for Modeling Bladed Disk Vibration," AIAA Paper No. 2003-1545.

Journal of Turbomachinery

Erratum

Erratum: "Development and Experimental Validation of a Compressor Dynamic Model" [Journal of Turbomachinery, 2005, 127(3), pp. 599–608]

M. Venturini

The error is very severe and, in my opinion, negatively affects the quality of the whole paper, since it causes a misunderstanding of the technical content presented.

Thus, the following sentence on p. 604, second column, line 14 of the printed version:

… both taken at quasi-imaginary spin orbit (ISO) conditions …

should be changed into:

… both taken at quasi-ISO conditions …

In fact, the acronym ISO stands for "International Organization for Standardization", and not for "imaginary spin orbit". Since the acronym ISO is a standard for machine performance evaluation and is well known in the field of turbomachines and of energy systems, I suggest to only maintain the acronym ISO.

